The Dissertation Committee for Faruk Omer Alpak Certifies that this is the approved version of the following dissertation:

Algorithms for Numerical Modeling and Inversion of Multi-Phase Fluid-Flow and Electromagnetic Measurements

Committee:

Carlos Torres-Verdín, Supervisor

Kamy Sepehrnoori, Co-Supervisor

Larry W. Lake

Leon S. Lasdon

Tarek M. Habashy

Algorithms for Numerical Modeling and Inversion of Multi-Phase Fluid-Flow and Electromagnetic Measurements

by

Faruk Omer Alpak, B.S., M.S.

Dissertation

Presented to the Faculty of the Graduate School of

The University of Texas at Austin

in Partial Fulfillment

of the Requirements

for the Degree of

Doctor of Philosophy

The University of Texas at Austin

May, 2005

Dedication

To my mother Mine Emine Alpak, my father Osman Alpak, my grandmother Sıdıka Ruacan, and my grandfather Ferruh Ruacan with all my love and affection.

Acknowledgements

I would like to extend my sincerest gratitude to my supervisor Dr. Carlos Torres-Verdín and to my co-supervisor Kamy Sepehrnoori for their support, guidance, constructive criticism, and patience throughout my time at The University of Texas at Austin. I feel honored to have been their student. Likewise, I am immensely grateful to have had the honor to work with and to learn from Dr. Tarek M. Habashy and Dr. Elisabeth B. Dussan V. of Schlumberger-Doll Research. Furthermore, I would like to extend my sincerest appreciation to my committee members, Dr. Larry W. Lake and Dr. Leon S. Lasdon for taking the time to read and correct my dissertation. I am grateful for all the help I received from Dr. Vladimir L. Druskin, Dr. Leonid Knizhnerman, Hani Elshahawi, Dr. Aria Abubakar, Dr. Barbara Anderson, Dr. Sheng Fang, and Dr. Daniel Georgi. I would also like to thank to my friends Baris Guler, Emmanuel Toumelin, and Maika Gambus-Ordaz for their continuous help and support. Special thanks go to my life-partner Peggy Rijken for her infinite support and patience with me. I would like to sincerely thank to Kyle Graves and Trey Prinz of SGI, Margaret Valentine and Reynaldo Casanova of UT for allowing me to focus on my research work without the distraction of computer problems and bureaucracy.

I would like to extend my sincere gratitude and appreciation to Schlumberger-Doll Research and Shell International Exploration and Production for providing me with

the opportunity to extend my knowledge and experience through summer internships. I am also thankful to the donors and philanthropists for the fellowships and scholarships I have received during my stay at UT. I would also like to acknowledge Anadarko Petroleum Corporation, Baker Atlas, BP, ConocoPhillips, ExxonMobil, Halliburton, The Mexican Institute for Petroleum, Precision Energy Services, Schlumberger, Shell International Exploration and Production, Statoil, Occidental Petroleum, Petrobras, and TOTAL for funding of my work through The University of Texas at Austin's Joint Industry Research Consortium on Formation Evaluation.

Algorithms for Numerical Modeling and Inversion of Multi-Phase Fluid-Flow and Electromagnetic Measurements

Publication No._____

Faruk Omer Alpak, Ph.D.

The University of Texas at Austin, 2005

Supervisor: Carlos Torres-Verdín

Co-Supervisor: Kamy Sepehrnoori

The focus of this dissertation is the estimation of petrophysical properties of rock formations based on the combined use of electromagnetic and fluid-flow measurements. Traditionally, borehole electromagnetic measurements are interpreted independently in terms of spatial variations of electrical resistivity. The estimated spatial variations of electrical resistivity are subsequently interpreted in terms of variations of fluid saturation and porosity. Such a strategy can lead to erroneous conclusions concerning the petrophysical evaluation of rocks because the spatial distribution of electrical resistivity is often governed by the interplay between salt concentration, absolute permeability, relative permeability, and capillary pressure. To date, no consistent effort has been advanced to use the physics of multi-phase fluid flow as the leading phenomenon in the interpretation of borehole electromagnetic measurements.

This dissertation develops several efficient nonlinear inversion algorithms that quantitatively combine borehole electromagnetic and fluid-flow phenomena. These

inversion algorithms also provide a measure of uncertainty and non-uniqueness in the presence of noisy and imperfect measurements. The combined use of electromagnetic and fluid-flow measurements drastically reduces non-uniqueness and uncertainty of the estimated petrophysical parameters and, therefore, increases the accuracy of the estimates. Specific problems considered in this dissertation are the estimation of spatial distributions of porosity, permeability, and fluid saturation, as well as the estimation of relative permeability and capillary pressure.

Joint and independent nonlinear inversions are performed for large-scale petrophysical properties from in-situ permanent sensor data and near-borehole scale petrophysical variables of rock formations from wireline formation tester and electromagnetic induction logging measurements. For cases where fluid-flow related measurements are absent, the coupled dual-physics inversion strategy allows quantitative interpretation of electromagnetic measurements consistent with the physics of fluid flow.

It is conclusively shown that the simultaneous use of fluid-flow and electromagnetic data sets reduces non-uniqueness in the inverted petrophysical model.

Table of Contents

List of Tables

List of Figures

Chapter 1: Introduction

1.1 PROBLEM STATEMENT

This dissertation considers inverse problems that combine the fields of borehole geophysics, reservoir engineering, petrophysics, and formation evaluation. The specific problem of interest is the quantitative estimation of spatial distributions of absolute permeability, porosity, relative permeability, and capillary pressure from borehole geophysical measurements. In this dissertation, the term *borehole geophysical measurements* is used in a broad sense to include wireline formation tester, electromagnetic induction logging, acoustic logging, nuclear logging, and in-situ downhole permanent sensor measurements.

Although borehole geophysical measurements are sensitive to a wide variety of petrophysical parameters, the focus of this dissertation is restricted to fluid-flow and electromagnetic measurements. Aside from the data-type categorization based on measurement physics, another point of emphasis is the acquisition platform. In this dissertation, we work with fluid-flow and electromagnetic measurements acquired for two entirely different operations, namely, reservoir monitoring via permanent sensors and openhole logging for petrophysical reservoir evaluation. More specifically, from the viewpoint of acquisition platform, measurements of interest to this dissertation are acquired with (or simulated for) the following hardware: (1) arrays of in-situ permanent sensors of pressure and dc resistivity; (2) wireline formation testers and/or multi-frequency array induction imager tools. Despite the differences in governing physics, spatial resolution, time-scale, and volume of investigation of in-situ permanent sensors and openhole logging tools, the inverse problem of estimating petrophysical parameters from measurements acquired by these platforms can be cast as an optimization problem.

Therefore, a robust and efficient optimization framework taking advantage of accurate, robust, and rapid forward modeling algorithms can flexibly accommodate joint and/or independent inversions of fluid-flow and/or electromagnetic measurements acquired either by permanent sensors or openhole logging tools. Such is the strategy considered in this dissertation. For convenience, we make use of the term *borehole fluid-flow and electromagnetic measurements* to establish a common reference for measurements associated with the multi-physics inversion approach entertained in this dissertation.

1.2 MOTIVATION

Quantitative interpretation of measurements acquired with in-situ permanent sensors and openhole logging tools provide valuable information about petrophysical parameters of hydrocarbon reservoirs. From the reservoir management viewpoint, accurate determination of petrophysical parameters is important for the accurate evaluation of recoverable reserves and for performing accurate predictions of recovery. Admittedly, information provided by the inversion of measurements subject to this dissertation is at best at the near-wellbore to inter-well spatial scale. Nonetheless, accurately determined and focused, yet, spatially sparse petrophysical information is clearly more valuable than no information at all. In turn, inversion-rendered hard petrophysical parameters can potentially reduce the frequency of expensive rock-core measurements.

On the other hand, our approach to joint and independent inversion of multi-physics permanent sensor and borehole measurements ensures consistency in the petrophysical model from the fluid-flow physics viewpoint. This is achieved through inclusion of fluid-flow measurements in the set of inverted measurements, which implicitly constrains the petrophysical parameter domain to honor flow schedules, or more precisely, production/injection data.

The impact of integrated petrophysical inversion propagates to the process of history matching as well. In the absence of guidance of geostatistical penalty on the minimized cost function, automatic history matching process is guided by the measured data misfit that constitutes the cost function. Experience shows that, for such cases, the absence of geostatistical guidance or a-priori information causes near-wellbore permeabilities and porosities to dominate the outcome of history matching process. This is simply because of the rapidly diminishing sensitivity of production data with respect to near-wellbore permeabilities and porosities as a function of radial distance away from well locations. One can therefore conclude that the inclusion of dynamic, flow-based measurements early in the petrophysical evaluation of hydrocarbon reservoirs generates data that are consistent with the physics of fluid flow, hence leading to physically more consistent calibration of seismic data and geostatistical interpolation/extrapolation. In turn, the integration of petrophysical data has immense potential in improving initial reservoir models for automatic history matching.

1.2.1 In-Situ Permanent Pressure Sensor and DC Resistivity Electrode Measurements

In-situ permanent sensors allow the possibility of real-time monitoring of dynamic changes in formation properties due to primary or enhanced hydrocarbon recovery. Prototypes of in-situ permanent sensors include pressure gauges, dc resistivity electrodes, and seismic sensors. From the multi-physics data integration viewpoint, in-situ permanent sensors provide a wealth of information. In contrast to sensor development and deployment issues, advances reported in the interpretation of data acquired with in-situ permanent sensors have been scarce.

Oil-producing companies have shown increased interest in instrumenting their hydrocarbon fields with in-situ pressure sensors. Recent advances in smart well

completion technologies have enabled the dynamic acquisition of in-situ pressure measurements with sensors in direct hydraulic contact with rock formations. As opposed to standard bottom-hole permanent pressure gauges, in-situ pressure sensors are deployed behind casing to remain in direct hydraulic communication with rock formations. Prototype deployments have been tested in field operations that included intelligent completions. In-situ pressure sensors allow the possibility of monitoring real-time dynamic variations of reservoir conditions due to primary or enhanced recovery. In consequence, a feedback loop can be enforced to modify the production scheme in a way that optimizes the recovery of existing hydrocarbon assets. In addition to the immediate impact of in-situ sensors as tools for real-time, reactive reservoir management and control, the usage of in-situ pressure sensors has long-term benefits. Devising an optimal management strategy for hydrocarbon reservoirs requires more than a tool for instantaneous monitoring and control. Precise knowledge of the spatial distribution of petrophysical properties is essential for accurate reservoir delineation, management, and production forecasting. From the formation evaluation viewpoint, large volumes of flow-related data constitute an attractive prospect for robust and accurate characterization of reservoirs. In addition to static information in the form of geostatistical, seismic, and geologic data, usage of dynamic measurements remains imperative to construct accurate reservoir models amenable to production forecast. While a great deal of laboratory and field work has been undertaken to advance hardware prototypes, relatively little has been done to quantify the spatial resolution and reliability of in-situ permanent pressure data to detecting hydrocarbon reservoir properties. A literature review on the subject of in-situ permanent sensors is included in a subsequent section of this chapter.

1.2.2 Wireline Formation Tester and Electromagnetic Array Induction Logging Measurements

Common use of water-base muds in overbalanced drilling leads to water-base mud filtrate invasion in hydrocarbon-bearing formations. In addition, the salinity contrast between the in-situ and invading aqueous phases (water phase) leads to a salinity gradient in the near-borehole region. Signatures of water-base mud filtrate invasion are apparent on wireline formation tester transient-pressure and water-cut measurements as well as electromagnetic array induction imaging measurements. Wireline formation testers (see, for instance, Pop et al., 1993; Ayan et al., 2001) and electromagnetic array induction logging tools (see, for example, Hunka et al., 1990) are industry-standard platforms for conducting transient-pressure, water-cut, and electromagnetic measurements. The spatial extent of water-base mud-filtrate invasion is predominantly a complex nonlinear function of formation permeability, porosity, relative permeability, capillary pressure, invasion rate, invasion time, viscosity/density contrast, and mudcake properties. Sensitivity of above-listed measurement types to mud-filtrate invasion and presence of a-priori information about mudcake properties, invasion time, and invasion rate can potentially allow us to estimate petrophysical parameters, namely, permeability, porosity, and parametric forms of two-phase relative permeability and capillary pressure functions from wireline formation tester and electromagnetic array induction logging measurements jointly, and for some restrictive cases, perhaps even independently. Our vision for integrated petrophysical analysis stems from physics. In fact, the physics of multi-phase fluid-flow and electromagnetic-induction phenomena in porous media can be readily linked by means of an appropriate saturation equation. For the cases where a-priori information about the properties of the flowing fluids (i.e., viscosity, density, compressibility, etc.) are known, a coupled-physics approach for the quantitative

interpretation of geoelectrical measurements can be used to directly estimate a petrophysical model. Although single-physics quantitative interpretation/inversion of wireline formation tester data and array induction logging measurements is a mature discipline, their joint sensitivity with respect to the underlying petrophysical material properties of hydrocarbon reservoirs is a relatively unexplored area of research. A relevant literature review will be given in a subsequent section of this chapter.

1.2.3 Challenges for Multi-Physics Integrated Inversion of Borehole Fluid-Flow and Electromagnetic Measurements

Having established the motivations for integrated petrophysical inversion, let us focus our attention to the prevailing challenges:

(1) Development of an extensive understanding of sensitivities of measurements with respect to variable and non-variable parameters of the model is the foremost requirement for successful multi-physics inversion. Therefore, analysis of the joint sensitivity of borehole fluid-flow and electromagnetic measurements with respect to acquisition geometry, number of sensors, number of sampling locations, measurement noise level, etc. is as important as the evaluation of the joint sensitivity of borehole fluid-flow and electromagnetic measurements with respect to petrophysical model parameters.

(2) Development of reliable methods for the evaluation of uncertainties for models attained through nonlinear inversion. Perhaps, the most challenging aspect of inverse problems is the non-uniqueness of the solution. Due to the ill-posed nature of inverse problems, evaluation of the uncertainty in the inverted model emerges as an inherent requirement for rigor. A rigorous answer to the question "*What constitutes a good solution*

to the inverse problem (at hand)?" should involve not only the reconstructed model but also attached uncertainties of the parameters constituting the model. However, evaluation of the uncertainties for nonlinear inverse problems such as the ones investigated in this dissertation is not as straightforward as in the case of linear inverse problems.

(3) The spatial support of fluid-flow measurements differs from that of electromagnetic measurements. For the joint inversion of multi-physics data robust strategies are necessary to put various different types of measurements into equal footing by addressing the problem of resolution discrepancy among various types of measurements governed by different, yet, coupled physics.

(4) One of the central requirements for rigorous multi-physics inversion is the need for fast, robust, and accurate optimization platforms for joint and independent inversion of borehole fluid-flow and electromagnetic measurements. The rigorous incorporation of physical constraints on the inverted model parameters is a requirement for physically consistent inversions. On the other hand, evaluation of sensitivity coefficients for Newton-based optimization methods constitutes a bottleneck for the iterative nonlinear inversion computations. In order to integrate multi-physics inversion to the day-to-day engineering workflow, improvements are necessary in this area. For inverse problems with potential multiple local minima, Newton-based local optimization algorithms need to be hybridized with global optimization algorithms that incur minimum compromise of computational efficiency.

(5) Robust and accurate forward modeling of vast volumes of data is a demand put forth by rigorous inversion algorithms. The physics of in-situ permanent sensor transient-pressure and wireline formation tester fluid-flow measurements are both governed by multi-phase multi-component fluid flow in porous media. On the other hand, low frequency electromagnetics constitutes the underlying physics of in-situ electrode array and electromagnetic induction logging measurements. Precise modeling of fluid-flow in porous media and electromagnetic wave propagation require computationally demanding numerical algorithms based on finite-difference and/or finite-element discretizations. Achievement of an optimal balance between robust and accurate descriptions of the governing physics of various different types of measurements and physically-consistent approximations ensuring computational efficiency is a challenging subject for rigorous multi-physics inversion.

1.2 OBJECTIVES

One of the objectives of the work described in this dissertation is to develop a rigorous and efficient multi-physics modeling and optimization framework for the nonlinear joint modeling and inversion of borehole fluid-flow and electromagnetic measurements. Emphasis is placed on the development of improved optimization algorithms for inverse modeling. Accurate, robust, and rapid modeling algorithms are formulated, developed, and implemented within the multi-physics inversion framework. The effort is focused on measurements that originate from multi-phase multi-component fluid flow and from low- to induction-frequency electromagnetics. Our objective, however, extends beyond the computationally robust, accurate, and efficient modeling

and inversion framework. An additional objective is to put the multi-physics modeling and inversion framework to work. Our vision is to develop a physical understanding of joint sensitivities, resolution, and attending uncertainties of borehole fluid-flow and electromagnetic measurements and inverted petrophysical model parameters thereof.

1.3 LITERATURE REVIEW

The literature of multi-physics inversion techniques and applications for borehole geophysical measurements is scarce, in our viewpoint, owing to computational challenges stemming from both inverse and forward modeling as well as requirement of multi-disciplinary expertise. In the following sections, we present brief reviews of previous efforts relevant to the multi-physics inversion approach considered in this dissertation.

1.3.1 Review of the Inversion of In-Situ Permanent Pressure Sensor and DC Resistivity Electrode Array Measurements

The availability of permanently installed downhole pressure, resistivity, and temperature sensors has opened a new window of opportunities to probe hydrocarbon reservoirs. Permanent sensors and monitoring systems provide continuous streams of measurements that facilitate real-time reservoir management and, therefore, help to increase hydrocarbon recovery. The benefits of permanent downhole pressure gauges used as a part of the well completion have been reported in several publications, i.e., Baker et al. (1995) and Athichanagorn et al. (1999). Even more valuable data sets can be acquired with pressure gauges cemented behind casing in direct hydraulic communication with the formation. In-situ sensors of this type are placed in the annulus between the formation and the casing and hence remain exposed to the formation. Patents have been granted for cemented formation pressure sensors (Babour et al., 1995) and cemented resistivity arrays (Babour et al., 1997). Oilfield experiments have been conducted to test the practical feasibility and the added value of in-situ permanent sensors (see, for

instance, van Kleef et al., 2001; Bryant et al., 2002a and 2002b). In addition to sensor development and deployment issues, advances have also been attained in the interpretation of data acquired with in-situ permanent sensors.

In contrast to sensor development and deployment issues, advances reported in the interpretation of data acquired with in-situ permanent sensors have been scarce. Athichanagorn et al. (1999) describe a wavelet analysis technique for the interpretation of permanent downhole pressure measurements and discuss practical issues related to the processing of large amounts of data. Belani et al. (2000) describe the utilization of permanent pressure sensors to monitor pressure transients with repeated fall-off tests. In the latter development, a method is described to jointly interpret cemented pressure- and resistivity-sensor data into estimates of saturation, front location, and fluid mobility ratios. Raghuraman and Ramakrisnan (2001) also combined in-situ permanent resistivity array measurements with cemented pressure-sensor data to quantitatively constrain fracture thickness, fracture absolute fluid permeability, and fracture porosity within an actual reservoir. Charara et al. (2002) performed a numerical experiment to demonstrate the use of permanent resistivity and transient-pressure measurements for time-lapse saturation monitoring. Wang and Horne (2000) integrated permanent resistivity sensor and production data to improve the estimation of spatial distributions of absolute fluid permeability.

1.3.2 Review of the Integrated Petrophysical Inversion of Wireline Formation Tester and Electromagnetic Induction Logging Measurements

Robust and accurate determination of fluid-flow related petrophysical parameters from borehole measurements is one of the fundamental problems of quantitative geophysical interpretation. Geoelectrical measurements exhibit strong sensitivity to the spatial distributions of fluid saturation and salt concentration. Therefore, introduction of

concepts of fluid flow to the analysis of geoelectrical borehole measurements can significantly improve current interpretation algorithms based solely on the estimation of electrical resistivity.

Two-phase (or, occasionally, three-phase) multi-component displacement phenomenon, which takes place during mud-filtrate invasion, provides a basis for the quantitative petrophysical interpretation of electrical conductivity around the borehole. Tobola and Holditch (1991), and Yao and Holditch (1996) reported the successful use of time-lapse electromagnetic-induction log responses to estimate reservoir absolute permeability by means of a history matching method for the case of fresh mud-filtrate invading low-permeability gas reservoirs. Semmelbeck et al. (1995) also attempted to estimate absolute permeability for low-permeability gas sands from array induction measurements. Ramakrishnan and Wilkinson (1997 and 1999) developed a method for the estimation of fractional flow curves from conductivity profiles around the borehole using the physics of fluid flow. Epov et al. (2002) performed inversions of high-frequency electromagnetic logging measurements to yield resistivity and salt concentration profiles consistent with two-phase hydrodynamic analysis of mud-filtrate invasion.

1.4 OUTLINE OF CHAPTERS

This dissertation is organized in three parts: Part I, consisting of Chapters 2 through 4, deals with the physical and mathematical foundations, formulation, and numerical solution of forward and inverse modeling problems of interest. Part II, which comprises Chapters 5 through 7, is devoted to the single- and dual physics inversion of data acquired with in-situ permanent pressure and dc resistivity electrode arrays. Part III, which encompasses Chapters 8 through 10, focuses on the joint and independent

inversion of borehole fluid-flow and induction frequency electromagnetic logging measurements.

In Chapter 2, we summarize a general framework for the joint and independent inversion of multi-physics borehole geophysical measurements for reservoir evaluation and engineering. The inversion framework is designed for inverse problems where parameterization of the unknown model is possible. Formulation of the inversion framework takes the inversion framework of Habashy and Abubakar (2004) as a point of origin and is described in great detail in Appendix A. Within this context, we present an extensive review of Newton-based techniques for minimization as well as a survey of various approaches to determine the regularization parameter. We implement a novel, robust, and simple method for choosing this regularization parameter with the aid of a recently developed multiplicative regularization analysis (Habashy and Abubakar, 2004). Habashy and Abubakar's (2004) framework is further extended for enhancing the efficiency of inversion without compromising rigor and robustness. In this context, we develop and implement a novel cascade inversion technique (Torres-Verdín et al., 2000). The cascade inversion technique provides significant acceleration of the inversion process without resorting to oversimplification of the inverse problem structure. For inverse problems with potential multiple local minima, we formulate an efficient helper computational protocol that extends the Newton-based core of the algorithm to global optimization. By combining all the techniques mentioned above, we arrive at an effective and robust parametric inversion framework for borehole geophysical measurements. At this point it is worthwhile to point out that in the following chapters we make use of various different combinations of inversion techniques and features described under the general inversion framework of Chapter 2 and Appendix A. One exception to this rule is Appendix B, where we present a state-of-the-art inversion technique for inverse problems

of two-phase flow with a relatively large number of model parameters and where the sensitivity coefficients are computed using an adjoint method (Wu et al., 1999).

In Chapter 3, we develop and validate a novel numerical algorithm for the simulation of axisymmetric single-phase fluid flow phenomena in porous and permeable media. In this new algorithm, the two-dimensional parabolic partial differential equation of fluid flow is transformed into an explicit finite-difference operator problem. The latter is solved by making use of an Extended Krylov Subspace Method (EKSM) constructed with both positive and inverse powers of the finite-difference operator. A significant advantage of the method of solution presented in this work is that simulations of pressure can be obtained at a multitude of times with practically the same efficiency as that of a single-time simulation. Moreover, the usage of inverse powers of the finite-difference operator provides a substantial increase in efficiency with respect to that of standard Krylov subspace methods. Tests of numerical performance with respect to analytical solutions for point and line sources validate the accuracy of the developed method of solution. We also validate the algorithm by making comparisons between analytical and numerical solutions in the Laplace transform domain. Additional tests of accuracy and efficiency are performed against a commercial simulator for spatially complex and anisotropic models of permeable media. The work on rapid and accurate simulation of fluid-flow in porous and permeable media is also published in Alpak et al. (2003c). Numerical solution of dc electrical conduction phenomena in 2D axisymmetric media is accomplished by making use of a differential-difference approximation of the problem (Druskin and Knizhnerman, 1987). The numerical solution for the boundary value problem of electrostatics is implemented using a semi-discrete numerical approach that combines the method of straight lines with an incomplete Galerkin formulation.

Chapter 4 describes a dual-physics modeling algorithm for the simulation of multi-phase fluid-flow and electromagnetic measurements. The physics of fluid flow is linked to electromagnetics by means of a saturation equation. Efficient commercial as well as in-house simulation software are cast in the form of a coupled dual-physics modeling algorithm. This algorithm is also described in detail in Alpak et al. (2003b) and Alpak et al. (2004a).

In Chapter 5, we address the inverse problem of simultaneously estimating spatial distributions of absolute permeability and porosity from measurements of transient-pressure acquired with in-situ permanent sensors. We pose the inverse problem as the minimization of a quadratic cost function that quantifies the misfit between the measured and numerically simulated data. Weighted and Regularized Gauss-Newton (WRGN) nonlinear optimization technique is used to minimize the quadratic cost function subject to physical constraints. We also make use of a dual-grid cascade inversion technique that alternates the use of coarse and fine finite-difference grids to accelerate the inversion. Several examples of inversion are performed with noise-free and noisy synthetic measurements aimed at understanding the role played by the flow-rate function and the location, spacing, and number of permanent sensors into the accuracy and stability of the inverted spatial distributions of permeability. Following these proof-of-concept exercises of applicability, the inversion algorithm is used for the simultaneous estimation of spatial distributions of permeability and porosity. A dual-grid inversion technique is utilized for the quantitative interpretation of time-records of pressure acquired during an experimental field deployment of in-situ permanent sensors. The work presented in Chapter 5 has been published in Alpak et al. (2001) and in Alpak et al. (2004d).

A quantitative methodology is presented in Chapter 6 to jointly interpret in-situ transient-pressure and dc resistivity measurements acquired in a hypothetical water

injection experiment designed to displace movable oil in a hydrocarbon-bearing formation. Time-variable flow rates are enforced while injecting water into the surrounding rock formations, thereby producing a sequence of repeated transient-pressure pulses. The objective of the experiment is to estimate parametric spatial distributions of absolute fluid permeability and electrical resistivity. Geophysical inverse theory is used to approach the estimation problem in the presence of noisy measurements. Results shed new light to the independent and joint sensitivity of noisy in-situ transient-pressure and dc resistivity measurements to detecting dynamic spatial distributions of resistivity and absolute fluid permeability. Examples of inversion are also included to assess the relative benefits of different types of sensor deployments. The work presented in Chapter 6 has been published in Alpak et al. (2002) and in Alpak et al. (2004b).

In connection with the inter-well scale inversion work regarding in-situ permanent sensor transient-pressure measurements described in Chapters 5 and 6, in Appendix B, we develop and validate a novel inversion algorithm for reservoirs subject to multi-phase flow. The specific application presented in Appendix B deals with the quantitative estimation of three-dimensional (3D) spatial distributions of permeability and porosity from pressure measurements acquired with in-situ permanent sensors. Using the novel inversion algorithm of Appendix B we efficiently perform an assessment the value of pressure data acquired with in-situ permanent sensors in 3D heterogeneous reservoir models subject to two-phase fluid flow. In this study, a pilot waterflood operation conducted with a conventional five-spot pattern is chosen as example for our numerical experiments. We assume in-situ permanent pressure sensors to be an integral part of the production-well completion and remain completely isolated from the hydraulics of the wellbore. Therefore, these sensors perform uncorrupted measurements of in-situ formation fluid pressures. The quantitative estimation of spatial distributions of

permeability and porosity is approached with a novel subspace approach and a Weighted and Regularized Gauss-Newton (WRGN) inversion algorithm. This inversion strategy incorporates an adjoint formulation for the efficient computation of model sensitivities. In our inversions, the physics of two-phase fluid-flow in the 3D spatial domain is rigorously incorporated to the assessment of distributions of petrophysical properties from in-situ permanent-sensor pressure data. The work presented in Appendix B is documented in detail in Alpak et al. (2005b).

In Chapter 7, we develop a novel algorithm for the integrated petrophysical evaluation of hydrocarbon-bearing formations using dual-physics measurements. Specific data sets used in this work are (a) time-lapse electromagnetic induction logging measurements acquired with an array induction logging tool, and (b) transient-pressure measurements acquired with a multi-probe wireline formation tester in a vertical borehole. Dynamic behavior of saturation and salt concentration distributions due to mud-filtrate invasion creates a two-phase three-component flow system. In this work, the inverse problem associated with dual-physics wireline measurements consists of the estimation of a two-dimensional (2D) axisymmetric petrophysical model described by layered parametric spatial distribution of porosity and vertical and horizontal absolute permeabilities. We pose the inverse problem of estimating layer petrophysical parameters from discrete time-lapse electromagnetic induction and transient-pressure measurements as an optimization problem. A weighted least-squares constrained optimization method is employed to solve the inverse problem. Tool responses within the framework of the iterative inversion scheme are numerically computed via simulating the dynamic physics of two-phase three-component flow that takes place during mud-filtrate invasion and subsequent formation testing. Time-lapse electromagnetic induction measurements are simulated in coupled mode to fluid flow. A conductive annulus is observed in all cases.

The work presented in Chapter 7 has been published in Alpak et al. (2003b) and in Alpak et al. (2004a).

Chapter 8 deals with a variant of the integrated petrophysical inversion algorithm of Chapter 7. The algorithm presented in Chapter 7 is adapted to the petrophysical evaluation of hydrocarbon-bearing rock formations using only borehole electromagnetic-induction measurements in Chapter 8. The methodology is based on the time-dependent nature of fluid saturation and salt concentration distributions in the immediate neighborhood of the wellbore due to mud-filtrate invasion. A rigorous formulation is used to account for the physics of two-phase, three-component transport of mass in the near-borehole region due to mud-filtrate invading hydrocarbon-bearing rock formations. The inverse problem consists of estimating parametric one-dimensional distributions of fluid permeability and porosity. As by-product, the inversion algorithm yields two-dimensional distributions of aqueous phase saturation, salt concentration, and electrical resistivity. As in the case of the inverse problem of Chapter 7, the inverse problem of estimating layer-by-layer petrophysical parameters from single- or time-lapse electromagnetic-induction measurements is posed as an optimization problem. A weighted least-squares constrained optimization method is employed to solve the inverse problem. Tool responses required within the framework of the iterative inversion scheme are numerically computed by simulating the two-phase three-component flow that takes place during mud-filtrate invasion. In turn, electromagnetic-induction measurements are simulated in coupled mode with the physics of fluid flow. Numerical inversion experiments are conducted using both noise-contaminated synthetic data and field logs. The inversion requires of a-priori knowledge of mud, petrophysical, and fluid parameters. An extensive analysis is performed of the accuracy and reliability of the inversion when

a-priori knowledge of such parameters is uncertain. The work presented in Chapter 8 is also documented in detail in Alpak et al. (2005a).

Chapter 9 introduces an extended version of the inversion algorithm of Chapters 7 and 8 for a more comprehensive in-situ petrophysical evaluation of hydrocarbon-bearing formations. The algorithm simultaneously honors a set of multi-physics data: (a) Pressure-transient, flowline fractional flow, and salt production rate measurements as a function of time acquired with a wireline-conveyed, dual-packer formation tester, and (b) borehole array electromagnetic induction measurements. Both time evolution and spatial distribution of fluid saturation and salt concentration in the near-borehole region are constrained by the physics of mud-filtrate invasion. The inverse problem consists of the simultaneous estimation of a two-dimensional axisymmetric spatial distribution of absolute permeability and parametric saturation functions for relative permeability and capillary pressure curves. For a given layer, both horizontal and vertical permeabilities are subject to inversion. Saturation functions of relative permeability and capillary pressure are parametrically represented using a modified Brooks-Corey model.

We simulate numerically the response of borehole logging instruments by reproducing the multi-phase, multi-component flow that takes place during mud-filtrate invasion and formation testing. A fully implicit finite-difference black-oil reservoir simulator with a brine tracking extension is used to simulate fluid-flow phenomena. Electromagnetic-induction measurements are coupled to the physics of fluid flow using a rapid integro-differential algorithm. Inversion experiments consider both noise-free and noise-contaminated synthetic data. Joint inversion results provide a quantitative proof-of-concept for the simultaneous estimation of transversely anisotropic spatial distributions of permeability and saturation-dependent functions. The stability and reliability of the inversions are conditioned by the accuracy of the a-priori information about the spatial

distribution of formation porosity and fluid PVT properties. For cases where multi-physics measurements lack the degrees of freedom necessary to accurately estimate all the petrophysical model parameters, we develop an alternative sequential inversion technique. The first step involves estimation of horizontal and vertical permeabilities from late-time transient-pressure measurements. Subsequently, the entire set of measurements is jointly inverted to yield saturation-dependent functions. The work presented in Chapter 9 has been published in Alpak et al. (2004c).

Chapter 10 concludes this dissertation by summarizing the main results and suggesting directions for further research.

1.5 LIST OF PUBLICATIONS

In relation to the work presented in this dissertation, the following journal and conference papers has been published or submitted for review:

Alpak, F. O., Dussan V., E. B., Habashy, T. M. and Torres-Verdín, C. [2003a]. Numerical simulation of mud-filtrate invasion and sensitivity analysis of array induction tools. *Petrophysics* **44**(6): 396-411.

Alpak, F. O., Habashy, T. M., Torres-Verdín, C. and Dussan V., E. B. [2003b]. Joint inversion of pressure and time-lapse electromagnetic logging measurements. Paper SS, *Transactions of the 44th Annual Logging Symposium: Society of Well Log Analysts*, Galveston, Texas, June 22–25.

Alpak, F. O., Habashy, T. M., Torres-Verdín, C. and Dussan V., E. B. [2004a]. Joint inversion of transient-pressure and time-lapse electromagnetic logging measurements. *Petrophysics* **45**(3): 251-267.

Alpak, F. O., Torres-Verdín, C. and Habashy, T. M. [2004b]. Joint inversion of transient-pressure and dc resistivity measurements acquired with in-situ permanent sensors: a numerical study. *Geophysics* **69**(5): 1173-1191.

Alpak, F. O., Torres-Verdín, C. and Habashy, T. M. [2005b]. Petrophysical inversion of borehole electromagnetic-induction logging measurements. *Geophysics* (submitted for review).

Alpak, F. O., Torres-Verdín, C., Habashy, T. M. and Sepehrnoori, K. [2004c]. Simultaneous estimation of in-situ multi-phase petrophysical properties of rock

formations from wireline formation tester and induction logging measurements. Paper SPE 90960, *Proceedings of the Annual Technical Conference and Exhibition: Society of Petroleum Engineers*, Houston, Texas, 26–29 September.

Alpak, F. O., Torres-Verdín, C. and Sepehrnoori, K. [2001]. Numerical simulation and inversion of pressure data acquired with permanent sensors. Paper SPE 71612, *Proceedings of the Annual Technical Conference and Exhibition: Society of Petroleum Engineers*, New Orleans, Lousiana, 30 September–3 October.

Alpak, F. O., Torres-Verdín, C. and Sepehrnoori, K. [2004d]. Estimation of axisymmetric spatial distributions of permeability from pressure-transient data acquired with in-situ permanent sensors: a numerical study. *Journal of Petroleum Science and Engineering* **44**: 231-267.

Alpak, F. O., Torres-Verdín, C., Sepehrnoori, K. and Fang, S. [2002]. Numerical sensitivity studies for the joint inversion of pressure and dc resistivity measurements acquired with in-situ permanent sensors. Paper SPE 77621, *Proceedings of the Annual Technical Conference and Exhibition: Society of Petroleum Engineers*, San Antonio, Texas, 29 September–2 October.

Alpak, F. O., Torres-Verdín, C., Sepehrnoori, K., and Fang, S. [2003d] Numerical sensitivity studies for the joint inversion of pressure and dc resistivity measurements acquired with in-situ permanent sensors. *Journal of Petroleum Technology* **55**(2): 70-72.

Alpak, F. O., Torres-Verdín, C., Sepehrnoori, K., Fang, S. and Knizhnerman, L. [2003c]. An extended Krylov subspace method to simulate single-phase fluid flow phenomena in axisymmetric and anisotropic porous media. *Journal of Petroleum Science and Engineering* **40**: 121-144.

Alpak, F. O., Wu Z. and Torres-Verdín, C. [2005b]. A quantitative study to assess the value of pressure data acquired with in-situ permanent sensors in three-dimensional heterogeneous reservoir models subject to two-phase fluid flow. *SPE Journal* (submitted for review).

PART I: MATHEMATICAL FOUNDATIONS, FORMULATION, AND NUMERICAL SOLUTION OF INVERSE AND FORWARD MODELING PROBLEMS

Chapter 2: A General Framework for the Constrained Parametric Inversion of Borehole Geophysical Measurements

2.1 INTRODUCTION

In inverse problems of borehole geophysics, one aims to determine the shape, location, and material property parameters of a near-borehole object from various types of measurements acquired within the borehole. A great majority of borehole geophysical measurements (wireline formation tester, electromagnetic induction logging, acoustic logging, downhole permanent sensor, etc.) depend on the petrophysical properties of the rock formation (fluid saturation, permeability, porosity, etc.) in a nonlinear fashion. This behavior, in turn, renders the inverse parameter estimation problem nonlinear. For simple forward models mainly in one-dimensional cases, a forward solver can potentially generate a database containing a full collection of simulated measurement data for a number of possible realizations of the model parameters. One can then select a particular realization with the best fit to the actually measured data. In practice, the execution of such an exhaustive search method is often impossible due to the large number of discrete unknown variables. Improvements of these Monte Carlo methods [see, for instance, Tarantola (1987)] are obtained when certain probability is taken into account as in the case of simulated annealing (Metropolis et al., 1953; Kirkpatrick et al., 1983; Geman and Geman, 1984; Černy, 1985) and genetic algorithms (Goldberg, 1989). The attractive feature of these inversion schemes is the pure simplicity and the feature that the algorithm will not trap in a local minimum. However, the major disadvantage is the prohibitively

large number of forward solutions to be generated and stored, especially, in the case of multi-dimensional forward models.

In this dissertation, we make use of an iterative approach where the model parameters are updated iteratively by a minimization of the misfit between the measured data and the predicted data. For this purpose, we make use of an L_2-norm based cost functional. Since the updates of the model parameters are determined from the misfit, in order to avoid the local minima of the nonlinear problem, one has to be precautious in handling the ill-posed nature of the inverse problem. In the case of borehole geophysical measurements, characteristically, the number of available measurement data is limited. Measurements are acquired only from a finite number of source-receiver positions leading to limited data diversity. In order to arrive at a reliable solution, parameterization of the model domain is required. Examples of parametric inversion of electromagnetic induction logging measurements can be found in Freedman and Minerbo (1991), Zhang et al. (1993), Gao (2002), Wang et al. (2003), and Barber et al. (2004). On the other hand, a certainly non-exhaustive list of example inversion algorithms for wireline formation tester measurements is as follows: Kuchuk et al. (1994), Onur and Kuchuk (1999), Ayan et al. (2001), Onur and Reynolds (2002), and Jackson et al. (2003). For the joint inversion of multi-physics measurements, a parametric inversion approach is essential to compensate for the resolution and volume of investigation mismatch between diverse types of measurements. In addition, subsequent to parameterization, the number of unknown model parameters is rendered manageable. In other words, the parameterization of the model domain leads to a non-underdetermined system. Enhanced convergence properties of the Newton-based algorithms justify their widespread use in parametric inversion applications in comparison to gradient-based algorithms.

2.2 THE COST FUNCTIONAL

We define the vector of residuals $\mathbf{e}(\mathbf{x})$ as a vector whose j^{th} element is the residual error (also referred to as the data mismatch) of the j^{th} measurement. The residual error is defined as the difference between the measured and the predicted normalized responses given by

$$\mathbf{e}(\mathbf{x}) = \begin{bmatrix} e_1(\mathbf{x}) \\ \vdots \\ e_M(\mathbf{x}) \end{bmatrix} = \begin{bmatrix} S_1(\mathbf{x}) - m_1 \\ \vdots \\ S_M(\mathbf{x}) - m_M \end{bmatrix} = \mathbf{S}(\mathbf{x}) - \mathbf{m}, \tag{2.1}$$

where M is the number of measurements. In equation (2.1), m_j is the normalized observed response (measured data) and S_j is corresponding to the normalized simulated response as predicted by the vector of model parameters, $\mathbf{x}$, given by

$$\mathbf{x} = \begin{bmatrix} x_1 \\ \vdots \\ x_N \end{bmatrix} = \mathbf{y} - \mathbf{y}_R, \tag{2.2}$$

where N is the number of unknowns. In the next section, we discuss various methods of normalizing the simulated and measured responses. We represent the vector of model parameters $\mathbf{x}$ as the difference between the vector of the actual model parameters $\mathbf{y}$ and a reference model (or background model) $\mathbf{y}_R$. The reference model includes all a-priori information on the model parameters such as those derived from independent measurements. We pose the inversion as the minimization of the following cost (or objective) functional, $C(\mathbf{x})$, of the form (Oldenburg, 1990)

$$C(\mathbf{x}) = \frac{1}{2}\left[\mu \left\{ \left\| \mathbf{W}_d \cdot \mathbf{e}(\mathbf{x}) \right\|^2 - \chi^2 \right\} + \left\| \mathbf{W}_x \cdot (\mathbf{x} - \mathbf{x}_p) \right\|^2 \right]. \tag{2.3}$$

The scalar factor μ $(0 < \mu < \infty)$ is a Lagrange multiplier (also called regularization parameter or damping coefficient). It is a trade-off parameter determining the relative importance of the two terms of the cost functional. The determination of μ will produce an estimate of the model $\mathbf{x}$ that has a finite minimum weighted norm (away from a prescribed model $\mathbf{x}_p$) and which globally misfits the data to within a prescribed value χ (determined from a-priori estimates of noise in the data). The second term of the cost functional is included to regularize the optimization problem. It safeguards against cases when measurements are redundant or lacking sensitivity to certain model parameters causing non-uniqueness of solution. It also suppresses any possible magnification of errors in our parameter estimations due to noise which is unavoidably present in the measurements. These error magnifications may result in undesirable large variations in the model parameters which may cause instabilities in the inversion. In equation (2.3), $\mathbf{W}_x^T \mathbf{W}_x$ is the inverse of the model covariance matrix representing the degree of confidence in the prescribed model $\mathbf{x}_p$. On the other hand, $\mathbf{W}_d^T \mathbf{W}_d$ is the inverse of the data covariance matrix, which describes the estimated uncertainties (due to noise contamination) in the available data set. It describes not only the estimated variance for each particular data point, but also the estimated correlation between errors. It therefore provides a point by point weighting of the input data according to a prescribed criterion (hence, can be used to reduce the effect of outliers in the data). If the measurement noise is stationary and uncorrelated, then $\mathbf{W}_d = diag\left\{\sigma_j\right\}$ where σ_j is the root-mean-square deviation (standard deviation) of the noise for the j^{th} measurement. The relationship

between the Bayesian inference approach and the minimization method posed above will also be pointed out in this work.

2.3 THE CONSTRAINED MINIMIZATION APPROACH

In order to impose a-priori information, such as positivity or physical maximum and minimum bounds (if available) on the inverted model parameters, **x**, we make use of nonlinear transforms such that

$$x_i = f(c_i, x_i^{\min}, x_i^{\max}), \quad -\infty < c_i < \infty, \quad i = 1, 2, \ldots, N. \tag{2.4}$$

In equation (2.4), $x_i^{\max}$ and $x_i^{\min}$ denote the upper and lower physical bounds on the model parameter x_i, respectively. These nonlinear transformations map a constrained minimization problem to an unconstrained one. Note that the above constraints will force the reconstruction of the model parameters to remain always within their physical bounds.

Self-evidently, there is an infinite number of nonlinear transformations $f(c_i, x_i^{\min}, x_i^{\max})$ that map a constrained minimization problem into an unconstrained one. Among the many we experimented with, three transformations, that were identified to perform the best, are presented in this work.

2.4 NORMALIZATION OF THE VECTOR OF RESIDUALS

In our implementation, we employ two possible forms of the cost functional of equation (2.3) that puts the various measurements on equal footings. The two forms differ in the way we define the vector of residuals **e**(**x**). In the first form we define **e**(**x**) as follows:

$$e_j(\mathbf{x}) = \frac{S_j(\mathbf{x})}{m_j} - 1, \tag{2.5}$$

and hence

$$\left\|\mathbf{e}(\mathbf{x})\right\|^2 = \sum_{j=1}^{M} \left| \frac{S_j(x)}{m_j} - 1 \right|^2 . \tag{2.6}$$

In the second form we define

$$e_j(\mathbf{x}) = \frac{S_j(\mathbf{x}) - m_j}{\left\|\mathbf{m}\right\| / M}, \tag{2.7}$$

and hence

$$\left\|\mathbf{e}(\mathbf{x})\right\|^2 = \frac{\sum_{j=1}^{M} \left| S_j(\mathbf{x}) - m_j \right|^2}{\left(\sum_{j=1}^{M} \left| m_j \right|^2 \right) \Big/ M^2}. \tag{2.8}$$

2.5 SUMMARY

For the implementation of the dual-physics inversion algorithm, we make use of a Weighted and Regularized Gauss-Newton (`WRGN`) least-squares optimization method that enforces data weights, model regularization, and model constraints. `WRGN` method is implemented to minimize the cost functional described by equation (2.3). A significant advantage of the `WRGN` method over alternative gradient-based minimizations methods such as Conjugate Gradient, Quasi-Newton, and Steepest Descent, is its nearly-quadratic

rate of convergence. This enhancement in the rate of convergence is possible because of the utilization of the Jacobian, or sensitivity matrix [see, for example, Nocedal and Wright (1999)] in computing the search direction. The inverted model parameters are constrained to be within their physical bounds using nonlinear transformations (Habashy and Abubakar, 2004). Such nonlinear transformations map a constrained minimization problem into an unconstrained one. A backtracking line search algorithm is used along the descent direction to guarantee a reduction of the cost functional from one iteration step to the next. The choice of the Lagrange multiplier is adaptively linked to the condition number of the Hessian matrix of the `WRGN` method. The weight of the misfit term in the cost functional is progressively increased with respect to the regularization term as the inversion algorithm iterates towards the optimum and non-uniqueness in the inversion reduces. In this fashion, the stability property of the solution obtained at each iteration level is enhanced without overbiasing the final solution to the stabilizing regularization term. Evaluation of the Hessian matrix is the most computationally intensive part of the inversion. Four alternative approximate update methods for the Hessian matrix which eliminate expensive computations are employed to accelerate the inversions. Explored approximation schemes are: Broyden symmetric rank-one, Powell-Symmetric-Broyden (`PSB`) rank-two, Davidson-Fletcher-Powell (`DFP`) rank-two, and Broyden-Fletcher-Goldfarb-Shanno (`BFGS`) rank-two update methods (Gill et al., 1981).

In addition to the above-listed algorithmic enhancements, we also developed a solution to the nonlinear inverse problem via a cascade sequence of auxiliary least-squares minimizations. The auxiliary minimizations are nonlinear inverse problems themselves, except that they are implemented with an approximate forward problem that is computationally more efficient to solve than the algorithm used to simulate the measurements. Any given auxiliary minimization in the cascade is fully self-contained

and yields a solution of the unknown model parameters. This solution, in turn, is used to perform a numerical simulation of the data to quantify its agreement with the input measurements. If the difference between the measured data and the simulated data is above the estimated noise threshold, it is input as data to the subsequent auxiliary inverse problem in the cascade. Otherwise, the inversion is brought to a successful completion. We describe the theory and operating conditions under which the cascade inversion technique converges to a solution equivalent to that of a single inversion implemented with the original forward problem. Depending on the choice of approximate forward problem and regardless of the optimization algorithm employed to solve the inverse problem, the cascade sequence of auxiliary minimizations can be made computationally more efficient than a single inversion performed with the original forward problem. In this dissertation, we consider a practical and flexible way to construct the approximate forward problem by using subset of the finite-difference grid used to simulate the measurements numerically, i.e., a dual-grid construction technique.

Finally, we hybridized the Weighted and Regularized Gauss-Newton (WRGN) method with an efficient stochastic global optimization algorithm, namely, Simultaneous Perturbation Stochastic Approximation (SPSA) method. The global optimization algorithm is used as a helper method to address the local minimum trapping problem associated with the Gauss-Newton based local optimization algorithms. Although global helper methods introduce additional computational burden to the inversion process, for inverse problems with potential multiple local minima, their added benefits crucial from the viewpoint of robustness.

Algorithmic improvements are implemented in a modular fashion such that arbitrary combinations of the described techniques can be utilized depending upon the

inversion strategy of the user. Details of our nonlinear inversion framework are described extensively in Appendix A.

Chapter 3: Rapid and Accurate Two-Dimensional Algorithms for Modeling Permanent Pressure and Electrode Array Responses

In this chapter, we focus on the mathematical modeling issues associated with permanent sensor arrays. Special focus of the presented work is permanent pressure sensor and dc resistivity electrode arrays. Accurate, robust, and fast algorithms are developed and validated in this chapter. The motivation behind the developments described in this work is the need for speed without the compromise of accuracy for nonlinear inversion. The central underlying assumption of the developed mathematical models is the two-dimensional axisymmetric spatial domain. In turn, permanent sensor arrays are assumed to be deployed in a vertical borehole.

3.1 An Extended Krylov Subspace Method to Simulate Single-Phase Fluid Flow Phenomena in Axisymmetric and Anisotropic Porous Media

For a long time now, analytical solutions have been developed to describe single-phase fluid flow phenomena in porous and permeable media. Analytical methods have also been applied to layered, laterally and radially composite systems. Recently, finite-difference, finite-element, and boundary integral methods have been successfully used to simulate single-phase fluid flow phenomena in the presence of complex and spatially heterogeneous media. Accuracy of the solution is of significant relevance for pulse and interference testing where the pressure is accurately measured with new-generation quartz gauges. Likewise, computational speed becomes of great importance for the inversion of pressure transient-flow rate measurements into spatial variations of permeability and porosity. Although three-dimensional (3D) numerical algorithms are available (Peaceman, 1977; Aziz and Settari, 1979; Knizhnerman et al., 1994), they are usually computationally prohibitive and, therefore, inefficient for history matching. Quite

often, a two-dimensional (2D) model represents a good compromise between computational efficiency and geometrical complexity for history matching of geometrically complex petrophysical models.

In this chapter we develop a novel forward modeling algorithm for single-phase fluid flow in 2D axisymmetric and anisotropic porous media. The algorithm is based on the use of an Extended Krylov Subspace Method (EKSM) introduced here for the first time to solve the pressure equation of single-phase fluid flow. The first implementation of the Lanczos method was reported by Lanczos (1950) in the context of numerical solutions to general linear algebraic systems. Initially, the Lanczos method was applied for solving linear systems (Paige and Saunders, 1975; Parlett, 1980; van der Vorst, 1987), and then for solving one-dimensional (1D) structural analysis and heat conduction problems (Nour-Omid and Clough, 1984; Nour-Omid, 1987) as well as multi-dimensional parabolic equations (Knizhnerman et al., 1994). Druskin and Knizhnerman (1988, 1989, 1991, 1994a, 1994b) developed a general numerical formalism to evaluate explicit matrix functionals by using a variant of the Lanczos method. Allers et al. (1994) used the Lanczos decomposition method for simulating subsurface electrical conduction phenomena. Druskin and Knizhnerman (1994b) also described an explicit 3D solver for the diffusion of electromagnetic fields in arbitrarily heterogeneous conductive media based on a global Krylov subspace (Lanczos) approximation. Dunbar and Woodbury (1989) implemented a Lanczos algorithm for solving linear systems that occur in groundwater flow problems whereas Knizhnerman et al. (1994) developed a 3D well model for the simulation of single-phase fluid flow in porous media.

The EKSM takes advantage of Krylov subspaces spanned by $\mathbf{A}^{-1}$, where $\mathbf{A}$ is a real and symmetric finite-difference operator arising from the spatial discretization of certain linear partial differential equations (PDEs). Druskin and Knizhnerman (1998)

reported a significant reduction in computation time and in the number of iterations via the EKSM compared to a conventional Spectral Lanczos Decomposition Method (SLDM) for a two and a half-dimensional (2.5D) elliptical problem.

With the motivation to construct a new, more efficient, and more accurate numerical algorithm, we develop and validate a new 2D axisymmetric solution for the numerical simulation of single-phase fluid flow in porous media. This is achieved by transforming the 2D parabolic PDE for fluid flow into a finite-difference operator problem that is defined as $\mathbf{u} = f(\mathbf{A}) \cdot \boldsymbol{\sigma}$, where $\mathbf{A}$ is a real and symmetric square matrix and $\mathbf{u}$ and $\boldsymbol{\sigma}$ are vectors. The solution for $\mathbf{u}$ is then pursued with an EKSM algorithm.

Quantitative interpretation of pressure transient data requires efficient simulations of large volumes of measurements. Moreover, pressure behavior in complex spatial distributions of formation properties cannot be simulated with traditional analytical approaches. The EKSM algorithm entails an accurate and efficient numerical solution for the simulation of single-phase fluid flow phenomena in 2D axisymmetric permeable media. Therefore, EKSM can be employed as the forward algorithm for iterative nonlinear inversion schemes to yield fluid flow parameters, such as permeability and porosity, from pressure transient measurements (Alpak et al., 2001; Alpak et al., 2004d).

3.2 SINGLE-PHASE FLUID FLOW MODELING USING EKSM

3.2.1 Physics of Single-Phase Fluid Flow in Permeable Media

We consider the single-phase flow of a Newtonian fluid in a rigid permeable medium occupying a domain $\Omega \subset R^3$ with a smooth and closed boundary, $\partial\Omega$. The continuity equation associated with the slightly compressible flow of a single-phase fluid can be obtained by applying conservation of mass over a representative control volume (Muskat, 1937), i.e.,

$$-\nabla \cdot \left[\rho(\mathbf{r},t)\mathbf{v}(\mathbf{r},t)\right] = \phi(\mathbf{r})\frac{\partial \rho(\mathbf{r},t)}{\partial t}, \tag{3.1}$$

where ρ is mass density, $\mathbf{v}$ is fluid velocity, ϕ is the time-invariant porosity distribution, $\mathbf{r}$ is a point in R^3, and t is time. According to Darcy's law, the constitutive equation for fluid velocity can be written as

$$\mathbf{v}(\mathbf{r},t) = -\frac{\overline{\overline{\mathbf{k}}}(\mathbf{r})}{\mu} \cdot \nabla p(\mathbf{r},t), \tag{3.2}$$

where p is pressure, μ is fluid viscosity, and $\overline{\overline{\mathbf{k}}}(\mathbf{r})$ is the second-order permeability tensor. For single-phase flow of a slightly compressible fluid with a constant compressibility, C_t, the pressure equation shown in equation (3.1) takes the form

$$\nabla \cdot \left[\overline{\overline{\mathbf{T}}}(\mathbf{r}) \cdot \nabla p(\mathbf{r},t)\right] = \phi(\mathbf{r}) C_t \frac{\partial p(\mathbf{r},t)}{\partial t}. \tag{3.3}$$

In the above formulation, we assume a fluid-independent permeability tensor, and tacitly neglect second-order terms by assuming small compressibility and pressure gradients. Also, $\overline{\overline{\mathbf{T}}}(\mathbf{r}) = \overline{\overline{\mathbf{k}}}(\mathbf{r})/\mu$ is commonly referred to as the mobility tensor. Both $\overline{\overline{\mathbf{T}}}(\mathbf{r})$ and $\phi(\mathbf{r})$ vary spatially and are assumed to be independent of pressure and time. Figure 3.1 is a graphical description of the spatial domain of the problem pursued in this work. It consists of open and closed sections of a vertical wellbore surrounded by porous and permeable rock formations.

We assume an initial condition for the time-dependent pressure field of the form

$$p(\mathbf{r},0) = 0 \text{ at } t = 0. \tag{3.4}$$

Along the open section of the wellbore, $\partial\Omega_1$, we prescribe a total volumetric flow rate, q_{sf}, as source condition given by

$$-\int_{\partial\Omega_1} T_r(\mathbf{r}) \frac{\partial p(\mathbf{r},t)}{\partial r}\, d\omega = q_{sf}(t) \text{ on } \partial\Omega_1 \text{ for } t > 0. \tag{3.5}$$

On the other hand, for the no-flow boundaries, $\partial\Omega_2$ (i.e., for the no-flow section of the wellbore and for the sealing upper, lower, and external limits of the formation), we assume

$$\frac{\partial p(\mathbf{r},t)}{\partial r} = 0 \text{ on } \partial\Omega_2 \text{ for } t > 0, \tag{3.6}$$

where $\bigcup_{i=1}^{2} \partial\Omega_i = \partial\Omega$, $\mathbf{r} : r = r_w$, $l_1 < z < l_2$, l_1 and l_2 are the vertical bounds of the open wellbore interval, and r_w is the radius of the internal cylindrical boundary of the wellbore. In equation (3.5) the radial mobility, T_r, is defined as

$$T_r(\mathbf{r}) = \frac{k_r(\mathbf{r})}{\mu}. \tag{3.7}$$

The prescribed internal boundary conditions in equations (3.5) and (3.6) over the cylindrical wellbore define a mixed boundary value problem. Also, we assume that the pressure (potential) along the open surface of the cylinder, $\partial\Omega_1$, is uniform, independent of r and z, and exclusively a function of time, i.e.,

$$p(r_w,t) = p_w(r_w,t) \text{ on } \partial\Omega_1 \text{ for } t > 0. \tag{3.8}$$

The no-flow boundary condition described in equation (3.6) equally applies to the closed exterior boundary of the reservoir.

3.2.2 Solution of the Pressure Diffusion Equation in Cylindrical Coordinates

A Green's function representation of the problem described above can be used to derive a canonical time-domain solution. Accordingly, the PDE satisfied by the Green's function and its associated initial and boundary conditions are given by

$$\nabla \cdot \left[\overline{\overline{\mathbf{T}}}(\mathbf{r}) \cdot \nabla G(\mathbf{r},t) \right] = \phi(\mathbf{r}) C_t \frac{\partial G(\mathbf{r},t)}{\partial t}, \tag{3.9}$$

$$G(\mathbf{r},t) = 0 \text{ at } t = 0, \tag{3.10}$$

$$-\int_{\partial\Omega_1} T_r(\mathbf{r}) \frac{\partial G(\mathbf{r},t)}{\partial r} \, d\omega = \delta(t) \text{ on } \partial\Omega_1 \text{ for } t > 0, \tag{3.11}$$

$$\frac{\partial G(\mathbf{r},t)}{\partial r} = 0 \text{ on } \partial\Omega_2 \text{ for } t > 0, \text{ and} \tag{3.12}$$

$$G(r_w,t) = G_w(r_w,t) \text{ on } \partial\Omega_1 \text{ for } t > 0. \tag{3.13}$$

Conceptually, the Green's function defined above corresponds to the pressure field due to a time-domain impulse of flow rate. For the problem at hand, we consider permeability anisotropy in the form of a diagonal tensor with the functions $k_r(\mathbf{r})$, $k_\theta(\mathbf{r})$, and $k_z(\mathbf{r})$ derived from principal permeabilities in the x, y, and z directions. Accordingly, as the permeabilities in the principal directions are given in Cartesian

coordinates, the coordinate transformation will yield $k_r(\mathbf{r})$, $k_\theta(\mathbf{r})$, and $k_z(\mathbf{r})$ such that $\overline{\overline{\mathbf{k}}}(\mathbf{r}) = \text{diag}\left[k_r(\mathbf{r})\ k_\theta(\mathbf{r})\ k_z(\mathbf{r})\right]$ and $\overline{\overline{\mathbf{T}}}(\mathbf{r}) = \overline{\overline{\mathbf{k}}}(\mathbf{r})/\mu$.

The initial and boundary value problem introduced earlier can be readily converted into a functional operator problem. To this end, we first remark that the asymptotic solution of the Green's function in equation (3.9) can be written as

$$G(\mathbf{r}) \approx G_1(\mathbf{r}) = \frac{\delta(r - r_w)H(z - l_1)H(l_2 - z)}{2\pi\ r_w(l_2 - l_1)C_t\phi(\mathbf{r})} \text{ as } t \to 0,\ \mathbf{r} \in \partial\Omega_1, \tag{3.14}$$

where H is Heaviside's step function (Knizhnerman et al., 1994). Therefore, the boundary and initial conditions associated with the canonical Green's function can be equivalently written as

$$-\int_{\partial\Omega_1} \frac{\partial G(\mathbf{r},t)}{\partial r}\, d\omega = 0 \text{ on } \partial\Omega_1 \text{ for } t > 0, \tag{3.15}$$

$$\frac{\partial G(\mathbf{r},t)}{\partial r} = 0 \text{ on } \partial\Omega_2 \text{ for } t > 0, \tag{3.16}$$

$$G(r_w,t) = G_w(r_w,t) \text{ on } \partial\Omega_1 \text{ for } t > 0, \tag{3.17}$$

$$G(\mathbf{r},0) = G_1(\mathbf{r}) \text{ at } t = 0. \tag{3.18}$$

As shown next, a fictitious domain can be introduced that allows one to define a corresponding spatial functional operator of the PDE implicitly as a product of another vector (Knizhnerman et al., 1994).

We describe Ω to be the spatial domain spanning $\mathbf{r}$, and $\overline{\Omega}_1$ and $\overline{\Omega}_2$ to be the fictitious outer domains, where, as indicated in Figure 3.1, the entire spatial domain of the problem can be defined as $\overline{\Omega} = \Omega \cup \overline{\Omega}_1 \cup \overline{\Omega}_2$ with $\partial\Omega \cap \partial\overline{\Omega}_1 = \partial\Omega_1$, and $\partial\Omega \cap \partial\overline{\Omega}_2 = \partial\Omega_2$. Therefore, one can write

$$\overline{\overline{\mathbf{T}}}(\mathbf{r}) = 0 \text{ for } \mathbf{r} \in \overline{\Omega}_2, \text{ and} \tag{3.19}$$

$$G_w(r_w, t) = G(\mathbf{r}, t)\,|_{r=r_w} = \frac{\int_{\partial\Omega_1} \overline{\overline{\mathbf{T}}}(\mathbf{r}) G(\mathbf{r}, t)\, d\Omega}{\int_{\partial\Omega_1} \overline{\overline{\mathbf{T}}}(\mathbf{r})\, d\Omega} \text{ for } \mathbf{r} \in \overline{\Omega}_1. \tag{3.20}$$

Consequently, the problem given by equation (3.9) and its boundary Ω can be defined as an equivalent PDE in $\overline{\Omega}$ subject to the boundary conditions given by equations (3.19) and (3.20). In equation (3.9), $G(\mathbf{r}, t)$ and the coefficients of the functional operator of the PDE shall be treated as arbitrary smooth functions when they are not defined by the conditions described in equations (3.19) and (3.20). We define $\bar{u}(\mathbf{r}, t)$ as the continuation of $u(\mathbf{r}, t)$, i.e.,

$$\bar{u}(\mathbf{r}, t) = u(\mathbf{r}, t) \text{ for } \mathbf{r} \in \Omega. \tag{3.21}$$

Attention is now focused on a hypothetical test case in which water is injected (or produced) from a vertical well into (or from) the surrounding rock formations. The specific geometrical model considered in this work is illustrated in Figure 3.2. For simplicity, but without sacrifice of generality, we assume that the permeability and porosity fields exhibit azimuthal symmetry around the axis of the injection well. Accordingly, we consider a 2D axisymmetric cylindrical coordinate system $(r - z)$

allowing permeability anisotropy in the form of a diagonal tensor with the functions $k_r(\mathbf{r})$ and $k_z(\mathbf{r})$. In this 2D cylindrical coordinate frame, the PDE satisfied by the Green's function is given by

$$\frac{1}{r}\frac{\partial}{\partial r}\left[rT_r\frac{\partial G(r,z,t)}{\partial r}\right]+\frac{\partial}{\partial z}\left[T_z\frac{\partial G(r,z,t)}{\partial z}\right]=\left[\phi(r,z)C_t\right]\frac{\partial G(r,z,t)}{\partial t}. \tag{3.22}$$

Making the change of variable

$$u(r,z,t)=(r\phi(r,z)C_t)^{1/2}G(r,z,t), \tag{3.23}$$

leads to

$$-A\left[u(r,z,t)\right]=\frac{\partial u(r,z,t)}{\partial t},\ \text{for}\ (r,z)\in\Omega, \tag{3.24}$$

where A is a functional operator defined as

$$A\left[u(r,z,t)\right]=-\left(r\phi(r,z)C_t\right)^{-1/2}\left[\frac{\partial}{\partial r}(rT_r)\frac{\partial}{\partial r}+\frac{\partial}{\partial z}(rT_z)\frac{\partial}{\partial z}\right]\left(r\phi(r,z)C_t\right)^{-1/2}u(r,z,t). \tag{3.25}$$

It can easily be shown that the functional operator A above is self-adjoint and nonnegative. Moreover, the change of variables introduced by equation (3.23) gives rise to the initial condition

$$\sigma=u(r,z,0)=\left(r\phi(r,z)C_t\right)^{1/2}G(r,z,0). \tag{3.26}$$

Using equation (3.14), the asymptotic solution of equation (3.26) can be expressed as

$$\sigma(r,z) \approx \left(r\phi(r,z)C_t\right)^{1/2} \frac{\delta(r-r_w)H(z-l_1)H(l_2-z)}{2\pi\, r_w(l_2-l_1)\phi(r,z)C_t} \text{ as } t \to 0. \tag{3.27}$$

The explicit solution to equation (3.24) is then given by

$$u(r,z,t) = \exp(-t\,A)\,\sigma(r,z)\,. \tag{3.28}$$

In order to solve numerically for $u(r,z,t)$, we approximate the functional operator A above by finite differences using a standard 5-point second-order stencil on a 2D axisymmetric spatial grid spanning the semiplane $(r > 0,\ z)$ (Aziz and Settari, 1979). In doing so, we render equation (3.28) discrete in space yet continuous in time. As a result of the spatial discretization, the functional operator A in equation (3.28) can be restated as a finite-difference operator in the form of a square symmetric nonnegative matrix $\mathbf{A}$ of dimension $L = (N-2)\times(M-2)$ where N and M are the number of grid points in the radial and the vertical directions, respectively. In turn, we transform equation (3.28) into a finite-difference operator problem described by

$$u(r,z,t) = \exp(-t\,\mathbf{A})\,\sigma(r,z)\,. \tag{3.29}$$

3.2.3 The EKSM for Computing $\exp(-t\,\mathbf{A})\,\sigma(r,z)$

The computation of $u(r,z,t)$ via equation (3.29) requires the evaluation of matrix $\mathbf{A}$ and its subsequent exponentiation, $\exp(-t\mathbf{A})$, for every possible value of t. This

computation can be performed in principle if one solves the eigenvalue problem for matrix $\mathbf{A}$. After solving this eigenvalue problem, one could solve for the vector $u(r,z,t)$ for as many values of t as needed without significant additional computations. We also remark that by having solved the eigenvalue problem for matrix $\mathbf{A}$ one could solve for vector $u(r,z,t)$ in response to several values of vector $\sigma(r,z)$ without an appreciable increase in computer operations. Each vector $\sigma(r,z)$ corresponds to the specific fluid source location in the (r,z) plane. For stationary fluid sources, one does not need to modify the vectors $\sigma(r,z)$.

Although obtaining a solution of vector $u(r,z,t)$ via a solution of the eigenvalue problem of matrix $\mathbf{A}$ provides valuable insight to the problem, a numerical solution implemented in this way would be impractical because of the often large size of matrix $\mathbf{A}$. Instead, to solve this problem we make use of the EKSM developed by Druskin and Knizhnerman (1998). With the EKSM, the vector $u(r,z,t)$ in equation (3.29) can be explicitly written as

$$u(r,z,t) \approx u_{k,m}(r,z,t) = \left\| \sigma(r,z) \right\| \mathbf{W} \exp(\mathbf{R}) e_1^{(k+m-1)}, \tag{3.30}$$

where $e_1 = (1, 0, \ldots, 0)^T$ is the unit vector of size $(k+m-1)$ and $\mathbf{W} = (q_1, \ldots, q_k, v_1, \ldots, v_{m-1})$ is an $n \times (k+m-1)$ matrix, i.e., $\mathbf{W}^T\mathbf{W} = \mathbf{I}$. Also, the Ritz matrix, $\mathbf{R}$, in augmented form can be written as

$$\mathbf{R} = \begin{bmatrix} \mathbf{G} & \mathbf{D} \\ \mathbf{D}^T & \mathbf{T} \end{bmatrix}, \tag{3.31}$$

where $\mathbf{G}$ is full matrix of size $k \times k$, i.e.,

$$\mathbf{G} = \mathbf{H}^{-1} + [r^T \mathbf{A}\, r]\,[\mathbf{H}^{-1} e_k]\,[\mathbf{H}^{-1} e_k]^T, \tag{3.32}$$

$\mathbf{T}$ is a $(m-1)\times(m-1)$ tridiagonal matrix given by

$$\mathbf{T} = \begin{pmatrix} a_1 & b_1 & & & 0 \\ b_1 & a_2 & b_2 & & \\ & . & . & . & \\ & & . & . & b_{m-2} \\ 0 & & & b_{m-2} & a_{m-1} \end{pmatrix}, \tag{3.33}$$

and $\mathbf{D}$ denotes a $(m-1)\times k$ rank 1 matrix with only the first nonzero column given by

$$\mathbf{D} = [b_0^{(1)}, \ldots, b_0^{(k)}]^T [e_1^{m-1}]^T. \tag{3.34}$$

Entries of matrices $\mathbf{W}$, $\mathbf{G}$, $\mathbf{T}$, $\mathbf{D}$, and $\mathbf{H}$ will be introduced in conjunction with the EKSM recurrence. First, let us introduce an extended Krylov subspace given by

$$\kappa^{k,m}(\mathbf{A},\sigma) = span\left\{ \mathbf{A}^{-k+1}\sigma, \ldots, \mathbf{A}^{-1}\sigma, \sigma, \ldots, \mathbf{A}^{m-1}\sigma \right\}, \tag{3.35}$$

where,

$$m \geq 1, \quad k \geq 1, \text{ and } \dim(\kappa^{k,m}) \leq (k+m-1). \tag{3.36}$$

In fact, $\kappa^{k,m}(\mathbf{A},\sigma) = \kappa^{k+m-1}(\mathbf{A}, \mathbf{A}^{-k+1}\sigma)$ is equivalent to a conventional Krylov subspace spanned with a different starting vector, $\mathbf{A}^{-k+1}\sigma$. The key concept of the EKSM is "extending" κ^m with inverse powers of $\mathbf{A}$. Druskin and Knizhnerman (1998) coined the

term "extended Krylov subspace" when developing a robust procedure to compute an orthonormal basis of $\kappa^{k,m}(\mathbf{A},\sigma)$ to solve the corresponding Ritz problem. In this work, we make use of an extended Krylov subspace method that employs both positive and inverse powers of $\mathbf{A}$ within the Lanczos procedure to evaluate the matrix exponential in equation (3.29). Extensive numerical experiments consistently showed superior computational efficiency for the extended Krylov subspace formulation over the use of only positive powers of $\mathbf{A}$. The inclusion of both positive and inverse powers of $\mathbf{A}$ provides a significant acceleration of convergence in comparison to the usage of only positive powers of $\mathbf{A}$. This behavior is due to both the nature of the matrix exponential in equation (3.29) and the choice of a cylindrical system of coordinates for the discretization of equation (3.29).

The EKSM recurrence starts with an economical scheme to compute an orthonormal basis of $\kappa^{k,m}(\mathbf{A},\sigma)$. Accordingly, the first k steps of the Lanczos recurrence are performed with $\mathbf{B}=\mathbf{A}^{-1}$ and σ. In this recurrence, an $n\times k$ matrix of Lanczos vectors, $\mathbf{Q}=\left(q_1,\ldots,q_k\right)$ is constructed together with a $k\times k$ tridiagonal symmetric Ritz matrix,

$$\mathbf{H}=\begin{pmatrix} \alpha_1 & \beta_1 & & & 0 \\ \beta_1 & \alpha_2 & \beta_2 & & \\ & . & . & . & \\ & & . & . & \beta_{k-1} \\ 0 & & & \beta_{k-1} & \alpha_k \end{pmatrix}. \tag{3.37}$$

The relationship between **Q** and **H** is given by Parlett (1980) as

$$\mathbf{BQ}-\mathbf{QH}=r\,[e^{(k)}]^T,\quad \mathbf{Q}^T\mathbf{Q}=\mathbf{I},\quad r=\beta_k q_{k+1}. \tag{3.38}$$

The vector v_1 is obtained from the formula

$$b_0^{(1)} v_1 = \mathbf{A}\, q_1 - \sum_{i=1}^{k} c_i q_i, \tag{3.39}$$

where the coefficients c_i are selected to make v_1 orthogonal to q_i, $i = 1, \ldots, k,$ and $b_0^{(1)} > 0$ is determined by the condition $\| v_1 \| = 1.$ The vector v_2 is computed in an analogous fashion via

$$b_1 v_2 = \mathbf{A}\, v_1 - a_1 v_1 - \sum_{i=1}^{k} b_0^{(i)} q_i, \tag{3.40}$$

where the coefficients $b_0^{(i)}$ and a_1 are selected to make v_2 orthogonal to q_i, $i = 1, \ldots, k,$ and v_1, respectively.

We employ computationally more convenient forms of equations (3.39) and (3.40) derived by Druskin and Knizhnerman (1998). An equivalent form for equation (3.39) can be obtained as

$$b_0^{(1)} v_1 = -e_k^T \mathbf{H}^{-1} e_1 \left\{ \mathbf{A}\, r + r^T \mathbf{A}\, r\, \mathbf{Q}\mathbf{H}^{-1} e_k \right\}, \tag{3.41}$$

and subsequently via

$$b_0^{(i)} = \frac{b_0^{(1)}}{e_k^T \mathbf{H}^{-1} e_1} e_k^T \mathbf{H}^{-1} e_i, \qquad i = 2, \ldots, k, \tag{3.42}$$

thus yielding an equivalent form for equation (3.40) given by

$$b_1 v_2 = \mathbf{A}\, v_1 - a_1 v_1 - \frac{b_0^{(1)}}{e_k^T \mathbf{H}^{-1} e_1} \mathbf{Q}\mathbf{H}^{-1} e_k , \tag{3.43}$$

where one can show that

$$b_0^{(1)} = -[e_k^T \mathbf{H}^{-1} e_1][v_1^T \mathbf{A}\, r]. \tag{3.44}$$

The vector $\mathbf{Q}\mathbf{H}^{-1} e_k$ appears both in equations (3.41) and (3.43). We make use of an effective conjugate gradient (CG) type recursive scheme to compute this vector without having to store all of the entries of matrix $\mathbf{Q}$.

Once an orthonormal basis of the form $(q_1, \ldots, q_k, v_1, \ldots, v_i)$ for $\kappa^{k,\, i+1}$, $i \geq 2$, has been constructed, the corresponding three-term Gram-Schmidt recurrence necessary to construct the orthonormal basis for $\kappa^{k,m}$ is obtained from

$$b_i v_{i+1} = \mathbf{A}\, v_i - a_i v_i - b_{i-1} v_{i-1}, \qquad 2 \leq i \leq m-1. \tag{3.45}$$

Subsequently, matrices $\mathbf{R}$, $\mathbf{G}$, $\mathbf{T}$, and $\mathbf{D}$ are computed from equations (3.31), (3.32), (3.33), and (3.34), respectively. The final solution $u_{k,m}(r, z, t)$ can then be computed via equation (3.30). In summary, the step-by-step implementation of the `EKSM` outlined above is as follows:

1. Enter k and m.
2. Compute k steps of the Lanczos procedure using $\mathbf{A}^{-1}$ and σ.
3. Compute $\mathbf{Q}$, $\mathbf{H}$, and r.
4. Compute $r^T \mathbf{A}\, r$.
5. Invert $\mathbf{H}$.

6. Compute $\mathbf{QH}^{-1}e_k$.
7. Compute $b_0^{(1)}$ and v_1 via equation (3.41) and normalize.
8. Compute $b_0^{(2)}, \ldots, b_0^{(k)}$ via equation (3.42).
9. Compute v_2, a_1, and b_1 via equation (3.43) and normalize.
10. Perform the recurrence in equation (3.45) and compute **T**.
11. Compute **G** and **D**.
12. Compute **R**.
13. Compute $u_{k,m}(r,z,t) = \| \sigma(r,z) \| \mathbf{W} \exp(\mathbf{R}) e_1^{(k+m-1)}$.

Once $u(r,z,t)$ is computed via the EKSM, substitution from equation (3.23) yields the corresponding Green's function $G(r,z,t)$.

Druskin and Knizhnerman (1998) report a behavior of the EKSM similar to that of the SLDM as characterized by the loss of orthogonality of **W**. They conclude that, as in the case of the SLDM, the loss of orthogonality of **W** in the Lanczos recurrence is not detrimental to the convergence of the EKSM results. This means that the error bounds are still satisfied within the desired accuracy in the presence of computer roundoff. Details of convergence properties of the EKSM are extensively discussed by Druskin and Knizhnerman (1998).

3.2.4 Computation of pressure

For practical problems, the boundary condition at the open section of the wellbore is commonly time-dependent as described by equation (3.5). Hence, subsequent to obtaining a solution for the Green's function, pressure due to an arbitrary time-domain flow rate function can be computed by means of the convolution operation

$$p(r,z,t) = p_o - \int_{-\infty}^{t} q_{sf}(\tau)\left[G(r,z,t-\tau) + \delta(t-\tau)\Delta p_{skin}\right] d\tau, \qquad (3.46a)$$

where Δp_{skin} represents the pressure drop due to the presence of skin factor, p_o indicates the initial formation pressure, and q_{sf} is the flow rate on the open section of the well (see Figures 3.1 and 3.2).

The EKSM algorithm can also be used to compute wellbore pressure. For this application, we may have a considerable borehole volume below the flow-rate measurement point in the wellbore. Conventionally, the flow rate is not measured at the sandface but rather at the wellhead. With the wellbore storage effect, the pressure solution given by equation (3.46a) can be modified to yield wellbore pressure as follows:

$$p(r,z,t) = p_o - \int_{-\infty}^{t} \left[q_m(\tau) + C\frac{dp_w}{d\tau} \right] \left[G(r,z,t-\tau) + \delta(t-\tau)\Delta p_{skin} \right] d\tau \,, \qquad (3.46b)$$

where p_w stands for the wellbore pressure and C describes the wellbore storage coefficient.

The matrix exponential formulation for the pressure impulse response (Green's function) shown in equation (3.29) provides an efficient way to compute the Laplace transform of the Green's function, namely,

$$U(r,z,s) = \left[s\mathbf{I} + \mathbf{A} \right]^{-1} \sigma(r,z), \qquad (3.47)$$

where s is the Laplace-transform variable. Thus, the EKSM formulation provides added flexibility for obtaining efficient solutions both in time and Laplace domains. In a similar fashion, a numerical solution for the pressure derivative with respect to time can be obtained directly from equation (3.29) with practically no additional computer overhead.

3.3 VALIDATION OF THE EKSM ALGORITHM

Both accuracy and performance of the EKSM algorithm described above are tested using a number of example cases exhibiting various degrees of geometrical complexity. The EKSM results are compared to analytical solutions for simple cases and to results obtained with the commercial simulator, ECLIPSE 100™ (GeoQuest, 2000), for relatively more complex flow geometries. In these comparisons, we compute the absolute percent error of the EKSM pressure simulations with respect to the simulations performed with either analytical solutions or ECLIPSE 100™. The numerical finite-difference grid used in the EKSM algorithm is refined until the simulation results converge to an acceptable level of accuracy. This level of accuracy is quantified in terms of the maximum absolute percent error. We target an accuracy level of 1% for relatively simple flow systems. The accuracy level is relaxed to 4% maximum absolute percent error for comparisons performed in relatively more complex flow systems, such as in the case of anisotropic layers that exhibit interlayer crossflow.

3.3.1 Pressure Response of a Point Source of Flow Rate in an Unbounded Homogeneous and Isotropic Medium

We simulate the pressure impulse response of the simple 2D radial homogeneous and isotropic unbounded reservoir depicted in Figure 3.3(a). The reservoir is constructed with large geometrical dimensions to match, in an asymptotic fashion, the equivalent response of an unbounded medium. Figure 3.3(a) illustrates the fluid injection source and its associated flow paths. The injection source is assumed to be a cylindrical point source and is constructed numerically with an infinitesimal cylindrical ring around the wellbore. Reservoir and fluid parameters associated with the simulations are detailed in Table 3.1. As the result of an extensive gridding study, we determine that a grid of size $r \times z \equiv 105 \times 286$ (see Figure 3.3(b)) provides acceptable accuracy in the EKSM

simulations. For simplicity, we assume that $\Delta p = p_o - p = 0$ at $t = 0$. EKSM simulation results are compared against solutions computed with an analytical formulation describing the pressure response of a point source in unbounded media (Raghavan, 1993), namely,

$$p(r,t) = q \frac{\exp\left(-\dfrac{r^2}{4kt/(\phi\mu C_t)} \right)}{8\,\pi^{3/2}\left[kt/(\phi\mu C_t)\right]^{3/2}}. \tag{3.48}$$

Figure 3.3(c) shows comparisons of the pressure change computed at a location in close proximity to the wellbore within the reservoir. Solutions are computed for a number of permeability values. The agreement between the EKSM and the analytical solution is very good. Differences between the two solutions are consistently below 1%.

3.3.2 Pressure Response of a Line Source of Flow Rate in an Unbounded Homogeneous and Isotropic Medium

The model for this test case is similar to the one described in the previous section except for the nature of the fluid injection source, considered here to be an infinite line. An infinite line source is numerically constructed by way of tightly spaced infinitesimal cylindrical sources exhibiting uniform flow rates and covering the open section of the well into the reservoir (Figures 3.1 and 3.4(a)). For the simulation, we make use of a finite-difference grid of size $r \times z \equiv 249 \times 126$. This grid is shown in Figure 3.4(b). We compare EKSM pressure impulse responses computed at two radial locations against the corresponding analytical expression of pressure given by Raghavan (1993),

$$p(r,t) = q\frac{\exp\left(-\dfrac{r^2}{4kt/(\phi\mu C_t)}\right)}{\left[4\pi kt/(\phi\mu C_t)\right]}. \tag{3.49}$$

Figure 3.4(c) shows the simulation results superimposed on the analytical solutions computed for two remote sensing locations: one in close proximity to the wellbore and the other relatively deeper into the reservoir. The agreement between the EKSM results and analytical solutions is remarkable. For the simulation times of interest, errors are consistently below 1%.

3.3.3 Commingled Layered Reservoir Model

Figure 3.5(a) describes a multilayer commingled reservoir with no-flow boundary conditions imposed on its external boundaries. A no-crossflow condition is imposed among the homogeneous and isotropic layers. We numerically model the injection flow rate by way of a truncated-line source equivalent to a fully penetrated well. Pressure response at the wellbore is computed using the EKSM. These results are compared against the analytical solution derived in the Laplace transform domain by Kuchuk and Wilkinson (1991), namely,

$$\Delta\bar{p}_w(s) = \frac{q_{inj}}{\left[2\pi s^{3/2}\sum_{i=1}^{3}\dfrac{\alpha_i\beta_i K_1(\alpha_i\sqrt{s})}{K_0(\alpha_i\sqrt{s}) + S_i\alpha_i\sqrt{s}K_1(\alpha_i\sqrt{s})}\right]}, \tag{3.50}$$

where

$$\Delta\bar{p}_w(s) = \frac{p_o}{s} - p_w(s),\ \ \beta_i = \frac{(kh)_i}{\mu_i},\quad \eta_i = \frac{k_i}{(\phi\,\mu\,C_t)_i},\quad \text{and } \alpha_i = \frac{(r_w)_i}{\sqrt{\eta_i}}. \tag{3.51}$$

For simplicity, in the simulations we assume $S_i = 0,$ where $i = 1, 2, \ldots, n$ and $(r_w)_1 = (r_w)_2 = \ldots = (r_w)_n$. A summary of the simulation parameters is given in Table 3.1. Figure 3.5(b) shows the $r \times z \equiv 117 \times 281$ nodes of the finite-difference grid used to compute the EKSM results. As displayed in Figure 3.5(c), the agreement between the EKSM and the analytical results is quite good. Relative errors are smaller than 1% except for the very early times. At very early times, the truncated line source underestimates the results of the analytical expression. This behavior can be attributed to the discrete numerical implementation of an otherwise physically continuous truncated line source.

3.3.4 Pressure Fall-Off Analysis in Injection Wells

In this section we undertake the simulation of pressure responses for several complex models of subsurface distributions of axisymmetric permeability. The central objective of these simulations is to validate the EKSM algorithm as well as to develop an understanding of the sensitivity of some reservoir parameters to pressure distributions imposed by an injection well. Benchmark comparisons are carried out against the widely used commercial simulator ECLIPSE 100™. We consider a simulation example resulting from the schedule of pressure fall-off subsequent to a 135 hr long constant downhole injection rate of 79.79 m^3/d (step-function excitation). Fluid injection is modeled using a truncated line source representing the response of a fully penetrated well across the formation of interest. The simulations are presented as time-domain pressure responses sampled in logarithmic time during a 100 hr long shut-in interval subsequent to a constant rate injection pulse. We make use of the same $r \times z \equiv 117 \times 281$ simulation grid illustrated in Figure 3.5(b) and of the same reservoir and fluid properties detailed in Table 3.1.

3.3.4.1 Homogeneous and Isotropic Reservoir Model

Figure 3.6(a) shows the example of a homogenous and isotropic reservoir model. We compute the fall-off pressure change as a function of time at a point vertically centered within the reservoir and in very close proximity to the wellbore. Pressure fall-off responses calculated with the EKSM algorithm for various permeability values are in excellent agreement with ECLIPSE 100™ simulations. Results of this simulation exercise are summarized in Figure 3.6(b). As expected, fast declining pressure fall-off responses are observed for increasingly large values of permeability. Relative errors between the EKSM and the ECLIPSE 100™ results are less than 1%.

A more practical version of the model described above is the one that includes variations of permeability in response to water and oil saturations (relative permeability). Such a model is illustrated in Figure 3.7(a). We assume a homogeneous and isotropic reservoir with a fully penetrating injection well and an inner boundary condition in the form of a uniform-flux truncated line source. Top, bottom, and external boundaries of the reservoir are assumed to abide by a no-flow condition. Except for irreducible water, the reservoir is assumed to be initially filled with oil of a small and constant compressibility. Water is injected into the well at a constant rate, thus displacing oil away from the wellbore. Although strictly speaking the displacement process should be described by two-phase continuity equations, we consider a commonly used simplification that approximates the saturation profile with a step change (shock saturation front). This assumption is equivalent to the case of a moving boundary two-zone composite reservoir model. We anticipate that the mean fluid properties of the invaded zone would roughly correspond to values at residual oil saturation. Presumably, fluid properties of the formation ahead of the saturation discontinuity, referred to as uninvaded zone, are determined by the properties of the in-situ oil. The idealized moving boundary (or the

water front) in the current context is expected to approximately coincide with the Buckley-Leverett discontinuity (Buckley and Leverett, 1941), or more precisely, the capillary transition region. A slow moving boundary is assumed. We describe the permeability field by computing effective single-phase permeabilities for the invaded (water) and uninvaded (oil) zones. Figure 3.7(a) shows the composite reservoir model constructed following these assumptions. Effective single-phase permeabilities are computed using end-point relative permeability values for a water-wet medium. The assumed saturation-relative permeability dependence for the medium is shown in Figure 3.7(b). We use only the end-point relative permeability values shown in that figure. Simulations of fall-off pressure response are performed for various locations of the water front (parameter *rbank*). A slow moving boundary assumption is imposed, i.e., we assume that the location of the fluid boundary remains stationary during the course of the pressure transient test. Figure 3.7(c) shows the comparison of simulation results obtained with both EKSM and ECLIPSE 100™ for the same pressure sampling location described in the previous case. In general, there is a good agreement between both results. Relative errors are within 1 to 4% for various locations of the saturation front. Comparison of the simulation results for homogeneous and composite reservoir models suggests that the pressure response is sensitive to both the single-phase permeability field and the location of the water front.

3.3.4.2 Reservoir Model Exhibiting Anisotropic Permeability

Vertical and horizontal permeabilities are commonly not equivalent in practical subsurface reservoir models. The ratio of the horizontal permeability, k_r, to the vertical permeability, k_z, is referred to as the anisotropy ratio, k_r/k_z. The EKSM algorithm developed in this work can be used for the simulation of pressure responses of anisotropic reservoirs describable with a 2D axisymmetric coordinate frame. Figure 3.8(a) shows an

example of an anisotropic reservoir model. Pressure responses due to this reservoir are computed with both the EKSM and ECLIPSE 100™ simulators assuming an observation point vertically centered in the reservoir and in close proximity to the wellbore. Simulation results are displayed in Figure 3.8(b) for various anisotropy ratios ranging from 1 to 30. The EKSM and ECLIPSE 100™ results agree within 1 to 4% of each other for the various simulation examples.

3.3.4.3 Two-Dimensional Multi-Layer and Multi-Block Reservoir Models

We simulate fall-off pressure changes in the presence of both a simple 2D three-layer model and a relatively more complex three-layer, nine-block reservoir model. Figure 3.9(a) illustrates the three-layer reservoir model and its associated rock properties. In both cases, pressure observation points are vertically centered within the layers at two different radial locations. Figure 3.9(b) shows the pressure changes simulated for the three-layer reservoir model at a point located in proximity to the wellbore (r = 0.1 m) at three vertical observation locations within the permeable medium. Pressure changes are computed with both the EKSM algorithm and ECLIPSE 100™, and are displayed as superimposed time domain variations. A similar plot is shown in Figure 3.9(c) that describes modeling results for a deeper radial location (r = 1.05 m) within three layer mid-depths. A percent error analysis indicates an agreement within 1% for both simulations.

Figure 3.10(a) describes the three-layer, nine-block reservoir model and its associated rock properties. Pressure observation locations are the same as in the previous case. Results of this simulation exercise are shown in Figure 3.10(b) in the form of time-domain pressure change at a location within the permeable medium in close proximity to the wellbore (r = 0.1 m). Figure 3.10(c), on the other hand, describes results obtained for

a deeper radial location (r = 1.05 m) within all three layer mid-depths. The EKSM and ECLIPSE 100™ numerical simulations agree within 1% of each other.

We also perform benchmark simulations of ECLIPSE 100™ and EKSM to assess computational efficiency. Results of our benchmark study are presented in Tables 3.2 and 3.3. All the simulations are performed on a SGI Octane 300 MHz computer. Comparison of simulation times indicates that EKSM provides approximately a one-and-one-half- to three-fold improvement in computational performance with respect to the commercial simulator for the test examples shown in Tables 3.2 and 3.3. Moreover, our benchmark studies suggest that the EKSM algorithm is suitable for solving large-scale inverse problems of single-phase fluid flow phenomena.

3.4 VARIABLE RATE INJECTION/PRODUCTION

The EKSM formulation described in this chapter provides added flexibility to compute pressure responses due to time-variable schedules of injection or production. This computation is performed directly from equation (3.46).

As an example of such a computation, we consider the reservoir model shown in Figure 3.10(a). Pressure changes are simulated at an observation point centered in the mid-layer in close proximity to the wellbore (r = 0.1 m). Figure 3.11 shows EKSM simulations obtained for several cases of time-variable injection rates. In this figure, the function $U(t)$ is given by

$$U(t-t_{shut}) = \begin{cases} 1 & for \quad t-t_{shut} < 0, \\ 0 & for \quad t-t_{shut} > 0, \end{cases} \tag{3.52}$$

where τ is the period for sinusoidal/cosinusoidal pulses, and γ is a positive constant for the exponential decay function. Simulations obtained with sinusoidal/cosinusoidal pulses

of flow rate clearly show a phase shift between the pressure change response and the pulsing rate function. Consistent with the physics of a slightly compressible fluid and pressure wave propagation, the pressure response exhibits a phase shift with respect to the excitation pulse by a constant amount. This phase shift increases with increasing values of compressibility, C_t.

Finally, the EKSM algorithm provides a simple and direct way to compute the pressure derivative with respect to time. From equation (3.46a), one can write

$$\frac{\partial p}{\partial t} = \frac{\partial}{\partial t}\left[\int_{-\infty}^{t} q_{sf}(\tau)\left[G(r,z,t-\tau) + \delta(t-\tau)\Delta p_{skin}\right] d\tau\right]. \tag{3.53}$$

Figure 3.12 shows examples of the computation of pressure derivatives associated with the injection/production schedules described in Figures 3.11(a) and 3.11(b). Figure 3.12(a) shows the pressure derivative and the injection rate as functions of time computed for the build-up time interval. Figure 3.12(b), on the other hand, displays pressure derivative behavior during the shut-in period resulting from the enforcement of step-function pulse excitation. Pressure derivative and pulsing rate behavior simulated for the sinusoidal pulse excitation displayed in Figure 3.11(b) are shown in Figure 3.12(c).

Pressure and pressure derivative responses of multirate tests can be readily evaluated with the formulations shown in equations (3.46a) and (3.53). Consequently, pressure test schedules with arbitrarily varying flow rates can be simulated via EKSM when the flow rate function can be approximated with a series of step-functions. An example simulation of an injection test is shown in Figures 3.13(a) and 3.13(b). Both actual and approximate flow rate schedules are superimposed on the pressure and the pressure derivative plots displayed in Figures 3.13(a) and 3.13(b), respectively.

3.5 A SEMI-DISCRETE NUMERICAL MODEL TO SIMULATE THE RESPONSE OF PERMANENTLY DEPLOYED ELECTRODE ARRAYS

In contrast to the conventional depth-profiling electrode logging tools, permanent resistivity arrays are stationary devices. The tool we consider in this work consists of an array of electrodes cemented in place within the annular space between an insulated casing and the formation. In the vertical direction, the array laid on an insulated part of the casing is spanning the zone of interest with a number of electrodes sufficient for the required lateral resolution of the system. A multi-conductor cable is serving as the interface between each electrode and a surface switch connected to a power module. The basic acquisition lies in sending current between one electrode and a surface stake and measuring the potential induced on the remaining electrodes with respect to a second surface stake. This operation is repeated until all the electrodes making up the array have been used as a source. This acquisition sequence is referred to as a monopole-monopole acquisition. The thickness of the rock formation straddled by the resistivity array and the resistivity contrast between the in-situ medium and the invading (or injected) fluid are the determining factors for the depth of investigation of resistivity array measurements (Delhomme et al., 1998). The basic structure of this tool is shown in Figure 3.14.

Unlike openhole electrical logging devices permanently deployed resistivity arrays offer the ability of recording long-term resistivity data. The applications for permanent resistivity imaging can be categorized into (a) water flood front monitoring from either an observatory or an injecting or producing well; (b) water coning monitoring in a producer at any deviation; (c) regional water-table monitoring from an observation well or from the heel part of a horizontal producing well (van Kleef et al., 2001). In this dissertation, we investigate the value in the permanent resistivity array measurements in inferring reservoir properties together with permanent sensor pressure data within a

quantitative joint inversion framework. The physical context for the permanent array measurements is a water injection experiment where the resistivity array is deployed in an injection well.

The governing equation of the resistivity problem can be derived from several basic laws of electrical theory. Ohm's law relates the current density $\mathbf{J}(\mathbf{r})$ to an isotropic conductivity $\sigma(\mathbf{r})$ and electric field intensity $\mathbf{E}(\mathbf{r})$ via

$$\mathbf{J}(\mathbf{r}) = \sigma(\mathbf{r})\ \mathbf{E}(\mathbf{r}). \tag{3.54}$$

Stationary electric fields of the dc resistivity problem can be expressed in terms of a scalar potential u as

$$\mathbf{E}(\mathbf{r}) = -\nabla u(\mathbf{r}). \tag{3.55}$$

The principle of conservation of charge over a volume and the utilization of continuity equation that applies to charge flow leads to the following relationship for point sources

$$\nabla \cdot \mathbf{J}(\mathbf{r}) = (\partial\rho / \partial t)\, \delta(\mathbf{r} - \mathbf{r}_S). \tag{3.56}$$

Combination of the equations (3.54), (3.55), and (3.56) yields

$$\nabla \cdot \left[\sigma(\mathbf{r}) \nabla u(\mathbf{r})\right] = -(\partial\rho / \partial t)\ \delta(\mathbf{r} - \mathbf{r}_S). \tag{3.57}$$

The charge source in the resistivity problem is the injected current; therefore, the right-hand side of equation (3.56) can be expressed as

$$(\partial\rho / \partial t)\,\delta(\mathbf{r} - \mathbf{r}_S) = I\,\delta(\mathbf{r} - \mathbf{r}_S), \tag{3.58}$$

where I is the electrical current injected into the source point. Substitution of the right-hand side of the equation (3.58) into equation (3.57) yields the partial differential equation to be solved numerically to simulate the electric potentials measured by the permanent dc resistivity array electrodes.

$$\nabla \cdot \left[\sigma(\mathbf{r})\nabla u(\mathbf{r})\right] = -I\ \delta(\mathbf{r} - \mathbf{r}_S). \tag{3.59}$$

Similar procedures for the derivation of governing partial differential equation are presented by Dey et al. (1979) and Lowry et al. (1989).

The solution methodology we propose in this work is in many aspects identical to the one of the axisymmetric problem of dc resistivity logging. According to the underlying postulation of the axisymmetric problem of dc resistivity logging or permanent dc resistivity electrodes, the solution is described in a cylindrical system of coordinates by reason of the main assumption of axisymmetricity in the underlying resistivity model. Vertical borehole geometry is inherently assumed leading to a notion of negligible three-dimensional effects in the resistivity response. The resistivity model of the rock formation is partitioned by plane-parallel boundaries into beds and each bed is divided by coaxial-cylindrical boundaries to represent physical hydrodynamic state of the geophysical problem. The employment of coaxial cylindrical boundaries is in fact a discrete approximation to the otherwise continuous variation of the bulk resistivity of the medium in radial direction due to the fluid saturation variation within the penetration

zone of the invading (or injected) fluid. Point sources of dc electric current are assumed along the axis of the borehole.

The potential $u(r,z)$ of a point source of current situated at the origin of the borehole axis satisfies in R^3 the equation

$$-\frac{\partial}{\partial r}(r\sigma(r,z)\frac{\partial}{\partial r}u(r,z))-\frac{\partial}{\partial z}(r\sigma(r,z)\frac{\partial}{\partial z}u(r,z))=\frac{I}{2\pi}\delta(r)\delta(z-z'), \tag{3.60}$$

subject to the boundary conditions

$$\lim_{r^2+z^2\to\infty} u=0, \tag{3.61}$$

and

$$\left.\frac{\partial u}{\partial r}\right|_{r=0}=0. \tag{3.62}$$

The forward problem of modeling the permanent array resistivity response is reduced to the computation of $u(r,z)$ at each electrode location making up the array.

If we replace R^3 by a cylinder such that $r\le R,$ the condition in the infinity represented by the asymptotic shown in equation (3.61) can be replaced by the conditions,

$$\lim_{z\to\infty} u=0, \tag{3.63}$$

and

$$u\big|_{r=R} = 0. \tag{3.64}$$

The relative error introduced to the solution for $u(r,z)$ by this physical substitution is in the order of $\sqrt{(r^2+z^2)/R}$ as reported by Druskin and Knizhnerman (1987). The numerical solution of dc electrical conduction phenomena in 2D axisymmetric media was accomplished by making use of a differential-difference approximation of the problem stated by the equations (3.60) through (3.64). The numerical solution for the above described boundary value problem is implemented using a semi-discrete numerical approach that combines the method of straight lines with an incomplete Galerkin formulation. Extensive numerical testing showed that the accuracy of the simulation algorithm remains within 1% of the existing analytical solutions. A modeling example for the response of a permanent electrode array is shown in Figure 3.15.

3.6 CONCLUDING REMARKS

An important feature of the EKSM developed in this chapter is its ability to provide pressure solutions in response to axisymmetric single-phase flow for a multitude of times with practically the same efficiency as that of a single time solution. Moreover, the EKSM formulation can be easily adapted to provide solutions of pressure in the Laplace transform domain without appreciable computer overhead. The same formulation requires only a minor modification to yield solutions of the time derivative of pressure. In addition, the EKSM formulation is also readily applicable for the simulation of variable flow rate schedules. In this work, we considered pressure change and pressure derivative responses for simple variable rate test schedules.

The high efficiency of the EKSM algorithm is primarily due to the usage of inverse powers of the finite-difference operator, **A**, when computing the pressure

solution. Extensive tests have shown that the simultaneous use of inverse and positive powers of **A** provides a significant acceleration in convergence compared to a conventional implementation of Lanczos recurrence. This property of the EKSM algorithm yields approximately one-and-a-half- to three-fold improvement in performance with respect to that of the commercial software used for comparisons. Sensitivity studies carried out to assess the influence of specific petrophysical parameters on pressure measurements also suggest that the EKSM algorithm possesses the degree of efficiency necessary to approach practical inverse problems. Comparisons of EKSM numerical simulation results with respect to those obtained using analytical solutions for point and line sources validate the accuracy of the developed numerical solver. These benchmark tests indicate that EKSM results and analytical solutions agree within 1% of each other. The accuracy of the EKSM algorithm is also assessed for various geometrically complex reservoir models by comparing EKSM simulations against numerical solutions computed using a commercial reservoir simulator, ECLIPSE 100™. Pressure responses from both simulators agree within 1-4% of each other.

A rapid and accurate numerical model for the simulation of permanent electrode array responses is developed with the central purpose of inversion. The solution method is based on the semi-discrete numerical approach that combines the method of straight lines with an incomplete Galerkin formulation.

Table 3.1: Summary of reservoir and fluid properties used in various test cases.

Parameter	**Value**
Fluid viscosity, μ, Pa.s	1.0×10^{-3}
Total compressibility, C_t, kPa^{-1}	2.9×10^{-6}
Wellbore radius, r_w, m	0.1
Skin factor, S	0.0
Step function pulse injection rate at downhole conditions, q, m^3/d	79.79

Table 3.2: Comparison of computation times associated with various test cases. Computational complexity is varied by changing the spatial discretization of the 1-layer 1-block reservoir model shown in Figure 3.6(a).

Machine: SGI OCTANE (300 MHz)	ECLIPSE 100™ (A)	EKSM (B)	Ratio of the CPU times (A)/(B)
Grid	$r\times z \equiv 105\times 200$	$r\times z \equiv 105\times 203$	-
CPU time (sec.)	12.71	5.38	2.36
Grid	$r\times z \equiv 125\times 200$	$r\times z \equiv 125\times 203$	-
CPU time (sec.)	15.00	8.13	1.85
Grid	$r\times z \equiv 117\times 281$	$r\times z \equiv 117\times 281$	-
CPU time (sec.)	20.68	11.56	1.79

Table 3.3: Comparison of computation times associated with various test cases. Simulation results from both simulators agree within 1% of each other for the test problems reported in this table.

Machine: SGI OCTANE (300 MHz)	ECLIPSE 100™ (A)	EKSM (B)	Ratio of the CPU times (A)/(B)
Grid	$r\times z \equiv 200\times 200$	$r\times z \equiv 117\times 281$	-
CPU time (sec.) [1-layer 1-block reservoir Fig. 3.6(a)]	31.00	11.56	2.68
CPU time (sec.) [3-layer 9-block reservoir Fig. 3.10(a)]	33.95	11.66	2.91

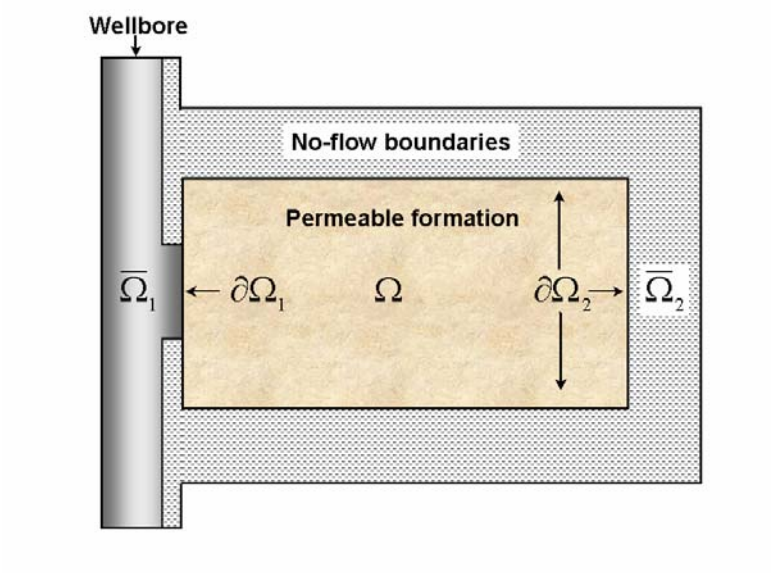

Figure 3.1: Graphical description of the spatial domain considered in the numerical solution of the pressure equation in an axisymmetric 2D cylindrical medium.

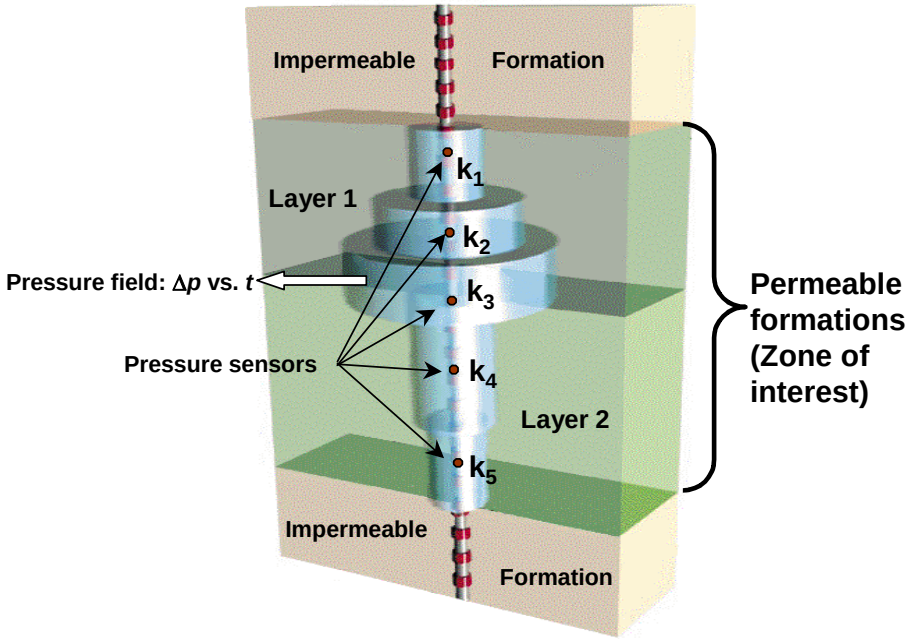

Figure 3.2: Graphical description of the simulation problem. Pressure gauges are deployed in direct hydraulic contact with the formation. Water is injected through an open interval along the well thereby displacing in-situ fluid. Invasion fronts in the form of cylinders are used to indicate variability in the vertical distribution of permeability.

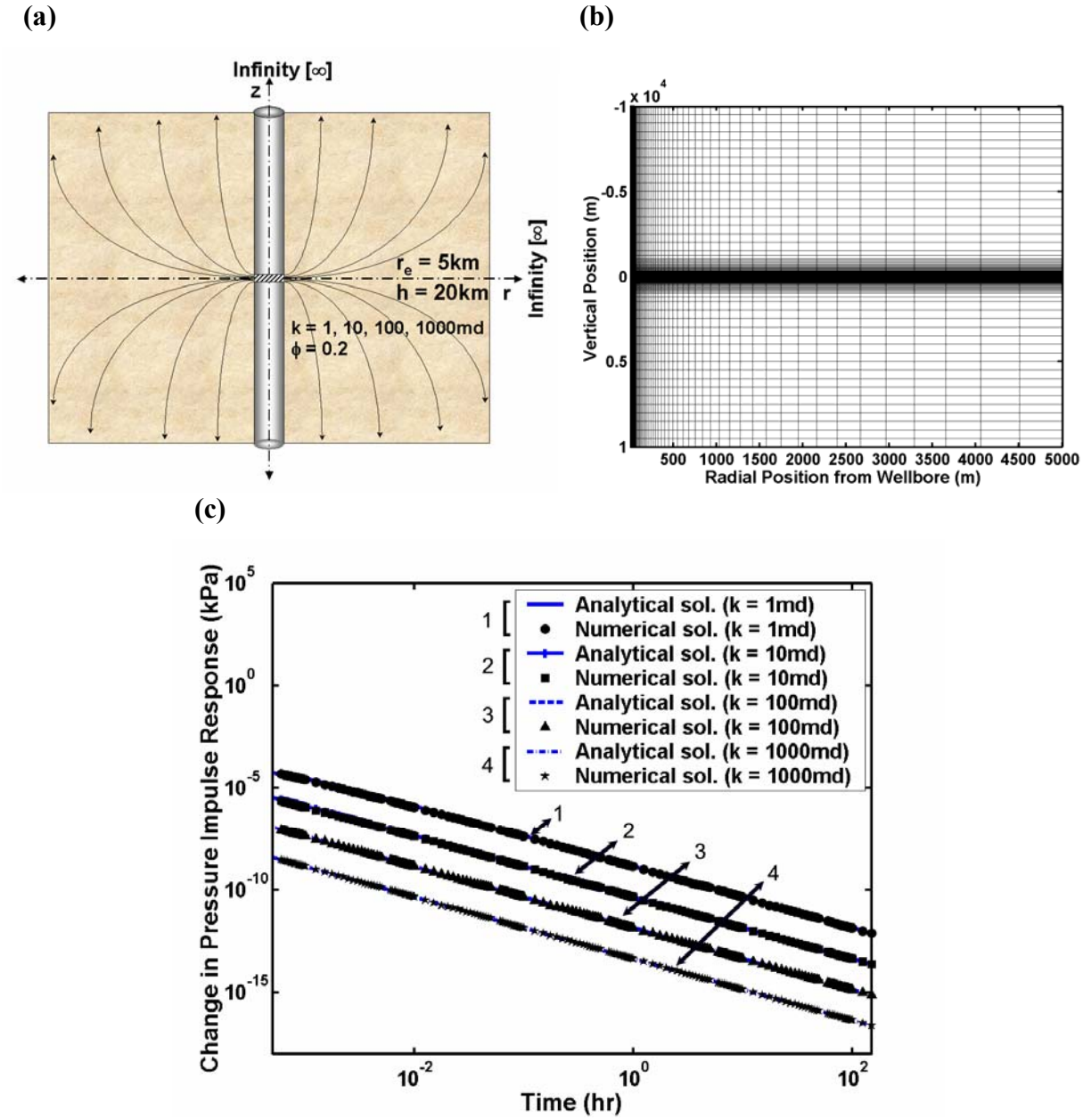

Figure 3.3: Homogeneous and isotropic reservoir model constructed to simulate the pressure response of a point source of flow rate in an unbounded permeable medium. (a) Description of the reservoir model. Pressure responses are computed for various permeability values. The associated reservoir and fluid properties are listed in Table 3.1. (b) Vertical cross-section of the 105×286 finite-difference simulation grid. (c) Comparison of numerical (EKSM) and analytical pressure impulse solutions in the time domain. Solutions are computed at a point vertically centered within the reservoir and in close proximity to the well boundary (r = 0.1 m).

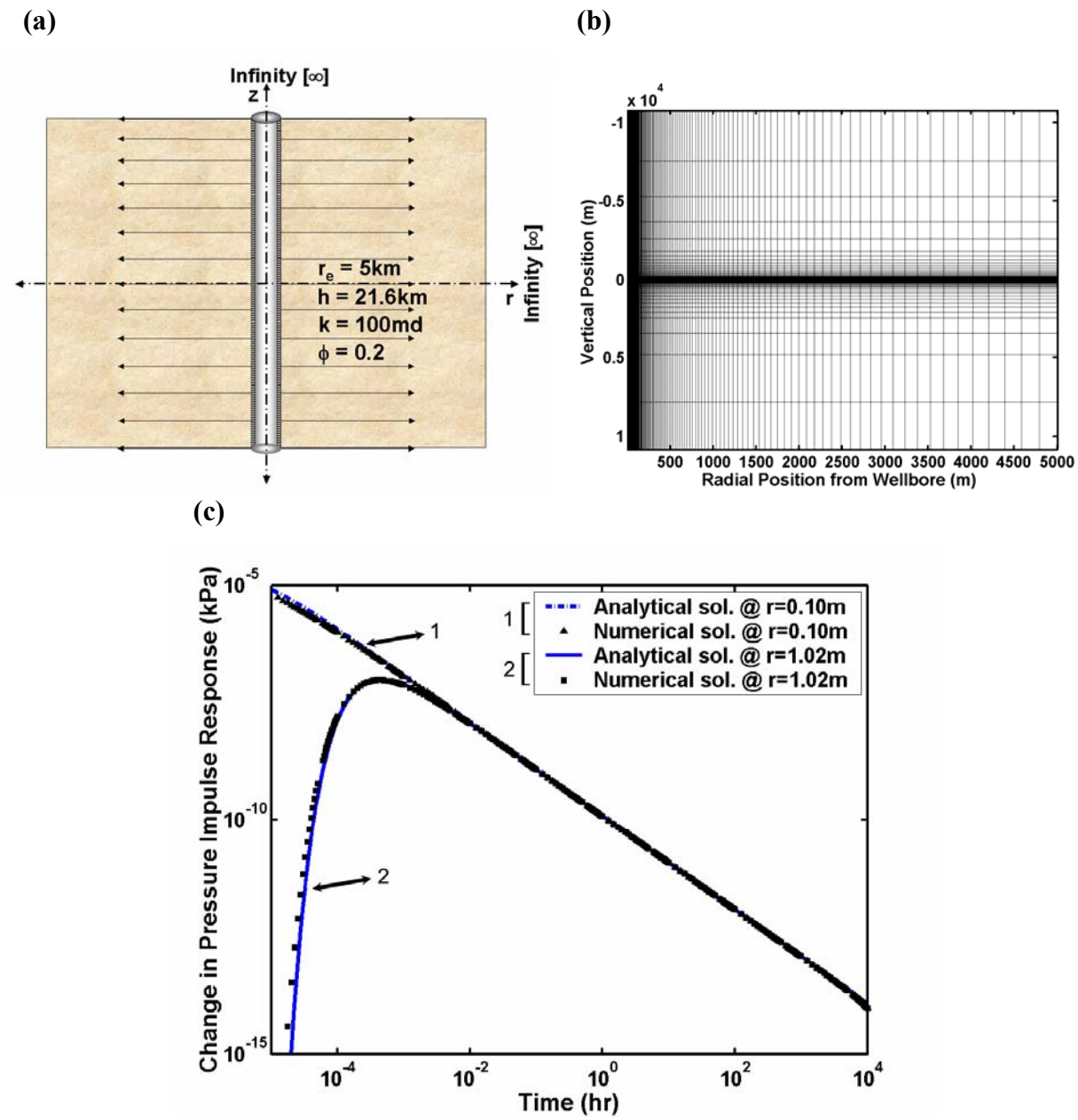

Figure 3.4: Homogeneous and isotropic reservoir model constructed to simulate the pressure response of a long line source of flow rate in an unbounded permeable medium. (a) Description of the reservoir model. The associated reservoir and fluid properties are listed in Table 3.1. (b) Vertical cross-section of the 249×126 finite-difference simulation grid. (c) Comparison of numerical (EKSM) and analytical pressure impulse solutions in the time domain. Solutions are computed at a point vertically centered within the reservoir and in close proximity to the well boundary (r = 0.1 m) and at a second point at (r = 1.02 m).

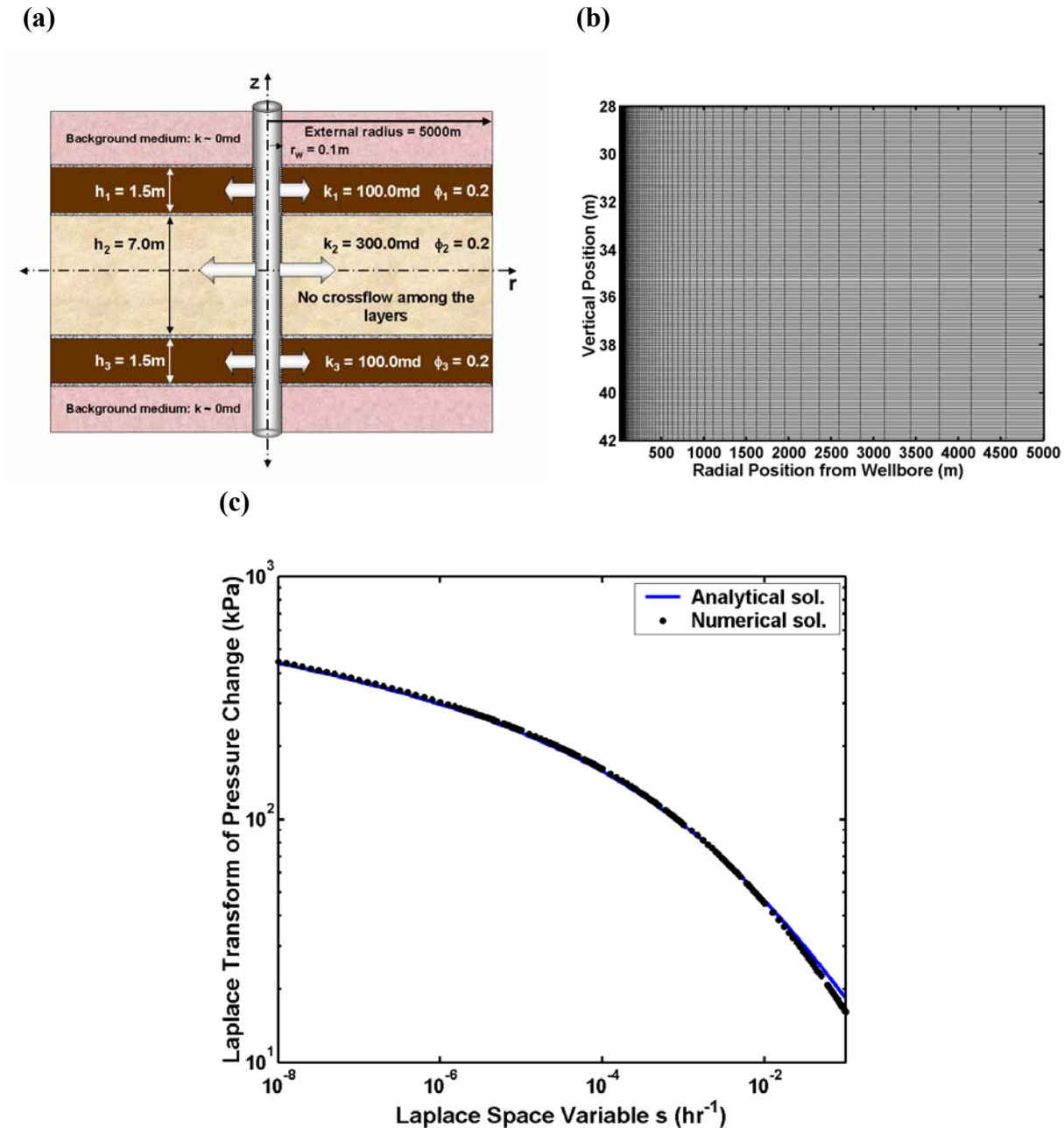

Figure 3.5: Three-layer commingled reservoir model. (a) Description of the reservoir model. The associated reservoir and fluid properties are listed in Table 3.1. No-flow condition is imposed to the top and bottom boundaries of the zone of interest. Each layer is homogeneous and isotropic. A no-crossflow condition is enforced among the layers. The injection flow rate is modeled by way of a truncated-line source equivalent to a fully penetrated well. (b) Vertical cross-section of the 117×281 finite-difference simulation grid. (c) Comparison of numerical (EKSM) and analytical wellbore pressure solutions in the Laplace transform domain.

(a)

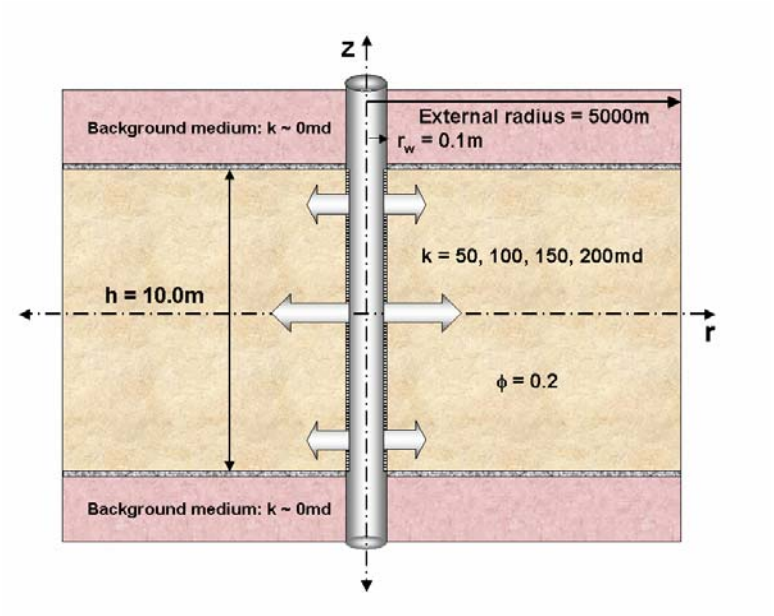

(b)

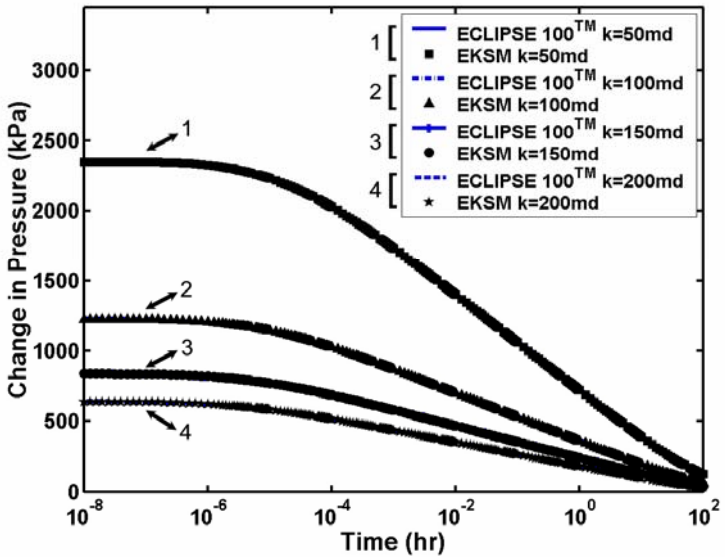

Figure 3.6: Homogeneous and isotropic permeability reservoir model. (a) Description of the reservoir model. The associated reservoir and fluid properties are listed in Table 3.1. The injection flow rate is modeled by way of a truncated-line source equivalent to a fully penetrated well. Pressure responses are simulated for various values of reservoir permeability. (b) Comparison of EKSM and ECLIPSE 100™ pressure fall-off response solutions in the time-domain. Solutions are computed at a point vertically centered within the reservoir and in close proximity to the well boundary (r = 0.1 m).

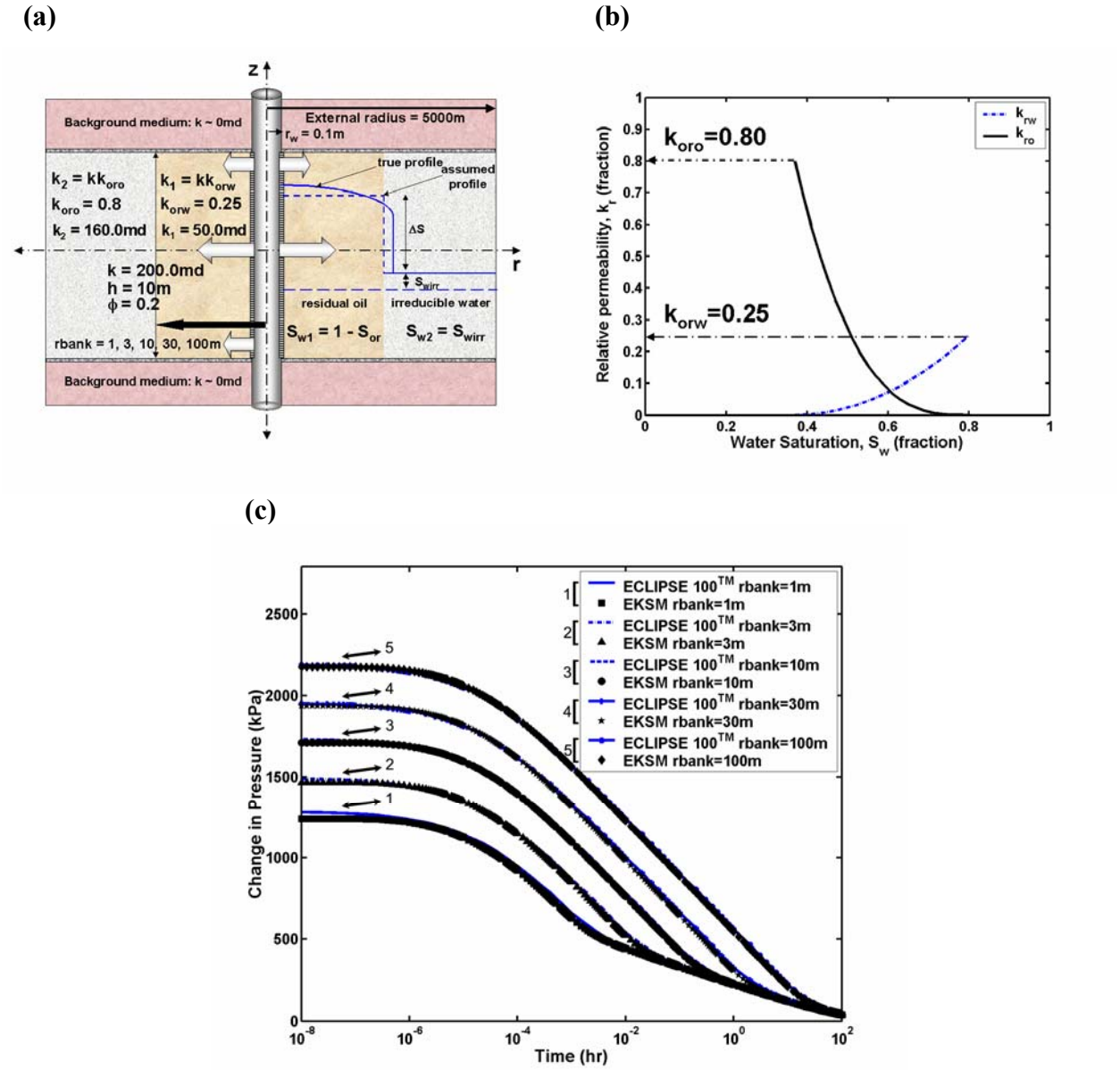

Figure 3.7: Composite water-oil bank reservoir model. (a) Description of the reservoir model. The associated reservoir and fluid properties are listed in Table 3.1. The injection flow rate is modeled by way of a truncated-line source equivalent to a fully penetrated well. Pressure responses are simulated for various locations of saturation front. (b) Assumed saturation-relative permeability dependence for the medium. The locations and values of end-point relative permeabilities employed in our simulations are indicated on the relative permeability curves. (c) Comparison of `EKSM` and `ECLIPSE 100`™ pressure fall-off response solutions in the time-domain. Solutions are computed at a point vertically centered within the reservoir and in close proximity to the well boundary (r = 0.1 m).

(a)

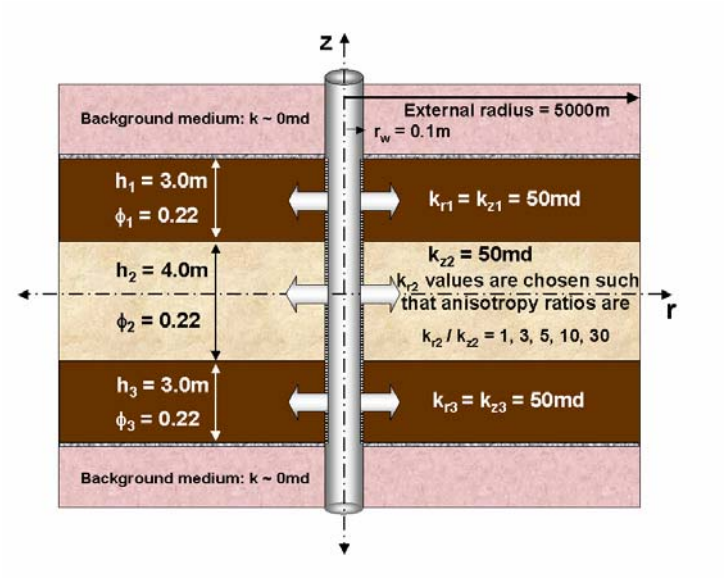

(b)

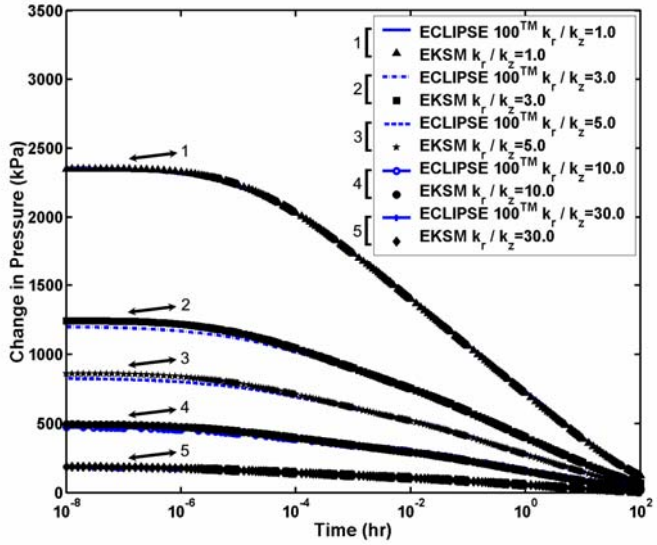

Figure 3.8: Reservoir model exhibiting anisotropic permeability. (a) Description of the reservoir model. Formation layers are in pressure communication. The associated reservoir and fluid properties are listed in Table 3.1. The injection flow rate is modeled by way of a truncated-line source equivalent to a fully penetrated well. Pressure responses are simulated for various permeability anisotropy ratios, namely, k_r / k_z.(b) Comparison of EKSM and ECLIPSE 100™ pressure fall-off response solutions in the time-domain. Solutions are computed at a point vertically centered within the reservoir and in close proximity to the well boundary (r = 0.1 m).

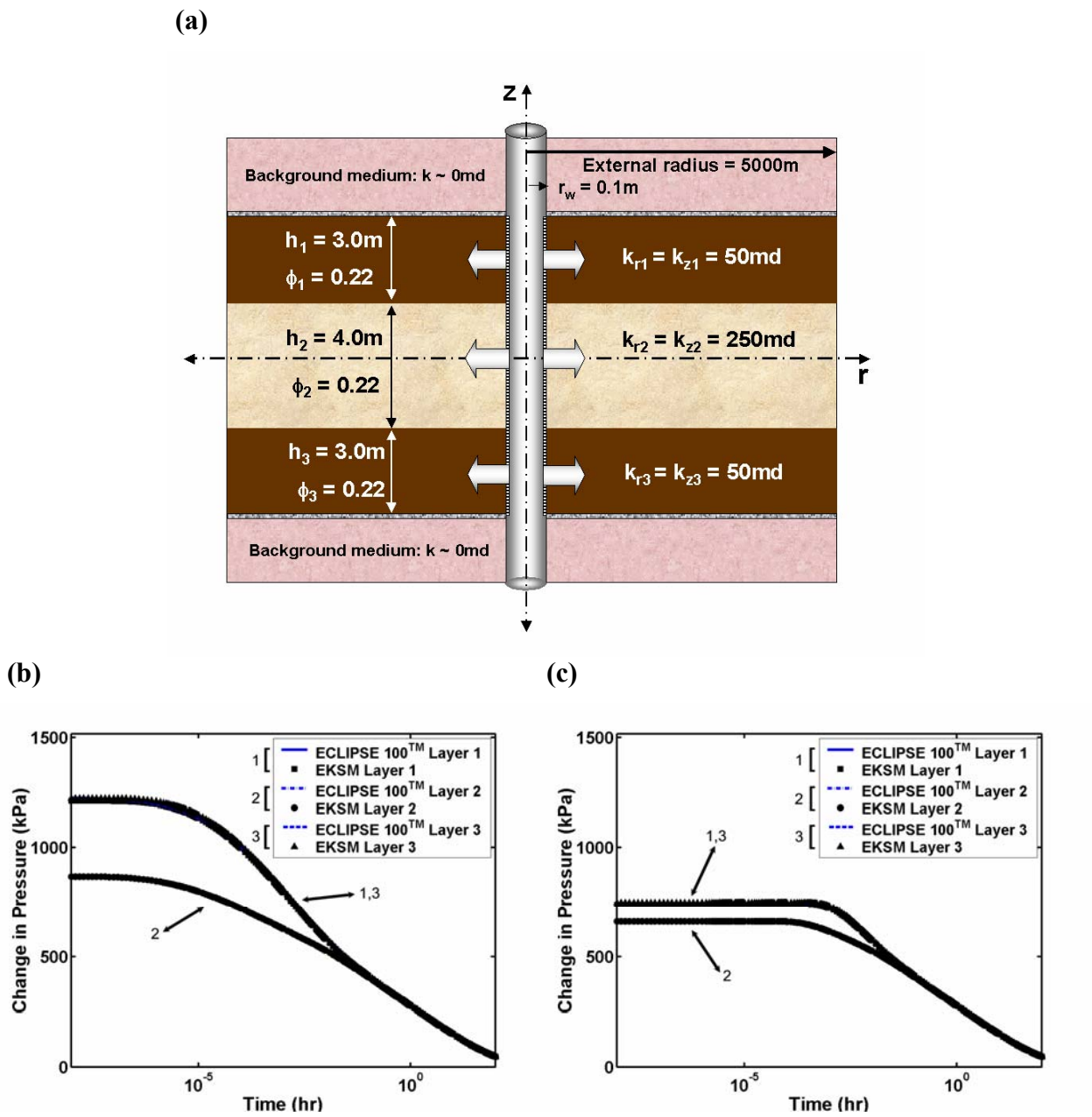

Figure 3.9: Three-layer reservoir model. (a) Description of the reservoir model. Formation layers are in pressure communication. The associated reservoir and fluid properties are listed in Table 3.1. The injection flow rate is modeled by way of a truncated-line source equivalent to a fully penetrated well. (b) Comparison of `EKSM` and `ECLIPSE 100`™ pressure fall-off response solutions in the time-domain. Solutions are computed at points vertically centered within each layer and in close radial proximity to the well boundary (r = 0.1 m). (c) Comparison of solutions of `EKSM` and `ECLIPSE 100`™ at a second set of locations relatively further in the reservoir (r = 1.05 m).

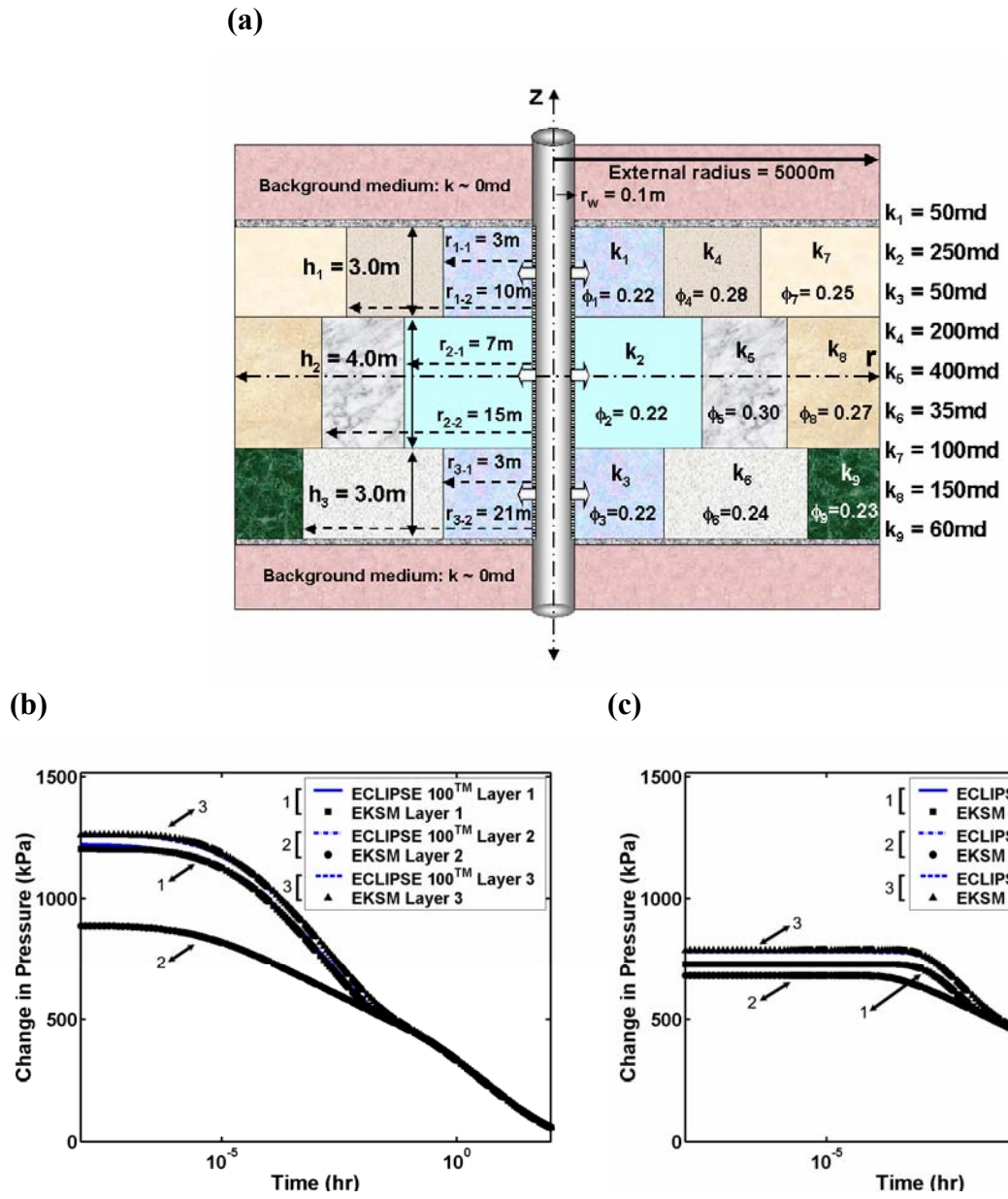

Figure 3.10: Three-layer, nine-block reservoir model. (a) Description of the reservoir model. Formation layers are in pressure communication. The associated reservoir and fluid properties are listed in Table 3.1. The injection flow rate is modeled by way of a truncated-line source equivalent to a fully penetrated well. (b) Comparison of EKSM and ECLIPSE 100™ pressure fall-off response solutions in the time-domain. Solutions are computed at points vertically centered within each layer and in close radial proximity to the well boundary (r = 0.1 m). (c) Comparison of solutions of EKSM and ECLIPSE 100™ at a second set of locations relatively further in the reservoir (r = 1.05 m).

(a) Step-function pulse: $q(t) = U(t - t_{shut})\, q_{inj}$

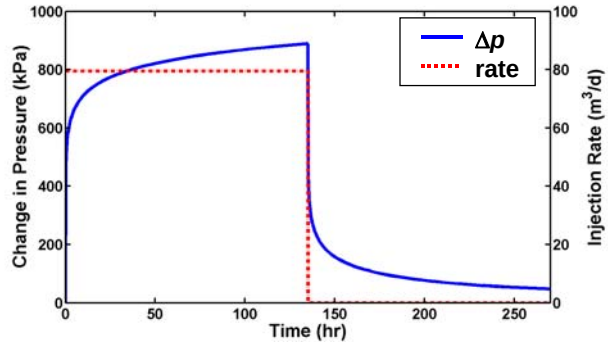

(b) Sinusoidal pulse: $q(t) = q_{\max} \sin\left[(\pi/\tau)\, t\right]$

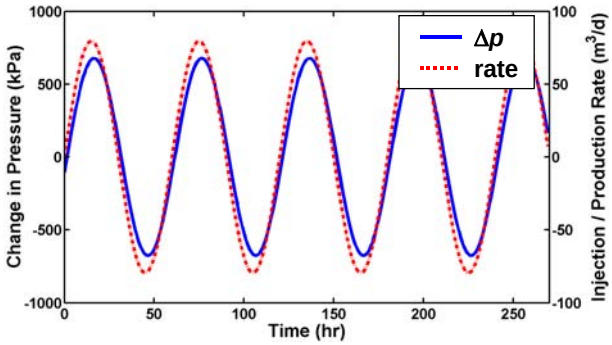

(c) Cosinusoidal pulse: $q(t) = q_{\max} \cos\left[(\pi/\tau)\, t\right]$

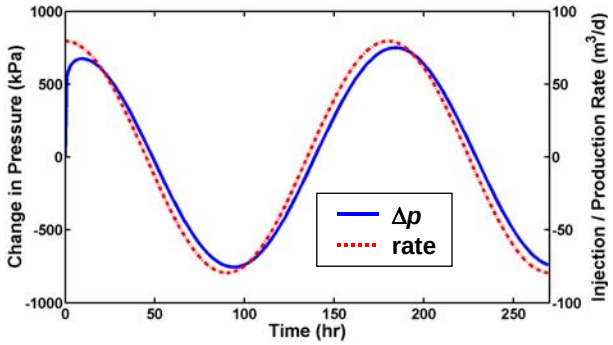

(d) Exponential decay: $q(t) = q_{\max} \exp(-\gamma t)$

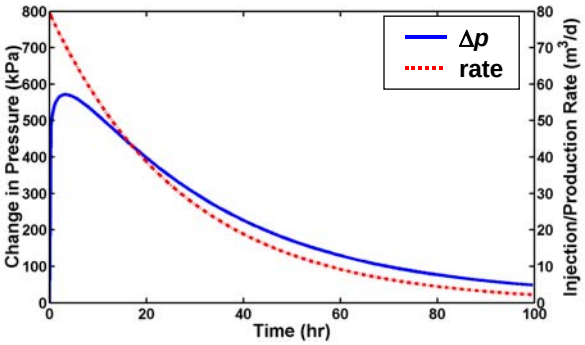

Figure 3.11: Simulated examples of pressure change as a function of time for variable injection/production schedules.

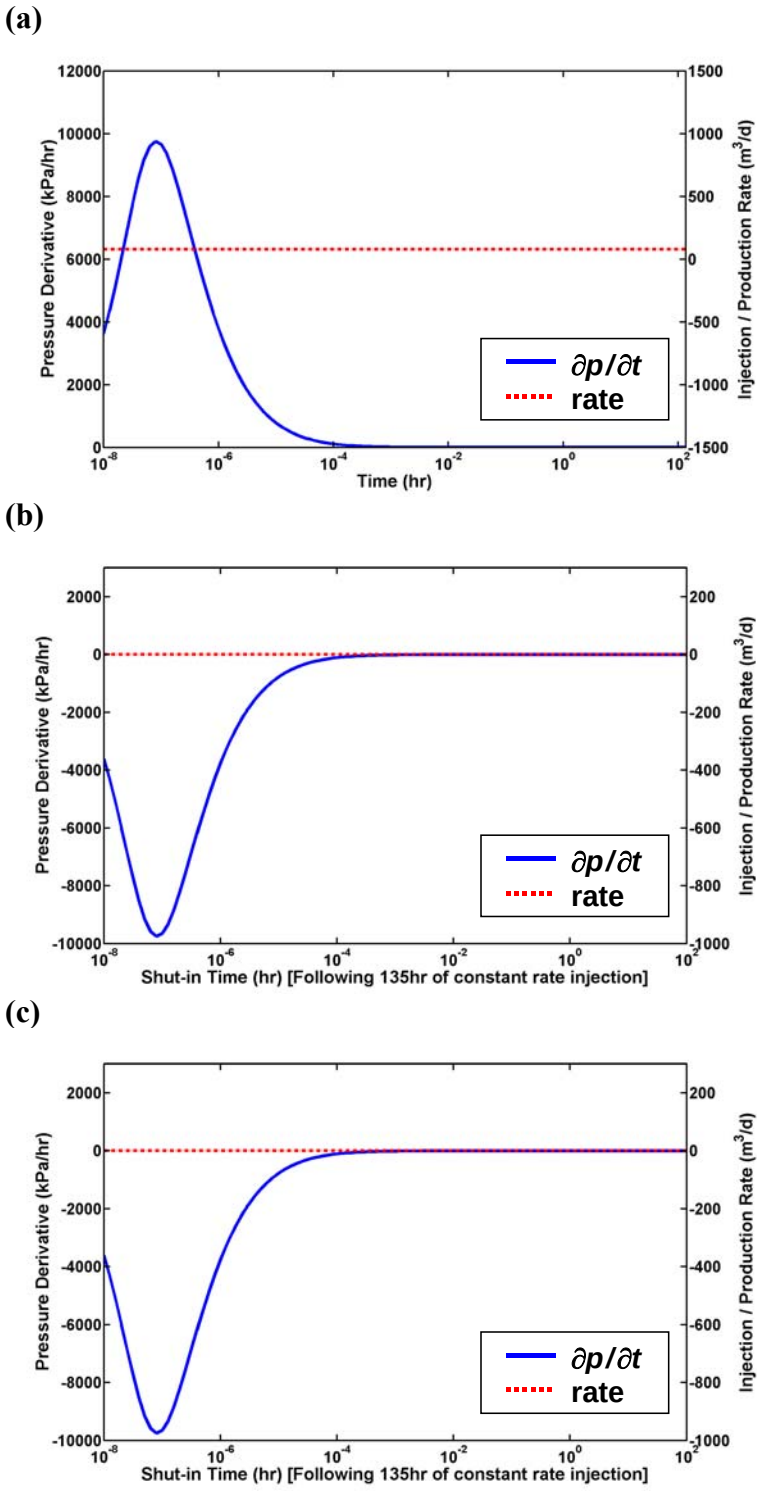

Figure 3.12: Pressure derivative and injection rate behavior during (a) build-up and (b) fall-off time intervals for the step-function excitation, and during (c) pulsation of the sinusoidal excitation.

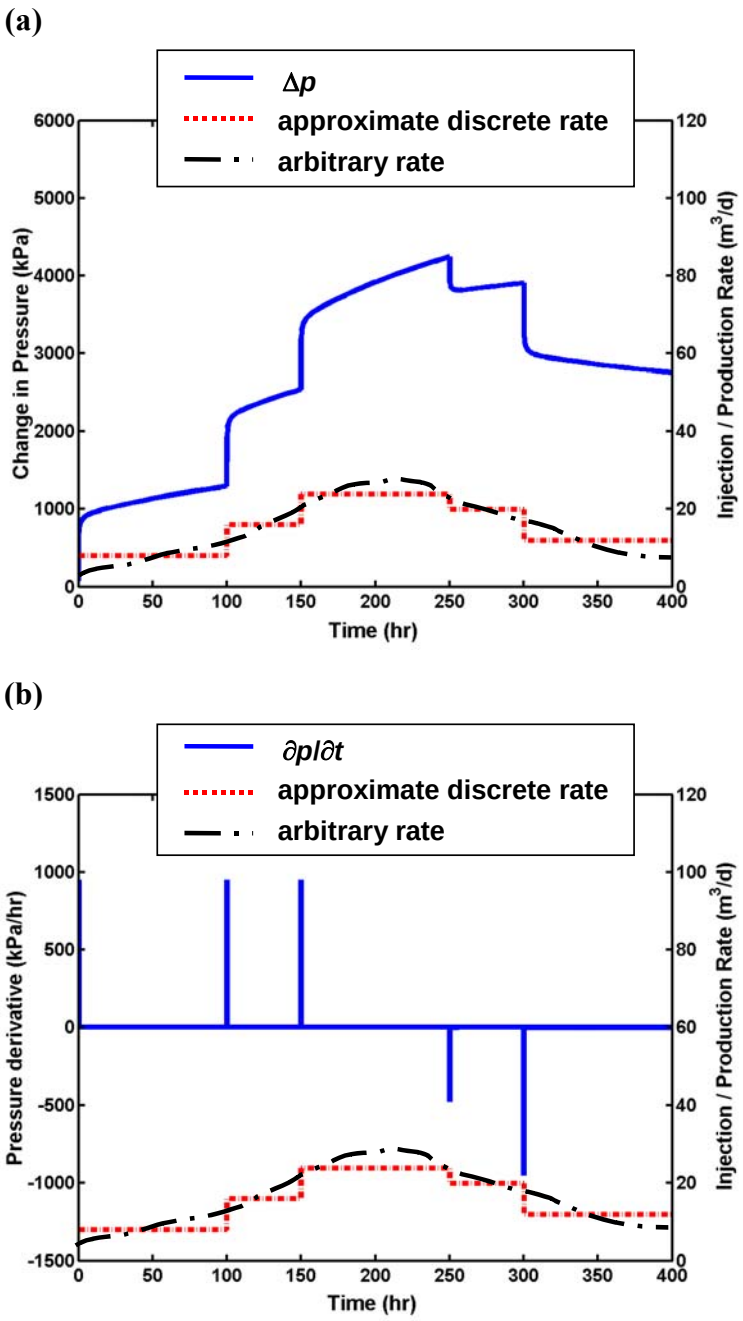

Figure 3.13: Simulated example of (a) pressure change and (b) pressure derivative as a function of time for an arbitrarily varying injection schedule. The actual injection schedule is approximated by a series of consecutive step-functions.

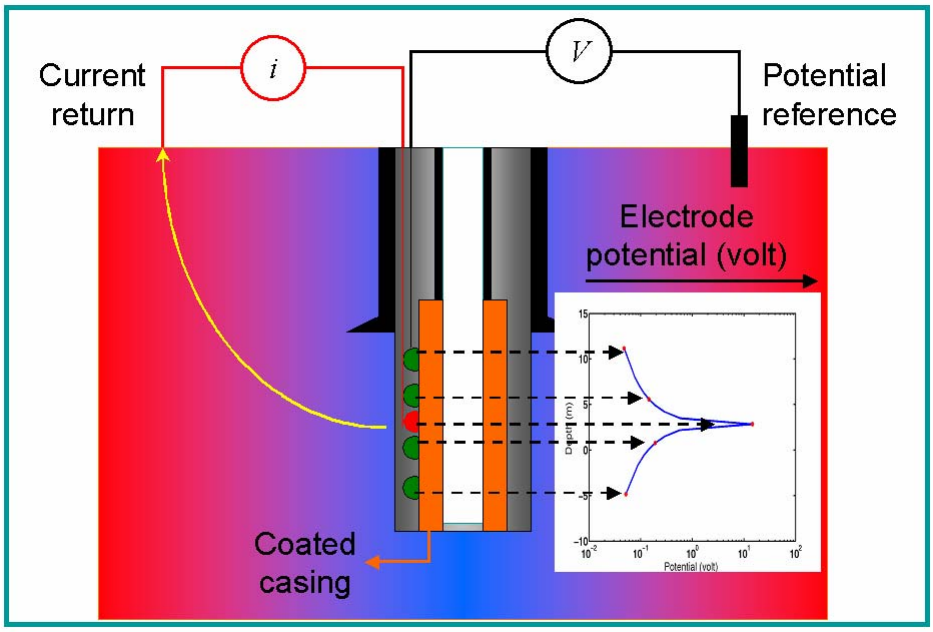

Figure 3.14: Schematic description of a permanent electrode array.

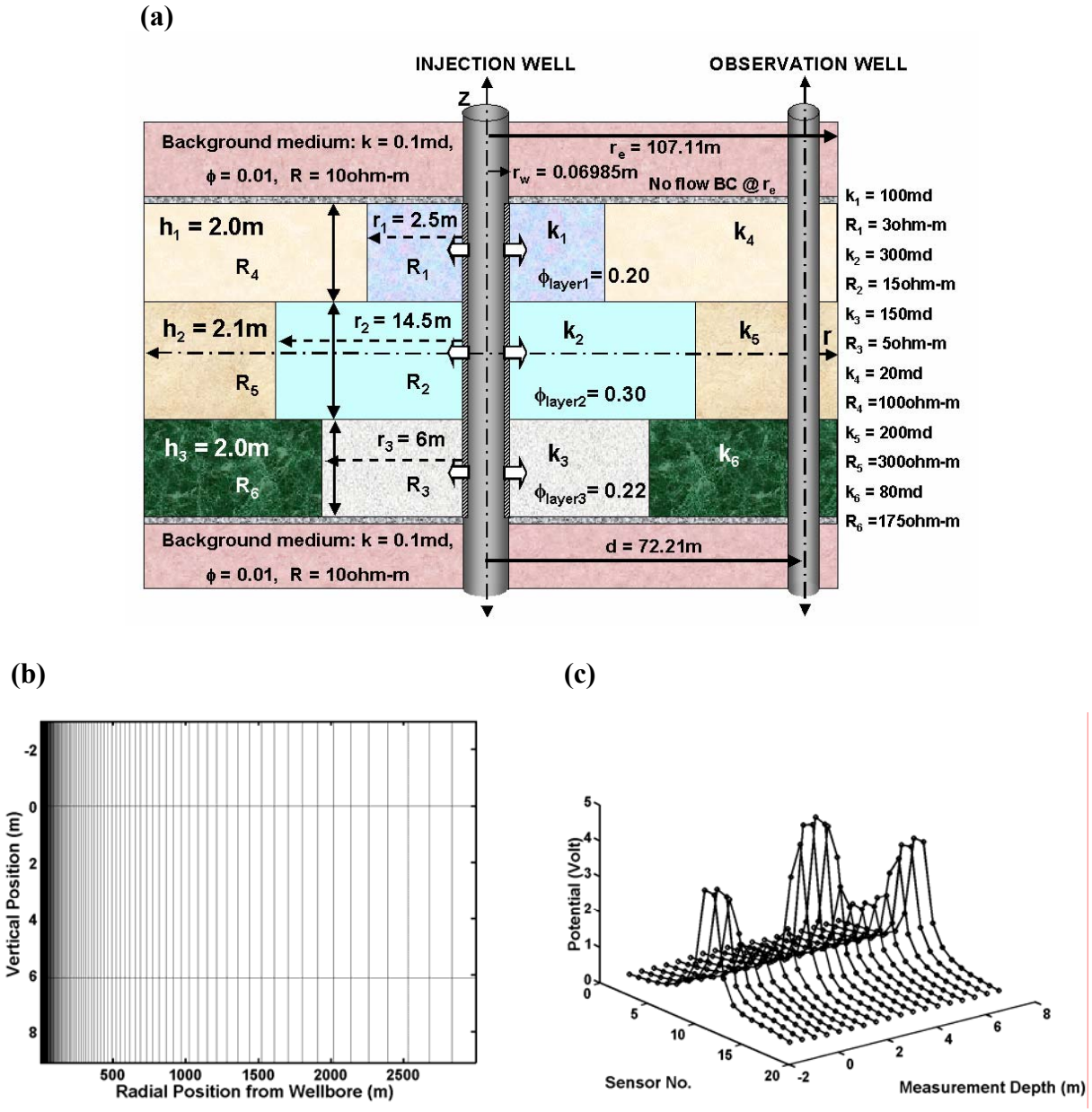

Figure 3.15: (a) Six-block formation model. Description of the permeable medium. The resistivity array, consisting of dc point-contact electrodes, is deployed only along the injection well. (b) Finite-difference radial grid constructed with 201 logarithmically distributed nodes. This mesh is used for the forward and inverse modeling of dc resistivity measurements. The forward modeling algorithm only requires the use of a radial grid. (c) dc electrical response: voltage measurements acquired with point-contact electrodes deployed along the injection well.

Chapter 4: Modeling and Inversion of Multi-Phase Flow and Electromagnetic Induction Logging Measurements

4.1 INTRODUCTION

This chapter describes dual-physics modeling algorithm for the simulation of multi-phase fluid flow and electromagnetic measurements. Physics of fluid flow is linked to electromagnetic domain by means of a saturation equation. Efficient commercial as well as non-commercial simulation software are cast under a coupled dual-physics modeling algorithm implemented using `FORTRAN 90` and `UNIX` shell scripts. Although not limited to, in this dissertation, we utilize the dual-physics modeling algorithm for the simulation of fluid-flow measurements acquired by a wireline formation tester and induction logging measurements acquired by means of a multi-frequency array induction imager sonde. In the current state of affairs, the time scale of fluid-flow measurements of wireline formation tester is much larger in comparison to the measurements of electromagnetic induction borehole survey. This fact is quite auspicious for the loose coupling of fluid-flow and electromagnetic induction modeling algorithms.

4.2 COMPUTATION OF THE RATE OF MUD-FILTRATE INVASION

In this work, we use a general numerical algorithm designed to simulate the physics of mud-filtrate invasion in vertical and highly deviated boreholes. This numerical scheme is adapted by Wu (2004) [also, see Wu et al. (2001), Wu et al. (2002), Wu et al. (2003)] from an existing multi-phase fluid-flow simulator developed by The University of Texas at Austin, and commercially referred to as `UTCHEM` (Delshad et al., 1996).

Numerical modeling of mud-filtrate invasion via `UTCHEM` yields an equivalent time-domain filtrate flow rate function. Given the pressure overbalance condition, invasion geometry, and mudcake properties, this function replicates time-dependent

behavior of the mudcake. Due to the fact that clay platelets form a mudcake with permeabilities in the order of 10^{-3} mD, the filtrate invasion rate is predominantly controlled by the mudcake, with minimal influence of the formation permeability (Ramakrishnan and Wilkinson, 1997). Extensive simulations conducted with UTCHEM are in agreement with the above observation. In turn, a numerically computed invasion rate schedule can be imposed as a local source condition (flux as a function of depth) to an effective fluid-flow simulator. As such, the physics of mud-filtrate invasion can be incorporated into a coupled algorithm for the simulation of multi-phase fluid-flow and electromagnetic induction phenomena.

4.3 FORWARD MODEL FOR DUAL-PHYSICS MEASUREMENTS

4.3.1 Simulation of Mud-Filtrate Invasion and Multi-Phase Flow Measurements

Invasion of water-base mud-filtrate into a partially saturated hydrocarbon-bearing porous medium and a subsequent multi-probe dual-packer formation test involve two-phase multi-component fluid transport. Time- and space-domain distributions of aqueous phase saturation, salt concentration, and pressure are modeled as advective transport of hydrocarbon and aqueous phases, and hydrocarbon, water, and salt components. Ions present in the system are assumed to be soluble only within the aqueous phase and lumped into a single salt component. In the formulation of the forward problem, we assume the existence of a salt concentration contrast between the in situ formation brine and the invading mud-filtrate. According to Ramakrishnan and Wilkinson (1997) diffusion has only a small effect at invasion radius length scales. In addition, equilibration of salt concentration among pores occurs at time scales smaller than the invasion time scale, whereupon local level aqueous phase salt concentrations remain the same from pore to pore. Therefore, for the problem of interest, we only consider

advective miscible transport of the salt component within the aqueous phase and neglect diffusional spreading of the interface between mud-filtrate and formation brine.

Simulation of isothermal two-phase flow in a partially saturated hydrocarbon-bearing medium requires mass balance and transport equations as well as a constitutive equation of state. We disregard the presence of chemical reactions, rock/fluid mass transfer, and diffusive/dispersive transport. The mass balance equation for the i^{th} fluid phase can be stated as follows (Aziz and Settari, 1979)

$$\frac{\partial(\rho_i \phi S_i)}{\partial t} + \nabla \cdot (\rho_i \mathbf{v}_i) = -q_{vi}, \quad i = 1, 2. \tag{4.1}$$

We model flow in the near-borehole region of a single vertical well intersecting a hydrocarbon-bearing horizontal reservoir in R^3. Consistent with the flow geometry imposed by the dual-packer module of the wireline formation tester, a cylindrical coordinate system is employed to accurately represent the dynamics of reservoir behavior in the spatial domain of interest. Spatial support for material balance equations is then $\Omega = \left\{(r, \theta, z) \in R^3 : \; r_w \le r \le r_e, \, 0 \le \theta \le 2\pi, \, 0 \le z \le h \right\}$. In equation (4.1), ρ, $\mathbf{v}$, ϕ, q_v, and S denote fluid density, fluid velocity vector, porosity, source/sink term, and phase saturation, respectively. The subscript i designates the phase index. Moreover, r_w, r_e, and h stand for borehole radius, external radius of the formation, and total formation thickness, respectively. No-flow boundary conditions are imposed on the upper, lower, and outer limits of the formation. The external boundary of the formation is located relatively far away from the wellbore. A constant rate internal boundary condition is imposed to the borehole wall time-step-by-time-step. In this fashion, time-variant invasion rate history and other formation test related rate schedules are incorporated into

our simulations in a time-stepwise discrete fashion. In our formulation, Darcy's law is the governing transport equation, i.e.,

$$\mathbf{v}_i = -\overline{\overline{\mathbf{k}}} \cdot \frac{k_{ri}}{\mu_i}\left(\nabla p_i - \gamma_i \nabla D_z\right), \quad i = 1, 2. \tag{4.2}$$

In equation (4.2), $\overline{\overline{\mathbf{k}}}$ is the absolute permeability tensor of the porous medium, k_r is the phase relative permeability, μ is the phase viscosity, p is the phase pressure, γ is the phase specific gravity, and D_z is the vertical location below some reference level. Finally, the constituent equation follows from the equation of state. The assumption is also made that both fluid-phase and rock compressibilities are constant over the pressure range of interest for the simulations that involve simultaneously flowing oleic and aqueous phases, and are given by

$$c_{fluid,i} = -\frac{1}{V_i}\frac{\partial V_i}{\partial p_i}\bigg|_T = \frac{1}{\rho_i}\frac{\partial \rho_i}{\partial p_i}\bigg|_T, \quad i = 1, 2 \tag{4.3}$$

and

$$c_{rock} = \frac{1}{\phi}\frac{\partial \phi}{\partial p_{avg.}}\bigg|_T, \tag{4.4}$$

respectively. In equation (4.4), $p_{avg.}$ stands for the average grid block pressure. The above assumption of constant fluid compressibility does not hold for the two-phase flow of gaseous and aqueous phases. Thus, in this case, gas compressibility is treated as a

function of the pressure-volume-temperature (PVT) properties of gas for each time-step. Capillary pressures and fluid saturations are governed by

$$P_c = p_{nw} - p_w, \tag{4.5}$$

and

$$S_{nw} + S_w = 1.0, \tag{4.6}$$

where the subscripts nw and w stand for nonwetting and wetting phases.

Advective transport of the salt component is simulated after a converged solution for the time-step has been found, and the interblock flows are determined. A mass conservation equation is solved to update the spatial distribution of salt concentrations, C_w, and is given by

$$\frac{\partial(\rho_w \phi S_w C_w)}{\partial t} + \nabla \cdot (\rho_w \mathbf{v}_w C_w) = -C_{wi} q_i. \tag{4.7}$$

In equation (4.8), C_{wi} and q_i stand for the concentration of invading mud-filtrate, and invasion rate at a given time-step, respectively.

Numerical modeling of the described two-phase, three-component fluid-flow problem in a permeable formation is accomplished using a finite difference-based reservoir simulator, namely, ECLIPSE 100™ in fully implicit, black-oil mode. Time- and space-domain distributions of aqueous phase saturation, salt concentration, and pressure due to mud-filtrate invasion and a subsequent formation tester drawdown-build-up sequence are simulated with ECLIPSE 100™. Our approach takes advantage of

various operating features available in the commercial reservoir simulator ECLIPSE 100™ (GeoQuest, 2000).

4.3.2 Saturation Model

Spatial distributions of aqueous phase saturation corresponding to each logging time are subsequently transformed into snapshots of electrical conductivity using Archie's law,

$$\sigma = (1/a)\,\sigma_w\,\phi^m\,S_w^n, \tag{4.8}$$

(Archie, 1942) applied grid-by-grid. In the above equation, σ, σ_w, and S_w denote formation conductivity, brine conductivity, and aqueous phase saturation, respectively. Porosity and saturation exponents m and n, and normalization parameter a are empirical constants.

In this work, the dual-physics simulation workflow may involve an arbitrary sequence events of involves acquisition single or multiple induction logs before the onset of a formation test. The rock formation, however, is exposed to a prescribed duration of water-base mud-filtrate invasion before the acquisition of the induction log. Therefore, subsequent to the simulation of mud-filtrate invasion, the computation of only a single snapshot of near-borehole conductivities is necessary to simulate the induction logging measurements.

4.3.3 Brine Conductivity Model

Spatial distributions of brine conductivity at each logging time are computed grid-by-grid using the following transformation from simulated salt concentrations (Zhang et al., 1999)

$$\sigma_w = \left[\left(0.0123 + \frac{3647.5}{C_w^{0.955}} \right) \frac{82}{1.8T + 39} \right]^{-1}, \tag{4.9}$$

where, C_w and T stand for salt concentration in [ppm] and formation temperature in [°C], respectively. As such, the dependency of grid block conductivity on the aqueous phase salt concentration is taken into account. The main assumption underlying the brine conductivity model is the instantaneous temperature equilibrium between invading and in situ aqueous phases.

4.3.4 Simulation of Electromagnetic Induction Logging Measurements

Forward modeling of array induction logging sonde response requires the solution of a frequency-domain electromagnetic induction problem described by the Maxwell's equations formulated for a diffusive electromagnetic field. The basic equations governing the local behavior of the diffusive electromagnetic field, assuming a time-harmonic variation of the form $e^{i\omega t}$, where $i^2 = -1$, ω is angular frequency, and t is time, present in an inhomogeneous, isotropic, and nonmagnetic medium, can be stated as follows:

$$\nabla \times \mathbf{E} + i\omega\mu \mathbf{H} = 0, \tag{4.10}$$

$$\nabla \times \mathbf{H} - \sigma \mathbf{E} = \mathbf{J}. \tag{4.11}$$

Here, $\mathbf{E}$ is the electric field vector, $\mathbf{H}$ is the magnetic field vector, and $\mathbf{J}$ is the external electric current source vector. The symbols $\sigma = \sigma(x, y, z)$ and μ denote the conductivity coefficient and the magnetic permeability, respectively. Consistent with the nature of low frequency electromagnetic induction applications, the displacement current is assumed to

be negligible. Equations (4.10) and (4.11) can be combined into the following equation for electric field **E**,

$$\sigma^{-1}\nabla\times\nabla\times\mathbf{E}+i\omega\mathbf{E}=-i\omega\sigma^{-1}\mathbf{J}. \tag{4.12}$$

For the numerical solution of equation (4.12), a finite difference-based algorithm `SLDMINV` (Druskin et al., 1999) on a set of staggered grid is employed using a Spectral Lanczos Decomposition Method that computes inverse powers of the stiffness matrix to yield multi-frequency simulations of induction tool responses in terms of magnetic field computations. Spatial distributions of conductivity, σ, are computed from fluid-flow simulation results for aqueous phase saturations and salt concentrations at each logging time. Conductivities computed from flow simulations on the 3D cylindrical grid are mapped to the 3D Cartesian grid of `SLDMINV` by means of a robust material-averaging stencil (Moskow et al., 1999). Simulation examples using `SLDMINV` are presented in Figures 4.1 and 4.2. The corresponding array induction logging tool responses are simulated by means of `SLDMINV` for each snapshot in time. Alternatively, for the electromagnetic modeling of induction logging measurements, equations (4.10) and (4.11) are solved using a rapid integro-differential algorithm, `KARID`, which assumes axial symmetry of both medium and impressed source (Tamarchenko and Druskin, 1988).

4.4 SUMMARY

Forward modeling of dual-physics measurements entails coupled simulations of mud-filtrate invasion, wireline formation test measurements, and induction-logging measurements. We utilize efficient three-dimensional finite difference-based algorithms to simulate multi-phase fluid-flow and electromagnetic induction phenomena. Time-

dependent spatial distributions of pressure, saturation, and salt concentration generated during water-base mud-filtrate invasion and a subsequent wireline formation test are modeled as two-phase advective transport of three components, namely, oil/gas, water, and salt. Coupling between two-phase flow and physics of electromagnetic induction is accomplished via Archie's saturation equation. Isothermal salt mixing taking place within the aqueous phase due to the invading and in situ salt concentration contrast is also taken into account by means of a brine conductivity model.

(a)

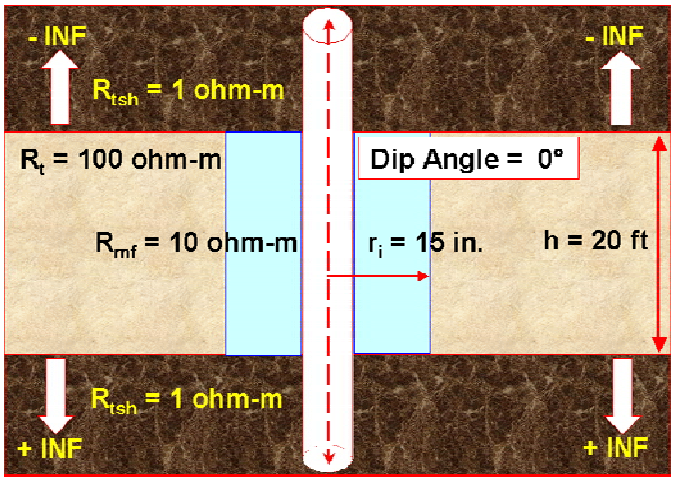

(b)

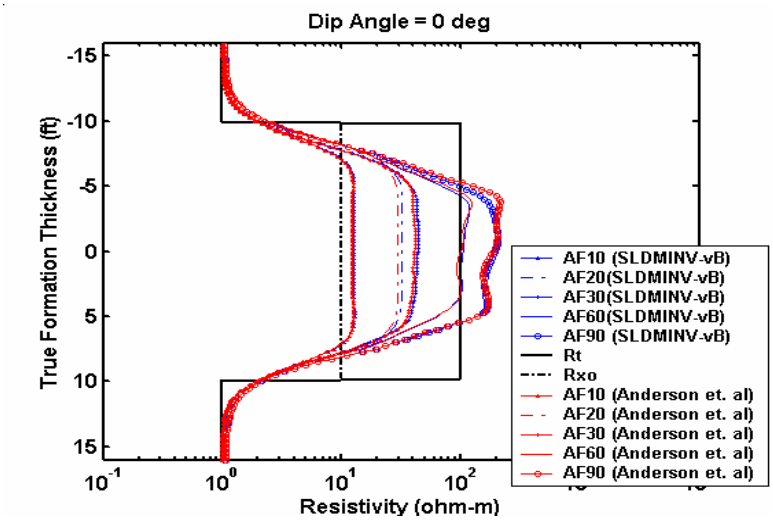

Figure 4.1: SLDMINV validation Case 1: (a) Vertical well test model with invasion. (b) Simulated array induction response obtained using SLDMINV is compared to the response obtained using a 2D semi-analytical model (Anderson et al., 1999).

(a)

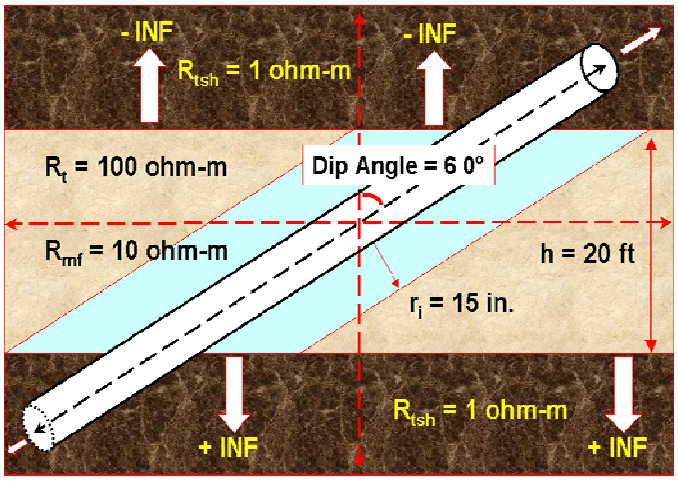

(b)

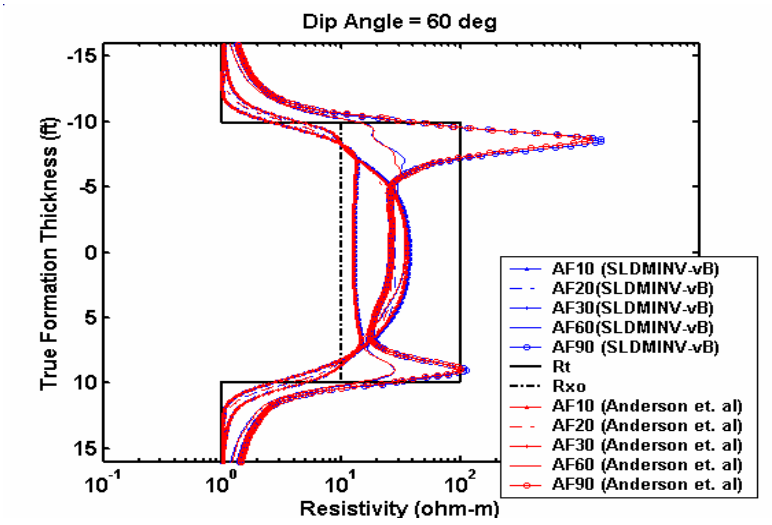

Figure 4.2: `SLDMINV` validation Case 2: (a) Inclined well test model with invasion. (b) Simulated array induction response obtained using `SLDMINV` is compared to the response obtained using an alternative 3D numerical model (Anderson et al., 1999).

PART II: INVERSION OF PERMANENT SENSOR DATA

Chapter 5: Estimation of Axisymmetric Spatial Distributions of Permeability and Porosity from Pressure-Transient Data Acquired with In-Situ Permanent Sensors

5.1 INTRODUCTION

The work described in this chapter appraises the spatial resolution properties of pressure-transient measurements acquired with in-situ permanent sensors. To this end, we consider a hypothetical water injection experiment and make use of an efficient parametric estimation technique adapted from the field of geophysical inverse theory. Our goal is to develop a robust and efficient algorithm to quantify the sensitivity of in-situ permanent sensor pressure-transient data to lateral and vertical variations in the distribution of permeability around the injection well. Inversion is also used to approach the simultaneous quantitative estimation of permeability and porosity.

The inversion algorithm used in this work for the estimation of reservoir parameters from in-situ permanent sensor pressure-transient data is similar to those procedures commonly used in the parametric interpretation of well-test measurements. Similar algorithms have been developed by researchers in an effort to systematically integrate dynamic measurements with static information to characterize hydrocarbon reservoirs.

A chronological list of select papers that describe examples of production-data inversion and dynamic data integration algorithms include: Jacquard and Jain (1965), Carter et al. (1974), Chen et al. (1974), Chavent et al. (1975), Gavalas et al. (1976), Carter et al. (1982), Lee and Seinfeld (1987), Yang et al. (1988), Anterion et al. (1989), Tang et al. (1989), Tan and Kalogerakis (1991), Makhlouf et al. (1993), Oliver (1994),

Bissel (1994), Bissel et al. (1994), Chu et al. (1995a and 1995b), Killough et al. (1995), Oliver et al. (1996), Reynolds et al. (1996), He et al. (1997), Landa and Horne (1997), Wen et al. (1998), Reynolds et al. (1999), Wu et al. (1999), Landa et al. (2000), He et al. (2000), Abacioglu et al. (2001), Li et al. (2001), Wu and Datta-Gupta (2002), Zhang and Reynolds (2002), and Zhang et al. (2003).

We also assess the applicability of the inversion algorithm to the interpretation of actual field data acquired during a field experiment conducted to test the deployment and reliability of pressure, electric, and fiber-optic measurement technologies for permanent reservoir monitoring (Bryant et al., 2002a; Raghuraman and Ramakrishnan, 2001). The spatial distributions of permeability, in some cases estimated simultaneously with porosity, are subsequently compared to core and wireline data.

The inversion algorithm employed in this work is based on a least-squares minimization technique that employs the Weighted and Regularized Gauss-Newton (WRGN) search method. Transient formation pressure measurements are nonlinearly related to variations in the spatial distribution of model parameters. Depending on the specific inversion problem, these model parameters may involve various combinations of spatial distributions of permeability, porosity, and other relevant geometrical model-zonation parameters as well as near-wellbore skin factors. The solution of the inverse problem is approached using a nonlinear fixed-point iteration method. A novel dual finite-difference gridding approach (Torres-Verdín et al., 2000) is implemented to reduce computational overhead. In addition, numerical simulation of in-situ pressure-transient measurements is performed with an efficient modeling code based on an Extended Krylov Subspace Method (EKSM) developed by Alpak et al. (2003c).

5.2 MATHEMATICAL MODEL FOR THE SIMULATION OF IN-SITU PRESSURE-TRANSIENT MEASUREMENTS

We focus our attention to a hypothetical test case in which water is injected from a vertical well into the surrounding oil-saturated rock formations. The assumption is made that the fluid properties of the injected water and the in-situ oil phase are approximately equal to each other to justify the assumption of a single-phase fluid-flow regime. Moreover, for simplicity but without sacrifice of generality, we assume that the spatial distributions of permeability and porosity exhibit azimuthal symmetry around the axis of the well. Permanent in-situ pressure gauges are assumed to be positioned along the well's water injection interval and to remain in direct hydraulic communication with the surrounding rock formations. The specific geometrical model and schematic details of the in-situ pressure-sensor experiment considered in this work are illustrated in Figures 5.1(a) and 5.1(b), respectively. In this work, we assume the availability of special completion designs and installation techniques that allow the deployment of in-situ permanent pressure sensors, similar to that described in Figure 5.1(b), along the open-to-flow sections of injection wells.

We solve the pressure-diffusion equation (3.3) to numerically simulate time-domain measurements acquired with in-situ pressure gauges for specific flow-rate schedules of single-phase fluid injection/production. The numerical computation of pressure is accomplished using a finite-difference formulation in cylindrical coordinates via the Extended Krylov Subspace Method (`EKSM`) (Alpak et al., 2003c). Details of this highly efficient method of solution are given in Chapter 3.

5.3 NONLINEAR INVERSION ALGORITHM

In the context of data acquired with in-situ permanent sensors, the inverse problem consists of estimating an axisymmetric spatial distribution of permeability or,

alternatively, axisymmetric spatial distributions of permeability and porosity, from a finite number of discrete time-domain measurements of transient pressure. Additionally, depending on the specific inverse problem, the unknown model may involve geometrical zonation parameters purposely included to render the solution method more efficient. In such cases, geometrical zonation parameters are chosen to be consistent with the geological properties of the formation of interest. We further assume that the unknown model function can be parameterized with a finite number of values.

Let $\mathbf{x}$ be the size-N vector of unknown parameters that fully describe the axisymmetric distributions of permeability (or permeability and porosity), and $\mathbf{x}_p$ a reference vector of the same size as $\mathbf{x}$ that has been determined from some a-priori information. We undertake the estimation of $\mathbf{x}$ from the measured in-situ permanent sensor pressure-transient data by minimizing the quadratic cost function described by equation (2.3) subject to physical constraints. The minimization problem is solved using the Weighted Regularized Gauss-Newton (`WRGN`) method described in detail in Chapter 2 and Appendix A. The upper and lower bounds enforced on $\mathbf{x}$ are intended to have the iterated solution yield only physically consistent results (e.g. permeability can only take positive values and porosity can only take values between zero and one).

5.4 NUMERICAL EXAMPLES

We first apply the foregoing nonlinear inversion procedure to the estimation of single-phase axisymmetric permeabilities. Data input to the inversion consist of synthetically-generated pressure-transient measurements acquired with in-situ permanent sensors. Following the validation of the inversion algorithm for the estimation of spatial distributions of permeability, we extend our investigations to numerical cases where profiles of permeability and porosity are estimated simultaneously. Several test examples are considered below.

5.4.1 Three-Layer, Six-Block Test Case

In this first test case, we construct a relatively simple reservoir model consisting of three layers and six blocks. The actual axisymmetric permeability distribution around the injection well is shown in Figure 5.2(a). Geometrical and fluid-flow parameters associated with this test case are listed in Table 5.1. Input data, assumed to consist of permanent sensor pressure-transient measurements, are synthetically generated using a single-phase fluid-flow simulator. We investigate two types of flow-rate time schedules (injection/production), namely, (a) a step-function pulse (conventional constant injection rate fall-off test) and (b) a sinusoidal pulse. The associated equations for injection/production flow-rate time schedules are as follows:

$$Step-function\ pulse: \quad q(t) = U(t - t_{shut}) \times q_{inj}, \tag{5.1}$$

where $U(t - t_{shut})$ is the unit step-function, given by

$$U(t - t_{shut}) = \begin{cases} 1 & for \quad t - t_{shut} < 0, \\ 0 & for \quad t - t_{shut} > 0, \end{cases} \tag{5.2}$$

and

$$Sinusoidal\ pulse: \quad q(t) = q_{\max} \times \sin\left[\left(\frac{\pi}{\tau}\right)t\right], \tag{5.3}$$

where $q_{\max}$ is the maximum attainable injection/production rate, and τ is the period of the sinusoidal pulse.

A finite-difference grid of size 105×281 (radial and vertical nodes, respectively) is constructed to perform the numerical simulations and inversions of pressure-transient data following an extensive sensitivity study. This grid, shown in Figure 5.2(b), consists of logarithmic steps in the radial direction and linear steps in the vertical direction within the zone of interest. The grid extends logarithmically into the upper and lower no-flow zones in the vertical direction to ensure the proper asymptotic behavior of the numerical solution. A coarser version of the above-described grid is shown in Figure 5.2(c). This coarse grid, which consists of 54×281 nodes, is used for the computation of auxiliary cost functions that are part of the dual-grid inversion algorithm described in a subsequent section of this chapter. Figures 5.3(a) and 5.3(b) are plots of the simulated pressure-transient data, Δp vs. t, together with the associated flow-rate schedule, q_{sf} vs. t, for step-function and sinusoidal flow-rate pulses, respectively. Notice that for the case of a step-function pulse, pressure-transient measurements are acquired during the shut-in time interval, whereas, for the case of the sinusoidal pulse, pressure-transient measurements are acquired at the same time the flow-rate pulse is taking place. Figure 5.3(b) shows a slight time delay between the pressure response and the injection/production flow-rate pulse. This behavior is consistent with the physics of slightly compressible fluid flow.

5.4.2 Noise-Free Three-Layer, Six-Block Test Case

We simulate pressure-transient data in the form of pressure changes, Δp, with respect to time, t, using a 135 hr long step-function pulse. Such a pulse amounts to 79.49 m^3/d of water injected along the borehole wall. Two alternative sensor-array deployments are considered in this example. In the first case, the measurement array consists of eleven equally-spaced pressure sensors. The second case involves an array of five distributed pressure sensors. In both cases the sensor array is deployed along the 10 m long zone of interest. Lateral boundaries as well as permeability values for each of the assumed six

blocks comprise the set of unknown parameters (a total of nine unknown parameters). Given that all of our model parameters are real and positive, we implement the convenient change of variable $\mu_j = \ln(m_j)$ for $j = 1, \ldots, N$. This change of variable is consistent with the fact that permeability usually exhibits a large degree of variability. Input data are simulated for the two alternative hypothetical sensor deployments. We initialize the inversion algorithm with a uniform permeability field of 5 mD and with radial block boundaries located at a uniform distance of 10 m away from the borehole wall. A plot of the actual permeability field is shown in Figure 5.4(a). This figure describes the permeability values assigned to each of the blocks as well as the radial locations of the corresponding block boundaries. Results for the inversion of noise-free Δp vs. t data simulated for eleven- and five-sensor measurement arrays are shown in Figures 5.4(b) and 5.4(c), respectively. Estimated parameters, namely, permeabilities and block-boundary locations, are within 0.7% of the actual input parameters. Post-inversion pressure-transient data corresponding to the above described inversion examples are shown in Figures 5.5(a) and 5.5(b) for the eleven- and five-sensor array configurations, respectively.

In the next numerical example, we repeat the inversion exercise described above assuming a sinusoidal flow-rate pulse such as the one described by equation (5.3) with a period, τ, of 60 hr, and a maximum injection rate of 79.49 m^3/d (q_{max}). The time interval for the pressure-transient measurements is chosen to be the same as in the previous case, i.e., 120 hr. Figures 5.4(d) and 5.4(e) summarize the results obtained for this second inversion exercise. It is observed that the inverted model parameters are all within 0.75% of the original values for all the inversions performed assuming a sinusoidal flow-rate pulse. Post-inversion pressure-transient data corresponding to the above described

inversion examples are shown in Figures 5.5(c) and 5.5(d) for the eleven- and five-sensor array configurations, respectively.

5.4.3 Noisy Three-Layer, Six-Block Test Case

In this inversion exercise, the objective is to assess the influence of noisy measurements on the inverted model parameters. We contaminate the simulated pressure-transient data with various amounts of additive random noise. Noise was synthesized numerically with a zero-mean Gaussian random number generator of standard deviation equal to a given percentage of the pressure-change amplitude. For reference, we consider the same three-layer, six-block model described in the previous example. A sinusoidal pulse is chosen for the flow-rate function and we examine deployments with eleven and twenty-three sensors evenly spaced along the well's injection interval. A plot of the actual permeability field is shown in Figure 5.6(a). Figure 5.6(b) describes the first set of inversion results obtained with an array of eleven pressure sensors and data contaminated with 1% random Gaussian additive noise. Pressure-transient measurements are acquired during a time interval of 120 hr. We notice that inverted parameters corresponding to blocks located away from the borehole are the most severely affected by the presence of noise. On the other hand, model parameters associated with near-borehole blocks remain relatively unscathed by the presence of noise.

A second test is conducted to assess the effect of sensor spacing and number of sensors in the inverted model parameters assuming data contaminated with several levels of noise. Pressure-transient data are simulated for a relatively dense array consisting of twenty-three in-situ permanent pressure sensors. Two of these sensors are positioned 0.5 m above and below the zone of interest, respectively, to enhance the sensitivity of pressure-transient data to upper and lower reservoir boundaries. Figure 5.6(c) describes the inversion results for the case of Δp vs. t input data contaminated with 1% Gaussian

random additive noise. Figures 5.6(d) and 5.6(e), on the other hand, show the model parameters inverted from pressure-transient data contaminated with 2% and 5% Gaussian random noise, respectively. As expected, the quality of the inversions degrades with increasing levels of noise in the input data. The largest relative errors in the estimated model parameters correspond to 1.2% and 2.5% for the cases of 2% and 5% Gaussian random additive noise, respectively.

5.4.4 Analysis of Inversion Results for the Three-Layer, Six-Block Test Case

In general, our study shows that for a reservoir model consisting of large variations of permeability in lateral and vertical directions, near-borehole parameters can be robustly estimated even in the presence of noisy measurements. Conversely, parameters corresponding to model features located away from the borehole remain adversely affected by even relatively small amounts of noise. This behavior is consistent with the diffusive nature of fluid pressure governed by single-phase flow in porous media, and there is practically little one can do about it. Measurement redundancy only partially helps to mitigate the deleterious effect of noise.

In the case of noisy measurements, the possibility also exists that the inversion be rendered unstable. A way to prevent such instability is to include a regularization term in the minimization of the cost function. This is accomplished by setting the matrix $\mathbf{W}_x^T \cdot \mathbf{W}_x$ in equation (2.32) equal to a unity diagonal matrix. The Lagrange multiplier, $\lambda = 1/\mu$, in equation (2.3) then takes the role of a regularization constant. For the inversions presented in this chapter, we have used a nonzero value of λ only in the cases of noisy pressure-transient measurements, and have set it to be a small percentage of the ratio between the largest and smallest eigenvalues of the matrix $\mathbf{J}^T(\mathbf{x}_k) \cdot \mathbf{W}_d^T \cdot \mathbf{W}_d \cdot \mathbf{J}(\mathbf{x}_k)$ in equation (2.32). The value of this percentage was chosen in proportion to the estimated noise level.

5.4.5 Twenty-Block Permeability Bank Test Case

We consider a relatively more complex test case as part of the assessment of in-situ permanent sensor pressure-transient measurements. This test case, shown in Figure 5.7(a), and described in Table 5.1, consists of twenty radial permeability blocks within the same vertical layer. In-situ permanent sensor pressure-transient data are simulated for this model assuming an injection flow-rate in the form of a 135 hr step-function. A uniform permeability value of 5 mD is assigned to all of the blocks to initialize the inversions. The sensor deployment consists of only one pressure gauge located at the mid-point of the vertical zone of interest. In this case, the inversion is formulated to render estimates of the twenty unknown permeability values. Figure 5.7(b) describes the inversion results for noise-free pressure-transient data. The inverted permeabilities are all within 0.65% of the original values.

5.4.6 Dual-Grid Inversion Technique Applied to the Three-Layer, Six-Block Formation

We implement a novel dual-grid strategy to reduce computer execution times associated with the inversion of a large number of unknown parameters. Details of the dual-grid nonlinear inversion technique are discussed extensively by Torres-Verdín et al. (2000) and described in Chapter2. A subset (54×281 nodes) of the fine finite-difference grid (105×281 nodes) is constructed to perform the dual-grid inversions. This coarse grid is shown in Figure 5.2(c). Minimization is performed solely on the coarse finite-difference grid, including computations of the Jacobian matrix. The fine grid is used only to perform periodic checks of the fit between numerically simulated and measured data.

Figure 5.8(a) describes the route to convergence of the dual-grid inversion procedure used to obtain the permeability model shown in Figure 5.8(b). All of the inverted model parameters are within 0.55% of the original values. In Figure 5.8(a), the

relative data misfit is plotted as a function of the number of data misfit evaluations. We compute the relative data misfit using the formula, namely,

$$\frac{\left\| \mathbf{W}_d \cdot [\mathbf{d}(\mathbf{x}) - \mathbf{d}^{obs}] \right\|^2}{\left\| \mathbf{W}_d \cdot \mathbf{d}^{obs} \right\|^2}, \tag{5.4}$$

which leads to $\mathbf{W}_d^T \cdot \mathbf{W}_d$, which, in turn, is a diagonal matrix with elements equal to the inverse of the measurement times the standard deviation of the noise. For the noise-free cases, $\mathbf{W}_d^T \cdot \mathbf{W}_d$ is set to a diagonal matrix with elements equal to the inverse of the measurement. In Figure 5.8(a) (left panel), the nonlinear inversion is completed with only five calls to the forward-modeling code implemented on the fine grid (105×281 nodes). Figure 5.8(a) (right panel) is a plot of the data misfit with respect to the iteration number within one of the successive auxiliary minimizations carried out on the coarse finite-difference grid (54×281 nodes). On the other hand, Figure 5.8(c) is a plot of the relative data misfit as a function of iteration number evaluated with the conventional single-grid (105×281 nodes) inversion approach used to obtain the permeability model shown in Figure 5.8(d). Table 5.2 shows a comparison of central processing unit (CPU) execution times required by the inversions performed with and without the dual-grid minimization approach. In this particular problem, the dual-grid inversion technique provides approximately a 2.8 fold reduction in CPU execution time with respect to the standard procedure. A comparison of the routes to convergence in the single- and dual-grid cases, shown in Figures 5.8(a) and 5.8(c), indicates a faster reduction of residuals as a function of iteration number for the dual-grid algorithm. This behavior is consistent with the CPU execution times described in Table 5.2.

5.4.7 Discussion on the Results of Additional Numerical Experiments

In addition to the numerical experiments described above, we performed several inversions of in-situ transient-pressure measurements using both step-function and sinusoidal pulse rate-schedules, including various levels of measurement-noise. Results of these numerical experiments helped us to develop some basic insights about the sensitivity of the data to model perturbations. As one of the significant points of that study, it was found that for relatively high levels of noise contamination, pressure data acquired in response to sinusoidal rate transients lent themselves to more accurate and stable reconstructions of the spatial distribution of permeability in comparison to pressure data acquired in response to a single step-function pulse of flow rate. It was also found that, for a step-function pulse of flow rate, the use of a repeated series of rate transients consistently improved the spatial resolution of the inverted distributions. A general conclusion from this study is that transient-pressure data acquired concomitantly with time variations of flow rates exhibited more sensitivity to spatial distributions of permeability and porosity, even in the presence of significant amounts of noise.

5.4.8 Assessment of the Vertical Resolution of In-Situ Permanent Sensor Pressure Transients Generated in Consistence with the Petrophysical Characterization of a Waterflood Volume in Mansfield Sandstone Reservoir

In 1999, a field experiment was conducted to test the feasibility and reliability of pressure, DC resistivity, and fiber optic measurements for permanent reservoir monitoring (Raghuraman and Ramakrishnan, 2001; Bryant et al., 2002a). In this experiment, two wells were drilled into the Mansfield sandstone reservoir to a depth of approximately 305 m in the Ashworth lease, Indiana, onshore USA. The principal objective of the experiment was to demonstrate the feasibility of monitoring water-front movement between an injection and an observation well. Bryant et al. (2002a) describe results and interpretation of the cemented resistivity array data and show how the

movement of the fluid front could be tracked at the injector well. Raghuraman and Ramakrishnan (2001) focus their interpretation work on the measurements acquired with a cemented in-situ permanent pressure gauge along the observation well. They also perform a sensitivity analysis of "continuous interference testing" to improve the spatial and petrophysical description of the reservoir. Raghuraman and Ramakrishnan's (2001) work clearly demonstrates the advantage of combining permanent sensor electrical resistivity and pressure data to reduce uncertainty in the estimation of reservoir petrophysical properties.

In this section of the chapter, we consider the inversion of pressure-transient measurements acquired with cemented in-situ permanent pressure sensors assuming a hypothetical deployment in the same reservoir volume described by Raghuraman and Ramakrishnan (2001). The objective is to assess vertical resolution properties of in-situ permanent sensors. We consider inversions of pressure-transient data acquired with various configurations of sensors deployed along the injection well, IW, and along the observation well, OW, both independently and jointly. For each sensor configuration, we make use of numerically simulated in-situ pressure-transient measurements to estimate spatial distributions of permeability. We also investigate cases where spatial distributions of permeability and porosity are subject to simultaneous quantitative estimation. In addition to noise-free measurement data, we consider more realistic in-situ pressure-sensor measurements contaminated with various levels of zero-mean Gaussian random noise.

A top view of the reservoir volume of interest is shown in Figure 5.9(a). The reservoir volume is enclosed by a square five-spot well pattern. The injector well, IW, is located in the center of four existing development wells, namely, PW1, PW2, PW3, and PW4. On the other hand, the monitoring well, OW, is offset 71 m between the injector

well and one of the development wells. In the actual field test, only one in-situ permanent pressure gauge was cemented behind casing in the well, OW, closer to the bottom of the reservoir. We assume that injection rate information is recorded at the injection well in a synchronized fashion with in-situ pressure measurements. In our numerical test cases, deployment of in-situ permanent pressure sensors is considered in both the injection well, IW, and the observation well, OW. In addition to joint inversions of data acquired in both wells, we perform independent inversions of single-well measurements.

For the forward modeling of measurements, a 2D axisymmetric cylindrical reservoir model is constructed with an equivalent reservoir volume to that of the waterflood cube. Here, we first assume that the waterflood pattern is confined within no-flow boundaries. This assumption leads to a rectangular reservoir volume with closed outer boundaries. Assuming a rectangular coordinate system with its origin located at the center of the volume, the vertices of the isolated reservoir section are given by the couplets $[x_1, x_2] = [-L/2, L/2]$, $[y_1, y_2] = [-L/2, L/2]$, and $[z_1, z_2] = [-h/2, h/2]$. Consistent with the assumption of 2D axisymmetric geometrical support for the solution of the partial differential equation (PDE) in equation (3.3), we replace the rectangular reservoir volume with a cylindrical spatial support of equivalent volume such that the location of the external boundary is given by $r_e = \sqrt{L^2 \pi} = 107.11$ m [see Figure 5.9(a)]. The latter assumption is a physically valid approximation to otherwise complex boundary conditions. This assumption also implicitly stipulates that the production rate at each of the wells PW1, PW2, PW3, and PW4 are approximately equivalent to the injection rate at well IW.

A fine grid of size 134×183 and a coarse subset of this grid of size 69×183 in the radial and vertical directions, respectively, are constructed to perform fast dual-grid inversions of the in-situ pressure-transient data. The main features of these grids are

similar to the ones shown in the set of simulation grids displayed in Figures 5.2(b) and 5.2(c). Simulations for a uniform permeability and porosity formation indicate that the pressure responses of fine and coarse grids agree within 2% of each other.

For the forward modeling of in-situ pressure-transient measurements, we also assume that one can approximately compute the pressure response of two-phase displacement phenomena governing the waterflood using the single-phase pressure-diffusion model described by equation (3.3). Consistent with the above approximation, we make use of saturation-averaged fluid PVT properties. The proximity of the values of water and oil fluid properties in this case constitutes the physical basis for the validity of the approximation. Saturation-averaged single-phase fluid parameters associated with this case are shown in Table 5.3 along with other relevant reservoir parameters.

Core- and log-based petrophysical evaluation of the Mansfield sandstone reservoir in the well IW was previously published by Bryant et al. (2002a). Based on the information provided by Bryant et al. (2002a), we constructed vertical profiles of permeability and porosity at well IW as shown in Figure 5.9(b). In this plot, core data are displayed along with the core- and log-based one-dimensional (1D) interpretations of vertical distributions of permeability and porosity. The value of the volumetric-average porosity is superimposed to the porosity profile. For the reservoir volume of interest mentioned above, we assume that 1D vertical variation of permeability and porosity adequately describes petrophysical heterogeneities. Vertical cross-sections of the corresponding 1D reservoir model are shown in terms of the spatial distribution of permeability in Figure 5.10(a), and of porosity in Figure 5.10(b). The locations of the injection well, IW, and observation well, OW, are clearly marked in these figures. Inversions performed for various sensor configurations and model domain assumptions are described below.

Case A: Figure 5.11(a) displays vertical locations of in-situ permanent pressure sensors with respect to 1D permeability and porosity profiles considered for this case. Superimposed plots of pressure and injection rate as a function of time for the injection well, IW, are shown in Figure 5.11(b). Figure 5.11(c) displays superimposed plots of pressure and injection rate as a function of time for the observation well, OW. In this case, we regard the layer-by-layer porosities as a-priori information for the inversions. Locations of layer boundaries remain fixed and are chosen based on the wireline and core data. Vertical locations of five in-situ permanent pressure sensors are selected according to the available layer-boundary location information. Pressure-transient data are simulated for in-situ pressure sensors installed at the injection well, IW, and at the observation well, OW. Subsequently, in-situ pressure-transient data simulated for the acquisition at IW and OW are entered to the inversion, both independently and jointly.

In the nonlinear inversions, we make use of a two-level inversion strategy. We first invert the measurement data for a homogeneous reservoir permeability model. The initial guess for the homogeneous permeability does not assume a-priori information and is chosen to be 7 mD. For the case of porosity, we stipulate the value of volume-averaged porosity, shown in Figure 5.9(b), for the homogeneous reservoir. In our inversion algorithm, nonlinear iterations are allowed to proceed until the normalized misfit is reduced to the level of the standard deviation of noise or until subsequent iterations do not cause any significant change in the inverted homogeneous permeability. For those cases in which a homogenous permeability model entails a reduction of data misfit to the noise level, we conclude that the measurements lack the necessary degrees of freedom to resolve finer features of the model such as those of thin horizontal layers. Beyond this point the addition of spatial structure to the model will only serve to fit the measurement noise. For the cases where the inversion of a homogeneous permeability model is

concluded with a data misfit level above the noise level, the seven-layer model is initialized with the inverted homogeneous permeability value. Nonlinear inversions are performed with the seven-layer structure until the misfit is reduced to the level of the standard deviation of the noise, i.e., $\chi = \sigma_{noise}$. In the hypothetical cases of noise-free data, we set $\chi = 1.0 \times 10^{-5}$.

Comparisons of the inverted seven-layer (1D) permeability profiles with respect to the actual seven-layer permeability model for the Mansfield-sandstone reservoir volume are shown in Figures 5.11(d), 5.11(e), and 5.11(f). Inversion results are shown in Figure 5.11(d) for the case of noise-free measurements. Figures 5.11(e) and 5.11(f), on the other hand, display inversion results for the cases where the measurement data are contaminated with 2% and 5% zero-mean Gaussian random noise, respectively. Vertical locations of the in-situ sensors are indicated with small circles on the profiles of inverted permeability.

Analysis of Case A: Given the sensor configuration designed on the basis of layer-boundary locations and assisted with layer-by-layer porosities in Case A, the inverted permeability profile compares very well to the original profile when performing the inversion with only noise-free IW sensor data. The same conclusion holds for the joint inversion of noise-free IW & OW sensor data. However, for the noise-free inversion of OW sensor data, some inaccuracies are apparent in the inverted profile of permeability. When the level of measurement noise increases, the permeability profiles inverted with IW data and IW & OW data still remain very close to the original permeability profile for relatively thick layers. For the inversion of IW and IW & OW measurements, the inverted permeability profile monotonically deteriorates with increasing levels of noise. This observation holds particularly for the permeability of thin layers and for the permeability of layers that are most distant to a sensor. In general,

inversions performed with IW & OW data yield slightly more accurate permeability profiles than those obtained with the inversion of IW data.

Inversions performed with noisy OW data are very peculiar. For these cases, a homogeneous permeability model is sufficient to reduce the data misfit to the level of the standard deviation of noise. Hence, OW measurements contaminated with 2% and 5% noise lack the degrees of freedom necessary to resolve the seven-layer vertical structure of the actual permeability profile. On the other hand, the inversion of noise-free OW data yields an approximation of the original permeability model.

The relatively low spatial resolution of OW data in comparison to IW data does not come as a surprise when one visually inspects the noise-free measurements shown Figures 5.11(b) and 5.11(c) simulated for wells IW and OW, respectively. In Figure 5.11(c), all the sensors deployed along OW indicate a similar time-record of pressure. There are many possible spatial distributions of permeability that fit the same OW in-situ sensor data. One such spatial distribution is the seven-layer permeability model shown in Figure 5.11(d). Pressure transients due to the injection source-condition at the open flow intervals of each reservoir layer penetrated by IW equilibrate to an average pressure in the vicinity of the observation well, OW. This phenomenon is due to hydraulic communication among reservoir layers. Consequently, in-situ pressure responses measured at the observation well remain sensitive only to average medium properties. If the porous medium consisted of two non-communicating flow units, one would expect that in-situ pressure-sensor measurements performed in well OW would remain sensitive to spatial variations of permeability. For an array of in-situ pressure sensors in well OW (Case A), a homogeneous permeability model remains the highest spatial complexity in the permeability distributions that can be resolved from the noisy measurements. Having reached the above conclusions on the very limited spatial resolution available from in-situ

pressure-transient data acquired in well OW, for the cases investigated subsequent to Case A, we did not consider additional inversion examples that include the exclusive use of data acquired in well OW. In-situ pressure-transient measurements acquired in well OW are only used in conjunction with measurements acquired in well IW to further constrain the inversions.

Case B: In this case, sensor configuration, measurement schedule, and inversion strategy remain the same as the ones in Case A. We assume that instead of layer-by-layer porosities, only the volumetric-average value of the porosity is known. This average porosity value, shown in Figure 5.9(b), is stipulated for each layer in the inversions. First, only injection well, IW, in-situ pressure-sensor data are input to the inversion. Next, we consider the joint inversion of simultaneously measured pressure-transient data acquired with in-situ pressure sensors at the injection well, IW, and at the observation well, OW.

Comparisons of the inverted seven-layer (1D) permeability profiles with respect to the actual seven-layer permeability model for the Mansfield-sandstone reservoir volume are shown in Figures 5.12(a), 5.12(b), and 5.12(c). Inversion results are shown in Figure 5.12(a) for the case of noise-free measurements. Figures 5.12(b) and 5.12(c), on the other hand, display inversion results for the cases where measurement data are contaminated with 2% and 5% zero-mean Gaussian random noise, respectively.

Analysis of Case B: Conclusions drawn for Case A about the inversions of IW data and IW & OW data remain valid for Case B. In comparison to Case A, in Case B we observe a slight general deterioration of the inverted profile of permeability. This slight deterioration is more apparent for thin layers and for layers located away from the nearest sensor location. Yet, the main features of the permeability profile are recovered even in the presence of 5% measurement noise.

Case C: We consider a symmetric five-sensor array of in-situ permanent pressure sensors. Layer-boundary information is assumed to be decoupled from design of the in-situ sensor array. Everything else about this inversion case remains the same as in Case B. Similar to the previous case, IW in-situ pressure-sensor data are inverted in an independent fashion from OW data. For the purpose of comparison, we also perform joint inversions pressure-transient data acquired with in-situ pressure sensors simultaneously at the wells IW and OW.

Figure 5.13(a) displays vertical locations of in-situ permanent pressure sensors with respect to the 1D permeability and porosity profiles considered for this case. Superimposed plots of pressure and injection rate as a function of time for the injection well, IW, are shown in Figure 5.13(b). Figure 5.13(c) displays superimposed plots of pressure and injection rate as a function of time for the observation well, OW. Comparisons of the inverted seven-layer (1D) permeability profiles with respect to the actual seven-layer permeability model for the Mansfield-sandstone reservoir volume are shown in Figures 5.13(d), 5.13(e), and 5.13(f). Inversion results are shown in Figure 5.13(d) for the case of noise-free measurements. Figures 5.13(e) and 5.13(f), on the other hand, display inversion results for the cases where the measurements were contaminated with 2% and 5% zero-mean Gaussian random noise, respectively.

Analysis of Case C: A symmetric array of five pressure sensors is considered in this case in lieu of an array in which vertical locations for the sensors are selected on the basis of layer boundaries (Cases A and B). There are minimal differences between inversion results obtained with noise-free measurements for Cases B and C. However, in Case C, permeability profiles obtained from inversions of noisy data are negatively affected by the introduction of a symmetric in-situ pressure array. Here, the in-situ sensor array is designed independent of the unknown permeability model. Therefore, errors in

the inverted model increase especially for thin layers and for layers located relatively farther from the nearest sensor. In Case C, inversions of IW data remain in general slightly more accurate in comparison to the joint inversions of IW & OW data. Estimations of the permeability profile are quite accurate for measurements contaminated with 2% noise. Yet, for the case of 5% measurement noise, the estimated permeabilities for thin layers and for layers located relatively far away from the nearest sensor deteriorate significantly.

Case D: Simultaneous inversions of 1D permeability and porosity profiles are performed for the same sensor configuration and spatial-model structure described for Case C. For the inversion of a homogeneous formation model, we assume 7 mD and 0.05 (fraction) as the initial guesses for homogeneous permeability and porosity, respectively. Comparisons of the inverted seven-layer permeability profiles with respect to the actual seven-layer permeability model for the Mansfield-sandstone reservoir volume are shown in Figures 5.14(a), 5.14(b), and 5.14(c). Similarly, comparisons of the inverted seven-layer porosity profiles with respect to the actual seven-layer porosity model are shown in Figures 5.14(d), 5.14(e), and 5.14(f). Inversion results are shown in Figures 5.14(a) and 5.14(d) for the case of noise-free measurement data. Figures 5.14(b) and 5.14(e), on the other hand, display inversion results for the case where measurement data were contaminated with 2% zero-mean Gaussian random noise. Inversion results for the case where measurement data were contaminated with 5% zero-mean Gaussian random noise are shown in Figures 5.14(c) and 5.14(f).

Analysis of Case D: Simultaneous inversion of 1D permeability and porosity profiles yields accurate results in the presence of noise-free in-situ permanent pressure sensor data. When compared to inversion results obtained for the case where the volumetric-average porosity is known (Case C), inversions of noisy measurements yield

slightly more inaccurate results. However, it is observed that estimation errors increase significantly for permeability and porosity values associated with relatively thin layers. For example, at 2% noise level, the comparison of the inversion results shown in Figures 5.13(b) and 5.14(b) indicate that the estimation of permeabilities for the fifth and sixth layers (from the top to bottom) is highly inaccurate in Case D in comparison to Case C. At 5% noise level, the same features cannot be resolved for both Cases C and D. Estimations of permeability and porosity values associated with thick layers do not exhibit much difference for Cases C and D.

The simultaneously inverted porosity profile appears to be more sensitive to the deleterious effect of noise in comparison to the permeability profile. Porosity estimates become more inaccurate with increasing levels of measurement-noise. Likewise, inverted porosity values remain relatively closer to the actual porosity values for thick layers in comparison to thin layers.

Even though porosity profiles are affected by the presence of noise, the inverted permeability profiles are relatively less sensitive to the presence of noise. We conclude that in-situ permanent sensor pressure-transient measurements are primarily sensitive to local spatial distribution of permeability. Their sensitivity to porosity remains of secondary order. For all of the inversion exercises considered in Case D, use of either IW or IW & OW data together does not have a significant impact on the inverted profiles of permeability and/or porosity.

Case E: In this case, we replace the symmetric five-sensor in-situ permanent pressure-sensor array configuration of Case D with a symmetric three-sensor array. Comparisons of the inverted seven-layer permeability profiles with respect to the actual seven-layer permeability model are shown in Figures 5.15(a), 5.15(b), and 5.15(c). Similarly, comparisons of the inverted seven-layer porosity profiles with respect to the

actual seven-layer porosity model are shown in Figures 5.15(d), 5.15(e), and 5.15(f). Inversion results are shown in Figures 5.15(a) and 5.15(d) for the case of noise-free measurements. On the other hand, Figures 5.15(b) and 5.15(e) display inversion results for the case where the measurements are contaminated with 2% zero-mean Gaussian random noise. Inversion results for the case where measurements are contaminated with 5% zero-mean Gaussian random noise are shown in Figures 5.15(c) and 5.15(f).

Analysis of Case E: In general, inversions performed with noise-free data yield equally accurate permeability and porosity values with respect to those obtained with noise-free data in Case D. Inversions performed with noisy data, however, increasingly depart from the original model profiles. Also, in general, inversions performed with noisy data exhibit a significant departure from the actual profiles for both permeability and porosity. Finally, when inversion results of Case E are compared to the ones obtained in Case D, it was found that a reduction in the number of sensors consistently reduced the number of degrees of freedom available in the input data to accurately estimate the profiles of permeability and porosity.

5.5 DISCUSSION ON THE UNDERLYING ASSUMPTIONS OF THE INVERSION

In order to provide a quantitative basis of comparison and appraisal of the numerical exercises of inversion, in this work, we have made several simplifying assumptions. Flow rates are in general known at surface conditions. Moreover, sandface flow-rate data may involve rate transients due to wellbore storage in injection wells. Rate transients due to wellbore storage effects may also occur in production wells. In such cases, rate transients will be present in surface flow-rate information. In the numerical inversion exercises described in this work, we assume that flow rates are accurately known at sandface conditions, and that flow-rate schedules are devoid of transients caused by the compression/expansion of fluids in the wellbore. The latter assumption

renders wellbore storage effects nonexistent. Moreover, given that, by definition, permanent sensor pressure-transient measurements are acquired within the formation of interest rather than at the surface, wellbore storage effects are irrelevant on transient-pressure measurements performed with in-situ pressure-sensor hardware. One critical point here is the assumption of knowledge of sandface flow rate data, which in turn is used a-priori for the inversion. In the absence of a downhole flowmeter that can accurately measure sandface flow-rate data, one can resort to surface flow-rate information. In such cases, consistent modeling of measurements requires knowledge of governing parameters of the physics of wellbore storage. As shown in equation (3.46b), the EKSM forward modeling algorithm can be readily modified to make use of surface flow-rate measurements. On the other hand, uncertainty in wellbore storage parameters can be quantified by performing a set of inversions of in-situ pressure-transient measurements using the most probable flow-rate schedules and by subsequently performing a statistical analysis of the inversion results.

Although in this work we did not quantitatively investigate a case where one or more flow units exhibited transversely anisotropic permeability, the inversion algorithm can be readily used to perform parametric inversions of vertical as well as horizontal permeabilities. In fact, the inversion and simulation algorithms are formulated in a sufficiently general manner to estimate the horizontal and vertical permeabilities of rock formations that exhibit transverse permeability anisotropy. The key issue for such inversion exercises would be the design of an optimal sensor deployment to maximize information about vertical and horizontal permeabilities borne by in-situ transient-pressure measurements.

The formulation adopted in this work for the simulation of in-situ permanent pressure measurements quantitatively incorporates the effect of skin factor (see,

equations (3.46a) and (3.46b)). However, for the numerical examples investigated in this work, we assume that the in-situ pressure measurements are not affected by skin. The rationale underlying this assumption is explained as follows: We assume that the well is fully-penetrating, that flow rates are sufficiently low to curb turbulence effects in the near-wellbore region, and that hydraulic communication between the formation and each of the pressure-sensors is established via shaped charges that can perforate a hydraulic conduit beyond the depth of the original skin layer (due to both mud-filtrate invasion and drilling-induced formation damage). We also assume that skin caused by the shaped charges themselves is negligible.

For cases in which the above assumptions do not hold, an approximate estimate of the skin factor can be used while performing the inversion. An alternative approach would be to add a skin factor parameter to the set of inverted parameters and to perform inversions of not only permeabilities but also of the skin factor.

The mathematical model assumed by the inversion algorithm described in this work was developed for reservoirs that approximately satisfy the requirements of a 2D axisymmetric geometry, transverse permeability anisotropy, single-phase flow, and no-flow outer boundary conditions. Depending on the complexity of the problem of interest, more generic three-dimensional and multi-phase flow reservoir models could be interfaced with the inversion algorithm.

On a different note, in the proof-of-concept numerical examples described in this work, we assume that the thicknesses of layers describing the formation of interest are known a-priori. Because of this assumption, other than absolute permeabilities, block-boundary locations were the only type of variable subject to inversion for the case of a three-layer, six-block reservoir. Remaining cases, however, did not involve the inversion of any type of zonation parameter concerning the model's geometrical properties. Rather,

these inversion exercises were exclusively focused to the reconstruction of permeability values. Moreover, in all of the investigated cases, the inversion was concluded with the successful satisfaction of the goodness-of-fit criterion, i.e. χ^2. The reason for using such an approach is as follows: In general, when working with real data sets, the goal is to invert a countable set of parameters that together define the unknown model. For example, let us assume that the unknown true model is a three-layer, six-block reservoir (as in the first case analyzed in this work). If a three-layer model, or a single-layer model with skin heterogeneity, or a single-layer model with a fracture were assumed instead, the measure of goodness-of-fit could be used as a quantitative indicator to rank possible model scenarios. Accordingly, in the numerical examples analyzed in this work, we first attempted to match the measurements with a single-layer, zero-skin medium. None of the estimated single-layer models satisfied the goodness-of-fit criterion. Yet, we observed that the corresponding model yielded an average permeability approximately equal to the volumetric mean of all the block permeabilities. This strategy indicates that preliminary single-layer inversion results provide a good, unbiased initial guess for subsequent, spatially more complex inversions. At this point, however, instead of quantifying multiple reservoir model scenarios and ranking them on the basis of a goodness-of-fit indicator, we assumed the availability of a-priori information about the layer-thicknesses.

5.6 INVERSION OF FIELD DATA

We now apply the inversion technique described above to the interpretation of actual transient-pressure data acquired during the Mansfield oilfield experiment. Details of this experiment are described in Section 5.4.8. The monitoring well was instrumented with a cemented formation pressure gauge. Flow rate and pressure data at the injection well were recorded continuously in addition to the continuous acquisition of data from a cemented sensor. To approach the interpretation of the Mansfield reservoir data, we

assume that one can approximately compute the pressure response of two-phase waterflood displacement with the single-phase pressure-diffusion model described by equation (3.3). Accordingly, we make use of saturation-averaged fluid PVT properties. Saturation-averaged single-phase fluid parameters associated with this case are shown in Table 5.3 along with other relevant reservoir parameters.

Figure 5.16(a) shows the complete time-records of pressure acquired in the injection and observation wells in response to the injection rate schedule shown in Figure 5.16(b). During the course of the experiment, the reservoir volume between the injection and the observation well was diagnosed to be hydraulically fractured (Raghuraman and Ramakrishnan, 2001). It was concluded that abnormally low reservoir pressure was responsible for the development of a horizontal fracture. From the interpretation of the sensor data it was found that the horizontal fracture acted as a hydraulic conduit between the injection and observation wells (Raghuraman and Ramakrishnan, 2001). Given that the fluid flow model described in this work was developed to simulate slightly compressible Darcy flow in porous media, we only make use of the pressure record acquired before the onset of hydraulic fracturing (a 400 hr record) to estimate the corresponding spatial distribution of permeability. In this time interval, pressure data were acquired in response to a fairly constant injection rate of 3.18 m^3/d.

As seen in Figure 5.16(a), during the time interval of interest, pressure in the observation well decreases even though injection of water continues undisturbed in the injection well. This behavior is not consistent with the physics of fluid flow in permeable media unless there is a permeability barrier blocking the hydraulic communication between the two wells. However, it was reported during the experiment that a leak in the hydraulic isolation of the cemented gauge caused the zone around the cemented gauge to over-pressurize and eventually to release a sudden pressure pulse recorded by the in-situ

pressure gauges. From Figures 5.16(a) and 5.16(b) it is clear that the gauge signal responded to rate transients but the time at which the gauge started reading the formation pressure is not obvious. By contrast, wellbore-pressure and rate measurements in the injection well remained consistent with the time behavior of an injection experiment. This observation led us to concentrate our inversion work exclusively on the time-record of wellbore pressure and flow rate measured at the injection well.

Prior to inverting the measured field data, we performed an extensive sensitivity study that involved various degrees of complexity in the assumed reservoir models, i.e., cylindrical vs. Cartesian, single-phase vs. two-phase, etc. This sensitivity study indicated that measurements acquired at the injection well were consistent with the assumptions of the forward modeling algorithm only between the 235^{th} and the 380^{th} hour of the pressure time-record. This observation led us to consider only data acquired during that time interval to be suitable for inversion.

An analysis of the pressure data acquired in the injection well indicated negligible wellbore storage effects. The time-record of pressure measurements was first subjected to inversion to yield a homogeneous model of isotropic reservoir permeability. In this case, we assumed a homogeneous reservoir porosity equal to 0.168 (fraction). Such a porosity value was derived from the volumetric average of the core and wireline data shown in Figure 5.9(b). The inversion yielded a homogeneous reservoir permeability of approximately 6.2 mD. Repeated inversions started from various initial guesses for permeability yielded similar results. However, for all of the inverted homogeneous reservoir models, the measure of goodness-of-fit, χ^2, indicated a poor fit of the measurements. The latter observation is summarized in Figure 5.16(c), where the post-inversion data fit is plotted for one of the homogeneous reservoir cases, thereby corroborating the relatively large data misfit.

For the subsequent inversions we introduced various combinations of unknown model parameters in addition to permeability. More specifically, we investigated the possibility of inverting the well's skin factor, a homogeneous vertical permeability, and a homogeneous reservoir porosity together with the homogeneous reservoir permeability. As shown in Figure 5.16(d), only the simultaneous quantitative estimation of homogeneous and isotropic reservoir permeability and a homogeneous porosity provided an excellent fit to the analyzed portion of the data. Inversion exercises performed with different initial guesses successfully converged toward a reservoir permeability of 23 mD and a porosity of 0.03 (fraction). Although the estimated reservoir permeability is within the range of rock-core and wireline permeability data, the estimated values of reservoir porosity were considerably low when compared to the porosity range of the measured rock-core and wireline data. Next, in order to reconcile the layered model constructed on the basis of the rock-core and wireline data with the pressure time-record under investigation, we performed inversions with the seven-layer reservoir model described in Section 5.4.8. None of the inversions performed for the seven-layer reservoir model and its variations (additional skin and anisotropy factors, etc.) provided an adequate fit to the measurements.

Finally, spatial distributions of unknown permeability, k, as well as unknown porosity, ϕ, were inverted assuming cellular reservoir models. Here, to describe the model domain, we constructed 2D cellular models of size 5×5, 10×10, and 20×20 in the radial and vertical directions, respectively. Preliminary studies suggested that the sensitivity of pressure data to permeability and porosity consistently decreased away from the observation location into the reservoir. Because of this, wellbore-pressure measurements (injection well) remained highly sensitive to spatial variations of porosity and permeability in the near-wellbore region. In keeping with such a behavior, we

designed a cellular mesh for inversion with logarithmic increments in the radial direction away from the injection well. The inversion was performed by constructing a model vector, $\mathbf{x}$, which incorporated cell permeabilities and porosities, namely, $\mathbf{x} = [k_1, k_2, \ldots, k_n, \phi_1, \phi_2, \ldots, \phi_n]^T$, where $n = 5 \times 5,\ 10 \times 10$, and 20×20.

In order to accelerate the multi-parameter inversions, we constructed fine and coarse finite-difference grids to be used in the numerical simulations of pressure. The fine grid consisted of 134×183 nodes in the radial and vertical directions, respectively, whereas the coarse grid was constructed as a subset of the fine grid with 134×99 nodes in the radial and vertical directions, respectively. Numerical simulations performed for a homogeneous permeability and porosity reservoir indicated that the pressure responses of fine and coarse grids agreed within 2% of each other.

We initialized the inversions with a constant average permeability equal to 23 mD obtained from matching the field data to a uniform reservoir and a porosity value of 0.168 (fraction) derived from the core and wireline data shown in Figure 5.9(b). Among the inversions performed using 2D model grids of the sizes described above, only the model reconstruction using a 10×10 mesh produced a fit to the data comparable to that shown in Figure 5.16(d). Inversions performed with 5×5 model grids consistently failed to provide an accurate fit to the measured pressure record. By contrast, inversions performed with a 20×20 model grid over-parameterized the estimation problem and failed to converge within a reasonable number of iterations. Spatial distributions of permeability and porosity inverted simultaneously for the case of a 10×10 grid model are shown in Figures 5.17(a) and 5.17(b), respectively. For a majority of the model cells located in close proximity to the well, the estimated permeability remains within the same value range of the measured rock-core and wireline data. Deeper into the reservoir, however, the estimated values of permeability are relatively large, especially, at the

bottom of the reservoir. In a similar fashion, porosity values estimated in the vicinity of the well are high compared to porosity values estimated farther into the reservoir. In fact, a majority of porosity values estimated in the near-borehole region fall within the range of rock-core and wireline porosities, namely, 0.12 to 0.18 (fraction). However, farther into the reservoir, inverted values of reservoir porosity are considerably lower, of the order of 0.05 (fraction). This result probably explains why the injectivity decreased after 400 hours of water injection rather than relatively earlier in the waterflood experiment. As shown in Figure 5.17(b), the reconstructed spatial distribution of porosity exhibits progressively lower resolution with distance away from the borehole. This feature of the reconstructed porosity model comes as the direct consequence of the loss of sensitivity of wellbore-pressure measurements to spatial variations of porosity located farther away from the borehole. Albeit much less pronounced, the same observation concerning resolution and data sensitivity is made for the reconstruction of the spatial distribution of permeability. The latter result can be attributed to the relatively higher sensitivity of pressure-transient measurements to spatial variations of permeability than to spatial variations of porosity.

5.7 SUMMARY AND CONCLUDING REMARKS

A proof-of-concept was carried out to quantify the sensitivity of in-situ permanent sensor pressure-transient measurements to detecting spatial distributions of permeability. An additional set of numerical examples investigated the possibility of simultaneously inverting permeability and porosity. The study was based on the assumption of a synthetic reservoir model subject to single-phase fluid flow, and on the availability of an array of permanent pressure gauges deployed along a vertical well. It was assumed that the well was subject to water injection and that pressure gauges were positioned in direct hydraulic communication with the surrounding rock formations. Properties of the injected

water and in-situ oil phases were assumed approximately equal to each other in consistency with the assumption of single-phase fluid-flow behavior. For simplicity, we also assumed that the rock formations exhibited azimuthal symmetry around the axis of the injection well. Techniques borrowed from the field of geophysical inverse theory were used to perform the sensitivity study. As part of this work, we introduced an efficient dual-grid approach that substantially reduced computation times required by the inversion algorithm.

Numerical test cases considered in this work indicate that in-situ permanent pressure sensors have the potential of accurately detecting spatial distributions of permeability. This conclusion holds for relatively low levels of measurement noise as well as for the simultaneous estimation of spatial distributions of permeability and porosity. Unlike standard pressure-transient measurements acquired within a borehole, pressure-transient measurements acquired with in-situ sensors are highly sensitive to rock-formation properties as well as to hydraulic communication among formations. A great deal of flexibility in the acquisition system is provided by (a) the location, spacing, and number of permanent sensors, (b) the time sampling schedule of the measurements, and (c) the way in which the injection flow rate is pulsed to produce a perturbation in the pressure field.

The sensitivity studies described in this work also showed that noisy pressure-transient measurements could considerably bias the detection of spatial variations of permeability located far away from the sensor array. This behavior is due to the diffusive nature of the flow of fluids in porous media, and there is hardly anything one can do about it. However, it was found that both sensor redundancy and an appropriate selection of flow-rate schedule (e.g. a low-frequency sinusoidal pulse) could improve the sensitivity of the in-situ pressure array to permeability variations located far away from

the borehole wall. Numerical experiments of inversion described in this work also indicate that pressure sensors located along the injection well provide higher spatial resolution in the estimation of permeability distributions than an array of sensors located away from the injection well.

In addition to synthetic proof-of-concept inversion exercises, we applied a dual-grid inversion algorithm to the interpretation of field data. In the latter case, it was shown that the inversion algorithm possessed the necessary efficiency and expediency to estimate large-scale spatial distributions of reservoir permeability and porosity from relatively large volumes of wellbore-pressure data. Data from the field experiment consisted of time-records of pressure acquired in a well used for water injection. The lack of in-situ pressure data severely curtailed the sensitivity of the measurements to spatial variations of permeability and porosity in the reservoir. Simultaneous inversion of permeability and porosity provided the most consistent reservoir model that successfully reproduced the measurements. However, the estimated distributions of permeability and porosity only provided information about the large-scale effective medium properties of the formation of interest.

Table 5.1: Geometrical and fluid-flow parameters for the three-layer, six-block test cases and for the twenty-block permeability bank test case considered in this work.

Parameter	**Value**
Initial pressure, p_o [kPa]	17236.89
Single-phase fluid viscosity, μ_o [Pa.s]	1.00×10^{-3}
Total compressibility, C_t [kPa^{-1}]	2.90×10^{-6}
Effective porosity, ϕ [fraction]	0.20
Wellbore radius, r_w [m]	0.10
Reservoir external radius, r_e [m]	5000.00
Reservoir thickness, h [m]	10.00
Injection rate, q (step-function pulse) [m^3/d]	79.49
Maximum attainable injection rate, $q_{\max}$ (sinusoidal pulse) [m^3/d]	79.49

Table 5.2: Comparison of CPU execution times for inversions performed with and without a dual finite-difference grid approach for a three-layer, six-block test case. Inversions were performed on a 300 MHz SGI OCTANE workstation.

Grid I size (outer loop)	Grid II size (inner loop)	CPU time [s]
105×281 nodes	-	7804.05
105×281 nodes	54×281 nodes	2807.19

Table 5.3: Geometrical and fluid-flow parameters for the Mansfield sandstone reservoir.

Parameter	**Value**
Initial pressure, p_o [kPa]	1378.95
Single-phase fluid viscosity, μ_o [Pa.s]	3.00×10^{-3}
Total compressibility, C_t [kPa^{-1}]	1.32×10^{-6}
Wellbore radius (injection well), r_w [m]	6.90×10^{-2}
Reservoir external radius, r_e [m]	107.11
Reservoir thickness, h [m]	6.40

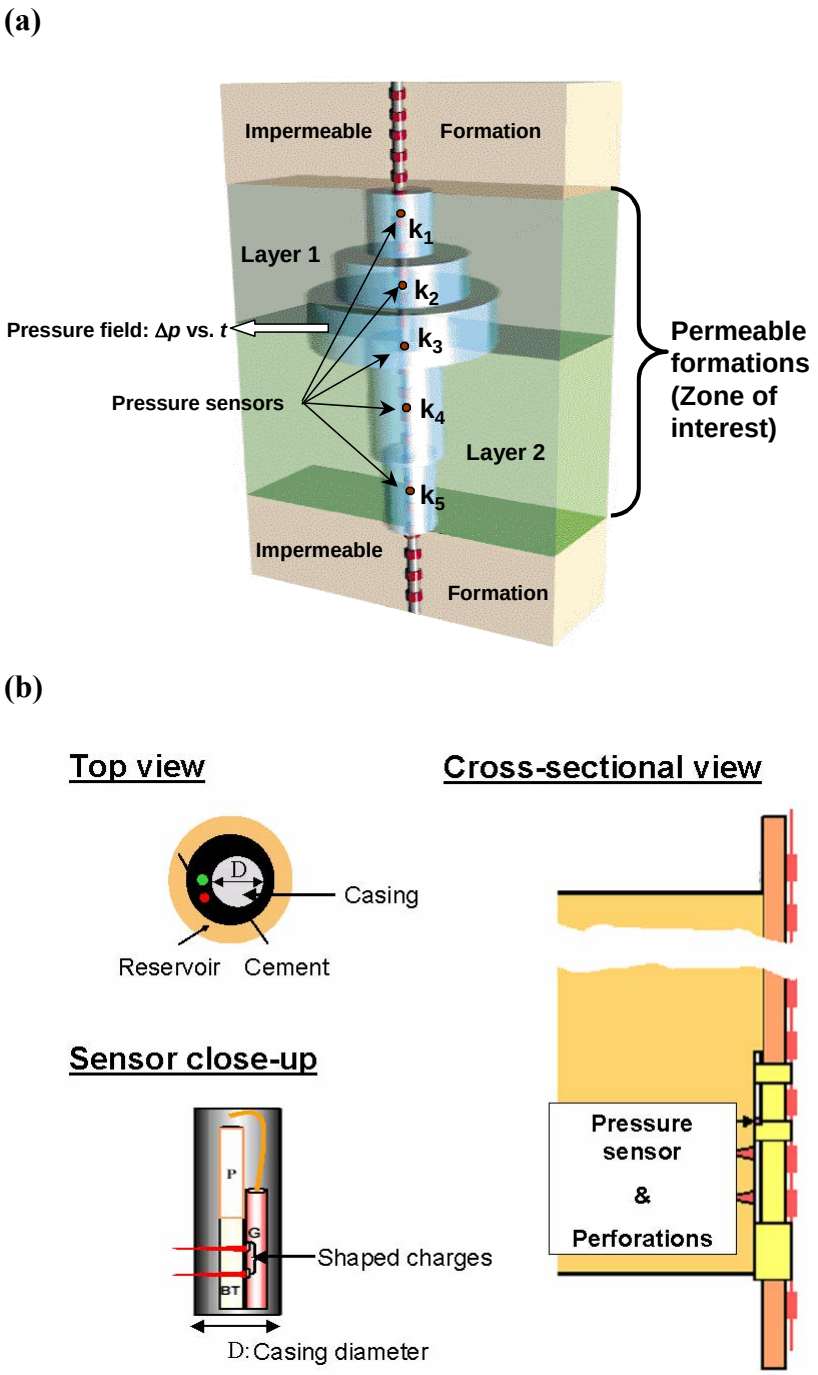

Figure 5.1: (a) Graphical description of a generic in-situ permanent sensor installation. Pressure gauges are deployed in direct hydraulic communication with the formation. In this example, water is injected through an open interval thereby displacing in-situ oil. Water invasion fronts in the form of cylinders are used to indicate variability in the vertical distribution of permeability. (b) Graphical description of the components of an in-situ pressure gauge. The gauge is cemented behind casing and operates in direct hydraulic communication with the formation (Babour et al., 1995).

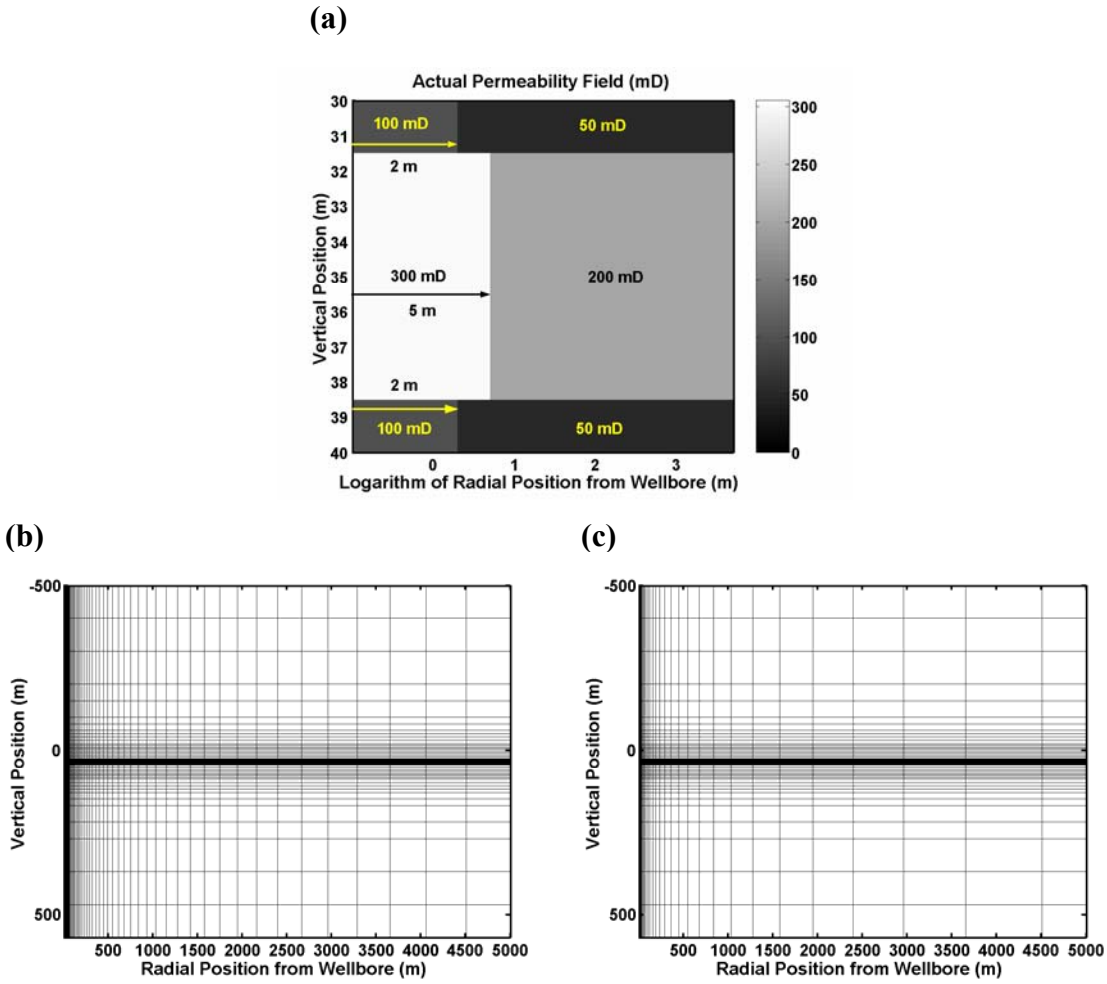

Figure 5.2: (a) Actual permeability model for a three-layer, six-block reservoir with hydraulically-communicating layers. (b) Finite-difference grid used for the numerical simulation and inversion examples presented in this chapter (except for the multi-block test case). (c) Coarse finite-difference grid enforced in the minimization of the auxiliary cost function for the dual-grid inversion method.

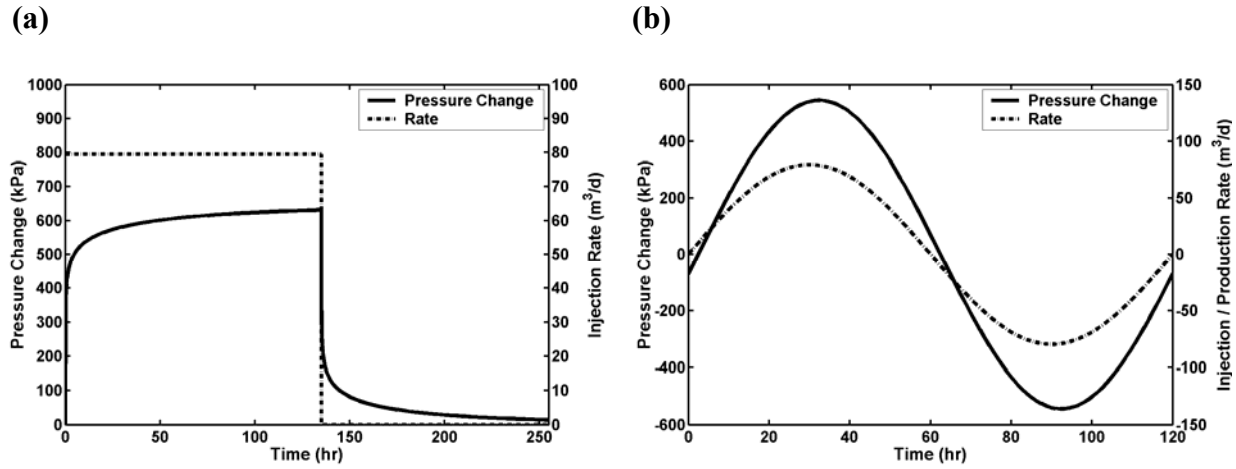

Figure 5.3: Examples of flow-rate schedules and of their associated pressure-transient data: (a) Step-function flow-rate pulse and (b) sinusoidal flow-rate pulse.

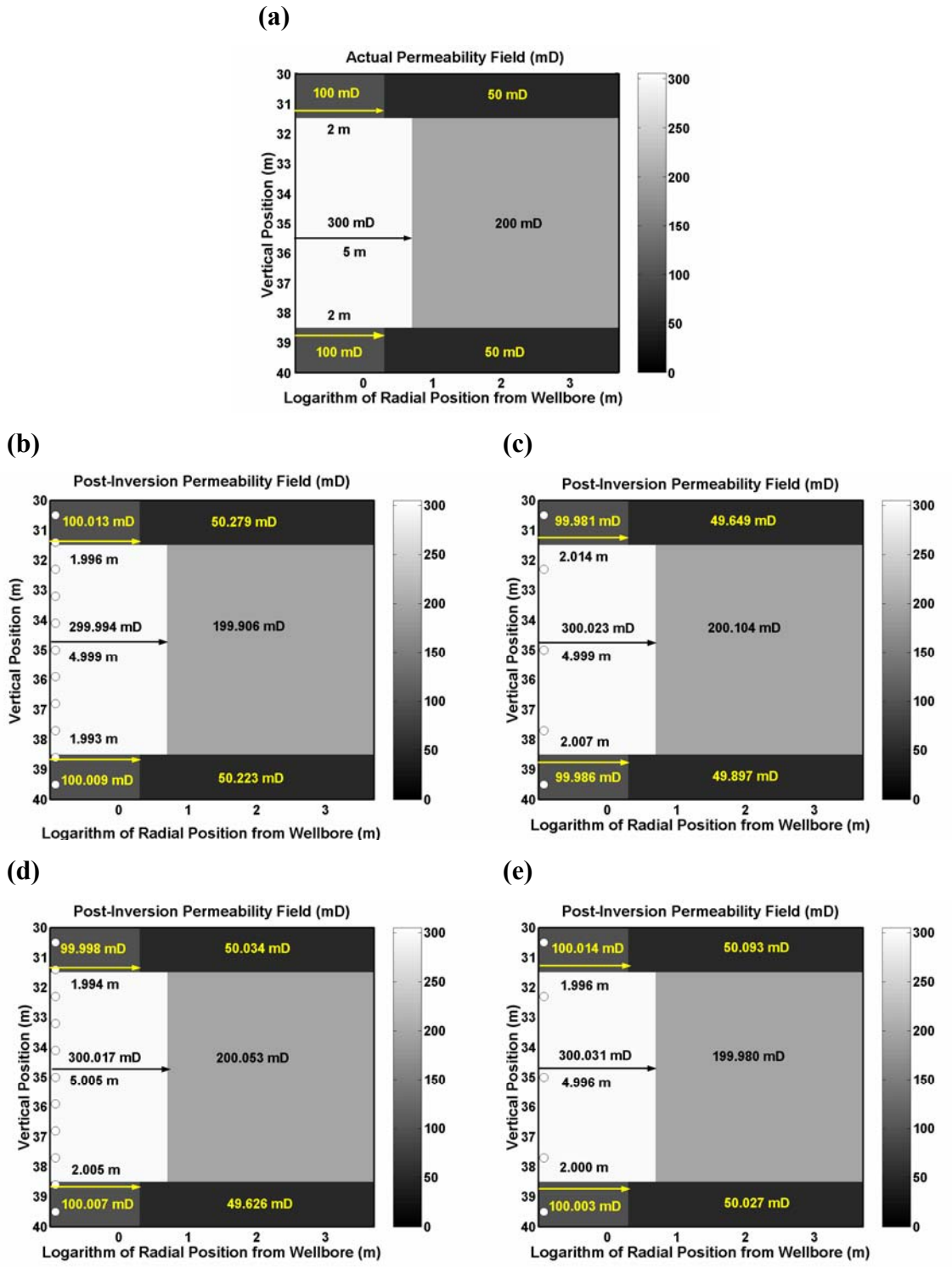

Figure 5.4: See caption on the following page.

Figure 5.4: Comparison of inverted and actual permeability models. (a) The actual permeability model. Inversions are carried out using noise-free pressure-transient data. Results from inversion are shown for the following data sets: (b) pressure-transient data acquired by eleven equally-spaced sensors in response to a 135 hr step-function pulse, (c) pressure-transient data acquired by five distributed sensors in response to a 135 hr step-function pulse, (d) pressure-transient data acquired by eleven equally-spaced sensors in response to a $\tau = 60$ hr sinusoidal pulse, (e) pressure-transient data acquired by five distributed sensors in response to a $\tau = 60$ hr sinusoidal pulse. In all cases, pressure-sensor locations are indicated with small circles.

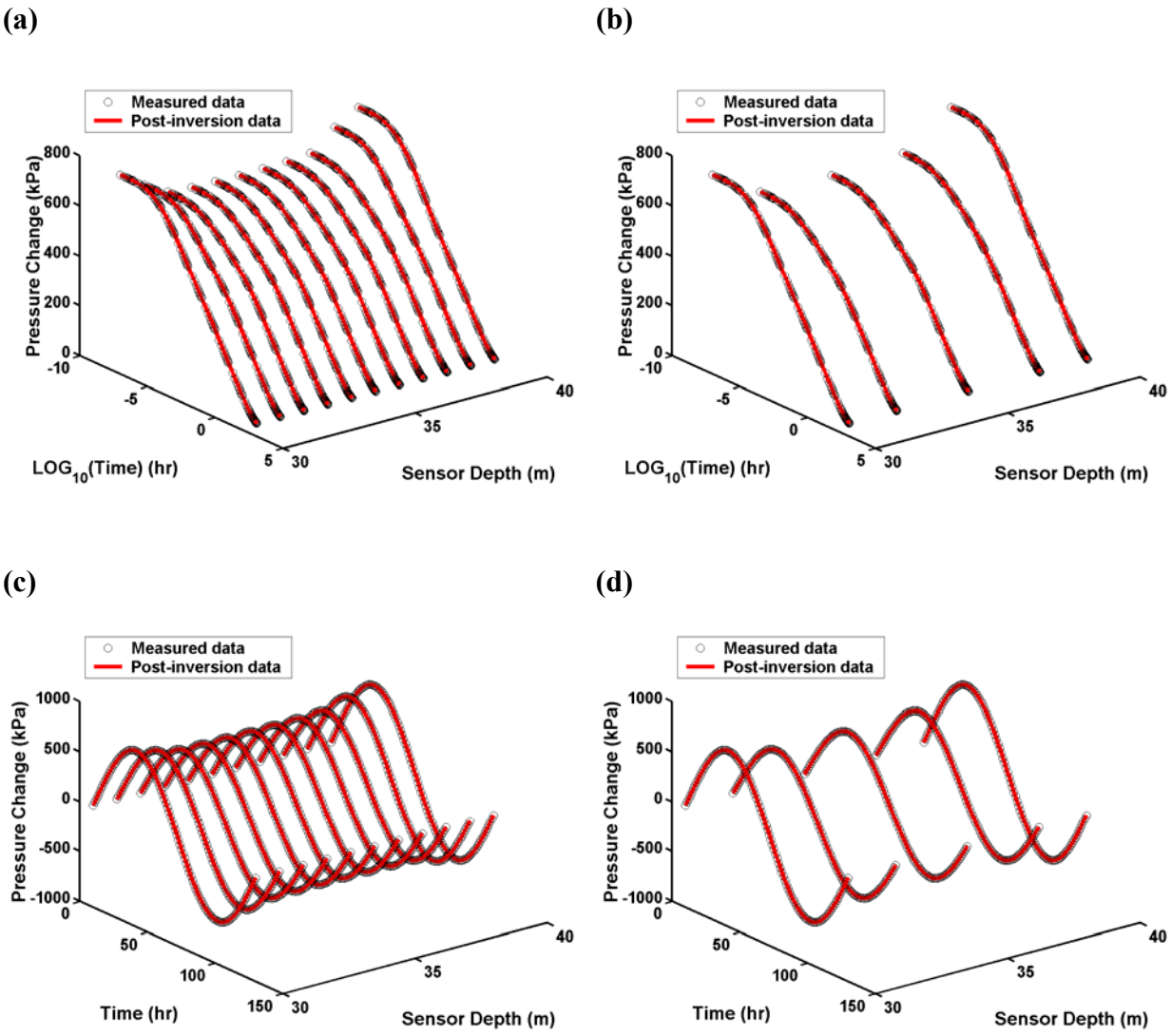

Figure 5.5: Plots of post-inversion pressure-transient data for the cases where measurements are acquired with (a) eleven equally-spaced sensors in response to a 135 hr step-function pulse, (b) five distributed sensors in response to a 135 hr step-function pulse, (c) eleven equally-spaced sensors in response to a $\tau = 60$ hr sinusoidal pulse, and (d) five distributed sensors in response to a $\tau = 60$ hr sinusoidal pulse.

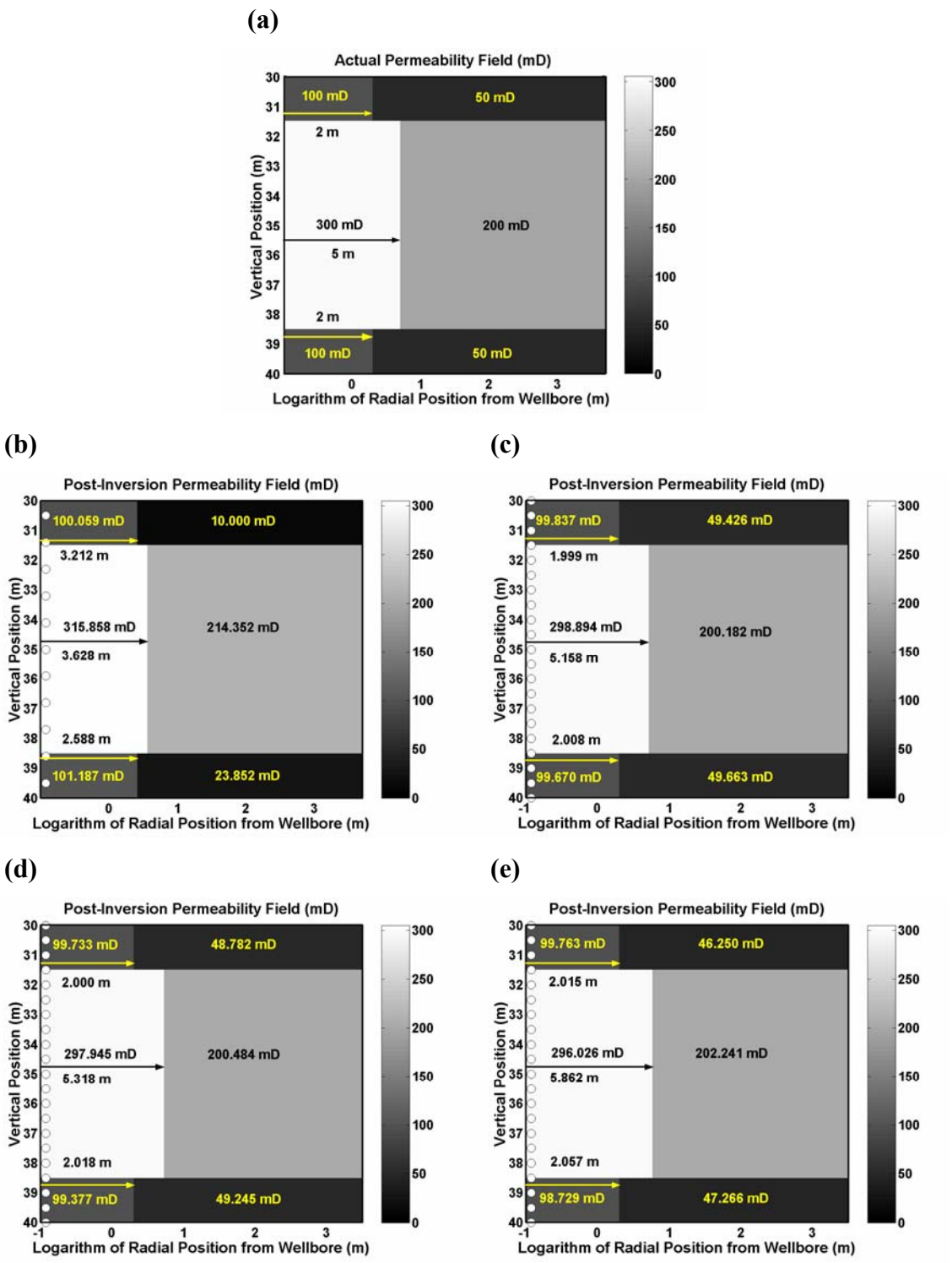

Figure 5.6: See caption on the following page.

Figure 5.6: Comparison of inverted and actual permeability models. (a) The actual permeability model. Inversions are carried out using noisy pressure-transient data acquired in response to a $\tau = 60$ hr sinusoidal pulse. Pressure-transient data were contaminated with additive zero-mean Gaussian random noise. Inversion results are shown for the following values of noise standard deviation and type of sensor configuration: (b) 1% white noise, eleven sensors; (c) 1% white noise, twenty-three sensors; (d) 2% white noise, twenty-three sensors; (e) 5% white noise, twenty-three sensors. In all cases, pressure-sensor locations are indicated with small circles.

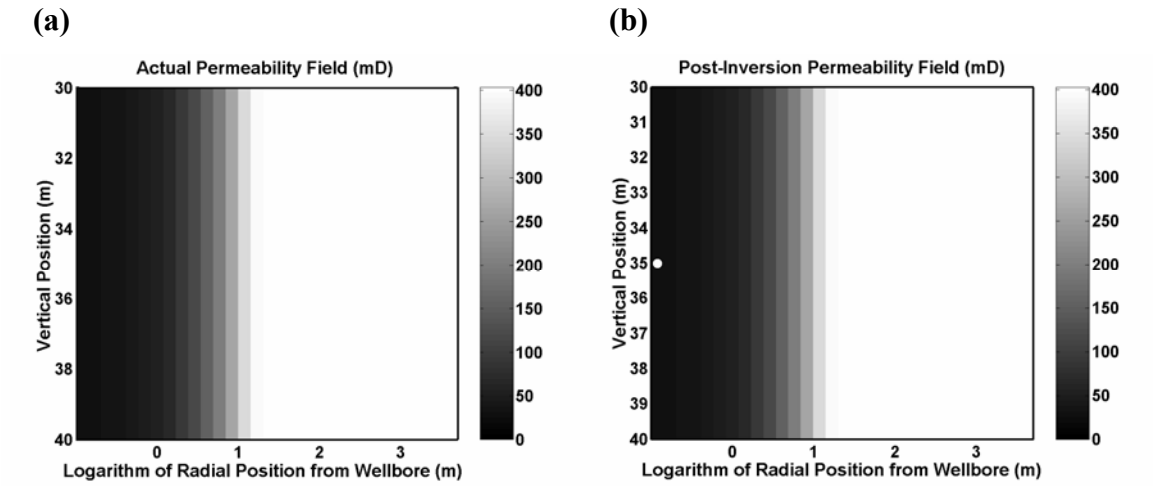

Figure 5.7: (a) Actual and (b) inverted permeability models for a single-layer, twenty-block permeability bank reservoir. Inversion was performed assuming transient data originating from the pressure fall-off response of the reservoir sampled at a single sensor location. The pressure sensor is located in the mid-depth of the reservoir as indicated with the small circle.

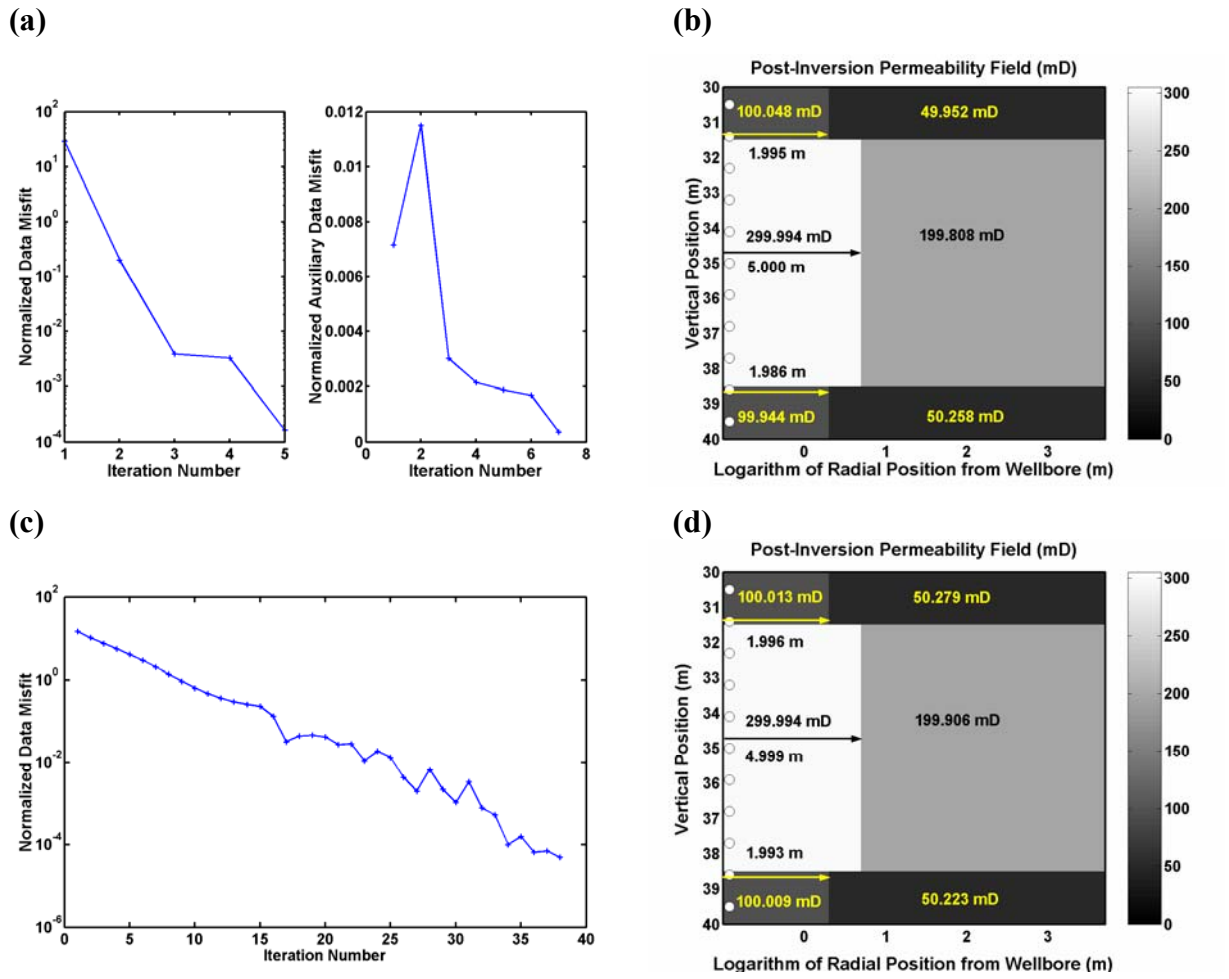

Figure 5.8: Plots of normalized data misfit versus iteration number in the search for a minimum of the cost function and corresponding inversion results. The actual permeability field is shown in Figure 5.2(a). (a) Inversion is performed with a dual-grid inversion technique. Left panel shows the evolution of the normalized data misfit with respect to iteration number evaluated with the fine grid (105×281 nodes). Right panel shows the normalized data misfit as a function of the iteration number within one of the auxiliary cost functions constructed with the coarse grid (54×281 nodes). (b) Post-inversion permeability field estimated using a dual-grid approach. (c) Normalized data misfit evaluated using a fine finite-difference grid (105×281 nodes). (d) Post-inversion permeability field estimated using a fine finite-difference grid. Pressure-sensor locations are indicated with small circles.

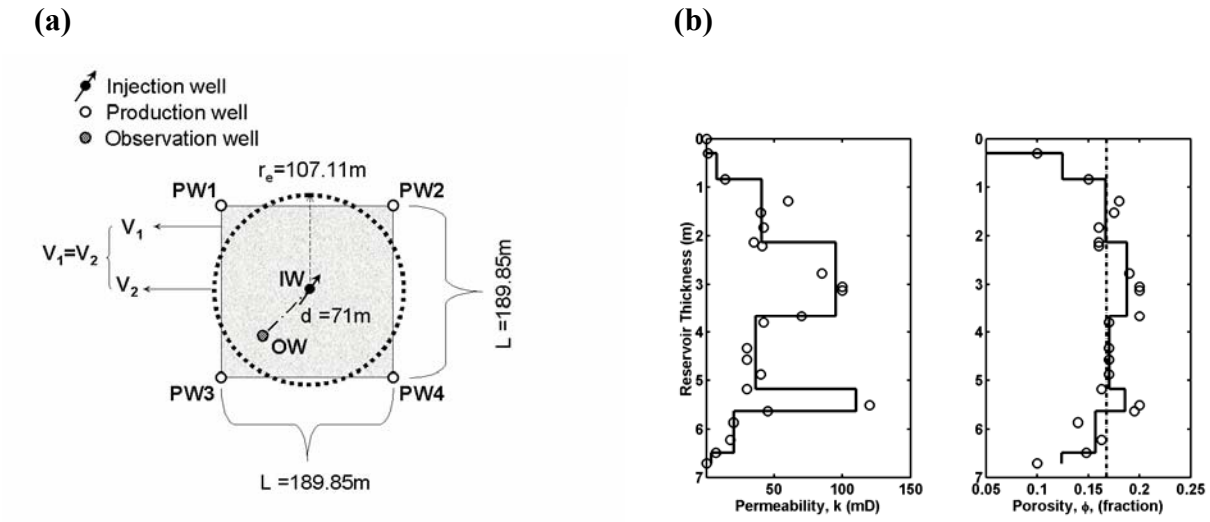

Figure 5.9: (a) Top view of the reservoir volume subjected to waterflood. The reservoir section is enclosed by a square five-spot pattern. We assume that the injection rate information is recorded at the injection well (IW). In our numerical test cases, we consider the deployment of in-situ permanent pressure sensors in both the injection well, IW, and the observation well, OW. (b) Petrophysical evaluation of the Mansfield sandstone reservoir in well IW. Core data are superimposed on the core- and log-based 1D interpretation of permeability and porosity profiles. The value of the volumetric-average porosity is also shown on the porosity profile.

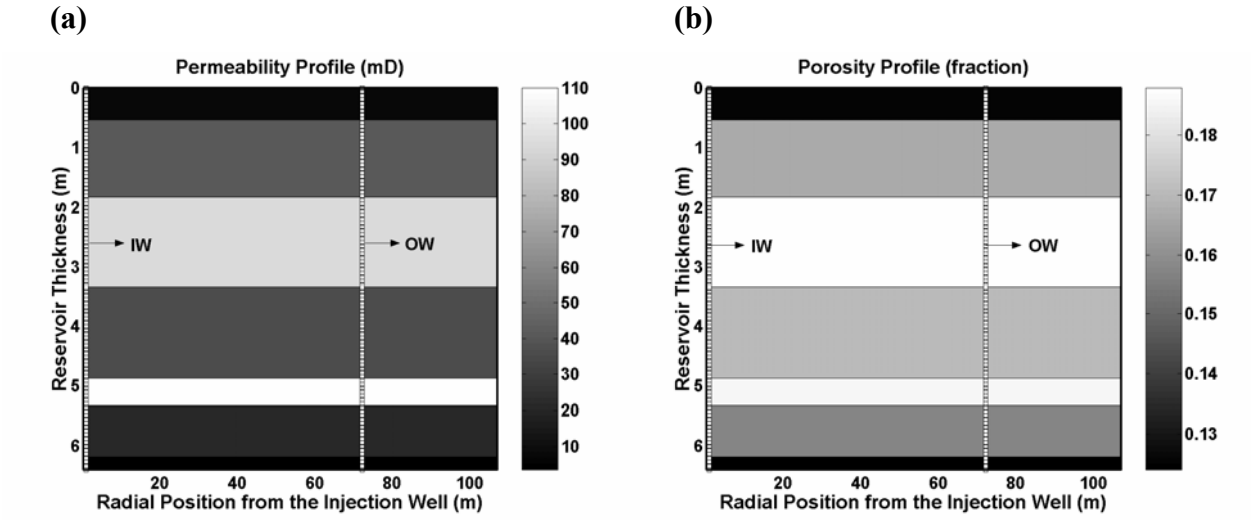

Figure 5.10: One-dimensional (1D) (a) permeability and (b) porosity models used to characterize the reservoir volume of interest. Spatial locations of the injection (IW) and observation (OW) wells are indicated with vertical lines penetrating through the reservoir.

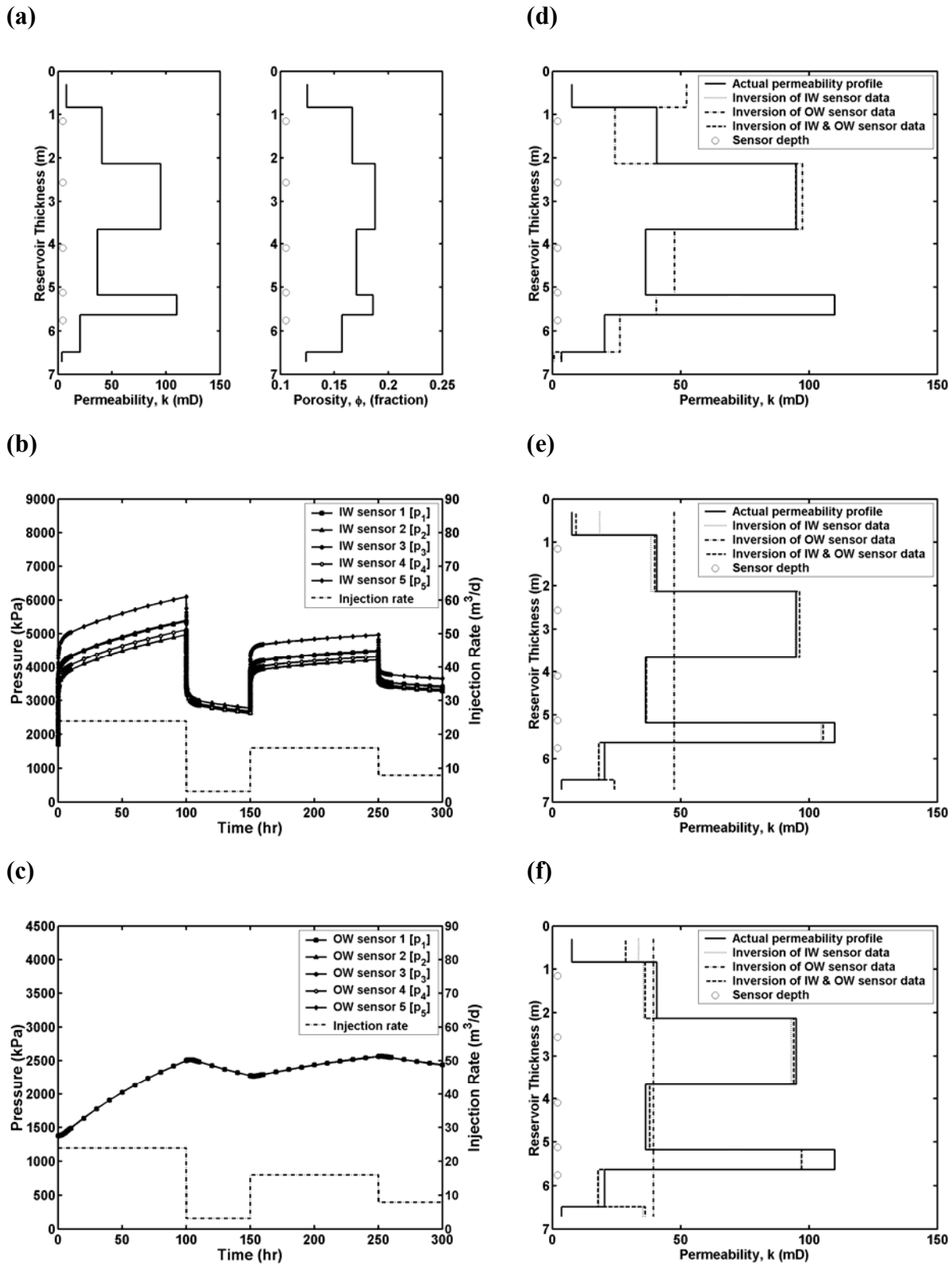

Figure 5.11: See caption on the following page.

Figure 5.11: (a) Vertical locations of in-situ permanent pressure sensors (Case A) with respect to 1D permeability and porosity profiles. (b) Superimposed plots of pressure and injection rate as a function of time for the injection well, IW. (c) Superimposed plots of pressure and injection rate as a function of time for the observation well, OW. Comparisons of the inverted seven-layer (1D) permeability profiles with respect to the actual seven-layer permeability model for the Mansfield-sandstone reservoir volume (Case A). In this case, we assume that the layer-by-layer porosities are known, and hence, used as a-priori information in the inversions. Inversion results are shown for the cases where (d) measurement data are noise-free, (e) measurement data are contaminated with 2% zero-mean Gaussian random noise, and (f) measurement data are contaminated with 5% zero-mean Gaussian random noise. Vertical locations of the in-situ sensors are superimposed to the inversion results and are indicated with small circles.

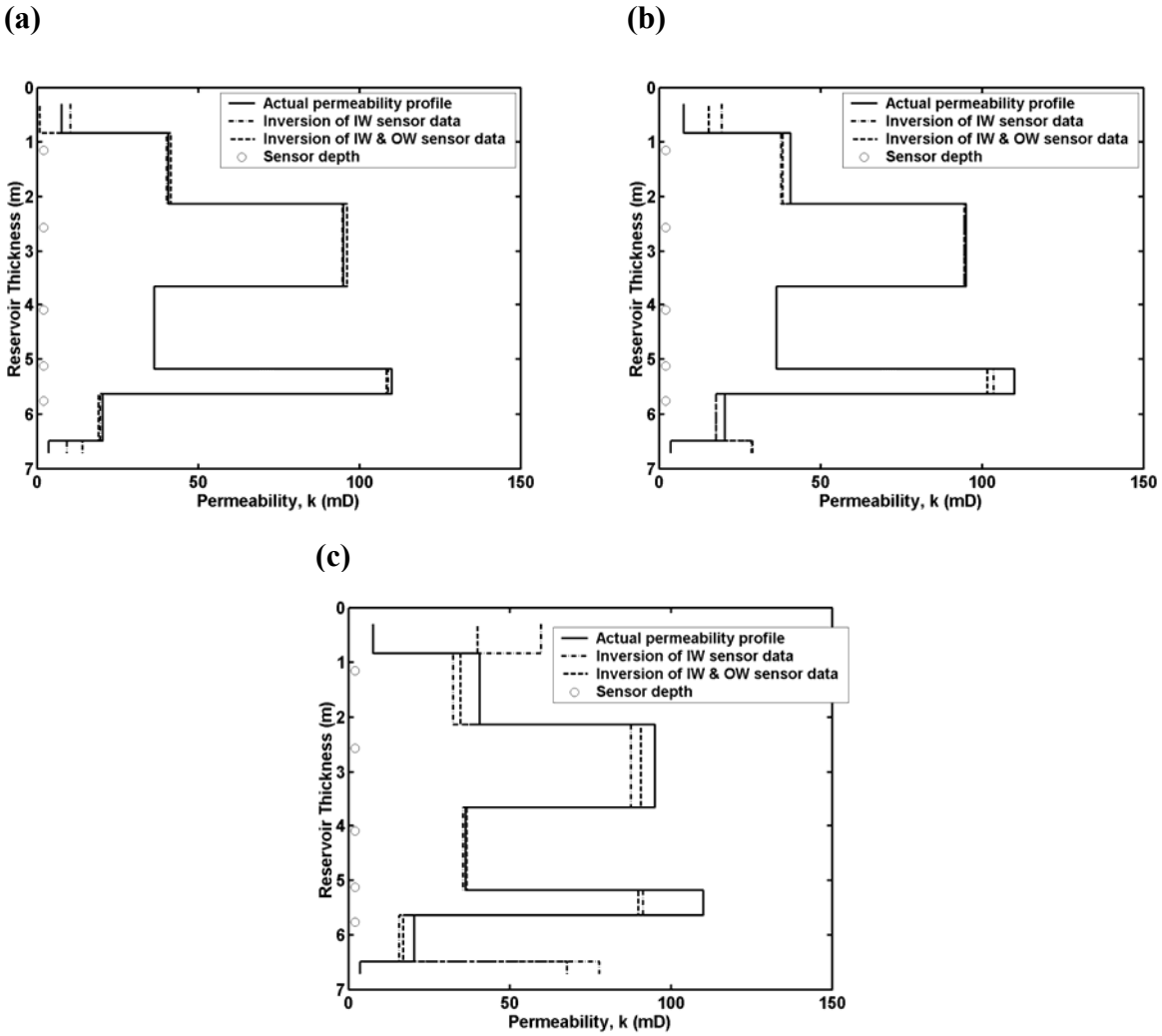

Figure 5.12: Comparisons of the inverted seven-layer (1D) permeability profiles with respect to the actual seven-layer permeability model for the Mansfield-sandstone reservoir volume (Case B). In this case, we assume that instead of layer-by-layer porosities, only the volumetric-average of the porosity is known. We stipulate this average porosity value, shown in Figure 5.9(b), in place of the porosity values of each layer in the inversions. Inversion results are shown for the cases where (a) measurement data are noise-free, (b) measurement data are contaminated with 2% zero-mean Gaussian random noise, and (c) measurement data are contaminated with 5% zero-mean Gaussian random noise. Vertical locations of the in-situ sensors are superimposed to the inversion results and are indicated with small circles.

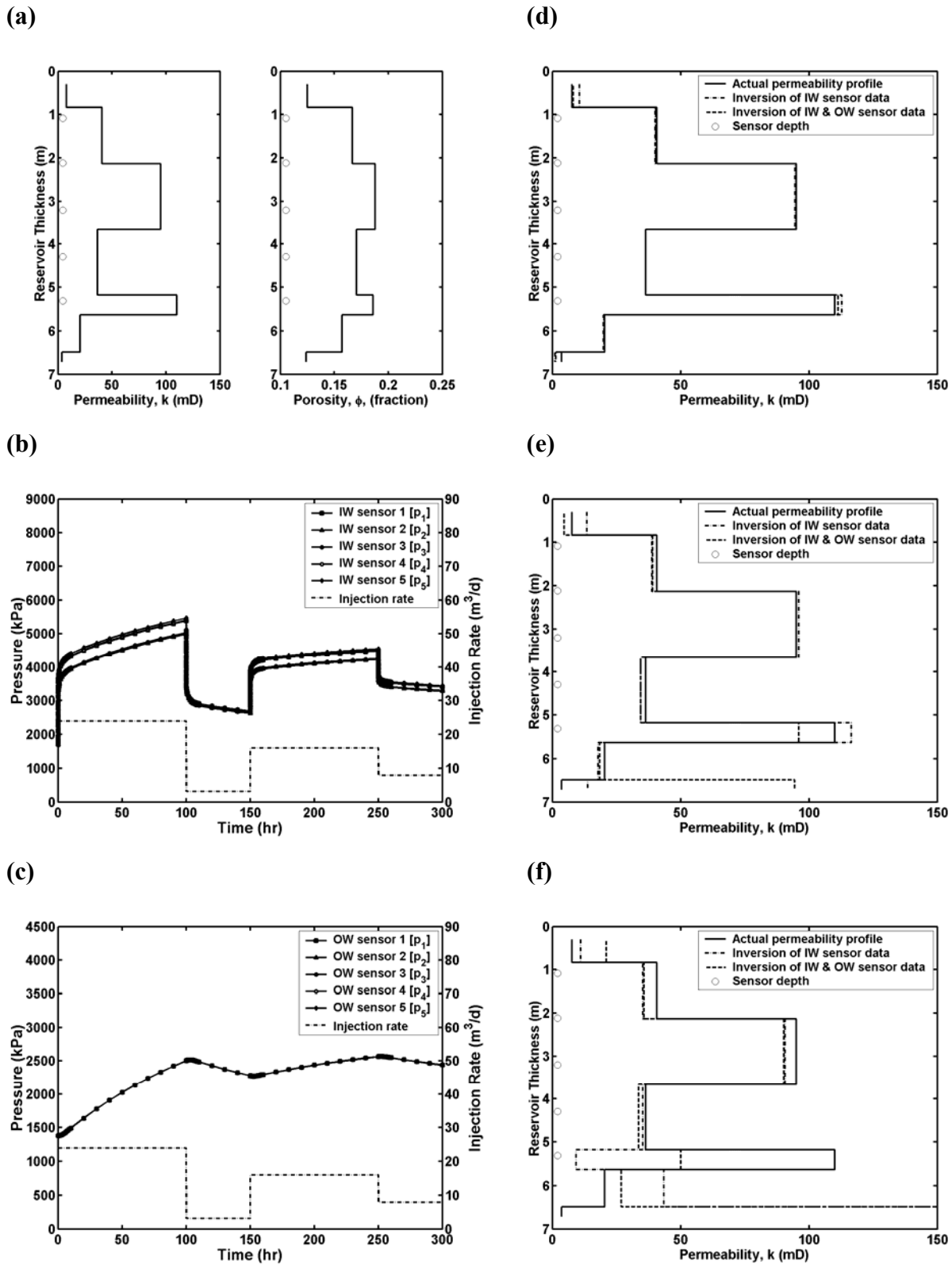

Figure 5.13: See caption on the following page.

Figure 5.13: (a) Vertical locations of in-situ permanent pressure sensors (Case C) with respect to 1D permeability and porosity profiles. (b) Superimposed plots of pressure and injection rate as a function of time for the injection well, IW. (c) Superimposed plots of pressure and injection rate as a function of time for the observation well, OW. Comparisons of the inverted seven-layer (1D) permeability profiles with respect to the actual seven-layer permeability model for the Mansfield-sandstone reservoir volume (Case C). In this case, we assume that instead of layer-by-layer porosities, only the volumetric-average of the porosity is known. We stipulate this average porosity value, shown in Figure 5.9(b), in place of the porosity values of each layer in the inversions. We also consider a symmetric five-sensor permanent in-situ pressure array. In this case, layer-boundary information is decoupled from the in-situ sensor array design. Inversion results are shown for the cases where (d) measurement data are noise-free, (e) measurement data are contaminated with 2% zero-mean Gaussian random noise, and (f) measurement data are contaminated with 5% zero-mean Gaussian random noise. Vertical locations of the in-situ sensors are superimposed to the inversion results and are indicated with small circles.

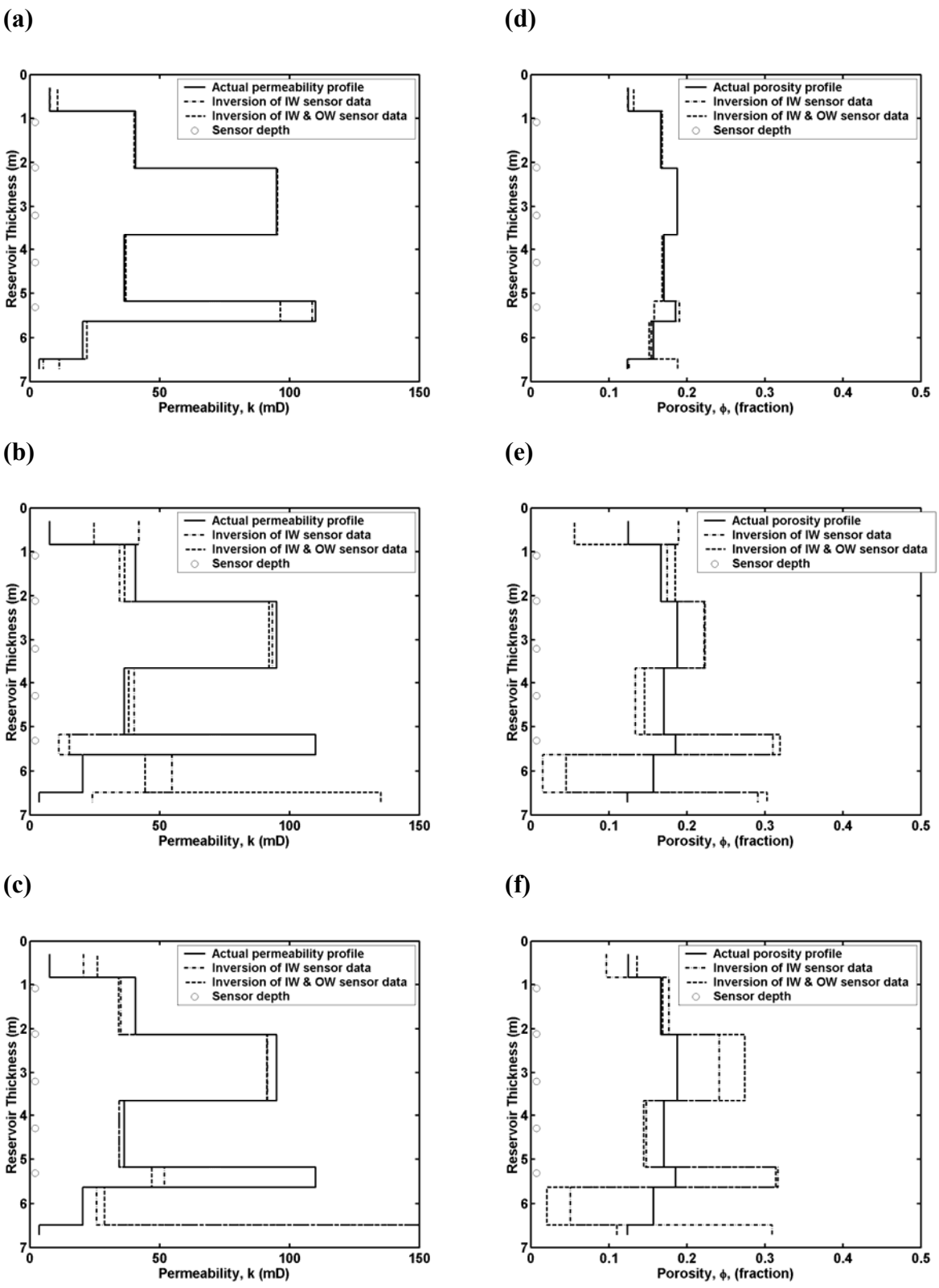

Figure 5.14: See caption on the following page.

Figure 5.14: Comparisons of the simultaneously inverted seven-layer (1D) permeability and porosity profiles with respect to actual seven-layer permeability-porosity model for the Mansfield-sandstone reservoir volume (Case D). The measurement hardware consists of a symmetric five-sensor permanent in-situ pressure array. Inversion results for the permeability profile are shown for the cases where (a) measurement data are noise-free, (b) measurement data are contaminated with 2% zero-mean Gaussian random noise, and (c) measurement data are contaminated with 5% zero-mean Gaussian random noise. Inversion results for the porosity profile are shown for the cases where (d) measurement data are noise-free, (e) measurement data are contaminated with 2% zero-mean Gaussian random noise, and (f) measurement data are contaminated with 5% zero-mean Gaussian random noise. Vertical locations of the in-situ sensors are superimposed to the inversion results and are indicated with small circles.

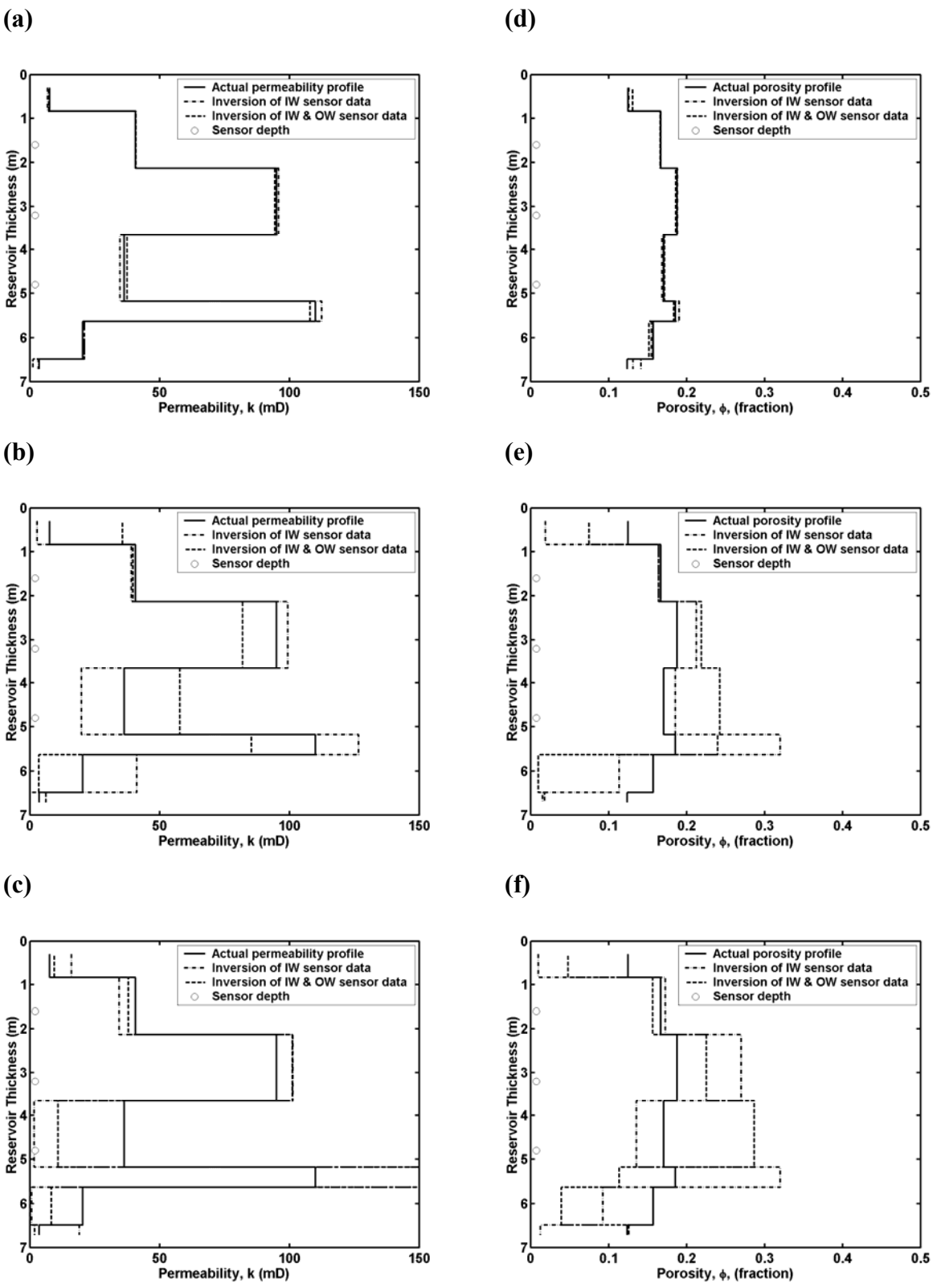

Figure 5.15: See caption on the following page.

Figure 5.15: Comparisons of the simultaneously inverted seven-layer (1D) permeability and porosity profiles with respect to actual seven-layer permeability-porosity model for the Mansfield-sandstone reservoir volume (Case E). The measurement hardware consists of a symmetric three-sensor permanent in-situ pressure array. Inversion results for the permeability profile are shown for the cases where (a) measurement data are noise-free, (b) measurement data are contaminated with 2% zero-mean Gaussian random noise, and (c) measurement data are contaminated with 5% zero-mean Gaussian random noise. Inversion results for the porosity profile are shown for the cases where (d) measurement data are noise-free, (e) measurement data are contaminated with 2% zero-mean Gaussian random noise, and (f) measurement data are contaminated with 5% zero-mean Gaussian random noise. Vertical locations of the in-situ sensors are superimposed to the inversion results and are indicated with small circles.

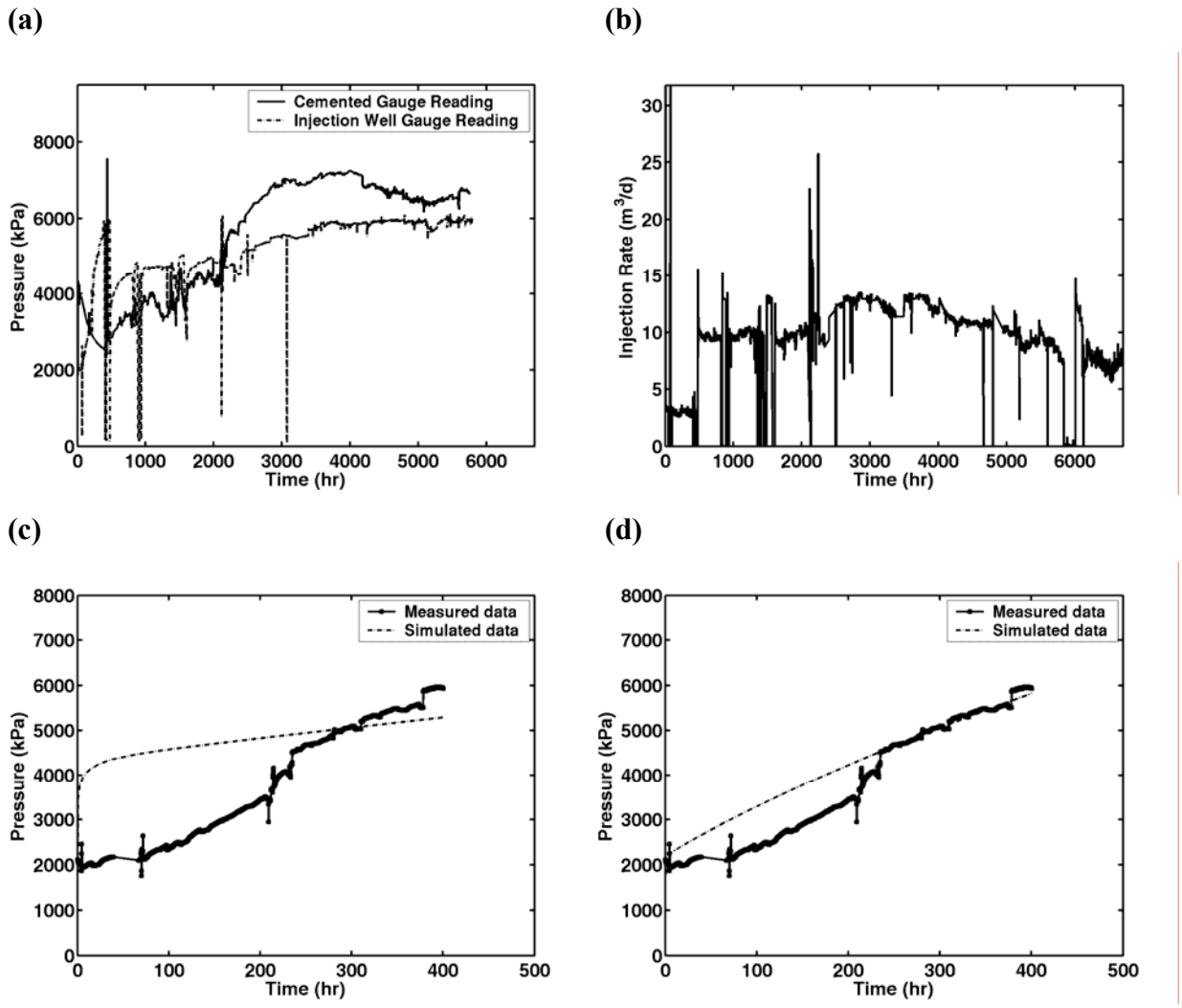

Figure 5.16: Complete injection and observation well pressure records are shown in panel (a). Complete injection rate history is shown in panel (b). Note that the reservoir volume around the injection well was hydraulically fractured approximately 403 hours after the onset of injection. Post-inversion data fits are also shown above for the cases where injection-well measurements used for inversion consist of time-records of pressure acquired between 235 through 380 hours of the field test. Measured data are first utilized to invert a homogeneous reservoir permeability. The corresponding post-inversion data fit is as shown in panel (c). In this case, we assume a fixed homogeneous reservoir porosity of 0.168 (fraction) that corresponds to the volumetric average derived from core and wireline data. Panel (d) shows the post-inversion data fit for the case where both homogeneous reservoir permeability and porosities are inverted simultaneously from the measurement data.

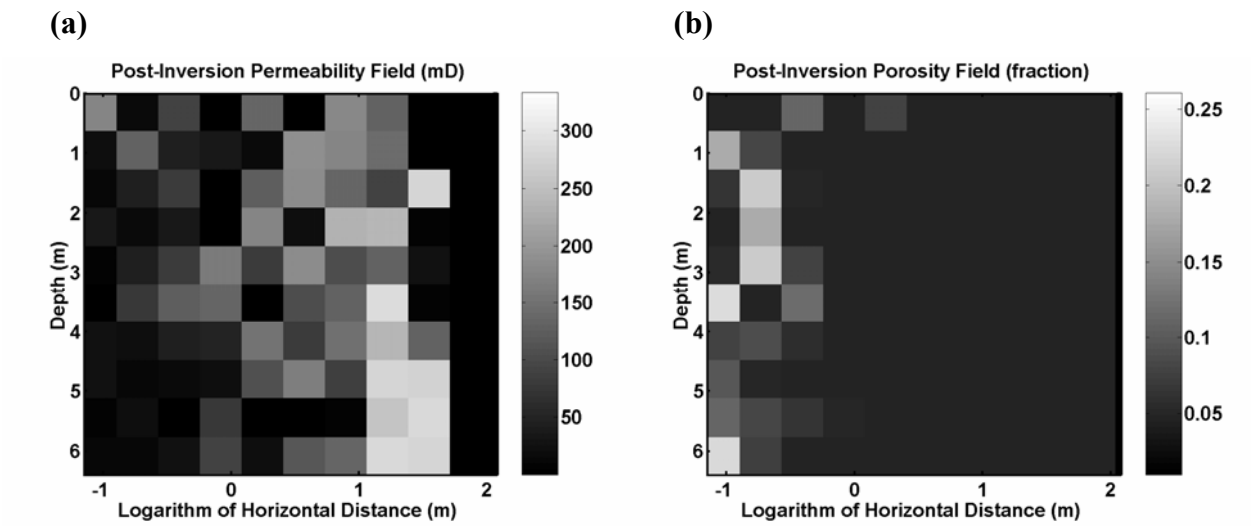

Figure 5.17: Simultaneous reconstructions of spatial distributions of (a) permeability and (b) porosity obtained for the case of a 10×10 cellular model.

Chapter 6: Joint Inversion of Transient-Pressure and DC Resistivity Measurements Acquired with In-Situ Permanent Sensors

6.1 INTRODUCTION

In-situ permanent sensors allow the possibility of inferring real-time images of the spatial distribution of fluid-flow parameters in the vicinity of a well and also between existing wells. Interpretation work, therefore, aims to quantify how a variation in the measurements acquired with in-situ permanent sensors will translate into a variation in the spatial distribution of fluid-flow properties. It is also imperative to optimally design the spacing and number of permanent sensors in light of both existing reservoir conditions and potentially deleterious measurement noise.

The problem considered consists of mapping discrete time- and space-domain variations of in-situ transient-pressure measurements as well as discrete space-domain measurements of dc resistivity voltages, into spatial distributions of resistivity and absolute fluid permeability of the porous medium. In order to establish a proof of concept for the joint inversion algorithm developed in this work, we make use of synthetic examples where measurements are numerically generated using accurate simulation algorithms. Numerical examples involve cases where synthetically generated measurements are contaminated with various degrees of random Gaussian noise. In this work, the inversion study is focused to the case of two-dimensional (2D) axisymmetric spatial models of permeability and electrical resistivity. A cylindrical permeable medium with an injection well at its center is assumed as the reservoir geometry. We also assume the petrophysical layers describe the spatial heterogeneity of the formation of interest. The specific geometrical model considered in this chapter is illustrated in Figure 6.1. A layer-by layer spatial distribution of porosity is assumed available from well-log

measurements such as density and/or neutron logs. On the other hand, fluid viscosity and compressibilities are assumed known from fluid sample analysis. Here, we would like to point out that in practical field applications, the parameters that we assume to be known may not be known at all or their values may involve various degrees of uncertainty depending on the amount and spatial extent of measurements acquired within the particular formation of interest. Nonetheless, the assumptions made above involve measurable quantities and they become increasingly relevant with the quality and spatial extent of the measurements listed above.

We focus the analysis to two measurement strategies for in-situ transient-pressure data. In the first strategy, transient-pressure measurements are acquired during the shut-in period subsequent to a constant step-injection rate pulse. In the second strategy, a more complete time record of pressure measurements is acquired during one injection and two fall-off periods of a multi-pulse cycle. In both cases, borehole resistivity surveys are performed at the end of the transient-pressure acquisition period. During fall-off periods, injection is stopped. The transient response of formation pressure generated by the change of injection rate (q_{inj} becomes zero) is recorded by in-situ sensors. On the other hand, during the subsequent injection period, the process of water injection resumes. As such, a new pressure-transient is generated due the injection-rate pulse (when injection rate is increased from zero to q_{inj}). In this work, we also investigate the sensitivity of the inversion to the presence of random measurement noise.

6.2 IN-SITU PERMANENT SENSORS

6.2.1 Pressure Sensors

In-situ permanent pressure sensors are cemented behind casing. Direct hydraulic communication between in-situ pressure sensors and surrounding rock formations is

established via special perforation techniques that make use of shaped charges. Deployment practices of in-situ pressure sensors require novel well completion techniques to ensure the accurate placement, and hence, the reliable operation of these sensors. As such, techniques for the placement of in-situ permanent pressure sensors are subject of active research and field test applications. Current practices described in the open literature generally involve in-situ pressure sensors deployed across observation and production wells. Installation of in-situ pressure sensors across injection wells, on the other hand, represents a more challenging task, because the isolation of the in-situ sensor from the wellbore hydraulics becomes increasingly nontrivial. However, for hydrocarbon-bearing formations undergoing a waterflood operation, our numerical sensitivity study (Alpak et al. 2001; Alpak et al., 2004d) presented in Chapter 5 showed that in-situ transient-pressure measurements acquired across injection wells have higher spatial sensitivity to the spatial distribution of permeability in comparison to the measurements acquired in a distant observation well. Therefore, in this work, we assume the availability of special completion designs and installation techniques that allow the deployment of in-situ permanent pressure sensors along the open-to-flow sections of injection wells.

6.2.2 Electrode Arrays

The electrical tool considered in this work, consists of an array of electrodes cemented in-place within the annular space between electrically insulated casing and the formation. In the vertical direction, the array is deployed outside the electrically insulated part of the casing. A multi-conductor cable serves as the interface between each electrode and a surface switch connected to a power module. The basic acquisition consists of establishing a dc current circuit between one of the electrodes and a surface grounding point, and of measuring the potential induced on the remaining electrodes with respect to

a surface reference electrode. This operation is repeated until all the electrodes in the array have been used as dc current sources. The depth of investigation of the resistivity array is controlled by both the thickness of the rock formation straddled by the array and the resistivity contrast between the background rock formations and the injected fluid (Delhomme et al., 1998).

Unlike openhole electrical logging devices, permanently deployed resistivity arrays offer the possibility of performing long-term and time-lapse measurements. Applications for permanent resistivity monitoring can be categorized into (a) water flood front monitoring from either an observation or an injector/producer well, (b) water coning monitoring from a producer well, and (c) regional water-table monitoring from an observation well or from the heel part of a horizontal producing well (van Kleef et al., 2001).

6.3 PETROPHYSICAL MODEL

The inversion approach developed in this work is based on the cooperative use of electrical and fluid-flow measurements acquired in porous and permeable rocks. Injection of water into otherwise hydrocarbon-saturated rocks causes a variation of electrical resistivity due to the contrast in electrical resistivity between in-situ and injected fluids. When water is injected through the wellbore, the original distribution of resistivity becomes space dependent within the surrounding rock formation. In the presence of a homogeneous rock formation, the spatial distribution of fluid saturation resulting from injection becomes symmetric with respect to the axis of the borehole. Under some restrictive assumptions, the radial distribution of fluid saturation away from the injection well can be approximately described with sharp radial boundaries between coaxial, cylindrical blocks (Ramakrishnan and Kuchuk, 1993). In this chapter, we assume that fluid saturation within each block remains constant.

When density and viscosity of water and in-situ oil saturating the porous medium are close to each other, an approximate single-phase flow model can be formulated for simulating time- and space-domain distributions of formation pressure in the two-phase flow environment. In this formulation, one makes use of the dependence of effective permeabilities on end-point saturations and on end-point relative permeabilities. Note that, the effective permeability of a porous medium for a given phase i is defined as the product of the absolute permeability of the porous medium and the relative permeability of the porous medium with respect to that phase, i.e., $k_{eff,i}(S_i) \equiv kk_{ri}(S_i)$. Then, relative and effective permeabilities of a porous medium for a given phase i depend on the saturation of that phase, S. In this work, we assume negligible capillary effects. We further assume that the densities and viscosities of the injected and in-situ fluids are close to each other. Then, we can make the first order assumption that the injected and in-situ fluids are separated by a sharp front. In this case, residual oil saturation prevails behind the injected-water front, where the water saturation is given by $S_w = S_{wor} (\equiv 1 - S_{or})$. Similarly, irreducible water saturation prevails ahead of the advancing water front, where $S_w = S_{wirr}$. Therefore, the radial saturation profile is represented by a jump discontinuity. In other words, instead of a relatively smoother Buckley-Leverett (Buckley and Leverett, 1941) type of saturation variation, we assume that sharp boundaries separate the leading and trailing saturation zones for each layer. Then, behind the injected water front, the effective permeability of the porous medium for the water phase equals $k_{eff,w} = kk_{rw}(S_{wor}) = kk^o_{rw}$, where k^o_{rw} is the end-point relative permeability for water phase. Nevertheless, again behind the injected water front, the effective permeability of the porous medium for the in-situ oil phase is $k_{eff,o} = kk_{ro}(S_{wor}) = 0$, because $k_{ro}(S_{wor}) = 0$. On the other hand, ahead of the advancing water front, the effective permeability of the porous medium for the water phase equals $k_{eff,w} = kk_{rw}(S_{wirr}) = 0$,

because $k_{rw}(S_{wirr}) = 0.$ Yet, the effective permeability of the porous medium for the oil phase is nonzero and is given by $k_{eff,o} = kk_{ro}(S_{wirr}) = kk_{ro}^{o},$ where k_{ro}^{o} is the end-point relative permeability for oil phase. We assume that during the time-scale of transient-pressure measurements, the location of the front remains stationary. This assumption is valid for injection rates that produce slow moving fronts in waterflood operations. Consequently, the spatial distribution of effective permeabilities can be described by means of $k_{eff,w} \equiv k_I$ behind the front and $k_{eff,o} \equiv k_{II}$ ahead of the water front. As such, for the approximate single-phase flow model, which assumes a slowly moving front within the measurement time scale of pressure transients, the layer-by-layer distribution of effective permeabilities can be described by means of a model that consist of a two-zone equivalent absolute fluid permeability per layer. For the fluid-flow domain, the parameters k_I, k_{II}, and r, where r is the distance of the injected water front from the center of the injection well, remain as the primary variables governing the physics of transient-pressure measurements.

The above-described approach renders the simulation of in-situ pressures equivalent to a problem of single-phase flow of a slightly compressible fluid (water + oil) in an inhomogeneous permeable medium. Having made the above assumption, the governing PDE of the flow problem in a 2D axisymmetric geometry is solved by using a robust and efficient method described in Chapter 3. In this work, we also assume a negligible salinity gradient between injected and in-situ irreducible water. Consequently, for a water injection application in an axisymmetric single-well geometry, the above described equivalent permeability segments per horizontal layer naturally coincide with the coaxial-cylindrical resistivity blocks that are used to describe the spatial distribution of fluid saturation. This observation emphasizes the fact that the near-borehole petrophysical model is consistent in both electrical resistivity and fluid-flow domains. We

approximate the effects of fluid saturation variability within each horizontal layer (due to two-phase flow) using lumped elements described in terms of behind- and ahead-of-the-front equivalent permeabilities and resistivities. Permeabilities and resistivities behind and ahead of the front are spatially constrained by means of the location of the injected water front. In our petrophysical model, the (end-point) saturations that describe the radial saturation variability are utilized implicitly within the equivalent permeability concept. As such, no assumption is required about the specific values of these saturations. Spatial heterogeneity in the vertical direction is assumed in the form of horizontal flow units (or layers) intersecting the coaxial-cylindrical blocks that describe the fluid saturation distribution. Figure 6.2 is a graphical description of the parametric model assumed in this work to describe the spatial distributions of permeability and electrical resistivity between the injector and the observation well, and between the observation well and the outer boundary of the reservoir.

From a measurement viewpoint, the properties of the spatial distributions of resistivity can be estimated with dc electrical measurements (i.e. voltages). On the other hand, the spatial distribution of permeability governs the in-situ transient-pressure response of rock formations surrounding the injection well. Although spatial variations of electrical resistivity and permeability can cause uncoupled perturbations of in-situ transient-pressure and electric voltage measurements, as described above, an indirect coupling exists between the description of the physics of fluid-flow phenomena and the physics of dc electrical phenomena. In effect, the parameter, r, that defines the radial location of each petrophysical block is common to the description and numerical simulation of the two types of measurements. We assume that additional petrophysical information about the segmentation blocks, i.e., the thickness and porosity of each flow unit, is readily available from other types of ancillary borehole measurements (e.g.

density and gamma ray logs). In general, information about the above listed parameters involves various degrees of uncertainty. Quantitative interpretation of the borehole measurements for these parameters, and of their probabilistic integration into the fluid-flow model represent nontrivial tasks that remain outside the scope of this work. Within a given horizontal layer, we consider two coaxial cylindrical blocks (Figure 6.2). Accordingly, the inner radial boundary of the first cylindrical block is equal to the wellbore radius, whereas the outer radial boundary of the second cylindrical block is equal to the distance between the injector and producer wells. The common radial boundary between the two cylindrical blocks is identified as r_i, where the subscript i is used to designate the specific horizontal layer under consideration. Thereafter, we jointly invert the two types of measurements to yield values of electrical resistivity and permeability within each petrophysical block, as well as the radial boundary location between the two coaxial cylindrical blocks.

The joint inversion approach, formulated for the petrophysical model described above, constrains the outcome of the inversion to honor measurements in both resistivity and fluid-flow domains. Subsequent to the joint inversion, using the inverted resistivity distribution, average fluid saturations behind and ahead of the front can be readily estimated by enforcing an appropriate saturation equation, i.e., Archie's law (Archie, 1942), that honors the underlying physics of resistivity-saturation coupling.

The motivation in developing a joint inversion approach for transient-pressure and dc resistivity measurements is to estimate petrophysical models that are consistent with the two types of measurements. As shown below, such a strategy provides an efficient way to reduce non-uniqueness in the inversions otherwise performed independently with the two sets of measurements.

6.4 NUMERICAL TECHNIQUES USED FOR MODELING AND INVERSION OF IN-SITU PERMANENT SENSOR MEASUREMENTS

Quantitative studies have been performed to assess the value of transient in-situ permanent pressure-sensor measurements to detecting permeability variations in the proximity of a sensor deployment (Alpak et al., 2004d). In this work, components of the petrophysical model under investigation consist of permeability and electrical resistivity. It is assumed that the unknown petrophysical model can be parameterized with a finite and discrete number of variables. The corresponding inverse problem is solved by minimizing a quadratic cost function written as the sum of the square differences between the measured data and the data yielded by a forward modeling algorithm. A nonlinear optimization algorithm based on the Weighted and Regularized Gauss-Newton (WRGN) method is used to minimize the quadratic cost function. This minimization strategy requires the computation of the Jacobian (sensitivity) matrix whose entries consist of first-order variations of the cost function. Construction of the Jacobian matrix is the most computationally demanding component of the nonlinear inversion algorithm. Extensive research work in geophysical inverse theory has been undertaken to approximate, eliminate, and economize the computation of the Jacobian matrix. Torres-Verdín and Habashy (1994) and Ellis et al. (1993) describe alternative approaches for the effective computation of the Jacobian matrix. The inversion algorithm developed for the work of this chapter is based on an efficient least-squares minimization technique adapted from the work of Torres-Verdín et al. (2000).

A novel dual-grid approach is integrated to the Weighted and Regularized Gauss-Newton (WRGN) method to accelerate the inversion. The dual-grid inversion algorithm relies on the iterative forward modeling of transient-pressure and dc resistivity measurements. Accurate and computationally efficient forward modeling algorithms are

used to simulate the measurements within the context of the inversion framework. These forward modeling algorithms are also used to generate synthetic measurements that are subsequently inverted in our numerical proof-of-concept studies. Simulations are consistently performed on numerical grids finer than the block scale parameterization assumed for the petrophysical model.

6.4.1 Numerical Simulation of In-Situ Permanent Sensor Measurements

For the modeling of subsurface fluid flow, the assumption is made that the density and viscosity of the injected water and of the in-situ oil phases are approximately equal to each other to justify the notion of a slightly compressible, single-phase fluid-flow regime. Here, the compressibility used to describe the thermodynamic nature of the single-phase fluid is considered as a volumetric average of the compressibilities of the injected water and in-situ oil phases. As such, we consider the single-phase flow of a Newtonian fluid in a rigid porous medium occupying a bounded domain $\Omega \in R^3$ with a smooth boundary $\partial\Omega$. From the material properties aspect of the flow problem at hand, two-dimensional axisymmetric permeable medium assumption is made for the spatial domain. We make use of the same single-phase flow formulation described in Chapter 3 and solve the governing initial boundary value problem using a code that implements the Extended Krylov Subspace Method (`EKSM`). This code is referred to as `EKSM`.

6.4.2 Numerical Simulation of In-Situ DC Electrode Responses

Physics of in-situ DC resistivity electrode responses are governed by the equation of electrostatics shown in equation (3.60) for the 2D spatial domain of interest. In this work, a solution of equation (3.60) subject to boundary conditions of equations (3.61) and (3.62) is approached with a numerical algorithm based on the semi-discrete numerical approach that combines the method of straight lines with an incomplete Galerkin

formulation, NKARD, described by Druskin and Knizhnerman (1987). Within the joint inversion framework described in this work, we make use of both NKARD and EKSM.

6.4.3 Cost Function

For the estimation of the 2D axisymmetric spatial distribution of petrophysical parameters of interest, permeability and electrical resistivity are assigned a constant value within each petrophysical block. Let $\mathbf{x}$ be the size-N vector of unknown parameters that fully describe the axisymmetric distribution of petrophysical parameters, and $\mathbf{x}_p$ a reference vector of the same size as $\mathbf{x}$ that has been determined from some a-priori information. We undertake the estimation (inversion) of $\mathbf{x}$ from the measured data by minimizing a quadratic cost function described by equation (2.3) subject to physical constraints. The minimization problem is solved via using the Weighted and Regularized Gauss-Newton (WRGN) method described in detail in Chapter 2 and Appendix A. The upper and lower bounds enforced on $\mathbf{x}$ are intended to have the iterated solution yield only physically consistent results (e.g. permeability and resistivity can only take positive values). The inversion algorithm employed in this chapter also takes advantage of a novel cascade optimization technique that incorporates a dual finite-difference gridding approach to accelerate the inversion associated with a large number of unknown model parameters. This highly efficient least-squares minimization technique is described in detail in Appendix A as well.

6.4.4 Computation of the Lagrange Multiplier

The first additive term on the right-hand side of equation (2.3) drives the inversion toward fitting the measurements within the desired χ value. The sole presence of such a term in the cost function, $C(\mathbf{x})$, will yield multi-valued solutions of the inverse problem as a result of both noisy measurements as well as insufficient and imperfect data

sampling. Enforcing an extremely small data misfit may result in petrophysical models with exceedingly large model norms (Torres-Verdín and Habashy, 1994). The second additive term on the right-hand-side of equation (2.3) is used to reduce non-uniqueness and to stabilize the inversion in the presence of noisy and sparse measurements. In this context, the Lagrange multiplier, μ, controls the relative weight of the two additive terms in the cost function. The developments considered in this chapter make use of an efficient strategy for the computation of the regularization parameter described in Torres-Verdín and Habashy (1994). We implemented a search for the Lagrange multiplier such that a data misfit reduction of ξ, where $0.5 \le \xi \le 1.0$, was imposed at each iteration with respect to the data misfit achieved at the previous iteration. The search for an optimal Lagrange multiplier demanded typically five to ten evaluations of data misfit at each iteration. Such evaluations did not compromise the efficiency of the inversion primarily due to the fast forward modeling algorithms `EKSM` and `NKARD`, and partly due to the dual-grid algorithm used to minimize the quadratic cost function.

6.4.5 Measurement and Model Vectors

In the above cost function, the measurement vector $\mathbf{m}$ is constructed from discrete real values of dc resistivity data gathered in the form of electric potentials (voltage differences), u, and/or space-time samples of pressure, p, in the following organized fashion:

$$\mathbf{m} = [u_1, u_2, \ldots, u_j, p_{j+1}, \ldots, p_M]^T, \text{ where } j = 1, 2, \ldots, M. \tag{6.1}$$

In equation (6.1), M is the number of measurements and the superscript T indicates transpose. The types of entries to be included in the measurement vector will depend on the inversion approach. For the option of an independent inversion, only either discrete

pressure or electric potential values will be included in the measurement vector. Each value of the index j represents a measurement taken at a particular sensor location, current source depth (for resistivity surveys), or time (for transient-pressure data). An inversion performed with a single measurement type will be intended to yield only estimates of its associated petrophysical parameters. The joint inversion approach will make use of both types of measurements, and will be intended to produce (a) estimates of resistivity and permeability for each petrophysical block, and (b) the location of the oil-water interface for each layer.

Similarly, the model vector can be assembled as

$$\boldsymbol{\psi} = [R_1, R_2, \ldots, R_\alpha, r_{\alpha+1}, \ldots, r_\beta, k_{\beta+1}, \ldots, k_N]^T, \tag{6.2}$$

where R_i and k_i denote block resistivity and permeability, respectively. The parameters r_i specify the location of the oil-water interface for each layer. In definition (6.2) the subscripts α, $\beta - \alpha$, $N - \beta$, and N are the number of resistivities, block-boundary locations, permeabilities, and total number of parameters that constitute the model subject to inversion, respectively. By denoting the model parameters as ψ_i, where $i = 1, 2, \ldots, N$, one can restate definition (6.2) as follows:

$$\boldsymbol{\psi} = [\psi_1, \psi_2, \ldots, \psi_N]^T. \tag{6.3}$$

A model vector constructed with only the model parameters R and $r = r_R$ is used for the independent inversion of electrical voltages. Likewise, an independent inversion of in-situ transient-pressure measurements will involve only the model parameters k and $r = r_k$. For both joint and independent inversion approaches, an arbitrary combination of

individual model parameters can be estimated depending on the extent of information available a-priori for the unknown model.

Given that all of the model parameters involved in the inversion are real and positive, we implement the change of variable $x_i = \ln(\psi_i)$, where $i = 1, 2, \ldots, N$. This change of variable is consistent with the fact that both electrical resistivity and permeability often exhibit a large range of variability. The vector of transformed model parameters is denoted by $\mathbf{x}$.

6.5 Sensitivity Studies for the Joint Inversion of Permanent Sensor Measurements

The foregoing nonlinear inversion algorithm is applied to the estimation of petrophysical model parameters, namely, permeabilities and electrical resistivities assuming a 2D axisymmetric geometry. A central objective of this work is to advance a proof of concept for the cooperative use of in-situ transient-pressure and dc resistivity measurements. Attention is focused on a hypothetical test case in which water is injected from a vertical well into the surrounding oil-saturated rock formations to displace movable oil. Permanent in-situ pressure sensors are assumed to be positioned along the well's water injection interval as well as along a vertical observation well located some distance away from the injection well. We also assume that the resistivity array is deployed only along the injection well.

6.5.1 Six-Block Test Case

The actual petrophysical model is described in Figure 6.3(a). This figure shows a vertical cross-section of the axisymmetric spatial distributions of permeability, layer-by-layer porosity, and resistivity around a vertical injection well. The spatial distribution of porosity is assumed to be known from ancillary measurements such as seismic and well-log data. A vertical observation well is located 72.2 m away from the injection well. Both

the injection and the observation wells are equipped with 15 in-situ permanent pressure sensors, 11 of which are installed across the formation of interest and are evenly distributed along the corresponding well. In addition, two sensor couples are deployed at the top and bottom of the reservoir within the sealing nonpermeable layers.

We assume a resistivity array consisting of 18 uniformly distributed point-contact electrodes deployed along the injection well. Reservoir and fluid-flow parameters associated with this inversion exercise are listed in Table 6.1. Data input to the inversion were simulated numerically using the forward modeling codes EKSM and NKARD.

A finite difference grid of size 134×249 in the radial and vertical directions, respectively, was constructed to perform the numerical simulations and inversions of in-situ transient-pressure measurements. This grid, shown in Figure 6.3(b), consists of logarithmic steps in the radial direction, and a combination of logarithmic and linear steps in the vertical direction. Figure 6.3(c) displays a plot of the simulated time-varying pressure responses, Δp vs. t, for all of the sensors deployed along the injection and observation wells. The associated time record of flow-rate measurements, q vs. t, is superimposed to the plot of simulated transient pressures. Due to hydraulic communication among reservoir blocks, the sensitivity of in-situ transient-pressure measurements to time variations of injection flow rate is relatively smaller along the observation well than along the injection well, as shown in Figure 6.3(c).

For the simulation of the dc electrical measurements, a 201-node, logarithmically distributed radial mesh was entered into NKARD. The spatial distribution of nodes for this grid is shown in Figure 6.4(a). Upper and lower reservoir boundaries are displayed together with the radial nodes. Figure 6.4(b) shows the electric potential measurements simulated along the electrode arrays as a function of both sensor number and depth.

Single-time electric voltages measured at the end of the water injection schedule constitute the electrical data input to the inversion algorithm.

We first investigate the joint and independent inversions of in-situ transient-pressure measurements acquired during a fall-off period (subsequent to a constant step-injection rate pulse), and electrical measurements acquired during a resistivity survey at a time corresponding to the end of the pressure fall-off period. More specifically, transient-pressure measurements acquired during the first fall-off period of the multi-pulse cycle, shown in Figure 6.3(c), were considered as input data to the inversion. In this acquisition strategy, transient-pressure measurements are recorded during the time-interval between the 100^{th} and the 150^{th} hour of the flow rate pulse schedule. In the case of joint inversion, transient-pressure measurements are inverted in conjunction with electrical measurements. Alternatively, a more complete time record of measurements acquired during one injection and two fall-off periods of the multi-pulse cycle is inverted both independently and in conjunction with electrical measurements. For these two latter cases, we considered transient-pressure measurements acquired during the first fall-off, second injection, and second fall-off periods of the multi-pulse cycle displayed in Figure 6.3(c) as input. Henceforth, we refer to the latter measurement set as multi-pulse and to the former type of measurement set as single-pulse in-situ transient-pressure measurements.

We perform both independent and joint inversions of the spatial distribution of permeability and resistivity. For the independent inversions, only in-situ transient measurements are used when estimating permeability, and only electric potential measurements are used when estimating resistivity. Next, we conduct joint inversions of the spatial distribution of permeability and resistivity. Figure 6.5 shows vertical cross-sections (radial distance vs. vertical location) of the actual and inverted spatial

distributions of permeability obtained using both independent and joint inversion approaches. Inversion results obtained with the usage of single- and multi-pulse transient-pressure responses for both inversion approaches are also shown in Figure 6.5. The spatial locations of in-situ pressure sensors deployed along the injection and observation wells are displayed on the same cross-section plots. Analogous sets of plots for the spatial distributions of electrical resistivity are shown in Figure 6.6. The spatial location of the 18-electrode dc resistivity array is superimposed to the cross-section of resistivity shown in Figure 6.6. For the estimation of model parameters k (permeability) and r (radial boundary location), the mean value of each individual parameter was used as the initial guess for the inversions. However, for electrical resistivity, R, the initial guess was constructed from the mean value of each vertical set of segments. Experiments performed with other initial guess locations indicated that the inversion algorithm did not yield estimations biased by the change of the initial guess. In all cases, inversion results converged to the global minimum, rendering post-inversion model-domain errors smaller than 1%. Although model domain percent errors were relatively small for this exercise, results obtained with the joint inversion approach consistently yielded smaller model-domain percent errors than those yielded by independent inversions. For instance, for the independent inversion of the spatial distribution of permeability using multi-pulse in-situ transient-pressure measurements, the maximum model domain error was 0.294%, whereas for an equivalent joint permeability-resistivity inversion, the maximum model domain error decreased to 0.102%. Comparison of inversion results attained with the use of single- and multi-pulse in-situ transient-pressure measurements did not indicate a significant advantage of one approach over the other for those cases that assumed noise-free measurements. Relative data misfits computed with the formula

$$\frac{\left\| \mathbf{W}_d \cdot \left[S(\mathbf{x}^k) - \mathbf{m} \right] \right\|^2}{\left\| \mathbf{W}_d \cdot \mathbf{m} \right\|^2} \tag{6.4}$$

yielded misfit values smaller than 1.0×10^{-4} for all of the noise-free inversions considered in this section. In-situ transient-pressure data-domain fits for the injection and observation well are shown in Figures 6.7(a) and 6.7(b), respectively. In addition, Figure 6.7(c) displays post-inversion data-domain fits for the measured dc resistivity voltages. Excellent data fits were common for inversions performed with noise-free measurements. Numerical experiments also showed that the regularization term in the cost function was not necessary for the stability and convergence of the inversion algorithm when noise-free measurements were used. Robustness to multiple starting points and well convergence behavior without requiring regularization indicate the relative well-posedness of the inverse problem at hand.

A study was also performed to assess the influence of noisy measurements on the inverted six-block model parameters. We first considered a test example wherein single- and multi-pulse transient-pressure measurements were contaminated with 1% zero-mean random Gaussian noise. Independent inversions of transient-pressure measurements were performed to assess the impact of noise. Post-inversion reconstructions of the permeability domain are shown in Figure 6.8 for both single- and multi-pulse transient pressure measurements along with the actual permeability distribution. Percent error maps for the quantitative estimation of permeability values in each parametric block are also shown for the investigated cases. Note that these error maps do not quantify the error in the reconstruction of block-boundary locations (parameter r). Inversion results indicate accurate reconstructions of the near-borehole permeability distribution in the vicinity of the injection well. However, inversion results for the permeability blocks away

from the injection well are negatively influenced by the deleterious effect of noise. A similar test example was considered wherein dc resistivity measurements were contaminated with 1% zero-mean random Gaussian noise. We first investigated the independent inversion of dc resistivity measurements. Post-inversion reconstructions of the resistivity domain are shown in Figure 6.9 along with the actual resistivity distribution. A percent error map for the quantitative estimation of resistivity values in each parametric block is also shown in Figure 6.9. Note that this error map does not quantify the error in the reconstruction of block-boundary locations (parameter r). Similar to the independent inversion of noisy transient-pressure measurements, inversion results indicate accurate reconstructions of the model parameter (in this case, resistivity) distribution in the vicinity of the injection well. Yet, inversion results for the resistivity blocks away from the injection well are negatively influenced by the deleterious effect of noise.

In order to provide a quantitative proof of concept for the merit of the joint inversion algorithm, we first considered the test example wherein both the simulated in-situ multi-pulse transient-pressure and dc voltage measurements were contaminated with 1% zero-mean additive random noise simulated with a Gaussian pseudorandom number generator. Noisy in-situ transient-pressure and dc resistivity (voltage) measurements were then inverted jointly to yield the coupled spatial distributions of permeability and resistivity. Inversion results indicate accurate reconstructions of the spatial distributions of permeability and resistivity. Subsequently, joint inversion of transient-pressure and dc resistivity measurements was repeated for the case where the noise level in the measurements was increased to 2%. Figure 6.10 compares the spatial distributions of permeability and resistivity inverted from noisy measurements with the actual spatial distributions of these parameters. A comparison of the spatial distributions of

permeability and resistivity inverted from noisy and noise-free measurements is also shown in this plot. The noisy case shown in Figure 6.10 is the one where measurements were contaminated with 2% Gaussian random noise. Inversion results obtained with noisy measurements suggest a robust estimation of petrophysical parameters under the deleterious influence of measurement noise. For both permeability and resistivity, model parameters near the injection well were estimated more accurately than the ones for petrophysical blocks located farther away from the injection well.

Although joint inversion of the noisy measurements captures the spatial distribution of permeability quite accurately, the permeability values for blocks located farther away from the injection well are slightly less accurate in comparison to the permeability values for blocks closer to the injection well. On the other hand, while resistivity values for the blocks neighboring the injection well remain accurate, inversion results for resistivity values divert significantly from the actual values for blocks located away from the injection well. These observations are consistent with the spatial resolution properties of in-situ transient-pressure and dc resistivity measurements. Measurements acquired with the in-situ dc resistivity sensors exhibit high sensitivity to the resistivities in the vicinity of the injection well. In contrast to dc resistivity measurements, in-situ transient-pressure measurements inherently exhibit a larger depth of penetration. Deployment of in-situ pressure sensors in the observation well helps to further constrain the spatial distribution of permeabilities. Therefore, permeability values for blocks located far away from the injection well are more accurately reconstructed than the values of resistivity for the same blocks.

For inversions performed with noisy measurements, stability was achieved by setting the matrix $\mathbf{W}_x^T \cdot \mathbf{W}_x$ equal to a unity diagonal matrix. The Lagrange multiplier, μ, then takes the role of a Wiener regularization constant (Treitel and Lines, 1982). We

implemented an adaptive Lagrange multiplier search technique such that at the initial steps of the iteration, a relative misfit reduction of at least 75% was enforced at each iteration with respect to the data misfit achieved at the previous iteration (Torres-Verdín and Habashy, 1994). This approach assigns small μ values (i.e., large λ values, since $\lambda = 1/\mu$) when $\Delta(\mathbf{x}^k) = \mathbf{x}^{k+1} - \mathbf{x}^k$ undergoes large variations in the initial steps of the iteration process. On the other hand, when $\Delta(\mathbf{x}^k)$ undergoes small variations, μ takes large values (i.e., small λ values). Hence, in the later steps of the minimization, more weight is allocated to the data misfit term of the cost function of equation (2.3).

6.5.2 Application of a Dual-Grid Technique in Conjunction with the Joint Inversion Approach

When developing a methodology for joint inversion, we attempted to take full advantage of the large amount of information supplied by multiple types of permanent sensors. Usage of large data sets, however, causes the inversion algorithm to lose the efficiency necessary to perform real-time estimation of petrophysical properties. One way to overcome this problem is to use nonconventional, yet, fast and robust inversion schemes. To that end, a dual-grid inversion approach was implemented based on the cascade minimization technique introduced in Appendix A. The algorithm consists of an inner loop in which the Jacobian matrix is approximated with finite-difference simulations performed on a coarse grid while an outer loop controls the global convergence through updates of data misfit computed with a fine finite-difference grid. Inner and outer loops can be designed in a flexible manner to improve convergence and to substantially reduce computation times. The computational performance of coarse-grid inner loop calculations can be further improved with the use of Broyden's rank-one update formula for the Jacobian matrix. In Appendix A, we present the necessary convergence condition to be satisfied by the dual-grid inversion procedure. Table 6.2

shows a comparison of CPU times (clocked on a 300 MHz SGI Octane machine) required to perform the inversions of the six-block test case using various minimization strategies. The formation model considered for this inversion exercise is a slightly larger version of the six-block example described in the previous section. Central processing unit (CPU) execution times shown in Table 6.2 indicate that simple modifications to the inversion algorithm can produce sizable increments in computer efficiency, thereby making it feasible to invert large measurement sets into large spatial distributions of reservoir petrophysical properties.

6.5.3 Multi-Block Test Case

A relatively more complex test case was designed to further assess the spatial resolution properties of arrays of in-situ permanent sensors of pressure and dc electrical voltage. This test case consisted of 15 permeability block segments, and 6 resistivity block segments. Again, spatial distributions of permeability and resistivity are linked via block-boundary (water front) locations of the first and second radial petrophysical blocks for each horizontal layer. The remaining blocks in the permeability model reflect the spatial heterogeneity of intrinsic fluid absolute permeability. Therefore, in this case, instead of a layer-by-layer uniform spatial distribution of permeability ahead of the water front, we investigate the inversion of laterally varying spatial distributions of permeability for each horizontal layer ahead of the front. The block-boundary locations other than the first one are not constrained by the resistivity data anymore, therefore, within the course of the inversion they are not allowed to vary. The locations of these block boundaries are assumed to be known from other types of measurements, i.e., seismic data acquired prior to the waterflood operation. Transient-pressure and resistivity measurements exhibit joint sensitivity only to the location of the first block-boundary that describes the location of the front within each horizontal layer. Therefore, the location of

the first block-boundary for each horizontal layer is pursued by the inversion along with the values of permeability and resistivity within each petrophysical block.

While generating the synthetic reservoir, we first assumed the permeability model, and consistently linked the spatial distribution of porosity to the spatial distribution of permeability via the correlation given by $\phi(\mathbf{r}) = 0.1 \times \log_{10}[k(\mathbf{r})] + 0.05$, that holds for shaly sandstone formations (Dussan et al., 1994). For the purpose of inversion, the spatial distribution of porosity is assumed to be known from other types of ancillary information such as seismic and well-log data. We considered the same well and sensor deployment geometries described in the previous case. Transient-pressure measurements were simulated assuming the same multiple flow rate pulse schedule used in the six-block test case. Multi-pulse pressure measurements recorded between the 100^{th} and the 300^{th} hour of the flow rate pulse schedule were input to the inversion. The inversion also included dc electrical voltages acquired at a single snapshot corresponding to the end of the transient-pressure record. In addition to the inversions of noise-free measurements, we alternatively considered the case where both the simulated multi-pulse in-situ transient-pressure and voltage measurements were contaminated with 2% zero-mean random Gaussian noise. For the noisy case, we make use of the same regularization strategy utilized for the inversions of noisy data in case of the six-block formation.

Figures 6.11 and 6.12 describe results from joint inversions performed with both noise-free and noisy measurements. The actual spatial distributions of permeability and resistivity are shown in Figures 6.11(a) and 6.12(a), respectively. Figure 6.11(b) displays noise-free joint inversion results for the spatial distribution of permeability, and Figure 6.12(b) shows joint inversion results for the spatial distribution of resistivity. Spatial distributions of permeability and resistivity obtained with the joint inversion of noisy measurements are displayed in Figures 6.11(c) and 6.12(c), respectively. Inversion results

obtained from noise-free measurements indicate an accurate reconstruction of the spatial distributions of permeability and resistivity. No regularization was required for this case. Transient-pressure measurements acquired in both the injection and observation wells appear to have sufficient sensitivity to resolve the radially-heterogeneous distribution of permeability. Resistivity measurements in the injection well, on the other hand, help to accurately constrain the location of the water-oil interface.

For the case of joint inversion of noisy measurements, permeability and resistivity values for blocks closest to the injection well are estimated more accurately than for blocks located farther away from the injection well. The same regularization approach used for the inversion of noisy measurements in the case of six-block formation is utilized in this case. Estimated block-boundary (fluid front) locations for the first and second radial petrophysical blocks remained consistent with the actual locations. Yet, reconstructions of both permeability and resistivity values beyond the block-boundary locations depart significantly from the original values. Inversion results obtained with noisy measurements are indicative of the resolution properties inherent to both types of measurements. Voltages measured by this array lack the length penetration necessary to resolve resistivity values far away from the injection well. In contrast to dc resistivity measurements, in-situ transient-pressure measurements exhibit a longer depth of penetration. However, their lateral resolution is not sufficient to resolve the spatial details of the original permeability model. Farther away from the injection well, only an average value for permeability can be reconstructed for each layer. In this case, deployment of in-situ pressure sensors in the observation well did not help to further constrain the spatial distribution of permeabilities. The lateral resolution of in-situ transient-pressure measurements acquired in the observation well is limited due to the equilibration of in-situ transient-pressure responses away from the injection well. This equilibration is due to

hydraulic communication among petrophysical blocks. As a result, in-situ transient-pressure measurements acquired in the observation well can only resolve a relatively simple distribution of volumetric average permeabilities for each layer. More spatially complex variations of permeability and resistivity can be reconstructed with the joint inversion of in-situ transient-pressure and dc resistivity measurements for significantly low noise levels.

6.5.4 Discussion on the Inversion Results

Undoubtedly, permeable rock formations to be encountered in practical applications will be more spatially and petrophysically complex than the idealized synthetic models assumed in this chapter. Despite the spatial complexity of the underlying petrophysical model, the inversion results described in our numerical experiments indicate that the joint use of in-situ transient-pressure and resistivity measurements improve the accuracy of the quantitative estimation of resistivity and permeability. Comparisons of the inversion results obtained from independent and joint inversions of noisy measurements (for the six-block formation case) clearly indicate that the concomitant use of transient-pressure and resistivity measurements reduces non-uniqueness in the estimated model. On the other hand, the inversion tools developed in this chapter could also be used to design the deployment of sensors to optimally detect and quantify reservoir properties constrained by specific geometrical and petrophysical conditions.

Having established a quantitative proof of concept for the joint inversion of resistivity and transient-pressure measurements, we remark that the assumptions placed on the fluid-flow model can be further relaxed by using a multi-phase flow formulation for modeling transient-pressure responses as well as spatial distributions of fluid saturation. Furthermore, the salinity contrast between the injected and in-situ fluids can

be taken into account by solving a transport equation, namely, convection-diffusion equation in addition to multi-phase flow equations. Using a multi-phase, multi-component flow simulator, spatial distributions of fluid saturations and salt concentrations can be iteratively modeled in addition to other fluid-flow measurements such as pressure and fractional rates of flowing phases. Therefore, spatial distributions of fluid saturations and salt concentrations can be simulated in response to perturbations to spatial distributions of petrophysical parameters, for example, absolute fluid permeability and formation porosity within a joint inversion framework. Subsequently, spatial distributions of fluid saturations and salt concentrations can be used for computing spatial distributions of resistivity using appropriate saturation and salt concentration equations. As such, perturbations to petrophysical parameters, i.e., permeability and porosity, can be propagated to the resistivity domain. An electromagnetic (or dc resistivity) simulator can be used to simulate resistivity measurements in response to the perturbed resistivity model. In conclusion, quantitative estimations of spatial distributions of permeability and porosity can be performed honoring both fluid-flow and resistivity domain measurements. One possible limitation of the described algorithm is the computational cost of multi-phase fluid-flow simulations within an iterative inversion algorithm that requires the computation of the Jacobian matrix. However, for an inversion problem that can be described using a reasonable number of model parameters, and that requires a relatively short timescale of multi-phase flow, the described joint inversion approach remains practical. A successful application of the multi-phase joint inversion algorithm will be described in Chapter 8 for the simultaneous estimation of layer-by-layer permeability and porosities from electromagnetic induction logging and wireline formation tester transient-pressure measurements.

6.6 SUMMARY AND CONCLUDING REMARKS

The inversion results considered in this chapter can be regarded as a proof-of-concept exercise to appraise the spatial resolution properties of transient-pressure and dc resistivity measurements acquired with in-situ permanent sensors. For all of the cases investigated, the joint inversion of in-situ transient-pressure and dc resistivity measurements improved the accuracy of estimations performed separately with either measurement set. This was possible because simultaneous use of the two measurement sets naturally reduced non-uniqueness and hence improved stability. However, coupling of the two measurement sets is nontrivial. Ideally, a rigorous multi-phase fluid-flow formulation should be used to drive the simulation and inversion of the two measurement sets. The inversion exercises presented in this chapter were based on an approximate formulation of multi-phase flow that allowed us to couple pressure-diffusion and electrical phenomena through geometrical parameters. More challenging work remains ahead to couple the two phenomena in more complicated cases of fluid saturation transitions and salt mixing between injected and connate formation water.

Technical issues explored in this chapter included: (1) noisy and imperfect data sampling strategies and (2) modalities for the flow rate excitation of in-situ transient-pressure measurements. A multitude of sensor and measurement configurations could be further explored to appraise the relative influence of these issues on the accuracy and stability of the inversions. The inversion examples investigated in this chapter suggest that the cooperative use of in-situ transient-pressure and in-situ dc resistivity measurements does provide an efficient way to detect and quantify petrophysical changes due to fluid-flow dynamics in the vicinity of the sensors. However, because of the underlying diffusion phenomena governing the two sets of measurements, the spatial resolution of the inversion deteriorates with distance away from sources and detectors. It

is envisioned that the deployment of arrays of in-situ permanent sensors should be designed to selectively adjust the sensitivity and resolution to shallow and deep spatial regions in the reservoir.

Table 6.1: Petrophysical and fluid-flow parameters used in the construction of the synthetic reservoir models considered in this chapter.

Parameter	**Value**
Fluid viscosity, μ [Pa.s]	0.001
Total compressibility, C_t [kPa^{-1}]	2.90×10^{-6}
Wellbore radius, r_w [m]	0.06895
Reservoir external radius, r_e [m]	107.11
Reservoir thickness, h [m]	6.10
Injection rate, q (step-function pulse), [m^3/d]	31.80

Table 6.2: Comparison of CPU execution times for the use of conventional and dual-grid inversion techniques. Inversions were performed on a 300 MHz SGI OCTANE workstation.

Grid I size (outer loop) Jacobian computed via Fréchet derivatives	**Grid II size (inner loop) Jacobian computed using Broyden's rank-one update formula**	**CPU time [s]**
$r \times z$ (EKSM) - r (NKARD)	$r \times z$ (EKSM) - r (NKARD)	
105 × 304 - 105 nodes	Broyden update formula not utilized	8566.7
105 × 304 - 105 nodes	105 × 304 - 105 nodes	6448.9
105 × 304 - 105 nodes	54 × 204 - 54 nodes	4486.8

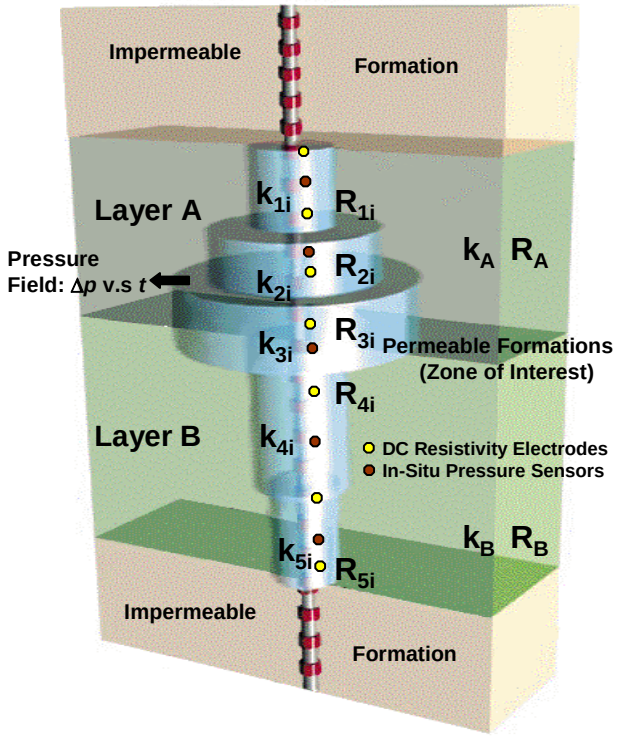

Figure 6.1: Graphical description of a generic in-situ permanent-sensor installation along a vertical well. In-situ pressure sensors and point-contact dc electrodes are deployed in direct hydraulic communication with the formation. In this example, water is injected through an open well interval thereby displacing in-situ oil. Water fronts in the form of cylinders with variable radii are used to indicate variability in the vertical distribution of permeability and electrical resistivity.

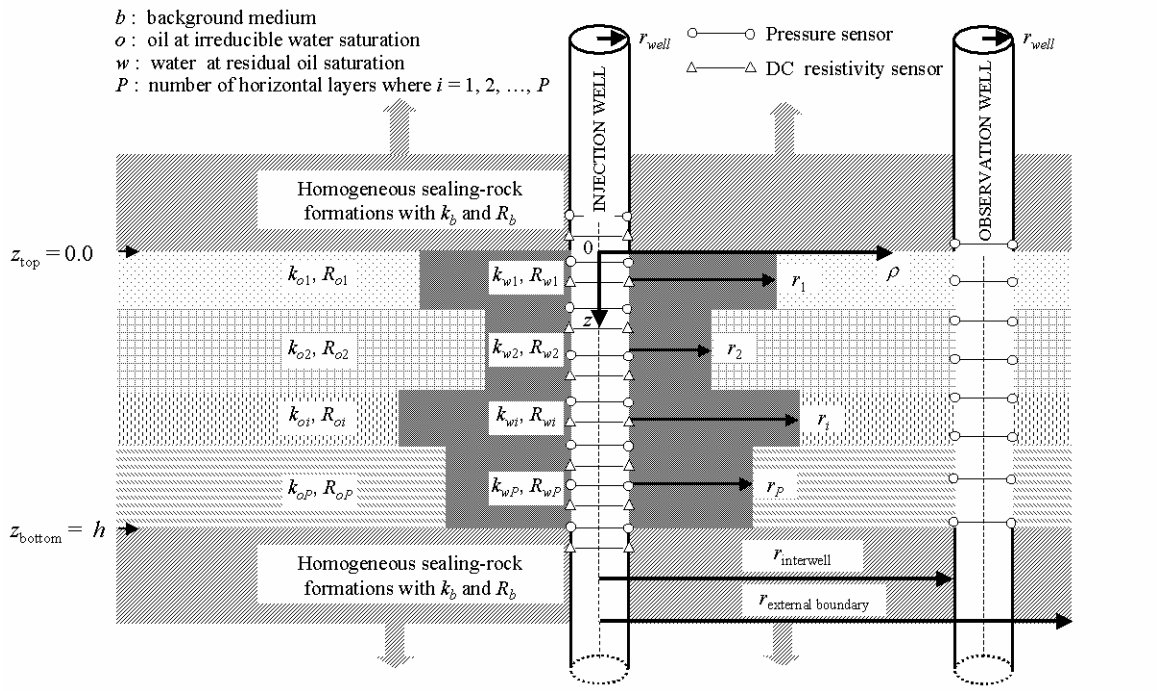

Figure 6.2: Graphical description of the parametric petrophysical model adopted for the joint inversions of in-situ measurements of pressure and dc resistivity. The petrophysical model is axial symmetric with respect to the axis of the injection well. Pressure and dc resistivity sensors are deployed along the injection well while only pressure sensors are deployed along the observation well. The parametric description of the petrophysical model consists of a fixed number of horizontal layers. There are two concentric cylindrical blocks within each horizontal layer. The first cylindrical block has an inner radius equal to the borehole radius and a variable outer radius. The second cylindrical block has an outer radius equal to the distance between the injection well and the outer boundary of the reservoir, and an inner radius equal to the outer radius of the first cylindrical block. Permeability and electric resistivity are assumed constant within a given cylindrical block.

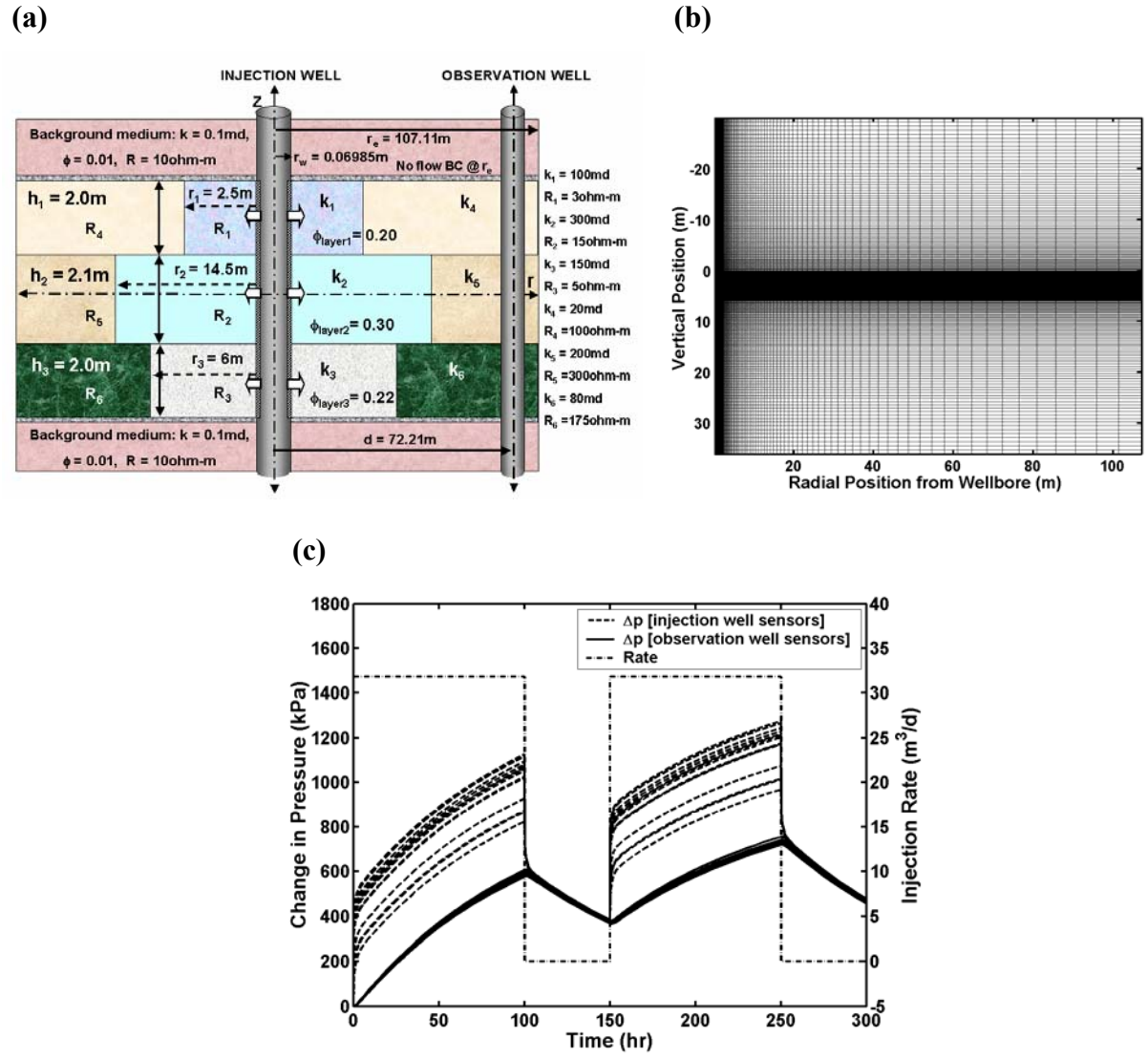

Figure 6.3: Six-block formation model. (a) Description of the permeable medium. The associated reservoir and fluid properties are listed in Table 6.1. Injection flow rates are modeled with a truncated-line source equivalent to a fully penetrated well. Both injection and observation wells are equipped with in-situ permanent pressure sensors. The resistivity array, consisting of dc point-contact electrodes, is deployed only along the injection well. (b) A finite-difference grid of size 134×249 in the r and z directions, respectively, is used for the forward and inverse modeling of in-situ transient-pressure measurements. (c) Superimposed plots of pressure change and flow rate as a function of time. The flow rate history consists of a periodic schedule of a 100 hr-long injection pulse followed by a 50 hr-long fall-off period.

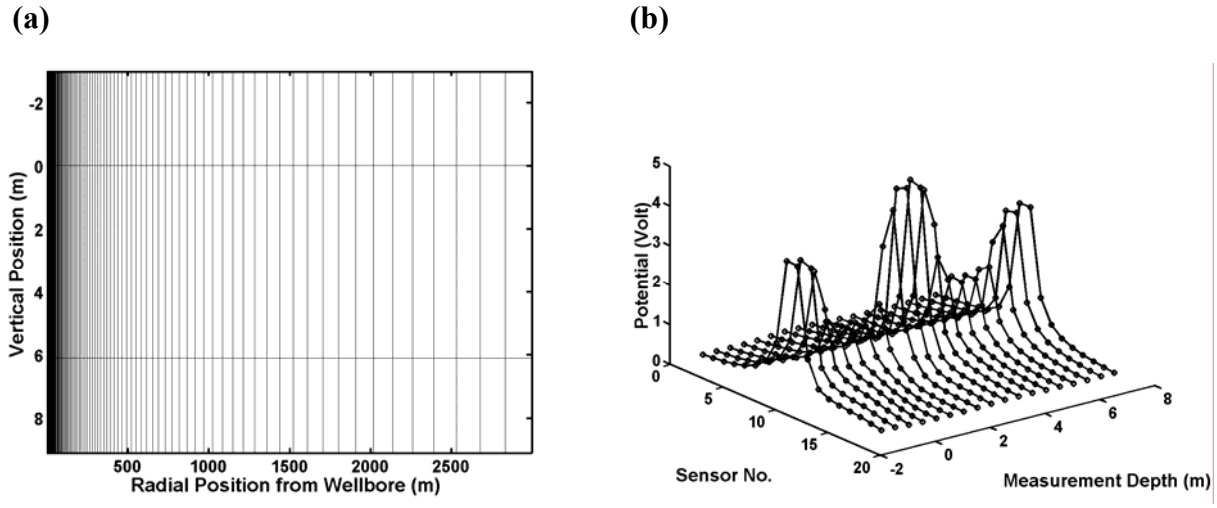

Figure 6.4: (a) Finite-difference radial grid constructed with 201 logarithmically distributed nodes. This mesh is used for the forward and inverse modeling of dc resistivity measurements. The forward modeling algorithm only requires the use of a radial grid. (b) dc electrical response: voltage measurements acquired with point-contact electrodes deployed along the injection well.

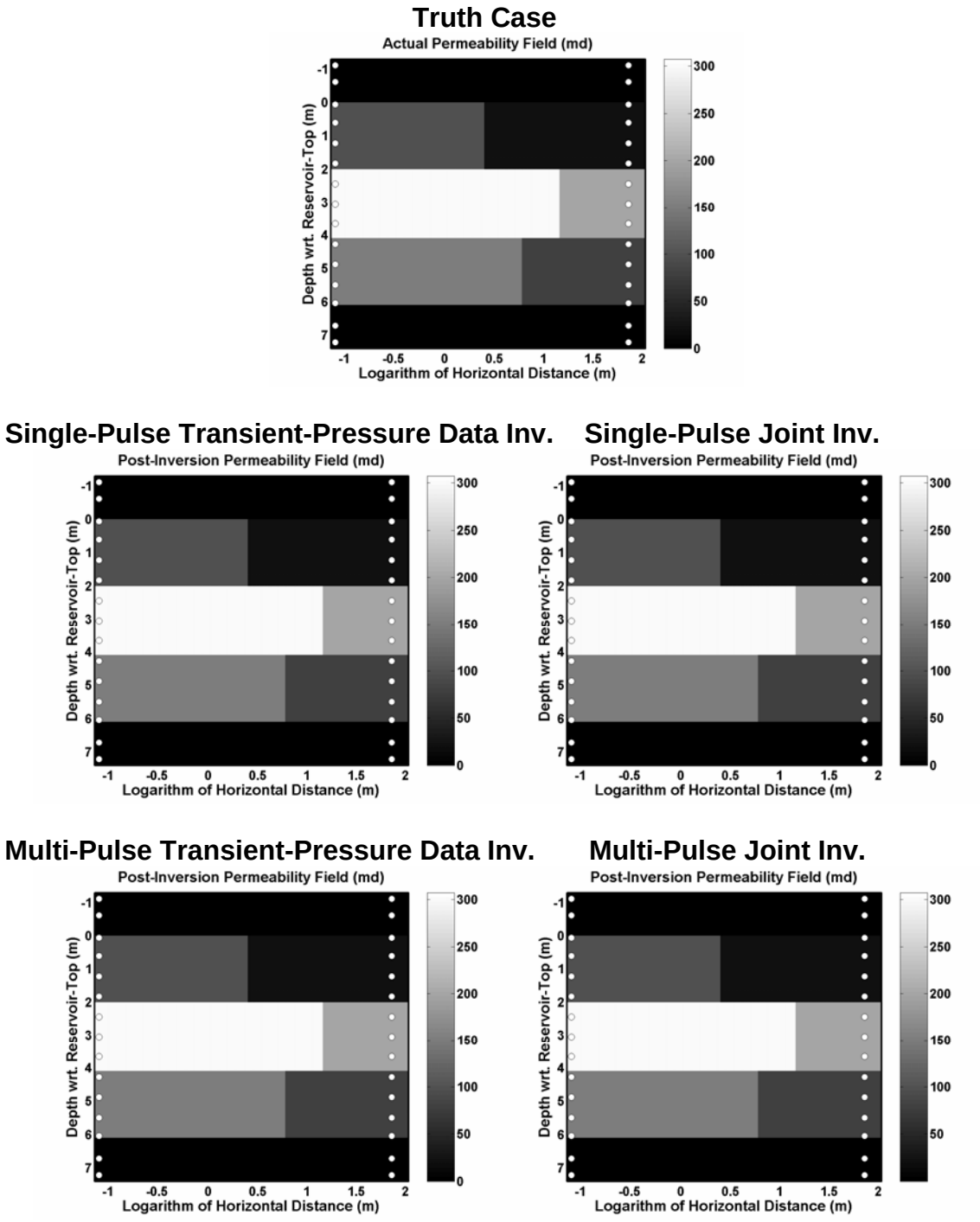

Figure 6.5: Six-block formation example. Actual and post-inversion spatial distributions of permeability. Parametric estimations are performed with independent inversions of noise-free single- and multi-pulse in-situ transient-pressure measurements, and alternatively, with joint inversions of noise-free single- and multi-pulse in-situ transient-pressure and dc resistivity measurements. Locations of in-situ pressure sensors in the injection and observation wells are indicated with small circles.

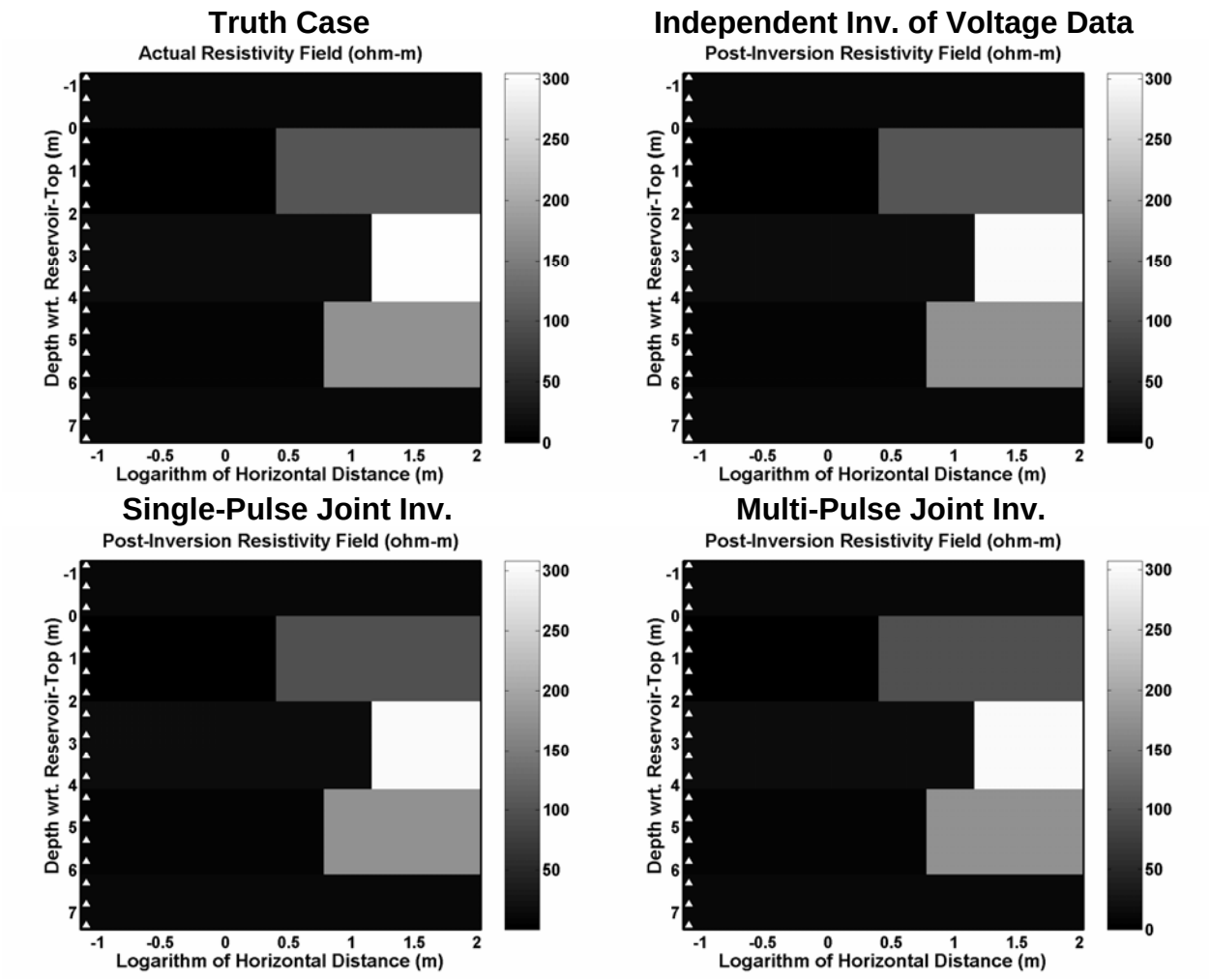

Figure 6.6: Six-block formation example. Actual and post-inversion spatial distributions of resistivity. The estimated spatial distributions are obtained from independent inversions of noise-free dc resistivity measurements, and alternatively, from joint inversions of noise-free single- and multi-pulse in-situ transient-pressure and dc resistivity measurements. Locations of in-situ contact electrodes (resistivity sensors) in the injection well are indicated with small triangles.

(a)

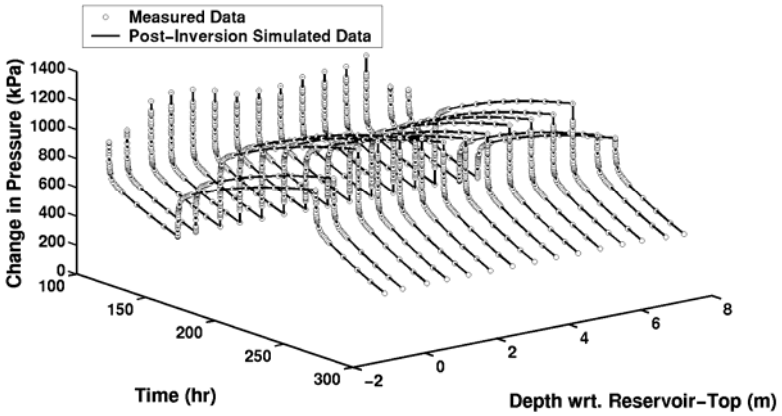

(b)

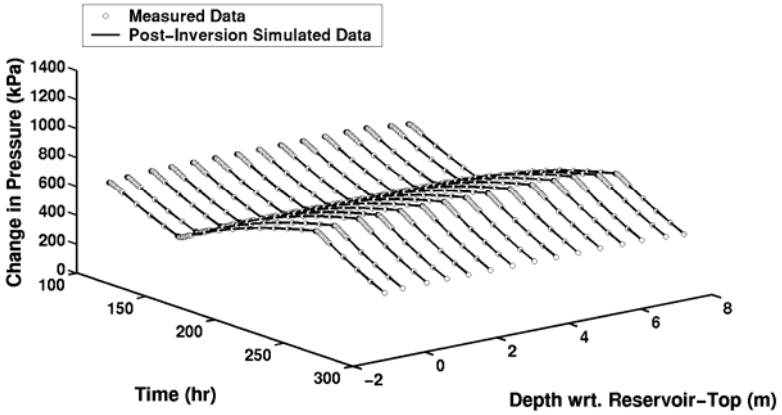

(c)

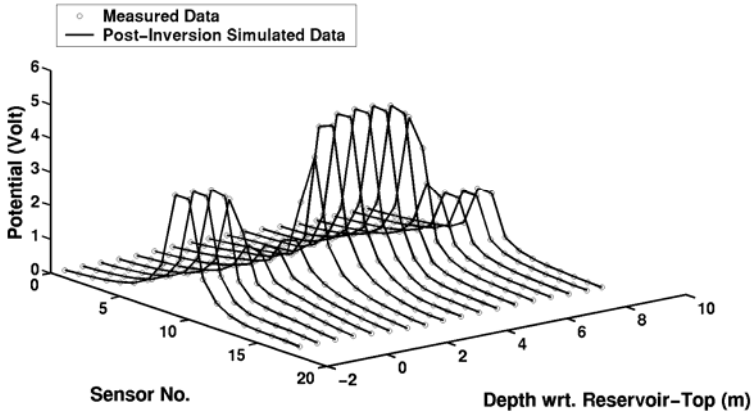

Figure 6.7: Six-block formation example. Plots of measured and post-inversion simulated in-situ transient pressures along the (a) injection and (b) observation well. (c) Plots describing measured and post-inversion dc resistivity voltages along the injection well. Inversion of the spatial distribution of permeability and resistivity was performed jointly from noise-free multi-pulse in-situ transient-pressure and dc resistivity measurements.

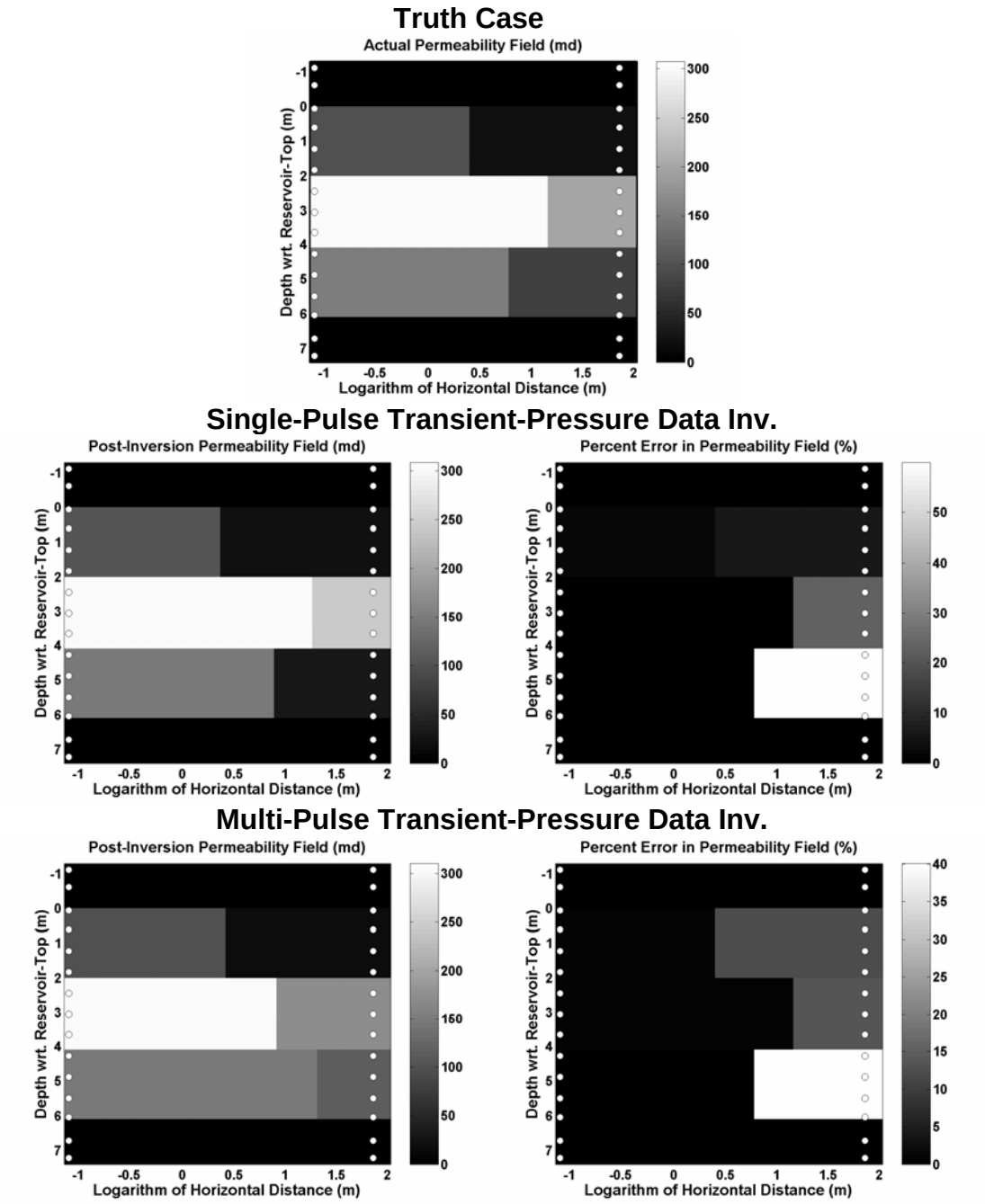

Figure 6.8: Six-block formation example. Comparisons of the inverted spatial distributions of permeability with the actual spatial distribution. Model domain percent errors are also shown. The inverted spatial distributions of permeability were obtained using noisy single- and multi-pulse transient-pressure measurements, respectively. Transient-pressure measurements are contaminated with 1% zero-mean Gaussian random noise. Locations of in-situ pressure sensors in the injection and observation wells are indicated with small circles.

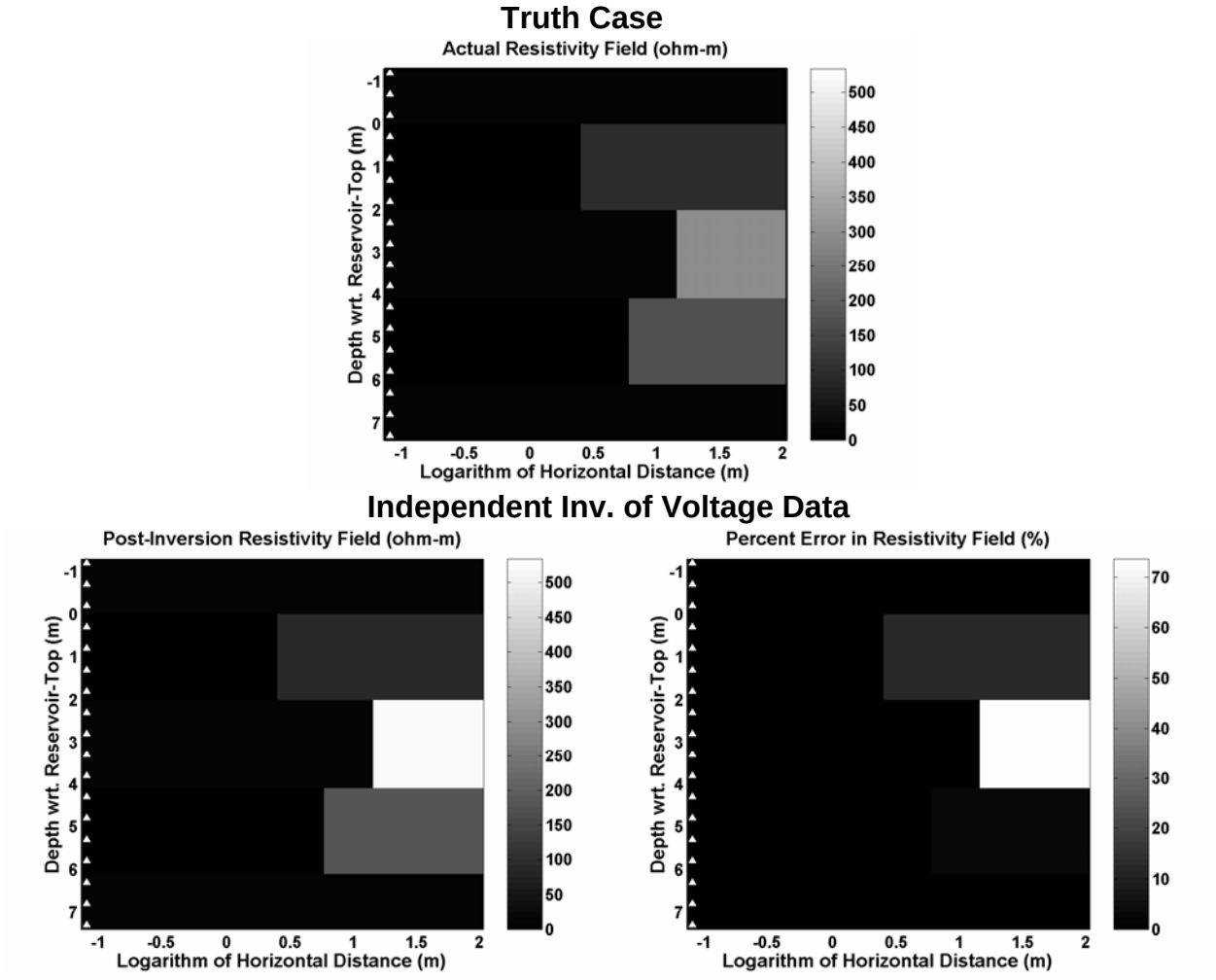

Figure 6.9: Six-block formation example. Comparison of the inverted spatial distribution of resistivity with the actual spatial distribution. Model domain percent errors are also shown. The inverted spatial distribution of resistivity was obtained using noisy dc resistivity measurements contaminated with 1% zero-mean Gaussian random noise. Locations of in-situ contact electrodes (resistivity sensors) in the injection well are indicated with small triangles.

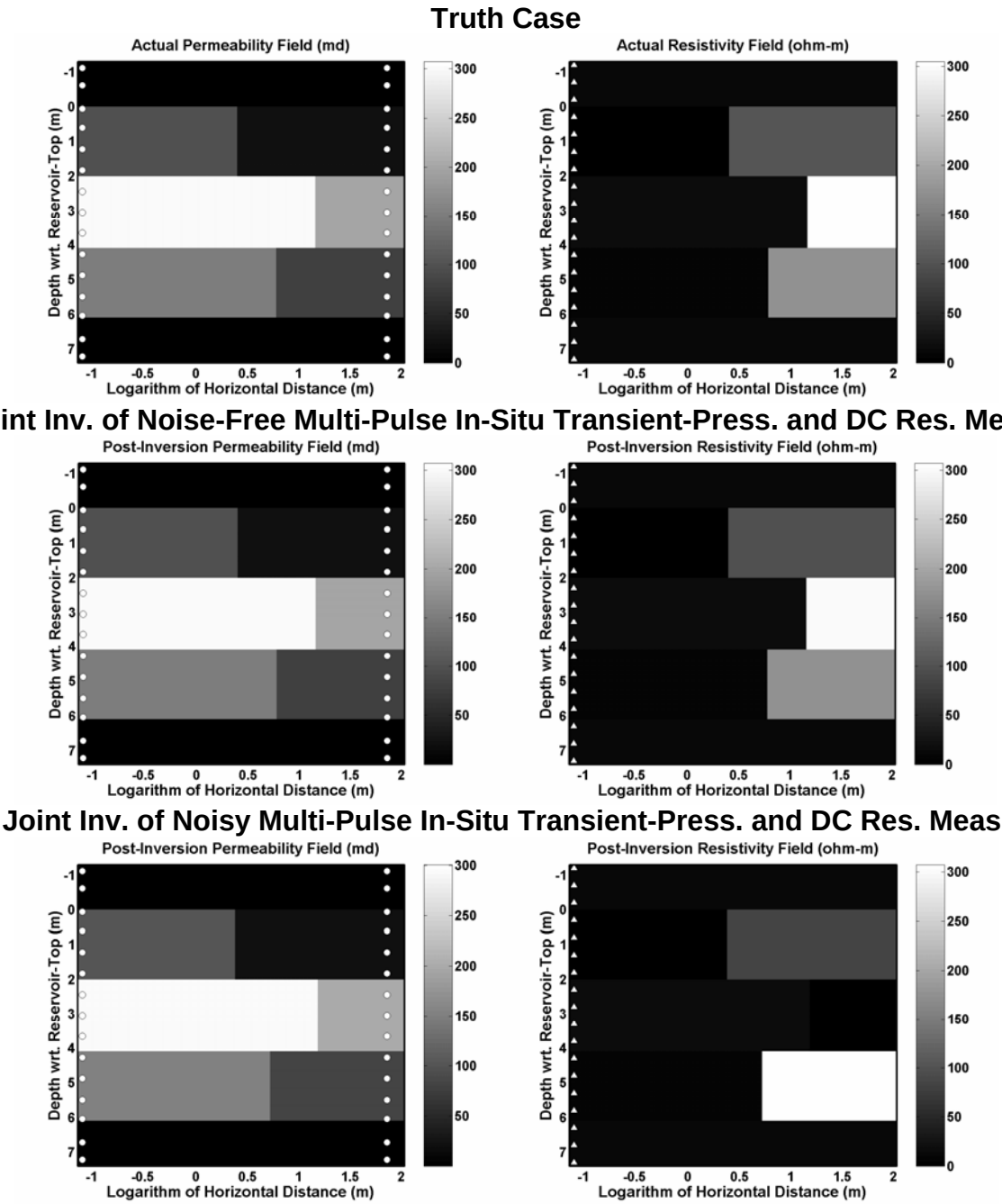

Figure 6.10: Six-block formation example. Comparisons of the inverted spatial distributions of permeability and resistivity with the actual spatial distributions. The inverted spatial distributions of permeability and resistivity were obtained using both noise-free and noisy multi-pulse transient-pressure and dc resistivity measurements, respectively. For the case of noisy data, 2% zero-mean Gaussian random noise was added to both transient pressure and dc voltage measurements. Locations of in-situ pressure sensors in the injection and observation wells are indicated with small circles, and locations of in-situ contact electrodes (resistivity sensors) in the injection well are indicated with small triangles.

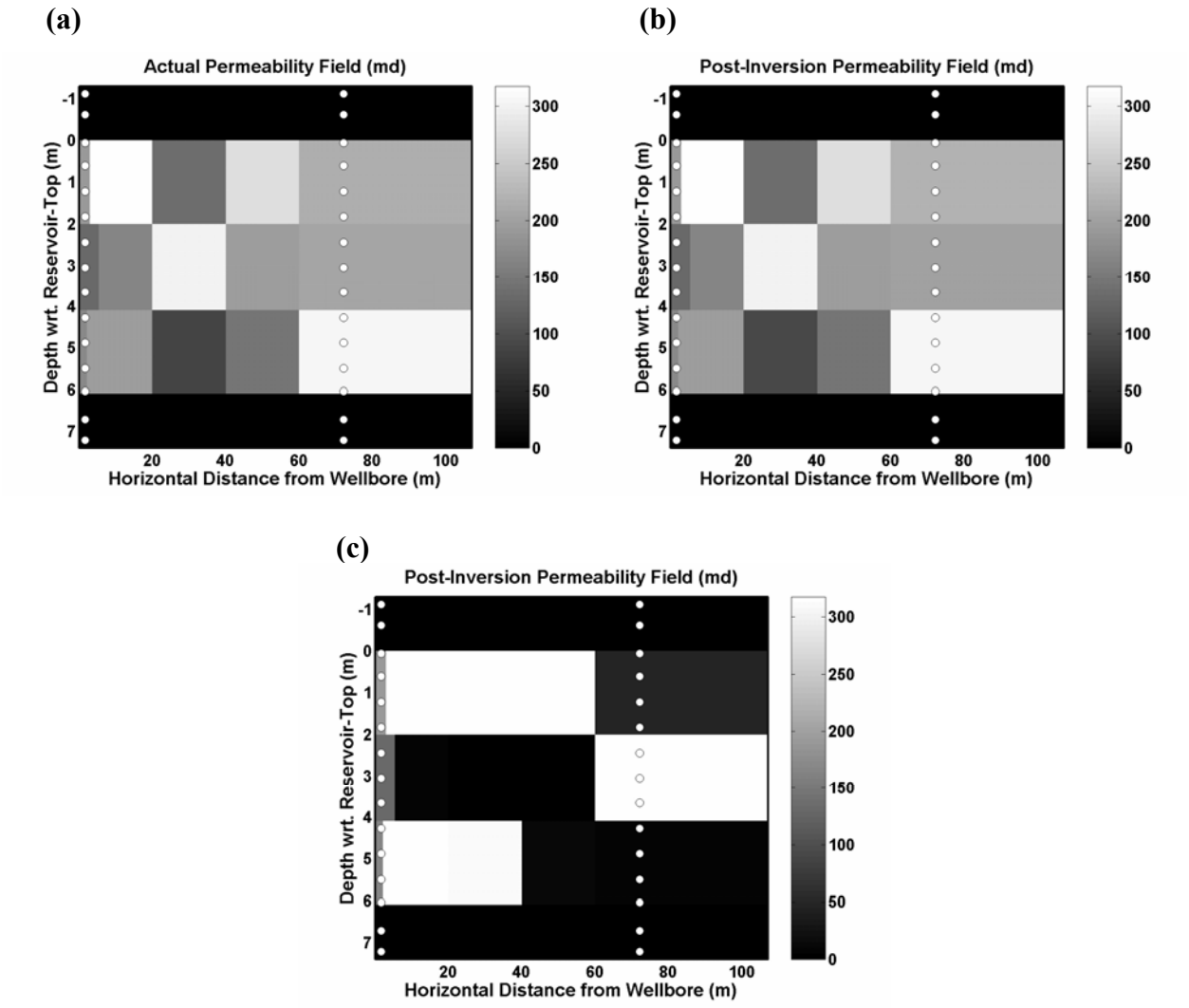

Figure 6.11: Multi-block formation example. Comparisons of inverted and actual spatial distributions of permeability. (a) Actual spatial distribution of permeability. The inverted spatial distribution of permeability was obtained using (b) noise-free and (c) noisy multi-pulse transient-pressure and dc resistivity measurements, respectively. For the inversions with noisy data, 2% zero-mean Gaussian random noise was added to both transient-pressure and dc voltage measurements. Locations of in-situ pressure sensors in the injection and observation wells are indicated with small circles.

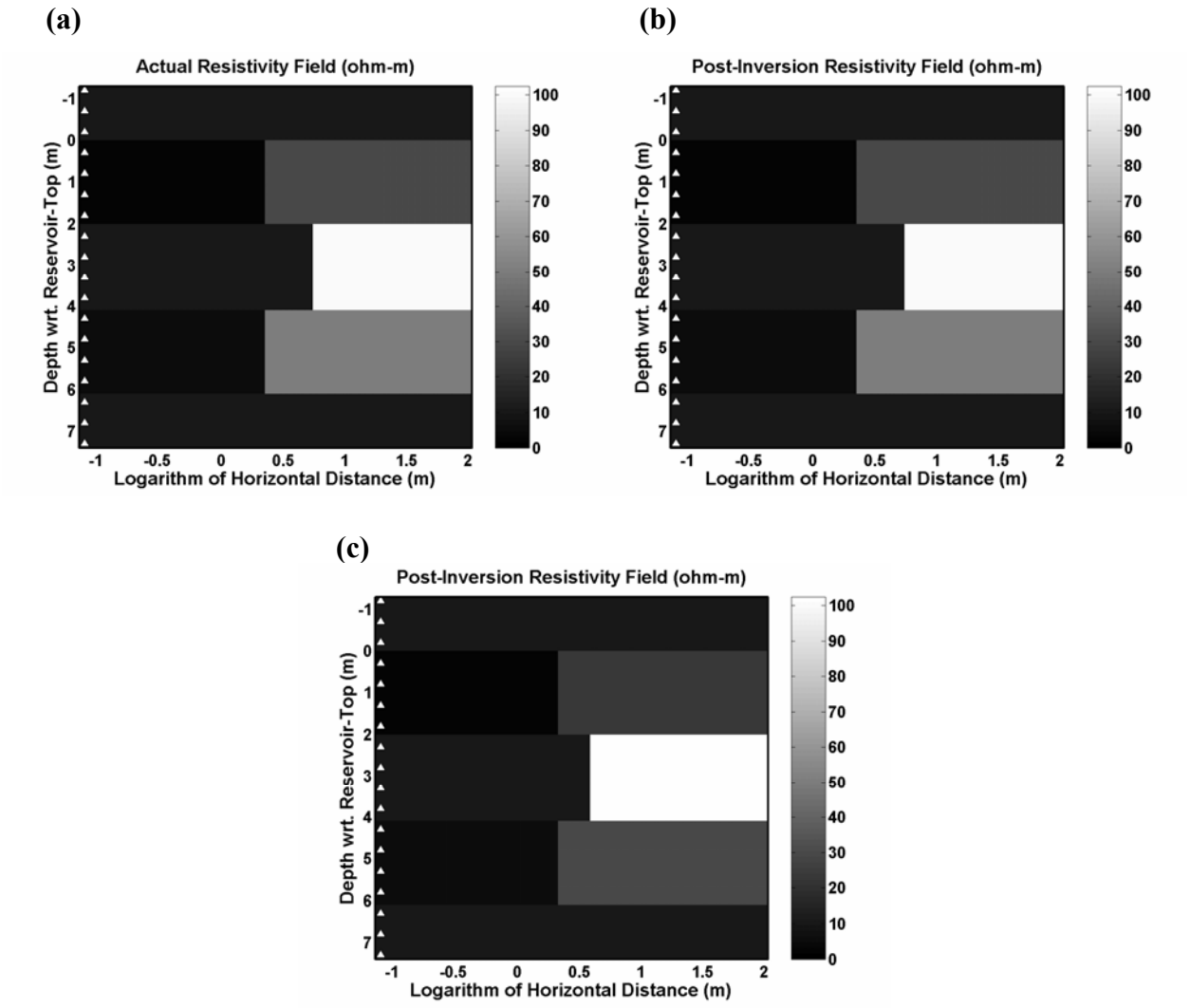

Figure 6.12: Multi-block formation example. Comparisons of inverted and actual spatial distributions of resistivity. (a) Actual spatial distribution of resistivity. The inverted spatial distribution of resistivity was obtained using (b) noise-free and (c) noisy multi-pulse in-situ transient-pressure and dc resistivity measurements, respectively. For the inversions with noisy data, 2% zero-mean Gaussian random noise was added to both transient-pressure and dc voltage measurements. Locations of in-situ contact electrodes in the injection well are indicated with small triangles. Note that in the frames of this figure, the horizontal distance is presented on a logarithmic scale unlike in the case of plots that show the spatial distribution of permeability for the multi-block formation example.

PART III: INTEGRATED PETROPHYSICAL INVERSION

Chapter 7: Joint Inversion of Transient-Pressure and Time-Lapse Electromagnetic Logging Measurements

7.1 INTRODUCTION

Inspired by the aforementioned dual-physics efforts summarized in Chapter 1, the objective of the work reported in this chapter is to develop a robust, accurate, and efficient algorithm for the parametric joint inversion of electromagnetic induction and transient formation-pressure measurements. The inversion algorithm will yield petrophysical properties, namely, layer-by-layer horizontal and vertical absolute permeabilities, and porosities of the hydrocarbon-bearing formations. Inversion of dual-physics measurements is posed as an optimization problem where a quadratic objective function is minimized subject to physical constraints on the model. A modification of the gradient-based iterative Gauss-Newton optimization technique, namely, the Weighted and Regularized Gauss-Newton (`WRGN`) method is utilized for the inversions (Gill et al., 1981; Nocedal and Wright, 1999). At each iterative step, the solution of the forward problem is required. Forward modeling of dual-physics measurements entails coupled simulations of mud-filtrate invasion, wireline formation test measurements, and induction-logging measurements. We utilize efficient three-dimensional finite difference-based algorithms to simulate multi-phase fluid-flow and electromagnetic induction phenomena (Aziz and Settari, 1979; Druskin et al., 1999). Details of the coupled physics algorithm developed for the simulation of fluid flow and electromagnetic measurements is described in Chapter 4. Time-dependent spatial distributions of pressure, saturation, and salt concentration generated during water-base mud-filtrate invasion and a subsequent wireline formation test are modeled as two-phase advective transport of three

components, namely, oil/gas, water, and salt. Coupling between two-phase flow and physics of electromagnetic induction is accomplished via Archie's saturation equation. Isothermal salt mixing taking place within the aqueous phase due to the invading and in situ salt concentration contrast is also taken into account by means of a brine conductivity model (Zhang et al., 1999).

Proof-of-concept examples of the joint inversion method are successfully conducted for single-well two-dimensional (2D) axisymmetric models that involve noisy and noise-free synthetically generated electromagnetic induction and transient-pressure measurements. In one of these examples, we carry out joint as well as independent inversions of induction-logging and dual-packer formation tester measurements for the purpose of comparison. For all of the investigated cases, the effect of mud-filtrate invasion is rigorously taken into account by making use of a novel numerical algorithm that simulates the physics of mud-filtrate invasion. The reported work confirms that the intrinsic value of each piece of data considerably improves when used in a cooperative, integrated fashion, and under a common petrophysical model. Consequently, measurement types that are considered to be of low vertical resolution but of large depth of investigation (i.e., transient-pressure measurements) can be efficiently integrated with measurements that exhibit a relatively shallow depth of investigation but higher vertical resolution (i.e., induction-logging measurements) into a common petrophysical model.

7.2 THE INVERSE PROBLEM AND THE INVERSION ALGORITHM

In the inverse problem, time-lapse measurements of the vertical component of total magnetic field, H_z, are conducted at multiple receiver locations, frequencies, and at various logging times with a depth-profiling sonde [see, for example, Figure 7.1(a)]. In addition, we consider the availability of multi-probe transient-pressure measurements, $p(t)$, acquired by a wireline formation tester shown in Figure 7.1(b). As formulated in

Chapter 4, the forward model for coupled dual-physics measurements is a nonlinear function of the spatial distribution of absolute permeabilities and porosities and other relevant rock and fluid properties. In this chapter, we assume the availability of other rock and fluid properties from various logs and laboratory experiments. The objective of our work is the joint inversion of layer-by-layer horizontal and vertical absolute permeabilities and porosities from time-lapse electromagnetic induction and transient-pressure measurements.

In this chapter, we focus only on vertical variability in the petrophysical model. Horizontal geological layers of various thicknesses characterize the reservoir geometry. The vector of model parameters, $\mathbf{x}$, is made up of the layer-by-layer parametric spatial distribution of horizontal and vertical absolute permeabilities, and porosities. A schematic of the model domain parameterization is shown in Figure 7.2. Here, we assume the availability of information about the locations of layer boundaries from other types of logs such as borehole images. Based on the extent of the available measurement data and a-priori information, an arbitrary combination of the above mentioned petrophysical parameters can be included in $\mathbf{x}$.

7.3 PROOF OF CONCEPT NUMERICAL EXAMPLES

A vertical borehole is considered to intersect a hydrocarbon-bearing horizontal formation comprising of a single thick-layer in our first test case. In addition to the permeable layer, sealing upper and lower shoulder beds are included in the geoelectrical model [see Figure 7.3(a)]. From the onset of drilling, the permeable formation is subject to dynamic water-base mud-filtrate invasion. At the first logging time, an array induction log is recorded across the formation. The tool assumed for the acquisition of electromagnetic induction measurements is the Array Induction Imager Tool, AIT™, described schematically in Figure 7.1(a). This sonde is used to ensure the availability of

data with multiple depths of investigation (Hunka et al., 1990). The second available data type is multi-probe transient formation-pressure measurements acquired with the Modular Formation Dynamics Tester, MDT™. A dual-packer/probe module configuration with two vertical observation probes is considered as the measurement platform (Pop et al., 1993; Ayan et al., 2001). Figure 7.1(b) shows a schematic of the packer and probe modules. Soon after the first induction log is recorded, the multi-probe formation tester configuration is deployed across the formation of interest to conduct transient-pressure measurements. Time-series of pressure responses are recorded at two observation probe locations, and at the center of the dual-packer open interval in response to a controlled flow rate pulse. A post transient-test electromagnetic induction log senses the perturbed two-phase flow field caused by the formation tester experiment. This measurement schedule involves acquisition of dual-physics data and, is here referred to as log-test-log strategy.

Given favorable flow conditions and sufficient test duration, transient-pressure measurements conducted by the dual-packer and tandem observation probes contain significant information about horizontal and vertical permeabilities (k_h and k_v), when reliable a-priori information about the group ϕC_t [product of porosity and total compressibility] is available (Ayan et al., 2001). Here, we assume the availability of laboratory measurements of fluid properties that allow reliable the determination of total compressibility, C_t (for slightly compressible phases, i.e., aqueous and oleic phases), or its dependence on pressure (for a compressible, i.e., gaseous phase). Additionally, in our forward model, movement of saturations and salt concentrations due to advective transport of fluids is robustly linked to spatial distributions of conductivity via a saturation equation. Thus, provided that the choice of saturation equation is appropriate for the formation of interest, information about porosity, ϕ, can be robustly extracted

from time-lapse electromagnetic measurements within the framework of a joint inversion scheme.

With the purpose of establishing a basis of comparison for the joint inversion approach, we also considered the inversion of time-lapse electromagnetic data alone for the zeroth order homogeneous and isotropic single-layer formation model. This schedule involves acquisition of two induction logs performed at two separate times. The formation is subject to mud-filtrate invasion during the time gaps between drilling, the first log, and the second log. This schedule is referred to as time-lapse log strategy.

Formation rock and fluid properties, specific instrumental details, and scheduling of the above described measurement strategies are listed in Table 7.1. We used a $31\times1\times30$ grid in the cylindrical coordinate system as the result of extensive finite-difference gridding studies to produce computationally efficient, internally consistent, and accurate numerical simulations. This grid is uniform in the vertical and azimuthal directions. Block sizes increase logarithmically in the radial direction away from the borehole. A vertical cross-section of this grid is shown in Figure 7.4. Capillary pressure effects are assumed to be negligible. The relative permeability function used for this case is illustrated in Figure 7.5(a).

The following schedule is assumed for log-test-log strategy. The first induction log is recorded at the 3rd day of mud-filtrate invasion. A subsequent wireline formation test is scheduled to last 300 min. During the formation test, fluid is withdrawn from the formation at a constant liquid rate of 30 rbbl/d [55 cc/sec = 4.75 m^3/d] for 100 min. As such, the total produced fluid volume amounts to 2 rbbl [3.67 cc]. The formation pressure drawdown response is observed across the dual-packer interval and at the observation probes. Subsequently, the tool is shut down for another 200 min and the formation pressure build-up response is recorded. In the example cases, we only consider the use of

transient-pressure data sampled during the build-up period of the formation test. Upon conclusion of the formation test, the second induction log is recorded. For the time-lapse log strategy, the first induction log is also recorded at the 3rd day of invasion. Yet, the formation is subjected to mud-filtrate invasion for a week before the second induction log is recorded at the 10th day.

For Case 1, simulated mud-filtrate invasion history until the first logging time is shown in Figure 7.6(a). Rate history is rendered into a two-step rate schedule via integral averaging of the early time-transient into an early-time equi-volume step-rate. For the time-lapse logging strategy, the invasion rate schedule is extended further until the second logging time. As shown in Figure 7.6(b), the rate domain response of the removal of mudcake due to drill-string trip-out at the first logging time is also incorporated into the mud-filtrate invasion history.

Joint inversions of time-lapse magnetic field and transient-pressure measurements (log-test-log schedule) and inversions of time-lapse magnetic field measurements (time-lapse log schedule) are performed to yield isotropic formation absolute permeability, k, and porosity, ϕ. True and initial guess permeability and porosity values are $k = 100$ mD, $\phi = 0.25$, and $k = 40$ mD, $\phi = 0.12$, respectively. The effect of noise on the inversion results is assessed by adding zero-mean Gaussian random noise to the synthetically-generated measurements. Inversion results are reported in Table 7.2 along with the number of Gauss-Newton iterations required to achieve convergence. Joint inversion of dual-physics data is performed using two data weighting strategies for each noise level. In the first strategy, both electromagnetic and transient-pressure data are weighted uniformly. In the second strategy, weight coefficients of electromagnetic data are made equal to three times of those used for transient-pressure data. In this case, the inversion is clearly biased to fit the electromagnetic data. At low noise levels, all measurement and

inversion strategies yield accurate estimations. In comparison to other approaches, the uniform-weight joint inversion strategy consistently requires fewer number of Gauss-Newton (WRGN) iterations for all investigated noise levels. When the weights of electromagnetic data are increased, inversion results for permeability at high noise levels deteriorate. Moreover, the number of required Gauss-Newton iterations increases in comparison to uniform-weight joint inversion. In general, results indicate that the joint inversion approach yields more accurate permeability values at high noise levels in comparison to the inversion of time-lapse electromagnetic measurements.

For all of the investigated cases, inversion results for porosity are robust in the presence of additive random Gaussian measurement noise of up to 8%. It is also observed that the quality of inverted porosity values deteriorates significantly above the 10% noise-level. For one-dimensional layered formation models, the multi-resolution acquisition strategy provides sufficient degrees of freedom to resolve porosity values from measurements contaminated with relatively high levels of noise. The first-order sensitivity of multi-resolution induction-logging measurements with respect to a variation of the spatial distribution of conductivity is related to the sensitivity of the measurements with respect to a perturbation of porosity via Archie's equation. Spatial distributions of fluid saturation and salt concentration are rendered by the reservoir simulator for the various time-snapshots of electromagnetic data acquisition. The important assumption in this process is the knowledge about the governing parameters of the assumed saturation-conductivity relationship. Additionally, the vertical sampling strategy used for the induction-logging measurements ensures the presence of redundant measurement points within each layer thereby improving the stability and robustness of the inversion.

For both log-test-log and time-lapse log inversion strategies, we reconstruct the conductivity domains sensed by the induction sonde at two logging times. This is

accomplished by performing flow simulations using the inverted petrophysical parameters. Figure 7.7 shows the reconstructed spatial distributions of electrical conductivity for log-test-log and time-lapse log strategies for the two logging times. In the illustrated case, simultaneous inversion for permeability and porosity is carried out using dual-physics data contaminated with 7% Gaussian random noise. The estimated spatial distributions of near-borehole conductivity clearly indicate the development of a conductive annulus for all of the investigated cases. Presence of conductive annuli has been discussed in the past by several authors, including Dumanoir et al. (1957), Ramakrishnan and Wilkinson (1997), Zhang et al. (1999), George et al. (2003), and Torres-Verdín et al. (2003). Our numerical simulations confirm that the invasion of fresh water-base mud-filtrate into a hydrocarbon-bearing zone saturated with a conductive brine leads to the development of a conductive annulus zone in the near-borehole region. The contrast of salt concentration between the invading and the in situ aqueous phases, the petrophysical properties of the rock-formation, and the PVT properties of the fluid phases govern the existence, spatial distribution, and time-evolution of the conductive annulus.

Near-borehole cross-sections of electrical conductivity simulated (using the inverted model parameters) for logging instances of both log-test-log and time-lapse log acquisition strategies are shown in the panels of Figure 7.7. As shown in Figures 7.7(a) and 7.7(c), for both acquisition strategies the spatial distributions of conductivity at the first logging time (3rd day of invasion) are almost identical. The effect of gravity on the spatial distribution of aqueous phase saturations and, consequently, on the spatial distribution of conductivity at the top and the bottom of the formation can be clearly identified in Figures 7.7(a) and 7.7(c). Since the invading aqueous phase exhibits a higher

density compared to the in situ oleic phase, the invading aqueous phase has a natural tendency to move to the bottom of the formation.

Spatial distribution of near-borehole conductivity is also simulated for the snapshot of time that corresponds to the conclusion of the formation test. As shown in Figure 7.7(b), fluid withdrawal by means of the dual-packer module during the drawdown period of the formation test perturbs the near-borehole conductivity distribution. The packer-sealed interval, which corresponds to the 17^{th} through 20^{th} ft of the 30 ft-thick formation, and the flow field generated by the simultaneously-flowing aqueous and oleic phases are clearly identifiable in the conductivity image.

For the time-lapse log acquisition strategy, mud-filtrate invasion proceeds with the rate schedule shown in Figure 7.6(b) for another week subsequent to the acquisition of the first induction log at the 3^{rd} day of mud-filtrate invasion. As shown in Figure 7.7(d), at the 10^{th} day of invasion when the second induction-logging measurements are acquired, the conductive annulus is found to be spread further in the radial direction. The reconstructed conductivity image exhibits more severe gravity effects at the top and the bottom of the formation in comparison to the one shown for the 3^{rd} day of mud-filtrate invasion.

In the second numerical example (Case 2), we consider a vertically anisotropic formation with the following true model parameters: horizontal permeability, $k_h = 100$ mD, vertical permeability, $k_v = 20$ mD, and porosity, $\phi = 0.25$. All other parameters remain the same as in the previous case. We assume a-priori knowledge about horizontal permeability and stipulate the true value. Only joint inversion of uniformly weighted time-lapse magnetic field and transient-pressure data at various levels of Gaussian random noise is investigated for the simultaneous estimation of vertical permeability and porosity. Initial-guess values for vertical permeability and porosity are $k_v = 50$ mD and

$\phi = 0.15,$ respectively. Inversion results are reported in Table 7.3 along with the required number of Gauss-Newton iterations for convergence. Inversion results indicate that the estimation of vertical permeability remains robust up to 3% Gaussian random noise level. Yet, at investigated noise levels higher than 3%, strong non-uniqueness renders the estimation of vertical permeability inaccurate. Unlike the estimation of vertical permeability, inverted porosity values are consistently accurate even at high noise levels. Extensive inversions conducted in this case indicate that the presence of multi-probe transient formation-pressure data yields a significant improvement in the simultaneous estimation of vertical permeability and porosity.

In the third numerical example (Case 3), we again consider a vertically anisotropic formation. In this case, true values of model parameters are as follows: horizontal permeability, $k_h = 50$ mD, vertical permeability, $k_v = 5$ mD, and porosity, $\phi = 0.18.$ All other information about the problem remains the same as that of Case 1. Joint inversion of uniformly weighted time-lapse magnetic field and transient-pressure data at various levels of Gaussian random noise is investigated for the simultaneous estimation of horizontal and vertical permeabilities, and porosity. Initial guesses for model parameters are as follows: $k_h = k_v = 100$ mD and $\phi = 0.25.$ Inversion results are listed in Table 7.4. Inversions indicate that for up to 5% Gaussian random noise level, the estimation of horizontal permeability remains robust. However, at noise levels higher than 5%, strong non-uniqueness renders the estimation of horizontal permeability inaccurate. The model parameter that is most sensitive to the deleterious effect of noise is vertical permeability. The highest noise level that yields consistent inversion results for this parameter is 3%. Inverted porosity values remain consistently accurate even at high noise levels. Yet, a slight deterioration trend in the inversion results for porosity is observed when the noise level in the dual-physics data increases.

In the last numerical example (Case 4), we consider a dry-gas saturated formation made up of three anisotropic layers of various thicknesses shown in Figure 7.3(b). Crossflow of fluids is allowed among the flow units. Formation rock and fluid properties, specific instrumental details, and scheduling of the above described measurement strategies are listed in Table 7.1. Layer-by-layer relative permeability and capillary pressure functions used for this numerical case are illustrated in Figures 7.5(b) and 7.5(c). Simulated and averaged mud-filtrate invasion histories until the first logging time are shown in Figure 7.6(c) for each flow-unit. Only log-test-log strategy is considered with the same measurement schedule as in the previous case except that the first logging time is assumed to be the 1st day of mud-filtrate invasion. During the formation test, the packer module is set across the lower-most layer and observation probes are located such that each probe is in contact with a separate layer. Joint inversion of uniformly weighted time-lapse magnetic field and transient-pressure data at various levels of Gaussian random noise is investigated for the simultaneous estimation of horizontal and vertical permeabilities, and porosity for each layer. Actual and initial guess values for the model parameters as well as inversion results are reported in Table 7.5. Inversion results clearly demonstrate the sensitivity of vertical permeability values in response to the effect of noise. Only at 1% noise level vertical permeability values are accurately reconstructed. Estimation of horizontal permeability and porosity values appear to be more robust in the presence of measurement noise in comparison to the estimation of vertical permeability values. High noise level negatively affects the estimation of model parameters of the most-permeable middle-layer. The quality of the estimation of model parameters for the top- and bottom-most layers is relatively higher in comparison to that of the middle-layer.

7.4 NUMERICAL EXAMPLES FOR THE QUANTIFICATION OF UNCERTAINTY

In this set of examples, a vertical borehole is considered to intersect a hydrocarbon-bearing horizontal formation comprising of three layers in our numerical formation model. In addition to the permeable layers, sealing upper and lower shoulder beds are included in the geoelectrical model as shown in Figure 7.8. From the onset of drilling, the permeable formation is subject to dynamic water-base mud-filtrate invasion. At the first logging time, an array induction log is recorded across the formation. Similar to the single-layer examples described above, the tool assumed for electromagnetic induction measurements is the Array Induction Imager Tool, AIT™, schematically shown in Figure 7.1(a). The second available data type is multi-probe formation pressure-transient measurements acquired with the Modular Formation Dynamics Tester, MDT™. A dual-packer/probe module configuration with two vertical observation probes is considered as the measurement platform (Pop et al., 1993; Ayan et al., 2001). Figure 7.1(b) shows a schematic of the packer and probe modules.

We assume the availability of laboratory PVT measurements of fluid and rock properties that can be robustly incorporated into the reservoir simulator to describe the PVT dependent nature of the two-phase flow in permeable media. For the three-layer formation model, we initially assume that the layers are isotropic in terms of permeability, we therefore enforce $k_h = k_v$ as shown in Figure 7.8.

Subsequent to the acquisition of the first induction log, the multi-probe formation tester configuration is deployed across the formation of interest to conduct pressure-transient measurements. Time-series of pressure responses are recorded at two observation probe locations, and at the center of the dual-packer open interval in response to a controlled flow rate pulse. This measurement schedule involves acquisition of dual-physics data and, is here referred to as log-test strategy. Alternatively, we investigate the

case where an additional post transient-test electromagnetic induction log senses the perturbed two-phase flow field caused by the formation tester experiment. This alternative measurement schedule is here referred to as log-test-log strategy. In modeling the measurement sequences described above, mud-filtrate invasion is simulated for the entire history of the near-borehole, since the moment of drilling until the acquisition of the last measurement.

On a case-by-case basis, the uncertainty in the inversion outcome is quantitatively analyzed by computing the Estimator's Covariance Matrix and the Cramer-Rao bounds described in Appendix A. The uncertainty analysis provides us with error bounds on the inversion results for each inverted parameter. With the purpose of establishing a basis of comparison to the joint inversion approach that involves either log-test or log-test-log acquisition strategies, we further suggest an inversion-based sensitivity study. In this sensitivity study, we additionally consider independent inversions of pressure-transient measurements (test strategy), and single- and dual-snapshot electromagnetic induction logging measurements (log and log-log strategy, respectively). As in the case of log-test and log-test-log strategies, the formation is considered to be subject to mud-filtrate invasion during the entire time-interval encompassing each measurement strategy. A quantitive analysis of the uncertainty in inversion results is carried out via computing the Estimator's Covariance Matrix and the Cramer-Rao bounds as in the case of joint inversion approach. For all of the measurement strategies, synthetically generated measurements are contaminated with random Gaussian noise with standard deviation corresponding to 1%, 3%, and 5% of the norm of each individual measurement.

Mudcake, formation rock and fluid properties, specific instrumental details, and scheduling of the above described measurement strategies are listed in Table 7.6. We use a $121\times1\times30$ grid in the cylindrical coordinate system as the result of extensive finite-

difference gridding studies to produce computationally efficient, internally consistent, and accurate numerical simulations. This grid is uniform in the vertical and azimuthal directions. Block sizes increase logarithmically in the radial direction away from the borehole. We also use a relatively fine cylindrical finite-difference grid of size $141\times1\times30$ for fluid-flow simulations performed in generating the synthetic measurements. A comparison of the simulation results obtained within the framework of the grid refinement study are displayed in Figure 7.9(a) for pressure-transient response, in Figure 7.9(b) for near-borehole distribution of aqueous phase saturation at the first logging time [1.5 days], and in Figure 7.9(c) for near-borehole distribution of salt concentration at the first logging time [1.5 days] and at the grid point corresponding to the center depth of the dual-packer interval. Simulations performed using fine and coarse finite-difference grids agree within 1% of each other. Layer-by-layer relative permeability and capillary pressure functions used for this numerical case are illustrated in Figures 7.10(a) and 7.10(b). Averaged mud-filtrate invasion history, imposed on the fluid-flow simulator as the source condition, is shown in Figure 7.11. For the log-log strategy, the invasion rate schedule is extended further until the second logging time [3rd day]. As shown in Figure 7.11, the rate domain response of the removal of mudcake due to drill-string trip-out at the first logging time [1.5th day] is also incorporated into the mud-filtrate invasion history. The post-ruboff average invasion is rate is computed in using the same averaging approach as in the case of the pre-ruboff average rate.

The following schedule is assumed for the log-test strategy. The induction log is recorded at the 1.5th day of mud-filtrate invasion. A subsequent wireline formation test is scheduled to last 200 min. During the formation test, fluid is withdrawn from the formation at a constant liquid rate of 21.09 rbbl/d [38.66 cc/sec = 3.34 m^3/d] for 100 min and the formation pressure drawdown response is observed across the dual-packer

interval and at the observation probes. Subsequently, the tool is shut down for another 100 min and the formation pressure build-up response is recorded. Here, we assume a minimal time is spent to establish contact with the formation and pressure-transient test is run during two-phase flow time-interval by excluding the pretest duration with the aim of reducing the total test duration. Certainly, the formation test in our example is run solely to acquire two-phase pressure-transients without the constraint of sampling quality. For the log-test-log schedule, upon conclusion of the formation test, a second induction log is recorded.

For the single-snapshot log strategy, the induction log is recorded at the 1.5^{th} day of invasion. For the dual-snapshot log strategy, in addition to the induction log acquired at the 1.5^{th} day of invasion, an additional induction log is acquired at the 3^{rd} day of invasion to track the changes in the saturation and salt concentration distributions in the near-borehole region due to mud-filtrate invasion. As far as the independent inversion of pressure-transient measurements is concerned, pressure data recorded at the test-log strategy are used in inversions. Two-phase displacement, production, and shut-in due to mud-filtrate invasion, formation-test drawdown, and formation test build-up are fully simulated within the context of iterative inversion.

The drawdown and build-up schedule imposed on the packer-sealed interval is shown in Figure 7.12(a). Noise-free pressure-transient measurements numerically generated for the observation probe locations and the packer-sealed interval are shown in Figure 7.12(b). Near-borehole logarithmic conductivity distributions, as sensed by the AIT™ tool, are presented in Figure 7.13(a) for the 1.5^{th} day, and in Figure 7.13(c) for the 3^{rd} day of mud-filtrate invasion. On the other hand, synthetically generated, noise-free electromagnetic induction logging measurements, acquired across the shown conductivity distributions, are displayed for logging times that encompass log [Figure 7.13(b)] and

log-log [Figures 7.13(b) and (d)] measurement strategies. Normalized time-lapse variations due mud-filtrate invasion are shown for both the logarithmic conductivity distribution and electromagnetic induction logging measurements in Figures 7.13(e) and 7.13(f), respectively. Similarly, logarithmic conductivity distributions and electromagnetic induction logging measurements simulated for the pre- and post-formation test measurement times are shown in Figures 7.14(a) through 7.14(d) for log-test-log and log-test measurement strategies. Normalized changes in the conductivity domain, and hence, in the electromagnetic induction logging measurements due formation test are quantitatively presented in Figures 7.14(e) and 7.14(f), respectively. Note that, in this example, we incorporate the effect of capillary forces in the two-phase displacement by using the capillary pressure curves shown in Figures 7.10(b). However, for the cases where viscous forces dominate over capillary forces, the effect of capillary pressure is negligible. In order to demonstrate the effect of capillarity, we simulated our base case for log-test-log schedule by assuming negligible capillary pressures. Simulation results are displayed in Figures 7.15(a) through 7.15(f) in a similar arrangement to case where we did not neglect capillary effects [frames of Figure 7.14]. Comparisons of the simulated conductivity domains shown in Figures 7.14 and 7.15 clearly demonstrate the front-diffusing effect of capillarity. Consequently, the signatures of the two-phase fluid displacement, which appear in terms of time-lapse changes in apparent conductivity channels, are sharper yet volumetrically more isolated for the case where capillarity is negligible. On the contrary, for the case where capillary forces are at work, time-lapse changes in apparent conductivity are smoother and volumetrically wide-extent. Simulated pressure-transient responses, for the case where capillary effects are negligible, are shown in Figure 7.16 for the flow-rate schedule shown in Figure 7.12(a).

Permeability and porosity profiles yielded by the independent inversions of pressure-transient measurements (test strategy) are shown in Figures 7.17(a) and 7.17(b) for 1%, in Figures 7.17(c) and 7.17(d) for 3%, and in Figures 7.17(e) and 7.17(f) for 5% noise level, respectively. True and initial guess profiles for the model parameters subject to inversion are also shown in these figures to quantify the accuracy and robustness of the inversion results. On the other hand, the degree of uncertainty of inversion results are quantitatively analyzed by computing the Estimator's Covariance Matrix and the 99.7% probability level Cramer-Rao bounds. Computed bounds provide error bars for each inverted model parameter. Similarly, the results of the inversions and post-inversion uncertainty analyses are shown for the log strategy in Figure 7.18, for the log-test strategy in Figure 7.19, for the log-log strategy in Figure 7.20, and for the log-test-log strategy in Figure 7.21.

A three-layer formation exhibiting permeability anisotropy is also considered for inversion. Synthetic single-time electromagnetic induction logging and wireline formation tester pressure-transient measurements (for a 1.5 day-long mud-filtrate invasion) are generated for the formation model shown in Figure 7.22 using the same reservoir fluid properties and measurement schedules used for the isotropic case. Formation layers are assumed to be in hydraulic communication. The locations of the formation tester packer and probe measurement locations are also shown in Figure 7.22. Horizontal and vertical permeability, and porosity profiles yielded by the independent inversions of pressure-transient and electromagnetic measurements (log-test strategy) are shown in Figures 7.23(a), 7.23(b), and 7.23(c) for 1%, in Figures 7.24(a), 7.24(b), and 7.24(c) for 3%, and in Figures 7.25(a), 7.25(b), and 7.25(c) for 5% noise level, respectively.

7.5 DISCUSSION OF THE DUAL-PHYSICS INVERSION RESULTS

Inversion results indicate that pressure-transient measurements contain first-order information about layer permeabilities. However, the presence of only pressure-transient measurements is not sufficient to resolve both permeabilities and porosities simultaneously. Additional independent information is needed for robust estimations of model parameters as indicated by results of single data-type inversions of pressure-transient measurements. In turn, the main contribution of electromagnetic induction logging measurements is in providing first-order information about near-wellbore porosities. As indicated by the independent inversions of single-snapshot electromagnetic induction logging measurements, it is possible to obtain robust and accurate simultaneous inversions of permeabilities and especially porosities from induction logging measurements at relatively low levels of noise. Yet, the sensitivity of the induction logging measurements exhibits a quickly diminishing trend when the noise-level in the induction data increases. Introduction of additional electromagnetic induction logging measurements acquired at different time of mud-filtrate invasion helps to further constrain permeabilities. Hence, this approach yields slight improvement in the inversion results for the absolute permeability profile and results in slight enhancement in reducing the uncertainty of the absolute permeability inversions. Yet, improvements in the inversion results and the reduction in the uncertainty of the inversion outcome are relatively less significant when compared to case where we combine both pressure-transient and electromagnetic induction logging measurements. Inversion results of the data acquired in log-test and log-test-log strategies indicate that the simultaneous use of dual-data sets effectively reduces the non-uniqueness, improves the stability of the optimization scheme, and yield more accurate inversions. The constructive impact of dual-physics data sets becomes increasingly significant when the measurements contain

high levels of noise. Addition of pressure-transient measurements to the inversion results in significant enhancement in the inversion results for permeabilities while the inversion results for porosities still very robust with respect to the deleterious influence of noise. Consistent with the improvements in the inversion results, joint inversion approach also reduces uncertainty in the estimation. On the other hand, the comparison of the results obtained from log-test and log-test-log joint inversion strategies exhibit only minor improvements in permeability and porosity profiles when an additional post formation-test electromagnetic induction logging measurements are added to the inversions. In summary, log-test measurement strategy, and hence, the joint inversion of single-snapshot electromagnetic induction logging and pressure-transient measurements embodies the most optimal approach that provides a relatively high degree of noise robustness, accuracy, and minimal non-uniqueness in inversions while avoiding the potentially expensive additional second induction log acquisition.

Having established the merit in the joint inversion of electromagnetic induction logging and wireline formation tester pressure-transient measurements, inversion of dual-physics data is applied to a three-layer reservoir exhibiting permeability anisotropy. For this case, log-test acquisition strategy is considered only. For 1%, 3%, and 5% random Gaussian noise levels, inverted values of horizontal permeability and porosity remain fairly consistent with the actual profiles. Although the reconstruction exhibits inaccuracies, for 1% and 3% noise levels, the trend of inverted vertical permeability values for first and second layers (from the top of the formation) remain consistent with the actual trend. For 5% noise level the reconstruction error significantly increases for the vertical permeability of these layers. The reconstruction of the vertical permeability of the bottom-most (third) layer profoundly diverges from the actual values for all levels of noise. For each noise level, the reconstructed value of vertical permeability exceeds the

scale of the plots, and hence, it is not shown. Overall, for all layers inverted vertical permeability values diverge from the actual vertical permeability profile for all levels of noise contamination.

While reconstructions of horizontal permeability and porosity profiles remain accurate and error bounds are sufficiently narrow for all investigated noise levels, the reconstruction of the vertical permeability profiles exhibit significant inaccuracies. The error bounds are also relatively larger for the inversion of vertical permeability profiles in comparison to other model parameters subject to inversion. In this three hydraulically communicating anisotropic layer case, certainly, there are a limited number of pressure sensors (or measurement locations in the vertical direction) that can provide pressure differential information. Therefore, there are limited degrees of freedom in the measurements for the inversion algorithm to resolve the vertical permeabilities of three different layers. Given the MDT™ tool configuration used in this case, the reconstruction of vertical permeability (simultaneously with horizontal permeability and porosity) is expected to be more accurate for a single-layer formation in comparison to a three-layer formation. This conclusion is verified in a proof-of-concept study for such a formation presented in the previous section.

7.6 SUMMARY AND CONCLUDING REMARKS

A dual-physics parametric inversion algorithm is developed and successfully employed to perform quantitative joint and independent interpretations of time-lapse electromagnetic induction and formation tester transient-pressure measurements. The benefit of the inversion algorithm is the quantitative estimation of layer-by-layer horizontal and vertical absolute permeabilities, and porosities.

Inversion results indicate that the simultaneous use of dual-data sets effectively reduces the non-uniqueness and improves the stability of the optimization scheme. The

positive impact of dual-physics data sets becomes significant when the measurements contain high levels of noise.

Parametric joint inversion of multi-probe transient formation-pressure and time-lapse electromagnetic induction measurements can yield layer-by-layer horizontal and vertical near-wellbore permeabilities as well as porosities. In this case, the transient-pressure test needs to be designed to ensure sensitivity of the transient data to the petrophysical parameters of the layers of interest. Model parameters that are most affected by the deleterious effect of noise are vertical permeabilities. Estimation of porosity is very robust with respect to the effect of measurement-noise for the investigated layered formation models; (a) because of the presence of multi-resolution array induction-logging measurements, and (b) because of the assumed knowledge about the parameters governing the saturation equation, namely, Archie's law.

Time-lapse electromagnetic induction measurements conducted across invaded beds can potentially yield significant information about the near-wellbore porosities and absolute permeabilities when interpreted within the framework of multi-phase fluid flow. Transient-pressure measurements contain first-order information about near-wellbore absolute permeabilities. Introduction of electromagnetic induction measurements to the inversion helps to further constrain absolute permeabilities. In effect, the main contribution of electromagnetic measurements is in providing first-order information about near-wellbore porosities, thereby, enabling the algorithm to simultaneously invert both near-wellbore permeabilities and porosities from noisy measurements.

Table 7.1: Summary of geometrical, petrophysical, and fluid parameters employed in the construction of the reservoir models. The hydrocarbon-saturated formation is invaded by the water-base mud. Note that we use the following encoding to distinguish data for various cases: (A) Cases 1, 2, and 3 [two-phase flow of oleic and aqueous phases, single-layer formation], and (B) Case 4 [two-phase flow of gaseous and aqueous phases, 3-layer formation]. Information about measurement schedules is also tabulated.

Variable	Units	Values
Mudcake permeability (A), (B)	[mD]	0.01, 0.03
Mudcake porosity (A), (B)	[fraction]	0.40, 0.60
Mud solid fraction (A), (B)	[fraction]	0.50, 0.20
Mudcake maximum thickness (A), (B)	[in]	1.00, 0.10
Formation rock compressibility (A), (B)	[psi^{-1}]	5.00×10^{-9}, 5.00×10^{-9}
Aqueous phase viscosity (mud-filtrate) (A), (B)	[cp]	1.274, 1.000
Aqueous phase density (mud-filtrate) (A), (B)	[lbm/cuft]	62.495, 74.040
Aqueous phase formation volume factor (mud-filtrate) (A), (B)	[rbbl/stb]	0.996, 1.000
Aqueous phase compressibility (mud-filtrate) (A), (B)	[psi^{-1}]	2.55×10^{-6}, 1.00×10^{-6}
Oleic phase viscosity (A)	[cp]	0.355
Oleic phase API density (A)	[ºAPI]	42
Oleic phase density (A)	[lbm/cuft]	50.914
Oleic phase formation volume factor (A)	[rbbl/stb]	1.471
Oleic phase compressibility (A)	[psi^{-1}]	1.904×10^{-5}
Fluid density contrast (A)	[lbm/cuft]	11.581
Viscosity ratio (water-to-oil) (A)	[dimensionless]	3.589
Initial water saturation (A)	[fraction]	0.30
Irreducible water saturation (A)	[fraction]	0.30
Residual oil saturation (A)	[fraction]	0.20
End-point relative permeability for aqueous phase (A)	[fraction]	0.25
End-point relative permeability for oleic phase (A)	[fraction]	0.80
Curvature parameter for aqueous phase relative permeability (A)	[dimensionless]	3.00
Curvature parameter for oleic phase relative permeability (A)	[dimensionless]	2.00
Gaseous phase viscosity [f(p) for T=const.] (B)	[cp]	0.01087@14.7 psia
Gaseous phase density [f(p) for T=const.] (B)	[lbm/cuft]	0.061@14.7 psia
Gaseous phase formation volume factor [f(p) for T=const.] (B)	[rbbl/Mscf]	139.203@14.7 psia
Initial water saturation (B)	[fraction]	Layer 1: 0.55, Layer 2: 0.50, Layer 3: 0.55
Irreducible water saturation (B)	[fraction]	Layer 1: 0.55, Layer 2: 0.50, Layer 3: 0.55
Residual gas saturation (B)	[fraction]	Layer 1: 0.03, Layer 2: 0.03, Layer 3: 0.03
End-point relative permeability for aqueous phase (B)	[fraction]	Layer 1: 0.12, Layer 2: 0.18, Layer 3: 0.12
End-point relative permeability for gaseous phase (B)	[fraction]	Layer 1: 0.50, Layer 2: 0.38, Layer 3: 0.50
Curvature parameter for aqueous phase relative permeability (B)	[dimensionless]	Layer 1: 3.00, Layer 2: 2.50, Layer 3: 3.00
Curvature parameter for gaseous phase relative permeability (B)	[dimensionless]	Layer 1: 2.00, Layer 2: 1.70, Layer 3: 2.00
Capillary pressure parameter for the gas-water system (B)	[psi × $[mD]^{1/2}$]	Layer 1: 30.00, Layer 2: 80.00, Layer 3: 50.00
Capillary pressure exponent for the gas-water system (B)	[dimensionless]	Layer 1: 2.50, Layer 2: 2.50, Layer 3: 2.50
Formation pressure (formation top is the reference depth) (A), (B)	[psia]	3000.00, 96.00
Mud hydrostatic pressure (A), (B)	[psia]	3600.00, 1153.00
Wellbore radius (A), (B)	[ft]	0.354, 0.350
Formation outer boundary location (A), (B)	[ft]	984.252, 984.252
Formation bed thickness (A)	[ft]	30.00
Formation bed thickness (B)	[ft]	Layer 1: 15.00, Layer 2: 6.00, Layer 3: 9.00
Relative depth of the top impermeable shoulder (A), (B)	[ft]	0.00, 0.00
Relative depth of the bottom impermeable shoulder (A), (B)	[ft]	30.00, 30.00
Pre rub-off mud-filtrate invasion duration (A)	[days]	Time-lapse log: 3, Log-test-log: 3
Post rub-off mud-filtrate invasion duration (A)	[days]	Time-lapse log: 7, Log-test-log: 0
Mudcake rub-off time ($t_{first\ log}$) (A)	[days]	Time-lapse log: 3, Log-test-log: 3
Second logging time ($t_{second\ log}$) (A)	[days]	Time-lapse log: 10, Log-test-log: 3.208
Formation horizontal permeability (A)	[mD]	Case 1: 100.00, Case 2: 100.00, Case3: 50.00
Formation vertical permeability (A)	[mD]	Case 1: 100.00, Case 2: 20.00, Case3: 5.00
Formation porosity (A)	[fraction]	Case 1: 0.25, Case 2: 0.25, Case 3: 0.18
Pre rub-off mud-filtrate invasion duration (B)	[days]	Log-test-log: 1
Post rub-off mud-filtrate invasion duration (B)	[days]	Log-test-log: 0
Mudcake rub-off time ($t_{first\ log}$) (B)	[days]	Log-test-log: 1
Second logging time ($t_{second\ log}$) (B)	[days]	Log-test-log: 1.208
Formation horizontal permeability (B)	[mD]	Layer 1: 6.83, Layer 2: 40.98, Layer 3: 14.33
Formation vertical permeability (B)	[mD]	Layer 1: 0.93, Layer 2: 4.53, Layer 3: 0.37
Formation porosity (B)	[fraction]	Layer 1: 0.139, Layer 2: 0.137, Layer 3: 0.125
Formation temperature (A), (B)	[ºF]	220, 96
Formation brine salinity (A), (B)	[ppm]	120000, 200000
Mud-filtrate salinity (A), (B)	[ppm]	5000, 2000
a-constant in the Archie's equation (A), (B)	[dimensionless]	1.00, 1.00
m-cementation exponent in the Archie's equation (A), (B)	[dimensionless]	2.00, 2.00
n-water saturation exponent in the Archie's equation (A), (B)	[dimensionless]	2.00, 2.00
Mud conductivity (A), (B)	[mS/m]	2631.58, 387.60
Upper and lower shoulder bed conductivities (A), (B)	[mS/m]	1000.00, 400.0
Logging interval (A), (B)	[ft]	2.00, 2.00

SPECIFIC INFORMATION FOR LOG-TEST-LOG SCHEDULE:		
Drawdown duration (A), (B)	[min]	100.00, 100.0
Build-up duration (A), (B)	[min]	200.00, 200.0
Drawdown rate (A), (B)	[rbbl/d]	30.00, 1.50
3ft interval sealed by the dual-packer (DP) module (A), (B)	[ft]	[18.50, 21.50], [23.50, 26.50]
Location of the first observation probe (A), (B)	[ft]	5.00, 10.00
Location of the second observation probe (A), (B)	[ft]	13.00, 18.00
Location of the pressure measurement conducted by DP module (A), (B)	[ft]	20.00, 25.00

Table 7.2: Inversion results for formation permeability, k, and porosity, ϕ, for Case 1, where, k_{true} = 100 mD and $k_{initial\ guess}$ = 40 mD, and ϕ_{true} = 0.25 and $\phi_{initial\ guess}$ = 0.12. Inversion results for k are reported in millidarcies [mD], and results for ϕ are tabulated in volume fractions. For each inversion, the number of Gauss-Newton iterations necessary for convergence is also reported.

Inversion results for formation permeability, k			
Additive, Gaussian random noise level	Joint inversion Weight ratio: 1:1	Joint inversion Weight ratio: 1:3	Inversion of time-lapse EM data
0%	100.00	100.50	100.01
1%	100.63	101.66	99.67
3%	99.98	103.64	100.60
5%	96.98	103.70	103.03
6%	94.42	101.24	105.78
7%	91.47	98.00	109.42
8%	86.98	85.13	70.86
Inversion results for formation porosity, ϕ			
Additive, Gaussian random noise level	Joint inversion Weight ratio: 1:1	Joint inversion Weight ratio: 1:3	Inversion of time-lapse EM data
0%	0.25	0.25	0.25
1%	0.25	0.25	0.25
3%	0.25	0.25	0.25
5%	0.25	0.25	0.25
6%	0.25	0.25	0.25
7%	0.25	0.25	0.25
8%	0.25	0.25	0.25
Required number of Gauss-Newton iterations for convergence			
Additive, Gaussian random noise level	Joint inversion Weight ratio: 1:1	Joint inversion Weight ratio: 1:3	Inversion of time-lapse EM data
0%	6	9	4
1%	4	5	4
3%	4	4	5
5%	4	14	14
6%	4	11	14
7%	4	9	12
8%	5	40	34

Table 7.3: Joint inversion [weight ratio: 1:1] results for vertical permeability, k_v, and porosity, ϕ, for Case 2. In this case, the value of horizontal permeability, k_h, is stipulated as a-priori information. Formation properties are: $k_{h\ true}$ = 100 mD, $k_{v\ true}$ = 20 mD, and ϕ_{true} = 0.25. The starting point for inversion is given by $k_{v\ initial\ guess}$ = 50 mD and $\phi_{initial\ guess}$ = 0.15. For each inversion, the number of Gauss-Newton iterations necessary for convergence is also reported.

Additive, Gaussian random noise level	Stipulated horizontal permeability, k_h [mD]	Inverted vertical permeability, k_v [mD]	Inverted porosity, ϕ [fraction]	Number of Gauss-Newton iterations
0%	100	20.00	0.25	9
1%	100	20.90	0.25	23
3%	100	23.29	0.25	23
5%	100	51.87	0.25	6
8%	100	50.42	0.25	3

Table 7.4: Joint inversion [weight ratio: 1:1] results for horizontal and vertical permeability, k_h and k_v, and porosity, ϕ, for Case 3, where, actual formation properties are: $k_{h\ true}$ = 50 mD, $k_{v\ true}$ = 5 mD, and ϕ_{true} = 0.18. The starting point for inversion is given by $k_{h\ initial\ guess}$ = $k_{v\ initial\ guess}$ = 100 mD. For each inversion, the number of Gauss-Newton iterations necessary for convergence is also reported.

Additive, Gaussian random noise level	Inverted horizontal permeability, k_h [mD]	Inverted vertical permeability, k_v [mD]	Inverted porosity, ϕ [fraction]	Number of Gauss-Newton iterations
0%	50.00	5.00	0.180	10
3%	49.55	4.89	0.180	11
5%	47.66	4.90	0.180	34
8%	40.75	8.18	0.179	28

Table 7.5: Inversion results for horizontal and vertical absolute permeabilities, k_h and k_v, and porosities, ϕ, in the case of a 3-layer gas reservoir with its layers exhibiting vertical anisotropy [Case 4]. Actual formation properties are shown below. Initial guesses are as follows: $k_{h\ initial\ guess}$ = 12.39 mD, $k_{v\ initial\ guess}$ = 0.71 mD (volume weighted arithmetic mean of horizontal and volume weighted harmonic mean of vertical permeabilities) and $\phi_{initial\ guess}$ = 0.18. For each inversion, the number of Gauss-Newton iterations necessary for convergence is also reported.

Inversion results for layer 1 [Joint inversion], where, $k_{h\ true}$=6.83 mD, $k_{v\ true}$=0.93 mD, and ϕ_{true}=0.139				
Additive, Gaussian random noise level	k_h [mD]	k_v [mD]	ϕ [fraction]	Number of Gauss-Newton iterations
1%	6.82	0.94	0.139	17
3%	6.83	0.78	0.139	61
5%	6.88	0.62	0.139	15
8%	7.00	0.40	0.139	7
Inversion results for layer 2 [Joint inversion], where, $k_{h\ true}$=40.98 mD, $k_{v\ true}$=4.53 mD, and ϕ_{true}=0.137				
Additive, Gaussian random noise level	k_h [mD]	k_v [mD]	ϕ [fraction]	Number of Gauss-Newton iterations
1%	44.63	1.69	0.137	17
3%	64.18	22.08	0.138	61
5%	92.47	1.29	0.138	15
8%	165.01	1.76	0.140	7
Inversion results for layer 3 [Joint inversion], where, $k_{h\ true}$=14.33 mD, $k_{v\ true}$=0.37 mD, and ϕ_{true}=0.125				
Additive, Gaussian random noise level	k_h [mD]	k_v [mD]	ϕ [fraction]	Number of Gauss-Newton iterations
1%	14.33	0.37	0.125	17
3%	14.33	0.46	0.125	61
5%	14.32	0.50	0.125	15
8%	14.24	0.86	0.124	7

Table 7.6: Summary of geometrical, petrophysical, mudcake, fluid, and sensor parameters for the reservoir model used in the inversion-based sensitivity study.

Variable	Units	Values
Mudcake permeability	[mD]	0.010
Mudcake porosity	[fraction]	0.400
Mud solid fraction	[fraction]	0.500
Mudcake maximum thickness	[cm]	1.270
Formation rock compressibility	[kPa^{-1}]	7.252×10^{-10}
Aqueous phase viscosity (mud-filtrate)	[Pa.s]	1.274×10^{-3}
Aqueous phase density (mud-filtrate)	[g/cm^3]	1.001
Aqueous phase formation volume factor (mud-filtrate)	[res. m^3/std. m^3]	0.996
Aqueous phase compressibility (mud-filtrate)	[kPa^{-1}]	3.698×10^{-7}
Oleic phase viscosity	[Pa.s]	3.550×10^{-4}
Oleic phase API density	[ºAPI]	42
Oleic phase density	[g/cm^3]	0.816
Oleic phase formation volume factor	[res. m^3/std. m^3]	1.471
Oleic phase compressibility	[kPa^{-1}]	2.762×10^{-6}
Viscosity ratio (water-to-oil)	[dimensionless]	3.589
Formation pressure at the formation top (at the reference depth = 0 m)	[MPa]	20.684
Mud hydrostatic pressure	[MPa]	24.821
Wellbore radius	[m]	0.108
Formation outer boundary location	[m]	300.000
Formation temperature	[ºC]	104.444
a-constant in the Archie's equation	[dimensionless]	1.000
m-cementation exponent in the Archie's equation	[dimensionless]	2.000
n-water saturation exponent in the Archie's equation	[dimensionless]	2.000
Mud conductivity	[mS/m]	2631.579
Upper and lower shoulder bed conductivities	[mS/m]	1000.000
Logging interval	[m]	6.096×10^{-1}
Specific Information for the Wireline Formation Test:		
Drawdown duration	[min]	100.000
Build-up duration	[min]	100.000
Drawdown rate	[m^3/d]	3.339
Interval sealed by the dual-packer (DP) module (wrt. to the formation top)	[m]	5.639 to 6.553
Location of the first observation probe (wrt. to the formation top)	[m]	1.524
Location of the second observation probe (wrt. to the formation top)	[m]	3.962
Location of the pressure measurement conducted by DP module (wrt. to the formation top)	[m]	6.096

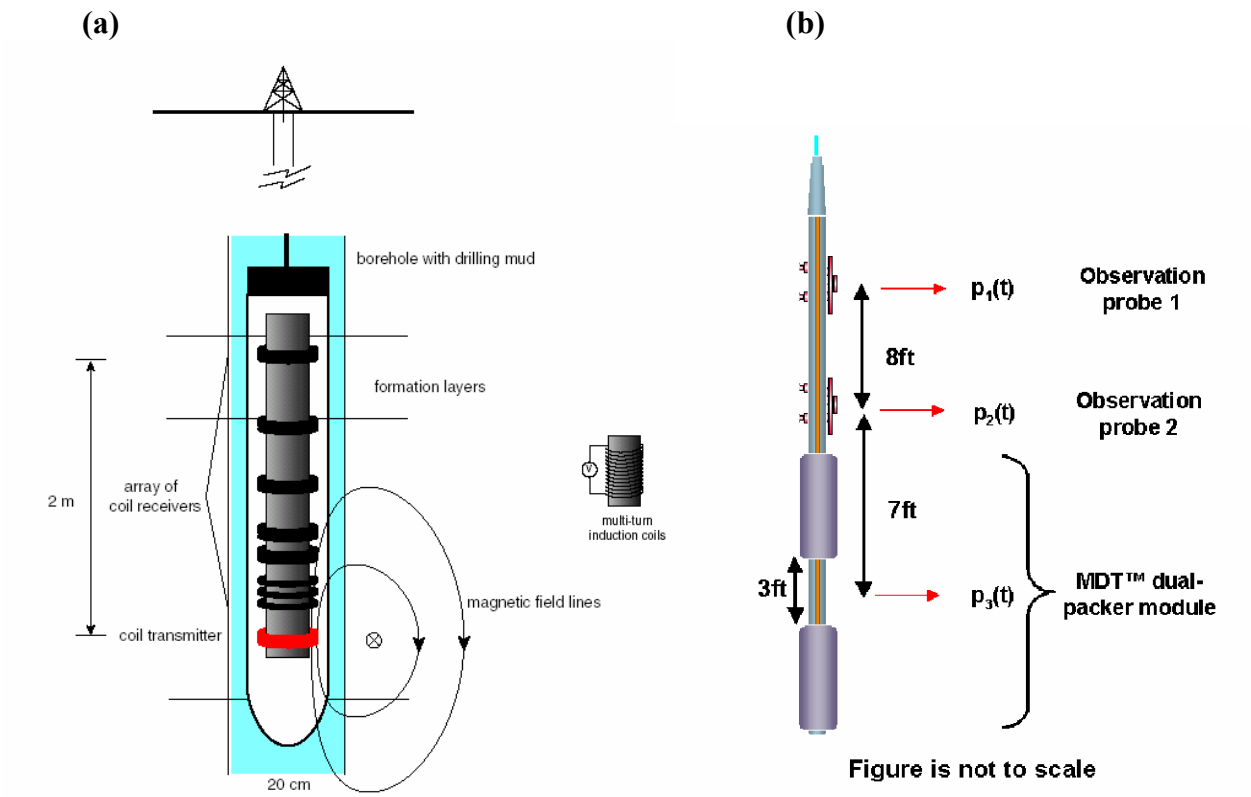

Figure 7.1: (a) Induction logging with AIT™: A multi-turn coil supporting a time-varying current generates a magnetic field that induces electrical currents in the formation. An array of receiver coils measures the magnetic field of the source and the secondary currents (Figure from Oristaglio and Blok, 1995). (b) Schematic of MDT™ multi-probe wireline tester packer/probe modules. The dual-packer module is combined with two vertical observation probes. Transient-pressure measurements are acquired at three vertical locations in response to rate schedules imposed by a downhole pump. Fluid flow takes place through the packer open interval.

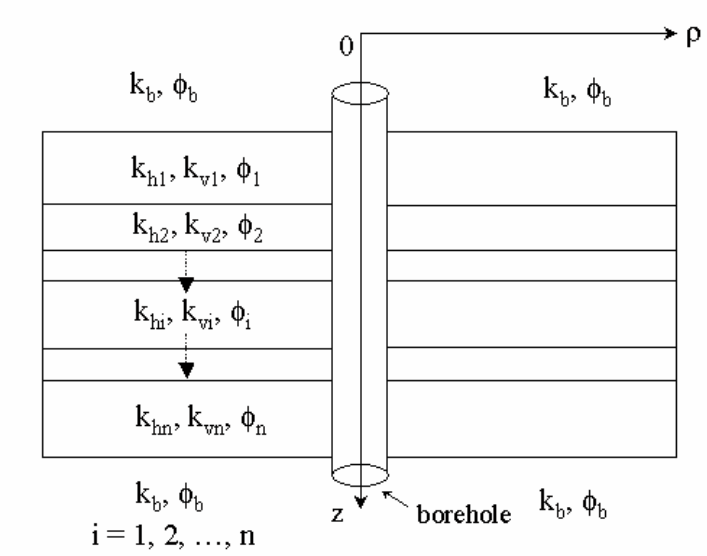

Figure 7.2: Parameterization of the model domain in terms of horizontal geological layers. Model parameters are layer-by-layer horizontal and vertical absolute permeabilities, and porosities denoted by k_h, k_v, and ϕ, respectively.

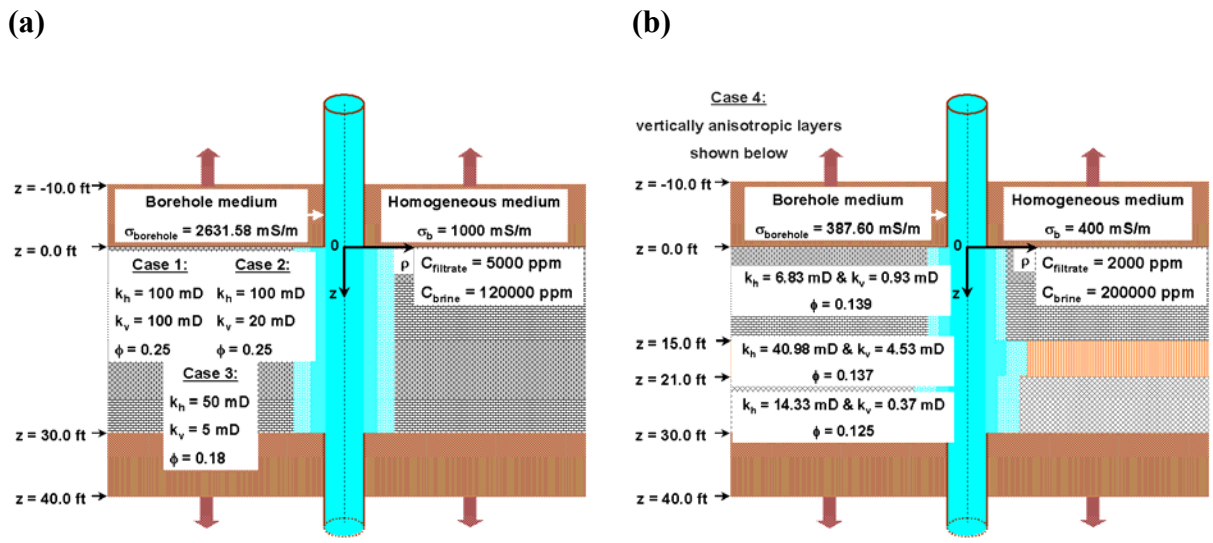

Figure 7.3: Two-dimensional vertical cross-sections of the investigated formations of interest intersected by a vertical borehole. Example cases are considered for a 30 ft-thick (a) single-layer, isotropic and anisotropic oil saturated formations, and (b) a 3-layer, anisotropic dry-gas saturated formation. In both cases, the permeable zones of interest are subject to water-base mud-filtrate invasion. Presence of a conductivity contrast between invading and in-situ aqueous phases is assumed. Actual values of the model parameters for the investigated inversion cases and geoelectrical properties of the shoulder beds are shown above.

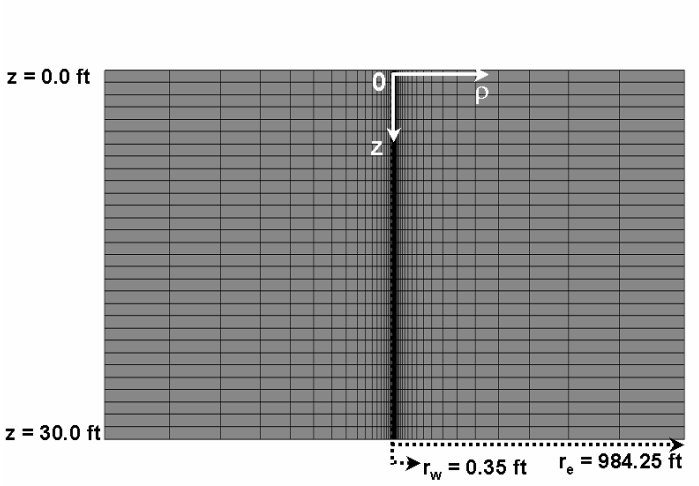

Figure 7.4: Two-dimensional vertical cross-section of the finite-difference grid employed for fluid-flow simulations. The grid is of dimensions, $r \times \theta \times z \equiv 31 \times 1 \times 30$, and is set up in a cylindrical coordinate system.

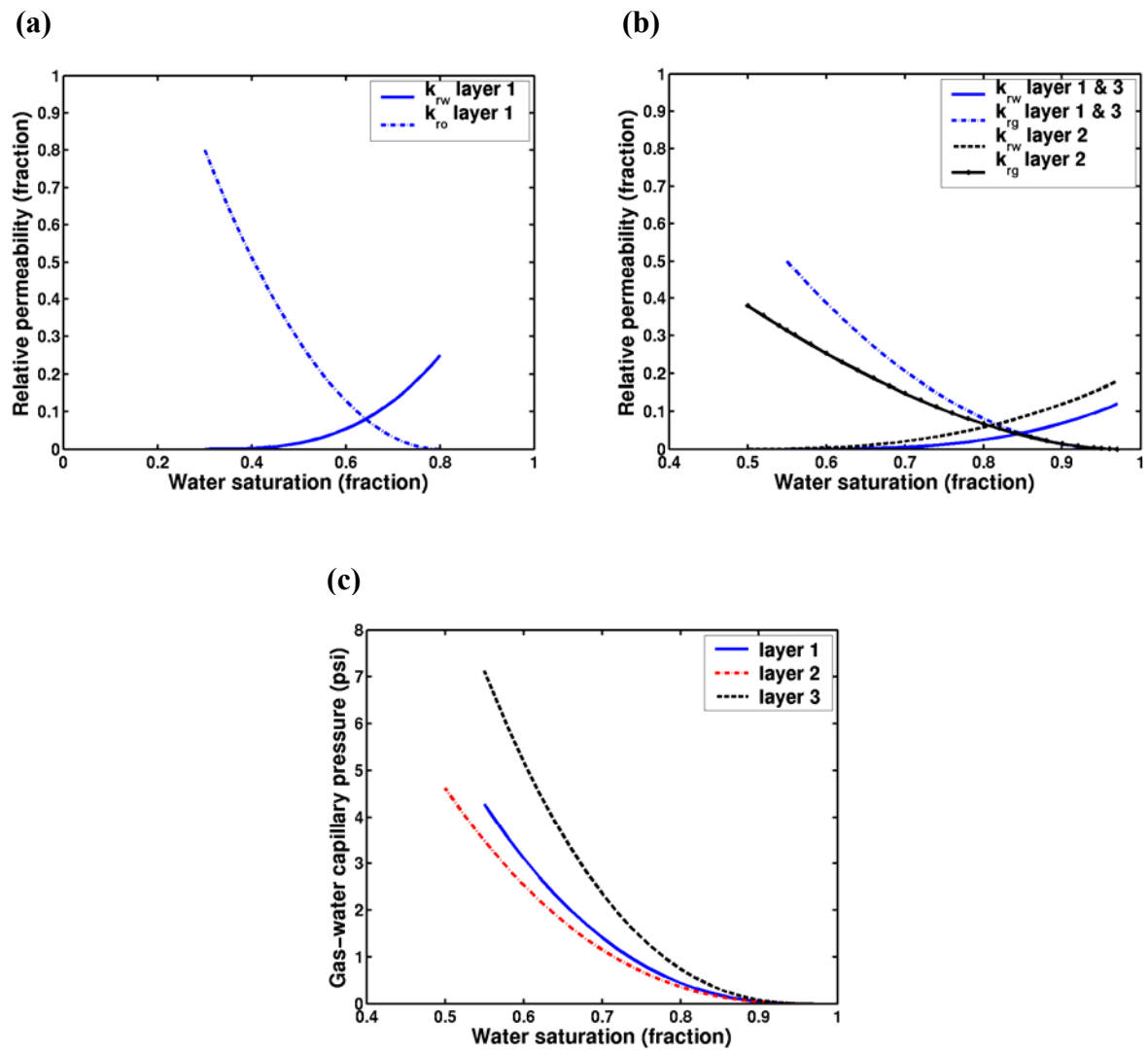

Figure 7.5: (a) Relative permeability curves employed in two-phase fluid-flow simulations for Cases 1, 2, and 3. Capillary effects are assumed to be negligible. Layer-by-layer (b) relative permeability and (c) capillary pressure curves employed to model simultaneous flow of gaseous and aqueous phases for Case 4. In this case, each layer is treated as a separate saturation region with intrinsic saturation-dependent functions.

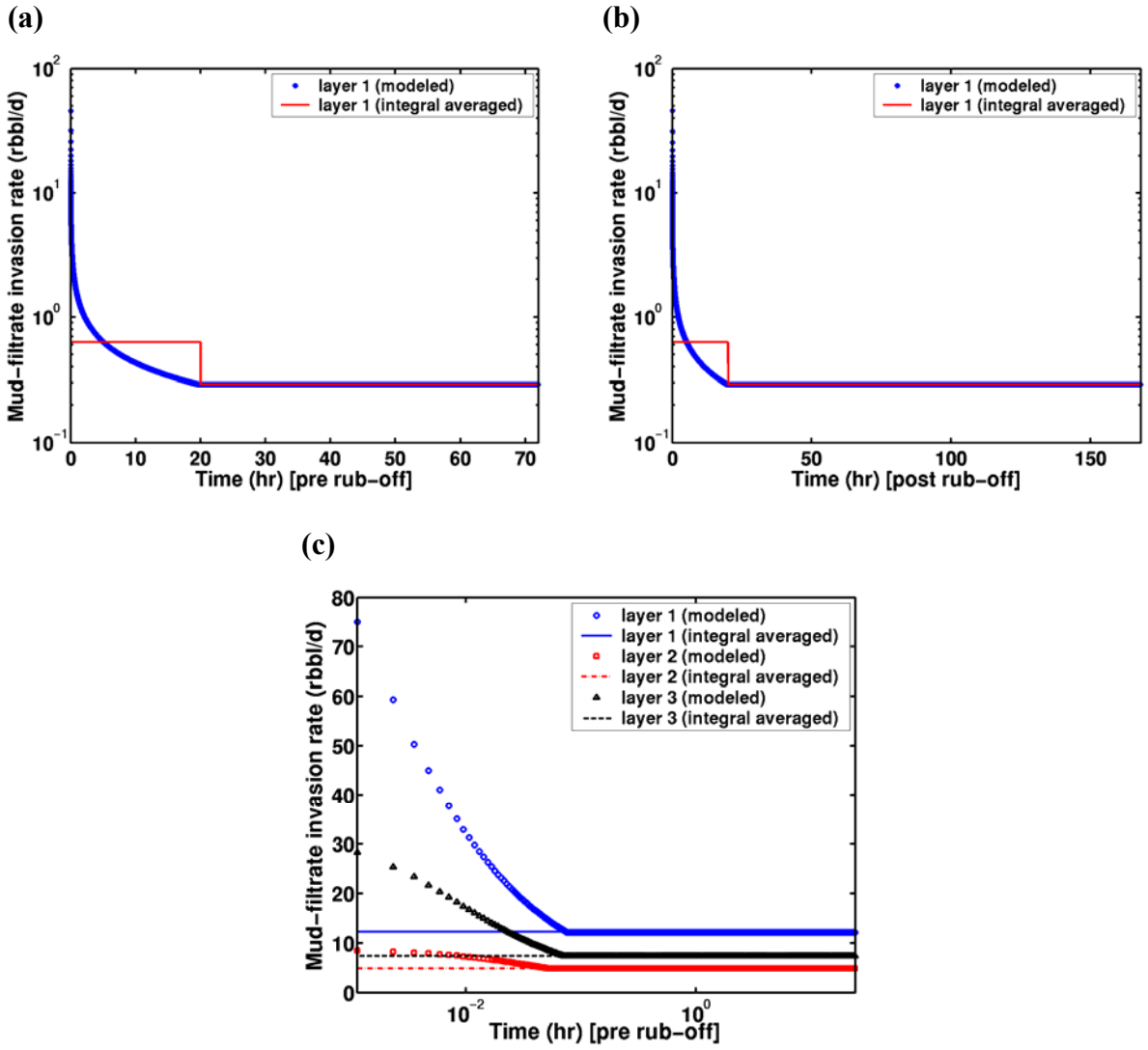

Figure 7.6: Simulated (via using UTCHEM) and averaged (a) pre- and (b) post rub-off mud-filtrate invasion schedules for the single-layer formation [Cases 1, 2, and 3]. Simulation results are integral averaged via maintaining the total filtrate volumetric balance, and are expressed in terms of step-wise rate schedules for pre and post rub-off durations. (c) Simulated and integral averaged mud-filtrate invasion histories computed until the first logging time for each flow unit in case of the 3-layer formation [Case 4]. In this case, a single-step averaging scheme is used for each layer due to the short durations of the early-time transients.

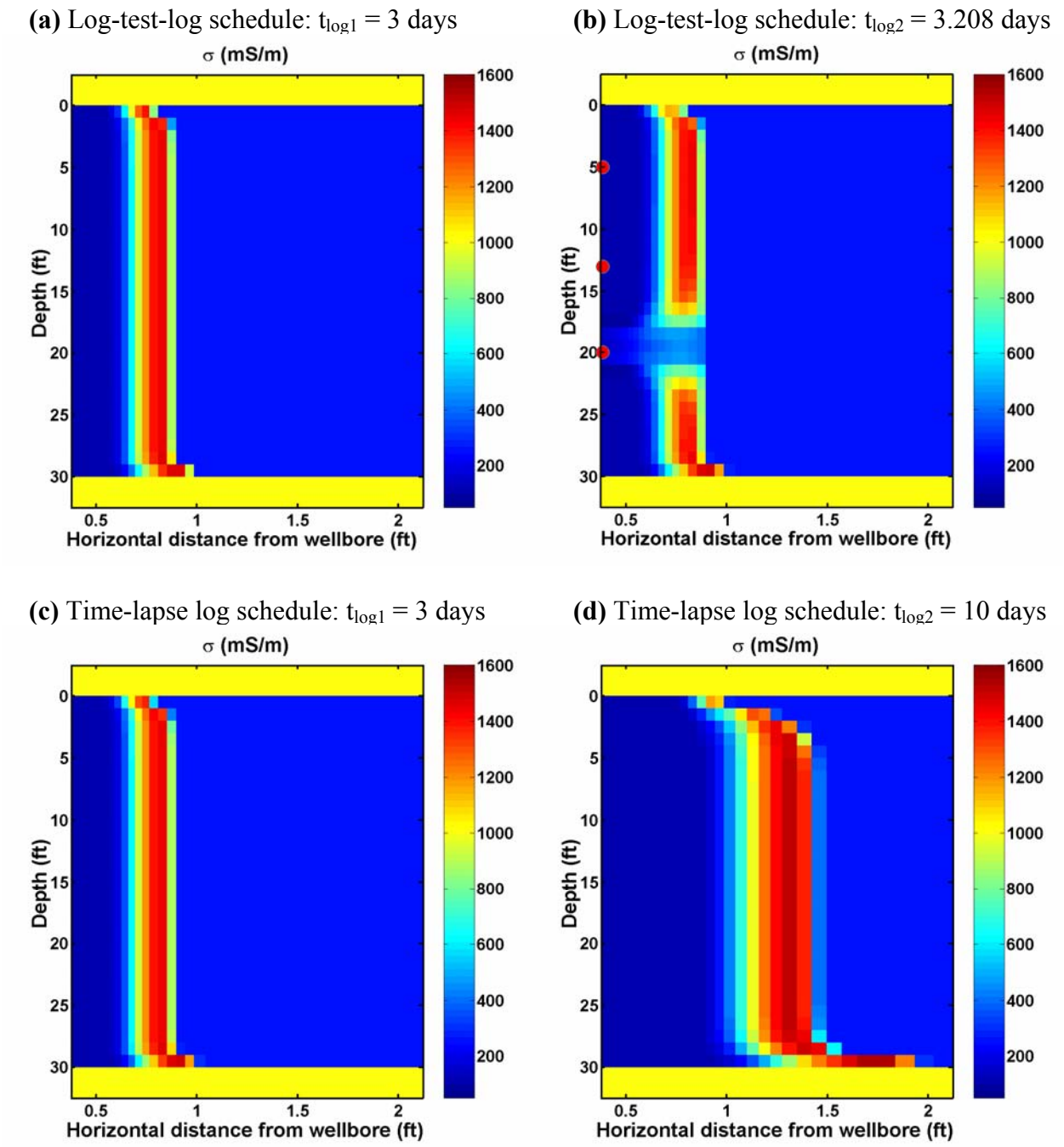

Figure 7.7: Two-dimensional vertical cross-sections of the post-inversion conductivity domain reconstruction at two logging times for both log-test-log and time-lapse log schedules [Case 1]. In this case, simultaneous inversion for layer permeability and porosity is carried out using dual-physics data contaminated with 7% Gaussian random noise.

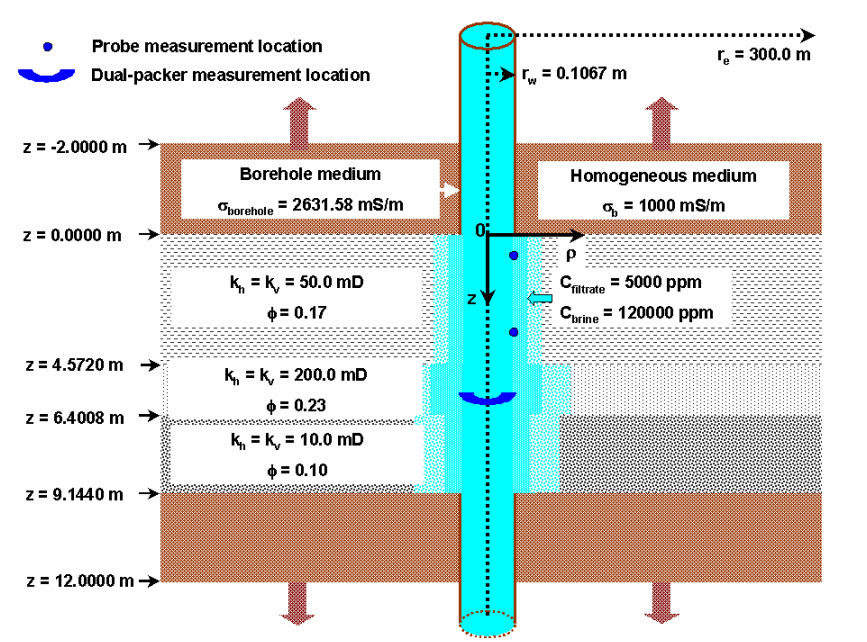

Figure 7.8: Formation model for the inversion-based sensitivity study. Two-dimensional vertical cross-section of the permeable formation intersected by a vertical borehole. The three-layer formation is subject to water-base mud-filtrate invasion.

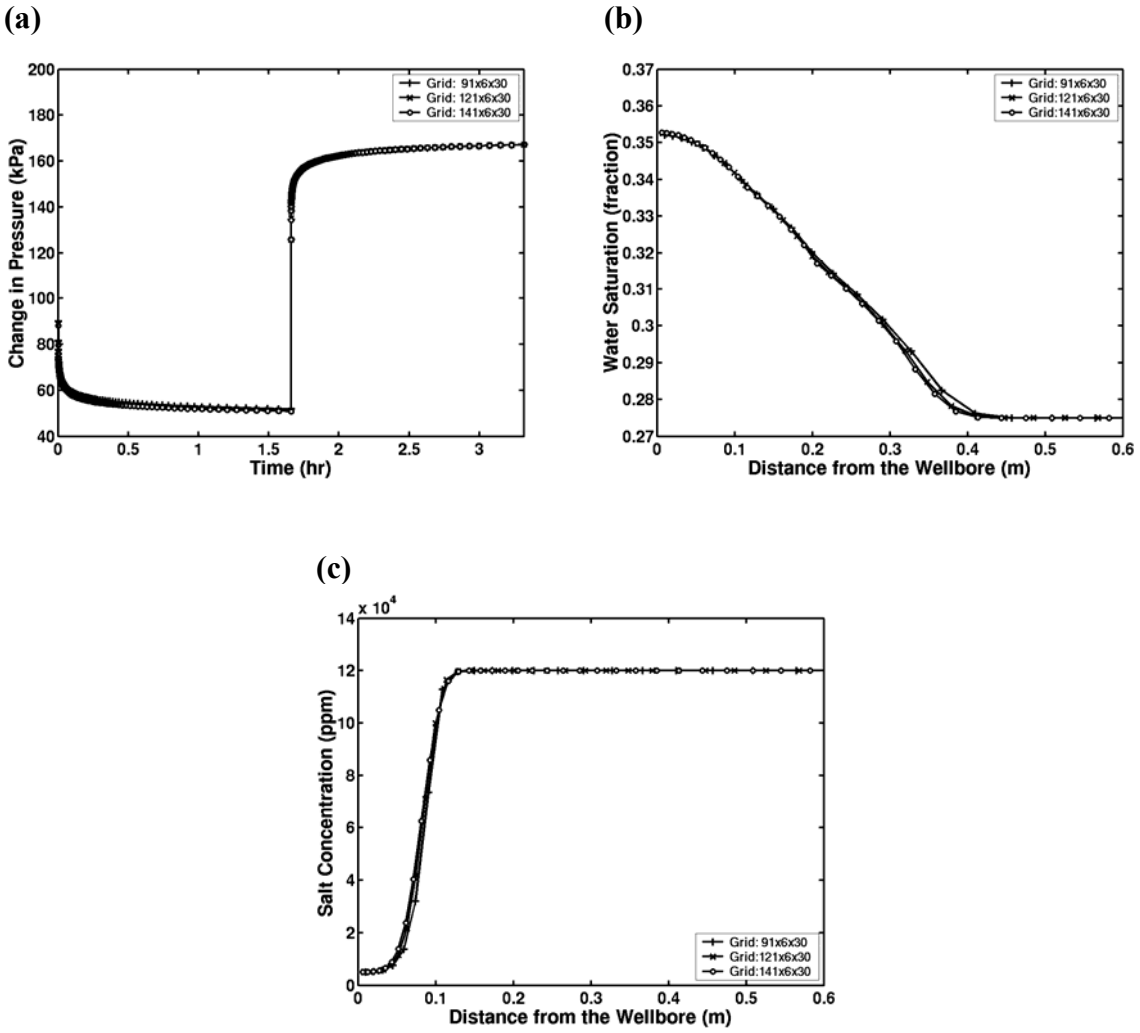

Figure 7.9: Refinement study for the radial grid of the fluid-flow simulator. Numerical solutions yielded by the finite-difference fluid-flow simulator are shown for various radial discretizations. (a) Pressure-transient solution at the dual-packer, (b) near-wellbore water saturation profile at the center depth of the dual-packer interval, and (c) near-wellbore salt concentration profile at the center depth of the dual-packer interval.

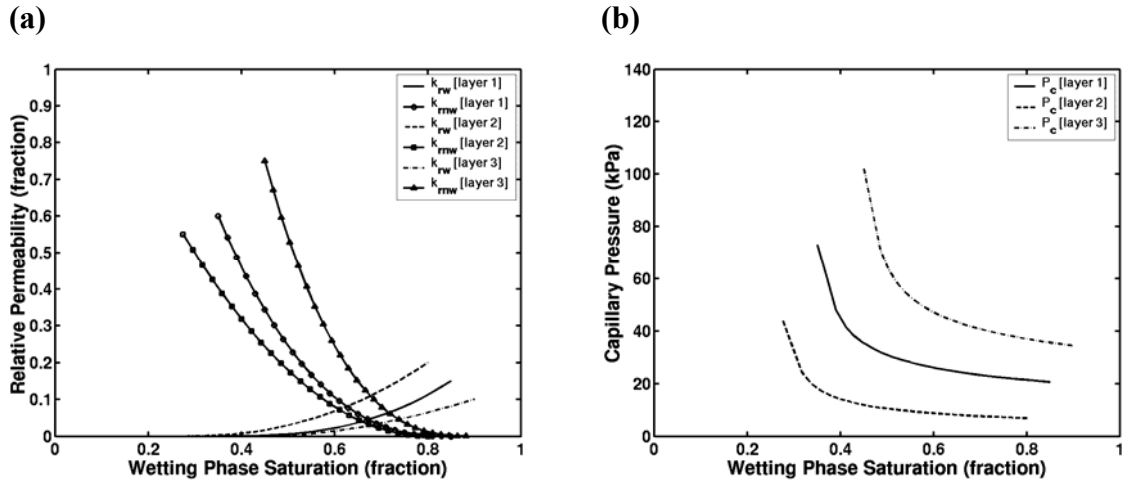

Figure 7.10: Layer-by-layer (a) relative permeability, and (b) capillary pressure functions used in fluid-flow simulations for the formation model of the inversion-based sensitivity study.

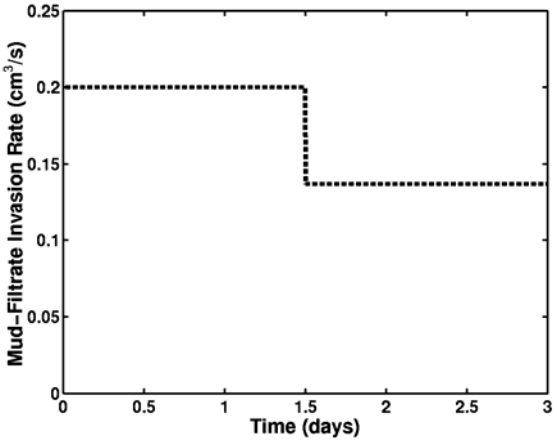

Figure 7.11: Time-average of the mud-filtrate invasion rate for pre and post rub-off periods.

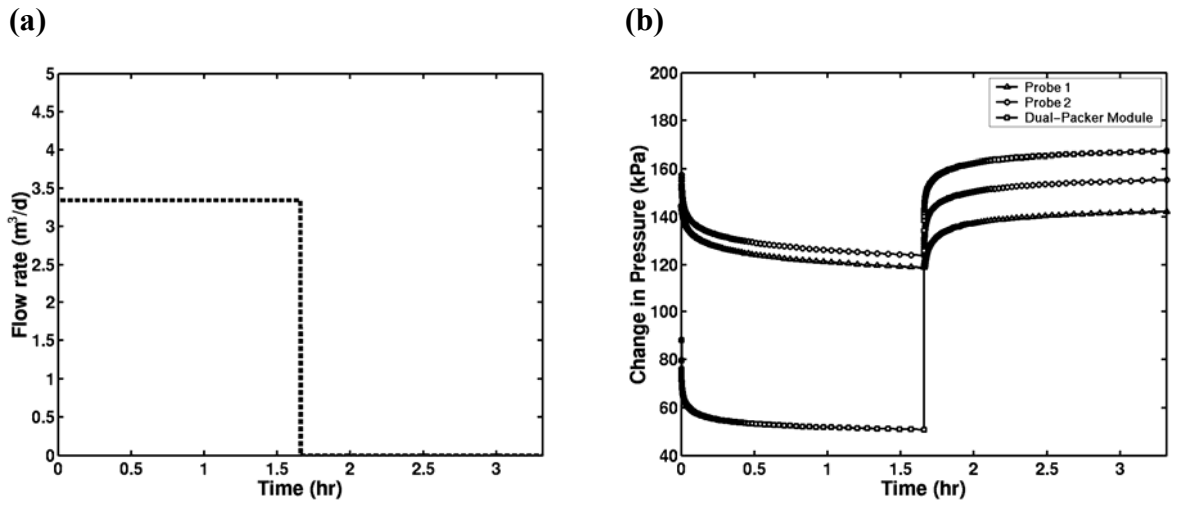

Figure 7.12: (a) Imposed flow-rate schedule for the dual-packer module. (b) Synthetic pressure-transient measurements simulated for the acquisition via dual-packer module and observation probes.

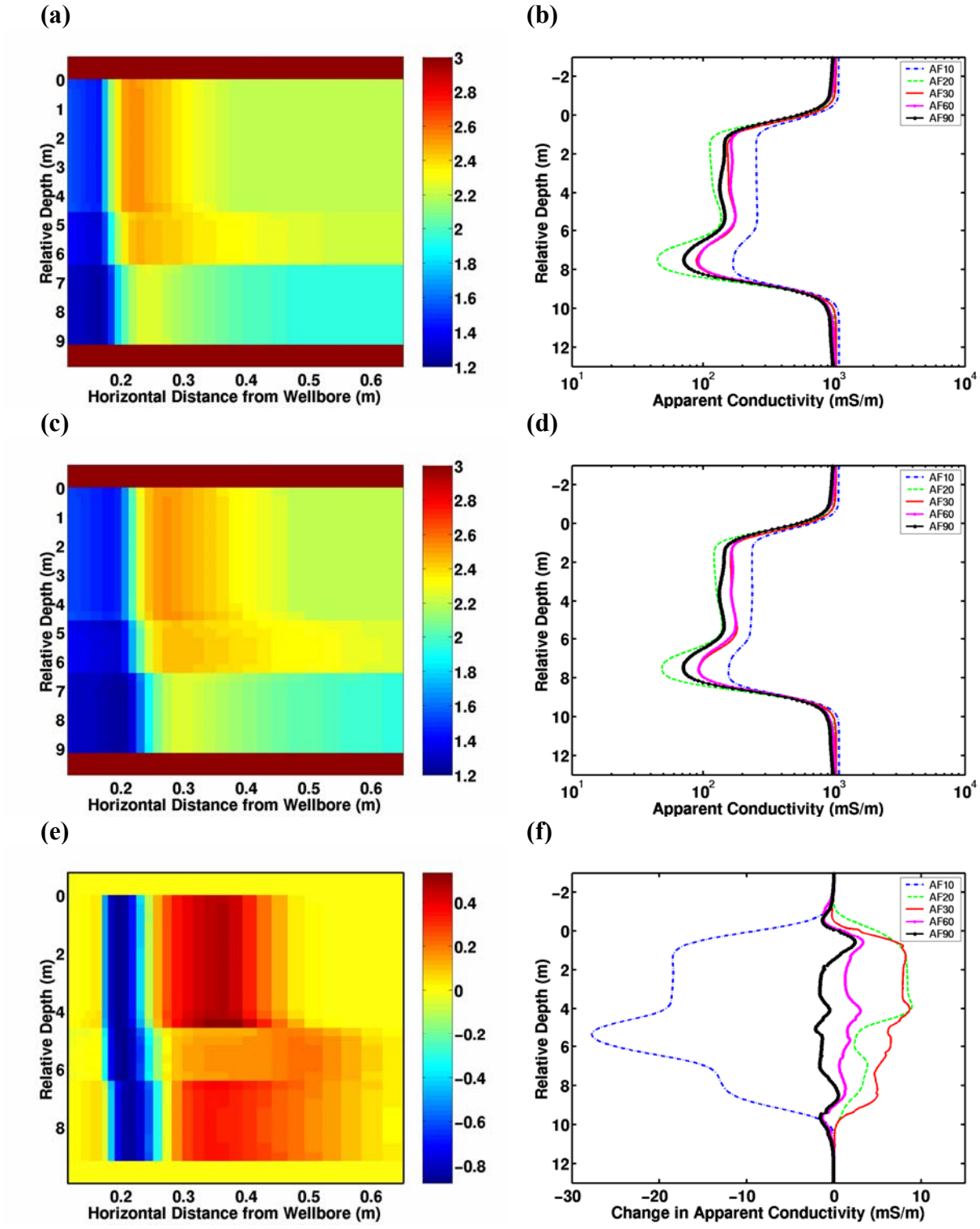

Figure 7.13: See caption on the following page.

Figure 7.13: Dual-snapshot log measurement strategy. (a) Conductivity domain represented in logarithmic scale $[\log_{10}[\sigma]]$ at $t_{\log 1} = 1.5$ day, and (b) the corresponding electromagnetic induction logging measurement. (c) Conductivity domain in logarithmic scale $[\log_{10}[\sigma]]$ at $t_{\log 2} = 3.0$ day, and (d) the corresponding electromagnetic induction logging measurement. (e) Normalized variation in the conductivity domain $[\sigma_2(\mathbf{r}) - \sigma_1(\mathbf{r})]/\sigma_1(\mathbf{r})$, and (f) the change in the induction log response from $t_{\log 1}$ to $t_{\log 2}$, namely, $[\sigma_{app.t2} - \sigma_{app.t1}]$.

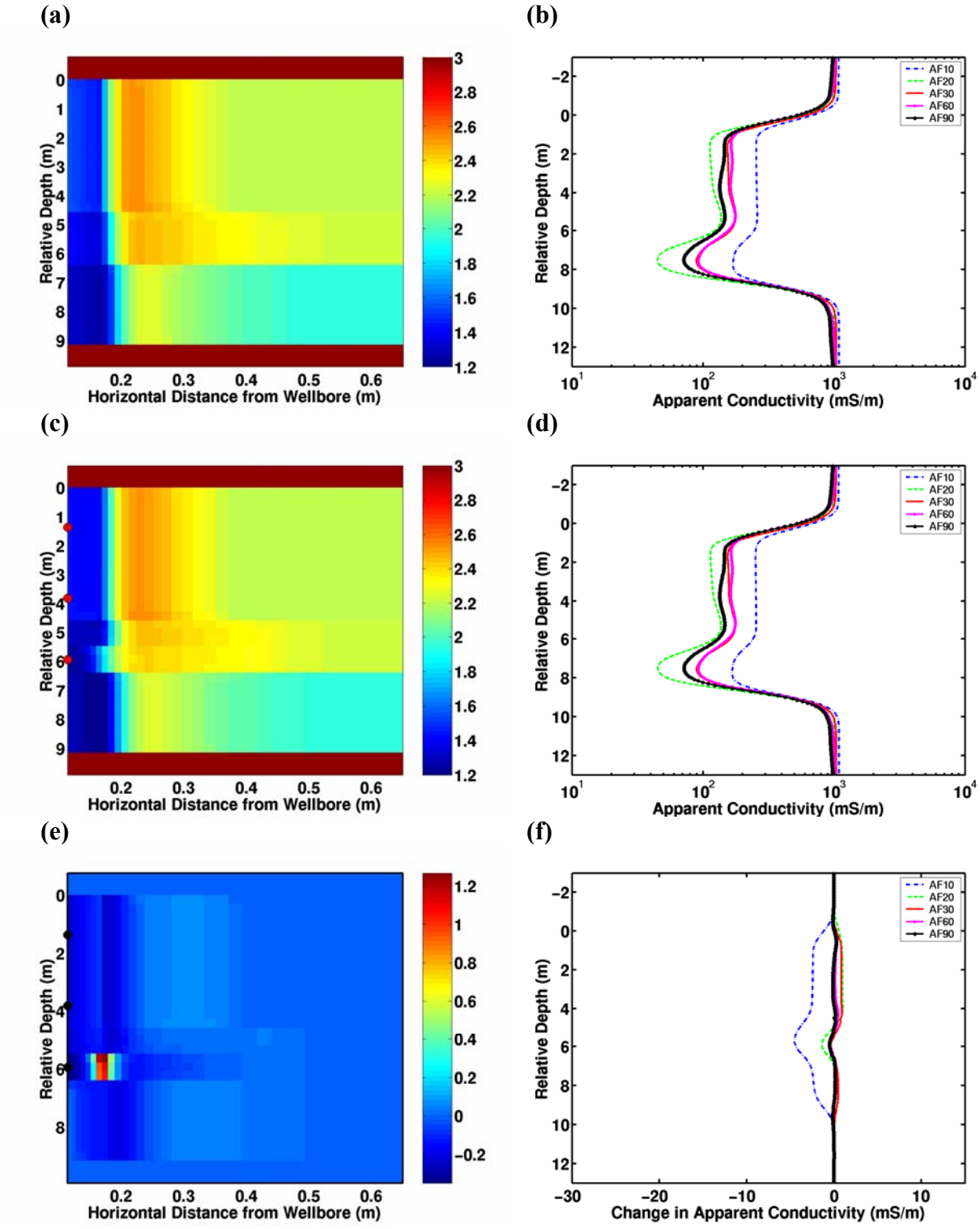

Figure 7.14: See caption on the following page.

Figure 7.14: Log-test-log measurement strategy. (a) Conductivity domain in logarithmic scale $[\log_{10}[\sigma]]$ at $t_{\log 1} = 1.5$ day, and (b) the corresponding electromagnetic induction logging measurement. (c) Conductivity domain in logarithmic scale $[\log_{10}[\sigma]]$ at $t_{\log 2} = 1.64$ day (right after the formation test), and (d) the corresponding electromagnetic induction logging measurement. (e) Normalized variation in the conductivity domain $[\sigma_2(\mathbf{r}) - \sigma_1(\mathbf{r})]/\sigma_1(\mathbf{r})$, and (f) the change in the induction log response from $t_{\log 1}$ to $t_{\log 2}$, namely, $[\sigma_{app.t2} - \sigma_{app.t1}]$. Formation tester measurement locations are shown using small circles on the conductivity domain plots corresponding to $t_{\log 2}$.

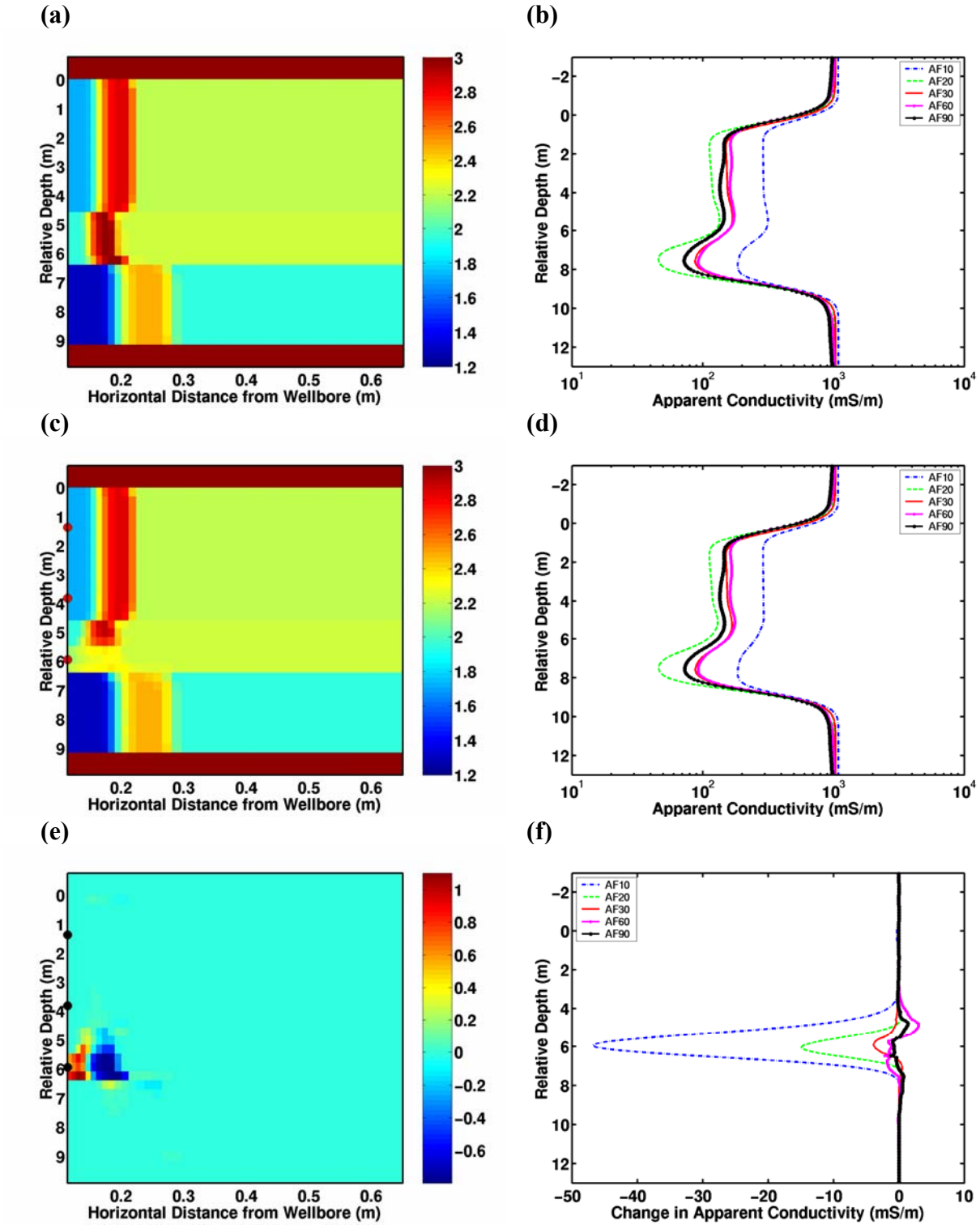

Figure 7.15: See caption on the following page.

Figure 7.15: Log-test-log measurement strategy [negligible capillary pressure effects]. (a) Conductivity domain in logarithmic scale $[\log_{10}[\sigma]]$ at $t_{\log 1} = 1.5$ day, and (b) the corresponding electromagnetic induction logging measurement. (c) Conductivity domain in logarithmic scale $[\log_{10}[\sigma]]$ at $t_{\log 2} = 1.64$ day (right after the formation test), and (d) the corresponding electromagnetic induction logging measurement. (e) Normalized variation in the conductivity domain $[\sigma_2(\mathbf{r}) - \sigma_1(\mathbf{r})]/\sigma_1(\mathbf{r})$, and (f) the change in the induction log response from $t_{\log 1}$ to $t_{\log 2}$, namely, $[\sigma_{app.t2} - \sigma_{app.t1}]$. Formation tester measurement locations are shown using small circles on the conductivity domain plots corresponding to $t_{\log 2}$.

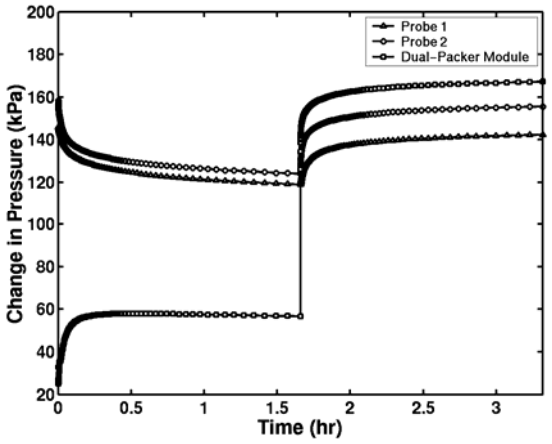

Figure 7.16: Synthetic pressure-transient measurements simulated for acquisition via dual-packer module and observation probes for the case where capillary effects are negligible.

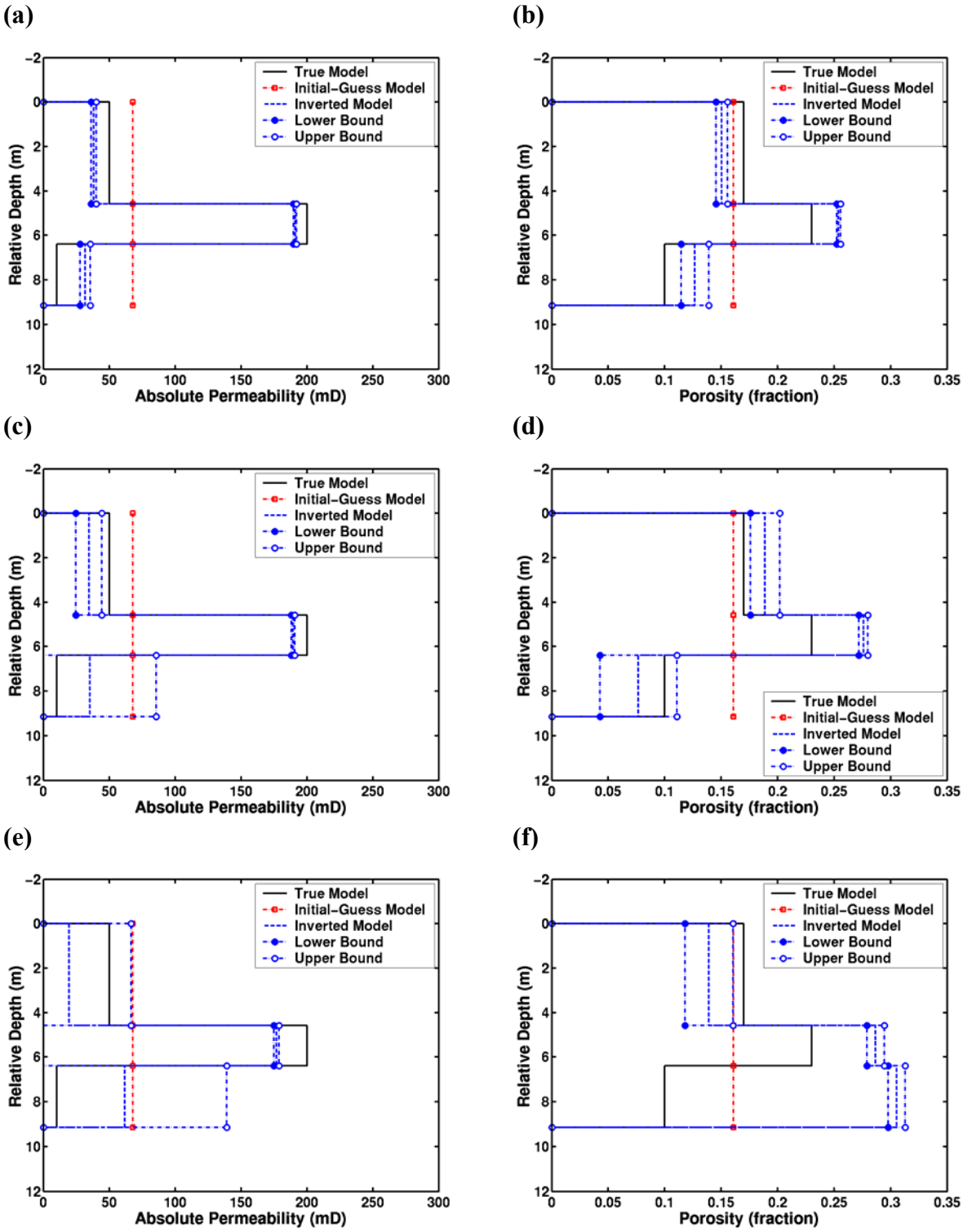

Figure 7.17: See caption on the following page.

Figure 7.17: Permeability and porosity profiles yielded by the inversions of pressure-transient measurements acquired by the dual-packer module and observation probes subsequent to a 1.5 day-long mud-filtrate invasion (test strategy). The Cramer-Rao bounds [with 99.7% probability] on the inversion results are computed post-convergence. Inversion results are shown for the cases where measurements are contaminated with 1% [(a) and (b)], 3% [(c) and (d)], and 5% [(e) and (f)] Gaussian, random noise.

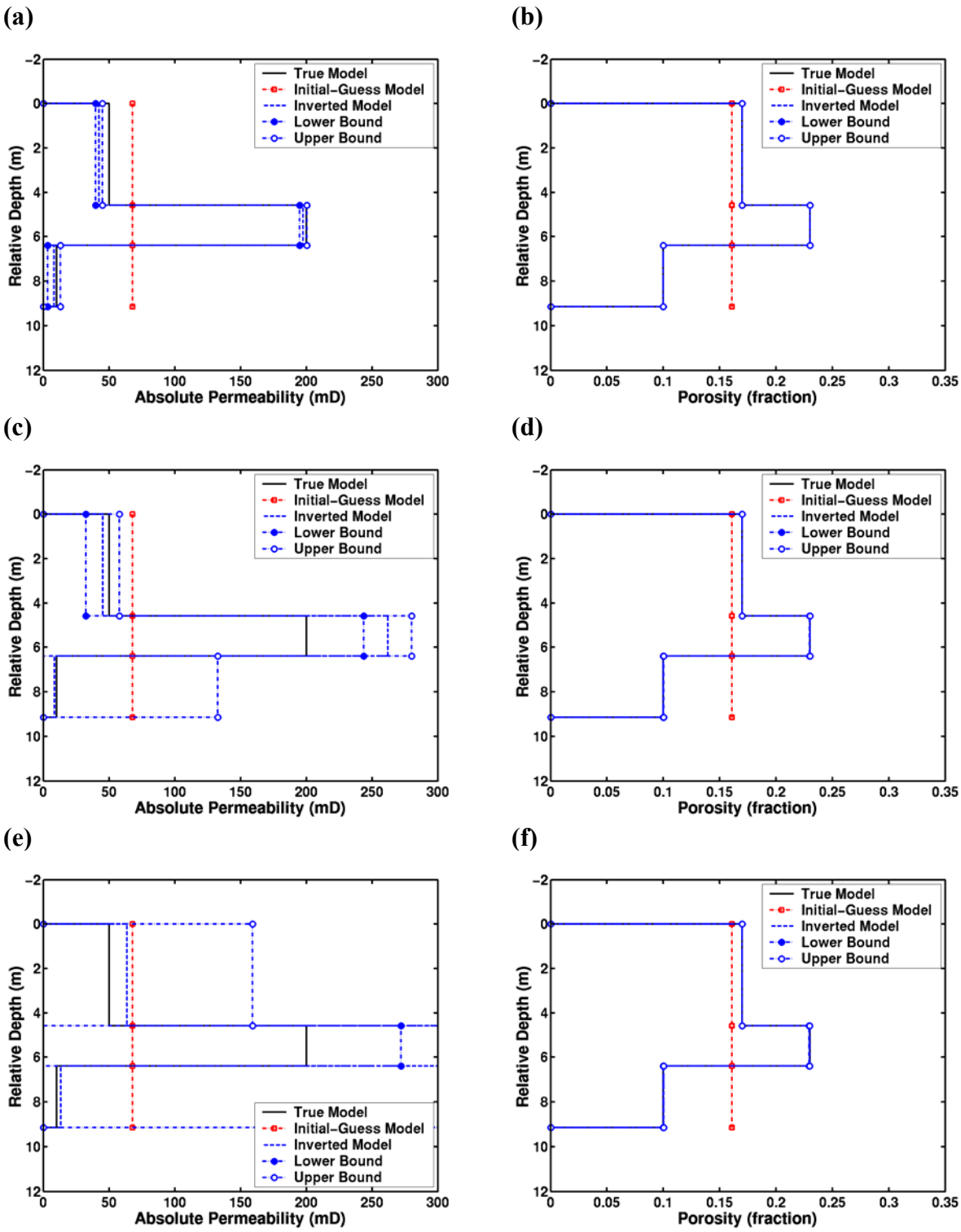

Figure 7.18: See caption on the following page.

Figure 7.18: Permeability and porosity profiles yielded by the inversions of single-time induction logging measurements acquired by the AIT™ configuration subsequent to a 1.5 day-long mud-filtrate invasion (log strategy). The Cramer-Rao bounds [with 99.7% probability] on the inversion results are computed post-convergence. Inversion results are shown for the cases where measurements are contaminated with 1% [(a) and (b)], 3% [(c) and (d)], and 5% [(e) and (f)] Gaussian, random noise.

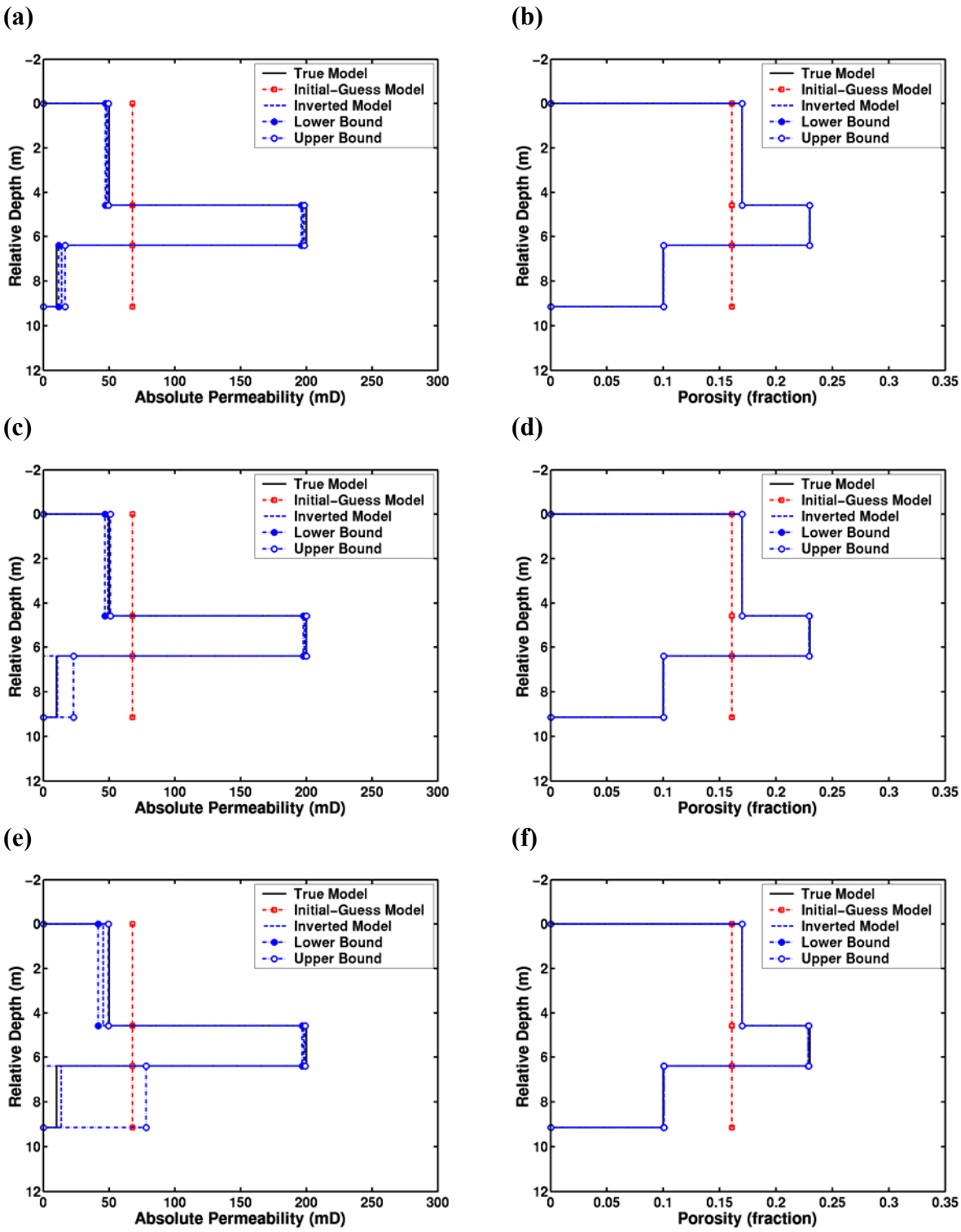

Figure 7.19: See caption on the following page.

Figure 7.19: Permeability and porosity profiles yielded by the joint inversions of single-time induction logging measurements acquired by the AIT™ configuration, and pressure-transient measurements acquired by the dual-packer module and observation probes subsequent to a 1.5 day-long mud-filtrate invasion (log-test strategy). The Cramer-Rao bounds [with 99.7% probability] on the inversion results are computed post-convergence. Inversion results are shown for the cases where measurements are contaminated with 1% [(a) and (b)], 3% [(c) and (d)], and 5% [(e) and (f)] Gaussian, random noise.

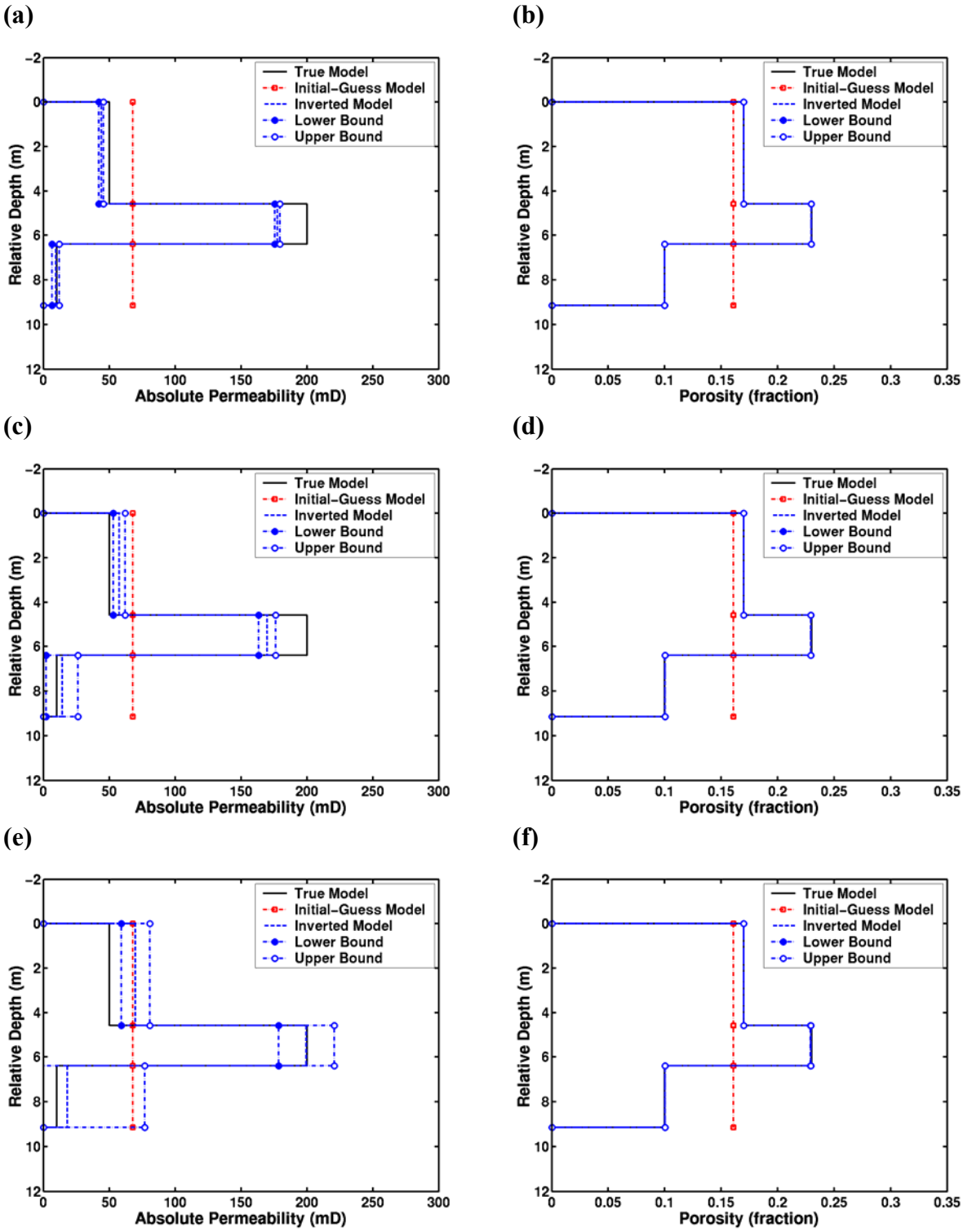

Figure 7.20: See caption on the following page.

Figure 7.20: Permeability and porosity profiles yielded by the joint inversions of two-snapshot induction logging measurements acquired by the AIT™ configuration (log-log strategy). The first induction log was acquired subsequent to a 1.5 day-long mud-filtrate invasion. A second induction log was acquired at the 3rd day of mud-filtrate invasion. The Cramer-Rao bounds [with 99.7% probability] on the inversion results are computed post-convergence. Inversion results are shown for the cases where measurements are contaminated with 1% [(a) and (b)], 3% [(c) and (d)], and 5% [(e) and (f)] Gaussian, random noise.

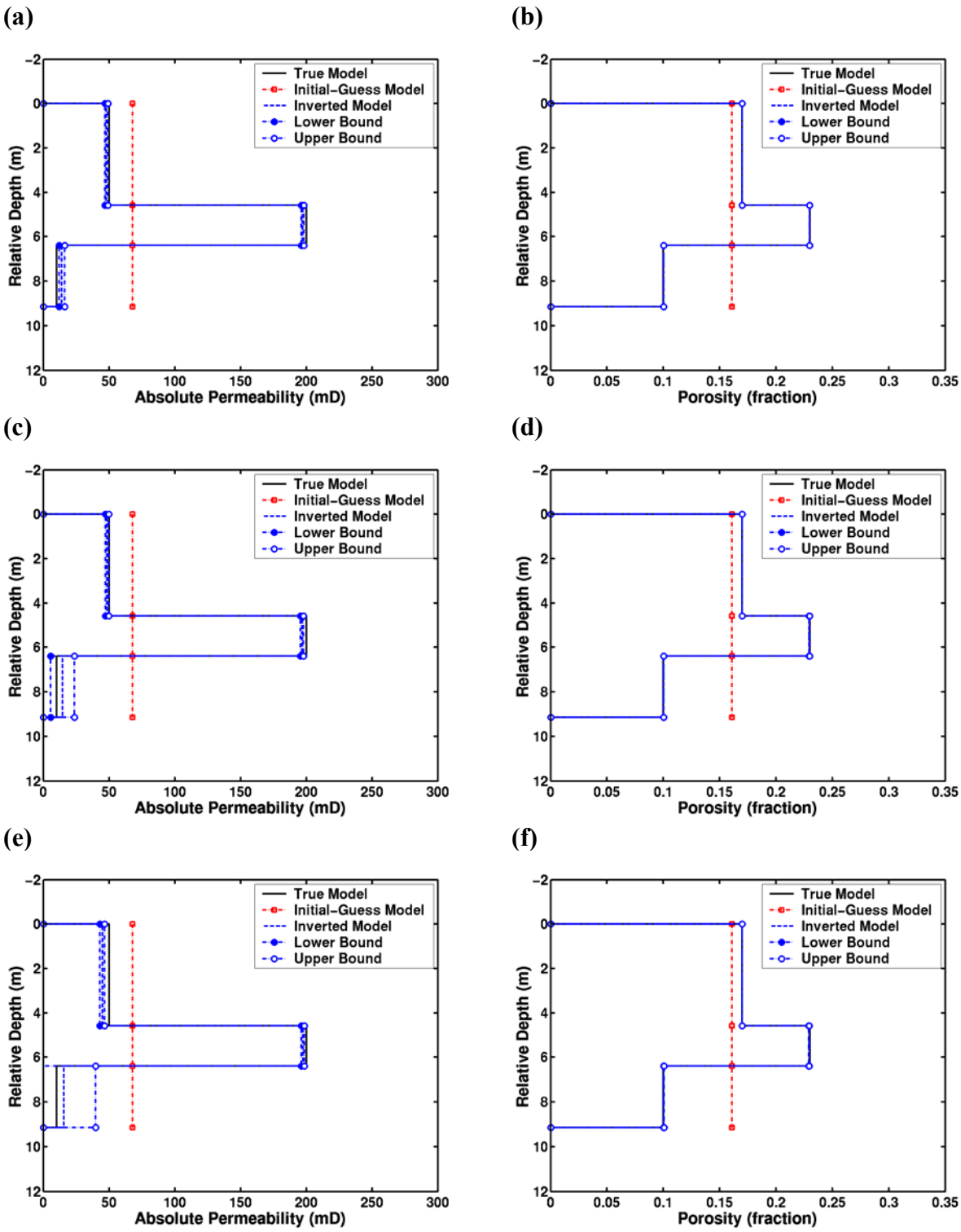

Figure 7.21: See caption on the following page.

Figure 7.21: Permeability and porosity profiles yielded by the joint inversions of two-snapshot induction logging measurements acquired by the AIT™ configuration, and pressure-transient measurements acquired by the dual-packer module and observation probes (log-test-log strategy). The first induction log and the formation test were conducted subsequent to a 1.5 day-long mud-filtrate invasion. A second induction log was acquired right after the formation test. The Cramer-Rao bounds [with 99.7% probability] on the inversion results are computed post-convergence. Inversion results are shown for the cases where measurements are contaminated with 1% [(a) and (b)], 3% [(c) and (d)], and 5% [(e) and (f)] Gaussian, random noise.

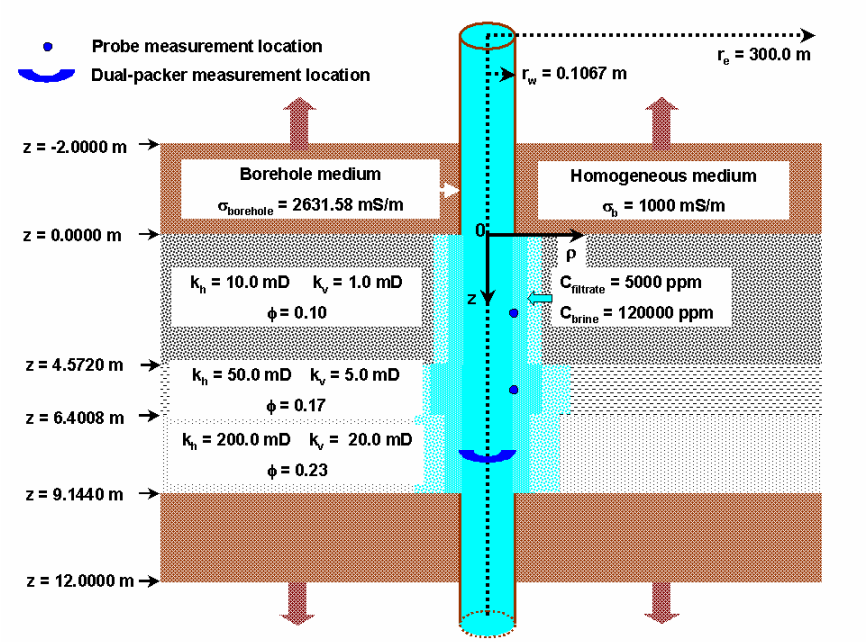

Figure 7.22: Two-dimensional vertical cross-section of the anisotropic formation intersected by a vertical borehole. The three-layer formation is subject to water-base mud-filtrate invasion.

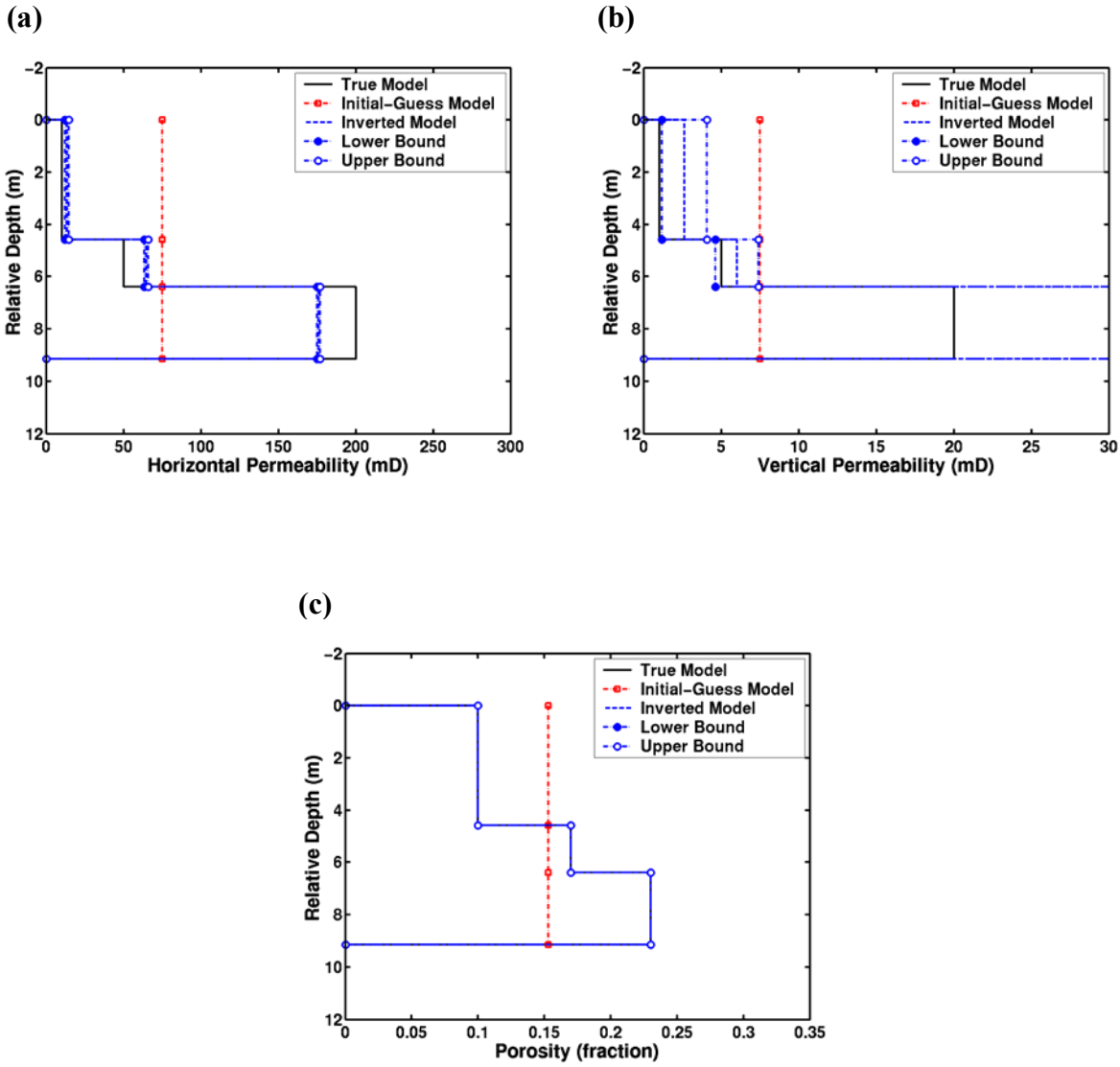

Figure 7.23: (a) Horizontal and (b) vertical permeability, and (c) porosity profiles yielded by the joint inversions of single-time induction logging measurements acquired by the AIT™ configuration, and pressure-transient measurements acquired by the dual-packer module and observation probes subsequent to a 1.5 day-long mud-filtrate invasion (log-test strategy). The Cramer-Rao bounds [with 99.7% probability] on the inversion results are computed post-convergence. Inversion results are shown for the cases where measurements are contaminated with 1% Gaussian, random noise.

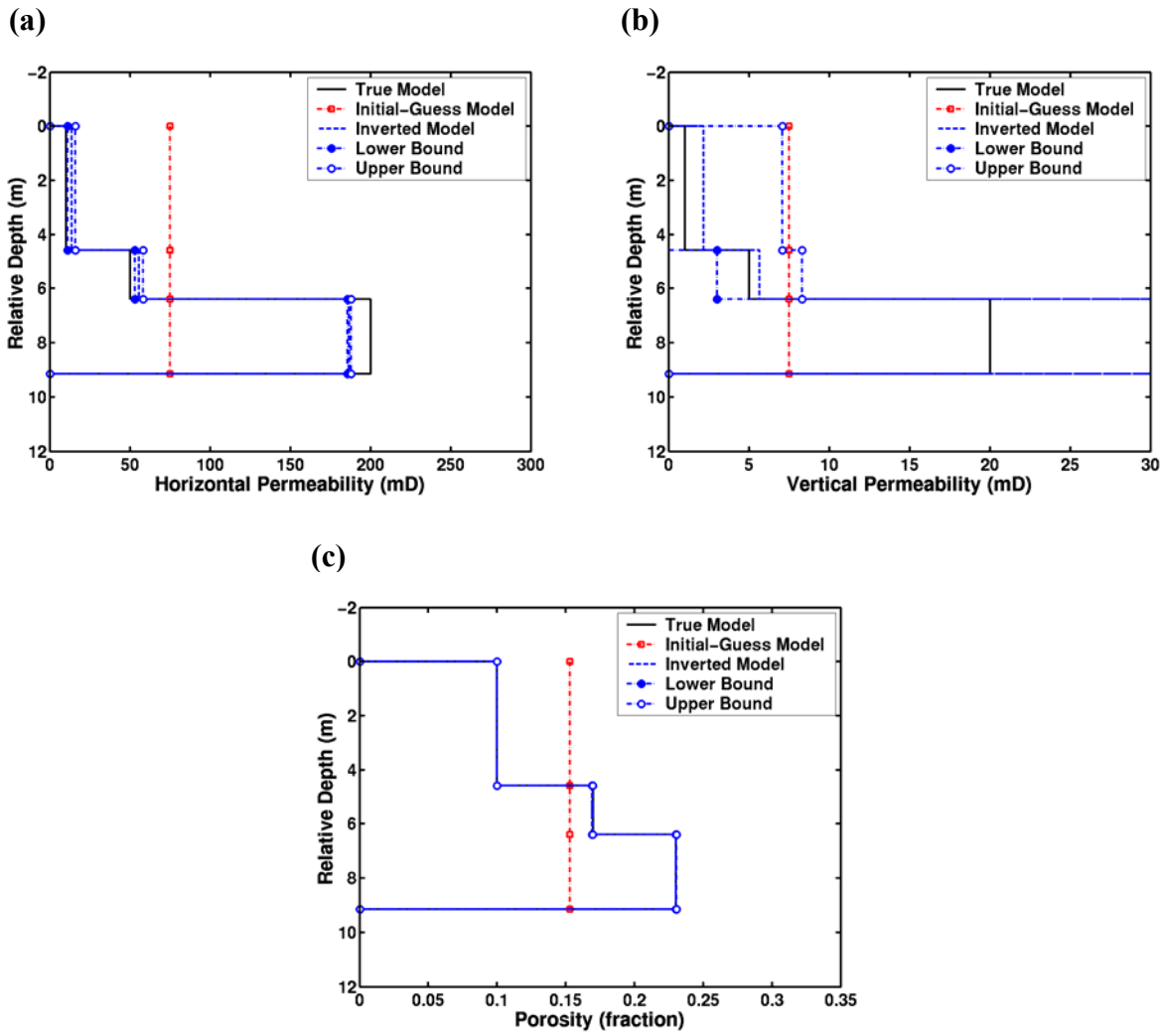

Figure 7.24: (a) Horizontal and (b) vertical permeability, and (c) porosity profiles yielded by the joint inversions of single-time induction logging measurements acquired by the AIT™ configuration, and pressure-transient measurements acquired by the dual-packer module and observation probes subsequent to a 1.5 day-long mud-filtrate invasion (log-test strategy). The Cramer-Rao bounds [with 99.7% probability] on the inversion results are computed post-convergence. Inversion results are shown for the cases where measurements are contaminated with 3% Gaussian, random noise.

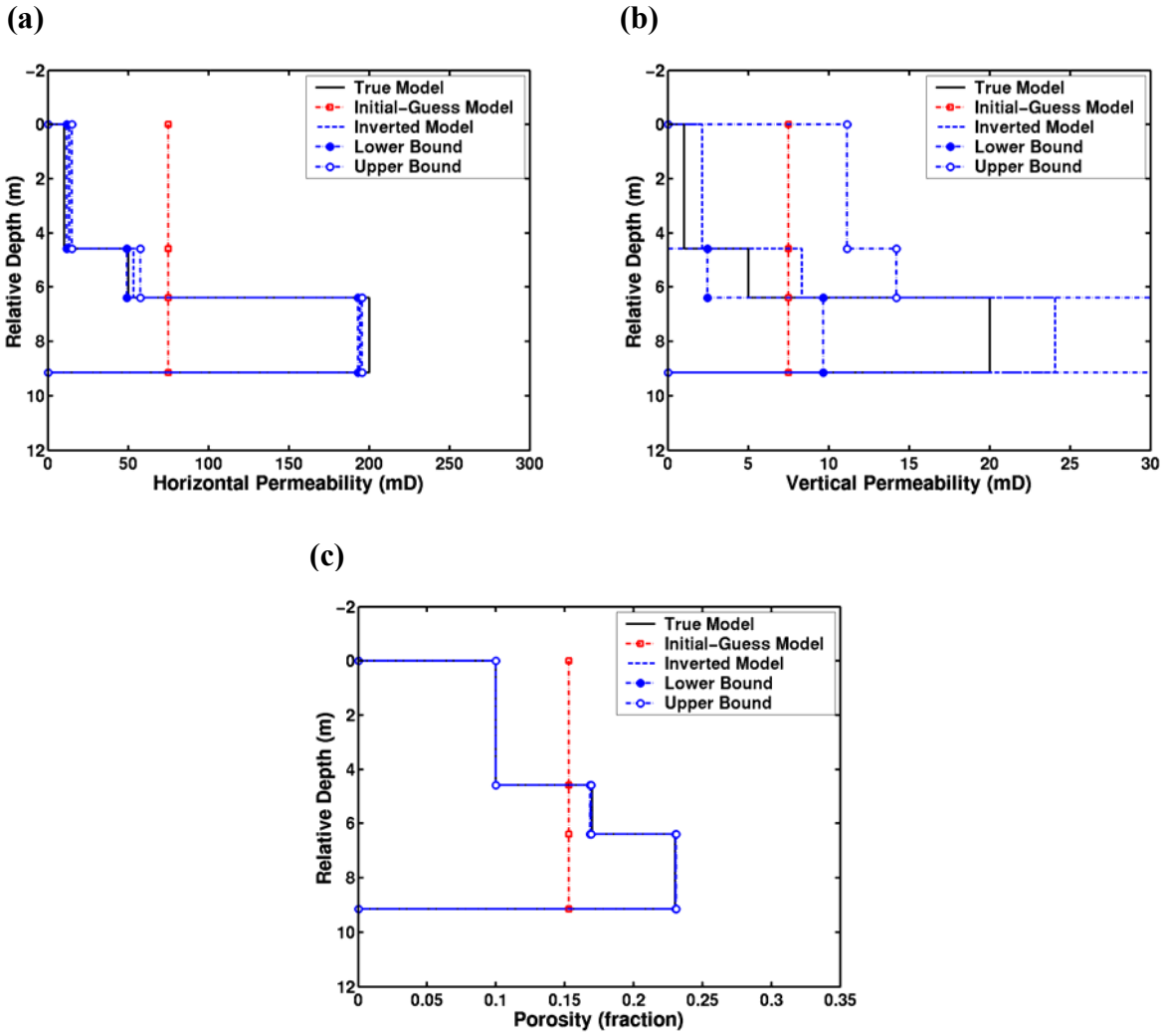

Figure 7.25: (a) Horizontal and (b) vertical permeability, and (c) porosity profiles yielded by the joint inversions of single-time induction logging measurements acquired by the AIT™ configuration, and pressure-transient measurements acquired by the dual-packer module and observation probes subsequent to a 1.5 day-long mud-filtrate invasion (log-test strategy). The Cramer-Rao bounds [with 99.7% probability] on the inversion results are computed post-convergence. Inversion results are shown for the cases where measurements are contaminated with 5% Gaussian, random noise.

Chapter 8: Petrophysical Inversion of Borehole Electromagnetic-Induction Logging Measurements

8.1 INTRODUCTION

The objective of our work is to develop a stable, accurate, and efficient algorithm for the parametric inversion of electromagnetic-induction measurements. The inversion algorithm will yield petrophysical properties, namely, layer-by-layer fluid permeabilities, and porosities of the hydrocarbon-bearing formations. Inversion of electromagnetic-induction measurements is posed as an optimization problem where a quadratic objective function is minimized subject to physical constraints on the model. A modification of the iterative Gauss-Newton optimization technique, namely, the Weighted and Regularized Gauss-Newton (WRGN) method is utilized for the inversions. At each iterative step, the solution of the forward problem is required. Forward modeling of electromagnetic-induction measurements entails coupled simulations of mud-filtrate invasion and the subsequent diffusive electromagnetic wave propagation phenomena. We make use of efficient finite-difference algorithms to simulate fluid-flow and electromagnetic-induction phenomena. Space- and time-domain distributions of aqueous phase saturation and salt concentration generated during the process of water-base mud-filtrate invasion is modeled as two-phase convective transport of three components, namely, oil/gas, water, and salt. Coupling between two-phase flow and electromagnetic-induction physics is accomplished via Archie's saturation equation (Archie, 1942). Salt mixing phenomenon taking place within the aqueous phase due to the invading and in-situ salt concentration contrast is also taken into account assuming a brine conductivity model.

Numerical examples of the coupled-physics inversion method are conducted for single-well two-dimensional (2D) axisymmetric near-borehole models. An inversion-

based sensitivity study is conducted for the simultaneous estimation of layer-by-layer absolute permeability and porosities from synthetically-generated electromagnetic-induction measurements contaminated with various levels of random Gaussian noise. For simplicity, from this point onward in the chapter, we refer to the absolute fluid permeability of rock formations simply as permeability. Inversions are performed for the cases, where perturbations are made to the a-priori information about rock and fluid properties. Uncertainty is quantified with the use of Cramer-Rao bounds (Habashy and Abubakar, 2004). The outcome of the sensitivity study provides a proof of concept for the robust estimation of permeability and porosity values from array electromagnetic-induction measurements. The coupled-physics inversion algorithm is further applied to field logs. Estimated permeability and porosity values remain consistent with available rock-core laboratory measurements.

8.2 PETROPHYSICAL INVERSION OF INDUCTION-LOGGING MEASUREMENTS

The objective of our work is the inversion of layer-by-layer permeability and porosity values from single- or dual-time electromagnetic-induction measurements. In the inverse problem, single- or multiple-time measurements of the vertical component of the total magnetic field are conducted at multiple receiver locations and frequencies with a depth-profiling instrument [see, for example, Figure 8.1]. In Chapter 4, we describe the forward model for coupled-physics induction-logging measurements as a nonlinear function of the spatial distribution of permeabilities, porosities, and other relevant rock and fluid properties. We initially assume the availability of saturation and pressure dependent rock and PVT dependent fluid properties from ancillary logs and laboratory experiments. It is important to emphasize that this assumption is relaxed in an inversion-based sensitivity study where we introduce perturbations to the a-priori known

parameters. In this sensitivity study, we will assess the impact of uncertainties in the a-priori known information on the outcome of the inversion.

8.3 AN INVERSION-BASED NUMERICAL SENSITIVITY STUDY

The assumed model consists of a vertical borehole that penetrates a hydrocarbon-bearing horizontal formation composed of three isotropic layers. In addition to the permeable layers, sealing upper and lower shoulder beds are included in the geoelectrical model shown in Figure 8.3. The reservoir is assumed to be buried in a shale background. As such, from the fluid-flow modeling point of view, upper, lower, and outer boundaries are assumed to exhibit no-flow conditions. The external boundary of the reservoir is located 300 m away from the axis of the borehole. From the onset of drilling, the permeable formation is subject to dynamic water-base mud-filtrate invasion. We consider the acquisition of an array induction log across the formation at a specific logging time for the single-time logging strategy. However, the time-lapse logging strategy involves two times of electromagnetic-induction logging measurements during the process of mud-filtrate invasion. The tool assumed for electromagnetic-induction measurements is an array induction imager tool described schematically in Figure 8.1. This tool is used to ensure the availability of measurements with multiple depths of investigation (Hunka et al., 1990) for an enhanced assessment of the perturbations of the spatial distribution of the near-borehole conductivity caused by mud-filtrate invasion.

Specific mud, mudcake, formation fluid and rock properties, and further details of the acquisition geometry are listed in Table 8.1. We make use of a $121\times1\times30$ grid in the cylindrical coordinate system to perform the simulations. This grid is uniform in the vertical and azimuthal directions. Block sizes increase logarithmically in the radial direction away from the borehole. We make use of a finer cylindrical finite-difference grid of size $141\times1\times30$ for fluid-flow simulations performed to generate the synthetic

measurements. Simulations performed using fine and coarse finite-difference grids agree within 1% of each other.

Layer-by-layer relative permeability and capillary pressure functions used for this numerical case are illustrated in Figures 8.4(a) and 8.4(b). The spatial distribution of initial aqueous and oleic phase saturation is derived from the hydrodynamic equilibrium state for the virgin (uninvaded) formation of interest. The averaged mud-filtrate invasion history, which is imposed on the fluid-flow simulator as the source condition, is shown in Figure 8.4(c). Rate history simulated with `UTCHEM` is rendered into a single-step rate schedule via integral averaging that maintains volumetric balance. In this case, the early-time rate-transient is short-lived in comparison to the stabilized rate and, therefore, the averaged invasion rate remains very close to the stabilized rate. This result also justifies the use of the single-step, equi-volume average rate. For the time-lapse logging strategy, the invasion-rate schedule is extended further until the second logging time (3^{rd} day). As shown in Figure 8.4(c), the rate-domain response of the removal of mudcake due to drill-string trip-out (rub-off) at the first logging time (1.5^{th} day) is also incorporated into the time history of the process of mud-filtrate invasion. The post-ruboff average invasion rate is computed using the same averaging approach as in the case of the pre-ruboff average rate. For all of the measurement strategies, synthetically generated measurements are contaminated with random Gaussian noise with standard deviation corresponding to 1% and 3% of the norm of each individual measurement.

8.3.1 Simulations of Near-Borehole Aqueous Phase Saturation, Salt Concentration, and Electrical Conductivity Distributions

We investigate the resistive invasion of water-base mud into hydrocarbon-bearing formations where the salinity of the in-situ brine is higher than that of mud-filtrate. In our example, mud-filtrate has a salt concentration of 5,000 ppm, whereas, the in-situ brine

has a salt concentration of 120,000 ppm. Simulated near-borehole oleic phase saturation and salt concentration distributions are shown in Figure 8.5 for the 1.5th and 3rd day of mud-filtrate invasion. Note that the spatial distribution of near-borehole oleic phase saturation can also be viewed as the spatial distribution of near-borehole aqueous phase saturation, since the saturation identity relationship, $S_w(\mathbf{r}) = 1 - S_o(\mathbf{r})$, holds for the two-phase immiscible flow of aqueous and oleic phases. The time-evolution of the spatial distribution of near-borehole conductivity is illustrated in Figure 8.6. Snapshots of conductivity are shown for the 1.5th, 3rd, 4.5th, 8.5th, and 12th day of mud-filtrate invasion. Spatial distributions of electrical conductivity are derived from the spatial distributions of aqueous phase saturation and salt concentration as described in Chapter 4.

The presence of a conductive annulus was discussed in the past by several authors, including Dumanoir et al. (1957), Ramakrishnan and Wilkinson (1997), and Zhang et al. (1999). In our example numerical simulations, we observe that invasion of water-base mud-filtrate into a hydrocarbon-bearing zone containing irreducible brine (with salt concentration much higher than the salinity of mud-filtrate) is responsible for the presence of a conductive annulus zone. This observation is consistent with the results of an in-depth study of the conductive annulus performed by Torres-Verdín et al. (2003).

8.3.2 Simulations of Synthetic Electromagnetic-Induction Logging Measurements

Electromagnetic-induction logging measurements simulated for the 1.5th, 3rd, 4.5th, 8.5th, and 12th day of mud-filtrate invasion are displayed in Figure 8.7. At relatively early stages of mud-filtrate invasion, the sensitivity of electromagnetic-induction measurements to time-dependent changes in the near-borehole conductivity distribution become apparent in the shallow investigating arrays (10, 20, and 30 inch arrays) in comparison to arrays with a longer depth of investigation (60 and 90 inch arrays). As mud-filtrate invasion proceeds, the sensitivity of electromagnetic-induction

measurements to perturbations in conductivity propagates further to include deeper investigating arrays.

From the geological point of view, the signature of mud-filtrate invasion in the electromagnetic-induction measurements becomes more apparent across relatively more permeable beds. Transport of mass of fluid components occurs faster in high-permeability beds, leading both the phase saturation and salt concentration fronts, and hence, the electrical conductivity perturbation to extend further into the reservoir. For the space and time scales of transport phenomena taking place within the depth of investigation of the array imager tool, relatively large changes in the electrical conductivity domain of permeable beds lead to relatively large changes in the magnitude of electromagnetic-induction measurements.

The above observations are further confirmed by a time-lapse analysis of the electromagnetic-induction logging measurements displayed in Figure 8.8. We compute the change in the electromagnetic-induction logging responses from $t_{\log 1}$ to $t_{\log 2}$, i.e., $\Delta\sigma_{\text{app.}} = \sigma_{\text{app. t}\log 2} - \sigma_{\text{app. t}\log 1}$. Changes in the log response are shown for $t_{\log 1} = 1.5$ day and $t_{\log 2} = 3$ day, $t_{\log 2} = 4.5$ day, $t_{\log 2} = 8.5$ day, $t_{\log 2} = 12$ day in Figures 8.8(a), 8.8(b), 8.8(c), and 8.8(d), respectively.

8.3.3 Inversions of Noisy Synthetic Electromagnetic-Induction Logging Measurements

Electromagnetic-induction logging measurements acquired at the 1.5^{th} day of mud-filtrate invasion are inverted to yield layer-by-layer values of permeability and porosity. Saturation-dependent functions, saturation equation parameters, and PVT properties of the fluids are assumed known from fluid sample and rock-core laboratory measurements.

Inversion results are presented along with true and initial-guess parameters. Uniform initial-guess values are chosen for both permeability and porosity. These uniform values are derived from the actual profiles by volumetrically averaging the true values of permeability and porosity, respectively. Figure 8.9(a) shows inversion results for permeability. On the other hand, Figure 8.9(b) displays inversion results for porosity for the case where the synthetic measurements are contaminated with 1% random Gaussian noise. A similar set of inversion results is shown in Figures 8.9(c) and 8.9(d) for a random Gaussian measurement-noise level of 3%. In the next numerical experiment, noise-contaminated time-lapse electromagnetic-induction logging measurements acquired at the 1.5^{th} and 3^{rd} day of invasion are input to the inversion algorithm. Figures 8.10(a) and 8.10(b) display inversion results for the random Gaussian noise level of 1%. Inverted permeability and porosity values for the 3% random Gaussian measurement-noise level are displayed in Figures 8.10(c) and 8.10(d). The inverted permeability values indicate sensitivity to the increasing noise level. Among the three layers, the deleterious effect of measurement noise appears to have the most effect on the permeability values inverted for the mid-layer. By contrast, an excellent reconstruction of porosity values is achieved for all of the numerical inversion experiments. We also observe a clear improvement in the reconstructions of permeability when using additional measurements acquired at the 3^{rd} day during the process of mud-filtrate invasion. For the 3% measurement-noise level, the inverted permeability values appear to improve gradually. Interestingly, however, the permeability values inverted with the time-lapse approach for 1% measurement-noise level are less accurate in comparison to the ones obtained with the single-snapshot approach. We attribute this behavior to the random nature of measurement noise and emphasize the fact that in each case we make use of a different realization of noise. The added value of the additional log-acquisition is marginally observable for the 3% noise

level. Therefore, one cannot expect to have a major impact on the inverted results with the use of additional measurements at the 1% noise level.

The effect of the time of mud-filtrate invasion on the inverted permeability and porosity values is quantified in the following set of results. Electromagnetic-induction measurements are simulated for log-acquisition times that correspond to the 4.5^{th} and 12^{th} day of mud-filtrate invasion. For these cases, we extend the mud-filtrate invasion rate computed via UTCHEM for the pre-ruboff invasion period shown in Figure 8.4(c) to the time of log-acquisition. The simulated measurements are contaminated with 3% random Gaussian noise, and input to the inversion algorithm. Initial-guess values are kept the same as in the previous case. Inversion results in the form of simultaneously estimated permeability and porosity values for the log-acquisition at the 4.5^{th} day of invasion are shown in Figures 8.11(a) and 8.11(b), respectively. Similar results are displayed in Figures 8.11(c) and 8.11(d) for the inversion of an electromagnetic-induction log simulated for the 12^{th} day of invasion. Note that the same inversion exercise can be viewed from the point of the invasion rate while keeping the log-acquisition time constant. As matter of fact, the measurements simulated for the 4.5^{th} day log-acquisition can be approximately thought of measurements acquired at the 1.5^{th} day of mud-filtrate invasion with an invasion rate equal to three times the original rate. Similarly, the measurements simulated for the 12^{th} day log-acquisition can be approximately thought of measurements acquired at the 1.5^{th} day of mud-filtrate invasion with an invasion rate equal to eight times the original rate.

For the case where the electromagnetic-induction log is recorded at the 12^{th} day of mud-filtrate invasion, the inverted permeability and porosity values accurately match the true model for all layers despite the 3% Gaussian, random measurement noise. In fact, comparisons of the permeability values estimated from inversions of 3% noise-

contaminated, single-snapshot electromagnetic-induction measurements for the 1.5th, 4.5th, and 12th day of mud-filtrate invasion indicate an improving trend as the duration of invasion increases. A combined analysis of the time-evolution of near-borehole electrical conductivity profiles (Figure 8.6) together with simulated electromagnetic-induction logging measurements (Figure 8.7), and their time-lapse sensitivity (Figure 8.8) provide a quantitative explanation to the above observation. Multi-phase flow during mud-filtrate invasion leads to spatial variations of conductivity in the radial direction due to the movement of the aqueous phase saturation and salt concentration fronts. Of course, there are effects due to multi-phase displacement in the vertical direction (cross-flow) because of the density contrast between the two fluid phases. Nonetheless, these effects are secondary in comparison to radial transport. The sensitivity of the electromagnetic-induction measurements to near-borehole spatial distribution of permeability increases with time of invasion in comparison to measurements acquired at the early stages of invasion. We conclude that, for the problem at hand, radial variations of conductivity due to multi-phase flow are directly related to permeability. When the spatial variations of conductivity are contained within the depth of investigation of the array imager tool, electromagnetic-induction measurements are sensitive to permeability. Eventually, when mud-filtrate invasion progresses and the spatial variations of conductivity are located deeper than the depth of investigation of the array imager tool, the sensitivity of the electromagnetic-induction measurements to permeability diminishes.

On the other hand, the underlying sensitivity of electromagnetic-induction measurements to the spatial distribution of porosity is inherent from the overall spatial distribution of electrical conductivity within the tool's volume of investigation. Therefore, the sensitivity of electromagnetic-induction measurements to the spatial distribution of porosity remains regardless of the depth of invasion. In all of the

numerical inversion experiments, an excellent reconstruction of porosity values is achieved. It is a well-established fact that electromagnetic-induction logging measurements exhibit strong sensitivity to the near-borehole spatial distributions of electrical conductivity. Therefore, electromagnetic-induction logging measurements are conventionally inverted to reconstruct the near-borehole electrical conductivity profiles for the purpose of estimating the spatial distribution near-borehole fluid saturations. In order to achieve this objective, the use of an appropriate saturation equation such as Archie's law (Archie, 1942) is necessary. For rock formations where the saturation-conductivity relationship established by Archie (1942) is valid, we observe that the spatial distribution of electrical conductivity is a nonlinear function of the spatial distribution of in-situ brine conductivity, porosity, and aqueous phase saturation along with the additional power-law parameters, m and n as shown in equation (4.8). Therefore, for rock formations where the power-law parameters are known with high certainty, the sensitivity of electromagnetic-induction logging measurements to the near-borehole spatial distribution of conductivity can be propagated to the spatial distribution of porosity. Within the framework of this novel petrophysical inversion algorithm, the spatial distribution of electrical conductivity is described as a function of the spatial distribution of porosity, brine conductivity, and aqueous phase saturation. In turn, the spatial distribution of brine conductivity and aqueous phase saturation are formulated as exclusive functions of the spatial distributions of permeability and porosity via a multi-phase flow formulation. Using such a formulation, the high-sensitivity of electromagnetic-induction logging measurements to the spatial distribution of electrical conductivity is propagated to the spatial distributions of permeability and porosity. In the described concentration-saturation-conductivity coupling, the role of the spatial distribution of porosity is readily apparent in equation (4.8) as opposed to the spatial

distribution of permeability. Specifically, in this case, each electromagnetic-induction array provides information about the same porosity for a given depth since we consider a layered reservoir. Moreover, since we consider a depth-profiling borehole-logging tool, data are sampled densely in the vertical direction. As such, for the cases where the Archie's saturation relationship is deemed valid, the spatial heterogeneity of porosity can be described by horizontal layers, and a near-borehole fluid-flow simulator is coupled to the inversion framework, multi-array electromagnetic-induction logging measurements provide an overdetermined system for the inversion of layer-by-layer porosity values. Therefore, electromagnetic-induction measurements are expected to exhibit a relatively higher order of sensitivity to the spatial distribution of porosity in comparison to the spatial distribution of permeability. In fact, our numerical experiments consistently indicate an excellent reconstruction of porosity values in comparison to the varying degrees of accuracy attained in the reconstructions of permeability values.

Having established physical insights to the time-evolution of sensitivities of electromagnetic-induction logging measurements with respect to the spatial distributions of permeability and porosity, we select the electromagnetic-induction logging measurements simulated for the 12^{th} day of mud-filtrate invasion, (or equivalently, for the 1.5^{th} day of mud-filtrate invasion with a rate of eight times the original rate of invasion) for the next numerical experiment. In this set of inversions, we contaminate the simulated measurements with 1%, 3%, 5%, 8%, 12%, 15%, and 21% Gaussian random noise. In order to assess the robustness of the inversion to the choice of the initial-guess values, for this set of experiments we select a new set of uniform initial permeability and porosity values. The outcome of the inversions are shown in Figures 8.12(a) and 8.12(b) for the measurement-noise level of 1%, in Figures 8.12(c) and 8.12(d) for the measurement-noise level of 3%, in Figures 8.12(e) and 8.12(f) for the measurement-noise level of 5%,

in Figures 8.12(g) and 8.12(h) for the measurement-noise level of 8%, in Figures 8.12(i) and 8.12(j) for the measurement-noise level of 12%, in Figures 8.12(k) and 8.12(l) for the measurement-noise level of 15%, and in Figures 8.12(m) and 8.12(n) for the measurement-noise level of 21%. Noise generated for the simulated measurements is additive, random, Gaussian, and the standard deviation of the noise level is specified, for instance, 15%. Note that this does not necessarily mean that each measurement point will involve a 15% error.

Inversions indicate accurate reconstructions of permeability and porosity values for both 1% and 3% noise levels despite the drastic change in the initial-guess values. A comparison of inversion results for the 3% noise level attained using the uniform initial-guess values of the previous case, shown in Figures 8.11(c) and 8.11(d), and using the new uniform initial-guess values, shown in Figures 8.12(c) and 8.12(d), provides a quantitative proof-of-validity for the robustness of our petrophysical inversion algorithm to initial-estimate values of permeability and porosity. For 5%, 8%, and 12% measurement-noise levels, the inverted permeability values deviate considerably from the true values. Estimated porosity values, however, remain unchanged with respect to the negative influence of measurement noise. From the 15% measurement-noise level onward, however, the inverted porosity values start to deviate from the true values. In general, at these very high noise levels, the quality of the reconstructed permeability values is significantly poorer than the quality of the reconstructed porosity values.

At a first glance, the robustness of the inversion for porosity at higher levels of measurement noise appears to be unrealistic. However, a quantitative analysis reveals that, for layered reservoirs, all channels of the multi-resolution electromagnetic-induction logging measurements exhibit sensitivity with respect to porosity. In such cases, lateral continuity of the porosity is the depositional characteristic. When spatial fluid saturation

and salt concentration information is provided by the near-borehole fluid-flow simulator, and when the governing parameters of the underlying saturation-conductivity relationship are accurately known, the sensitivity of electromagnetic-induction measurements to a local change in electrical conductivity can be interpreted as the sensitivity with respect to porosity. Since for a layered reservoir there are no radial variations of porosity, electromagnetic-induction logging measurements with multiple radial lengths of investigation at a given depth show sensitivity to the same porosity-layer. Another feature of the inversions that contributes to the strong sensitivity of the measurements with respect to porosity is the measurement sampling strategy used for the above-described numerical examples. The sampling strategy used for induction-log acquisition ensures the presence of multiple measurement points within each layer.

In the next numerical inversion experiment, we investigate the added value of a time-lapse inversion approach. For this experiment, we make use of electromagnetic-induction logging measurements acquired at the 1.5^{th} and 12^{th} day of mud-filtrate invasion. In comparison to the previous time-lapse case, in this inversion exercise we integrate additional measurements with enhanced sensitivity to permeability to the 1.5^{th} day log-acquisition. Note that in the previous numerical inversion experiments, we already quantitatively proved the presence of improved sensitivity of the 12^{th} day electromagnetic-induction measurements to near-borehole permeability values. Time-lapse measurements are corrupted with 1% and 3% Gaussian random noise. Inversions are initialized with uniform permeability and porosity values that are farther away from the true values as in the previous numerical experiments. Reconstructions of permeability and porosity values for 1% noise level are shown in Figures 8.13(a) and 8.13(b), respectively. Similar inversion results are displayed in Figures 8.13(c) and 8.13(d) for the measurement-noise level of 3%. Inverted permeability values at 3% measurement-noise

level are more accurate than single-snapshot inversions of 1.5^{th} day measurements as well as 12^{th} day measurements regardless of the choice of initial-guess value. Although the inverted permeability values at 1% measurement-noise level still indicates a good reconstruction, the results are less accurate than single-snapshot inversions of 1.5^{th} day measurements as well as 12^{th} day measurements. It is found that when the noise level is below 1% the results of the inversion remain unchanged. This behavior is consistent with the permeability values inverted with the previously investigated time-lapse study for 1% noise level. We attribute this behavior to the random nature of measurement noise and emphasize the fact that in each case we make use of a different realization of noise. Inversion results for porosity remain very accurate in all of the inversion cases because the estimation of porosity from the given set of electromagnetic-induction measurements is an overdetermined problem.

A quantitative appraisal of the uncertainty of the inversion results is carried out with the calculation of Cramer-Rao bounds using an approximation to the estimator's covariance matrix. The Cramer-Rao error bounds provide a probabilistic range for each model parameter inverted from noisy measurements. Computation of these error limits is described in detail in Appendix A. The assumption underlying the approximate computation of the estimator's covariance matrix is that the errors in the measurements are purely random and comply with the Gaussian distribution.

For the purpose of appraising the uncertainty of the inversion results on a set of numerical inversion experiments, we select the electromagnetic-induction logging measurements simulated for the 12^{th} day of mud-filtrate invasion, or equivalently, for the 1.5^{th} day of mud-filtrate invasion with a rate of eight times the original rate of invasion. In this set of inversions, we corrupt the simulated measurements with 1% and 3% Gaussian random noise. In this set of inversions, we make use of the same finite-

difference numerical mesh that we used in generating the synthetic measurements ($141\times1\times30$) to prevent any systematic error (although less than 1%) from affecting the outcome of the uncertainty analysis. Inverted values of permeability and porosity along with the computed upper and lower uncertainty bounds are shown in Figures 8.14(a) and 8.14(b) for the measurement-noise level of 1%, and in Figures 8.14(c) and 8.14(d) for the measurement-noise level of 3%. Inversion results indicate relatively small uncertainty bounds on the reconstructed model parameters at both levels of measurement noise. For some model parameters the true value of the parameter falls outside the probabilistic uncertainty bounds yielded by the inversion. In fact, this behavior is observed for the inverted permeability value of the mid-layer at both noise levels of 1% and 3%. For cases where the relative flatness of the cost function (as a function of the iteration number) is high with respect to a given model parameter in the vicinity of the minimum, the uncertainty range derived from the estimator's covariance matrix may turn out be small to include the true value of the model parameter, despite the fact that inverted result is accurate. Characteristically, for the inversions at hand, uncertainty bounds for the estimated porosity values are lower than the ones estimated for permeability values at a given level of measurement noise.

For the same synthetic case described above, numerically simulated electromagnetic-induction logging measurements are also used to invert permeability values only. In this case, the spatial distribution of porosity is assumed to be known from other measurements such as density and neutron logs. Inverted values of permeability are shown along with error bounds and initial-guess values in Figure 8.15(a) for 1% measurement-noise level, and in Figure 8.15(b) for 3% measurement-noise level. Estimated permeability values are comparable to the ones obtained with the simultaneous inversion approach. The inversion of porosity values in the simultaneous inversion

approach is robust. As such, for the independent inversion of permeability values, a-priori knowledge about porosity values does not improve the accuracy of the results.

8.3.4 Sensitivity of the Petrophysical Inversion Results to Uncertainty in A-Priori Information

In the previous section, the investigated cases involved the assumption that saturation equation parameters, PVT properties of the fluids, and saturation-dependent functions were known a-priori from fluid sampling and rock-core laboratory measurements. This assumption concerns quantities that are measurable and becomes increasingly relevant with the quality of sampling and laboratory analysis. However, for a newly-discovered hydrocarbon-bearing formation, knowledge of a-priori information about saturation equation parameters, PVT properties of the fluids, and relative permeability and capillary pressure functions may be limited or may involve various degrees of uncertainty. In this section of the chapter, the primary objective is to quantitatively assess the robustness of the petrophysical inversion algorithm with respect to inaccuracies in a-priori information. For this purpose, a sensitivity study is carried out where inversions of electromagnetic-induction logging measurements are conducted with perturbed input parameters for saturation equation, viscosity ratio, oleic phase compressibility, and saturation-dependent functions. For the inversions with perturbed a-priori information, we use synthetically-computed electromagnetic-induction logging measurements. Electromagnetic-induction logging measurements simulated for the 12^{th} day of mud-filtrate invasion, (or equivalently, for the 1.5^{th} day of mud-filtrate invasion with a rate of eight times the original rate of invasion) are selected for the numerical experiment. Uniform initial-guess values of 100 mD and 25% are assumed for permeability and porosity, respectively. While generating the measurement vector, accurately-simulated measurements are contaminated with 1% random Gaussian noise.

As in the case of inversions conducted with unperturbed a-priori information, we make use of a relatively coarser $121\times1\times30$ numerical mesh in the cylindrical coordinate system.

8.3.4.1 Inversions with Perturbed Saturation Equation Parameters

We first perform inversions for the purpose of quantifying the sensitivity of inversion results to the simultaneous perturbations in Archie's parameters m and n. Panels (a) and (b) of Figure 8.16 show inversion results for permeability and porosity values, respectively, for the perturbed m and n set no. 1 shown in Table 8.2. Similarly, panels (c) and (d) of Figure 8.16 display inversion results for the perturbed parameter set no. 2. Finally, panels (e) and (f) of Figure 8.16 show inverted permeability and porosity values, respectively, for the perturbed parameter set no. 3 given in Table 8.2.

In the first test case, a 5% percent positive perturbation is performed on the parameter m, whereas the parameter n is subjected to a 5% negative perturbation. Inversion results indicate that at perturbation levels that correspond to the 5% of the original parameter (set no. 1), the petrophysical inversion algorithm yields acceptable values of permeability and porosity. When the magnitude of the perturbation is increased to 10% and the sign of the perturbations remain unchanged (set no. 2), the inverted values do not significantly change with respect to those of the original model. However, we observe a slight deterioration in the quality of the reconstruction of porosity. For the same perturbation level, a reversal of the sign of the perturbation for the parameter n (set no. 3) amplifies the model reconstruction errors for both permeability and porosity. An extensive number of inversion exercises indicate that petrophysical inversions result in acceptable reconstructions of permeability and porosity values up to a perturbation level of 5%. However, above 5% perturbation level the quality of inversion results for permeability values deteriorates significantly due to an amplification of non-uniqueness.

The quality of the reconstruction of porosity values becomes a matter of perturbation direction which is also a very undesirable outcome.

8.3.4.2 Inversions with Perturbed Oleic Phase Viscosity and Compressibility

Next, we investigate the sensitivity of inversion results to simultaneous perturbations in viscosity ratio and oleic phase compressibility. The objective of this study is to perform petrophysical inversions under the influence of an inaccurate displacement efficiency prescribed for the multi-phase fluid-flow forward model. The displacement efficiency is a strong function of the mobility ratio which is predominantly governed by the ratio of viscosities of the displaced and displacing fluids. In our case, water-base mud-filtrate (aqueous phase) is displacing the in-situ liquid oil (oleic phase). Therefore, perturbations done on the oleic phase viscosity can be interpreted as modifications done on the displacement efficiency. If the ratio of the viscosities of the displaced fluid with respect to the displacing fluid (for the case at hand, μ_o / μ_w) is less than one, then the displacement phenomenon proceeds with a favorable viscosity ratio. If the viscosity ratio is greater than one, then the displacement phenomenon takes place with an adverse viscosity ratio. In general, viscosity, density, and compressibility of the fluid phases are interrelated. For instance, high viscosity oils usually exhibit high density and low compressibility. In other words, lighter oils are less viscous and relatively more compressible. In order to maintain the consistency of the perturbation analysis, we considered a simultaneous modification of the oleic phase viscosity and compressibility for a given level of oleic phase density. Panels (a) and (b) of Figure 8.17 show inversion results for permeability and porosity, respectively, for the perturbed parameter set no. 1 shown in Table 8.3. The viscosity ratio of this case is equal to the relatively adverse value of 3.14, as opposed to the actual favorable viscosity ratio of 0.28. Similarly, panels (c) and (d) of Figure 8.17 display inversion results for the perturbed parameter set no. 2

where we consider the use of a favorable viscosity ratio of 0.08. Finally, Figures 8.17(e) and 8.17(f) show inverted permeability and porosity values, respectively, for the perturbed parameter set no. 3 listed in Table 8.3. In this case, we perform inversions by assuming a more adverse viscosity ratio equal to 7.8.

For the investigated cases, inversion results for porosity remain robust with respect to perturbations on the viscosity ratio and oleic phase compressibility. The inverted permeability values, on the other hand, exhibit limited sensitivity to these perturbations. Overall, the inverted permeability values agree well with the actual permeability values.

8.3.4.3 Inversions with Perturbed Saturation-Dependent Functions

For the synthetic numerical experiments described in this chapter, we make use of parametric relative permeability and capillary pressure functions described independently for each petrophysical layer. Within the context of the forward model, a multi-phase flow simulator uses these saturation-dependent functions via a modified Brooks-Corey model (Lake, 1989; Semmelbeck et al., 1995) to compute transmissibilities associated with numerical gridblocks. The modified Brooks-Corey model is described by the following parametric equations for phase relative permeabilities:

$$S_{wD} = \frac{S_w - S_{wirr}}{1 - S_{wirr} - S_{or}}, \tag{8.1}$$

$$k_{rw}(S_{wD}) = k_{rw}^{o}\left[S_{wD}\right]^{e_w}, \tag{8.2}$$

and

$$k_{ro}(S_{wD}) = k_{ro}^{o}\left[1 - S_{wD}\right]^{e_o}, \tag{8.3}$$

The capillary pressure between aqueous and oleic phases is given by

$$P_c(S_{wD}) = P_{ce}\left[S_{wD}\right]^{-1/\alpha}. \tag{8.4}$$

In the above equations, S_w stands for the saturation of the aqueous phase, and S_{wirr} and S_{or} denote irreducible aqueous and residual oleic phase saturation, respectively. A normalized aqueous phase saturation, S_{wD}, is computed using equation (8.1). Saturation-dependent aqueous and oleic phase relative permeability functions, $k_{rw}(S_{wD})$ and $k_{ro}(S_{wD})$, respectively, are computed using end-point aqueous and oleic phase relative permeabilities, k_{rw}^{o} and k_{ro}^{o}, and curvature parameters, e_w and e_o. On the other hand, the saturation-dependent capillary pressure between oleic and aqueous phases, $P_c(S_{wD})$ is parameterized using the entry capillary pressure, P_{ce} and the pore-size distribution index, α (Semmelbeck et al., 1995). Relative permeability and capillary pressure functions described by equations (8.1) through (8.4) reflect drainage conditions. Imbibition relative permeabilities are assumed to be the same as drainage, in other words, the hysteresis in the saturation-dependent functions is assumed to be negligible.

A study is carried out to quantify the sensitivity of inversion results to perturbations in the saturation-dependent functions, namely, relative permeability and capillary pressure functions. Figures 8.18(a) and 8.18(b) show inversion results for permeability and porosity, respectively, assuming that the relative permeability and capillary pressure functions for layer no. 1 hold for all three layers. Similarly, panels (c) and (d) of Figure 8.18 display inversion results obtained by assuming that the relative permeability and capillary pressure functions for layer no. 2 hold for all three layers.

Finally, panels (e) and (f) of Figure 8.18 show inversion results for permeability and porosity, respectively, assuming that the relative permeability and capillary pressure functions for layer no. 3 hold for all three layers. The sensitivity study is extended using various combinations of the perturbed parameters for saturation-dependent functions. These perturbed parameters are documented in Table 8.4. Corresponding inversion results for each perturbed set are shown in Figures 8.19 and 8.20.

In comparison to the inverted porosity values, permeability values have consistently been identified as the parameter that is the most sensitive to the deleterious effect of measurement noise and to the negative influence of inaccuracies in the a-priori information. However, for the numerical experiments where we introduce significant inaccuracies to the description of the governing relative permeability and capillary pressure data, inverted permeability as well as porosity values both exhibit significant deviations from the actual values. Despite this fact, in a great majority of the investigated cases, where inversions were performed under the influence of perturbed saturation-dependent functions, inverted porosity values consistently agreed well with the true model. The quality of the inverted permeability values, on the other hand, appears to be highly case-dependent. Inaccurate descriptions of saturation-dependent functions combined with noisy measurements render the permeability-porosity inverse problem more non-unique in comparison to other types of perturbations considered in this work.

8.3.4.4 Perturbations on the Estimated Duration of Mud-Filtrate Invasion

We also assess the impact of an error in the estimated time duration of the process of mud-filtrate invasion. This inversion-based sensitivity study can also be viewed as introducing uncertainty to the mud-filtrate invasion rate since we use a constant time-average rate of mud-filtrate invasion. Electromagnetic-induction logging measurements simulated for the 12^{th} day of mud-filtrate invasion are selected for the numerical

experiment. We introduce ± 1 day and ± 3 days error for the estimated duration of mud-filtrate invasion.

Inversion results are shown in Figures 8.21(a) and 8.21(b) for a perturbation of $+1$ day, 8.21(c) and 8.21(d) for a perturbation of -1 day, 8.21(e) and 8.21(f) for a perturbation of $+3$ days, and 8.21(g) and 8.21(h) for a perturbation of -3 days, respectively. Inversions results indicate that introducing an error of ± 1 day has a minimal effect on the accuracy of the inverted values of permeability and porosity. An error of ± 3 days in the assumption of the duration of mud-filtrate invasion, however, has dire consequences on the accuracy of the inverted values of permeability, while the inverted porosity values remain unscathed. These latter conclusions about the impact of accurate estimation of mud-filtrate invasion duration on the accuracy of the inverted petrophysical parameters are also directly applicable for the accurate estimation of the rate of mud-filtrate invasion.

8.3.5 Full One-Dimensional Inversion of Permeability from Electromagnetic-Induction Logging Measurements

For full one-dimensional (1D) inversion of electromagnetic-induction logging measurements, we parameterize the 9.144 m (30 ft) thick three-layer (geological layers) formation (shown in Figure 8.3), into thirty uniform thin numerical layers of thickness equal to 0.3048 m (1 ft). We assume the availability of porosity values from other ancillary logs (such as bulk density). Electromagnetic-induction logging measurements simulated for the 12^{th} day of mud-filtrate invasion, (or equivalently, for the 1.5^{th} day of mud-filtrate invasion with a rate of eight times the original rate of invasion) are selected for the numerical experiment. A uniform initial-guess value of 100 mD is assumed for the permeability of all the layers. While generating the measurement vector, accurately-simulated measurements (on a $141 \times 1 \times 30$ grid) were contaminated with 1% and 3%

random Gaussian noise. For the inversions, we make use of a relatively coarser $121 \times 1 \times 30$ numerical mesh.

Results for full 1D inversions of permeability from electromagnetic-induction logging measurements are shown in Figure 8.22. Figure panels 8.22(a) and 8.22(b) show inversion results for cases where the measurements are contaminated with 1% and 3% random Gaussian noise, respectively. Inversion results indicate a fairly accurate reconstruction of the near-wellbore permeabilities for the 1% noise-contamination case. However, for 3% measurement-noise level, the deleterious effect of noise significantly reduces the accuracy of the inverted permeability values.

8.4 PETROPHYSICAL INVERSION OF FIELD DATA

The study presented in this work is focused on a gas-bearing carbonate formation intersected by wells X-1 and X-2 approximately 100 m away from each other. These wells were drilled with water-base muds of salinities in the range of 300 ppm to 2,000 ppm. On the other hand, the salinity of connate water is very high, of the order of 200,000 ppm. From the onset of drilling, the permeable formation is subject to water-base mud-filtrate invasion. Lithology in the gas-bearing zone consists of inter-layered carbonates along with fine-grained clastics and shales. A 10.67 m (35 ft) thick carbonate formation straddled by these two wells was selected as the permeable medium of interest for petrophysical inversion. Gas saturation of the formation is within 80% to 85%.

Well X-2 was drilled using a heavy fresh water-base mud, causing an overbalance pressure approximately equal to 7.3 MPa. Porosity of the gas-bearing formation is low, on the order of 15%, hence giving rise to deep invasion. A major challenge faced in the evaluation of this reservoir, using electrical measurements acquired in Well X-2, is the deep invasion of mud-filtrate adversely affecting the response of resistivity measurements. Dual Induction Imager Resistivity Tool logs (DIL™) acquired in well X-2,

shown in Figure 8.23, exhibit a reverse resistivity profile where, on average, deep dual induction (ILD™) readings (20-22 ohm-m) are lower than the medium dual induction (ILM™) readings (25-30 ohm-m). Both average ILD™ and ILM™ readings are lower than the shallow readings (90-100 ohm-m) indicated by the Spherically Focused Microresistivity Tool log (MicroSFL™) and Spherically Focused Resistivity log (SFL™) measurements. Here, we would like to point out that, in this section of the chapter, the spatial distribution of the geoelectrical property of the formation of interest is expressed in terms of resistivity, $R(\mathbf{r})$ [ohm-m], in contrast to the convention of the numerical sensitivity study where we expressed the same property in terms of conductivity, $\sigma(\mathbf{r})$ [mS/m].

A nearby well, here referred to as X-1, was drilled approximately 100 m away from well X-2. This well was drilled with a light water-base mud resulting in very shallow invasion. The overbalance pressure for well X-1 was much lower than the one for well X-2. Resistivity logs acquired in well X-1 showed a normally ordered resistivity profile across the same formation as shown in Figure 8.24. On average, Array Induction Imager Tool (AIT™) readings are for the 90-inch channel 50-60 ohm-m, for the 60-inch channel 40-50 ohm-m, and for the 10-inch channel 30-35 ohm-m. Well X-1 is considered a key well in the present study due to both shallow invasion and the availability of extensive log and rock-core data. Rock-core and log measurements acquired in well X-1 are used as a benchmark in the present work. This well provides a unique reference to quantify the robustness and accuracy of the petrophysical inversions of electromagnetic-induction logging measurements to yield estimates of permeability and porosity. Moreover, the complete suite of measurements also provides a benchmark to quantify the effect of mud-filtrate invasion on the resistivity logs acquired along the same formation in well X-2.

For the purpose of parametric petrophysical inversion of electromagnetic-induction logging measurements acquired in wells X-1 and X-2, a two-dimensional cylindrical formation model is constructed with a vertical well at its center. The vertical borehole is considered to intersect a gas-bearing reservoir consisting of isotropic permeable layers. The reservoir is assumed to be buried in a shale background. In turn, upper, lower, and outer boundaries are assumed to maintain no-flow conditions. In addition to the permeable layers of the reservoir, sealing upper and lower shoulder-beds are included in the geoelectrical model as shown in Figure 8.25(a) in the form of a vertical cross-section. Resistivities of the upper and lower shoulder beds are also displayed in Figure 8.25(a). Measurements conducted on mud-filtrate samples indicated that the salinity of the mud-filtrate in wells X-2 and X-1 is approximately equal to 2,000 ppm and 340 ppm, respectively. On the other hand, downhole fluid samples taken within the formation of interest revealed that the salinity of connate water is approximately 200,000 ppm. According to the interpretation of the rock-core data and density logs, three isotropic horizontal layers of thicknesses 4.57 m, 2.44 m, and 3.66 m form the formation of interest. Prior to the inversion of electromagnetic-induction logging measurements, values of permeability and porosity for each layer were estimated from rock-core analysis. These values are also displayed in Figure 8.25(a).

As in the previous case, we assume instantaneous temperature equilibrium between the mud-filtrate and the in-situ fluids. This assumption renders the mud-filtrate invasion phenomenon an isothermal flow of two fluid phases (namely, gaseous and aqueous phases) in a permeable rock formation. For the gaseous phase, laboratory PVT measurements are used to constrain fluid properties, i.e., density, viscosity, formation volume factor, z-factor, and compressibility relationships as a function of pressure. Laboratory measurements of density, viscosity, formation volume factor, and

compressibility as a function of salt concentration are used for the aqueous phase, more specifically, mud-filtrate. Numerical values of the PVT properties of the gaseous phase at a reference pressure of 1 atm (surface conditions) along with the PVT properties of the aqueous phase are reported in Table 8.5.

Extensive rock-core data were used to constrain relative permeability and capillary pressure functions for each flow unit (layer). Within the framework of petrophysical inversion, laboratory measurements of relative permeability derived from a set of cores, sampled from each of the reservoir layers, are input to the near-borehole fluid-flow simulator. These relative permeability curves are shown in Figure 8.25(b). A high irreducible aqueous phase saturation for each layer hints toward a strong water-wet nature. Certainly, in this case, the aqueous phase is the wetting phase, and the wetting/non-wetting convention of the relative permeability plot should be interpreted accordingly. Capillary pressure data, shown in Figure 8.25(c), is derived from laboratory measurements for the drainage cycle for the above layers. Because of the lack of laboratory capillary pressure for the imbibition cycle, the available drainage-cycle data is used for the numerical simulations of the imbibition process, namely, water-base mud-filtrate invasion in a strongly water-wet medium.

The use of Archie's law in the present study is justified given the clastic behavior of the carbonate sequence under consideration. Also, the high salinity of connate water makes it unnecessary to apply corrections for the presence of clay to Archie's equation. The parameters used in Archie's saturation equation are listed in Table 8.5. Spatial distribution of the initial aqueous phase saturation within the formation of interest was derived from the conventional inversion of the array induction logging measurements acquired at well X-1. Specifically, layer-by-layer spatial distributions of deep resistivity, R_t, are derived by inverting the deep-most channel (90 in) of the induction log for a more

finely layered medium. Here, we make use of an eight-layer parametric model to describe the spatial distribution of R_t. Layer thicknesses for the assumed eight layers are determined by analyzing the depth variability of the array induction log acquired in well X-1. Initial spatial distribution of the aqueous phase saturation is derived using Archie's law in conjunction with porosity estimates derived from rock-core data. The spatial distribution of gaseous phase saturation is readily computed using a saturation identity for two-phase flow and the spatial distribution of aqueous phase saturation. In turn, the saturation domain is described with a parameterization finer than the three-layer permeability-porosity parameterization derived from core data. Within the context of the petrophysical inversion algorithm, the estimated initial spatial distribution of aqueous and gaseous phase saturations (determined for the eight-layer saturation domain) are used to describe the initial condition for the simulation of mud-filtrate invasion via a fluid-flow simulator.

Samples of mud and mud-filtrate in well X-2 provided adequate information to constrain fundamental parameters governing the process of invasion such as mudcake growth and effective flow rate across the mudcake. Flow rate of mud-filtrate across the mudcake is modeled using `UTCHEM` (Wu et al., 2001) as a function of invasion time. Mudcake parameters required by this computation are documented in Table 8.5. However, for well X-1, mudcake parameters required for the computation of the rate of mud-filtrate invasion were not available. On the other hand, for both wells X-1 and X-2, the logging record indicated that the wells of interest were logged at a time approximately equal to four days after the onset of invasion. For filtrate invasion in well X-2, both dynamic growth of mudcake thickness and dynamic decrease of mudcake permeability are coupled to formation properties. This process results in a monotonic decrease of flow rate across the borehole wall. After a short initial spurt of mud-filtrate invasion, the rate

of flow is observed to reach a steady-state value specific to a particular layer. For the purpose of computing the time-domain flow-rate response of mudcake, we made use of permeability and porosity values derived from rock-core measurements. In the present work, the layer-dependent rate of mud-filtrate invasion is assumed to be the steady-state value yielded by the simulations of invasion. Since the mudcake parameters in well X-1 were not available, the mud-filtrate invasion rate in well X-1 was derived from a conventional inversion of electrical measurements. Using Archie's law, we determined the total volume of mud-filtrate that invaded the formation in well X-1. Subsequently, since the duration of invasion is known, an average mud-filtrate invasion rate was determined for well X-1. Rates of mud-filtrate invasion for wells X-1 and X-2 are eventually imposed as a source condition for the fluid-flow module integrated to the petrophysical inversion algorithm.

Electromagnetic-induction logging measurements acquired in both wells X-1 and X-2 exhibit an increasing shaliness trend at the bottom of the formation of interest. The spatial location of this trend predominantly corresponds to the volume encompassed by the third petrophysical layer derived from rock-core analysis. Therefore, for the petrophysical inversions, the third layer suggested by the rock-core analysis was divided into two separate layers. Inversions were then conducted using four parametric layers. A better way of performing the petrophysical inversion would be to parameterize the formation of interest using many small layers, and by performing a one-dimensional inversion of permeability and porosity without assuming the layer thicknesses. However, numerical experiments performed using such a model discretization were proved computationally very costly due to the increased number of forward simulations required for the computation of the Jacobian matrix.

We first investigate the petrophysical inversion of electromagnetic-induction logging measurements acquired in well X-2. Figure 8.26 shows permeability and porosity values yielded by the inversion of electromagnetic-induction measurements acquired with the DIL™ configuration. Inversion results are shown for two different uniform initial-guess values of permeability and porosity. Inverted values are shown in conjunction with permeability and porosity values derived from rock-core analysis. We make use of uniform initial-guess values to demonstrate the robustness of the petrophysical inversion algorithm. These initial-guess values are also shown in each panel of Figure 8.26 that displays a particular inversion result. Figure 8.27 describes the quality of the post-inversion data fit achieved by the inversions of DIL™ measurements. In this plot, we display the simulated data with respect to the actual filed measurements for the final iteration of the inversion algorithm. Subsequent to the quantitative estimation of permeability and porosity, we performed a simulation of the spatial distributions of near-borehole fluid saturations and salt concentration. A conductivity image was computed from the simulated profiles of aqueous phase saturation and salt concentration via Archie's equations. In addition to estimating permeability and porosity values from electromagnetic-induction measurements, the petrophysical inversion algorithm can also be used to estimate the spatial distribution of near-borehole conductivity around well X-2 as shown in Figure 8.28(a). In this figure, the cross-section of electrical conductivity is displayed in logarithmic scale, i.e., $\log_{10}[\sigma(\mathbf{r})]$. Post-inversion reconstructions of the near-borehole spatial distributions of gaseous phase saturation and salt concentrations are shown in Figures 8.28(a) and 8.28(b), respectively.

Figure 8.29 shows permeability and porosity values simultaneously estimated via inversions of electromagnetic-induction measurements acquired with the AIT™ configuration in well X-1. Inverted permeability and porosity values are shown for two

inversion examples where we make use of a three-layer and a four-layer parameterization of the formation of interest. Inverted values are shown in conjunction with permeability and porosity values yielded by rock-core analysis. In this case, we initialize the inversion with uniform permeability and porosity values. These initial-guess values are also shown in each panel of Figure 8.29 that displays a particular inversion outcome. Array induction imaging measurements acquired in well X-1 are shown together for each measurement-array (or channel) in Figure 8.30(a). In the remaining panels of Figure 8.30, the quality of the post-inversion data fit achieved by the inversions of AIT™ measurements is displayed independently for each measurement array. Data-domain fit is shown for the case of the four-layer permeable medium. Upon successful termination of the quantitative estimation of permeability and porosity, a simulation of the spatial distributions of near-borehole saturation and salt concentration was performed using the inverted permeability and porosity values. In turn, a conductivity image was obtained from the simulated spatial distributions of aqueous phase saturation and salt concentration using Archie's law. Post-inversion reconstruction of the spatial distribution of near-borehole conductivity around the borehole of well X-1 is shown in Figure 8.31(a). Post-inversion reconstructions of the near-borehole spatial distributions of gaseous phase saturation and salt concentration are shown in Figures 8.31(b) and 8.31(c), respectively. In a following inversion study, porosity values are fixed and equal to porosity values obtained from rock-core laboratory analysis. Field measurements are inverted to yield near-borehole permeability values only. Figure 8.32 shows permeability values yielded by the inversions of single-time electromagnetic-induction logging measurements acquired by the array induction imager configuration in well X-1. Two different initial-guess values of permeability are used for both data sets as shown in Figures 8.32(a) and 8.32(b).

In general, permeability values inverted from AIT™ measurements (acquired in well X-1) are more consistent with the permeability values measured from rock-core data in comparison to the permeability values inverted from DIL™ measurements (acquired in well X-2). This result is consistent with the results obtained from the numerical experiments where we analyzed inversions of synthetic measurements. We observed that the primary information about permeability is embedded within the acquired measurements that exhibit multiple radial lengths of investigation. Clearly, a five-array induction imaging tool configuration (AIT™) is more sensitive to the radial conductivity variations compared to a tool with only two arrays (DIL™). At a given depth, radial variations of conductivity are a complex nonlinear function of the corresponding radial variations of phase saturation and salt concentration. Because of this, radial variations of electrical conductivity are predominantly governed by the permeability of the formation. Therefore, as long as the radial conductivity variations occur within the depth of investigation of the electromagnetic-induction logging tool, and these variations are captured by multiple measurement-arrays, there exists sufficient sensitivity in the electromagnetic-induction measurements for a robust and accurate inversion of permeability (as in the case of well X-1). Fewer measurement arrays in conjunction with deep invasion produce less robust and more inaccurate inversions of permeability (as in the case of well X-2).

Porosity values inverted from both AIT™ and DIL™ measurements, on the other hand, agree well with the corresponding values measured from rock-core samples. Inversion results indicate that for the cases where laboratory measurements of saturation-dependent functions, namely, relative permeability and capillary pressures are available, and the parameters governing the saturation equation (Archie's law) are reliable, electromagnetic-induction logging measurements yield robust and accurate values of

formation porosity. Extensive inversion exercises indicated that knowledge of the spatial distribution of initial fluid saturations also plays a significant role in obtaining consistent porosity values.

The near-borehole conductivity image derived for well X-2 suggests a substantial length of mud-filtrate invasion. This result is consistent with the use of heavy mud and the qualitative interpretation of the dual induction log discussed above. The radius of invasion in the upper section of the formation is in the order of 1 m to 1.5 m. However, in the lower section of the formation, the radius of invasion decreases to approximately 0.5 m to 1.0 m. On the other hand, the near-borehole conductivity image derived for well X-1 suggests a relatively short length of mud-filtrate invasion. This result is consistent with the use of light mud and the qualitative interpretation of the array induction log discussed above. The radius of invasion in the upper section of the formation is of the order of 0.35 m to 0.45 m. However, in the lower section of the formation, the radius of invasion decreases to less than 0.1 m. Conductivity images around wells X-1 and X-2 also indicate the presence of a high-conductivity (low-resistivity) annulus in the transition region between the flushed and virgin zones.

8.5 SUMMARY AND CONCLUDING REMARKS

The synthetic and field data examples described in this chapter indicate that array induction measurements can be used to estimate the permeability and porosity of layered rock formations. This estimation is possible because of the physical link that exists between the physics of mud-filtrate invasion and the physics of electromagnetic logging measurements. During the process of mud-filtrate invasion, permeability and porosity play a dominant role in the time evolution of the spatial distributions of aqueous phase saturation and salt concentration in the near-borehole region. In this work, the link between porosity, saturation, and electrical conductivity is enforced through Archie's

law, whereas the link between permeability and electrical resistivity is enforced through both Archie's law and the time evolution of the process of mud-filtrate invasion.

Measurable sensitivity to permeability exists in borehole electromagnetic measurements that exhibit a selective deepening of the radial zone of response. The time evolution of the process of mud-filtrate invasion causes significant vertical and radial variations of aqueous phase saturation and salt concentration in the near-borehole region which can only be detected with array induction tools that exhibit multiple lengths of investigation. It is also shown that array induction measurements in general exhibit a measurable sensitivity to porosity regardless of the specific petrophysical conditions that govern the process of mud-filtrate invasion. We find that the estimation of permeability is much more sensitive to noisy electromagnetic measurements than the estimation of porosity.

The accurate estimation of permeability is largely controlled by a-priori information such as mud properties, time of invasion, relative permeability, capillary pressure, fluid viscosity, and initial aqueous phase saturation, among others. Inversion exercises considered in this chapter indicate that a-priori knowledge about pressure-volume-temperature dependent properties of the fluids play a secondary role in the accuracy of the estimated values of permeability and porosity. Another conclusion is the relative insensitivity of the inversion to acceptable ranges of uncertainty in mud-filtrate invasion parameters such as time of invasion and rate of invasion.

The petrophysical inversion algorithm described in this work can also be used to estimate spatial distributions of electrical conductivity. Cross-sections of electrical conductivity are a by-product of the inversion of permeability and porosity. However, as opposed to standard algorithms for the inversion of borehole electromagnetic measurements, the estimated spatial distributions of electrical conductivity described in

this work are consistent with the processes of salt mixing and fluid transport, and abide by the law of mass conservation. Given the inherent non-uniqueness of inversion, the enforcement of petrophysical conditions on the inversion provides a natural way to reduce uncertainty in the presence of noisy and inadequate borehole electromagnetic-induction measurements.

Table 8.1: Summary of geometrical, petrophysical, mudcake, fluid, and sensor parameters for the reservoir model used in the inversion-based sensitivity study.

Variable	Unit	Value
Mudcake permeability	[mD]	0.010
Mudcake porosity	[fraction]	0.400
Mud solid fraction	[fraction]	0.500
Mudcake maximum thickness	[cm]	1.270
Formation rock compressibility	[kPa^{-1}]	7.252×10^{-10}
Aqueous phase viscosity (mud-filtrate)	[Pa.s]	1.274×10^{-3}
Aqueous phase density (mud-filtrate)	[g/cm^3]	1.001
Aqueous phase formation volume factor (mud-filtrate)	[res. m^3/std. m^3]	0.996
Aqueous phase compressibility (mud-filtrate)	[kPa^{-1}]	3.698×10^{-7}
Oleic phase viscosity	[Pa.s]	3.550×10^{-4}
Oleic phase API density	[ºAPI]	42
Oleic phase density	[g/cm^3]	0.816
Oleic phase formation volume factor	[res. m^3/std. m^3]	1.471
Oleic phase compressibility	[kPa^{-1}]	2.762×10^{-6}
Viscosity ratio (water-to-oil)	[dimensionless]	3.589
Formation pressure at the formation top (at the reference depth = 0 m)	[MPa]	20.684
Mud hydrostatic pressure	[MPa]	24.821
Wellbore radius	[m]	0.108
Formation outer boundary location	[m]	300.000
Formation temperature	[ºC]	104.444
a-constant in the Archie's equation	[dimensionless]	1.000
m-cementation exponent in the Archie's equation	[dimensionless]	2.000
n-aqueous phase saturation exponent in the Archie's equation	[dimensionless]	2.000
Mud conductivity	[mS/m]	2631.579
Upper and lower shoulder bed conductivities	[mS/m]	1000.000
Logging interval used for inversion	[m]	6.096×10^{-1}

Table 8.2: Parameters of the Archie's equation used for the inversion-based perturbation sensitivity study. Note that the parameters of the Archie's equation are dimensionless.

Variable	Actual values	Perturbed set 1	Perturbed set 2	Perturbed set 3
a	1.00	1.00	1.00	1.00
m	2.00	2.10	2.20	2.20
n	2.00	1.90	1.80	2.20

Table 8.3: Oleic phase viscosity and compressibility values used for the inversion-based perturbation sensitivity study.

Variable	Actual values	Perturbed set 1	Perturbed set 2	Perturbed set 3
Compressibility, [kPa^{-1}]	2.762×10^{-6}	2.762×10^{-8}	2.762×10^{-4}	2.762×10^{-8}
Viscosity, [Pa.s]	3.550×10^{-4}	4.000×10^{-3}	1.000×10^{-4}	1.000×10^{-2}

Table 8.4: Layer-by-layer modified Brooks-Corey relative permeability and capillary pressure model parameters used for the inversion-based perturbation sensitivity study. Note that the parameters S_{wirr}, S_{or}, k^o_{rw}, and k^o_{ro} are reported in fractions. The parameters e_w, e_o, and α are dimensionless.

Layer 1	S_{wirr}	S_{or}	k^o_{rw}	k^o_{ro}	e_w	e_o	P_{ce} [kPa]	α
Actual	**0.350**	**0.150**	**0.150**	**0.600**	**2.750**	**2.500**	**20.684**	**3.000**
Set 1	0.300	0.100	0.100	0.700	2.000	2.000	6.895	1.500
Set 2	0.300	0.100	0.100	0.700	2.750	2.500	20.684	3.000
Set 3	0.400	0.100	0.200	0.550	2.750	2.500	20.684	3.000
Set 4	0.300	0.200	0.100	0.650	2.750	2.500	20.684	3.000
Set 5	0.350	0.150	0.150	0.600	2.750	2.500	10.342	2.500
Layer 2	S_{wirr}	S_{or}	k^o_{rw}	k^o_{ro}	e_w	e_o	P_{ce} [kPa]	α
Actual	**0.275**	**0.200**	**0.200**	**0.550**	**2.250**	**2.000**	**6.895**	**2.000**
Set 1	0.225	0.250	0.250	0.600	2.000	1.850	13.790	1.000
Set 2	0.225	0.250	0.250	0.600	2.250	2.000	6.895	2.000
Set 3	0.325	0.150	0.250	0.500	2.250	2.000	6.895	2.000
Set 4	0.225	0.250	0.150	0.600	2.250	2.000	6.895	2.000
Set 5	0.275	0.200	0.200	0.550	2.250	2.000	13.790	1.500
Layer 3	S_{wirr}	S_{or}	k^o_{rw}	k^o_{ro}	e_w	e_o	P_{ce} [kPa]	α
Actual	**0.450**	**0.100**	**0.100**	**0.750**	**1.750**	**2.750**	**34.474**	**3.500**
Set 1	0.350	0.150	0.150	0.800	1.500	2.500	27.579	2.500
Set 2	0.350	0.150	0.150	0.800	1.750	2.750	34.474	3.500
Set 3	0.500	0.050	0.150	0.700	1.750	2.750	34.474	3.500
Set 4	0.400	0.150	0.050	0.800	1.750	2.750	34.474	3.500
Set 5	0.450	0.100	0.100	0.750	1.750	2.750	17.237	4.000

Table 8.5: Summary of geometrical, petrophysical, mudcake, fluid, and sensor parameters for the reservoir model used in the inversions of field electromagnetic-induction measurements.

Variable	**Unit**	**Value**
Mudcake permeability (Well X-2)	[mD]	0.030
Mudcake porosity (Well X-2)	[fraction]	0.600
Mud solid fraction (Well X-2)	[fraction]	0.200
Mudcake maximum thickness (Well X-2)	[cm]	0.254
Formation rock compressibility	[kPa^{-1}]	7.252×10^{-10}
Aqueous phase viscosity (mud-filtrate)	[Pa.s]	1.000×10^{-3}
Aqueous phase density (mud-filtrate)	[g/cm^3]	1.186
Aqueous phase formation volume factor (mud-filtrate)	[res. m^3/std. m^3]	1.000
Aqueous phase compressibility (mud-filtrate)	[kPa^{-1}]	1.450×10^{-7}
Gaseous phase reference viscosity [f(p) for T=*const.*]	[Pa.s]	1.087×10^{-5} @ 1.0 atm
Gaseous phase reference density [f(p) for T=*const.*]	[g/cm^3]	9.781×10^{-4} @ 1.0 atm
Formation pressure at the formation top (at the reference depth = 0 m)	[MPa]	0.662
Mud hydrostatic pressure (Well X-2)	[MPa]	7.950
Wellbore radius	[m]	0.100
Formation outer boundary location	[m]	300.000
Formation temperature	[ºC]	35.556
a-constant in the Archie's equation	[dimensionless]	1.000
m-cementation exponent in the Archie's equation	[dimensionless]	2.000
n-aqueous phase saturation exponent in the Archie's equation	[dimensionless]	2.000
Mud conductivity	[mS/m]	387.600
Upper shoulder bed conductivity (Well X-1)	[mS/m]	200.000
Lower shoulder bed conductivity (Well X-1)	[mS/m]	327.900
Upper shoulder bed conductivity (Well X-2)	[mS/m]	200.000
Lower shoulder bed conductivity (Well X-2)	[mS/m]	400.000
Logging interval	[m]	7.620×10^{-2}

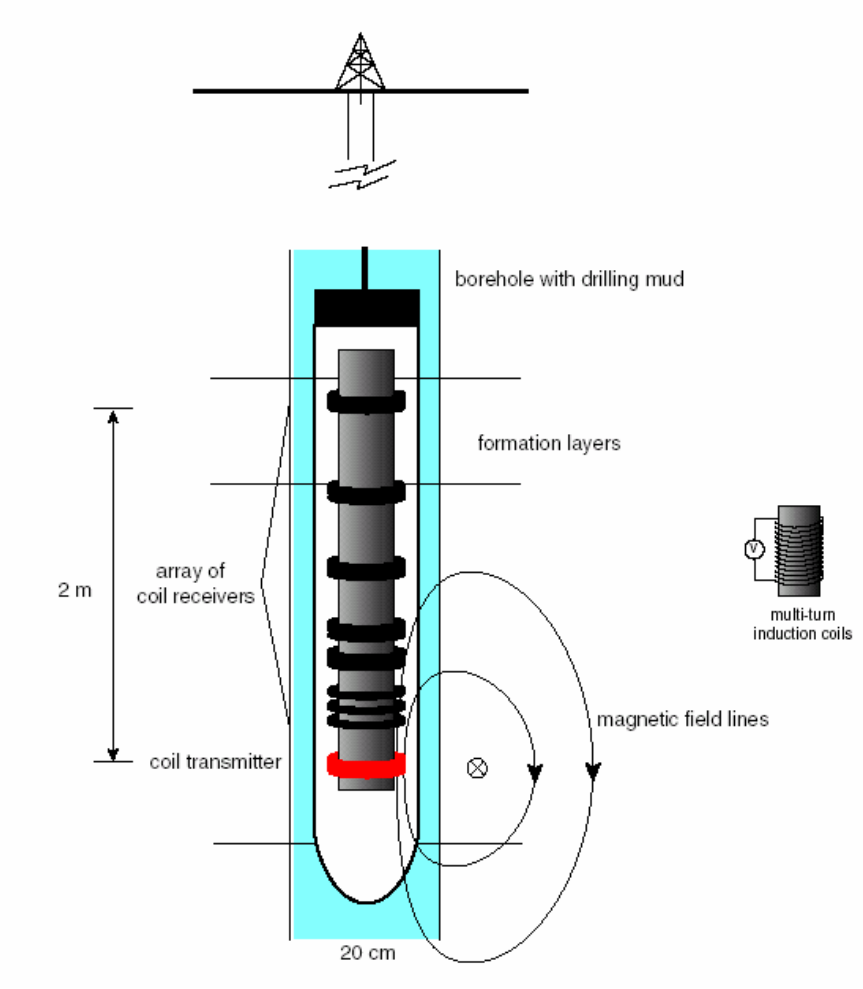

Figure 8.1: Simplified schematic description of the array induction imager tool measurement principle (Blok and Oristaglio, 1995): A multi-turn coil supporting a time-varying current generates a magnetic field that induces electrical currents in the formation. An array of receiver coils measures the magnetic field of the source and the secondary currents.

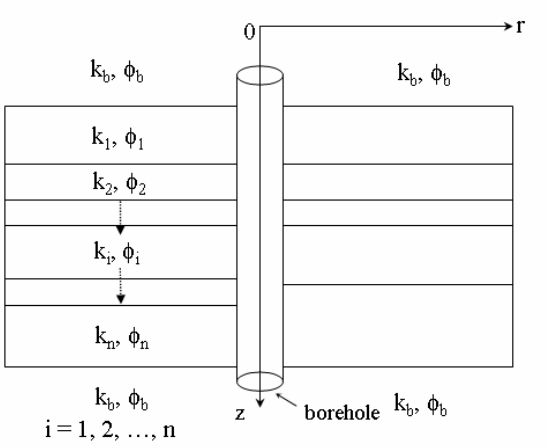

Figure 8.2: Parameterization of the model domain in terms of horizontal geological layers. Model parameters are layer-by-layer permeabilities and porosities denoted by k and ϕ, respectively.

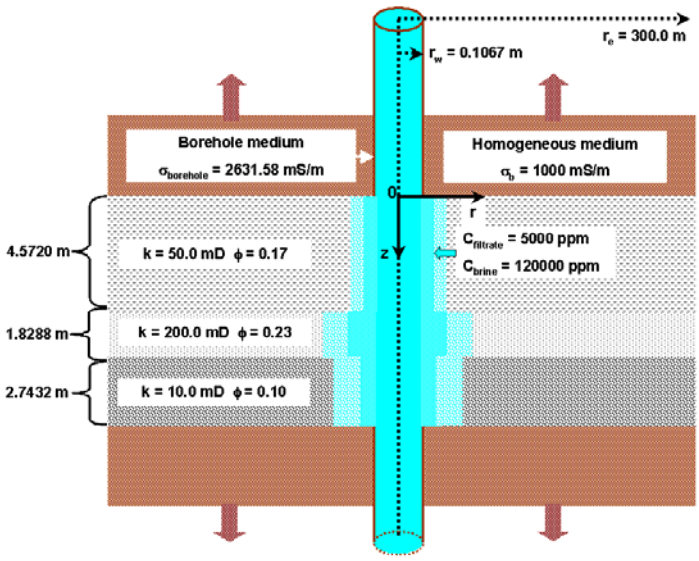

Figure 8.3: Formation model for the inversion-based sensitivity study. Two-dimensional vertical cross-section of the permeable formation intersected by a vertical borehole. The three-layer formation is subject to water-base mud-filtrate invasion.

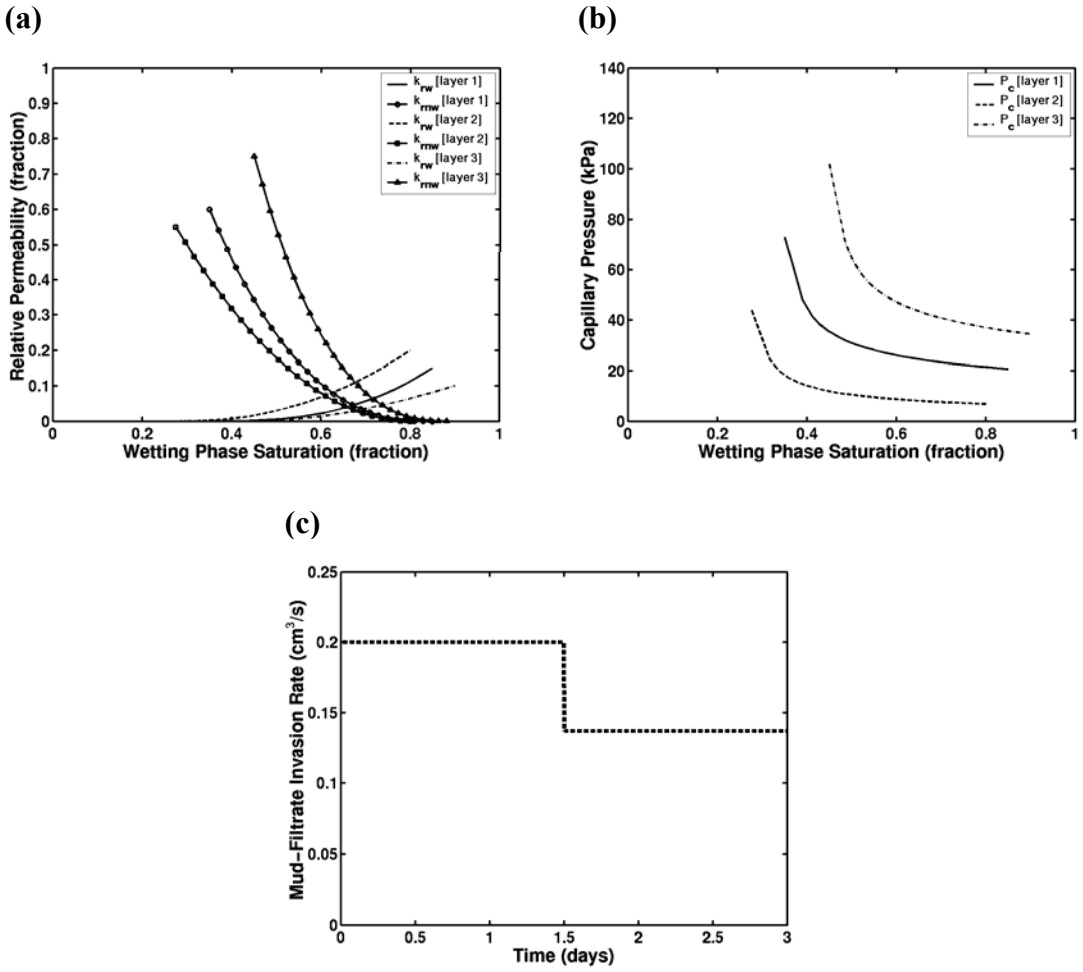

Figure 8.4: Layer-by-layer (a) relative permeability and (b) capillary pressure functions used in fluid-flow simulations for the formation model of the inversion-based sensitivity study. Relative permeability and capillary pressure functions for each layer are generated using the modified Brooks-Corey model. The parameters used in generating these saturation-dependent functions are listed in Table 8.4; actual model section. (c) Time-average of the mud-filtrate invasion rate for pre- and post-removal of mudcake.

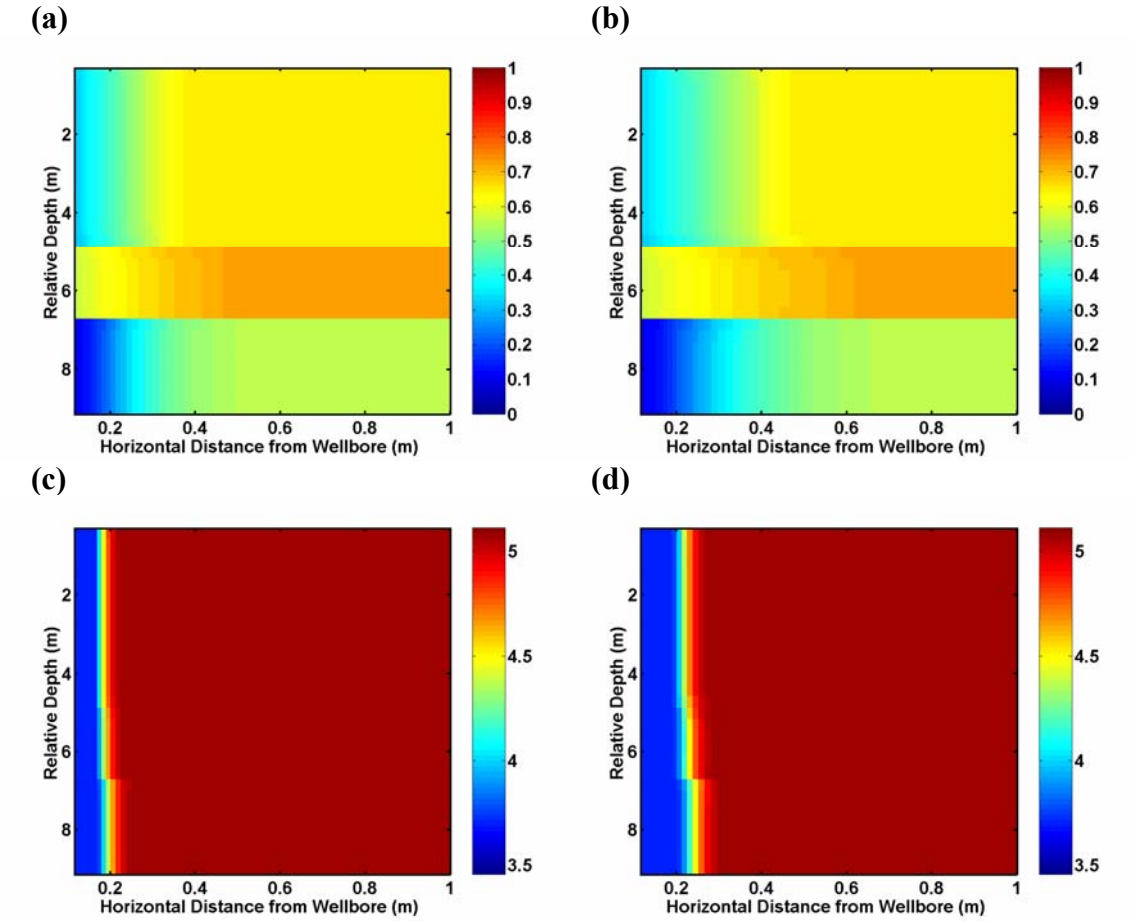

Figure 8.5: Spatial distribution of axisymmetric near-borehole oleic phase saturation at various instances after the onset of mud-filtrate invasion: (a) 1.5th day and (b) 3rd day. In these panels, the spatial distribution of oleic phase saturation $\{S_o(\mathbf{r}) = 1.0 - S_w(\mathbf{r})\}$ is reported in the unit of pore volume fractions. Similarly, the spatial distribution of axisymmetric near-borehole salt concentration at 1.5th and 3rd day of mud-filtrate invasion are shown in panels (c) and (d), respectively. In these plots, the spatial distribution of salt concentration is reported in the unit of part per million [ppm] using a logarithmic scale.

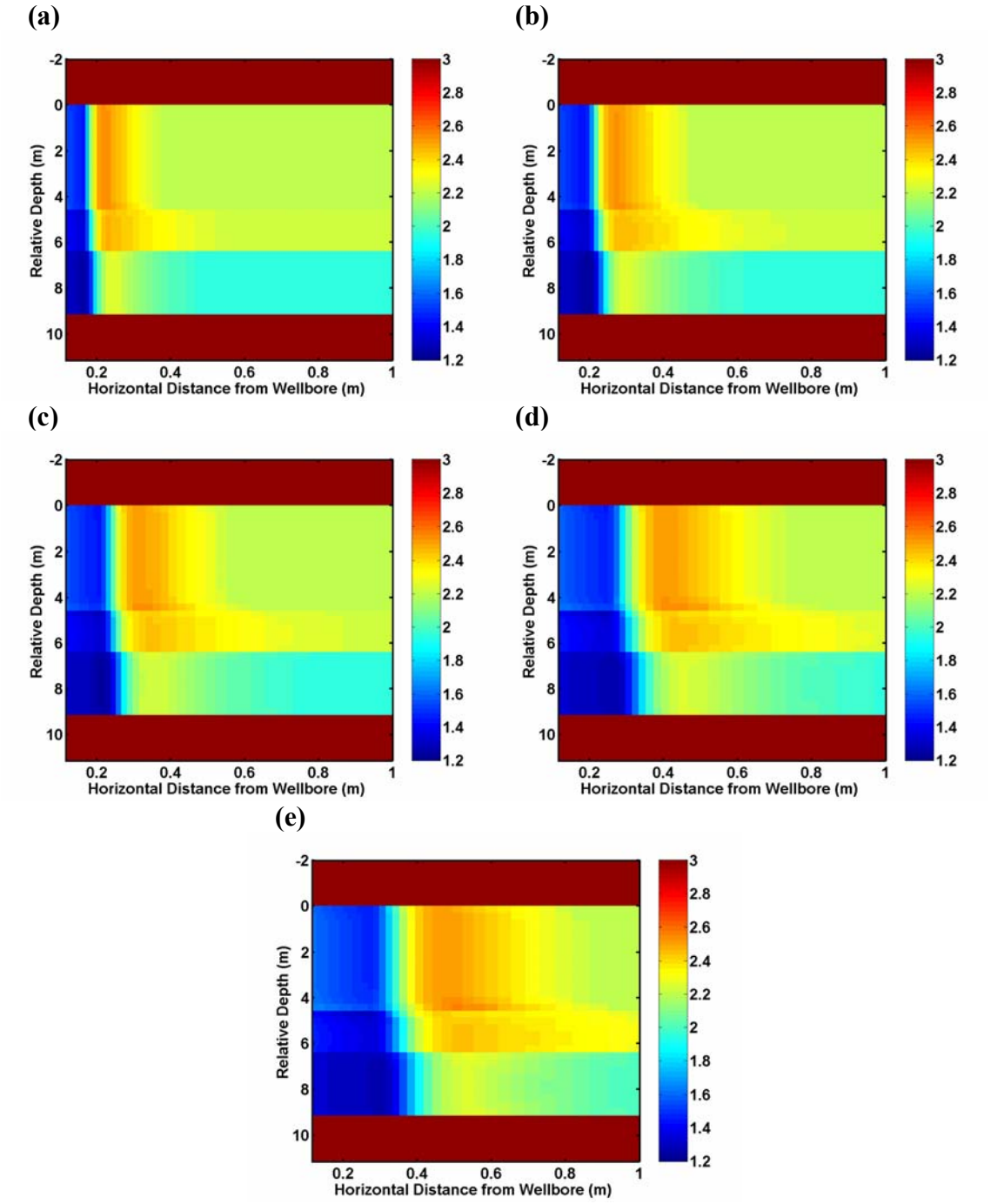

Figure 8.6: Spatial distribution of axisymmetric near-borehole conductivity at various instances of mud-filtrate invasion: (a) 1.5th day, (b) 3rd day, (c) 4.5th day, (d) 8.5th day, and (e) 12th day. Conductivity domain is shown in logarithmic scale, i.e., $\log_{10}[\sigma(\mathbf{r})]$.

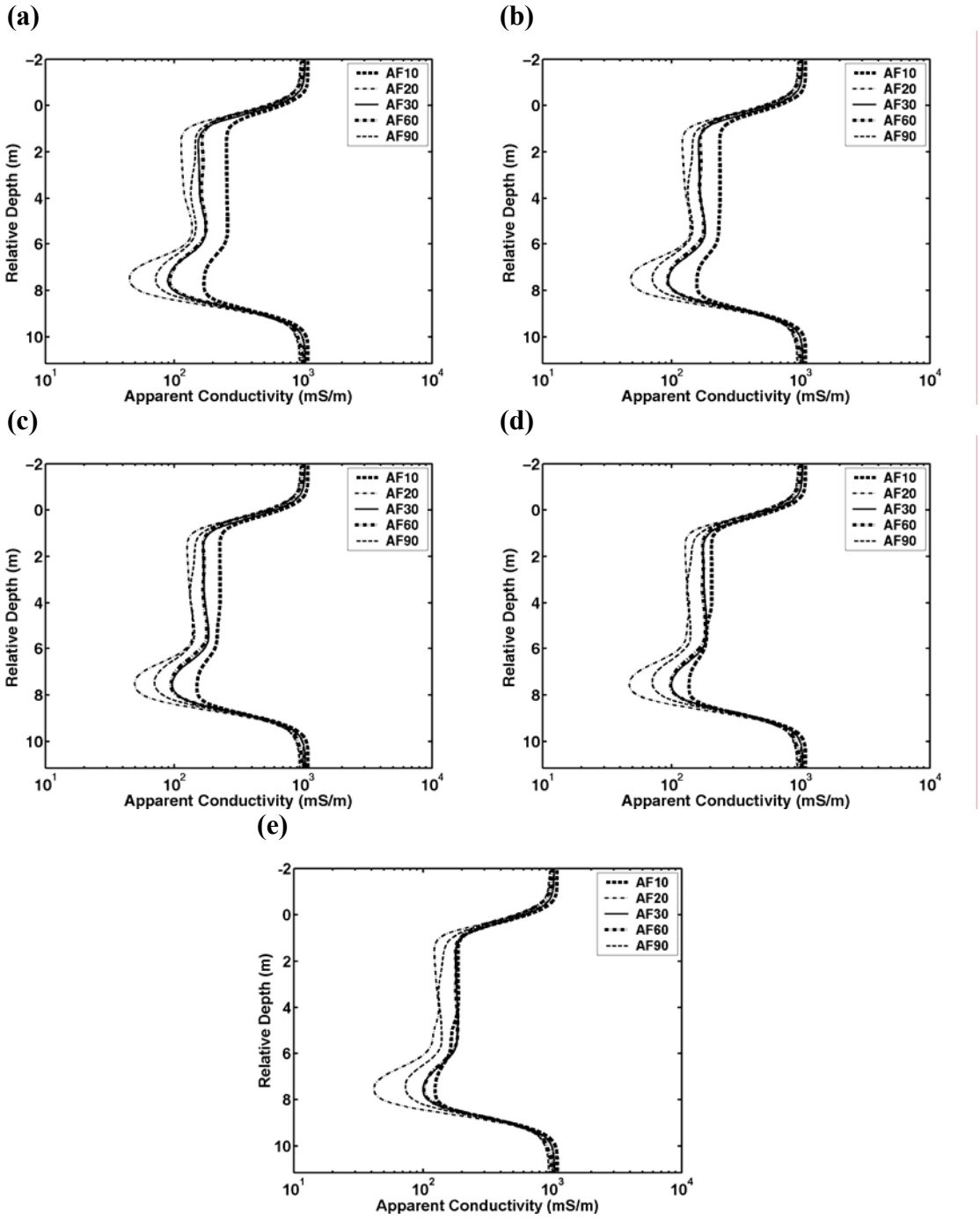

Figure 8.7: Electromagnetic-induction measurements simulated for logging times that correspond to (a) 1.5th, (b) 3rd, (c) 4.5th, (d) 8.5th, and (e) 12th day of mud-filtrate invasion.

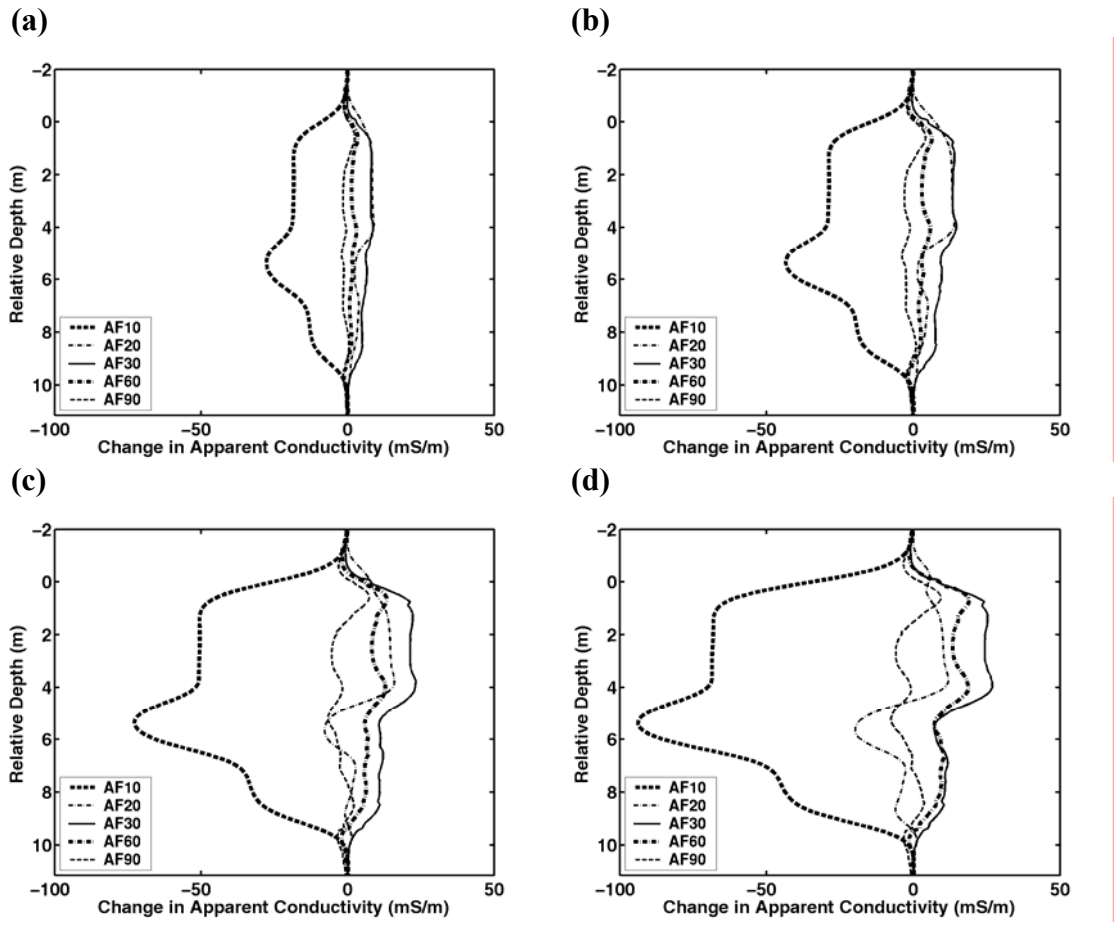

Figure 8.8: Change in the electromagnetic-induction log response from $t_{\log 1}$ to $t_{\log 2}$, i.e., $\Delta\sigma_{\text{app.}} = \sigma_{\text{app. t log 2}} - \sigma_{\text{app. t log 1}}$, where $t_{\log 1} = 1.5$ day and (a) $t_{\log 2} = 3$, (b) 4.5, (c) 8.5, and (d) 12 day, respectively.

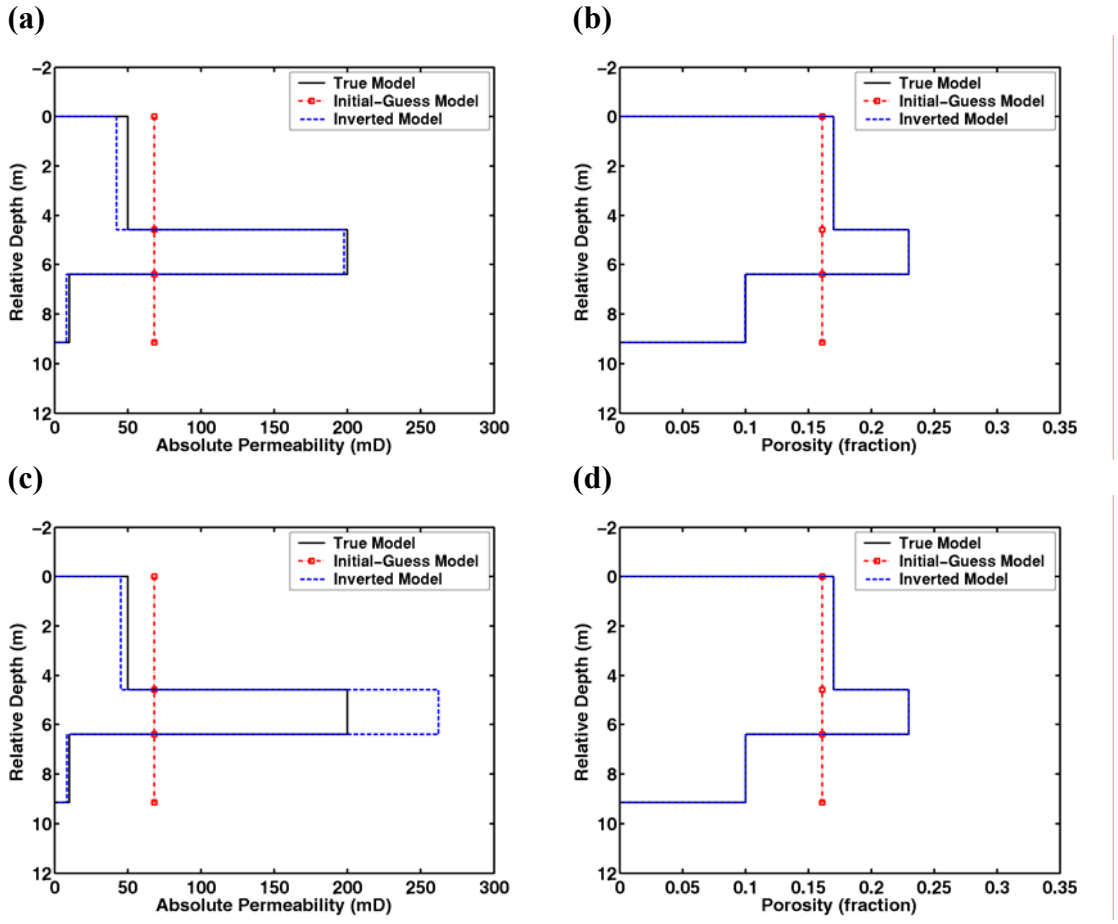

Figure 8.9: Permeability and porosity values yielded by the inversions of single-time electromagnetic-induction logging measurements acquired by the array induction imager configuration subsequent to a 1.5 day-long mud-filtrate invasion period. Inversion results are shown for the cases where measurements are contaminated with 1% and 3% Gaussian, random noise in panels {(a), (b)}, and {(c), (d)}, respectively.

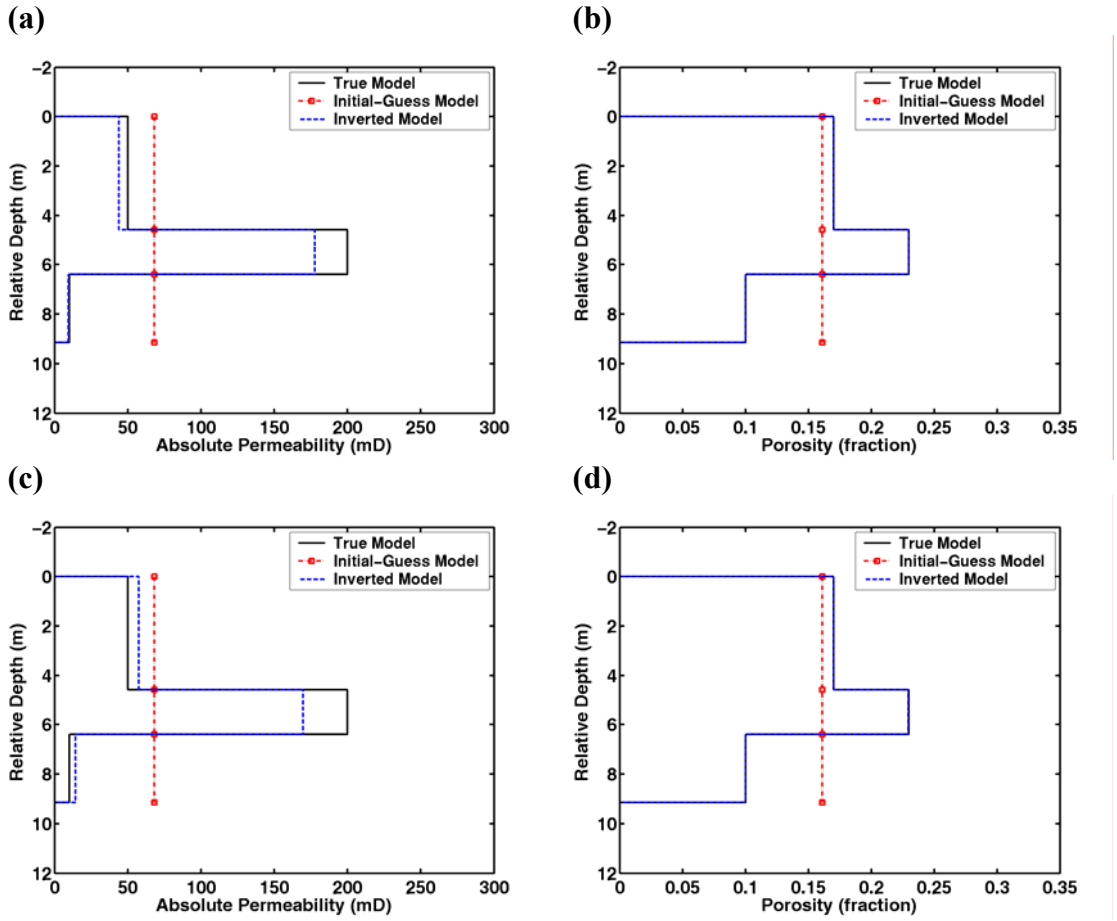

Figure 8.10: Permeability and porosity values yielded by the inversions of time-lapse electromagnetic-induction logging measurements acquired by the array induction imager configuration. Electromagnetic-induction measurements are acquired at the 1.5th and 3rd day of the mud-filtrate invasion timeline. Inversion results are shown for the cases where measurements are contaminated with 1% and 3% Gaussian, random noise in panels {(a), (b)}, and {(c), (d)}, respectively.

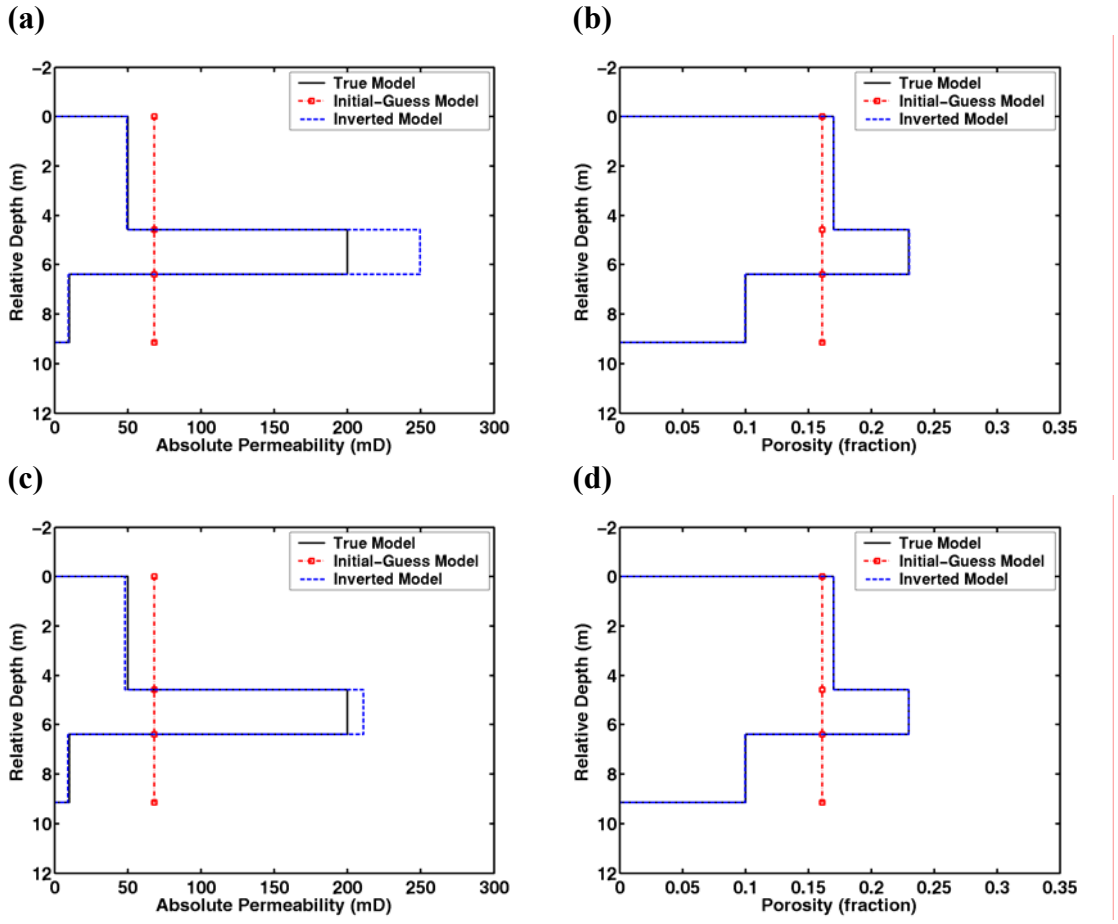

Figure 8.11: Permeability and porosity values yielded by the inversions of single-time electromagnetic-induction logging measurements acquired by the array induction imager configuration subsequent to a {(a), (b)} 4.5 days-long and {(c), (d)} 12 days-long mud-filtrate invasion period. Inversion results are shown for the cases where measurements are contaminated with 3% Gaussian, random noise.

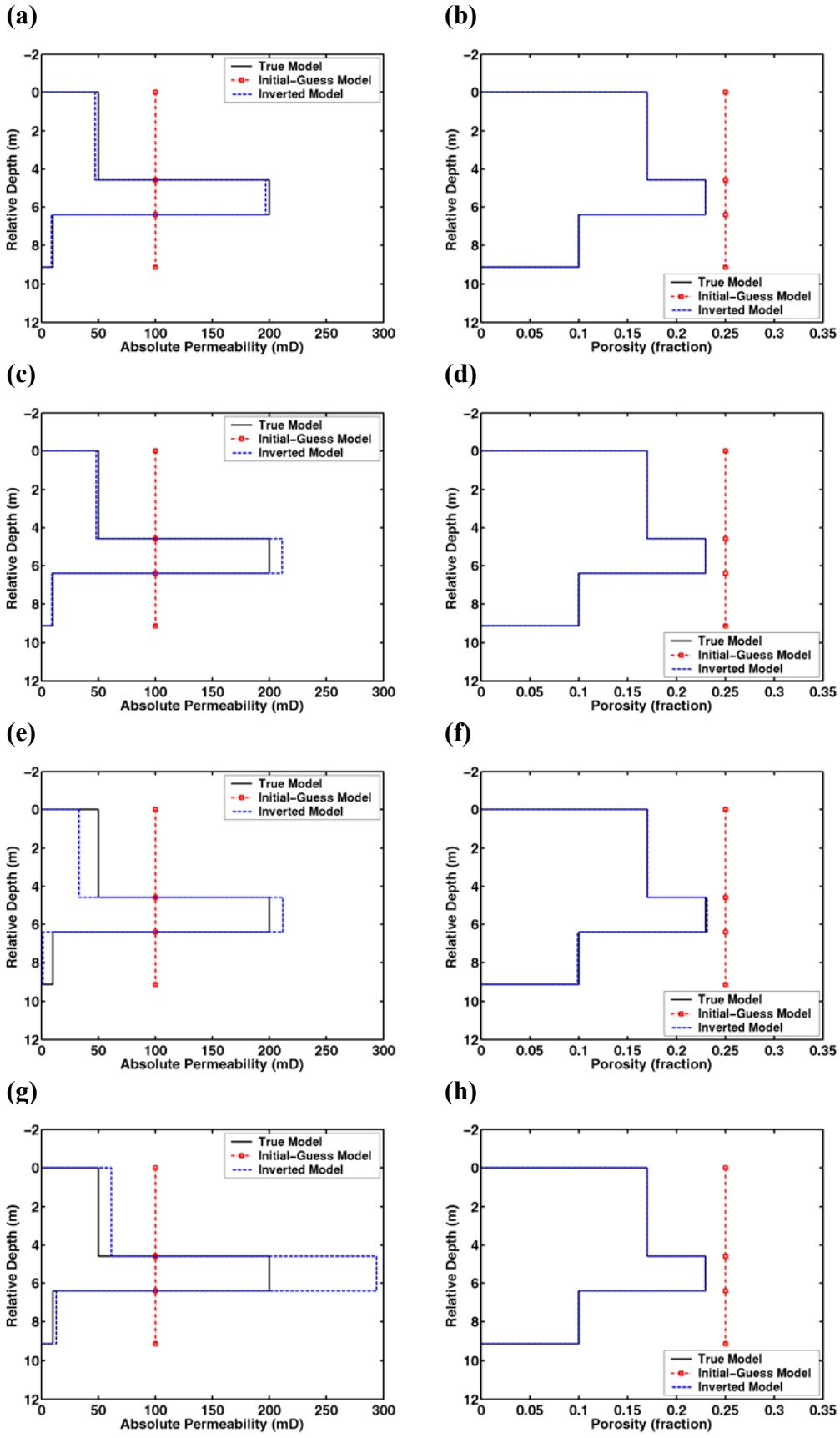
(a)
(b)
(c)
(d)
(e)
(f)
(g)
(h)
True Model
Initial-Guess Model
Inverted Model
Relative Depth (m)
Absolute Permeability (mD)
Porosity (fraction)

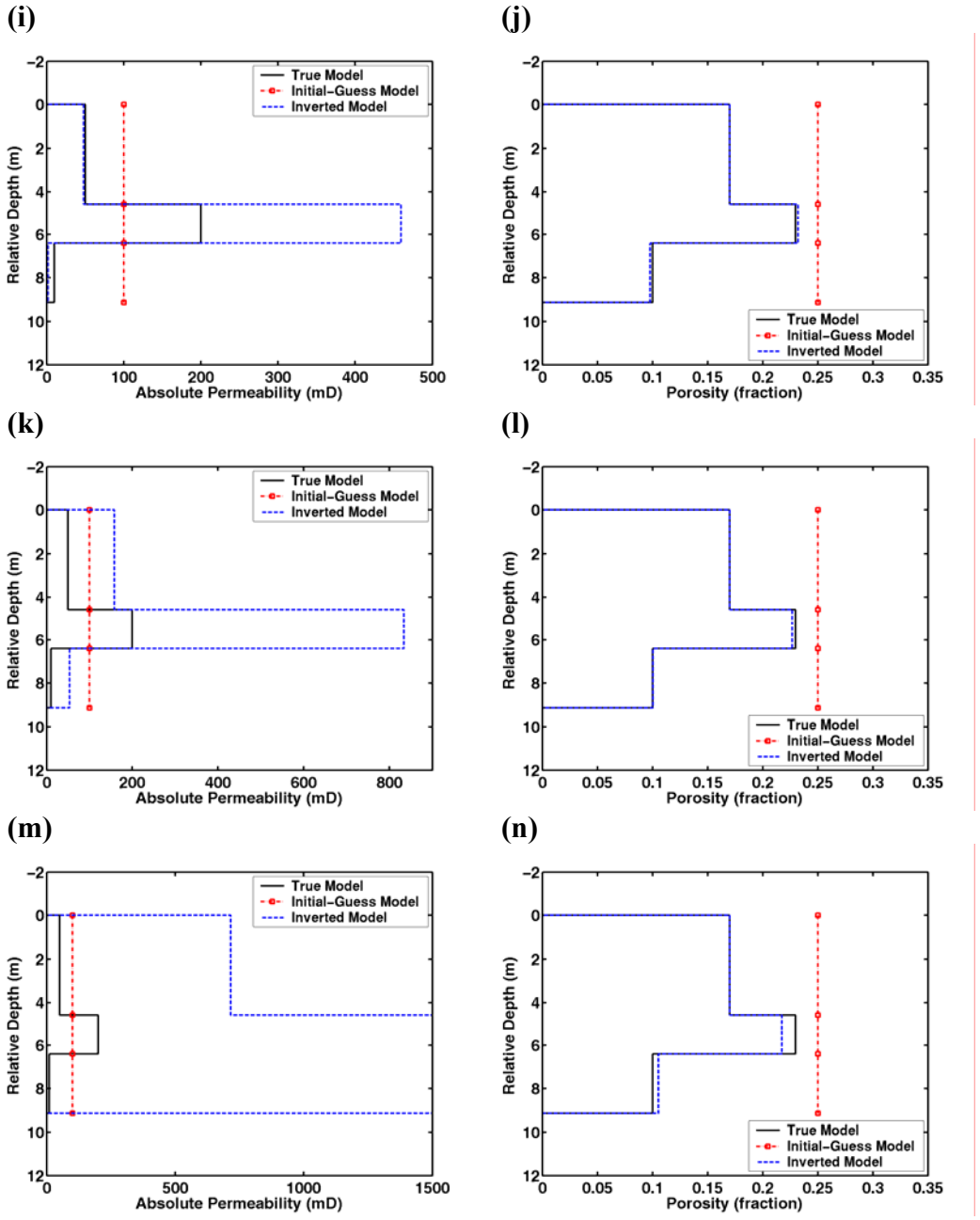

Figure 8.12: Permeability and porosity values yielded by the inversions of single-time electromagnetic-induction logging measurements acquired by the array induction imager configuration subsequent to a 12 days-long mud-filtrate invasion period. Inversion results are shown for the cases where measurements are contaminated with 1%, 3%, 5%, 8%, 12%, 15%, and 21% Gaussian, random noise in panels {(a), (b)}, {(c), (d)}, {(e), (f)}, {(g), (h)}, {(i), (j)}, {(k), (l)}, and {(m), (n)} respectively. In this example, initial-guess values are chosen to be further away from the volumetric mean values of permeability and porosity.

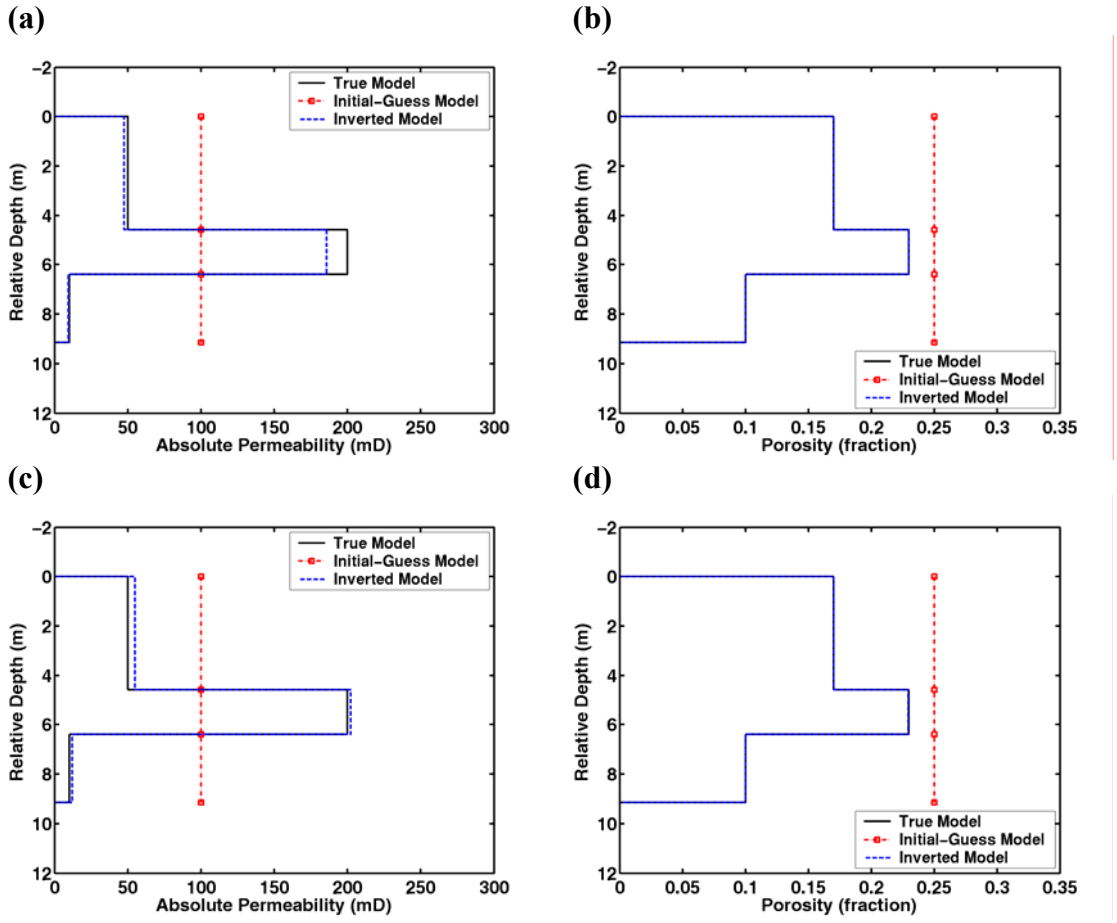

Figure 8.13: Permeability and porosity values yielded by the inversions of time-lapse electromagnetic-induction logging measurements acquired by the array induction imager configuration. Electromagnetic-induction measurements are acquired at the 1.5^{th} and 12^{th} day of the mud-filtrate invasion timeline. Inversion results are shown for the cases where measurements are contaminated with 1% and 3% Gaussian, random noise in panels {(a), (b)}, and {(c), (d)}, respectively. In this example, initial-guess values are chosen to be further away from the volumetric mean values of permeability and porosity.

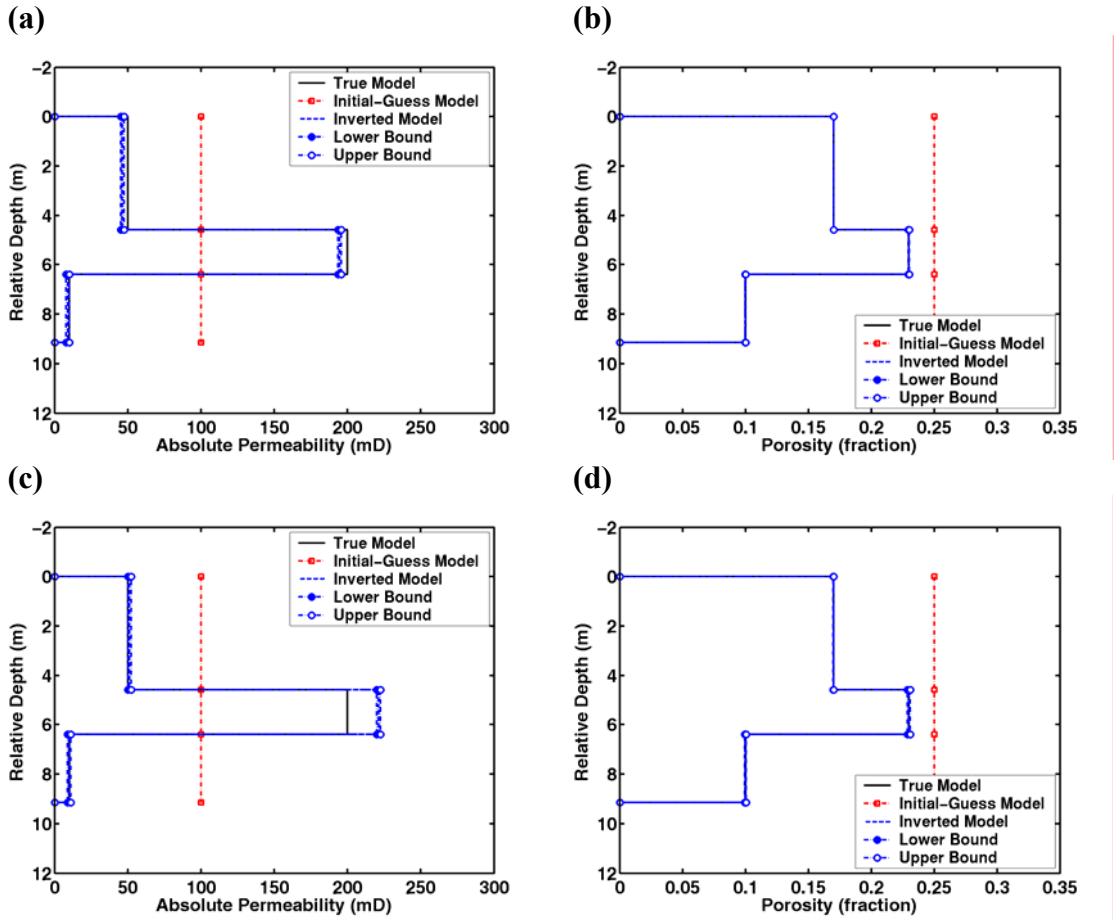

Figure 8.14: Permeability and porosity values yielded by the inversions of single-time electromagnetic-induction logging measurements acquired by the array induction imager configuration subsequent to a 12 days-long mud-filtrate invasion period. In this example, the numerical grid used for inversion is identical to the one used in generating the synthetic measurements. Inversion results are shown for the cases where measurements are contaminated with 1% and 3% Gaussian, random noise in panels {(a), (b)}, and {(c), (d)}, respectively. The computed Cramer-Rao upper and lower bounds for the inversion results are also shown for each case.

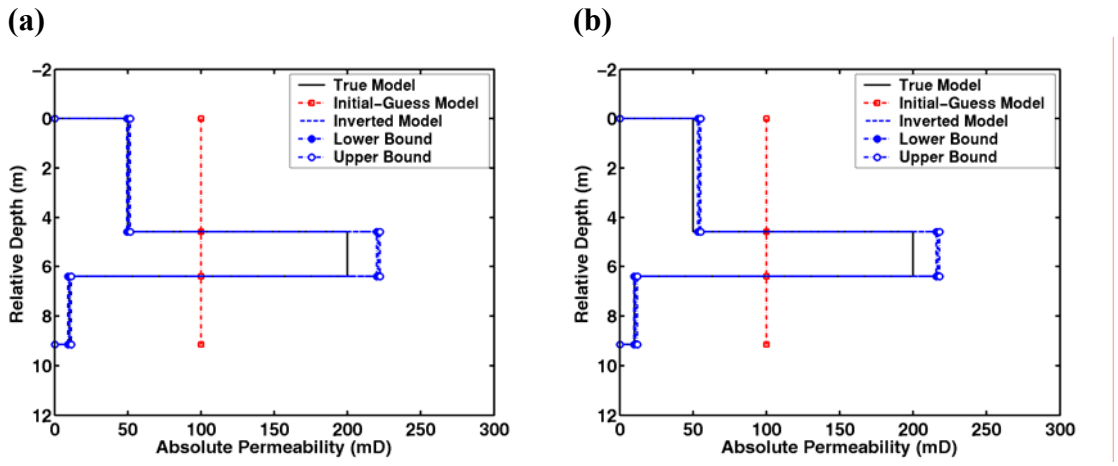

Figure 8.15: Permeability values yielded by the inversions of single-time electromagnetic-induction logging measurements acquired by the array induction imager configuration subsequent to a 12 days-long mud-filtrate invasion period. In this example, the numerical grid used for inversion is identical to the one used in generating the synthetic measurements. Inversion results are shown for the cases where measurements are contaminated with 1% and 3% Gaussian, random noise in panels (a) and (b), respectively. The computed Cramer-Rao upper and lower bounds for the inversion results are also shown for each case.

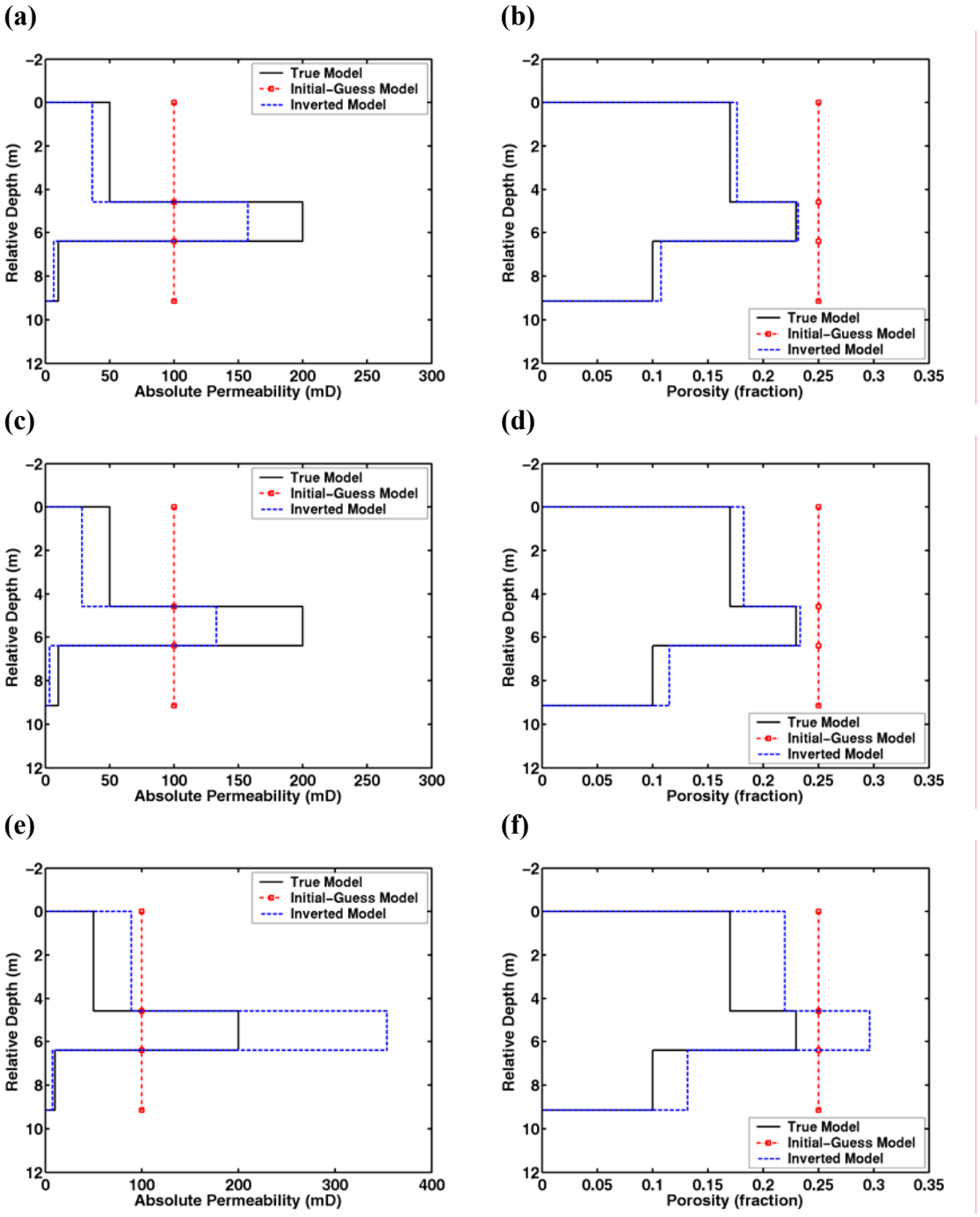

Figure 8.16: Sensitivity of inversion results to the perturbations in Archie parameters *m* and *n*. Panels (a) and (b) show inversion results for permeability and porosity values, respectively, for the perturbed parameter set 1 shown in Table 8.2. Similarly, panels (c) and (d) show inversion results for permeability and porosity values, respectively, for the perturbed parameter set 2 listed in Table 8.2. Finally, panels (e) and (f) show inversion results for permeability and porosity values, respectively, for the perturbed parameter set 3 listed in Table 8.2.

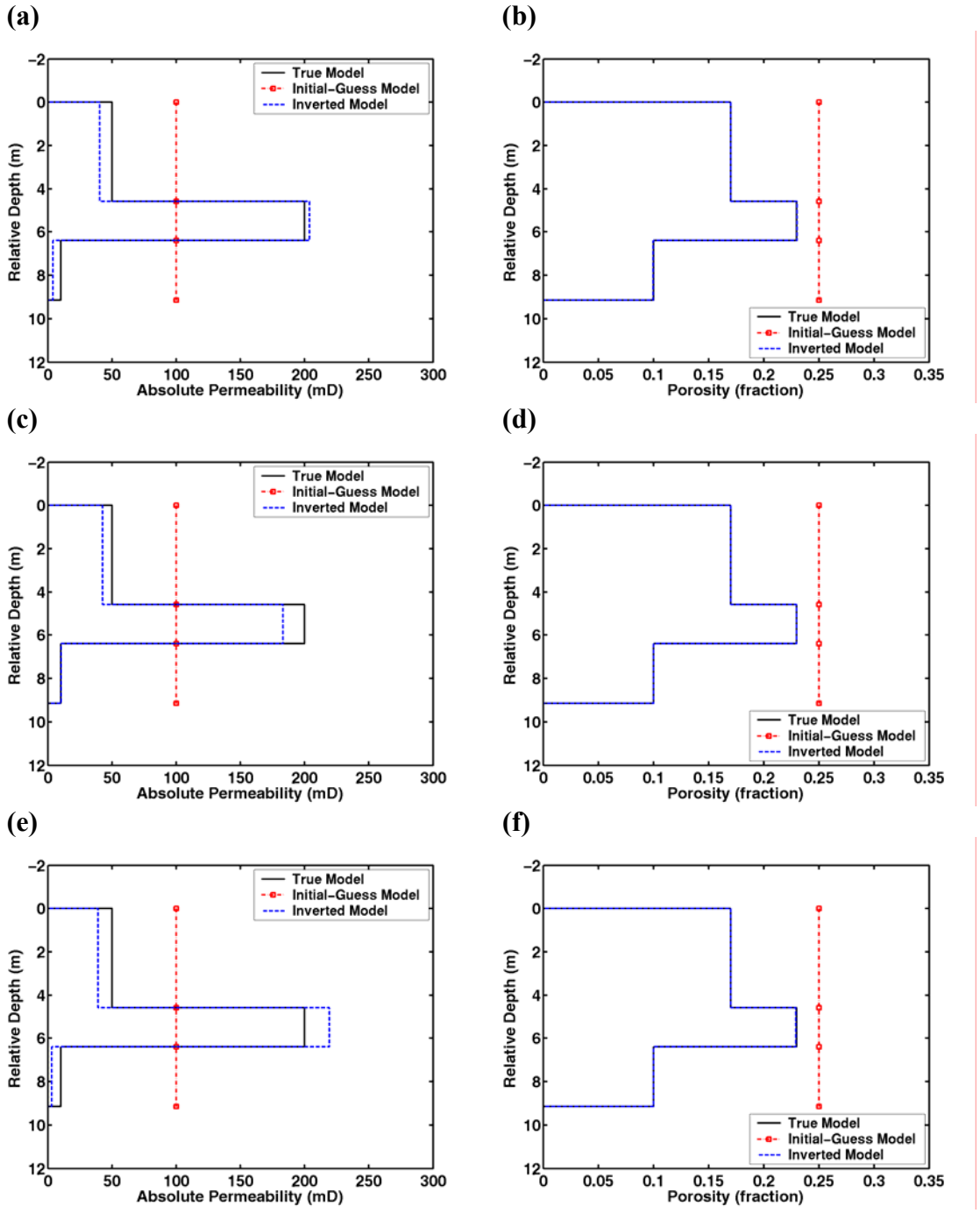

Figure 8.17: Sensitivity of inversion results to the perturbations in viscosity ratio and oleic phase compressibility. Panels (a) and (b) show inversion results for permeability and porosity values, respectively, for the perturbed parameter set 1 shown in Table 8.3. Similarly, panels (c) and (d) show inversion results for permeability and porosity values, respectively, for the perturbed parameter set 2 listed in Table 8.3. Finally, panels (e) and (f) show inversion results for permeability and porosity values, respectively, for the perturbed parameter set 3 listed in Table 8.3.

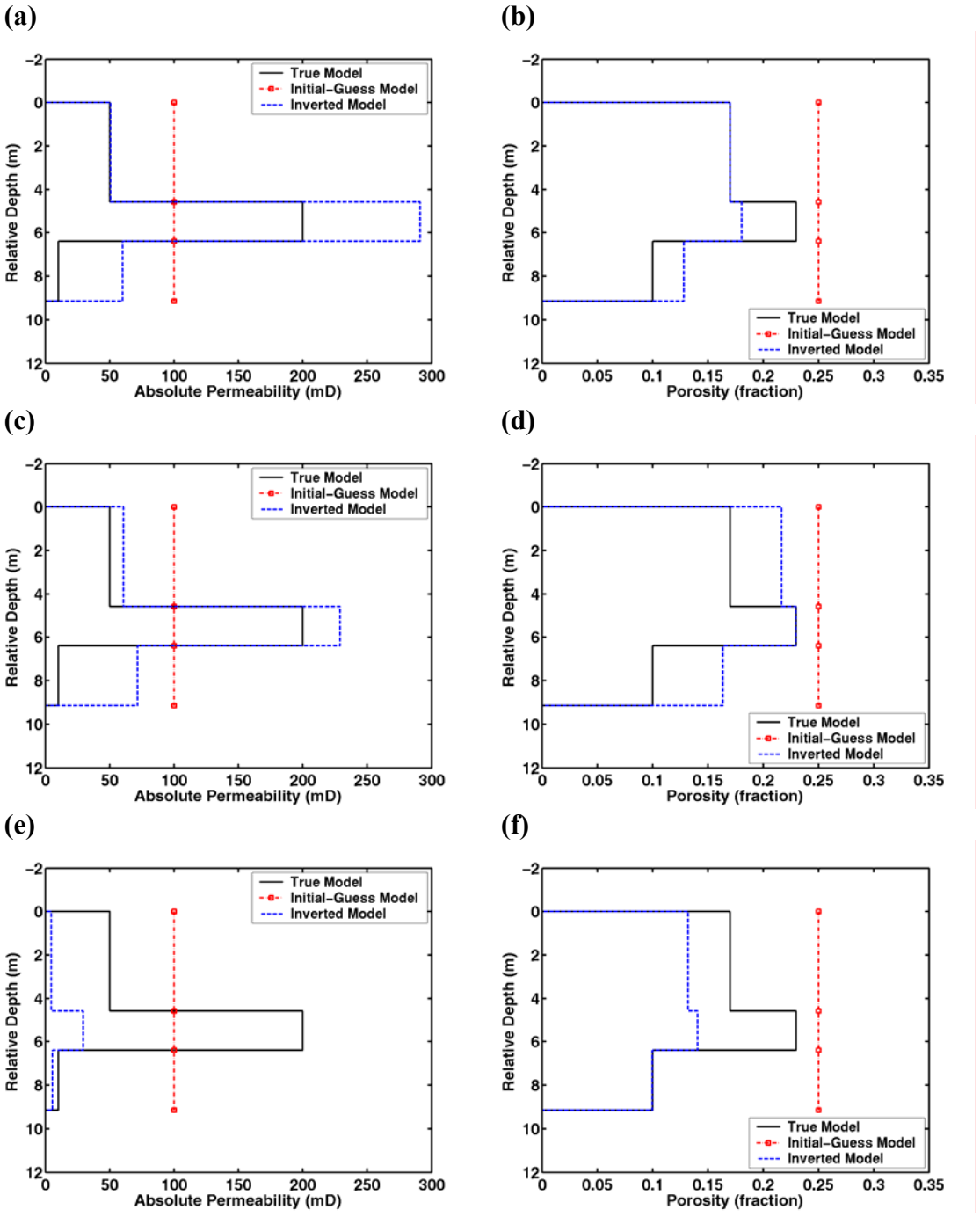

Figure 8.18: See caption on the following page.

Figure 8.18: Sensitivity of inversion results to the perturbations in saturation-dependent functions, namely, relative permeability and capillary pressure functions. Panels (a) and (b) show inversion results for permeability and porosity values, respectively, assuming that the relative permeability and capillary pressure functions for layer 1 hold for all three layers. Similarly, panels (c) and (d) show inversion results for permeability and porosity values, respectively, assuming that the relative permeability and capillary pressure functions for layer 2 hold for all three layers. Finally, panels (e) and (f) show inversion results for permeability and porosity values, respectively, assuming that the relative permeability and capillary pressure functions for layer 3 hold for all three layers.

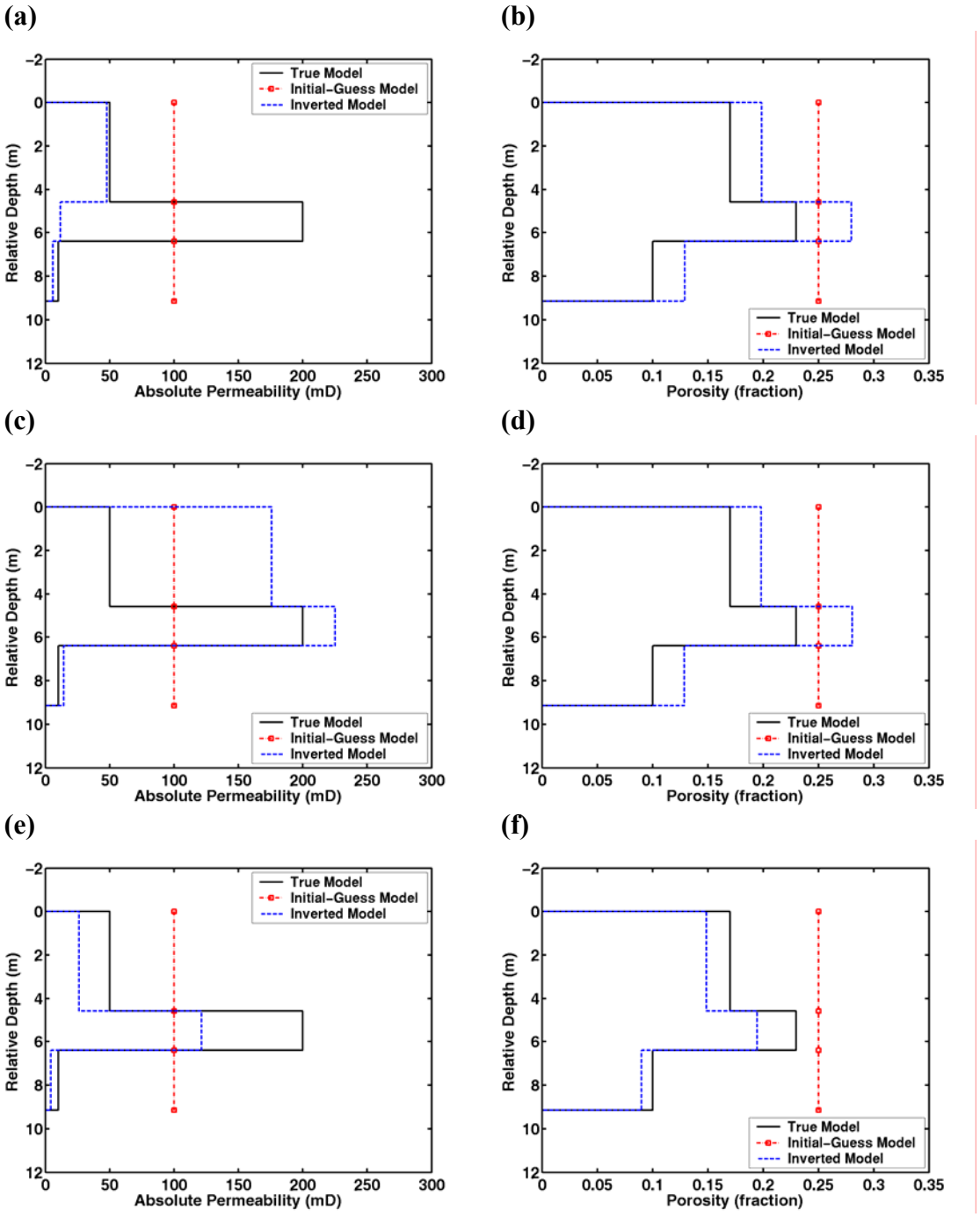

Figure 8.19: Sensitivity of inversion results to the perturbations in saturation-dependent functions, namely, relative permeability and capillary pressure functions. Panels (a) and (b) show inversion results for permeability and porosity values, respectively, for the perturbed parameter set 1 shown in Table 8.4. Similar inversion results are shown for perturbed parameter sets 2 and 3 are shown in panels {(c), (d)} and {(e), (f)}, respectively.

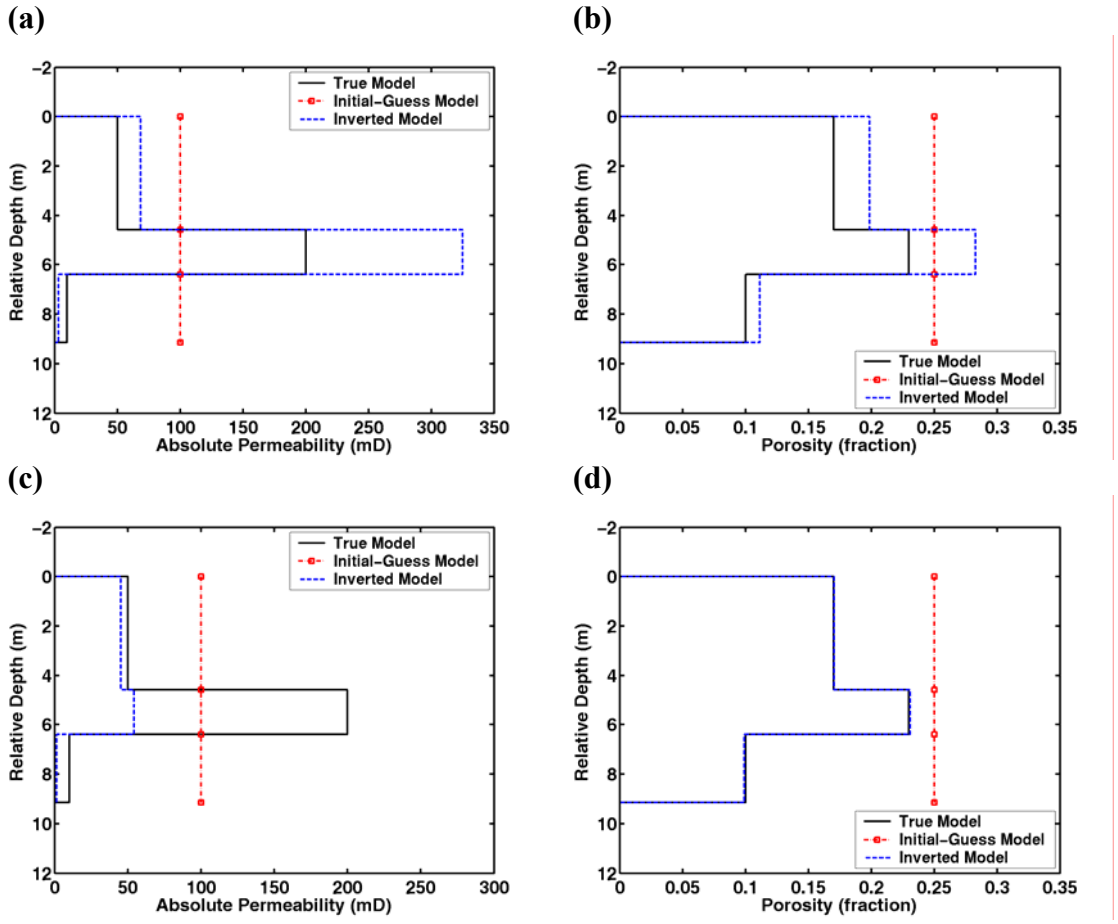

Figure 8.20: Sensitivity of inversion results to the perturbations in saturation-dependent functions, namely, relative permeability and capillary pressure functions. Panels (a) and (b) show inversion results for permeability and porosity values, respectively, for the perturbed parameter set 4 shown in Table 8.4. Similar inversion results are shown for the perturbed parameter set 5 are shown in panels (c) and (d).

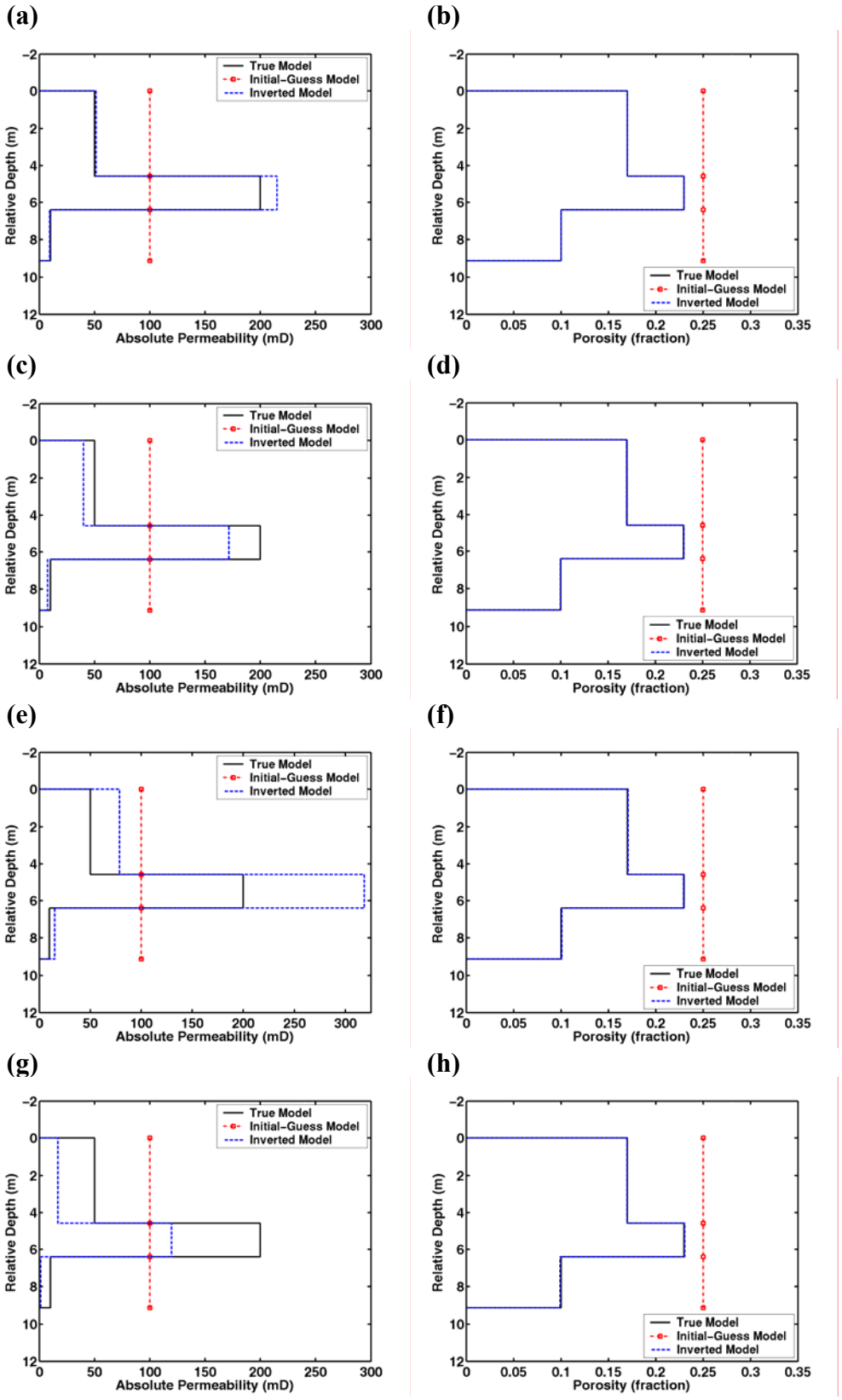

Figure 8.21: See caption on the following page.

Figure 8.21: Sensitivity of inversion results to the perturbations in mud-filtrate invasion duration. Inversion results are shown in panels (a) and (b) for a perturbation of $+1$ day, (c) and (d) for a perturbation of -1 day, (e) and (f) for a perturbation of $+3$ days, and (g) and (h) for a perturbation of -3 days, respectively. True mud-filtrate invasion duration is 12 days.

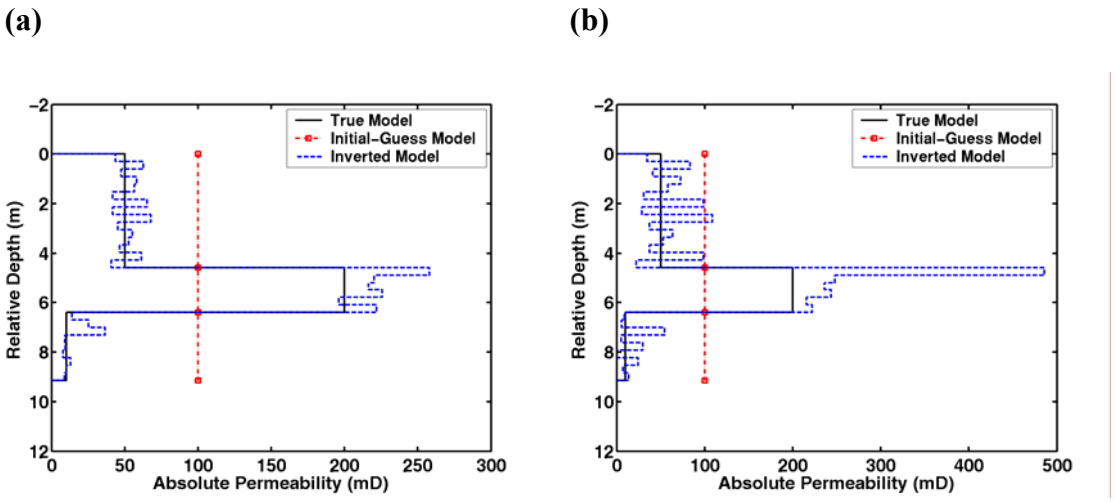

Figure 8.22: Full 1D inversion of permeability from electromagnetic-induction logging measurements. Panels (a) and (b) show inverted permeability profiles along with true and initial-guess values of permeability for cases where measurements are contaminated with 1% and 3% random Gaussian noise, respectively.

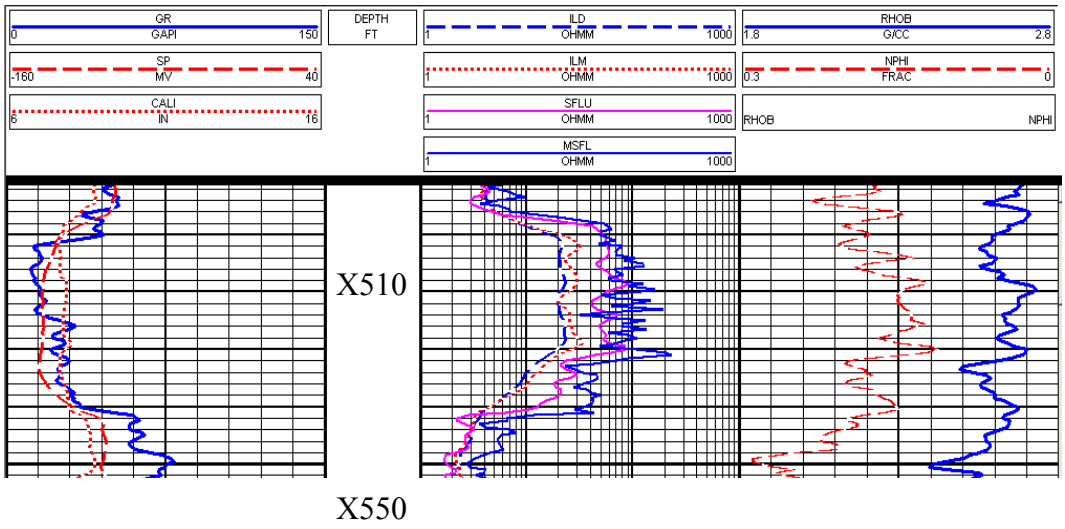

Figure 8.23: Plot of the basic suite of wireline logs including dual-induction measurements acquired along Well X-2.

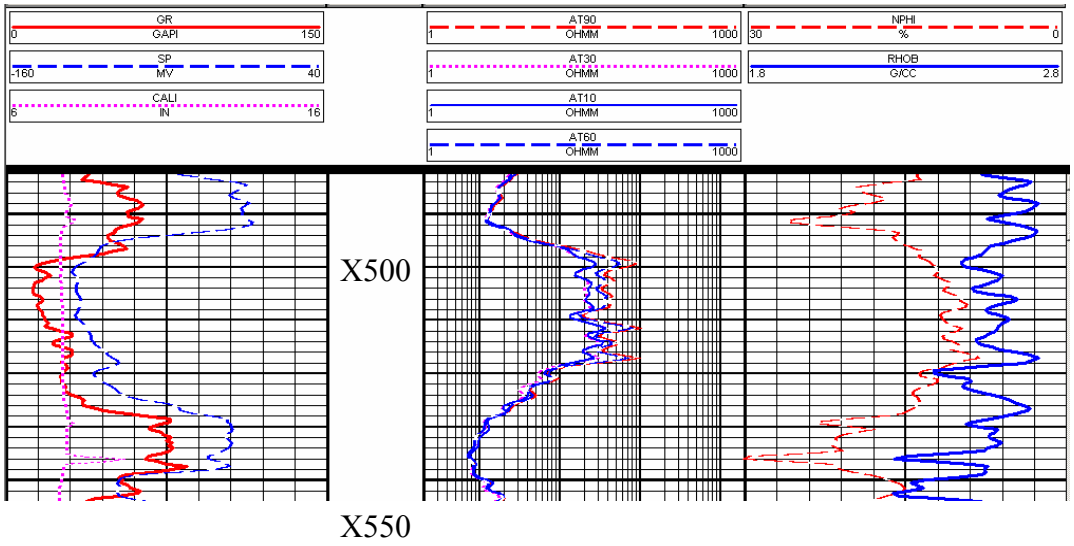

Figure 8.24: Plot of the basic suite of wireline logs including array induction measurements acquired along Well X-1.

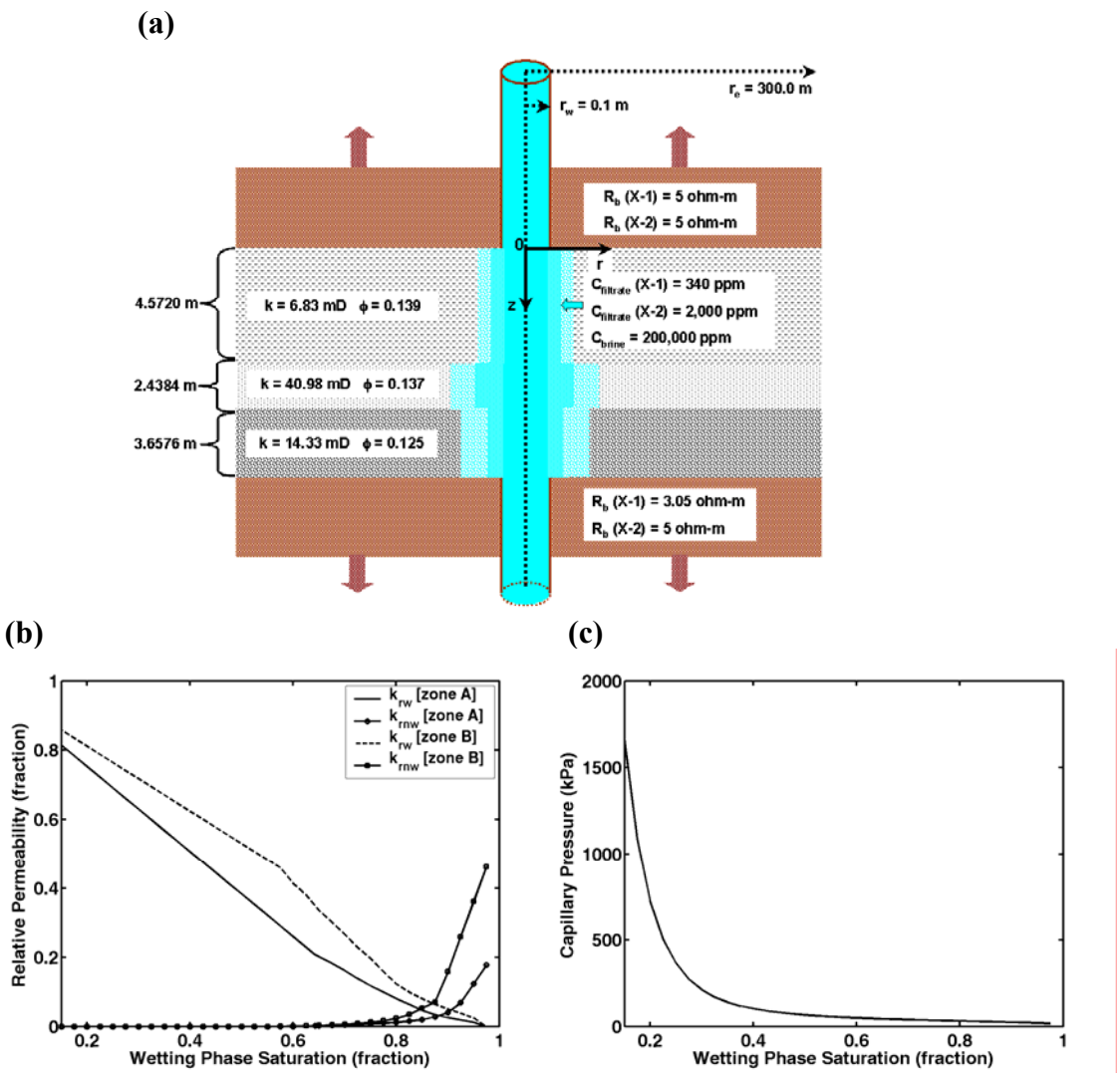

Figure 8.25: (a) Formation model for the inversions of field borehole electromagnetic-induction measurements acquired at wells X-1 and X-2. Two-dimensional vertical cross-section of the permeable formation intersected by a vertical borehole. The three-layer formation is subject to water-base mud-filtrate invasion. Permeability and porosity values obtained from core analysis are shown in the above cross-section. (b) Relative permeability and (c) capillary pressure functions used in fluid-flow simulations within the petrophysical inversion framework of field electromagnetic-induction logging measurements.

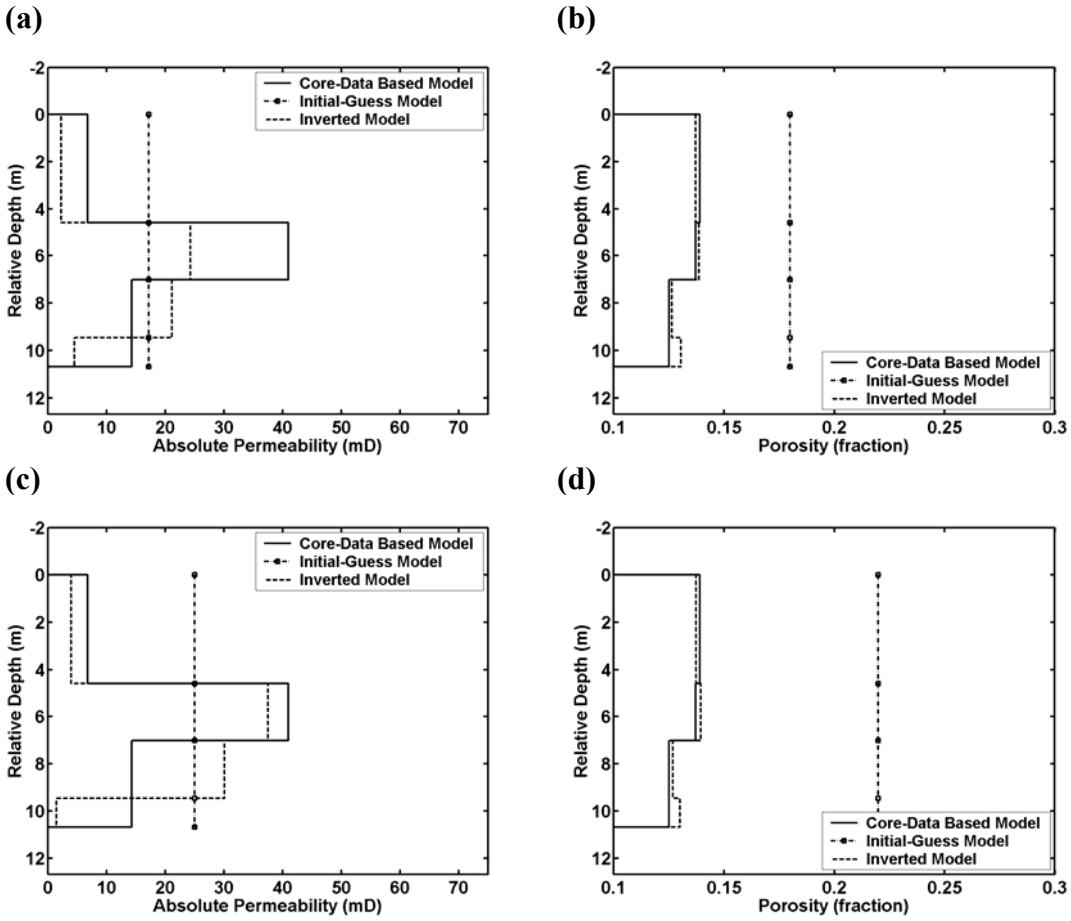

Figure 8.26: Permeability and porosity values yielded by the inversions of single-time electromagnetic-induction logging measurements acquired by the dual induction tool configuration at well X-2. Measurements were recorded subsequent to a 4 days-long mud-filtrate invasion period. Inversion results are shown for two initial-guess values of permeability and porosity for a four-layer description of the formation of interest.

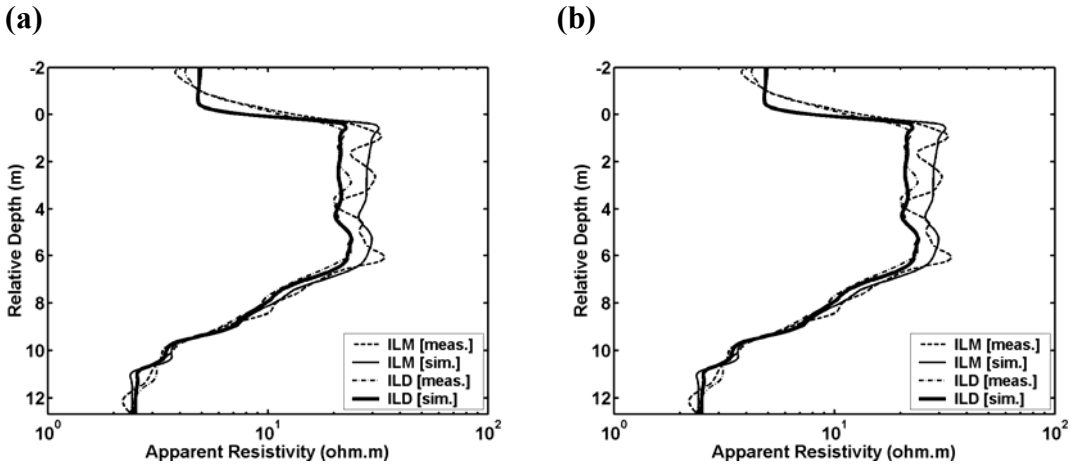

Figure 8.27: Post-inversion data match for dual induction tool measurements acquired at well X-2. Data matches are plotted for the inversions performed using (a) the initial-guess set 1 shown in panels (a) and (b) of Figure 8.26, and (b) the initial-guess set 2 shown in panels (c) and (d) of Figure 8.26.

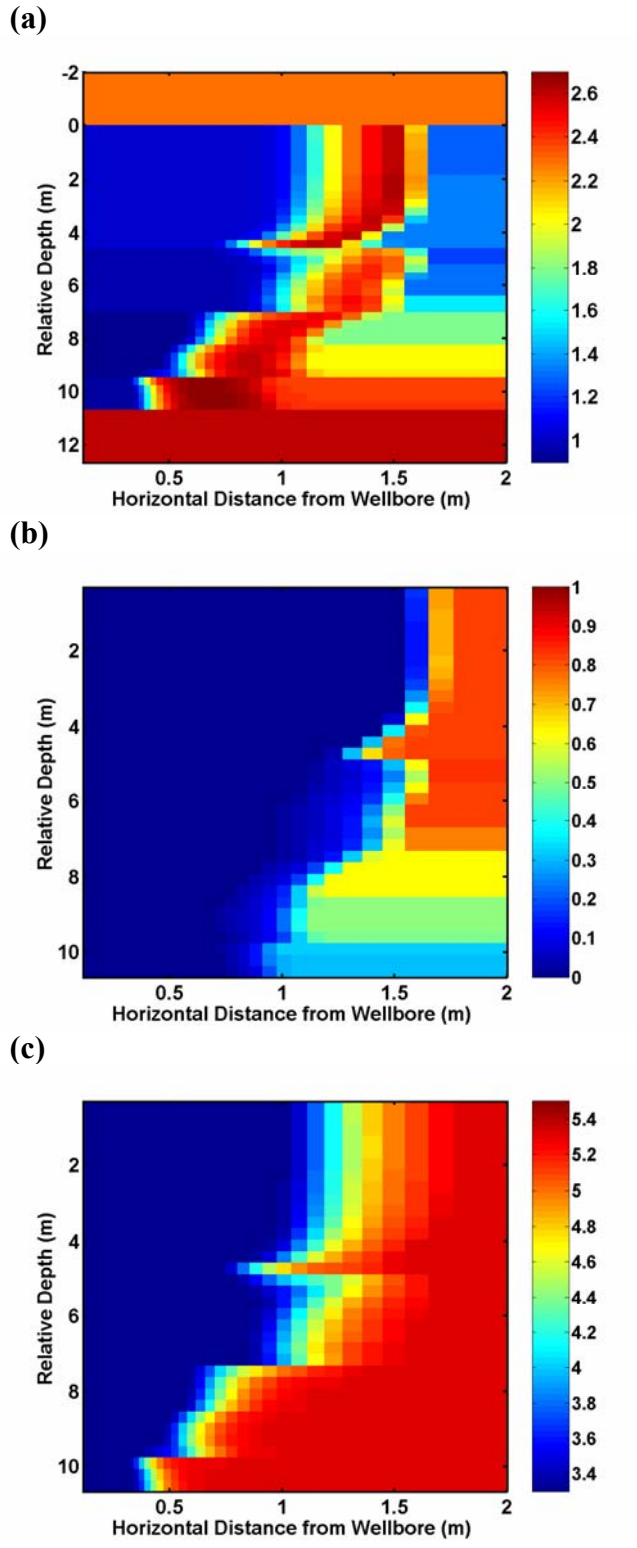

Figure 8.28: See caption on the following page.

Figure 8.28: Post-inversion simulations of spatial distributions of near-borehole (a) conductivity (shoulder-bed conductivities are also shown), (b) gaseous phase saturation, and (c) salt concentration at well X-2. Conductivity domain is shown in logarithmic scale, i.e., $\log_{10}[\sigma(\mathbf{r})]$. The spatial distribution of gaseous phase saturation $\left\{S_g(\mathbf{r}) = 1.0 - S_w(\mathbf{r})\right\}$ is reported in the unit of pore volume fractions and the spatial distribution of salt concentration is reported in the unit of part per million [ppm] using a logarithmic scale.

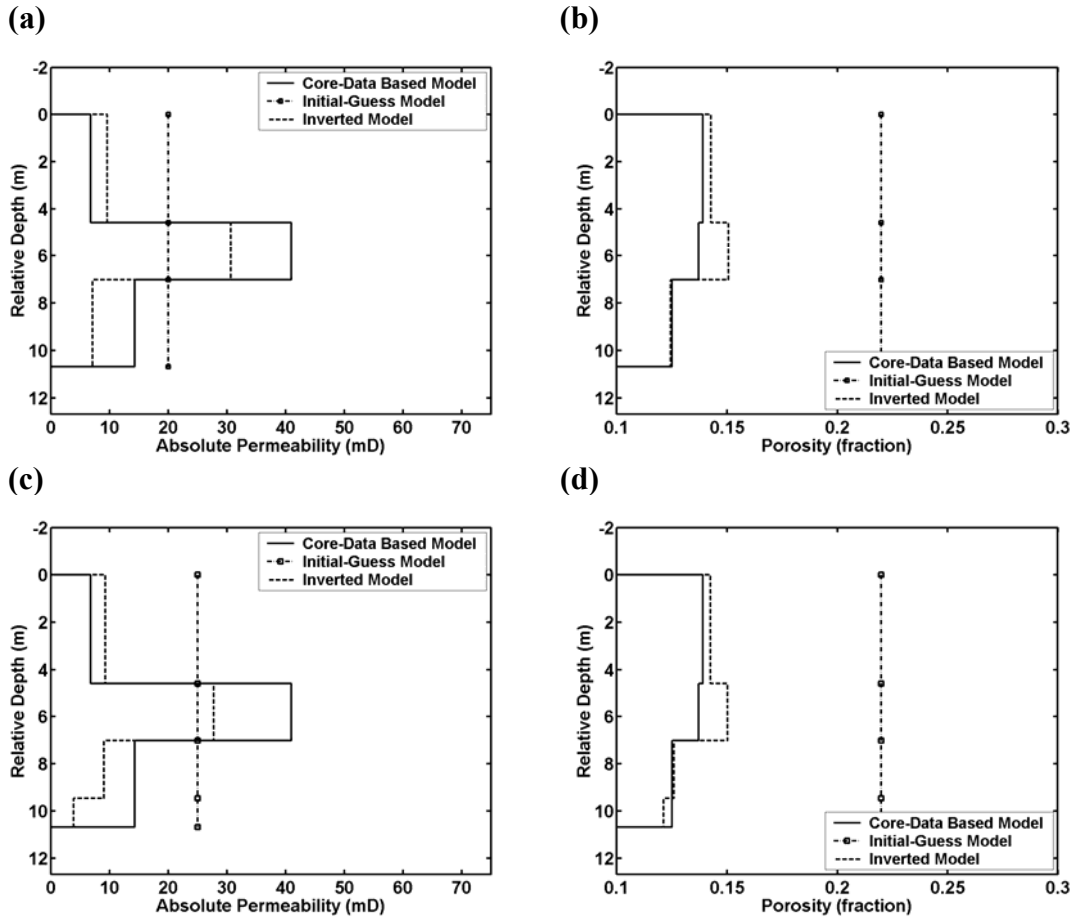

Figure 8.29: Permeability and porosity values yielded by the inversions of single-time electromagnetic-induction logging measurements acquired by the array induction imager configuration at well X-1. Measurements were recorded subsequent to a 4 days-long mud-filtrate invasion period. Inversion results are shown for two cases: (1) a three-layer description of the formation of interest (panels (a) and (b)), and (2) a four-layer description of the formation of interest (panels (c) and (d)).

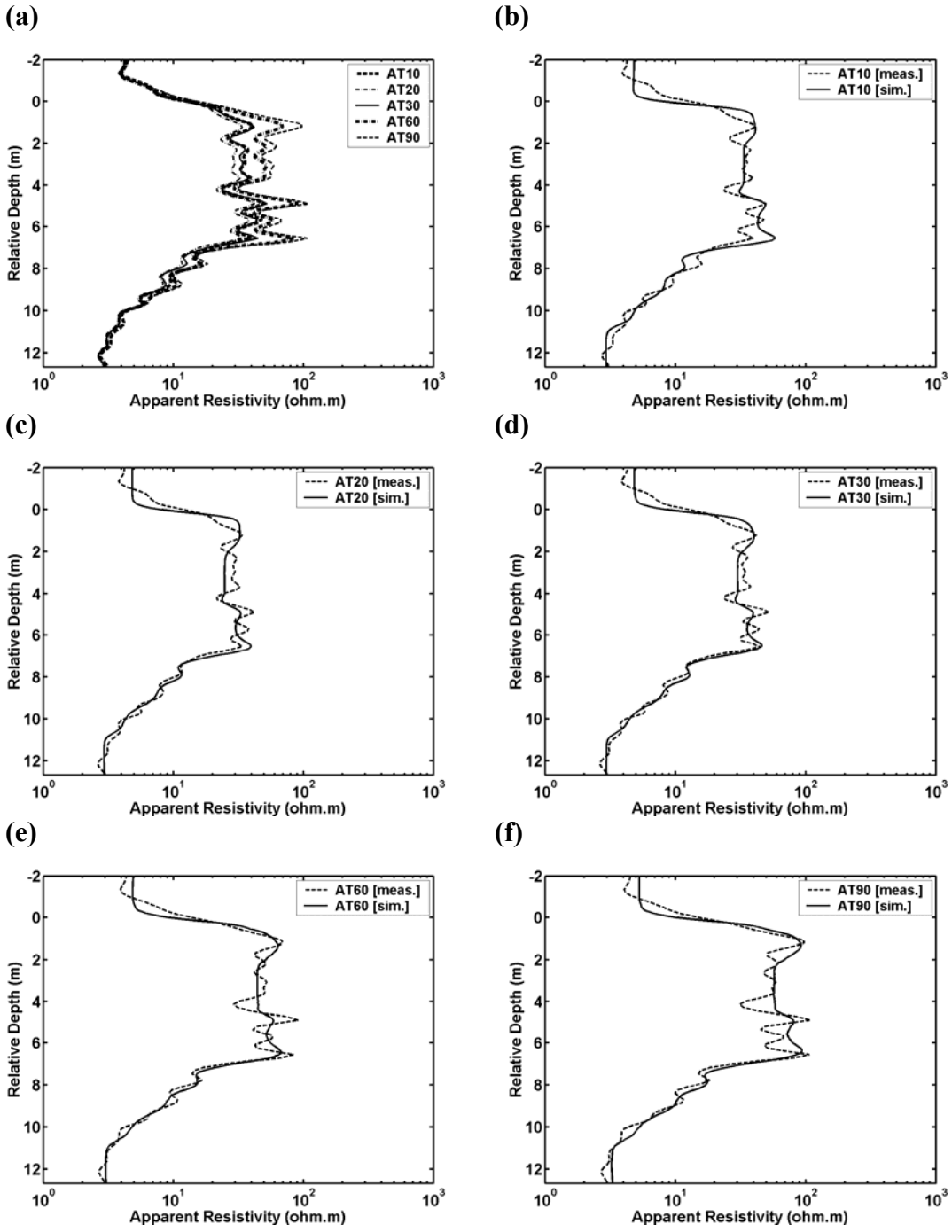

Figure 8.30: (a) Measured array induction logging data in well X-1 across the formation of interest. Panels (b), (c), (d), (e), and (f) show post-inversion data match for each array.

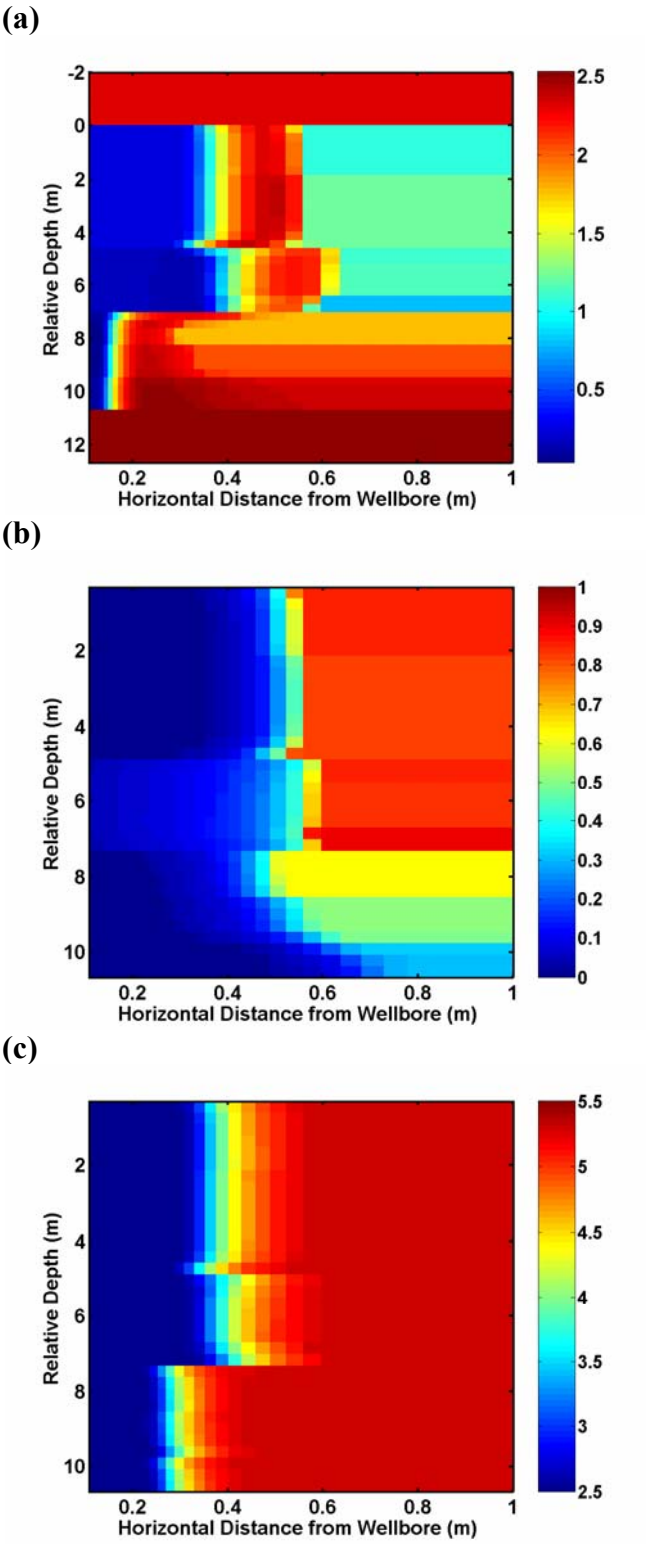

Figure 8.31: See caption on the following page.

Figure 8.31: Post-inversion simulations of spatial distributions of near-borehole (a) conductivity (shoulder-bed conductivities are also shown), (b) gaseous phase saturation, and (c) salt concentration at well X-1. Conductivity domain is shown in logarithmic scale, i.e., $\log_{10}[\sigma(\mathbf{r})]$. The spatial distribution of gaseous phase saturation $\left\{S_g(\mathbf{r}) = 1.0 - S_w(\mathbf{r})\right\}$ is reported in the unit of pore volume fractions and the spatial distribution of salt concentration is reported in the unit of part per million [ppm] using a logarithmic scale.

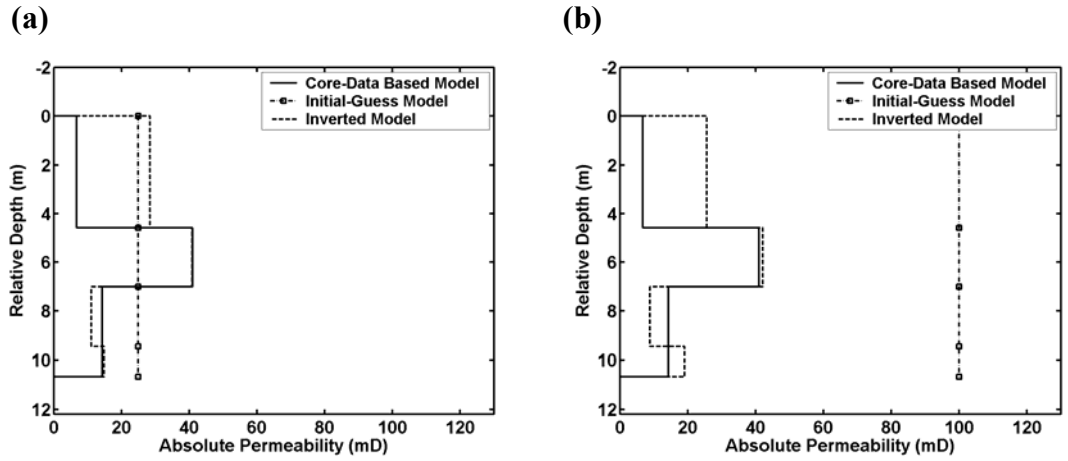

Figure 8.32: Permeability values yielded by the inversions of single-time electromagnetic-induction logging measurements acquired by the array induction imager configuration at well X-1. Measurements were recorded subsequent to a 4 days-long mud-filtrate invasion period. Two different initial-guess values of permeability are used for both data sets as shown in panels (a) and (b). Porosity values are fixed to the value determined from core data.

Chapter 9: Simultaneous Estimation of In-Situ Multi-Phase Petrophysical Properties of Rock Formations from Wireline Formation Tester and Induction Logging Measurements

9.1 INTRODUCTION

In Chapters 7 and 8, we quantitatively demonstrate that the physics of multi-phase fluid-flow and electromagnetic induction phenomena in porous media can be coupled by means of a fluid saturation equation. Thus, a multi-physics inversion algorithm for the quantitative joint interpretation of electrical and fluid-flow measurements can be formulated to estimate the underlying petrophysical model. The objective of the work reported in this chapter is to develop a robust, accurate, and efficient algorithm for the simultaneous, parametric joint inversion of induction logging, transient-pressure, flowline water-cut, and salt production rate measurements. The inversion algorithm yields two-phase flow petrophysical properties, namely, layer-by-layer horizontal and vertical absolute permeabilities, parametric representations of relative permeability and capillary pressure curves, and initial phase saturations of the hydrocarbon-bearing rock formations. We assume standard instrument geometries rather than proposing an experimental tool. However, we also explore the possibility of taking a first step toward the future of the joint interpretation of formation tester and induction logging measurements by introducing multi-pulse schedules for formation tester measurements. For more realistic cases where multi-physics measurements lack the degrees of freedom necessary to accurately estimate all the petrophysical model parameters, we develop an alternative sequential inversion technique. We first resort to the single-phase inversion of transient formation pressure measurements acquired at late times of the formation test, i.e., when the flow into the formation tester is dominated by (almost) single-phase fluid. Subsequently, simultaneous multi-physics inversion of the entire time record of

formation tester measurements is performed jointly with induction logging measurements.

For the inversion, we assume the availability of two important pieces of information: (a) properties of mudcake for the simulation of the process of mud-filtrate invasion in the presence of mudcake, (b) fluid sampling measurements to yield the PVT properties of the in-situ fluid phases and flowing components. Inversion of multi-physics measurements is posed as a constrained optimization problem. In turn, a quadratic cost function is minimized subject to physical constraints enforced on the unknown model. A hybrid global optimization technique is developed for inversion (see, Appendix A). Numerical examples of the joint inversion method are successfully conducted for two-dimensional axisymmetric reservoir models that involve noisy and noise-free synthetically generated induction logging, transient formation pressure, flowline water-cut, and salt production rate measurements. We focus our attention to the vertical variability of the petrophysical model. Horizontal geological layers of various thicknesses characterize the reservoir geometry. We assume the availability of information about the locations of layer boundaries from other types of logs such as borehole images. Based on the extent of the available measurement data and a-priori information, an arbitrary combination of the above-mentioned petrophysical parameters can be included into our inversion algorithm. Figure 9.1 shows the flowchart of the multi-physics algorithm developed in this work to solve the above-described integrated petrophysical inversion problem.

9.2 A HYBRID GLOBAL OPTIMIZATION ALGORITHM FOR INVERSION

The optimization technique implemented for the solution of the inverse problem considered in this work is based on a weighted least-squares method. In our implementation, the weighted least-squares algorithm makes use of the Weighted and Regularized Gauss-Newton (`WRGN`) search direction (Gill et al., 1981; Nocedal and Wright, 1999). Consistently, we refer to the minimization algorithm as the Weighted and

Regularized Gauss-Newton method, WRGN. In addition, two helper methods based on the Simultaneous Perturbation Stochastic Approximation (SPSA) technique (Spall, 1992; Spall, 1998; Spall, 2003; Chin, 1994) are introduced to overcome the common WRGN pitfall of a potential entrapment around a local minimum. When the helper method is active, the inversion algorithm marches toward the minimum with the steps of a global optimizer (SPSA). Once the model is deemed sufficiently close to the minimum, WRGN steps take over SPSA steps for ensuring rapid convergence. If local minimum entrapment is sensed (based on criteria reflecting invariance of the model or insufficient reduction of the cost function), the hybrid algorithm automatically switches back to SPSA steps. Convergence of the algorithm is accepted only if (approximately) the same model minimum is achieved after a prescribed number of global-local (WRGN-SPSA) interactions over the course of optimization. Appendix A provides technical details of this highly efficient hybrid inversion algorithm.

A quantitative analysis of the uncertainty in inversion results is carried out by computing the Cramer-Rao uncertainty bounds using an approximation to the Estimator's Covariance Matrix. The Cramer-Rao uncertainty bounds provide a probabilistic range for each model parameter inverted from noisy measurements. Computation of Cramer-Rao uncertainty bounds is described in detail in Appendix A. The assumption underlying the approximate computation of the Estimator's Covariance Matrix is that the errors in the measurements are purely random and comply with Gaussian distribution.

The inversion algorithm is formulated in a generic fashion to incorporate any parametric saturation function of relative permeability and capillary pressure that physically suits the problem of interest. For the purpose of parsimony in the numerical examples, we assume that two-phase relative permeability and capillary pressure curves can be described by a simple modified Brooks-Corey model. This model (Lake 1989; Honarpour et al., 1986) utilized for the parametric modeling of relative permeability and capillary pressure functions is described via following equations:

$$k_{r1}(S_1) = k_{r1}^o \left(\frac{S_1 - S_{1r}}{1 - S_{1r} - S_{2r}} \right)^{(3+2/\eta)}, \tag{9.1}$$

$$k_{r2}(S_1) = k_{r2}^o \left(\frac{1 - S_1 - S_{2r}}{1 - S_{1r} - S_{2r}} \right)^{(1+2/\eta)}, \tag{9.2}$$

and

$$P_c(S_1) = P_{ce} \left(\frac{S_1 - S_{1r}}{1 - S_{1r} - S_{2r}} \right)^{-1/\eta}. \tag{9.3}$$

In the above equations, S_1 and S_2 are saturations for fluid phases 1 and 2, k_{r1}^o and k_{r2}^o are end-point relative permeabilities for fluid phases 1 and 2, S_{1r} and S_{2r} are residual saturations for fluid phases 1 and 2, η is the pore size distribution index, P_c is the capillary pressure, and P_{ce} is the capillary entry pressure. Then, saturation functions of relative permeability and capillary pressure can be described by the parameter set $\mathbf{x}_{kr-Pc}$, such that

$$\mathbf{x}_{kr-Pc} = \left[k_{r1}^o, S_{1r}, k_{r2}^o, S_{2r}, \eta, P_{ce} \right]^T. \tag{9.4}$$

9.3 NUMERICAL EXAMPLES

In order to assess the applicability and efficiency of the proposed inversion algorithm, we constructed several realistic numerical examples. All reported inversions fit the measurement data to the level of prescribed noise since zero-mean additive random Gaussian noise is used to contaminate the measurements. For the inversions of noise-free measurements, we enforce a global misfit equal to $\chi^2 = 10^{-4}$.

9.3.1 Rock Formation Model

A vertical borehole is considered to intersect a hydrocarbon-bearing horizontal rock formation. For the sake of simplicity, we limit our analysis to the case of a single-layer formation. In addition to the permeable layer, sealing upper and lower shoulder beds are included in the geoelectrical model as shown in Figure 9.2. Details of formation rock and fluid properties are given in Table 9.1. The single-layer formation is assumed to exhibit transversely anisotropic permeability behavior described by the following diagonal tensor:

$$\overline{\overline{\mathbf{k}}} = diag\left[k_h \; k_h \; k_v\right]. \tag{9.5}$$

The ultimate goal of the inversion is the reconstruction of parametric two-phase relative permeability and capillary pressure curves, and horizontal and vertical permeabilities from multi-probe transient formation pressure, water-cut, salt production rate, and induction logging measurements. The vector of model parameters subject to inversion is given by

$$\mathbf{x} = \left[k_h, k_v, k_{r1}^o, S_{1r}, k_{r2}^o, S_{2r}, \eta, P_{ce}\right]^T. \tag{9.6}$$

We assume the availability of laboratory measurements of fluid compressibilities for slightly compressible fluid phases, namely, aqueous and oleic phases. Additionally, fluid viscosities, formation porosity, formation temperature, and saturation-equation parameters are assumed known from ancillary information. The formation of interest is assumed to be previously unexplored. Therefore, the reservoir pore volume is assumed to be saturated at irreducible aqueous phase saturation. In other words, initial aqueous phase saturation is equal to the irreducible aqueous phase saturation. Hence, the suggested

inversion algorithm yields the initial saturation condition of the formation of interest as by-product.

9.3.2 Simulated Measurement Hardware and Schedule

From the onset of drilling, the permeable formation is assumed to be subject to dynamic water-base mud-filtrate invasion. Mud-filtrate invasion is simulated using a constant integral-averaged invasion rate computed using `INVADE [UTCHEM]`. After a prescribed duration of mud-filtrate invasion (before the formation test), an array induction log is assumed to be recorded across the formation. The tool assumed for the simulated acquisition of electromagnetic induction measurements is the Array Induction Imager Tool, AIT™, described schematically in Figure 9.3. This sonde configuration is selected to ensure the availability of data with multiple depths of investigation (Hunka et al., 1990). The second available data type is multi-probe formation tester measurements. Measurements are simulated for acquisition with the Modular Formation Dynamics Tester, MDT™. A dual-packer/probe module configuration with two vertical observation probes is considered in order to estimate permeability anisotropy (Pop et al., 1993; Ayan et al., 2001). Figure 9.4 is a schematic of the dual-packer and probe modules. For the formation tester configuration, we assume the presence of an optical fluid analyzer to yield measurements of flowline water-cut. Also, for some of the numerical cases, we assume the presence of flowline resistivity measurements to provide measurements of salt concentration. In turn, time records of salt concentration measurements are used to compute the time functions of salt production rate.

Soon after the induction log is acquired, the multi-probe formation tester configuration is assumed to be deployed across the formation of interest to conduct transient-pressure, water-cut, and salt production rate measurements. Note that the latter measurement type is included in the measurement vector on a case-by-case basis. Time records of pressure are simulated for two observation probe locations, and at the center of the dual-packer open interval in response to a controlled flow rate pulse. Flowline water-

cut and salt production rate measurements are derived from simulated source condition values that correspond to the vertical sequence of gridblocks across to the open interval of the dual-packer. The source condition is represented as a well penetrating into multiple gridblocks. Tool and dual-packer open-interval storage effects are assumed negligible. The effect of (mud-filtrate) invasion-related skin contamination is rigorously accounted for by simulating the entire invasion process (via imposing the mud-filtrate invasion rate computed with `INVADE [UTCHEM]`). In the numerical cases subject to analysis, we parsimoniously assume that (mud-filtrate) invasion-related skin contamination is the dominant factor of skin. In other words, additional factors of skin stemming from partial penetration, etc. are negligible. Details of the simulated formation tester rate vs. time schedules will be described on a case-by-case basis. For the simulation of formation tester measurements, we assume a cylindrical coordinate frame and make use of a finite-difference grid with $31 \times 1 \times 30$ nodes in the radial, azimuthal, and vertical directions, respectively. This grid is uniform in the vertical direction. Block sizes increase logarithmically in the radial direction away from the borehole. Figure 9.6 shows a vertical cross-section of the simulation grid. For simplicity, henceforth we refer to the simulated events as if they were the events of a real-life workflow.

9.3.3 Case A

Subsequent to the duration of six-day long water-based mud-filtrate invasion, an induction log is recorded across the single-layer formation. Following the induction log acquisition, formation fluid is withdrawn from the formation using the dual-packer module. Two-phase formation fluid is withdrawn from the formation with a volumetric rate of 15 rbbl/d [2.38 m^3/d = 27.60 cc/s] for 4000 seconds [1.11 hours]. In order to generate a pressure transient without interrupting the clean-up process, the rate of fluid withdrawal is reduced to 5 rbbl/d [0.79 m^3/d = 9.2 cc/s] for 400 seconds [0.11 hours]. The flow rate history for the formation test is shown in Figure 9.6(a). Subsequently, the formation test is concluded. Multi-probe transient formation pressure and flowline water-

cut measurements are recorded during the formation test. A pre-inversion sensitivity study indicated that the most difficult parameters to estimate are pore size distribution index (η) and capillary entry pressure (P_{ce}). Therefore, we assume the availability of nuclear magnetic resonance (NMR) measurements that will allow the determination of the range of pore size distribution index and capillary entry pressure (Altunbay et al., 1998; Volokitin et al., 1999; Altunbay et al., 2001). Such an integrated petrophysics approach, allows us to enforce relatively narrower physical bounds and relatively closer initial-guess values for these parameters during the inversion process in comparison to other unknown parameters. Noise-free measurements of induction logging and formation tester are input to the inversion algorithm. Table 9.2 shows the actual and initial-guess model parameters along with the corresponding inversion results. Inversion results for Case A are also displayed in Figure 9.13 along with actual and initial-guess values of model parameters. End-point (residual) saturations of aqueous and oleic phases, capillary entry pressure, and pore-size distribution index are the model parameters that are accurately reconstructed by the multi-physics inversion algorithm. The poorest reconstruction is obtained for the oleic phase relative permeability. The quality of reconstruction for horizontal permeability still remains poor whereas the accuracy of the estimated vertical permeability is satisfactory.

The problem associated with the formation test described in Case A is two-fold: (1) The saturation range is not sampled entirely during the test as indicated by the unstabilized flowline water-cut measurements shown in Figure 9.7(a). In fact, the formation test failed to cover the saturation range in the vicinity of the oleic phase end-point. Consequently, the quality of the reconstruction for the end-point relative permeability of oleic phase remains poor. (2) Although the presence of auxiliary measurements considerably improves the estimation, horizontal and vertical permeability information is predominantly extracted from transient-pressure measurements within the multi-physics inversion framework. Presence of multiple transients of pressure increases

the redundancy of data and reduces the non-uniqueness in the inverted permeability model. The double rate-pulse approach used in Case A, which is similar to the conventional drawdown and build-up sequence (only without interrupting the water-cut measurements) obviously fails to provide the necessary degrees of freedom to accurately estimate horizontal and vertical permeabilities.

9.3.4 Case B

In order to overcome the limitations described in Case A, we replace the dual-pulse flow rate schedule of Case A with a multi-pulse schedule shown in Figure 9.6(b). The test duration is extended to 5 hours for enabling the formation test to provide information in the vicinity of the oleic phase end-point. As indicated by Figure 9.7(b), we remark that the water-cut trend has reached a pseudo steady-state behavior at the concluding stages of the formation test. In order to keep the formation in transient condition as long as possible during the formation test, the flow rate is modified every hour thereby creating a sequence of five transient time-series of measurements. In order to further constrain the inversion, we add the time record of salt production rate measurements to the data vector. Everything else about the formation model remains the same as in Case A. In this case (similar to Case A), noise-free measurements are input to the inversion. In the first inversion example (Case B1), we assume the availability of NMR measurements that allow the accurate determination of both pore-size distribution index and capillary entry pressure. Therefore, in Case B1, these parameters remain stipulated over the course of the inversion. In the second inversion example (Case B2), however, pore-size distribution index and capillary entry pressure are determined by the inversion. Over the course of the inversion, these model parameters are subject to the same physical bounds and initial-guess values used in Case A.

Table 9.2 shows the results of the inversion for Cases B1 and B2 along with actual and initial-guess model parameters. Inversion results for Case B1 are also displayed in Figure 9.13 along with actual and initial-guess values of model parameters.

Inversion results indicate an accurate reconstruction of horizontal and vertical permeabilities as well as of parameters that describe relative permeability and capillary pressure curves for Case B2. Actual, initial-guess, and inverted saturation functions of relative permeability (both in linear and log scales) and capillary pressure are shown in Figures 9.8 through 9.10 for Case B2. For this case, pre- and post-inversion formation tester data fits are shown in Figures 9.11(a) through 9.11(c) for transient-pressure, in Figure 9.11(d) for flowline water-cut, and in Figure 9.11(e) for salt production rate. On the other hand, the panels in Figure 9.12 show pre- and post-inversion fits of the electromagnetic induction logging data for one of the receiver locations and for three tool frequencies.

Interestingly, the accuracy of the reconstruction of horizontal permeability and oleic phase end-point relative permeability is marginal for Case B1. We attribute this behavior to the (limited) sensitivity of the inversion with respect to the adaptively computed regularization parameter. The selection of the regularization parameter is linked to the condition number of the `WRGN` Hessian matrix. Over the course of nonlinear iterations, when the condition number decreases below a pre-specified threshold, the regularization parameter is calculated as a small fraction of the largest eigenvalue of the `WRGN` Hessian matrix. Inversion results for Cases B1 and B2 exhibit limited sensitivity to the choice of this condition number and to the choice of a (small) regularization fraction. For Cases B1 and B2, the inverse problem solution appears to lie in the neighborhood of a relatively flat cost function. Therefore, inversion results of Cases B1 and B2 need to be interpreted as deterministic samples from such a flat neighborhood in model vs. cost-function vector space. Overall, multi-physics measurements provide satisfactorily accurate reconstructions of model parameters.

9.3.5 Case C

Both formation tester and induction logging measurements of Case B are contaminated with 1% random Gaussian noise. Everything else is kept invariant as in

Case B2. Table 9.3 reports three sets of inversion results. All model parameters are simultaneously inverted in Case C1. The comparison of inversion results of Case C1 with respect to inversion results of Case B2 indicates that the presence of measurement noise negatively affects the simultaneous inversion approach. Except for the inverted values of end-point saturations, inversion results for the values of the remaining model parameters exhibit inaccurate reconstructions. As a remedy to this problem, we assume that the model parameters that govern the capillary pressure function, namely, pore size distribution index and capillary entry pressure are known a-priori. The first inversion with stipulated capillary pressure model parameters, referred to as Case C2, involves a blind choice of criteria for the computation of the regularization parameter. The second set of inversion results (referred to as Case C3) provide reconstructions of model parameters for the case where we optimize the choice of criteria applied to the computation of regularization parameter through exhaustive experimentation (expert-mode inversion). Inversion results provide a quantitative proof-of-concept for the simultaneous estimation of a transversely anisotropic spatial distribution of permeability and saturation-dependent functions from noisy multi-phase flow and induction logging measurements. However, once again inversion results exhibit limited sensitivity to the choice of regularization parameter. Inversion results for Case C are also displayed in Figure 9.14 along with actual and initial-guess values of model parameters.

As demonstrated in Cases C1, C2, and C3, for the problem of simultaneous reconstruction of anisotropic permeability, and parametric MBC-type functions of relative permeability and capillary pressure, a-priori knowledge about pore size distribution index and capillary entry pressure are of primary importance. The more accurately these parameters are constrained; the better conditioned the inverse problem. Precise knowledge of the a-priori model for these parameters becomes crucial from the viewpoint of accuracy and non-uniqueness of the model parameters inverted from noisy field measurements. In fact, overall results for Case C indicate that the quality of prior

knowledge about pore-size distribution and capillary entry pressure parameters ultimately determines the reliability and accuracy of the inversion. Capillary pressure tests (conducted on cores of the same rock and fluid type as the ones in the formation of interest) and accurate interpretations of NMR measurements across the same formation may potentially provide the information necessary for the construction of a reliable a-priori model.

9.3.6 Case D

In Case D, we assume a three-day long process of mud-filtrate invasion. A realistic dual-pulse liquid production rate schedule, shown in Figure 9.6(c), is used for the formation test. Formation test measurements are acquired across the entire saturation range as suggested by the stabilized flowline water-cut measurements shown in Figure 9.7(c). We only consider multi-probe transient-pressure, water-cut, and induction logging measurements to construct the data vector. We also assume that the measurements are contaminated with Gaussian random noise of standard deviation equal to 1% and 3% (of the individual magnitude of each discrete measurement) in the respective cases (Cases D1 and D2). As a simple starting point for our analysis, we assume that information about horizontal and vertical permeabilities can be determined accurately from conventional single-phase transient formation pressure test analysis. We only estimate parameters that describe the relative permeability and capillary pressure curves. In turn, the inversion problem consists of estimating the parameters k_{r1}^{o}, S_{1r}, k_{r2}^{o}, S_{2r}, η, and P_{ce}. Since we assume the availability of a-priori information about permeability, for the purpose of testing the robustness of the inversion we relax the bounds applied to pore-size distribution and capillary-entry pressure parameters. We constrain the inversion with a relatively wide set of physical bounds for these parameters. In other words, we do not assume any a-priori information (such as core and NMR measurements) about these parameters. Table 9.4 summarizes the inversion results together with actual and initial-guess values of model parameters. At both levels of noise contamination (1% and 3%),

the inversion provides an accurate reconstruction of parameters that describe saturation functions of relative permeability and capillary pressure. Inversion results for Case D are also displayed in Figure 9.15 along with actual and initial-guess values of model parameters.

9.3.7 Case E

The inverse problem and the measurements of Case D are the same for Case E. However, in case E, we do not enforce the assumption of a-priori knowledge about horizontal and vertical permeabilities. We first attempt to simultaneously invert all model parameters (Case E1). Inversion results indicate that the multi-physics data set (contaminated with 1% random Gaussian noise) lacks the degrees of freedom necessary to simultaneously estimate all model parameters. The negative impact of insufficient redundancy in the transient data (pressure transients are generated in response to a dual-pulse schedule as opposed to the multi-pulse schedule of Case B) together with the absence of salt production rate measurements are apparent in the inversion results. Although the inversion converges to a misfit level equal to the level of noise (as expected for measurement data contaminated with zero-mean random Gaussian noise), the inversion results are far from being accurate. Extensive inversion runs with various regularization strategies lead us to conclude that the simultaneous inversion approach is riddled with model non-uniqueness.

Instead of resorting to NMR measurements to constrain the capillary pressure parameters (as described in Case B), in this case, we concentrate exclusively on the information content of transient formation pressure measurements. Based on single-phase inversions of transient-pressure measurements with average fluid properties and with various regularization weights, we determine the following ranges for horizontal and vertical permeabilities: 55 mD to 60 mD and 9 mD to 12 mD, respectively. Subsequently, we perform the inversion of parameters that describe relative permeability and capillary pressure curves. In the latter inversions, previously inverted horizontal and vertical

permeabilities remain fixed. We describe two examples with limiting values of horizontal and vertical permeability stipulated as a-priori information for the inversion (Cases E2 and E3). Table 9.5 displays the post-inversion reconstructions as well as the actual and initial-guess values of model parameters input to the inversion. Results indicate accurate reconstructions for end-point saturations and for the end-point relative permeability of the aqueous phase. Inversion results for pore size distribution index, capillary entry pressure parameters, and end-point relative permeability for the oleic phase exhibit limited sensitivity to the choice of stipulated horizontal and vertical permeabilities. Overall, the accuracy of the inverted parameters is satisfactory. Inversion results for Case E are also displayed in Figure 9.16 along with actual and initial-guess values of model parameters.

9.3.7 Case F

Limiting values of the ranges for horizontal and vertical permeability ([55-60 mD] and [9-12 mD] derived from single-phase analysis) are taken as initial-guess values. Everything else about this case remains the same as in Case E. Inversions are performed for all parameters. Results are shown for two cases. Case F1 uses initial-guess values of 55 mD and 9 mD for the horizontal and vertical permeability, respectively. Initial-guess values for other model parameters are the same as in Cases E2 and E3. Multi-physics measurements are contaminated with 1% noise. Actual, inverted, and initial-guess values for all model parameters are shown in Table 9.6. In Case F2, initial-guess values of horizontal and vertical permeability are changed to 60 mD and 12 mD, respectively. Initial-guess values for other model parameters remain the same as in Case F1. Multi-physics measurements are contaminated with 3% noise. Table 9.6 also displays the actual, inverted, and initial-guess values for all model parameters. Inversion results indicate satisfactory reconstructions of model parameters associated with relative permeability and capillary pressure curves under the deleterious influence of measurement noise. A slight improvement is obtained for the values of horizontal and vertical permeability compared to previous inversions. Inversion results for Case F are

also displayed in Figure 9.17 along with actual and initial-guess values of model parameters.

9.3.8 Case G: Sensitivity of Inversion Results with Respect to the Uncertainty in Fluid Viscosity Values

For the inversion studies described above, we assume that the viscosities of the aqueous and oleic phases (denoted by μ_w and μ_o, respectively) are a-priori known. In Case G, we relax this assumption by introducing perturbations to the true viscosity ratio, $\mu_o/\mu_w = 0.28$. This is accomplished by keeping the value of the aqueous phase viscosity constant and making perturbations to the value of the oleic phase viscosity. We select the measurement and inversion model characteristics of Case C3 as the base case. Therefore, in this inversion-based sensitivity study, we work with measurements contaminated with 1% random Gaussian noise. Table 9.7 displays the actual, inverted, and initial-guess values for all model parameters. Case G1 encompasses the base case where the inversion is performed using true values of fluid viscosities, hence, using the true viscosity ratio. Inversions are also performed with perturbed viscosity ratio values of 0.39, 0.59, and 0.78. Inversion results for these cases are reported in Cases G2, G3, and G4 of Table 9.7, respectively. Consistent with our expectations, the inversion case with the unperturbed viscosity ratio value (Case G1) yields a relatively accurate reconstruction of inverted model parameters. As an interesting outcome, the reconstruction of the values of model parameters still remains acceptable for perturbed viscosity ratio values of 0.39 (Case G2) and 0.59 (Case G3). However, the accuracy of the inverted model parameters significantly breaks down for values of viscosity ratio larger than 0.59.

We would like to point out that in the investigated perturbed cases, we assume that the model parameters that govern the capillary pressure function, namely, pore size distribution index and capillary entry pressure are known a-priori. In addition to the described sensitivity study, we performed extensive inversions under the influence of a perturbation to the fluid viscosity ratio. Inaccurate results were consistently obtained for

perturbed viscosity ratio inversions where capillary pressure model parameters are included in the simultaneous inversion together with the remaining model parameters. These inversions helped us reach the following conclusion: For cases where knowledge of fluid viscosities involves large uncertainty, accuracy of the inverted model parameters is constrained by information about the governing parameters of the capillary pressure saturation function. Inversion results for Case G are also displayed in Figure 9.18 along with actual and initial-guess values of model parameters.

9.3.9 Cramer-Rao Error Bounds

Table 9.8 shows Cramer-Rao uncertainty bounds for cases where the measurements input to the inversion are contaminated with zero-mean Gaussian random noise. The underlying theory of Cramer-Rao uncertainty bounds assumes that the measurement noise (misfit error) is uncorrelated and exhibits a uniform standard deviation. Therefore, noise-free inversion cases and inversion cases with biased noise, [in other words, inversion cases that make use of (inaccurately estimated) stipulated petrophysical parameters such as Case E], are not considered in the analysis. For all of the investigated cases, uncertainty bounds remain sufficiently small. This result indicates that the multi-physics approach introduced in this chapter successfully constrains the stability and non-uniqueness of the inversion.

9.4 Discussion of the Inversion Results

Within the context of numerical examples, we considered the use of multi-physics inversion to design an optimal data-acquisition schedule for the interpretation of formation tester measurements. In order for the multi-physics inversion algorithm to yield physically consistent reconstructions, the measurements must exhibit sufficient sensitivity to model parameters. A multi-pulse rate-schedule, presence of salt production rate information, and a sufficiently-long time sampling interval are essential for the accurate simultaneous reconstruction of all the model parameters. For water-based mud-

filtrate invasion, insufficient sampling of the saturation front significantly compromises the ability of the inversion to estimate the relative permeability end-point for the oleic phase.

Although not explored in this work, the multi-physics inversion approach can also be utilized to enhance the information content of electromagnetic induction logging measurements with respect to flow-related petrophysical properties of rock formations. Specifically, the number of induction frequencies or receivers can be chosen to provide selective deepening of the zone of response, and hence to improve the detection and assessment of the spatial distribution of fluid phase saturation. In turn, redundancy of electromagnetic data may further contribute to the accurate reconstruction of petrophysical model parameters. Future inversion-based sensitivity studies remain to be conducted for the near-borehole imaging of fluid saturation as a time function of multi-phase flow.

In most of the investigated cases, the WRGN minimization algorithm reached a reliable solution (neighborhood of global minimum) without resorting to SPSA-based helper methods. Nonetheless, the positive impact of SPSA-based helper methods on the inversion results emerged for Cases D2 and F2. For these cases the level of random Gaussian noise contamination was relatively larger (3%) in comparison to the noise contamination in remaining cases of inversion.

9.5 SUMMARY AND CONCLUDING REMARKS

We formulated and implemented a robust and accurate hybrid optimization algorithm for the simultaneous inversion of anisotropic formation permeabilities and parametric forms of relative permeability and capillary pressure curves. The hybrid inversion algorithm allows a two-way coupling between the (global) Simultaneous Perturbation Stochastic Approximation (SPSA) technique, and the (local) Weighted and Regularized Gauss-Newton (WRGN) technique.

The proof-of-concept inversion exercises considered in this work consistently show the added value of the multi-physics approach for the quantitative integration of several types of measurements into a two-phase fluid model of petrophysical variables. Multi-physics measurements successfully reduce non-uniqueness of the inversion. This conclusion is quantitatively supported by the Cramer-Rao uncertainty bounds computed subsequent to our inversions.

Use of multi-physics measurements within the hybrid optimization framework makes it possible to efficiently and stably approach the highly nonlinear inverse problem of simultaneously estimating anisotropic permeabilities and saturation functions of relative permeability and capillary pressure. However, the accuracy of the simultaneous inversion approach is subject to the availability of a-priori information about parameters that govern the capillary pressure function. Accurate reconstructions of anisotropic permeabilities, and parametric relative permeability and capillary pressure curves are obtained from synthetic multi-physics measurements contaminated with random Gaussian noise. For cases where knowledge of the fluid viscosities involves large uncertainty, accuracy of the inverted model parameters is constrained by information about the governing parameters of the capillary pressure saturation function.

A sequential inversion workflow was developed to approach estimation problems where formation tester and induction logging measurements lack the necessary degrees of freedom to simultaneously estimate all of the petrophysical model parameters. A single-phase pre-processing of late time multi-probe transient formation pressure measurements provides a closer starting point for the multi-physics inversion of horizontal and vertical permeabilities. This approach is efficient and accurate with conventional rate-pulse schedules and in the presence of noisy measurements.

Robustness of the multi-physics inversion with respect to end-point saturations can only be achieved with array induction measurements. This conclusion comes as the

result of extensive inversion practice performed with various combinations of measurement types.

Currently, the only undesirable feature of the developed simultaneous multi-physics inversion approach is the requirement of expert-mode input when all of the model parameters are estimated in the presence of noisy measurements. Careful adjustment of measurement and regularization weights is necessary to obtain accurate inversion results.

The parametric formulation of the multi-physics inversion problem allows one to use a relatively small number of model parameters. Moreover, when the initial-guess model is sufficiently close to the (global) minimum, the Weighted and Regularized Gauss-Newton search direction (or WRGN technique) provides rapid convergence. For the investigated problems, WRGN-based inversions required a maximum of 15 to 20 Gauss-Newton iterations to achieve convergence. However, the computation time required by the inversions increased 3 to 5 fold when a SPSA-based helper algorithm was activated together with the WRGN approach.

Table 9.1: Summary of geometrical, petrophysical, and fluid parameters for the single-layer anisotropic formation model.

Variable	Units	Values
Mudcake permeability	[mD]	0.01
Mudcake porosity	[fraction]	0.40
Mud solid fraction	[fraction]	0.50
Mudcake maximum thickness	[in]	1.00
Formation porosity	[fraction]	0.12
Formation rock compressibility	[psi^{-1}]	5.00e-09
Aqueous phase viscosity (mud-filtrate)	[cp]	1.274
Aqueous phase density (mud-filtrate)	[lbm/cuft]	62.495
Aqueous phase formation volume factor (mud-filtrate)	[rbbl/stb]	0.996
Aqueous phase compressibility (mud-filtrate)	[psi^{-1}]	2.55e-06
Oleic phase viscosity	[cp]	0.355
Oleic phase API density	[°API]	42
Oleic phase density	[lbm/cuft]	50.914
Oleic phase formation volume factor	[rbbl/stb]	1.471
Oleic phase compressibility	[psi^{-1}]	1.904e-05
Fluid density contrast	[lbm/cuft]	11.581
Viscosity ratio (water-to-oil)	[dimensionless]	3.589
Formation pressure (formation top is the reference depth)	[psia]	3000.00
Mud hydrostatic pressure	[psia]	3600.00
Wellbore radius	[ft]	0.354
Formation outer boundary location	[ft]	984.252
Formation bed thickness	[ft]	30.00
Relative depth of the top impermeable shoulder	[ft]	0.00
Relative depth of the bottom impermeable shoulder	[ft]	30.00
Mud-filtrate invasion duration	[days]	6.00 [Cases A, B, C, D, and G], 3.00 [Cases E and F]
Integral-averaged mud-filtrate invasion rate	[rbbl/d]	1.8
Integral-averaged mud-filtrate invasion velocity	[ft^3/s]	1.170e-04
Second logging time ($t_{second\ log}$)	[days]	3.208
Formation temperature	[°F]	220
Formation brine salinity	[ppm]	120000
Mud-filtrate salinity	[ppm]	5000
a-constant in the Archie's equation	[dimensionless]	1.00
m-cementation exponent in the Archie's equation	[dimensionless]	2.00
n-water saturation exponent in the Archie's equation	[dimensionless]	2.00
Mud conductivity	[mS/m]	2631.58
Upper and lower shoulder bed conductivities	[mS/m]	1000.00
Logging interval	[ft]	0.25
3ft interval sealed by the dual-packer (DP) module	[ft]	18.50-21.50
Location of the first observation probe	[ft]	5.00
Location of the second observation probe	[ft]	13.00
Location of the pressure measurement conducted by DP module	[ft]	20.00

Table 9.2: Petrophysical inversion results for the anisotropic formation model. Modified Brooks-Corey functions are used to represent two-phase relative permeability and capillary pressure curves. Noise-free, synthetically generated measurements are input to the inversion. Results are reported for Cases A1, A2, B1, and B2, respectively.

Variable	Units	Actual val.	Initial-guess val.	Inverted val.			
Initial water saturation (= Irreducible water saturation)	[fraction]	0.30	0.10	0.30	0.30	0.30	0.30
Residual oil saturation	[fraction]	0.20	0.10	0.20	0.20	0.20	0.20
End-point relative permeability for aqueous phase	[fraction]	0.20	0.50	0.12	0.13	0.19	0.21
End-point relative permeability for oleic phase	[fraction]	0.80	0.50	0.22	0.47	0.72	0.79
Pore size distribution index	[dimensionless]	2.00	2.50	N/A	1.95	N/A	2.01
Capillary entry pressure	[psi]	1.00	1.50	N/A	0.98	N/A	1.03
Formation horizontal permeability	[mD]	50.00	100.00	109.81	79.32	54.68	49.20
Formation vertical permeability	[mD]	10.00	50.00	84.27	14.75	10.66	9.61

Table 9.3: Petrophysical inversion results for the anisotropic formation model. Modified Brooks-Corey functions are used to represent two-phase relative permeability and capillary pressure curves. Synthetically generated measurements are contaminated with 1% random Gaussian noise. Inversion results are reported for Cases C1, C2, and C3, respectively.

Variable	Units	Actual val.	Initial-guess val.	Inverted val.		
Initial water saturation (= Irreducible water saturation)	[fraction]	0.30	0.10	0.30	0.30	0.30
Residual oil saturation	[fraction]	0.20	0.10	0.20	0.20	0.20
End-point relative permeability for aqueous phase	[fraction]	0.20	0.50	0.13	0.18	0.21
End-point relative permeability for oleic phase	[fraction]	0.80	0.50	0.51	0.68	0.83
Pore size distribution index	[dimensionless]	2.00	2.50	2.24	N/A	N/A
Capillary entry pressure	[psi]	1.00	1.50	1.22	N/A	N/A
Formation horizontal permeability	[mD]	50.00	100.00	78.19	58.21	48.00
Formation vertical permeability	[mD]	10.00	50.00	15.17	11.33	9.63

Table 9.4: Petrophysical inversion results for the anisotropic formation model. Modified Brooks-Corey functions are used to represent two-phase relative permeability and capillary pressure curves. Synthetically generated measurements are contaminated with 1% and 3% random Gaussian noise. Inversion results are reported for Cases D1 (1% noise) and D2 (3% noise), respectively. An italic font is used to identify values of stipulated petrophysical parameters.

Variable	Units	Actual val.	Initial-guess val.	Inverted val.	
Initial water saturation (= Irreducible water saturation)	[fraction]	0.30	0.10	0.30	0.30
Residual oil saturation	[fraction]	0.20	0.10	0.20	0.20
End-point relative permeability for aqueous phase	[fraction]	0.20	0.50	0.20	0.20
End-point relative permeability for oleic phase	[fraction]	0.80	0.50	0.80	0.80
Pore size distribution index	[dimensionless]	2.00	4.00	2.02	1.98
Capillary entry pressure	[psi]	1.00	2.00	0.99	0.97
Formation horizontal permeability	[mD]	50.00	*50.00*	N/A	N/A
Formation vertical permeability	[mD]	10.00	*10.00*	N/A	N/A

Table 9.5: Petrophysical inversion results for the anisotropic formation model. Modified Brooks-Corey functions are used to represent two-phase relative permeability and capillary pressure curves. Synthetically generated measurements are contaminated with 1% random Gaussian noise. Inversion results are reported for Cases E1, E2, and E3, respectively. An italic font is used to identify values of stipulated petrophysical parameters.

Variable	Units	Actual val.	Initial-guess val.			Inverted val.		
Initial water saturation (= Irreducible water saturation)	[fraction]	0.30	0.10	0.10	0.10	0.30	0.30	0.30
Residual oil saturation	[fraction]	0.20	0.10	0.10	0.10	0.20	0.19	0.20
End-point relative permeability for aqueous phase	[fraction]	0.20	0.50	0.50	0.50	0.16	0.19	0.17
End-point relative permeability for oleic phase	[fraction]	0.80	0.50	0.50	0.50	0.65	0.70	0.67
Pore size distribution index	[dimensionless]	2.00	2.50	4.00	4.00	1.93	2.48	2.00
Capillary entry pressure	[psi]	1.00	1.50	2.00	2.00	0.91	1.45	0.98
Formation horizontal permeability	[mD]	50.00	100.00	*55.00*	*60.00*	61.71	N/A	N/A
Formation vertical permeability	[mD]	10.00	50.00	*9.00*	*12.00*	12.41	N/A	N/A

Table 9.6: Petrophysical inversion results for the anisotropic formation model. Modified Brooks-Corey functions are used to represent two-phase relative permeability and capillary pressure curves. Synthetically generated measurements are contaminated with 1% and 3% random Gaussian noise. Inversion results are reported for Cases F1 (1% noise) and F2 (3% noise), respectively.

Variable	Units	Actual val.	Initial-guess val.		Inverted val.	
Initial water saturation (= Irreducible water saturation)	[fraction]	0.30	0.10	0.10	0.30	0.30
Residual oil saturation	[fraction]	0.20	0.10	0.10	0.19	0.20
End-point relative permeability for aqueous phase	[fraction]	0.20	0.50	0.50	0.21	0.17
End-point relative permeability for oleic phase	[fraction]	0.80	0.50	0.50	0.85	0.69
Pore size distribution index	[dimensionless]	2.00	4.00	4.00	2.68	2.05
Capillary entry pressure	[psi]	1.00	2.00	2.00	1.54	1.06
Formation horizontal permeability	[mD]	50.00	55.00	60.00	46.57	58.02
Formation vertical permeability	[mD]	10.00	9.00	12.00	8.86	11.48

Table 9.7: Petrophysical inversion results for the anisotropic formation model. Modified Brooks-Corey functions are used to represent two-phase relative permeability and capillary pressure curves. Synthetically generated measurements are contaminated with 1% random Gaussian noise. Inversion results are reported for Cases G1 (μ_o/μ_w = 0.28), G2 (μ_o/μ_w = 0.39), G3 (μ_o/μ_w = 0.59), and G4 (μ_o/μ_w = 0.78), respectively.

Variable	Units	Actual val.	Initial-guess val.	Inverted val.			
Initial water saturation (= Irreducible water saturation)	[fraction]	0.30	0.10	0.30	0.30	0.30	0.30
Residual oil saturation	[fraction]	0.20	0.10	0.20	0.20	0.19	0.20
End-point relative permeability for aqueous phase	[fraction]	0.20	0.50	0.21	0.18	0.26	0.08
End-point relative permeability for oleic phase	[fraction]	0.80	0.50	0.83	0.99	0.97	0.84
Pore size distribution index	[dimensionless]	2.00	N/A	N/A	N/A	N/A	N/A
Capillary entry pressure	[psi]	1.00	N/A	N/A	N/A	N/A	N/A
Formation horizontal permeability	[mD]	50.00	100.00	48.00	56.76	44.39	109.80
Formation vertical permeability	[mD]	10.00	10.00	9.63	11.51	4.62	25.24

Table 9.8: Cramer-Rao uncertainty bounds for cases where measurements are contaminated with zero-mean Gaussian random noise. The underlying theory of Cramer-Rao bounds assumes uncorrelated measurement noise (misfit error) with uniform standard deviation. Therefore, noise-free inversion cases and inversion cases with systematic errors [i.e., inversion cases that make use of (inaccurately estimated) stipulated petrophysical parameters such as Case E] are not considered in the analysis.

Variable		**Case C1**	**Case C2**	**Case C3**	**Case D1**	**Case D2**
Irreducible water saturation	[fraction]	3.74e-05	4.34e-05	3.71e-05	6.04e-05	1.82e-04
Residual oil saturation	[fraction]	2.99e-04	6.05e-04	2.32e-04	3.16e-04	9.18e-04
End-point relative permeability for aqueous phase	[fraction]	3.65e-03	1.98e-02	6.07e-03	2.67e-04	8.09e-04
End-point relative permeability for oleic phase	[fraction]	1.31e-02	6.75e-02	2.21e-02	6.61e-04	2.04e-03
Pore size distribution index	[dimensionless]	2.20e-02	N/A	N/A	1.89e-02	4.63e-02
Capillary entry pressure	[psi]	2.25e-02	N/A	N/A	1.28e-02	3.33e-02
Formation horizontal permeability	[mD]	1.02	1.09	1.03	N/A	N/A
Formation vertical permeability	[mD]	1.03	1.08	1.03	N/A	N/A
Variable		**Case F1**	**Case F2**	**-**	**-**	**-**
Irreducible water saturation	[fraction]	6.48e-05	1.84e-04	-	-	-
Residual oil saturation	[fraction]	3.21e-04	9.91e-04	-	-	-
End-point relative permeability for aqueous phase	[fraction]	2.06e-03	1.27e-02	-	-	-
End-point relative permeability for oleic phase	[fraction]	7.82e-03	4.41e-02	-	-	-
Pore size distribution index	[dimensionless]	1.19e-02	4.63e-02	-	-	-
Capillary entry pressure	[psi]	1.46e-02	3.48e-02	-	-	-
Formation horizontal permeability	[mD]	1.01	1.07	-	-	-
Formation vertical permeability	[mD]	1.01	1.06	-	-	-

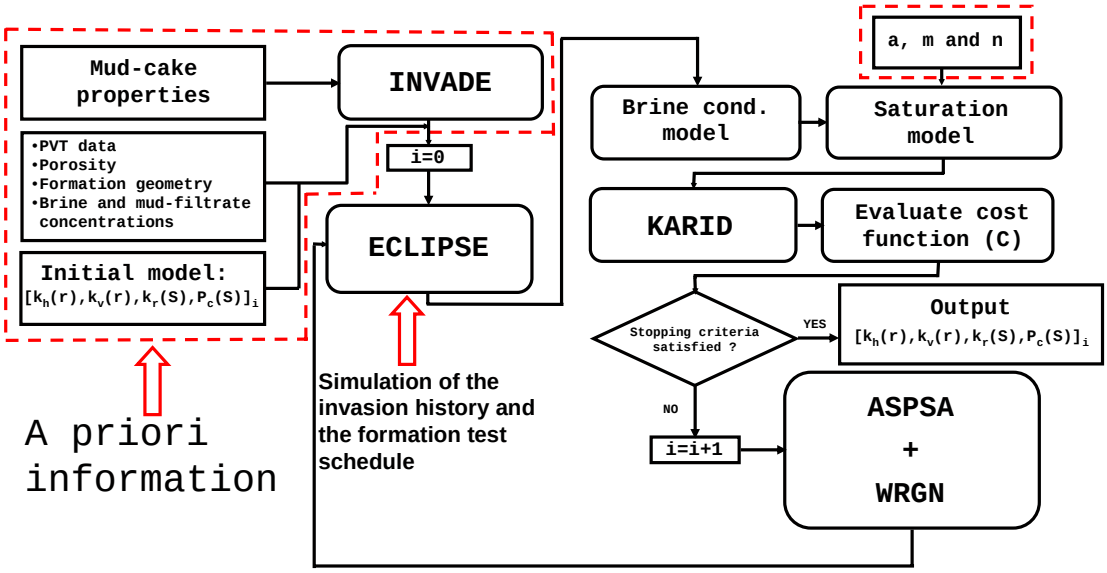

Figure 9.1: Flowchart describing the various components of the multi-physics inversion algorithm described in this chapter.

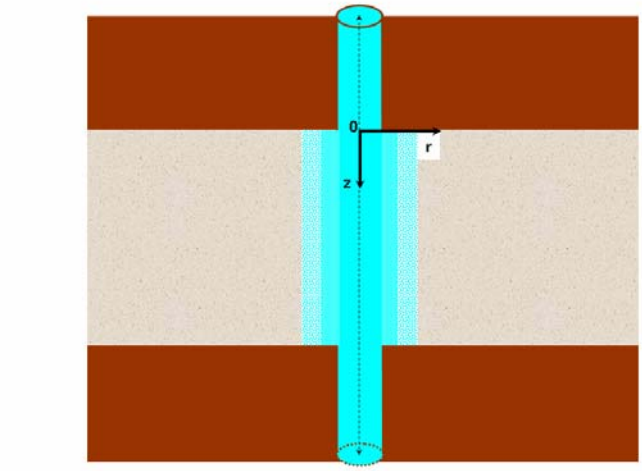

Figure 9.2: Graphical description of a single-layer rock formation model subject to water-based mud-filtrate invasion.

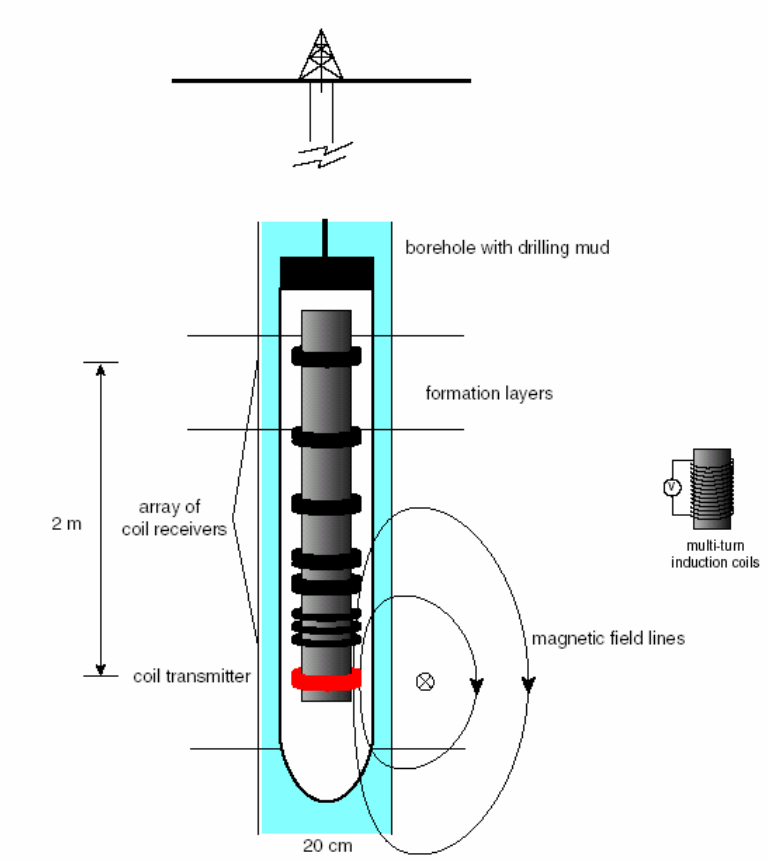

Figure 9.3: Induction logging with AIT™: A multi-turn coil supporting a time-varying current generates a magnetic field that induces electrical currents in the formation. An array of receiver coils measures the magnetic field of the source and the secondary currents (Hunka et al., 1990).

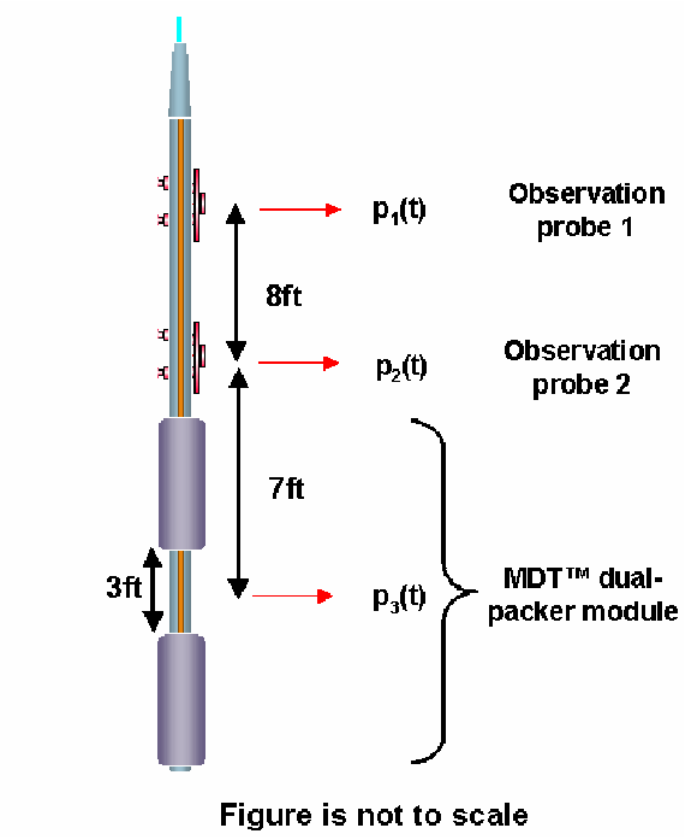

Figure 9.4: Schematic of MDT™ multi-probe wireline tester packer/probe modules. The dual-packer module is combined with two vertical observation probes. Transient-pressure measurements are acquired at three vertical locations in response to rate schedules imposed by a downhole pump. Fluid flow takes place through the packer open interval.

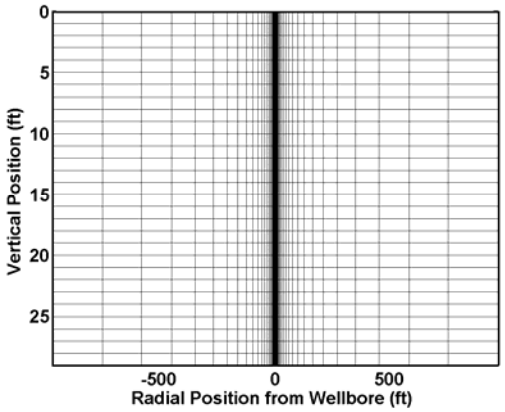

Figure 9.5: Two-dimensional vertical cross-section of the finite-difference grid used for fluid-flow simulations. The grid is constructed with a cylindrical coordinate frame and consists of 31x1x30 nodes in the radial, azimuthal, and vertical directions, respectively.

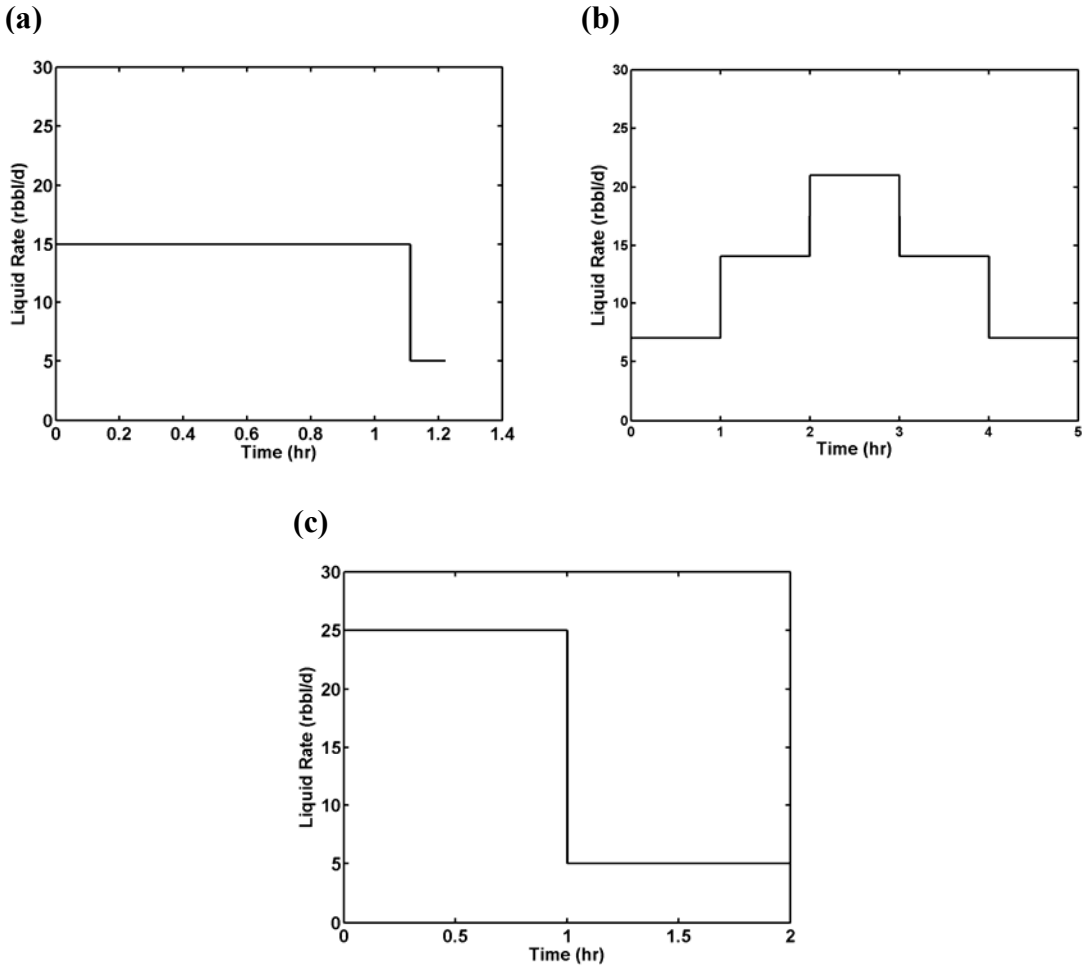

Figure 9.6: Time history of formation test flow rate (production pulse) for the various study cases considered in this chapter: (a) Case A; (b) Cases B, C, and G; (c) Cases D, E, and F.

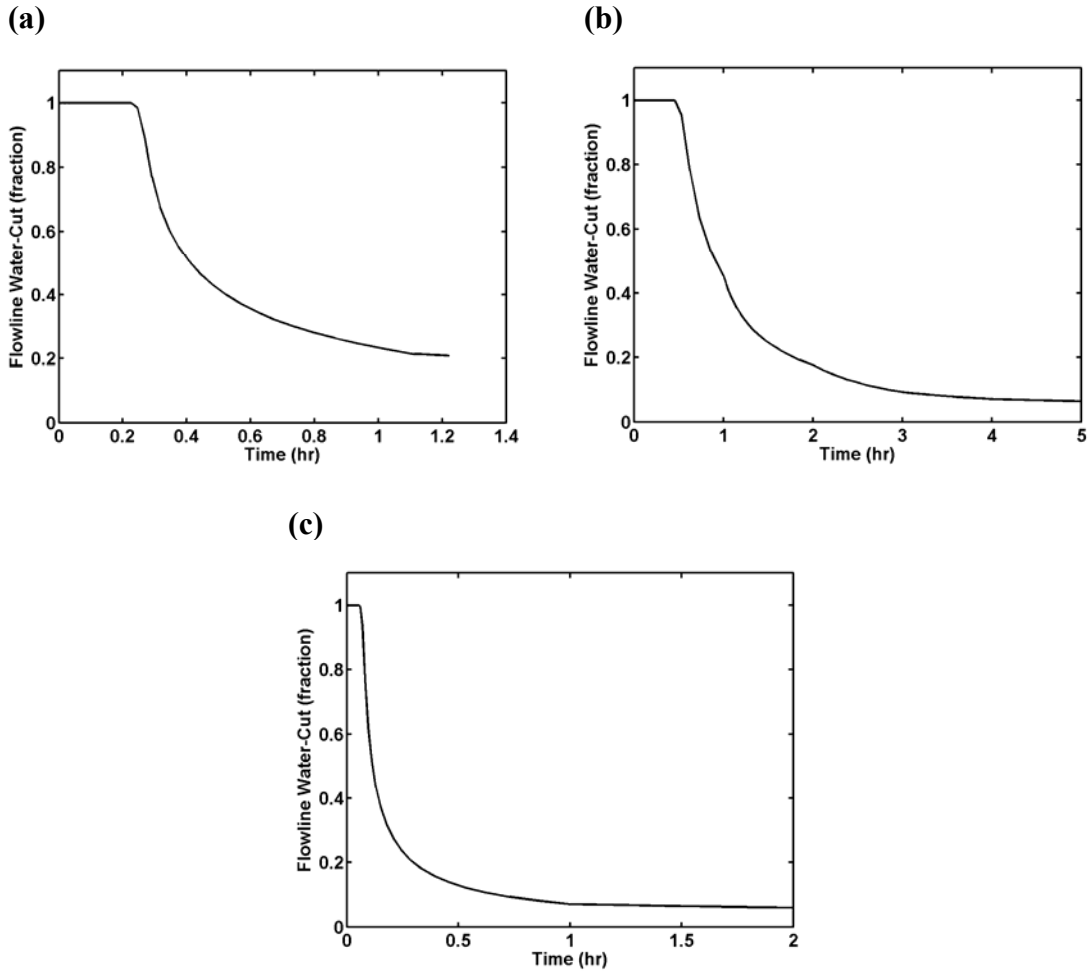

Figure 9.7: Water-cut measurements simulated for the acquisition of dual-packer measurements for the various study cases considered in this chapter: (a) Case A; (b) Cases B, C, and G; (c) Cases D, E, and F.

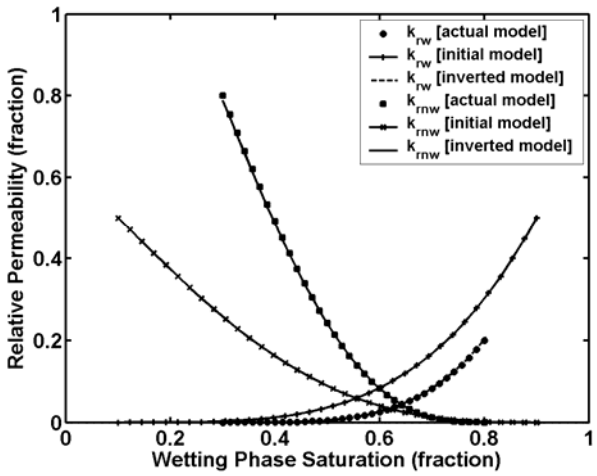

Figure 9.8: Reconstruction of the parametric two-phase relative permeability functions for Case B2.

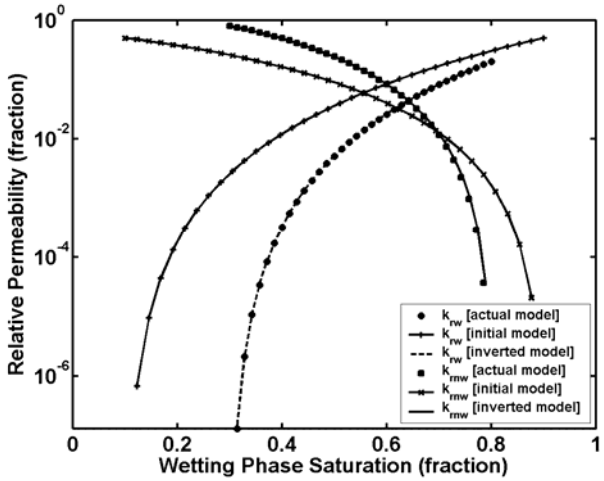

Figure 9.9: Reconstruction of the parametric two-phase relative permeability functions for Case B2. Relative permeability curves are plotted with a logarithmic scale.

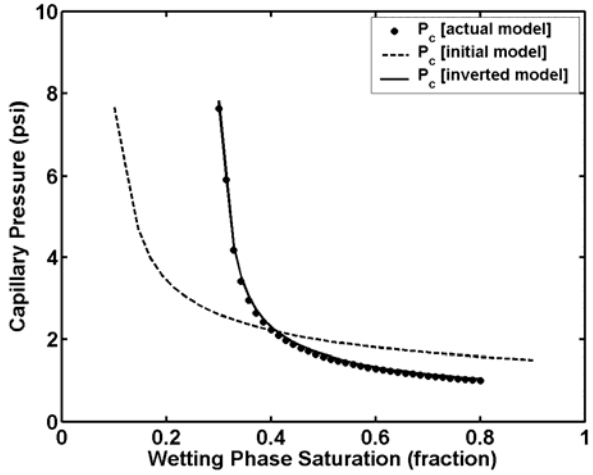

Figure 9.10: Reconstruction of the parametric capillary pressure function for Case B2.

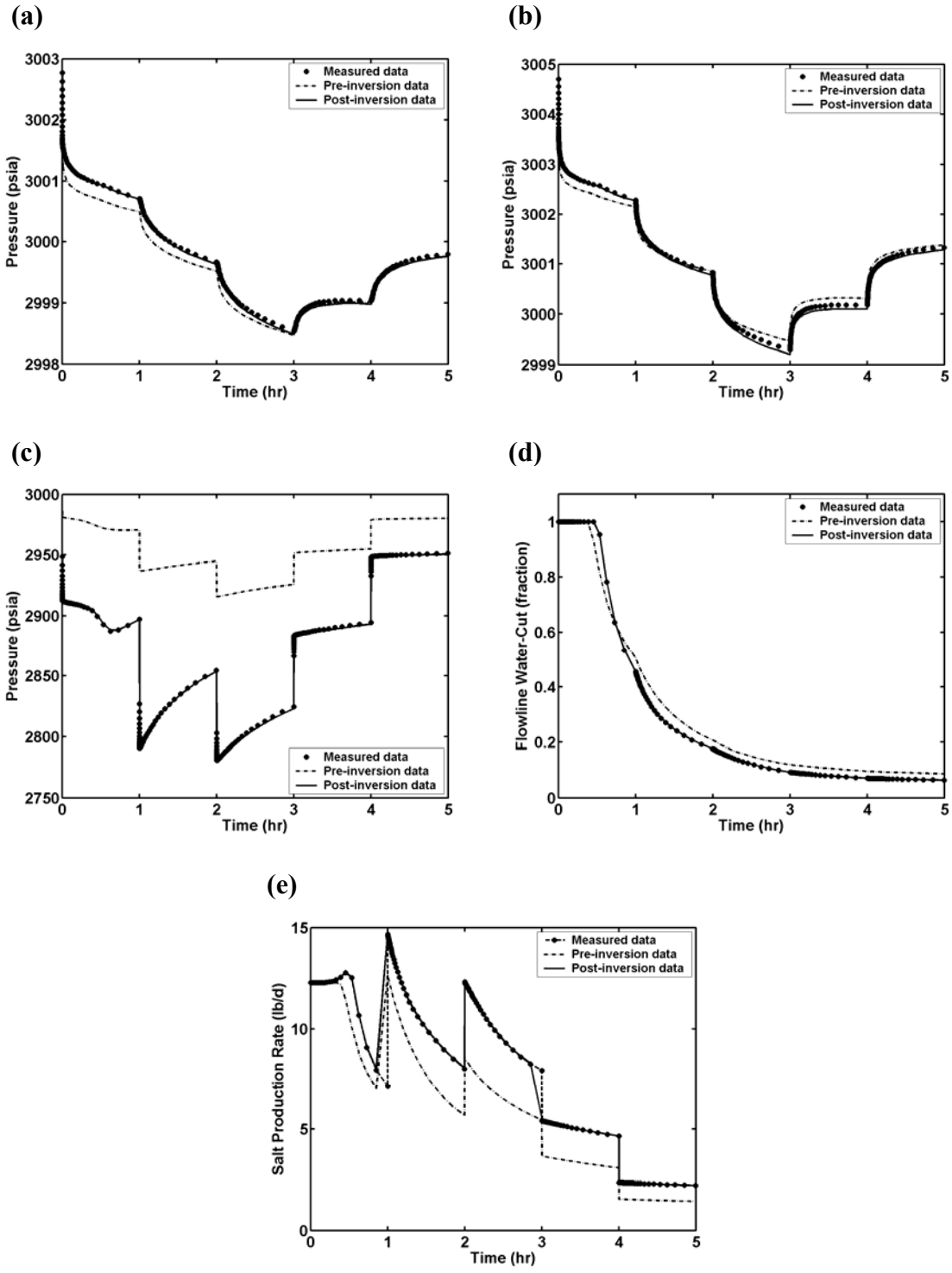

Figure 9.11: See caption on the following page.

Figure 9.11: Pre- and post-inversion data fits for transient-pressure measurements simulated for the acquisition by (a) the observation probe 1, (b) the observation probe 2, and (c) the dual-packer module. Panels (d) and (e) show pre- and post-inversion data fits for flowline water-cut and salt production rate measurements simulated for the acquisition by the dual-packer module. Data fits are shown for Case B2.

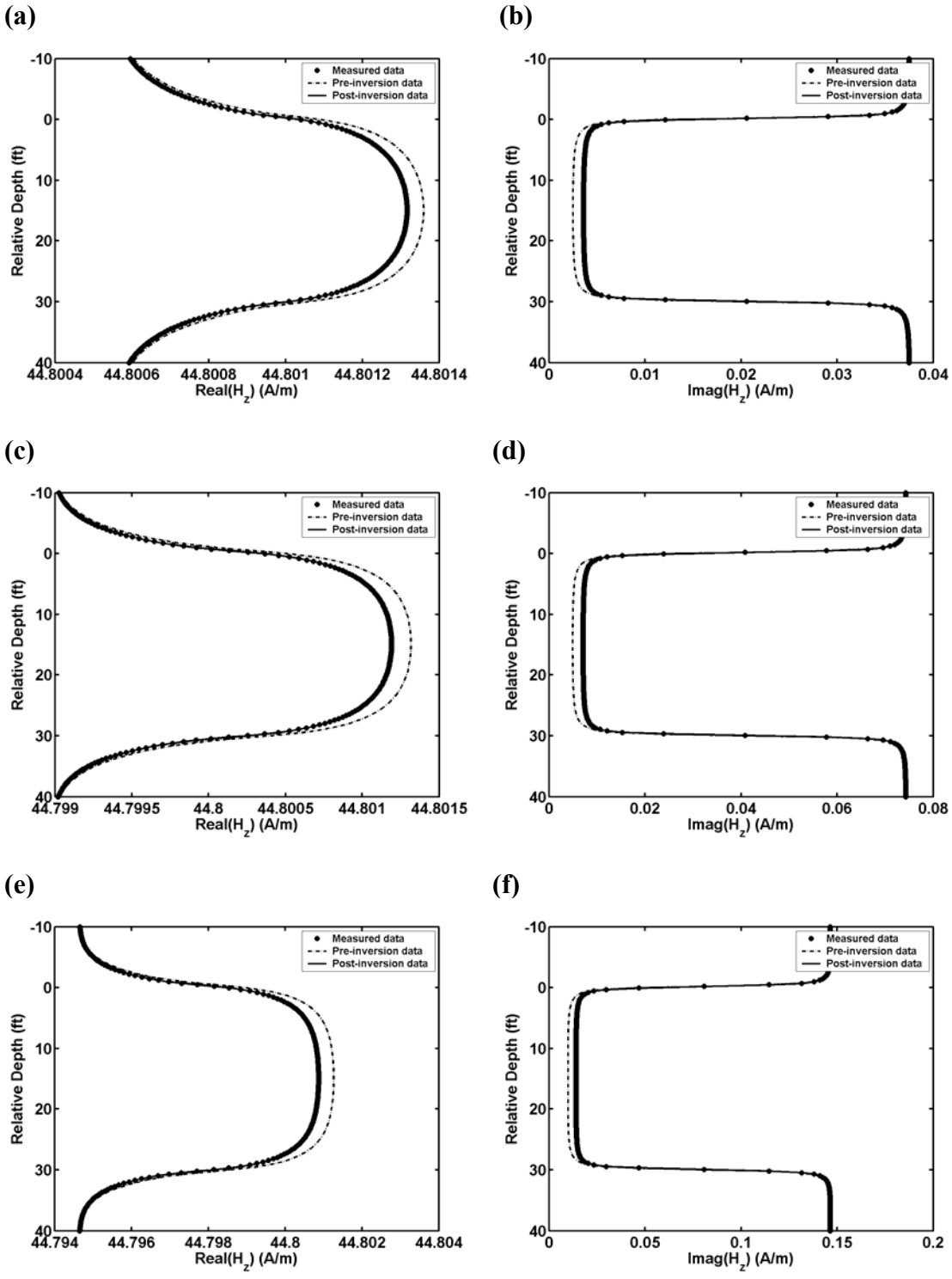

Figure 9.12: See caption on the following page.

Figure 9.12: Pre- and post-inversion data fits for electromagnetic induction logging measurements. Electromagnetic data are shown only for one receiver location for 3 frequencies: ~25 kHz in panels (a) and (b), ~50 kHz in frames (c) and (d), and ~100 kHz in panels (e) and (f). Complex-valued primary-field data are used to perform the inversions described in this chapter. Data fits are shown for Case B2.

(a)

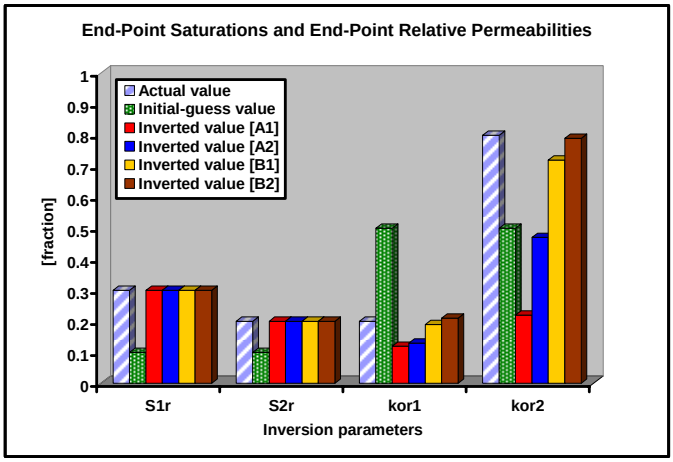

(b)

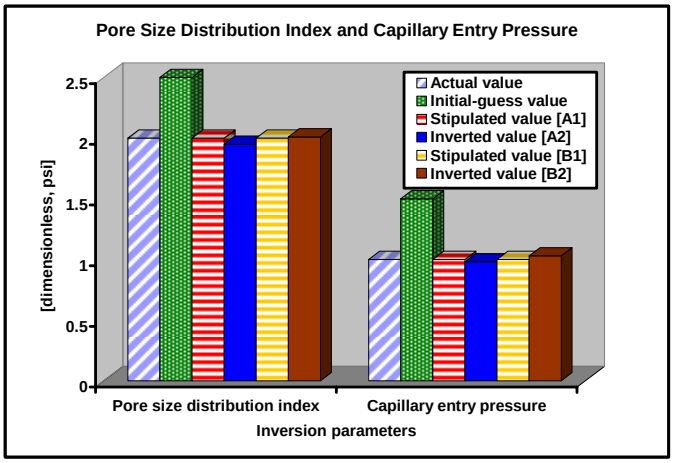

(c)

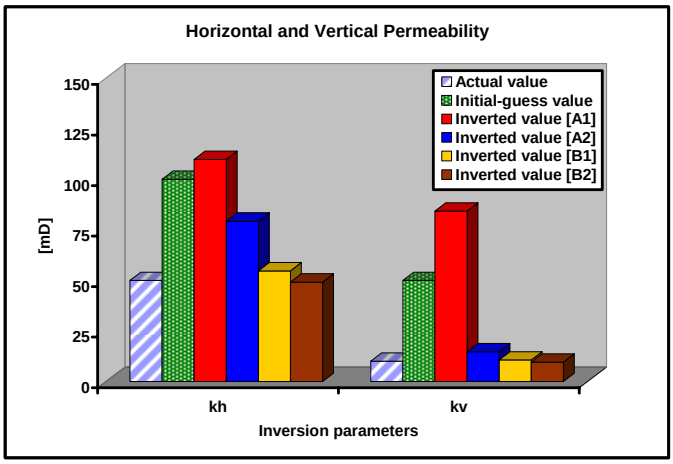

Figure 9.13: Inversion results for Cases A and B.

(a)

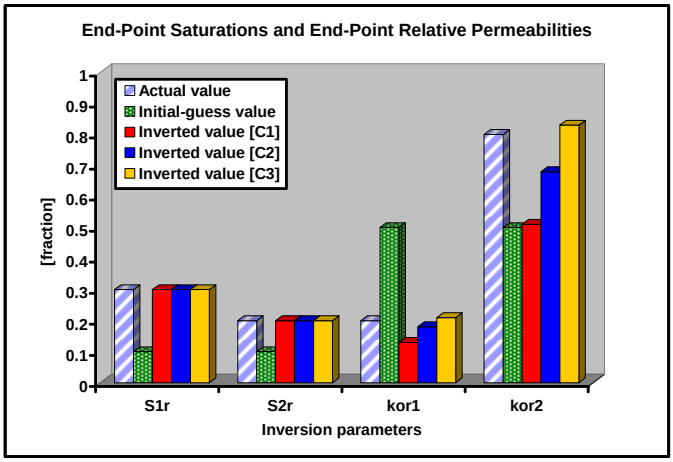

(b)

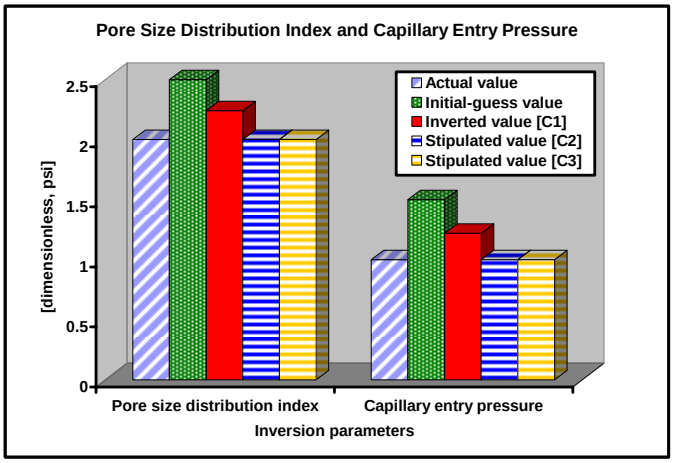

(c)

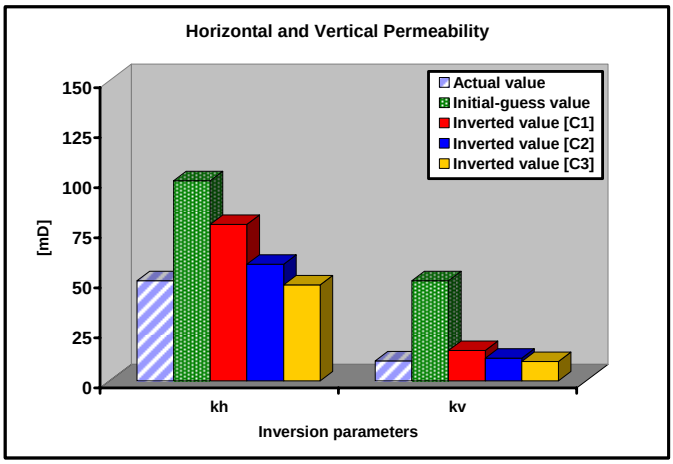

Figure 9.14: Inversion results for Case C.

(a)

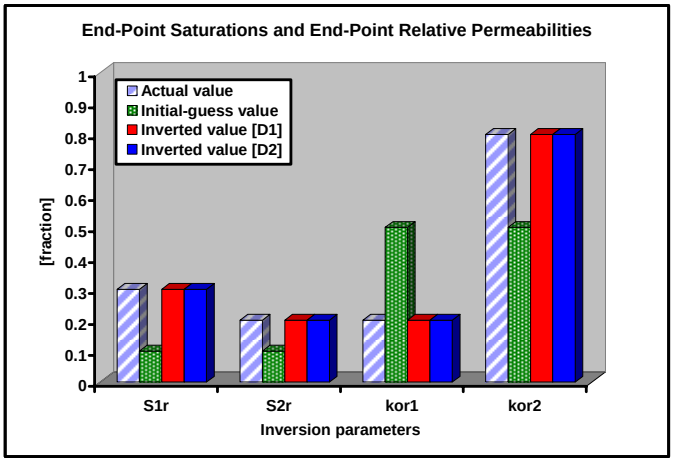

(b)

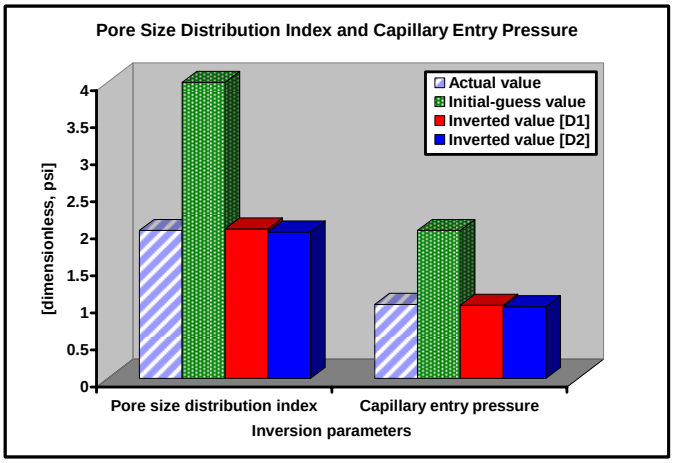

(c)

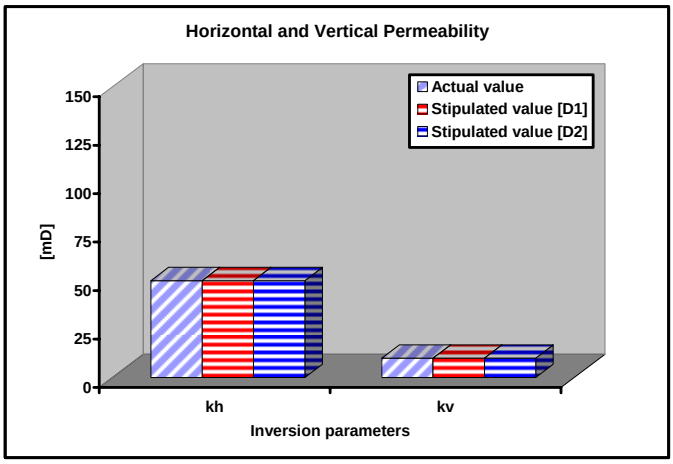

Figure 9.15: Inversion results for Case D.

(a)

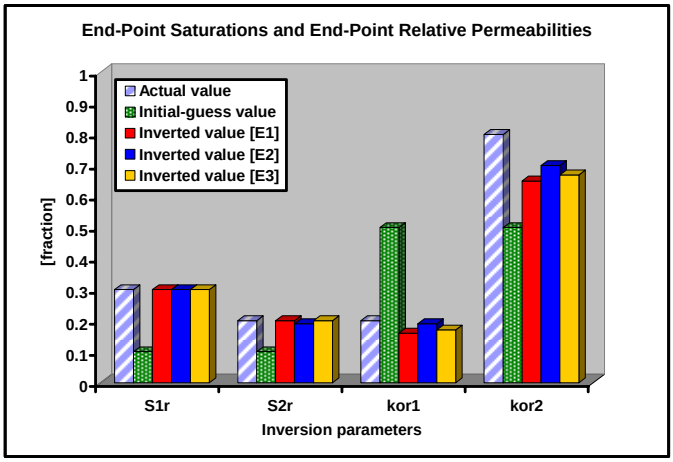

(b)

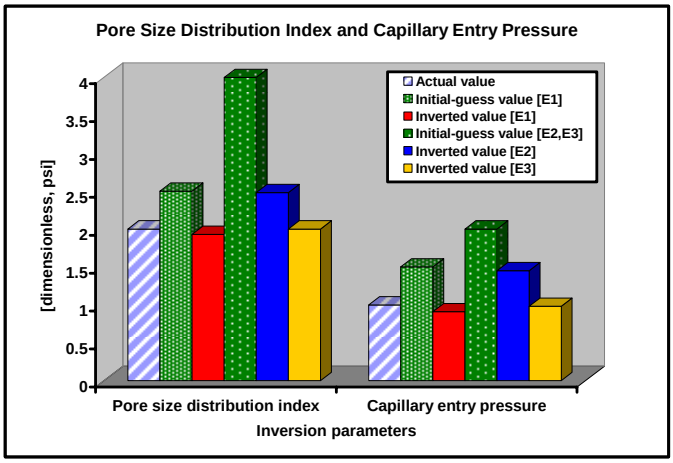

(c)

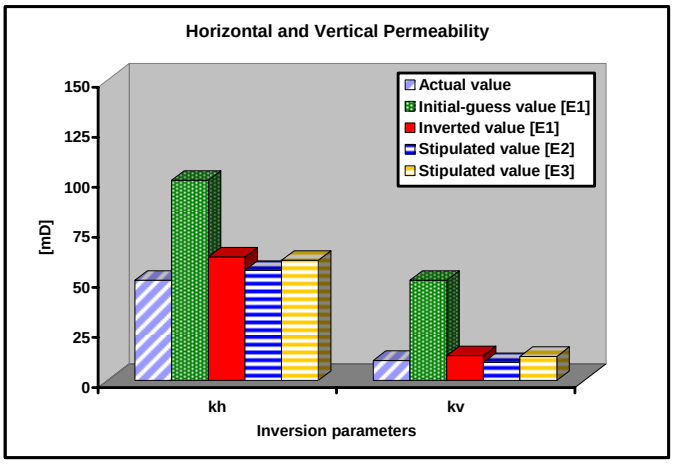

Figure 9.16: Inversion results for Case E.

(a)

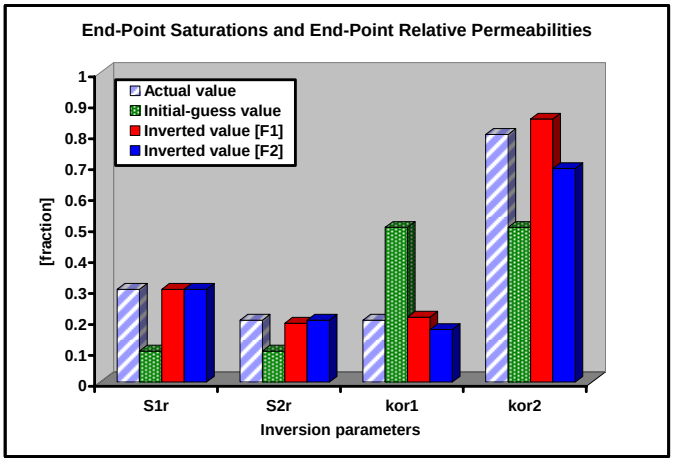

(b)

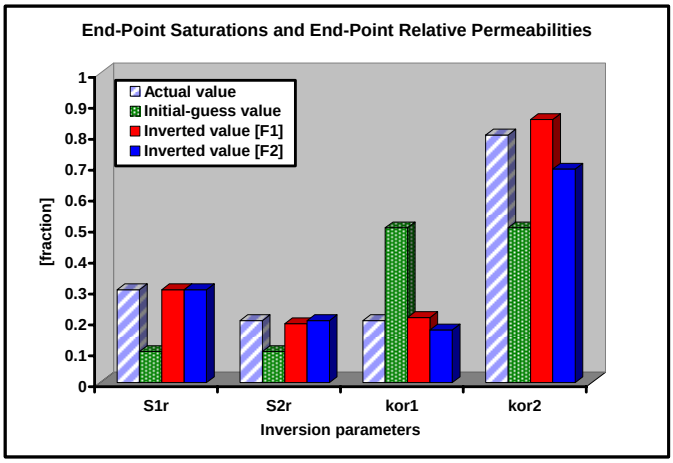

(c)

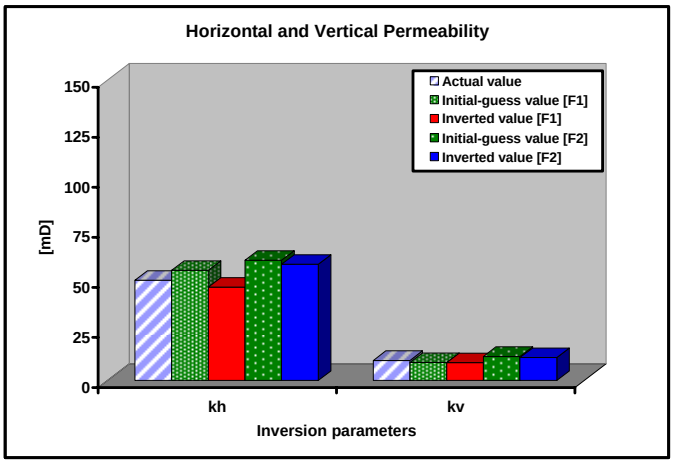

Figure 9.17: Inversion results for Case F.

(a)

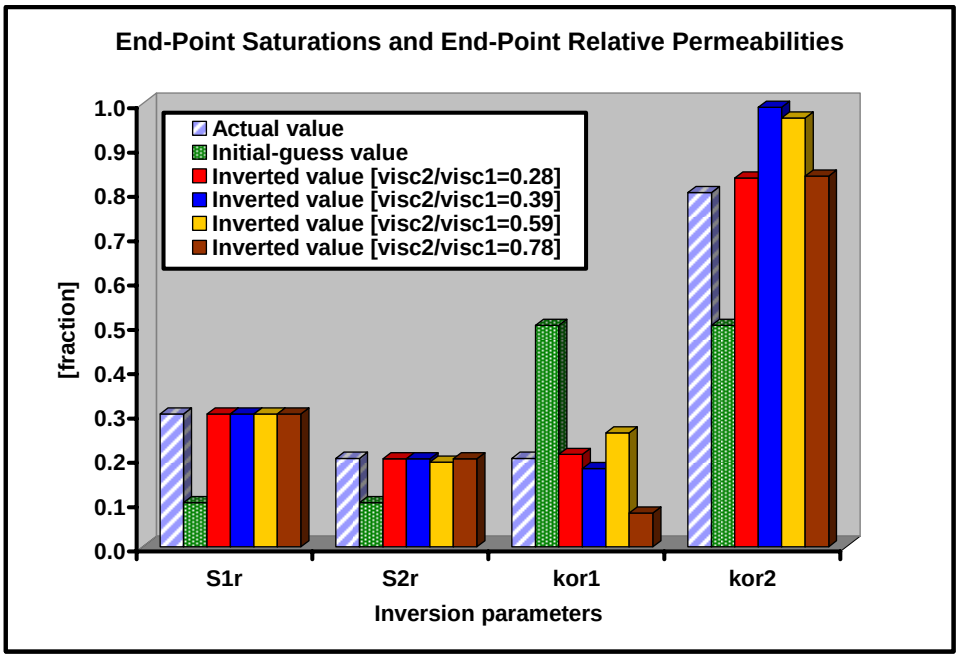

(b)

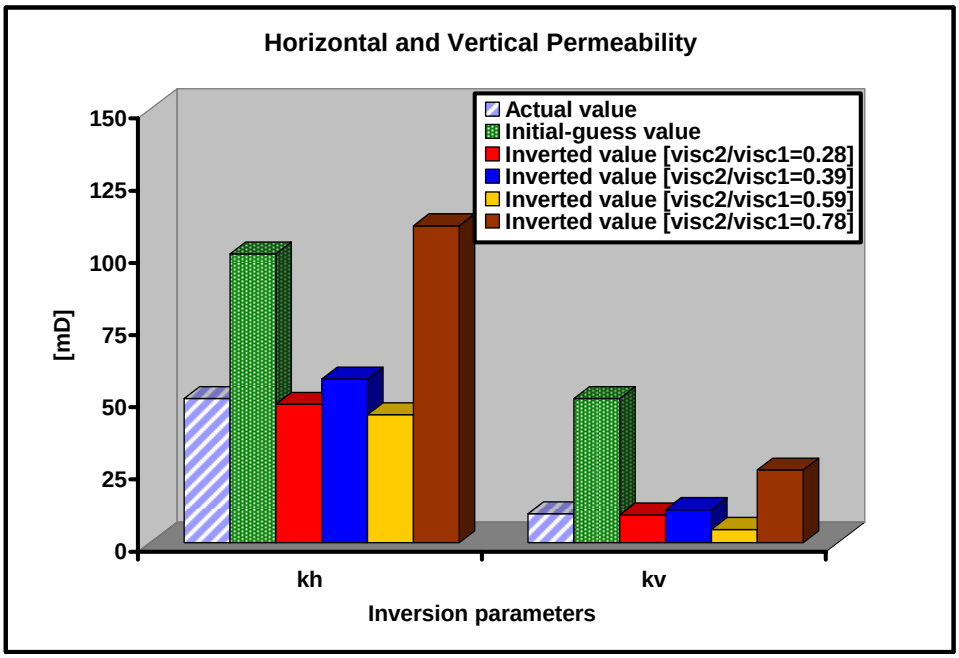

Figure 9.18: Inversion results for Case G.

Chapter 10: Summary, Conclusions, and Recommendations

The central objective of this dissertation is to develop a novel, efficient, accurate, and robust algorithm to quantitatively integrate borehole fluid-flow and electromagnetic measurements with rock and fluid properties in the estimation of petrophysical properties of hydrocarbon-bearing rock formations. From the mathematical point of view, this task embodies developments of robust numerical inversion algorithms as well as developments of accurate numerical solutions of partial differential equations governing the physics of the measurements. From the physical viewpoint, our workflow makes use of proof-of-concept numerical test cases and sensitivity studies. Emphasis is placed on applications of the petrophysical inversion framework to the quantitative interpretation of field data. In turn, validation studies are conducted using field data wherever available. Brief summaries of the primary aspects of the petrophysical modeling and inversion algorithms are presented in the first section of this chapter. Subsequent to these summaries, we itemize conclusions attained as a result of this dissertation work on a topical basis. In the final section of this chapter, taking the work presented in this dissertation as a point of reference, we propose avenues of further research.

10.1 SUMMARY

10.1.1 Summary of Developments on the Inversion Algorithms

A number of variants of Newton-type inversion techniques are formulated and implemented in this dissertation. Newton-type methods work efficiently for inversion applications where the number of inverted model parameters is limited which makes Newton-type techniques very desirable for parametric inversion algorithms. We formulate enhancements on the Newton-type inversion techniques using a family of nonlinear parameter transformations to impose physical bounds on the inverted model

parameters and an efficient line search procedure to accelerate the convergence. In turn, a robust and efficient algorithm based on the Weighted and Regularized Gauss-Newton (WRGN) technique was developed using an innovative multiplicative and a more conventional Tikhonov regularization approach. The formulation of the multiplicative regularization technique, originally developed for the gradient-based imaging algorithms, is extended and successfully applied to Newton-type parametric inversion algorithms.

We also describe a novel algorithm for nonlinear inversion that casts standard minimization procedures in the form of a cascade sequence of simpler, and hence, computationally more efficient, nonlinear inversions. In this work, we have chosen to construct simple nonlinear inversions using an approximate solution to the original forward problem. We propose the possibility of constructing an approximate forward problem by taking a subset of the finite-difference grid that is used to simulate the measurements. Other approximate forward problems could be used for the same purpose as long as they abide by the necessary requirements of convergence. On the other hand, the dual-grid approach proposed in this work is attractive because it allows great flexibility to adjust the degree of accuracy required to achieve a given rate of convergence.

In addition to the above described developments, we formulate and implement a robust and accurate hybrid optimization algorithm for inverse problems with potential multiple local minima. The hybrid inversion algorithm allows a two-way coupling between the (global) Simultaneous Perturbation Stochastic Approximation (SPSA) technique, and the (local) Weighted and Regularized Gauss-Newton (WRGN) technique.

10.1.2 Summary of Developments on the Modeling Algorithms

In this dissertation, we develop and validate a novel numerical algorithm for the simulation of axisymmetric single-phase fluid flow phenomena in porous and permeable

media. In this new algorithm, the two-dimensional parabolic partial differential equation for fluid flow is transformed into an explicit finite-difference operator problem. The latter is solved with an Extended Krylov Subspace Method (EKSM) constructed with both positive and inverse powers of the finite-difference operator. A significant advantage of the method of solution presented in this work is that simulations of pressure can be obtained at a multitude of times with practically the same efficiency as that of a single-time simulation. Moreover, the usage of inverse powers of the finite-difference operator provides a substantial increase in efficiency with respect to that of standard Krylov subspace methods. Tests of numerical performance with respect to analytical solutions for point and line sources validate the accuracy of the developed method of solution. We also validate the algorithm by making comparisons between analytical and numerical solutions in the Laplace transform domain. Additional tests of accuracy and efficiency are performed against a commercial simulator for spatially complex and anisotropic models of permeable media.

A rapid and accurate numerical model for the simulation of permanent electrode array responses is developed with the central purpose of inversion. The solution method is based on a semi-discrete numerical approach that combines the method of straight lines with an incomplete Galerkin formulation.

Forward modeling of dual-physics measurements entails coupled simulations of mud-filtrate invasion, wireline formation test measurements, and induction-logging measurements. We utilize efficient three-dimensional finite difference-based algorithms to simulate multi-phase fluid-flow and electromagnetic induction phenomena. Time-dependent spatial distributions of pressure, saturation, and salt concentration generated during water-base mud-filtrate invasion and a subsequent wireline formation test are modeled as two-phase advective transport of three components, namely, oil/gas, water,

and salt. Coupling between two-phase flow and physics of electromagnetic induction is accomplished via Archie's saturation equation. Isothermal salt mixing taking place within the aqueous phase due to the invading and in situ salt concentration contrast is also taken into account by means of a brine conductivity model.

10.1.3 Summary of Developments on the Inversion of Permanent Sensor Data

A proof-of-concept is carried out to quantify the sensitivity of in-situ permanent sensor pressure-transient measurements to detecting spatial distributions of permeability. An additional set of numerical examples investigate the possibility of simultaneously inverting permeability and porosity. The study is based on the assumption of a synthetic reservoir model subject to single-phase fluid flow, and on the availability of an array of permanent pressure gauges deployed along a vertical well. It is assumed that the well is subject to water injection and that pressure gauges are positioned in direct hydraulic communication with the surrounding rock formations. Properties of the injected water and in-situ oil phases are assumed approximately equal to each other in consistency with the assumption of single-phase fluid-flow behavior. For simplicity, we also assume that the rock formations exhibit azimuthal symmetry around the axis of the injection well. Techniques borrowed from the field of geophysical inverse theory were used to perform the sensitivity study. As part of this work, we introduced and made use an efficient dual-grid approach that substantially reduced computation times required by the inversion algorithm.

We also explored the technical issues arising from (1) noisy and imperfect data sampling strategies and (2) modalities for the flow rate excitation of in-situ transient-pressure measurements. A multitude of sensor and measurement configurations could be further explored to appraise the relative influence of these issues on the accuracy and stability of the inversion. Inversion examples suggest that the cooperative use of in-situ

transient-pressure and in-situ dc resistivity measurements does provide an efficient way to detect and quantify petrophysical changes due to fluid-flow dynamics in the vicinity of the sensors. However, because of the underlying diffusion phenomena governing the two sets of measurements, the spatial resolution of the inversion deteriorates with distance away from sources and detectors. It is envisioned that the deployment of arrays of in-situ permanent sensors should be designed to selectively adjust the sensitivity and resolution to shallow and deep spatial regions in the reservoir.

Having performed both joint and independent proof-of-concept inversions of in-situ permanent sensor pressure and dc resistivity measurements, we focus on the inversion of in-situ pressure data acquired during a two-phase flow process. A robust and efficient subspace inversion algorithm is developed for the inversion of fluid-flow measurements acquired in two-phase flow environments, i.e., waterflood operations. The subspace inversion algorithm is applied to the quantitative appraisal of in-situ permanent sensor pressure measurements in the estimation of spatial distributions of permeability and porosity. Reconstruction of model parameters yielded by permanent pressure sensor pressure data is rigorously compared to the spatial distributions of model parameters inverted from production measurements, namely, well bottom-hole pressure and water-oil ratio data, respectively.

10.1.3 Summary of Developments on the Petrophysical Inversion of Borehole Fluid-Flow and Electromagnetic Measurements

A dual-physics parametric inversion algorithm was developed and successfully employed to perform quantitative joint and independent interpretations of time-lapse electromagnetic induction and formation tester transient-pressure measurements. The benefit of the inversion algorithm is the quantitative estimation of layer-by-layer horizontal and vertical absolute permeabilities, and porosities.

Within the dual-physics modeling and inversion framework developed in this dissertation, we also develop a novel methodology for the petrophysical evaluation of hydrocarbon-bearing rock formations using only borehole electromagnetic-induction measurements. The methodology is based on the time-dependent nature of fluid saturation and salt concentration distributions in the immediate neighborhood of the wellbore due to mud-filtrate invasion. A rigorous formulation is used to account for the physics of two-phase, three-component transport of mass in the near-borehole region due to mud-filtrate invading hydrocarbon-bearing rock formations. The inverse problem consists of estimating parametric one-dimensional distributions of fluid permeability and porosity. As by-product, the inversion algorithm yields two-dimensional distributions of aqueous phase saturation, salt concentration, and electrical resistivity. The inverse problem of estimating layer-by-layer petrophysical parameters from single- or time-lapse electromagnetic-induction measurements is posed as an optimization problem. A weighted least-squares constrained optimization method is employed to solve the inverse problem. Tool responses required within the framework of the iterative inversion scheme are numerically computed by simulating the two-phase three-component flow that takes place during mud-filtrate invasion. In turn, electromagnetic-induction measurements are simulated in coupled mode with the physics of fluid flow. Numerical inversion experiments are conducted using both noise-contaminated synthetic data and field logs. The inversion requires of a-priori knowledge of mud, petrophysical, and fluid parameters. An extensive analysis is performed of the accuracy and reliability of the inversion when a-priori knowledge of such parameters is uncertain. Inversion results clearly indicate that multi-frequency and multi-resolution borehole electromagnetic measurements enable the accurate estimation of layer-by-layer absolute permeability and porosity.

As an extension of the above described coupled physics modeling and inversion framework, we formulated and implemented a robust and accurate hybrid optimization algorithm for the simultaneous inversion of anisotropic formation permeabilities and parametric forms of relative permeability and capillary pressure curves. The hybrid inversion algorithm allows a two-way coupling between a (global) Simultaneous Perturbation Stochastic Approximation (SPSA) technique, and the (local) Weighted and Regularized Gauss-Newton (WRGN) technique.

10.2 CONCLUSIONS

10.2.1 Rapid and Accurate Two-Dimensional Algorithms for Modeling Permanent Pressure and Electrode Array Measurements

(1) An important feature of the EKSM developed in this dissertation is its ability to provide pressure solutions in response to axisymmetric single-phase flow for a multitude of times with practically the same efficiency as that of a single time solution.

(2) The EKSM formulation can be easily adapted to provide solutions of pressure in the Laplace transform domain without appreciable computer overhead. The same formulation requires only a minor modification to yield solutions of the time derivative of pressure.

(3) The EKSM formulation is also readily applicable for the simulation of variable flow rate schedules. In this work, we considered pressure change and pressure derivative responses for simple variable-rate test schedules.

(4) The high efficiency of the EKSM algorithm is primarily due to the usage of inverse powers of the finite-difference operator, $\mathbf{A}$, when computing the pressure solution. Extensive tests have shown that the simultaneous use of inverse and positive powers of $\mathbf{A}$ provides a significant acceleration of convergence

compared to a conventional implementation of Lanczos recurrence. This property of the EKSM algorithm yields approximately a one-and-a-half- to three-fold improvement in performance with respect to that of the commercial software used for comparisons.

(5) Sensitivity studies carried out to assess the influence of specific petrophysical parameters on pressure measurements also suggest that the EKSM algorithm possesses the degree of efficiency necessary to approach practical inverse problems. Comparisons of the EKSM numerical simulation results with respect to those obtained using analytical solutions for point and line sources validate the accuracy of the developed numerical solver. These benchmark tests indicate that the EKSM results and analytical solutions agree within 1% of each other. The accuracy of the EKSM algorithm is also assessed for various geometrically complex reservoir models by comparing EKSM simulations against numerical solutions computed using a commercial reservoir simulator, ECLIPSE 100™ (GeoQuest, 2000). Pressure responses from both simulators agree within 1-4% of each other.

10.2.2 Estimation of Axisymmetric Spatial Distributions of Permeability and Porosity from Pressure-Transient Data Acquired with In-Situ Permanent Sensors

(1) Numerical test cases considered in this dissertation indicate that in-situ permanent pressure sensors have the potential of accurately detecting spatial distributions of permeability. This conclusion holds for relatively low levels of measurement noise as well as for the simultaneous estimation of spatial distributions of permeability and porosity. Unlike standard pressure-transient measurements acquired within a borehole, pressure-transient measurements acquired with in-situ sensors are highly sensitive to rock-formation properties as well as to hydraulic communication among formations. A great deal of flexibility in the acquisition

system is provided by (a) the location, spacing, and number of permanent sensors, (b) the time sampling schedule of the measurements, and (c) the way in which the injection flow rate is pulsed to produce a perturbation in the pressure field.

(2) The sensitivity studies described in this work also showed that noisy pressure-transient measurements could considerably bias the detection of spatial variations of permeability located far away from the sensor array. This behavior is due to the diffusive nature of the flow of fluids in porous media, and there is hardly anything one can do about it. However, it was found that both sensor redundancy and an appropriate selection of flow-rate schedule (e.g. a low-frequency sinusoidal pulse) could improve the sensitivity of the in-situ pressure array to permeability variations located far away from the borehole wall. Numerical experiments of inversion described in this work also indicate that pressure sensors located along the injection well provide higher spatial resolution in the estimation of permeability distributions than an array of sensors located away from the injection well.

(3) In addition to synthetic proof-of-concept inversion exercises, we applied a dual-grid inversion algorithm to the interpretation of field data. In the latter case, it was shown that the inversion algorithm possessed the necessary efficiency and expediency to estimate large-scale spatial distributions of reservoir permeability and porosity from relatively large volumes of wellbore-pressure data. Data from the field experiment consisted of time-records of pressure acquired in a well used for water injection. The lack of in-situ pressure data severely curtailed the sensitivity of the measurements to spatial variations of permeability and porosity in the reservoir. Simultaneous inversion of permeability and porosity provided the most consistent reservoir model that successfully reproduced the measurements.

However, the estimated distributions of permeability and porosity only provided information about the large-scale effective medium properties of the formation of interest.

10.2.3 Joint Inversion of Transient-Pressure and DC Resistivity Measurements Acquired with In-Situ Permanent Sensors

The inversion results considered in this project can be regarded as a proof-of-concept exercise to appraise the spatial resolution properties of transient-pressure and dc resistivity measurements acquired with in-situ permanent sensors. For all of the cases investigated, the joint inversion of in-situ transient-pressure and dc resistivity measurements improved the accuracy of estimations performed separately with either measurement set. This was possible because simultaneous use of the two measurement sets naturally reduced non-uniqueness and hence improved stability. However, coupling of the two measurement sets is nontrivial. Ideally, a rigorous multi-phase fluid-flow formulation should be used to drive the simulation and inversion of the two measurement sets. The inversion exercises presented in this dissertation are based on an approximate formulation of multi-phase flow that allowed us to couple pressure-diffusion and electrical phenomena through geometrical parameters.

10.2.4 Quantitative Study to Assess the Value of Pressure Data Acquired with In-Situ Permanent Sensors in Three-Dimensional Heterogeneous Reservoir Models Subject to Two-Phase Fluid Flow

(1) When compared to the true permeability and porosity fields, reconstructions of spatial distributions of model parameters yielded by noisy in-situ permanent pressure measurements are more accurate than reconstructions performed with noisy production measurements, namely, well bottom-hole pressure and water-oil ratio data. In both lateral and vertical directions the relative spatial resolution of

in-situ permanent sensor data is significantly higher than the resolution provided by well bottom-hole pressure and water-oil ratio measurements. Our test cases also indicate that the degree of sensitivity of in-situ permanent sensor measurements is higher for the spatial distributions of permeability than for the spatial distributions of porosity.

(2) Inversion results clearly show the added value of in-situ permanent sensor measurements in providing enhanced spatial resolution of permeability and to a relatively less degree for porosity. Having established a practical proof of concept for the value of dynamic in-situ pressure measurements in the absence of a-priori information, in-situ pressure measurements could be further integrated into the construction of static geostatistical reservoir models. Such a strategy could provide more accurate spatial descriptions of porosity and permeability and hence significantly reduce the uncertainty associated with the forecast of hydrocarbon production.

10.2.5 Joint Inversion of Transient-Pressure and Time-Lapse Electromagnetic Logging Measurements

(1) Inversion results indicate that the simultaneous use of dual-data sets effectively reduces non-uniqueness and improves the stability of the optimization scheme. The positive impact of dual-physics data sets becomes significant when the measurements contain high levels of noise.

(2) Parametric joint inversion of multi-probe transient formation-pressure and time-lapse electromagnetic induction measurements yields layer-by-layer horizontal and vertical near-wellbore permeabilities as well as porosities. In this case, the transient-pressure test needs to be designed to ensure sensitivity of the transient data to the petrophysical parameters of the layers of interest.

(3) Model parameters that are most affected by the deleterious effect of noise are vertical permeabilities.

(4) Estimation of porosity is very robust with respect to the effect of measurement noise for the investigated layered formation models. This is due to the presence of multi-resolution array induction-logging measurements and due to the assumed knowledge about the parameters governing the saturation equation, namely, Archie's law.

(5) Time-lapse electromagnetic induction measurements conducted across invaded beds yield significant information about the near-wellbore porosities and absolute permeabilities when interpreted within the framework of multi-phase fluid flow.

(6) Extensive sensitivity studies indicated that transient-pressure measurements encompass high sensitivity with respect to near-wellbore absolute permeabilities. Nonetheless, introduction of electromagnetic induction measurements to the inversion helps to further constrain the estimated absolute permeabilities.

(7) The main contribution of electromagnetic measurements is in providing first-order information about near-wellbore porosities, thereby enabling the algorithm to simultaneously invert both near-wellbore permeabilities and porosities from noisy measurements.

10.2.6 Petrophysical Inversion of Borehole Electromagnetic-Induction Logging Measurements

(1) The synthetic and field data examples described in this project indicate that array induction measurements can be used to estimate the permeability and porosity of layered rock formations. This estimation is possible because of the physical link that exists between the physics of mud-filtrate invasion and the physics of electromagnetic logging measurements. During the process of mud-filtrate invasion, permeability and porosity play a dominant role in the time evolution of

the spatial distributions of aqueous phase saturation and salt concentration in the near-borehole region. In this work, the link between porosity, saturation, and electrical conductivity is enforced through Archie's law, whereas the link between permeability and electrical resistivity is enforced through both Archie's law and the time evolution of the process of mud-filtrate invasion.

(2) Measurable sensitivity to permeability exists in borehole electromagnetic measurements that exhibit a selective deepening of the radial zone of response. The time evolution of the process of mud-filtrate invasion causes significant vertical and radial variations of aqueous phase saturation and salt concentration in the near-borehole region which can only be detected with array induction tools that exhibit multiple lengths of investigation. It is also shown that array induction measurements in general exhibit a measurable sensitivity to porosity regardless of the specific petrophysical conditions that govern the process of mud-filtrate invasion. We find that the estimation of permeability is much more sensitive to noisy electromagnetic measurements than the estimation of porosity.

(3) The accurate estimation of permeability is largely controlled by a-priori information such as mud properties, time of invasion, relative permeability, capillary pressure, fluid viscosity, and initial aqueous phase saturation, among others. Inversion exercises considered in this chapter indicate that a-priori knowledge about pressure-volume-temperature dependent properties of the fluids play a secondary role in the accuracy of the estimated values of permeability and porosity. Another conclusion is the relative insensitivity of the inversion to acceptable ranges of uncertainty in mud-filtrate invasion parameters such as time of invasion and rate of invasion.

(4) The petrophysical inversion algorithm described in this work can also be used to estimate spatial distributions of electrical conductivity. Cross-sections of electrical conductivity are a by-product of the inversion of permeability and porosity. However, as opposed to standard algorithms for the inversion of borehole electromagnetic measurements, the estimated spatial distributions of electrical conductivity described in this work are consistent with the processes of salt mixing and fluid transport, and abide by the law of mass conservation. Given the inherent non-uniqueness of inversion, the enforcement of petrophysical conditions on the inversion provides a natural way to reduce uncertainty in the presence of noisy and inadequate borehole electromagnetic-induction measurements.

10.2.7 Simultaneous Estimation of In-Situ Multi-Phase Petrophysical Properties of Rock Formations from Wireline Formation Tester and Induction Logging Measurements

(1) The proof-of-concept inversion exercises considered in this project consistently show the added value of the multi-physics approach for the quantitative integration of several types of measurements into a two-phase fluid model of petrophysical variables. Multi-physics measurements successfully reduce non-uniqueness of the inversion. This conclusion is quantitatively supported by the computed Cramer-Rao uncertainty bounds.

(2) Use of multi-physics measurements within the hybrid optimization framework makes it possible to efficiently and stably approach the highly nonlinear inverse problem of simultaneously estimating anisotropic permeabilities and saturation functions of relative permeability and capillary pressure. However, the accuracy of the simultaneous inversion approach is subject to the availability of a-priori information about parameters that govern the capillary pressure function.

Accurate reconstructions of anisotropic permeabilities, and parametric relative permeability and capillary pressure curves are obtained from synthetic multi-physics measurements contaminated with random Gaussian noise. For cases of uncertain knowledge of fluid viscosities, accuracy of the inverted model parameters is constrained by the information about governing parameters of the capillary pressure saturation function.

(3) A sequential inversion workflow was developed to approach estimation problems where formation tester and induction logging measurements lack the necessary degrees of freedom to simultaneously estimate all of the petrophysical model parameters. A single-phase pre-processing of late time multi-probe transient formation pressure measurements provides a closer starting point for the multi-physics inversion of horizontal and vertical permeabilities. This approach is efficient and accurate with conventional rate-pulse schedules and in the presence of noisy measurements.

(4) Robustness of the multi-physics inversion with respect to end-point saturations can only be achieved with array induction measurements. This conclusion comes as the result of extensive inversion practice performed with various combinations of measurement types.

(5) The only undesirable feature of the developed simultaneous multi-physics inversion approach is the requirement of expert-mode input when all of the model parameters are simultaneously estimated in the presence of noisy measurements. Careful adjustment of measurement and regularization weights is necessary to obtain accurate and reliable inversion results.

(6) The parametric formulation of the multi-physics inversion problem allows one to use a relatively small number of model parameters. Moreover, when the initial-

guess model is sufficiently close to the (global) minimum, the Weighted and Regularized Gauss-Newton search direction (used by the WRGN technique) provides rapid convergence. For the investigated problems, WRGN-based inversions required a maximum of 15 to 20 Gauss-Newton iterations to achieve convergence. However, the computation time required by the inversions increased 3 to 5 fold when a SPSA-based helper algorithm was activated together with the WRGN approach.

10.3 RECOMMENDATIONS FOR FURTHER RESEARCH

Several issues addressed in this dissertation deserve further investigation. Some directions for further research include the following:

(1) Extension of the EKSM algorithm to three-dimensional parabolic problems.

(2) Development of a fully-implicit multi-phase multi-component near-borehole fluid-flow simulator with adjoint sensitivity computation capabilities for the accelerated inversion of fluid-flow measurements.

(3) Implementation of a feedback loop for recovery optimization in response to newly acquired petrophysical information from the inversion of in-situ permanent sensor measurements.

(4) Extension of the multi-physics modeling and inversion framework to incorporate measurements acquired with in-situ seismic sensors.

(5) Application of the inverse modeling philosophy of this dissertation to the continuous in-situ seismic monitoring of enhanced recovery processes.

(6) Extension of the multi-physics modeling and inversion framework to incorporate measurements acquired by acoustic and nuclear logging tools.

(7) Joint inversion of wireline formation tester and electromagnetic induction logging measurements acquired at highly deviated and horizontal boreholes.

(8) Application of the petrophysical modeling and inversion framework to an extensive number of field cases with the purpose of developing a better understanding of its practical limitations.

(9) Multi-level parallelization of modeling and inversion algorithms of petrophysical inversion framework for enhanced computational efficiency.

Appendix A: A General Framework for the Constrained Parametric Inversion of Borehole Geophysical Measurements

A.1 INTRODUCTION

In this appendix, we first review the Newton based methods by putting them in a general framework. Our formulation of the inverse problem closely follows the formulation and notation of Habashy and Abubakar (2004). Nonetheless, this appendix does not constitute a mere repetition. Instead, we build upon their framework and propose novel ways of enhancing computational efficiency without the compromise of rigor for Newton-based optimization algorithms applied to the solution of inverse problems of borehole geophysics.

In order to enhance the performance of these Newton based methods, we constrained them with nonlinear transformations. The imposed constraints force the reconstruction of the unknown model parameters to lie within the physical bounds. In order to guarantee the error reducing nature of the algorithm, we adjust the iterative step using a line search algorithm. In this manner, we prevent the algorithm from jumping back and forth between two successive iterations. Since the inverse problem is essentially nonlinear, regularization of the Hessian matrix is needed for stability reasons. In the literature of inverse problems, the proper selection and application of the regularization parameter (also called as the Lagrange multiplier) is a central area of research. In our formulation of the regularization procedure, we are inspired from the work of van den Berg and Abubakar (2001) and van den Berg et al. (2003) on the multiplicative regularization for gradient-type algorithm. We extend the multiplicative regularization approach to Newton-type algorithms. In our formulation, in order to avoid the necessity of determining the appropriate regularization parameter, the regularizer is included as a

multiplicative constraint. In this way, the appropriate regularization parameter will be controlled by the optimization process itself. In fact, the misfit in the error in the space of the forward operator is selected as the regularization parameter. This implies that no a-priori knowledge on the model domain is needed. If noise is present, the misfit error of the forward operator will remain at a large value during the optimization process. Hence, the weight of the regularization factor will be more significant. In turn, the noise will, at all times, be suppressed in the inversion process. In this way, the parametric inversion algorithm is armed with a robust method to determine the weight of the regularization term. We emphasize the relationship between the L_2-norm minimization algorithms and the Bayesian inference approach. Equivalence between our L_2-norm based inversion algorithm and Bayesian inference approach is demonstrated. As an important implication of this demonstration, we derive a method for computing the error bounds on the nonlinear inversion outcome.

In the following section of this appendix, we develop a solution to the nonlinear inverse problem via a cascade sequence of auxiliary least-squares minimizations. The auxiliary minimizations are nonlinear inverse problems themselves, except that they are implemented with an approximate forward problem that is computationally more efficient to solve than the algorithm used to simulate the measurements. Any given auxiliary minimization in the cascade is fully self-contained and yields a solution of the unknown model parameters. This solution, in turn, is used to perform a numerical simulation of the data to quantify its agreement with the input measurements. If the difference between the measured data and the simulated data is above the estimated noise threshold, it is input as data to the subsequent auxiliary inverse problem in the cascade. Otherwise, the inversion is brought to a successful completion. We describe the theory and operating conditions under which the cascade inversion technique converges to a solution equivalent to that of

a single inversion implemented with the original forward problem. Depending on the choice of approximate forward problem and regardless of the optimization algorithm employed to solve the inverse problem, the cascade sequence of auxiliary minimizations can be made computationally more efficient than a single inversion performed with the original forward problem. In this dissertation, we consider a practical and flexible way to construct the approximate forward problem by using subset of the finite-difference grid used to simulate the measurements numerically, i.e., a dual-grid construction technique.

In the final section of this appendix, we hybridize the Weighted and Regularized Gauss-Newton (WRGN) method with an efficient stochastic global optimization algorithm, namely, Simultaneous Perturbation Stochastic Approximation (SPSA) method. The global optimization algorithm is used as a helper method to address the local minimum trapping problem associated with the Gauss-Newton based local optimization algorithms. Although global helper methods introduce additional computational burden to the inversion process, for inverse problems with potential multiple local minima, their added benefits crucial from the viewpoint of robustness.

A.2 THE COST FUNCTIONAL

We define the vector of residuals $\mathbf{e}(\mathbf{x})$ as a vector whose j^{th} element is the residual error (also referred to as the data mismatch) of the j^{th} measurement. The residual error is defined as the difference between the measured and the predicted normalized responses given by

$$\mathbf{e}(\mathbf{x}) = \begin{bmatrix} e_1(\mathbf{x}) \\ \vdots \\ e_M(\mathbf{x}) \end{bmatrix} = \begin{bmatrix} S_1(\mathbf{x}) - m_1 \\ \vdots \\ S_M(\mathbf{x}) - m_M \end{bmatrix} = \mathbf{S}(\mathbf{x}) - \mathbf{m}, \tag{A.1}$$

where M is the number of measurements. In equation (A.1), m_j is the normalized observed response (measured data) and S_j is corresponding to the normalized simulated response as predicted by the vector of model parameters, $\mathbf{x}$, given by

$$\mathbf{x} = \begin{bmatrix} x_1 \\ \vdots \\ x_N \end{bmatrix} = \mathbf{y} - \mathbf{y}_R, \tag{A.2}$$

where N is the number of unknowns. In the next section, we discuss various methods of normalizing the simulated and measured responses. We represent the vector of model parameters $\mathbf{x}$ as the difference between the vector of the actual model parameters $\mathbf{y}$ and a reference model (or background model) $\mathbf{y}_R$. The reference model includes all a-priori information on the model parameters such as those derived from independent measurements. We pose the inversion as the minimization of the following cost (or objective) functional, $C(\mathbf{x})$, of the form (Oldenburg, 1990)

$$C(\mathbf{x}) = \frac{1}{2}\left[\mu \left\{ \left\| \mathbf{W}_d \cdot \mathbf{e}(\mathbf{x}) \right\|^2 - \chi^2 \right\} + \left\| \mathbf{W}_x \cdot (\mathbf{x} - \mathbf{x}_p) \right\|^2 \right]. \tag{A.3}$$

The scalar factor μ $(0 < \mu < \infty)$ is a Lagrange multiplier (also called regularization parameter or damping coefficient). It is a trade-off parameter determining the relative importance of the two terms of the cost functional. The determination of μ will produce an estimate of the model $\mathbf{x}$ that has a finite minimum weighted norm (away from a prescribed model $\mathbf{x}_p$) and which globally misfits the data to within a prescribed value χ (determined from a-priori estimates of noise in the data). The second term of the cost functional is included to regularize the optimization problem. It safeguards against cases

when measurements are redundant or lacking sensitivity to certain model parameters causing non-uniqueness of solution. It also suppresses any possible magnification of errors in our parameter estimations due to noise which is unavoidably present in the measurements. These error magnifications may result in undesirable large variations in the model parameters which may cause instabilities in the inversion. In equation (A.3), $\mathbf{W}_x^T\mathbf{W}_x$ is the inverse of the model covariance matrix representing the degree of confidence in the prescribed model $\mathbf{x}_p$. On the other hand, $\mathbf{W}_d^T\mathbf{W}_d$ is the inverse of the data covariance matrix, which describes the estimated uncertainties (due to noise contamination) in the available data set. It describes not only the estimated variance for each particular data point, but also the estimated correlation between errors. It therefore provides a point by point weighting of the input data according to a prescribed criterion (hence, can be used to reduce the effect of outliers in the data). If the measurement noise is stationary and uncorrelated, then $\mathbf{W}_d = diag\{\sigma_j\}$ where σ_j is the root-mean-square deviation (standard deviation) of the noise for the j^{th} measurement. The relationship between the Bayesian inference approach and the minimization method posed above will also be pointed out in this work.

A.3 THE CONSTRAINED MINIMIZATION APPROACH

To impose a-priori information, such as positivity or physical maximum and minimum bounds (if available) on the inverted model parameters, $\mathbf{x}$, we make use of nonlinear transforms such that

$$x_i = f(c_i, x_i^{\min}, x_i^{\max}), \quad -\infty < c_i < \infty, \quad i = 1, 2, \ldots, N. \tag{A.4}$$

In equation (A.4), $x_i^{\max}$ and $x_i^{\min}$ denote the upper and lower physical bounds on the model parameter x_i, respectively. These nonlinear transformations map a constrained

minimization problem to an unconstrained one. Note that the above constraints will force the reconstruction of the model parameters to remain always within their physical bounds.

Self-evidently, there is an infinite number of nonlinear transformations $f(c_i, x_i^{\min}, x_i^{\max})$ that map a constrained minimization problem into an unconstrained one. Among the many we experimented with, three transformations, that were identified to perform the best, are presented in this work.

A.4 NORMALIZATION OF THE VECTOR OF RESIDUALS

We employ two possible forms of the cost functional of equation (A.3) that puts the various measurements on equal footings. The two forms differ in the way we define the vector of residuals $\mathbf{e}(\mathbf{x})$. In the first form we define $\mathbf{e}(\mathbf{x})$ as follows:

$$e_j(\mathbf{x}) = \frac{S_j(\mathbf{x})}{m_j} - 1, \tag{A.5}$$

and hence

$$\left\|\mathbf{e}(\mathbf{x})\right\|^2 = \sum_{j=1}^{M} \left| \frac{S_j(x)}{m_j} - 1 \right|^2 . \tag{A.6}$$

In the second form we define

$$e_j(\mathbf{x}) = \frac{S_j(\mathbf{x}) - m_j}{\left\|\mathbf{m}\right\| / M}, \tag{A.7}$$

and hence

$$\left\|\mathbf{e}(\mathbf{x})\right\|^2 = \frac{\sum_{j=1}^{M}\left|S_j(\mathbf{x}) - m_j\right|^2}{\left(\sum_{j=1}^{M}\left|m_j\right|^2\right)\Big/M^2}. \tag{A.8}$$

A.5 THE NEWTON MINIMIZATION METHOD

To solve the above nonlinear optimization problem, we employ a Newton minimization approach (Gill et al., 1981) which is based on a local quadratic model of the cost functional. The quadratic model is formed by taking the first three terms of the Taylor series expansion of the cost functional around the current k^{th} iteration ($\mathbf{x}_k$), as follows:

$$C(\mathbf{x}_k + \mathbf{p}_k) \approx C(\mathbf{x}_k) + \mathbf{g}^T(\mathbf{x}_k)\cdot\mathbf{p}_k + \frac{1}{2}\mathbf{p}_k^T\cdot\mathbf{G}(\mathbf{x}_k)\cdot\mathbf{p}_k, \tag{A.9}$$

where the superscript T indicates transposition and $\mathbf{p}_k = \mathbf{x}_{k+1} - \mathbf{x}_k$ is the step in $\mathbf{x}_k$ towards the minimum of the cost functional $C(\mathbf{x})$. The vector $\mathbf{g}(\mathbf{x}) = \nabla C(\mathbf{x})$ is the gradient vector of the cost functional $C(\mathbf{x})$ and is given by the following expression:

$$\mathbf{g}(\mathbf{x}) = \nabla C(\mathbf{x}) = \left[\, g_n \equiv \frac{\partial C}{\partial x_n};\, n = 1, 2, 3, \ldots, N \,\right], \tag{A.10a}$$

or in other words,

$$\mathbf{g}(\mathbf{x}) = \mu\,\mathbf{J}^T(\mathbf{x})\cdot\mathbf{W}_d^T\cdot\mathbf{W}_d\cdot\mathbf{e}(\mathbf{x}) + \mathbf{W}_x^T\cdot\mathbf{W}_x\cdot(\mathbf{x} - \mathbf{x}_p). \tag{A.10b}$$

In equation (A.10a), x_n is the n^{th} component of the model vector $\mathbf{x}$. In equation (A.10b), $\mathbf{J}(\mathbf{x})$ is the $M \times N$ Jacobian matrix, and is given by the following expression:

$$\mathbf{J}(\mathbf{x}) = \left[J_{mn} \equiv \frac{\partial e_m}{\partial x_n}; m = 1,2,3,\ldots,N; n = 1,2,3,\ldots,N \right], \tag{A.11a}$$

or in other words,

$$\mathbf{J}(\mathbf{x}) = \begin{bmatrix} \partial S_1/\partial x_1 & \cdots & \partial S_1/\partial x_j & \cdots & \partial S_1/\partial x_N \\ \vdots & \ddots & \vdots & \ddots & \vdots \\ \partial S_l/\partial x_1 & \cdots & \partial S_l/\partial x_j & \cdots & \partial S_l/\partial x_N \\ \vdots & \ddots & \vdots & \ddots & \vdots \\ \partial S_M/\partial x_1 & \cdots & \partial S_M/\partial x_j & \cdots & \partial S_M/\partial x_N \end{bmatrix}. \tag{A.11b}$$

On the other hand, $\mathbf{G}(\mathbf{x}) = \nabla\nabla C(\mathbf{x})$ is the Hessian of the cost functional $C(\mathbf{x})$ which is a real symmetric $N \times N$ matrix (not necessarily positive-definite) given by

$$\mathbf{G}(\mathbf{x}) = \nabla\nabla C(\mathbf{x}) = \left[G_{nm} \equiv \frac{\partial^2 C}{\partial x_n \partial x_m}; n,m = 1,2,3,\ldots,N \right], \tag{A.12a}$$

or in other words,

$$\mathbf{G}(\mathbf{x}) = \mathbf{W}_x^T \cdot \mathbf{W}_x + \mu \left[\mathbf{J}^T(\mathbf{x}) \cdot \mathbf{W}_d^T \cdot \mathbf{W}_d \cdot \mathbf{J}(\mathbf{x}) + \mathbf{Q}(\mathbf{x}) \right]. \tag{A.12b}$$

In equation (A.12b),

$$\mathbf{Q}(\mathbf{x}) = \sum_{m=1}^{M} f_m(\mathbf{x}) \mathbf{F}_m^T(\mathbf{x}), \tag{A.13}$$

where $f_m(\mathbf{x})$ is the m^{th} element of the weighted vector of residuals,

$$\mathbf{f}(\mathbf{x}) = \mathbf{W}_d \cdot \mathbf{e}(\mathbf{x}), \tag{A.14}$$

and

$$\mathbf{F}_m(\mathbf{x}) = \nabla\nabla f_m(\mathbf{x}) = \left[\frac{\partial^2 f_m}{\partial x_i \partial x_j}; i, j = 1, 2, 3, \ldots, N \right]. \tag{A.15}$$

Note that the full Hessian $\mathbf{G}(\mathbf{x})$ of the cost functional $C(\mathbf{x})$ includes second order information that accounts for curvature. The minimum of the right-hand side of equation (A.9) is achieved if $\mathbf{p}_k$ is a minimum of the quadratic functional

$$\phi(\mathbf{p}) = \mathbf{g}^T(\mathbf{x}_k) \cdot \mathbf{p} + \frac{1}{2} \mathbf{p}^T \cdot \mathbf{G}(\mathbf{x}_k) \cdot \mathbf{p}. \tag{A.16}$$

The functional $\phi(\mathbf{p})$ has a stationary point (a minimum, a maximum or a saddle point also called point of inflection) at $\mathbf{p}_o$, only if the gradient vector of $\phi(\mathbf{p})$ vanishes at $\mathbf{p}_o$, i.e.,

$$\nabla\phi(\mathbf{p}_o) = \mathbf{G} \cdot \mathbf{p}_o + \mathbf{g} = 0. \tag{A.17}$$

Thus, the stationary point is the solution to the following set of linear equations:

$$\mathbf{G} \cdot \mathbf{p}_o = -\mathbf{g}. \tag{A.18}$$

A.5.1 Case (1): Singular G

Equation (A.18) can be expressed as follows:

$$\mathbf{g} = -\sum_{j=1}^{N} \mathbf{G}_j p_j, \tag{A.19}$$

where G_j are the columns of the $N \times N$ matrix $\mathbf{G}$ and p_j is the j^{th} component of the vector $\mathbf{p}_o$.

If $\mathbf{G}$ is singular, then some of the columns of $\mathbf{G}$ can be expressed as a linear combination of others. Hence, the columns of $\mathbf{G}$ do not constitute a complete set of basis vectors that are sufficient to represent an arbitrary vector.

If the vector $\mathbf{g}$ cannot be expressed as a linear combination of the columns of $\mathbf{G}$ (i.e., $\mathbf{g}$ has a nonzero component in the null-space of $\mathbf{G}$), then the system of equations (A.15) is incompatible and does not have a solution. Thus, the stationary point $\mathbf{p}_o$ does not exist and the functional ϕ is unbounded above and below (i.e., has neither a maximum nor a minimum value). On the other hand, if the vector $\mathbf{g}$ can be expressed as a linear combination of the columns of $\mathbf{G}$, then the system of equations (A.18) is compatible and has more than one solution.

A.5.2 Case (2): Nonsingular G

In this case, equation (A.18) has a unique solution given by

$$\mathbf{p}_o = -\mathbf{G}^{-1} \cdot \mathbf{g} = -\sum_{j=1}^{N} \frac{1}{\lambda_j} \left(\mathbf{v}_j^T \cdot \mathbf{g} \right) \mathbf{v}_j. \tag{A.20}$$

The norm of $\mathbf{p}_o$ is given by

$$\left\| \mathbf{p}_o \right\| \equiv \left(\mathbf{p}_o^T \cdot \mathbf{p}_o \right)^{1/2} = \left[\sum_{j=1}^{N} \frac{1}{\lambda_j^2} \left(\mathbf{v}_j^T \cdot \mathbf{g} \right)^2 \right]^{1/2}, \tag{A.21}$$

where λ_j and $\mathbf{v}_j$ are the eigenvalues and the corresponding orthonormal eigenvectors of the $N \times N$ Hessian matrix $\mathbf{G}$ such that

$$\mathbf{G} \cdot \mathbf{v}_j = \lambda_j \mathbf{v}_j, \tag{A.22}$$

with

$$\mathbf{v}_i^T \cdot \mathbf{v}_j = \delta_{ij}. \tag{A.23}$$

At the stationary point $\mathbf{p}_o,$ given by equation (A.20), we have from equation (A.9)

$$C(\mathbf{x}_k + \mathbf{p}_o) \approx C(\mathbf{x}_k) - \frac{1}{2} \mathbf{g}^T(\mathbf{x}_k) \cdot \mathbf{G}^{-1}(\mathbf{x}_k) \cdot \mathbf{g}(\mathbf{x}_k) = C(\mathbf{x}_k) - \frac{1}{2} \sum_{j=1}^{N} \frac{1}{\lambda_j} \left(\mathbf{v}_j^T \cdot \mathbf{g} \right)^2 \tag{A.24}$$

The stationary point $\mathbf{p}_o,$ given by equation (A.20), is either a minimum, a maximum or a saddle point, depending on the definiteness of the matrix $\mathbf{G}$. If $\mathbf{G}(\mathbf{x}_k)$ is a positive-definite matrix, then the quadratic model of equation (A.9) is guaranteed to have a unique stationary point given by equation (A.20). From equation (A.24), the direction $\mathbf{p}_o$ is guaranteed to be a descent direction, since

$$C(\mathbf{x}_k + \mathbf{p}_o) - C(\mathbf{x}_k) \approx -\frac{1}{2} \sum_{j=1}^{N} \frac{1}{\lambda_j} \left(\mathbf{v}_j^T \cdot \mathbf{g} \right)^2 < 0. \tag{A.25}$$

In this case, we choose the search direction $\mathbf{p}_k = \mathbf{p}_o$. On the other hand, if $\mathbf{G}(\mathbf{x}_k)$ is indefinite (but nonsingular), then the quadratic model of equation (A.9) is guaranteed to have a unique stationary point (given by equation (A.20)). However, this stationary point is not necessarily a minimum. From equation (A.24), the direction $\mathbf{p}_o$ is not necessarily a descent direction, since $C(\mathbf{x}_k + \mathbf{p}_o) - C(\mathbf{x}_k)$ can be non-negative.

As it will be discussed in a subsequent section, the conditioning (singular or nonsingular nature) and the definiteness (positive- negative-definiteness or indefiniteness) of the matrix $\mathbf{G}$ can be adjusted by the proper choice of μ. The search direction $\mathbf{p}_k$ which is given by the vector that solves equation (A.18) is called the Newton search direction. The method that makes use of this vector as the search direction is called the full Newton search. The full Newton minimization approach is known to have a quadratic rate of convergence.

A.6 THE MODIFIED NEWTON MINIMIZATION METHOD

In the case where $\mathbf{G}(\mathbf{x}_k)$ is indefinite (but nonsingular), the direction of $\mathbf{p}_o$, given by equation (A.20), is not necessarily a descent direction. One popular strategy in modifying Newton's method is to construct a related positive-definite matrix $\mathbf{K}(\mathbf{x}_k)$ when $\mathbf{G}(\mathbf{x}_k)$ is indefinite. In this case, the search direction is given by the solution of

$$\mathbf{K} \cdot \mathbf{p}_o = -\mathbf{g}. \tag{A.26}$$

One way of constructing such a positive-definite matrix, is to construct $\mathbf{K}(\mathbf{x}_k)$ such that it has the same eigenvectors as $\mathbf{G}(\mathbf{x}_k)$ and with eigenvalues given by

$$\mu_j = \left|\lambda_j\right|. \tag{A.27}$$

This ensures that $\mathbf{K}(\mathbf{x}_k) = \mathbf{G}(\mathbf{x}_k)$ if $\mathbf{G}(\mathbf{x}_k)$ is positive-definite. The constructed positive-definite matrix $\mathbf{K}(\mathbf{x}_k)$ is hence given by the following expression

$$\mathbf{K} = \sum_{j=1}^{N} |\lambda_j| \mathbf{v}_j \mathbf{v}_j^T, \tag{A.28}$$

and the corresponding search direction is given by

$$\mathbf{p}_o = -\mathbf{K}^{-1} \cdot \mathbf{g} = -\sum_{j=1}^{N} \frac{1}{|\lambda_j|} \left(\mathbf{v}_j^T \cdot \mathbf{g} \right) \mathbf{v}_j, \tag{A.29}$$

whose norm is given by

$$\| \mathbf{p}_o \| \equiv \left(\mathbf{p}_o^T \cdot \mathbf{p}_o \right)^{1/2} = \left[\sum_{j=1}^{N} \frac{1}{\lambda_j^2} \left(\mathbf{v}_j^T \cdot \mathbf{g} \right)^2 \right]^{1/2}, \tag{A.30}$$

which is identical to that of the unmodified direction as shown in equation (A.21). For this search direction, we have from equation (A.9)

$$C(\mathbf{x}_k + \mathbf{p}_o) - C(\mathbf{x}_k) \approx -\sum_{j=1}^{N} \frac{1}{|\lambda_j|} \left[1 - \frac{1}{2} \mathrm{sgn}(\lambda_j) \right] \left(\mathbf{v}_j^T \cdot \mathbf{g} \right)^2 < 0. \tag{A.31}$$

Thus, the direction $\mathbf{p}_o$, given by equation (A.29), is guaranteed to be a descent direction. In this case, we choose $\mathbf{p}_k = \mathbf{p}_o$.

A.7 THE GAUSS-NEWTON MINIMIZATION METHOD

In the Gauss-Newton search method, one discards the second-order derivatives to avoid the expensive computation of second derivatives. Then, the Hessian reduces to

$$\mathbf{G}(\mathbf{x}) = \mathbf{W}_x^T \cdot \mathbf{W}_x + \mu \mathbf{J}^T(\mathbf{x}) \cdot \mathbf{W}_d^T \cdot \mathbf{W}_d \cdot \mathbf{J}(\mathbf{x}), \tag{A.32}$$

which is a positive semi-definite matrix. If λ_j and $\mathbf{v}_j$ are the eigenvalues and the corresponding orthonormal eigenvectors of the $N \times N$ real symmetric matrix $\mathbf{G}$

$$\mathbf{G} \cdot \mathbf{v}_j = \lambda_j \mathbf{v}_j, \tag{A.33}$$

such that

$$\mathbf{v}_i^T \cdot \mathbf{v}_j = \delta_{ij}. \tag{A.34}$$

Then,

$$\lambda_j = \frac{\mathbf{v}_j^T \cdot \mathbf{G} \cdot \mathbf{v}_j}{\left\| \mathbf{v}_j \right\|^2} = \left\| \mathbf{W}_x \cdot \mathbf{v}_j \right\|^2 + \mu \left\| \mathbf{W}_d \cdot \mathbf{J} \cdot \mathbf{v}_j \right\|^2 \geq 0, \tag{A.35}$$

Hence, as previously mentioned $\mathbf{G}$ is a positive semi-definite matrix. As indicated before and as will be discussed in the next section, the Hessian $\mathbf{G}$ can be constructed to be a positive-definite matrix by the proper choice of μ.

The search direction $\mathbf{p}_k$ that is given by the vector that solves equation (A.18) with the Hessian approximated by equation (A.32) is called the Gauss-Newton search direction. The method in which this vector is used as a search direction is called the

Gauss-Newton search. The Gauss-Newton minimization approach has a rate of convergence that is slightly less than quadratic but significantly better than linear. It provides quadratic convergence in the neighborhood of the minimum.

A.8 THE STEEPEST-DESCENT MINIMIZATION METHOD

In the case of large-scale optimization problems and to avoid the direct inversion of a large size matrix (the Hessian matrix $\mathbf{G}$) as is required by the Newton or Gauss-Newton minimization approaches, one can employ an iterative linear solver, e.g., a Lanczos method or a conjugate-gradient approach (Golub and Van Loan, 1993; Press et al., 1992). However, these iterative approaches are more efficient for sparse systems and tend to loose their advantage for systems that have full matrices similar to the problem at hand where the Hessian is a full matrix. Furthermore, the most computationally expensive part of the inversion is not actually in inverting the Hessian matrix but is by far in the evaluation of the elements of the Hessian (or Jacobian).

An alternative approach to iterative solvers that does not require the inversion of the Hessian matrix, is the steepest-descent method where the search direction is simply chosen to be along the negative of the gradient of the cost functional, i.e.,

$$\mathbf{p}_k = -\gamma_k \, \mathbf{g}(\mathbf{x}_k) \equiv -\gamma_k \, \mathbf{g}_k, \tag{A.36}$$

where γ_k is a positive step-length which must be chosen so that the cost functional $C(\mathbf{x}_k + \mathbf{p}_k)$ is "sufficiently decreased" after each iteration. It is thus clear that, unless the gradient vanishes, the search direction of equation (A.36) is a descent direction, since $\mathbf{p}_k$ and $\mathbf{g}_k$ are trivially bounded away from orthogonality $\left(\mathbf{g}_k^T \cdot \mathbf{p}_k = -\gamma_k \left|\mathbf{g}_k\right|^2 \neq 0\right)$.

We choose the step-length that maximizes the reduction in the value of cost functional $C(\mathbf{x}_k + \mathbf{p}_k)$. Substituting equation (A.36) into equation (A.9), we obtain

$$C(\mathbf{x}_k + \mathbf{p}_k) \approx C(\mathbf{x}_k) - \gamma_k \left|\mathbf{g}_k\right|^2 + \frac{1}{2}\gamma_k^2 \, \mathbf{g}_k^T \cdot \mathbf{G}_k \cdot \mathbf{g}_k. \tag{A.37}$$

whose minimum occurs when:

$$\gamma_k = \frac{\left|\mathbf{g}_k\right|^2}{\mathbf{g}_k^T \cdot \mathbf{G}_k \cdot \mathbf{g}_k} \tag{A.38}$$

Thus, the steepest-descent search direction is given by

$$\mathbf{p}_k = \mathbf{x}_{k+1} - \mathbf{x}_k = -\frac{\left|\mathbf{g}_k\right|^2}{\mathbf{g}_k^T \cdot \mathbf{G}_k \cdot \mathbf{g}_k}\mathbf{g}_k = -\frac{\left|\mathbf{g}_k\right|^2}{\left|\mathbf{W}_x \cdot \mathbf{g}_k\right|^2 + \mu\left|\mathbf{W}_d \cdot \mathbf{J}_k \cdot \mathbf{g}_k\right|^2}\mathbf{g}_k. \tag{A.39}$$

This steepest-descent direction is guaranteed to yield a convergent algorithm. This conclusion stems from the following facts: (1) Unless the gradient vanishes, the search direction of equation (A.39) is a descent direction, since $\mathbf{p}_k$ and $\mathbf{g}_k$ are trivially bounded away from orthogonality,

$$\mathbf{g}_k^T \cdot \mathbf{p}_k = -\frac{\left|\mathbf{g}_k\right|^4}{\left|\mathbf{W}_x \cdot \mathbf{g}_k\right|^2 + \mu\left|\mathbf{W}_d \cdot \mathbf{J}_k \cdot \mathbf{g}_k\right|^2} \neq 0. \tag{A.40}$$

(2) The value of the cost functional $C(\mathbf{x}_k + \mathbf{p}_k)$ is sufficiently decreased after each iteration such that

$$C(\mathbf{x}_k + \mathbf{p}_k) - C(\mathbf{x}_k) \approx -\frac{1}{2}\frac{\left|\mathbf{g}_k\right|^4}{\left|\mathbf{W}_x \cdot \mathbf{g}_k\right|^2 + \mu\left|\mathbf{W}_d \cdot \mathbf{J}_k \cdot \mathbf{g}_k\right|^2} < 0. \tag{A.41}$$

Unfortunately, global convergence of an algorithm does not ensure that it is an efficient method. For the quadratic approximation of the cost functional, given by equation (A.9), with $\mathbf{G}(\mathbf{x})$ approximated by equation (A.32), where it becomes a real symmetric positive-definite matrix, it can be shown that

$$C(\mathbf{x}_{k+1}) - C(\mathbf{x}_o) \approx \frac{(\kappa - 1)^2}{(\kappa + 1)^2} \{C(\mathbf{x}_k) - C(\mathbf{x}_o)\}, \tag{A.42}$$

where $\mathbf{x}_o$ is the value of the minimum of the cost functional where $\mathbf{g}(\mathbf{x}_o)$ vanishes and $\kappa = \lambda_{\max} / \lambda_{\min}$ is the condition number of the Hessian $\mathbf{G}$. From equation (A.42), it is clear that the rate of convergence of the steepest-descent method is linear as opposed to the quadratic rate of convergence of the full Newton minimization approach. Furthermore, the factor of reduction in the error at each iteration step can be very close to unity, depending on the condition number of the Hessian matrix $\mathbf{G}$, so that there is a very small gain in accuracy at each iteration. With the steepest-descent, the iteration is forced to traverse back and forth across the minimum rather than down towards the minimum. In practice, the steepest-descent method may typically require hundreds of iterations to achieve very little progress towards the final solution.

A.9 THE CONJUGATE-GRADIENT MINIMIZATION METHOD

One way to improve the convergence rate of the steepest-descent method (also called the gradient method) is by using a search direction which is a linear combination of the current gradient and the previous search direction. This type of method is called conjugate-gradient. The nonlinear conjugate-gradient method is modeled after the conjugate-gradient method for linear equations, see, for instance, Fletcher (1980).

Accordingly, it can be proven that quadratic functionals converge in exact arithmetic in N number of steps, where N equals to the number of unknowns. In the classical conjugate-gradient method (or the so-called Fletcher-Reeves conjugate-gradient direction) the search direction is given by

$$\mathbf{p}_k = \gamma_k \mathbf{s}_k, \tag{A.43}$$

where

$$\mathbf{s}_k = -\mathbf{g}_k + \frac{\left\| \mathbf{g}_k \right\|^2}{\left\| \mathbf{g}_{k-1} \right\|^2} \mathbf{s}_{k-1}. \tag{A.44}$$

Substituting equation (A.43) into equation (A.37), the weighting parameter γ_k is given by

$$\gamma_k = \frac{\left| \mathbf{s}_k \right|^2}{\mathbf{s}_k^T \cdot \mathbf{G}_k \cdot \mathbf{s}_k}. \tag{A.45}$$

Since our problem is nonlinear in terms of the inverted model parameters, after a number of iterations, the effectiveness of the Fletcher-Reeves direction will reduce. Hence, the steepest-descent direction must be restarted and iterations must be continued with new conjugate-gradient directions. The Polak-Ribière conjugate-gradient direction (Fletcher, 1980; Luenberger, 1984), however, avoids these restarting procedures. The Polak-Ribière conjugate-gradient direction is obtained by modifying equation (A.44) as follows:

$$\mathbf{s}_k = -\mathbf{g}_k + \frac{\left\langle \mathbf{g}_k, \mathbf{g}_k - \mathbf{g}_{k-1} \right\rangle}{\left\| \mathbf{g}_{k-1} \right\|^2} \mathbf{s}_{k-1}, \tag{A.46}$$

where $\langle \bullet, \bullet \rangle$ denotes the inner product operation. When there are no changes in the inverted model parameters, we have $\langle \mathbf{g}_k, \mathbf{g}_k - \mathbf{g}_{k-1} \rangle = 0$, therefore, the Polak-Ribière conjugate-gradient directions coincide with the Fletcher-Reeves directions. However, when the iterative scheme does not improve sufficiently, it leads to $\mathbf{g}_k \approx \mathbf{g}_{k-1}$. In such a case, we have $\mathbf{s}_k = -\mathbf{g}_k$. Hence, the Polak-Ribière conjugate-gradient directions become equivalent to the steepest-descent directions. Then, the updating is restarted automatically.

A.10 LINE-SEARCH METHODS FOR ACCELERATING CONVERGENCE

The search vector $\mathbf{p}_k$ of equation (A.18) is guaranteed to be a descent direction for the approximated quadratic form of the cost functional of equation (A.3). In other words, $\mathbf{p}_k$ is a descent direction for the approximated cost functional of equation (A.9). However, after taking this step, the new iterate $(\mathbf{x}_k + \mathbf{p}_k)$ may not sufficiently reduce the cost functional of equation (A.3). It may not even decrease its value, indicating that $C(\mathbf{x})$ is poorly modeled by a quadratic form in the vicinity of $\mathbf{x}_k$. One approach to alleviate this problem is to adopt a line-search algorithm (Dennis and Schnabel, 1983) where one searches for an appropriate real positive step-length υ_k along the search direction, $\mathbf{p}_k$, which yields an acceptable next iterate, $\mathbf{x}_{k+1} = \mathbf{x}_k + \upsilon_k \mathbf{p}_k$, that sufficiently decreases the value of cost functional. The search direction can be computed by either a Newton, a Gauss-Newton, a steepest-descent, or a conjugate-gradient method. However, for the sake of brevity we will only analyze the search direction determined via Gauss-Newton method.

Essentially, in the line-search algorithm one solves the following problem:

$$\upsilon_k = \arg\min_{\upsilon} \left\{ C(\mathbf{x}_k + \upsilon \mathbf{p}_k) \right\}. \tag{A.47}$$

Since υ is a scalar this minimization in principle can be carried out by using any nonlinear minimization routine (Press, 1992). However, if the evaluation of the cost functional is expensive, a full nonlinear determination of υ_k might not be feasible, since it will require multiple evaluations of the cost functional. It is therefore desirable to limit the number of such evaluations as much as possible. In this work, we adopt an algorithm whereby a step-length $\upsilon_k > 0$ is selected which reduces the value of cost functional such that the average rate of decrease from $C(\mathbf{x}_k)$ to $C(\mathbf{x}_k + \upsilon_k \mathbf{p}_k)$ is at least some prescribed fraction, α, of the initial rate of decrease at $\mathbf{x}_k$ along the direction $\mathbf{p}_k$, i.e.,

$$C(\mathbf{x}_k + \upsilon_k \mathbf{p}_k) \le C(\mathbf{x}_k) + \alpha \upsilon_k \delta C_{k+1}, \tag{A.48}$$

where $0 < \alpha < 1$ is a fractional number which, in practice, is set quite small (we set α to 1×10^{-4}) so that hardly more than a decrease in the value of cost functional is required. δC_{k+1} is the rate of decrease of $C(\mathbf{x})$ at $\mathbf{x}_k$ along the direction $\mathbf{p}_k$ and is given by

$$\delta C_{k+1} = \frac{\partial}{\partial \upsilon} C(\mathbf{x}_k + \upsilon \mathbf{p}_k)\bigg|_{\upsilon=0} = \mathbf{g}^T(\mathbf{x}_k) \cdot \mathbf{p}_k \tag{A.49}$$

The procedure we will adopt is to first employ the full Gauss-Newton search step and if $\upsilon_k = 1$ fails to satisfy the criterion given by equation (A.48), then backtrack (i.e., reduce υ_k) along the direction of the Gauss-Newton step until an acceptable next iterate $\mathbf{x}_{k+1} = \mathbf{x}_k + \upsilon_k \mathbf{p}_k$ is found.

If, at the $(k+1)^{\text{th}}$ iteration, $\upsilon_k^{(m)}$ is the current step-length that does not satisfy the condition of equation (A.48), we compute the next backtracking step-length, $\upsilon_k^{(m+1)}$, by searching for the minimum of the following functional

$$f(\upsilon) \equiv C(\mathbf{x}_k + \upsilon \mathbf{p}_k), \tag{A.50}$$

which we approximate by a quadratic expression as

$$f(\upsilon) \approx a + b\upsilon + c\upsilon^2, \tag{A.51}$$

where the real constants a, b, and c are determined from the current information on the cost functional $C(\mathbf{x})$ such that

$$f(\upsilon = 0) = C(\mathbf{x}_k), \tag{A.52}$$

$$\frac{df}{d\upsilon}(\upsilon = 0) = \delta C_{k+1}, \tag{A.53}$$

and

$$f(\upsilon = \upsilon_k^{(m)}) = C(\mathbf{x}_k + \upsilon_k^{(m)} \mathbf{p}_k), \tag{A.54}$$

from which we obtain

$$a = C(\mathbf{x}_k), \tag{A.55}$$

$$b = \delta C_{k+1}, \tag{A.56}$$

and

$$c = \frac{1}{\left\{\upsilon_k^{(m)}\right\}^2}\left[C(\mathbf{x}_k + \upsilon_k^{(m)}\mathbf{p}_k) - C(\mathbf{x}_k) - \upsilon_k^{(m)}\delta C_{k+1}\right]. \tag{A.57}$$

Thus, $\upsilon_k^{(m+1)}$, which is the minimum of $f(\upsilon)$, for $m = 0, 1, 2, \ldots$ is given by

$$\upsilon_k^{(m+1)} = -\frac{b}{2c} = -\frac{\left\{\upsilon_k^{(m)}\right\}^2}{2}\frac{\delta C_{k+1}}{C(\mathbf{x}_k + \upsilon_k^{(m)}\mathbf{p}_k) - C(\mathbf{x}_k) - \upsilon_k^{(m)}\delta C_{k+1}}, \tag{A.58}$$

from which it is clear that if $C(\mathbf{x}_k + \upsilon_k^{(m)}\mathbf{p}_k) > C(\mathbf{x}_k)$, then

$$0 < \upsilon_k^{(m+1)} < \frac{1}{2}\upsilon_k^{(m)} < \frac{1}{2^{m+1}}, \quad m = 0, 1, 2, \ldots, \tag{A.59}$$

whereas, if $C(\mathbf{x}_k + \upsilon_k^{(m)}\mathbf{p}_k) > C(\mathbf{x}_k) + \alpha\,\upsilon_k^{(m)}\delta C_{k+1}$, then

$$0 < \upsilon_k^{(m+1)} < \frac{1}{2(1-\alpha)}\upsilon_k^{(m)} < \frac{1}{\left[2(1-\alpha)\right]^{m+1}}, \quad m = 0, 1, 2, \ldots. \tag{A.60}$$

Thus, we start with $\upsilon_k^{(0)} = 1$ and proceed with the backtracking procedure of equation (A.58) until condition (A.48) is satisfied. In general, it is not desirable to decrease $\upsilon_k^{(m+1)}$ too much since this may excessively slow down the iterative process, requiring many iterations to achieve very little progress towards the minimum. To prevent this slow down, we set $\upsilon_k^{(m+1)} = 0.1\,\upsilon_k^{(m)}$ if $\upsilon_k^{(m+1)} < 0.1\,\upsilon_k^{(m)}$ (but with υ_k not to decrease below 0.1,

i.e., $\upsilon_{\min} = 0.1$ to guard against a too small value of υ) and then proceed with the iteration.

In order to take advantage of the newly acquired information on the cost functional beyond the first backtrack, one can replace the quadratic approximation of $f(\upsilon)$ of equation (A.51) by a cubic approximation. If υ_1 and υ_2 are two subsequent search steps, then according to the cubic approximation, the next search step is determined from

$$\upsilon = \frac{-b + \sqrt{b^2 - 3a\,\delta C_{k+1}}}{3a}, \tag{A.61}$$

where a and b given by

$$\begin{bmatrix} a \\ b \end{bmatrix} = \frac{1}{\upsilon_2 - \upsilon_1} \begin{bmatrix} 1/\upsilon_2^2 & -1/\upsilon_1^2 \\ -\upsilon_1/\upsilon_2^2 & \upsilon_2/\upsilon_1^2 \end{bmatrix} \begin{bmatrix} f(\upsilon_2) - \upsilon_2\ \delta C_{k+1} - C(\mathbf{x}_k) \\ f(\upsilon_1) - \upsilon_1\ \delta C_{k+1} - C(\mathbf{x}_k) \end{bmatrix}. \tag{A.62}$$

A.11 COMPUTATION OF THE LAGRANGE MULTIPLIER

There exist several criteria by which one can select the Lagrange multiplier μ. One such criterion (Oldenburg, 1990) is to substitute $\mu = e^{\vartheta}$ or $\mu = \vartheta^2$ (i.e., any transform which enforces μ's positivity) and to assign ϑ a real solution of the following nonlinear algebraic equation

$$\left\| \mathbf{W}_d \cdot \mathbf{e}(\mathbf{x}_k + \mathbf{p}_k(\vartheta)) \right\| = \chi. \tag{A.63}$$

Equation (A.63) results from setting $\partial C(\mathbf{x}, \mu)/\partial \mu = 0$. This method is known as the discrepancy principle. A different strategy for selecting μ is also described by Habashy

et al. (1986), in which a steepest-descent method is applied in the initial steps of the iteration process. This corresponds to choosing small values for μ, hence, allocating more weight on the second term of the cost functional of equation (A.3), since the first term is only crudely approximated by the quadratic model of equation (A.9). As the iteration progresses, the reconstructed model approaches its true value, thus resulting in equation (A.9) becoming more accurate, and hence more weight (corresponding to larger values of μ) is allocated on the minimization of the first term of the cost functional. As such, as the iterative procedure progresses, this approach increasingly resembles the Gauss-Newton method.

One of the working criteria for choosing μ is to bound it by the following inequality

$$\max\left\{small\ \tau_m\text{'}s\right\} \ll \frac{1}{\mu} \ll \min\left\{large\ \tau_m\text{'}s\right\}, \tag{A.64}$$

where τ_m are the eigenvalues of the positive-definite real symmetric matrix given by

$$\mathbf{H} = \left\{\mathbf{W}_x^{-1}\right\}^T \cdot \mathbf{J}^T(\mathbf{x}) \cdot \mathbf{W}_d^T \cdot \mathbf{W}_d \cdot \mathbf{J}(\mathbf{x}) \cdot \mathbf{W}_x^{-1}. \tag{A.65}$$

The second part of the above inequality guarantees that the spectral content of the inversion operator remains unaltered, whereas, the first part of the inequality regularizes the inversion problem by suppressing the null-space of the inversion operator. To illustrate this behavior, we define $\mathbf{u}_m$ as the orthonormal eigenvector corresponding to the eigenvalue τ_m of the matrix $\mathbf{H}$. In this case the solution to equation (A.18) with the Hessian matrix approximated by equation (A.32) is given by

$$\mathbf{p}_k = \mathbf{x}_{k+1} - \mathbf{x}_k = -\sum_{j=1}^{N} \frac{1}{1+\mu\tau_j} (\mathbf{u}_j^T \cdot \mathbf{W}_x^T \cdot \mathbf{g}_k)\, \mathbf{W}_x \cdot \mathbf{u}_j. \tag{A.66}$$

Hence, according to the criterion given in equation (A.64), we obtain

$$\mathbf{p}_k = -\sum_{large\{\tau_j's\}} \frac{1}{\tau_j} (\mathbf{u}_j^T \cdot \mathbf{W}_x^T \cdot \mathbf{g}_k / \mu)\, \mathbf{W}_x \cdot \mathbf{u}_j - \sum_{small\{\tau_j's\}} \mu (\mathbf{u}_j^T \cdot \mathbf{W}_x^T \cdot \mathbf{g}_k / \mu)\, \mathbf{W}_x \cdot \mathbf{u}_j. \tag{A.67}$$

From this expression it is clear that μ acts as a damping factor that suppresses (or filters out) the contributions of the small eigenvalues with the tendency of magnifying the noise in the data, and consequently, causing undesired large swings in $\mathbf{p}_k$. As such, the role of μ, which satisfies the condition of equation (A.64), is to damp out the large deviations of the $(k+1)^{\text{th}}$ iterate from the k^{th} iterate and to safeguard against unwanted large changes in $\mathbf{p}_k$ due to noise in the data. In the implementation, we choose the Lagrange multiplier as follows:

$$\frac{1}{\mu} = \beta \max_{\forall m} \{\tau_m\}, \; for \; \frac{\min_{\forall m} \{\tau_m\}}{\max_{\forall m} \{\tau_m\}} < \beta, \tag{A.68}$$

where β is a constant value determined via numerical implementation.

In order to illustrate the role of the ill-conditioning of the Hessian matrix on the error magnification due to the noisy data, we perturb the right-hand-side of equation (A.18) by $\delta\mathbf{g}$ and compute the corresponding perturbation $\delta\mathbf{p}$ in $\mathbf{p}$ as follows:

$$\mathbf{G} \cdot \delta\mathbf{p} \approx -\delta\mathbf{g}, \tag{A.69}$$

from which we obtain

$$\| \delta \mathbf{p} \| \leq \| \mathbf{G}^{-1} \| \| \delta \mathbf{g} \|. \tag{A.70}$$

Since the following expression holds

$$\| \mathbf{g} \| \leq \| \mathbf{G} \| \| \mathbf{p} \|, \tag{A.71}$$

we obtain

$$\frac{\| \delta \mathbf{p} \|}{\| \mathbf{p} \|} \leq \| \mathbf{G} \| \| \mathbf{G}^{-1} \| \frac{\| \delta \mathbf{g} \|}{\| \mathbf{g} \|} = cond(\mathbf{G}) \frac{\| \delta \mathbf{g} \|}{\| \mathbf{g} \|}. \tag{A.72}$$

The expression in equation (A.72) clearly indicates that the relative error in the estimator, $\| \delta \mathbf{p} \| / \| \mathbf{p} \|$, can be excessively magnified if the condition number of the Hessian matrix is large.

The effect of the presence of $small\{\tau_j's\}$ in the spectrum of $\mathbf{H}$ is to cause the minimum of the cost functional to be a flat valley. The presence of noise in the data will then result in multiple false local minima. The role of the regularizing parameter μ is to sharpen the minimum and to suppress other false local minima.

Eigenvectors with small eigenvalues are the source of non-uniqueness in the inversion problem, i.e., the cause of the ill-posedness of the inversion. The addition of an arbitrary weighted sum of these eigenvectors to any solution of the inverse problem, (namely, inverted model) may still make the resulting model fit the data. Thus, the

knowledge of the observed data will not enable us to construct the part of the model represented by the eigenvectors that correspond to small eigenvalues. Hence, these parts must be recovered from information other than that contained in the data. One approach to recover these components is to incorporate all possible a-priori information concerning the model of interest, thus narrowing down the class of admissible solutions. This goal can be accomplished via the construction of the reference model, $\mathbf{y}_R$, of equation (A.2) and the introduction of the regularization term in the cost functional of equation (A.3). If such a-priori information is not available, one may choose to tolerate the non-uniqueness, if the class of admissible solutions still contains useful and decisive information about the unknown model.

By making use of stationary phase argument, it can be shown that the eigenvectors corresponding to small eigenvalues encompass high spatial frequencies, and hence, they tend to be highly oscillatory. By suppressing these oscillatory eigenvectors as shown in equation (A.67), in effect, one constructs models with the least degree of complexity yielding the best fit of the data.

Evaluation of the eigenvalues of the Hessian matrix tends to be a computationally expensive operation. Guided by the above discussion, in order to enforce the inequality shown in equation (A.64) without evaluating the eigenvalues of the Hessian matrix, one can resort to an alternative approach. This approach relies on an implementation where the regularization parameter, μ, is adaptively varied as the nonlinear inversion iteration process progresses. Recently, van den Berg and Abubakar (2001) introduced an algorithm where the regularization parameter, μ, is automatically computed over the course of the inversion iterations. This approach poses the regularization as a multiplicative factor in the cost functional. Consequently, the regularization parameter is proportionally linked to the non-regularized cost functional. In conjunction with a

conjugate gradient type inversion algorithm, this regularization technique is shown to be very effective in inverting synthetic as well as experimental data (see, for example, Abubakar et al., 2003; van den Berg et al., 2003). In this work, we also adapted this multiplicative regularization technique for the Newton-type algorithms. For this purpose, we modified the cost functional given by the equation (A.3) as follows:

$$C_k(\mathbf{x}) = F(\mathbf{x})R_k(\mathbf{x}), \tag{A.73}$$

where $F(\mathbf{x})$ is the non-regularized cost functional given by

$$F(\mathbf{x}) = \frac{1}{2}\| \mathbf{W}_d \cdot \mathbf{e}(\mathbf{x}) \|^2 . \tag{A.74}$$

The regularization factor $R_k(\mathbf{x})$ is chosen to be

$$R_k(\mathbf{x}) = \eta_k \left(\| \mathbf{W}_x(\mathbf{x} - \mathbf{x}_p) \|^2 + \| \delta \|^2 \right), \tag{A.75}$$

where

$$\eta_k = \frac{1}{\| \mathbf{W}_x(\mathbf{x}_k - \mathbf{x}_p) \|^2 + \| \delta \|^2}, \tag{A.76}$$

in which δ is a constant parameter which is to be determined by numerical experimentation. One should note that the parameter δ is far more insensitive than the Lagrange multiplier. From the observation of equations (A.75) and (A.76), we expect that the parameter δ is only dependent on the type of measurements. The normalization in

the regularization factor $R_k(\mathbf{x})$ is chosen so that $R_k(\mathbf{x}=\mathbf{x}_k)=1$. This ensures that at the end of the optimization process the value of the regularization parameter will be close to unity. Then, the gradient of the cost functional $C(\mathbf{x})$ is given by the following expression:

$$\mathbf{g}_k=\mathbf{g}(\mathbf{x}=\mathbf{x}_k)=\mathbf{J}^T(\mathbf{x}_k)\cdot\mathbf{W}_d^T\cdot\mathbf{W}_d\cdot\mathbf{e}(\mathbf{x}_k)+\eta_k F(\mathbf{x}_k)\,\mathbf{W}_x^T\cdot\mathbf{W}_x\cdot(\mathbf{x}_k-\mathbf{x}_p), \qquad \text{(A.77)}$$

and the Hessian matrix of the cost functional $C(\mathbf{x})$ is given by

$$\begin{aligned}\mathbf{G}_k=\mathbf{G}(\mathbf{x}=\mathbf{x}_k)=&\mathbf{J}^T(\mathbf{x}_k)\cdot\mathbf{W}_d^T\cdot\mathbf{W}_d\cdot\mathbf{J}(\mathbf{x}_k)+\mathbf{Q}(\mathbf{x}_k)+\eta_k F(\mathbf{x}_k)\,\mathbf{W}_x^T\cdot\mathbf{W}_x\\&+\eta_k\left[\mathbf{W}_x^T\cdot\mathbf{W}_x\cdot(\mathbf{x}_k-\mathbf{x}_p)\right]^T\cdot\mathbf{J}^T(\mathbf{x}_k)\cdot\mathbf{W}_d^T\cdot\mathbf{W}_d\cdot\mathbf{e}(\mathbf{x}_k)\\&+\eta_k\left[\mathbf{J}^T(\mathbf{x}_k)\cdot\mathbf{W}_d^T\cdot\mathbf{W}_d\cdot\mathbf{e}(\mathbf{x}_k)\right]^T\cdot\mathbf{W}_x^T\cdot\mathbf{W}_x\cdot(\mathbf{x}_k-\mathbf{x}_p),\end{aligned} \qquad \text{(A.78)}$$

where $\mathbf{Q}(\mathbf{x}_k)$ is given by equation (A.13). If one uses the Gauss-Newton search direction, the equation (A.78) will be modified as follows:

$$\begin{aligned}\mathbf{G}_k=\mathbf{G}(\mathbf{x}=\mathbf{x}_k)=&\mathbf{J}^T(\mathbf{x}_k)\cdot\mathbf{W}_d^T\cdot\mathbf{W}_d\cdot\mathbf{J}(\mathbf{x}_k)+\eta_k F(\mathbf{x}_k)\,\mathbf{W}_x^T\cdot\mathbf{W}_x\\&+\eta_k\left[\mathbf{W}_x^T\cdot\mathbf{W}_x\cdot(\mathbf{x}_k-\mathbf{x}_p)\right]^T\cdot\mathbf{J}^T(\mathbf{x}_k)\cdot\mathbf{W}_d^T\cdot\mathbf{W}_d\cdot\mathbf{e}(\mathbf{x}_k)\\&+\eta_k\left[\mathbf{J}^T(\mathbf{x}_k)\cdot\mathbf{W}_d^T\cdot\mathbf{W}_d\cdot\mathbf{e}(\mathbf{x}_k)\right]^T\cdot\mathbf{W}_x^T\cdot\mathbf{W}_x\cdot(\mathbf{x}_k-\mathbf{x}_p).\end{aligned} \qquad \text{(A.79)}$$

In our numerical implementation, due to the lack of a-priori information, constructing a reliable $\mathbf{x}_p$ is practically not possible. In order to constrain the optimization process such that the inverted model parameters, $\mathbf{x}_k$, will not exhibit large jumps within two successive iterations, we choose $\mathbf{x}_p$ equal to the value of $\mathbf{x}$ at the previous iteration, namely, $\mathbf{x}_p=\mathbf{x}_{k-1}$. For this particular choice of $\mathbf{x}_p$, this multiplicative regularization

technique is equivalent with the standard additive one if we choose the Lagrange multipliers μ to vary as the iteration proceeds according to

$$\frac{1}{\mu} = \frac{F(\mathbf{x}_k)}{\|\delta\|^2} \tag{A.80}$$

The logic underlying the multiplicative regularization procedure is such that the regularization factor, μ, will be minimized due to the use of a larger weighting parameter in the beginning of the optimization process, because the value of $F(\mathbf{x}_k)$ is still large. In this case the search direction is predominantly steepest descent, which is a more appropriate approach to use in the initial steps of the iteration process. This is because the optimization using steepest-descent direction has the tendency of suppressing large swings in the search direction. As the iteration proceeds, the optimization process will increasingly minimize the data misfit error in the non-regularized cost functional when the regularization factor, $R_k(\mathbf{x})$, approaches a constant value close to one. In this case, the search direction increasingly corresponds to the full Newton search direction (or Gauss-Newton direction if one uses the approximate Hessian shown in equation (A.79)). Full Newton (or Gauss-Newton direction) is a more appropriate direction as the iteration process approaches to minimum of the cost functional, $F(\mathbf{x})$, where the quadratic model for the cost functional becomes more accurate. For the cases where measurement-noise is present in the data, the non-regularized cost functional, $F(\mathbf{x})$, will approximately remain at a certain value as the optimization process approaches the minimum. The presence of the weight introduced by the regularization factor, $R_k(\mathbf{x})$, will be more significant. The proposed regularization method ensures that the measurement-noise will at all times be suppressed during the inversion process at the same time the need for a larger regularization parameter will be fulfilled when the measurement data contains noise as

suggested by Rudin et al. (1992) and Chan and Wong (1998). We would like to emphasize the fact that for a normalized (dimensionless) cost functional, the parameter $\|\delta\|^2$, needs to be determined from the noise level of the measurements fed into the inversion algorithm.

A.12 APPROXIMATE UPDATE FORMULAS FOR THE HESSIAN MATRIX

Inversion methods described in the previous sections of this work represent powerful approaches. Yet, they have several disadvantages. One drawback is the need for the computation of the Jacobian matrix, $\mathbf{J}(\mathbf{x})$. In real-world problems of borehole geophysics, usually, model domains subject to inversion are structurally complex, consequently, analytical expressions for the derivatives of equation (A.11) are unavailable. For such cases, these derivatives should be computed numerically. Computational expense associated with the evaluation of finite-difference derivatives may prohibit a frequent use of numerical derivatives. There are, however, a number of quasi-Newton methods that provide computationally inexpensive approximation to the Jacobian for optimization. In this section, we summarize various updating schemes which effectively eliminate the direct computation of the Hessian matrix (Nocedal and Wright, 1999).

Let

$$\mathbf{s}_k = \upsilon_k \mathbf{p}_k = \mathbf{x}_{k+1} - \mathbf{x}_k \tag{A.81}$$

be the step taken from the k^{th} iterate, $\mathbf{x}_k$, to obtain the $(k+1)^{\text{th}}$ iterate, x_{k+1}. Expanding the gradient vector $\mathbf{g}$ about the k^{th} iterate, namely, $\mathbf{x}_k$, using Taylor series expansion, i.e., we obtain

$$g(\mathbf{x}_k + \mathbf{s}_k) = \mathbf{g}(\mathbf{x}_k) + \mathbf{G}(\mathbf{x}_k) \cdot \mathbf{s}_k + \ldots \tag{A.82}$$

or

$$\mathbf{g}_{k+1} = \mathbf{g}_k + \mathbf{G}_k \cdot \mathbf{s}_k + \ldots. \tag{A.83}$$

In any of the following update formulas, the updated Hessian matrix, denoted by $\mathbf{U}_{k+1}$, will be required to satisfy equation (A.83) approximated by the first two terms in the Taylor series expansion, i.e.,

$$\mathbf{g}_{k+1} = \mathbf{g}_k + \mathbf{U}_{k+1} \cdot \mathbf{s}_k \tag{A.84}$$

or

$$\mathbf{U}_{k+1} \cdot \mathbf{s}_k = \mathbf{q}_k \equiv \mathbf{g}_{k+1} - \mathbf{g}_k. \tag{A.85}$$

This condition is referred to as the quasi-Newton condition. The updated Hessian, $\mathbf{U}_{k+1}$, is obtained by updating the previous approximate Hessian, $\mathbf{U}_k$, to take into account the recently acquired information on the curvature of the cost functional quantified in equation (A.85). The Hessian matrix, $\mathbf{U}_k$ is the approximate Hessian matrix at the beginning of the k^{th} iteration, which reflects the curvature information that has already been accumulated. The matrix $\mathbf{U}_k$ is utilized to determine the k^{th} Gauss-Newton search direction, $\mathbf{p}_k$, by using equation (A.18)

$$\mathbf{U}_k \cdot \mathbf{p}_k = -\mathbf{g}_k \tag{A.86}$$

or

$$\mathbf{U}_k \cdot \mathbf{s}_k = -\upsilon_k \, \mathbf{g}_k . \tag{A.87}$$

A.12.1 The Rank-One Matrix Update

In this update, $\mathbf{U}_{k+1}$ is constructed from $\mathbf{U}_k$ by adding a symmetric matrix of rank-one (since the Hessian matrix is a symmetric matrix)

$$\mathbf{U}_{k+1} = \mathbf{U}_k + \mathbf{u}\,\mathbf{u}^T, \tag{A.88}$$

for some vector $\mathbf{u}$. Substituting into the quasi-Newton condition in equation (A.85), we obtain

$$\left(\mathbf{u}^T \cdot \mathbf{s}_k\right)\mathbf{u} = \mathbf{q}_k - \mathbf{U}_k \cdot \mathbf{s}_k, \tag{A.89}$$

from which we can easily deduce that

$$\mathbf{u} = \frac{1}{\left[\mathbf{s}_k^T \cdot \left(\mathbf{q}_k - \mathbf{U}_k \cdot \mathbf{s}_k\right)\right]^{1/2}}\left(\mathbf{q}_k - \mathbf{U}_k \cdot \mathbf{s}_k\right), \tag{A.90}$$

and hence, the update formula for $\mathbf{U}_{k+1}$ is given by

$$\mathbf{U}_{k+1} = \mathbf{U}_k + \frac{1}{\mathbf{s}_k^T \cdot \left(\mathbf{q}_k - \mathbf{U}_k \cdot \mathbf{s}_k\right)}\left(\mathbf{q}_k - \mathbf{U}_k \cdot \mathbf{s}_k\right)\left(\mathbf{q}_k - \mathbf{U}_k \cdot \mathbf{s}_k\right)^T . \tag{A.91}$$

In the above equation, it is assumed that $\mathbf{U}_k \cdot \mathbf{s}_k \neq \mathbf{q}_k$ and $\mathbf{s}_k^T \cdot \left(\mathbf{q}_k - \mathbf{U}_k \cdot \mathbf{s}_k\right) \neq 0$. The update formula of equation (A.91) can also be written as

$$\mathbf{U}_{k+1} = \mathbf{U}_k + \frac{1}{\mathbf{s}_k^T \cdot \left(\mathbf{q}_k + \upsilon_k \, \mathbf{g}_k\right)} \left(\mathbf{q}_k + \upsilon_k \, \mathbf{g}_k\right) \left(\mathbf{q}_k + \upsilon_k \, \mathbf{g}_k\right)^T . \tag{A.92}$$

The above update formula is called Broyden symmetric rank-one update. At this point, we would like to note that the quasi-Newton condition of equation (A.85) will continue to hold even if further rank-one matrices of the form $\mathbf{v}\mathbf{v}^T$ are added to $\mathbf{U}_{k+1}$ as long as the vector $\mathbf{v}$ is orthogonal to $\mathbf{s}_k$, i.e., $\mathbf{v}^T \cdot \mathbf{s}_k = 0$. Undoubtedly, the elements of $\mathbf{U}_{k+1}$ will change by each additional matrix.

A.12.2 Rank-Two Matrix Updates

In rank-two matrix updates, $\mathbf{U}_{k+1}$ is constructed from $\mathbf{U}_k$ by adding a symmetric matrix of rank-two. The general form of a symmetric rank-two matrix update is given by

$$\mathbf{U}_{k+1} = \mathbf{U}_k + \mathbf{u}\mathbf{u}^T + \alpha \left\{\mathbf{u}\mathbf{v}^T + \mathbf{v}\mathbf{u}^T\right\} + \mathbf{v}\mathbf{v}^T , \tag{A.93}$$

where $\mathbf{u}$ and $\mathbf{v}$ are any two different vectors and α is scalar. The Hessian matrix updates discussed in this section can all be derived from the following formula which satisfies the quasi-Newton condition of equation (A.85)

$$\mathbf{U}_{k+1} = \mathbf{U}_k + \frac{1}{\mathbf{s}_k^T \cdot \mathbf{v}} \left\{\left(\mathbf{q}_k + \upsilon_k \, \mathbf{g}_k\right) \mathbf{v}^T + \mathbf{v} \left(\mathbf{q}_k + \upsilon_k \, \mathbf{g}_k\right)^T\right\} - \frac{\mathbf{s}_k^T \cdot \left(\mathbf{q}_k + \upsilon_k \, \mathbf{g}_k\right)}{\left(\mathbf{s}_k^T \cdot \mathbf{v}\right)^2} \mathbf{v}\mathbf{v}^T . \tag{A.94}$$

Equation (A.94) holds for any arbitrary vector $\mathbf{v}$ that is not orthogonal to $\mathbf{s}_k$, i.e., $\mathbf{s}_k^T \cdot \mathbf{v} \neq 0$. Note that the rank-one matrix update of equation (A.92) can be derived from the rank-two matrix update of equation (A.94) by setting $\mathbf{v} = \mathbf{q}_k + \upsilon_k \, \mathbf{g}_k$.

A.12.2.1 The Powell-Symmetric-Broyden (PSB) Update

In Powell-Symmetric-Broyden update, the arbitrary vector $\mathbf{v}$ is chosen to be $\mathbf{s}_k$, to obtain the formula given by

$$\mathbf{U}_{k+1} = \mathbf{U}_k + \frac{1}{\| \mathbf{s}_k \|^2} \left\{ \left(\mathbf{q}_k + \upsilon_k \, \mathbf{g}_k \right) \mathbf{s}_k^T + \mathbf{s}_k \left(\mathbf{q}_k + \upsilon_k \, \mathbf{g}_k \right)^T \right\} - \frac{\mathbf{s}_k^T \cdot \left(\mathbf{q}_k + \upsilon_k \, \mathbf{g}_k \right)}{\| \mathbf{s}_k \|^4} \mathbf{s}_k \mathbf{s}_k^T. \quad \text{(A.95)}$$

A.12.2.2 The Davidson-Fletcher-Powell (DFP) Update

In Davidson-Fletcher-Powell update, the arbitrary vector $\mathbf{v}$ is chosen to be $\mathbf{q}_k$, to obtain the formula given by

$$\mathbf{U}_{k+1} = \mathbf{U}_k + \frac{\upsilon_k}{\mathbf{s}_k^T \cdot \mathbf{g}_k} \mathbf{g}_k \mathbf{g}_k^T + \frac{1}{\mathbf{s}_k^T \cdot \mathbf{q}_k} \mathbf{q}_k \mathbf{q}_k^T - \upsilon_k \left(\mathbf{s}_k^T \cdot \mathbf{g}_k \right) \mathbf{w}_k \mathbf{w}_k^T, \quad \text{(A.96)}$$

where

$$\mathbf{w}_k \equiv \frac{1}{\mathbf{s}_k^T \cdot \mathbf{q}_k} \mathbf{q}_k - \frac{1}{\mathbf{s}_k^T \cdot \mathbf{g}_k} \mathbf{g}_k. \quad \text{(A.97)}$$

Note that $\mathbf{w}_k$ is orthogonal to $\mathbf{s}_k$, i.e., $\mathbf{s}_k^T \cdot \mathbf{w}_k = 0$.

A.12.2.3 The Broyden-Fletcher-Goldfarb-Shanno (BFGS) Update

Since $\mathbf{w}_k$ is orthogonal to $\mathbf{s}_k$, consequently, any multiple of rank-one matrix $\mathbf{w}_k\mathbf{w}_k^T$ can be added to $\mathbf{U}_{k+1}$ without violating the quasi-Newton condition of equation (A.85). This leads to the following update formula

$$\mathbf{U}_{k+1} = \mathbf{U}_k + \frac{\upsilon_k}{\mathbf{s}_k^T \cdot \mathbf{g}_k}\mathbf{g}_k\mathbf{g}_k^T + \frac{1}{\mathbf{s}_k^T \cdot \mathbf{q}_k}\mathbf{q}_k\mathbf{q}_k^T - \alpha\upsilon_k\left(\mathbf{s}_k^T \cdot \mathbf{g}_k\right)\mathbf{w}_k\mathbf{w}_k^T, \tag{A.98}$$

where α is any scalar. In the case of the Broyden-Fletcher-Goldfarb-Shanno update, α is set equal to zero. Thus, we obtain

$$\mathbf{U}_{k+1} = \mathbf{U}_k + \frac{\upsilon_k}{\mathbf{s}_k^T \cdot \mathbf{g}_k}\mathbf{g}_k\mathbf{g}_k^T + \frac{1}{\mathbf{s}_k^T \cdot \mathbf{q}_k}\mathbf{q}_k\mathbf{q}_k^T. \tag{A.99}$$

Although it is possible to start the approximation of the Hessian matrix $\mathbf{U}_k$ by simply using the identity matrix, $\mathbf{I}$, in the current implementation, we prefer to spend the first N evaluations of the cost functional on finite-difference approximation to initialize $\mathbf{U}_k$. Finally, it has to be noted that, since $\mathbf{U}_k$ is not the exact Jacobian, it is not guaranteed that $\mathbf{p}_k$ is a descent direction for the cost functional of equation (A.9). Thus, the line search algorithm can fail to return a suitable step if $\mathbf{U}_k$ wanders far away from the true Jacobian. In this case, we reinitialize $\mathbf{U}_k$ using finite-difference approximation through evaluations of the cost functional.

A.13 CRITERIA FOR TERMINATING THE ITERATIVE PROCESS

The iteration process will stop if one of the following conditions occurs first:

(a) The root-mean-square of the relative error reaches a prescribed value η determined from estimates of noise in the data, i.e.,

$$\left\{\frac{1}{M}\left\|\mathbf{e}\right\|^2\right\}^2 \le \eta, \tag{A.100}$$

where η is a pre-determined a-priori information that has to be provided by the user. In the hypothetical case of noise-free data, $\eta = 0$.

(b) The differences between two successive iterates, $(k+1)^{\text{th}}$ and k^{th}, of the model parameters are within a prescribed tolerance factor, tol, of the current iterate, and thus, satisfying the following relationship

$$\sum_{j=1}^{N}\left| x_{j,k+1} - x_{j,k} \right| \le tol \times \sum_{j=1}^{N}\left| x_{j,k+1} \right|. \tag{A.101}$$

(c) The difference between the values of cost functional at two successive iterates, $(k+1)^{\text{th}}$ and k^{th}, of the model parameters is within a prescribed tolerance factor, $tole$, of the value of cost functional at the current iterate, and thus, satisfying the following relationship

$$\left| C(\mathbf{x}_{k+1}) - C(\mathbf{x}_k) \right| \le tole \times C(\mathbf{x}_{k+1}). \tag{A.102}$$

(d) The number of iterations exceeds a prescribed maximum number.

A.14 REGULARIZATION

As previously mentioned, the inversion problem is invariably ill-posed. One approach of narrowing down the solution of the inverse problem is to introduce a-priori information through use of a regularization term in the cost functional, as was done in the

case of the cost functional of equation (A.3). In this section, we will discuss several other choices of the regularization term.

Let us generalize the cost functional of equation (A.3) by redefining it as follows:

$$C(\mathbf{x}) = \frac{1}{2}\left[\mu \left\{ \left\| \mathbf{W}_d \cdot \mathbf{e}(\mathbf{x}) \right\|^2 - \chi^2 \right\} + R(\mathbf{x}, \mathbf{x}_p) \right], \tag{A.103}$$

where $R(\mathbf{x}, \mathbf{x}_p)$ is a generalized regularization term. The selection of $R(\mathbf{x}, \mathbf{x}_p)$ will bias the class of models to be inverted.

A.14.1 L_1 – Norm Regularization

The weighted L_q – norm of a vector $\mathbf{u}$ is defined as follows:

$$\left\| \mathbf{W} \cdot \mathbf{u} \right\|_q = \left[\sum_{i=1}^{N} \left| \sum_{j=1}^{N} W_{ij} u_j \right|^q \right]^{1/q}. \tag{A.104}$$

The L_1 – norm regularization term is hence given by

$$R(\mathbf{x}, \mathbf{x}_p) = \left\| \mathbf{W}_x \cdot (\mathbf{x} - \mathbf{x}_p) \right\|_1 = \sum_{i=1}^{N} \left| \sum_{j=1}^{N} W_{ij} (x_j - x_{pj}) \right|. \tag{A.105}$$

Unlike the L_2 – norm regularization term of equation (A.3), the L_1 – norm allows the inverted parameters to acquire large differences (large contrasts) relative to each other. However, as a point of caution we would like to point out that such a regularization term may introduce spurious artifacts due to the ill-posedness of the inversion problem combined with the presence of noise in the data.

The L_1-norm regularization term has the disadvantage that it derivative does not exist. Therefore, such a regularization approach is not compatible with the Newton-type methods where derivatives are required. An alternative approach to Newton-type methods is to employ linear programming schemes.

A.14.2 Maximum Entropy Regularization

In the maximum entropy regularization method, the regularization term is defined by

$$R(\mathbf{x}, \mathbf{x}_p) = -\sum_{j=1}^{N} r_j \ln(r_j), \tag{A.106}$$

where

$$r_j = \frac{t_j}{T},\ T = \sum_{j=1}^{N} t_j \ \Rightarrow\ \sum_{j=1}^{N} r_j = 1, \tag{A.107}$$

and the vector $\mathbf{t}$ is given by

$$\mathbf{t} = \mathbf{W}_x \cdot (\mathbf{x} - \mathbf{x}_p). \tag{A.108}$$

The advantage of the maximum entropy regularization term is that it provides the most probable estimation that is consistent with the measured data. Similar to the L_1-norm regularization term, yet, to a lesser extent owing to its inherent smoothing effect, it also allows the inverted parameters to acquire large differences (large contrasts). However, maximum entropy regularization method effectively suppresses the appearance of spurious artifacts resulting from the ill-posedness of the inversion problem and the

presence of noise in the data. Another inherent property of the maximum entropy regularization method is that it automatically enforces positivity on the model parameters without the necessity of imposing additional constraints. As shown in equation (A.106), term $R(\mathbf{x}, \mathbf{x}_p)$ has an infinite slope as any of the model parameters approaches to zero.

A.15 THE WEIGHTED LEAST SQUARES MINIMIZATION IN THE FRAMEWORK OF STOCHASTIC ESTIMATION

A.15.1 Preliminaries

In the stochastic framework, each data point m_i is assumed to be different from the corresponding simulated response $S_i(\mathbf{x})$ by a measurement error (or noise) denoted by e_i as shown in equation (A.1)

$$\mathbf{e} = S(\mathbf{x}) - \mathbf{m}. \tag{A.109}$$

One assumes that the measurement noise $\mathbf{e}$ is a random variable represented by a normal (Gaussian) distribution with zero mean. In this case, the probability distribution function for the measurement noise $\mathbf{e}$ is given by (Tarantola, 1987)

$$P(\mathbf{e}) = P_e \exp\left(-\frac{1}{2}\mathbf{e}^T \cdot \mathbf{\Lambda}_e^{-1} \cdot \mathbf{e} \right) = P_e \exp\left\{ -\frac{1}{2}\left[\mathbf{m} - S(\mathbf{x})\right]^T \cdot \mathbf{\Lambda}_e^{-1} \cdot \left[\mathbf{m} - S(\mathbf{x})\right] \right\}, \tag{A.110}$$

where P_e is a normalization constant and $\mathbf{\Lambda}_e$ is the noise covariance matrix. The above Gaussian distribution assumption will breakdown if the simulated response, $S(\mathbf{x})$, does not exactly and fully represent the physics of the measurement $\mathbf{m}$. In this case, the error will be biased by the degree of inaccuracy in the simulated response and hence will not possess a normal distribution.

The probability distribution function of equation (A.110) is also the conditional probability density $P(\mathbf{m}\,|\,\mathbf{x})$ of the data $\mathbf{m}$ given by the model $\mathbf{x}$ such that

$$P(\mathbf{m}\,|\,\mathbf{x}) = P_e \exp\left\{-\frac{1}{2}\left[\mathbf{m} - S(\mathbf{x})\right]^T \cdot \boldsymbol{\Lambda}_e^{-1} \cdot \left[\mathbf{m} - S(\mathbf{x})\right]\right\}. \tag{A.111}$$

In Bayesian inference approaches, this probability density function is also referred to as the likelihood function and is denoted by $L(\mathbf{x}\,|\,\mathbf{m})$. Maximizing the probability distribution function of equation (A.111) is equivalent to minimizing the negative of its logarithm which is also equivalent to the weighted least squares minimization of the first term of the cost functional of equation (A.3) with

$$\boldsymbol{\Lambda}_e^{-1} = \mathbf{W}_d^T \cdot \mathbf{W}_d. \tag{A.112}$$

This form of parameter estimation is called the maximum likelihood estimation such that

$$\mathbf{x}_{ML} = \arg\max_{\mathbf{x}} \left\{L(\mathbf{x}\,|\,\mathbf{m})\right\} = \arg\max_{\mathbf{x}} \left\{P(\mathbf{m}\,|\,\mathbf{x}\right\}, \tag{A.113}$$

or

$$\mathbf{x}_{ML} = \arg\min_{\mathbf{x}} \left\{-\frac{1}{2}\left[\mathbf{m} - S(\mathbf{x})\right]^T \cdot \boldsymbol{\Lambda}_e^{-1} \cdot \left[\mathbf{m} - S(\mathbf{x})\right]\right\}. \tag{A.114}$$

On the other hand, the joint probability density function, $P(\mathbf{x}, \mathbf{m})$, can be represented by Bayes' rule as follows:

$$P(\mathbf{x}, \mathbf{m}) = P(\mathbf{m})\,P(\mathbf{x}\,|\,\mathbf{m}) = P(\mathbf{x})\,P(\mathbf{m}\,|\,\mathbf{x}) = P(\mathbf{x})\,L(\mathbf{x}\,|\,\mathbf{m}). \tag{A.115}$$

From equation (A.115) we obtain the following expression for the conditional probability density of the model $\mathbf{x}$ given the data $\mathbf{m}$:

$$P(\mathbf{x}\,|\,\mathbf{m}) = \frac{P(\mathbf{x})\,L(\mathbf{x}\,|\,\mathbf{m})}{P(\mathbf{m})}, \tag{A.116}$$

where $P(\mathbf{x})$ and $P(\mathbf{m})$ are the prior (or marginal) probability density functions of the model $\mathbf{x}$ and the data $\mathbf{m}$, respectively. In the terminology of the Bayesian estimation approach, $P(\mathbf{x}\,|\,\mathbf{m})$ is referred to as the posterior probability density function, $P(\mathbf{x})$ is the prior probability density function, and $P(\mathbf{m})$ as the evidence. The prior probability density function $P(\mathbf{m})$ can be regarded as a normalization factor which makes the integral of the posterior probability density function $P(\mathbf{x}\,|\,\mathbf{m})$ with respect to the model vector $\mathbf{x}$ equal to unity, hence

$$P(\mathbf{m}) = \int d\mathbf{x}\; P(\mathbf{x})L(\mathbf{x}\,|\,\mathbf{m}). \tag{A.117}$$

The estimation problem of maximizing the posterior probability density function, $P(\mathbf{x}\,|\,\mathbf{m})$, is often called the maximum a posteriori estimation, i.e.,

$$\mathbf{x}_{MAP} = \arg\max_{\mathbf{x}} \left\{ P(\mathbf{x}\,|\,\mathbf{m}) \right\}, \tag{A.118}$$

which is equivalent to minimizing the negative of the logarithm of $P(\mathbf{x}\,|\,\mathbf{m})$, i.e.,

$$\mathbf{x}_{MAP} = \arg\min_{\mathbf{x}} \left\{ \frac{1}{2}\left[S(\mathbf{x}) - \mathbf{m}\right]^T \cdot \boldsymbol{\Lambda}_e^{-1} \cdot \left[S(\mathbf{x}) - \mathbf{m}\right] - \ln\left[\frac{P_e\,P(\mathbf{x})}{P(\mathbf{m})}\right] \right\}. \tag{A.119}$$

Maximum a posteriori estimation is also equivalent to the weighted least squares minimization problem defined by the cost functional of equation (A.103) with the regularization term given by

$$R(\mathbf{x}, \mathbf{x}_p) = -2 \ln \left[\frac{P_e \, P(\mathbf{x})}{P(\mathbf{m})} \right]. \tag{A.120}$$

From equations (A.114) and (A.119), $\mathbf{x}_{MAP}$ will reduce to $\mathbf{x}_{ML}$ in the absence of any a-priori information, i.e., with a uniform prior probability density function $P(\mathbf{x})$.

Introducing the additional assumption that the model $\mathbf{x}$ is a random variable represented by a normal distribution with mean $\mathbf{x}_p$, the prior probability density function is thus given by

$$P(\mathbf{x}) = P_x \exp\left\{ -\frac{1}{2} \left[\mathbf{x} - \mathbf{x}_p \right]^T \cdot \mathbf{\Lambda}_x^{-1} \cdot \left[\mathbf{x} - \mathbf{x}_p \right] \right\}, \tag{A.121}$$

where P_x is a normalization constant. The model covariance matrix $\mathbf{\Lambda}_x^{-1}$ is given by

$$\mathbf{\Lambda}_x^{-1} = \mathbf{W}_x^T \cdot \mathbf{W}_x. \tag{A.122}$$

Thus, in this case,

$$\mathbf{x}_{MAP} = \arg\min_{\mathbf{x}} \frac{1}{2} \left\{ \left[S(\mathbf{x}) - \mathbf{m} \right]^T \cdot \mathbf{\Lambda}_e^{-1} \cdot \left[S(\mathbf{x}) - \mathbf{m} \right] + \left[\mathbf{x} - \mathbf{x}_p \right]^T \cdot \mathbf{\Lambda}_x^{-1} \cdot \left[\mathbf{x} - \mathbf{x}_p \right] \right\}, \tag{A.123}$$

which is equivalent to the weighted least squares minimization problem defined by the cost functional of equation (A.3) with

$$\mu = 1,\ \boldsymbol{\Lambda}_e^{-1} = \mathbf{W}_d^T \cdot \mathbf{W}_d,\ \text{and}\ \boldsymbol{\Lambda}_x^{-1} = \mathbf{W}_x^T \cdot \mathbf{W}_x. \tag{A.124}$$

At this point, we would like to emphasize the fact that the above stochastic framework does not readily provide a means to accommodate a Lagrange multiplier μ as in the least squares approach defined by the cost functional of equation (A.3). As discussed above, the role of the Lagrange multiplier μ is important in eliminating degenerate inversions which are likely to achieve unrealistically small values of the residual errors to levels below the noise plateau χ. By judicially adjusting the Lagrange multiplier, μ, the residual errors will be brought into their expected statistical range. In the following sections, the Lagrange multiplier, μ, will be introduced in the exponent of the likelihood function, to obtain

$$P(\mathbf{x} \mid \mathbf{m}) = \frac{P_e\, P_x}{P(\mathbf{m})} \exp\{-C(\mathbf{x}, \mathbf{m})\}, \tag{A.125}$$

where $C(\mathbf{x}, \mathbf{m})$ is given by

$$C(\mathbf{x}, \mathbf{m}) = \frac{1}{2}\left\{\mu\left[S(\mathbf{x}) - \mathbf{m}\right]^T \cdot \boldsymbol{\Lambda}_e^{-1} \cdot \left[S(\mathbf{x}) - \mathbf{m}\right] + \left[\mathbf{x} - \mathbf{x}_p\right]^T \cdot \boldsymbol{\Lambda}_x^{-1} \cdot \left[\mathbf{x} - \mathbf{x}_p\right]\right\}. \tag{A.126}$$

Finally, it should be noted that the choice of which probability density, $P(\mathbf{e})$, may truly represent the experimental uncertainties for the data is not a straightforward matter. In principle, a careful examination of the experimental conditions under which the data were gathered can suggest an appropriate choice of the probability density for representing the

data uncertainties, however, such a task may not always be easy or even possible. The difficulty that arises in attempting to describe the statistics of the data, is that some of the uncertainties affecting the data are not statistical in nature. Because of these difficulties, the tendency sometimes is to assume a probability density which may result in biasing the estimation process leading to erroneous results.

A.15.2 The Fisher Information Matrix

Let us define a score function as the gradient with respect to the model parameters of the logarithm of the joint probability distribution function as shown by Scharf (1991)

$$\mathbf{s}(\mathbf{x}, \mathbf{m}) = \nabla_{\mathbf{x}} \ln\left[P(\mathbf{x}, \mathbf{m})\right]. \tag{A.127}$$

The score function "scores" values of $\mathbf{x}$ as the random vector $\mathbf{m}$ assumes its various values. Score values which are near to zero are "good" scores and scores which are different from zero are "bad" scores. The score function has mean zero, i.e.,

$$E\left\{\mathbf{s}(\mathbf{x}, \mathbf{m})\right\} = \int d\mathbf{m}\; P(\mathbf{x}, \mathbf{m}) \nabla_{\mathbf{x}} \ln\left[P(\mathbf{x}, \mathbf{m})\right] = \nabla_{\mathbf{x}} \int d\mathbf{m}\; P(\mathbf{x}, \mathbf{m}) = 0, \tag{A.128}$$

where E denotes the expected value. The Fisher Information Matrix is the covariance matrix of the score function and is denoted by $\mathbf{\Gamma}(\mathbf{x})$

$$\mathbf{\Gamma}(\mathbf{x}) = E\left\{\mathbf{s}(\mathbf{x}, \mathbf{m})\, \mathbf{s}^T(\mathbf{x}, \mathbf{m})\right\} = E\left\{\left[\nabla_{\mathbf{x}} \ln\left[P(\mathbf{x}, \mathbf{m})\right]\right]\left[\nabla_{\mathbf{x}} \ln\left[P(\mathbf{x}, \mathbf{m})\right]\right]^T\right\}. \tag{A.129}$$

From the identity

$$\nabla_{\mathbf{x}}\nabla_{\mathbf{x}} \ln\left[P(\mathbf{x}, \mathbf{m})\right] = \frac{1}{P(\mathbf{x}, \mathbf{m})}\nabla_{\mathbf{x}}\nabla_{\mathbf{x}} P(\mathbf{x}, \mathbf{m}) - \left[\nabla_{\mathbf{x}} \ln\left[P(\mathbf{x}, \mathbf{m})\right]\right]\left[\nabla_{\mathbf{x}} \ln\left[P(\mathbf{x}, \mathbf{m})\right]\right]^T \tag{A.130}$$

and from the equality

$$E\left\{\frac{1}{P(\mathbf{x}, \mathbf{m})}\nabla_{\mathbf{x}}\nabla_{\mathbf{x}} P(\mathbf{x}, \mathbf{m})\right\} = 0, \tag{A.131}$$

it follows that $\mathbf{\Gamma}(\mathbf{x})$ is also given by

$$\mathbf{\Gamma}(\mathbf{x}) = -E\left\{\nabla_{\mathbf{x}}\nabla_{\mathbf{x}} \ln\left[P(\mathbf{x}, \mathbf{m})\right]\right\}. \tag{A.132}$$

Using expression (A.132) and for the posterior probability density function of equation (A.125), the Fisher information matrix is given by the Hessian matrix of equation (A.12).

$$\mathbf{\Gamma}(\mathbf{x}) = \mathbf{G}(\mathbf{x}) = \mathbf{\Lambda}_x^{-1} + \mu\, \mathbf{J}^T(\mathbf{x}) \cdot \mathbf{\Lambda}_e^{-1} \cdot \mathbf{J}(\mathbf{x}), \tag{A.133}$$

where we have discarded second-order derivatives consistent with the Gauss-Newton optimization method. This assumption is justified since the residual error at the minimum of the cost functional is small enough such that the first-order term $\mathbf{J}^T(\mathbf{x}) \cdot \mathbf{\Lambda}_e^{-1} \cdot \mathbf{J}(\mathbf{x})$ of equation (A.12) will dominate over the second-order term $\mathbf{Q}(\mathbf{x})$ which is weighted by the residual errors. The Fisher information matrix is a measure of the information content in the data. It provides a sensitivity map of the data with respect to the model parameters.

A.15.3 The Estimator's Covariance Matrix and the Cramer-Rao Bounds

Subsequent to the estimation of the vector of the model parameters $\mathbf{x}$, one is interested in computing the estimator's covariance matrix denoted by $\boldsymbol{\Sigma}$ and defined by

$$\boldsymbol{\Sigma} = E\left\{\left[\mathbf{x}^* - E(\mathbf{x}^*)\right]\left[\mathbf{x}^* - E(\mathbf{x}^*)\right]^T\right\}, \tag{A.134}$$

where x^* is the estimator of the model parameter vector $\mathbf{x}$. A related parameter that attempts to quantify errors is the error covariance matrix denoted by $\boldsymbol{\Omega}$ and defined by

$$\boldsymbol{\Omega} = E\left\{\left[\mathbf{x}^* - \mathbf{x}\right]\left[\mathbf{x}^* - \mathbf{x}\right]^T\right\}. \tag{A.135}$$

The diagonal element, $E\left\{(x_n^* - x_n)^2\right\}$, is the mean-squared error between the estimator x_n^* and the true model parameter x_n. The off-diagonal element is the cross-covariance between the errors of two different parameters of the model. The error covariance matrix is related to the estimator's covariance matrix by

$$\boldsymbol{\Omega} = \boldsymbol{\Sigma} + \mathbf{B}, \tag{A.136}$$

where $\mathbf{B}$ is the bias-squared matrix for the estimator, given by

$$\mathbf{B} = \left[E\left\{\mathbf{x}^*\right\} - \mathbf{x}\right]\left[E\left\{\mathbf{x}^*\right\} - \mathbf{x}\right]^T. \tag{A.137}$$

The diagonal term of $\boldsymbol{\Omega}$ (the mean-squared error of the estimator) is therefore given by

$$E\left\{(x_n^* - x_n)^2\right\} = E\left\{\left[x_n^* - E\left\{x_n\right\}\right]^2\right\} + \left(E\left\{x_n^*\right\} - x_n\right)^2 = \mathrm{var}(x_n^*) + \left(E\left\{x_n^*\right\} - x_n\right)^2,$$

(A.138)

which is the sum of the variance of the estimator plus its bias-squared. The estimator $\mathbf{x}^*$ is said to be unbiased if

$$E\left\{\mathbf{x}^*\right\} = \mathbf{x}, \tag{A.139}$$

in this case $\mathbf{B} = 0$ and the error covariance matrix, $\mathbf{\Omega}$, is equal to the estimator's covariance matrix, $\mathbf{\Sigma}$, while the mean-squared error becomes the variance of the estimator. In this case, for an unbiased estimator, it can be shown that (Scharf, 1991)

$$\mathbf{\Sigma} = \mathbf{\Omega} \geq \mathbf{\Gamma}^{-1}, \tag{A.140}$$

which is the Cramer-Rao inequality that bounds the covariance matrix of an unbiased estimator from below by the inverse of the Fisher information matrix.

A similar and an approximate result can be obtained by expanding the exponent, $C(\mathbf{x}, \mathbf{m})$, of the posterior probability density function, $P(\mathbf{x} \mid \mathbf{m})$, of equations (A.125) and (A.126), respectively, around the estimator $\mathbf{x}^*$, to obtain

$$P(\mathbf{x} \mid \mathbf{m}) \approx \frac{P_e P_x}{P(\mathbf{m})} \exp\left\{-C(\mathbf{x}^*, \mathbf{m})\right\} \exp\left\{-\frac{1}{2}(\mathbf{x} - \mathbf{x}^*)^T \cdot \mathbf{G}(\mathbf{x}^*) \cdot (\mathbf{x} - \mathbf{x}^*)\right\}, \tag{A.141}$$

which shows that when the cost functional is approximated by a local quadratic form, the posterior probability density function is Gaussian in the model space. Furthermore, from

equation (A.141) one can trivially deduce that the estimator's covariance matrix, $\mathbf{\Sigma}$, is approximated by

$$\begin{aligned}\mathbf{\Sigma}(\mathbf{x}^*) &\approx \mathbf{G}^{-1}(\mathbf{x}^*) = \mathbf{\Gamma}^{-1}(\mathbf{x}^*) = \left[\mathbf{\Lambda}_x^{-1} + \mu\,\mathbf{J}^T(\mathbf{x}^*)\cdot\mathbf{\Lambda}_e^{-1}\cdot\mathbf{J}(\mathbf{x}^*)\right]^{-1} \\ &= \mathbf{\Lambda}_x - \mu\,\mathbf{\Lambda}_x\cdot\mathbf{J}^T(\mathbf{x}^*)\cdot\left[\mathbf{\Lambda}_e + \mu\,\mathbf{J}^T(\mathbf{x}^*)\cdot\mathbf{\Lambda}_x\cdot\mathbf{J}(\mathbf{x}^*)\right]^{-1}\cdot\mathbf{J}(\mathbf{x}^*)\cdot\mathbf{\Lambda}_x. \qquad \text{(A.142)}\end{aligned}$$

In deriving equation (A.141), the gradient $\mathbf{g}(\mathbf{x}^*)$ is set to zero, since it vanishes at the minimum of the cost functional, $C(\mathbf{x},\mathbf{m})$. In the case when the measurement noise is uncorrelated and with a uniform standard deviation, σ, then

$$\begin{aligned}\mathbf{\Sigma}(\mathbf{x}^*) &\approx \sigma^2\left[\sigma^2\mathbf{\Lambda}_x^{-1} + \mu\,\mathbf{J}^T(\mathbf{x}^*)\cdot\mathbf{J}(\mathbf{x}^*)\right]^{-1} \\ &= \mathbf{\Lambda}_x - \mu\,\mathbf{\Lambda}_x\cdot\mathbf{J}^T(\mathbf{x}^*)\cdot\left[\sigma^2\mathbf{I} + \mu\,\mathbf{J}^T(\mathbf{x}^*)\cdot\mathbf{\Lambda}_x\cdot\mathbf{J}(\mathbf{x}^*)\right]^{-1}\cdot\mathbf{J}(\mathbf{x}^*)\cdot\mathbf{\Lambda}_x. \qquad \text{(A.143)}\end{aligned}$$

The square root of the diagonal terms (variances) of the covariance matrix provide "error bars" describing the uncertainties in the estimated values of the model parameters. On the average, the true value of the i^{th} model parameter x_i will fall 68% of the time within $\pm\sqrt{\Sigma_{ii}}$ of the estimated value x_i^*, within $\pm 2\sqrt{\Sigma_{ii}}$, 95% of the time, and within $\pm 3\sqrt{\Sigma_{ii}}$, 99.7% of the time.

The interpretation of the off-diagonal elements (covariances) of the covariance matrix is not straightforward. A more meaningful indicator of error correlations is the correlation coefficient matrix, $\boldsymbol{\rho}$, defined by

$$\rho_{ij} = \frac{\Sigma_{ij}}{\sqrt{\Sigma_{ii}\Sigma_{jj}}}, \qquad \text{(A.144)}$$

which is bounded by the inequality

$$-1 \le \rho_{ij} \le +1. \tag{A.145}$$

If the correlation coefficient, ρ_{ij}, between the estimated parameters x_i^* and x_j^* is close to zero, then the uncertainties in estimating these two model parameters are uncorrelated. On the other hand, the uncertainties will be highly correlated (or anti-correlated), if the correlation coefficient is close to +1 (or –1). A strong correlation on the uncertainties, means that the two parameters have not been independently resolved by the data set, but that only some linear combination of the two parameters has been resolved.

A.16 NONLINEAR TRANSFORMATIONS FOR CONSTRAINED MINIMIZATION

There are an infinite number of nonlinear transformations that can map a constrained minimization problem to an unconstrained one. We make use of only the following three nonlinear transformations:

If $x_{\max}$ is an upper bound on the model parameter x and $x_{\min}$ is a lower bound, then in order to ensure that $x_{\min} < x < x_{\max}$ at all iterations, we introduce one of the following transformations:

A.16.1 First Nonlinear Transformation

$$x = f(c, x_{\min}, x_{\max}) = x_{\min} + \frac{x_{\max} - x_{\min}}{c^2 + 1} c^2, \quad -\infty < c < +\infty. \tag{A.146}$$

It is clear that

$$x \to x_{\min}, \text{ as } c \to 0, \tag{A.147}$$

$$x \to x_{\max}, \text{ as } c \to \pm\infty. \tag{A.148}$$

It is straightforward to show that

$$\frac{\partial S_j}{\partial c} = \frac{dx}{dc}\frac{\partial S_j}{\partial x} = 2\frac{x_{\max} - x}{x_{\max} - x_{\min}}\sqrt{(x_{\max} - x)(x - x_{\min})}\,\frac{\partial S_j}{\partial x}, \tag{A.149}$$

where S_j is the j^{th} measurement. The two successive iterates x_{k+1} and x_k of x are related by

$$x_{k+1} = x_{\min} + \frac{x_{\max} - x_{\min}}{c_{k+1}^2 + 1}c_{k+1}^2 = x_{\min} + \frac{x_{\max} - x_{\min}}{(c_k + q_k)^2 + 1}(c_k + q_k)^2, \tag{A.150}$$

where

$$c_k = \left(\frac{x_k - x_{\min}}{x_{\max} - x_k}\right)^{1/2}, \tag{A.151}$$

and $q_k = c_{k+1} - c_k$ is the Gauss-Newton search step in c towards the minimum of the cost functional. Defining

$$p = 2\frac{x_{\max} - x}{x_{\max} - x_{\min}}\sqrt{(x_{\max} - x)(x - x_{\min})}\;q = \frac{dx}{dc}q, \tag{A.152}$$

we obtain the following relationship between the two successive iterates x_{k+1} and x_k of x assuming an adjustable step-length υ_k along the search direction

$$x_{k+1} = x_{\min} + \frac{x_{\max} - x_{\min}}{\alpha_k^2 + (x_k - x_{\min})(x_{\max} - x_k)^3}\alpha_k^2, \tag{A.153}$$

where

$$\alpha_k = (x_k - x_{\min})(x_{\max} - x_k) + \frac{1}{2}(x_{\max} - x_{\min})\ \upsilon_k\ p_k. \tag{A.154}$$

Note that

$$x_{k+1} \to x_{\max},\ \text{if}\ x_k \to x_{\max}\ \text{ or }\ x_{\min}. \tag{A.155}$$

The variable p defined by equation (A.152) is the solution of the equation

$$\mathbf{G} \cdot \mathbf{p}_o = -\mathbf{g}. \tag{A.156}$$

Finally, one should note that this transformation of equation (A.146) introduces false minima at $x = x_{\max}$ and $x = x_{\min}$ since $\partial S_j / \partial c$ vanishes at both $x = x_{\max}$ and $x = x_{\min}$. Notice that, from equation (A.155), this transformation skews the emphasis towards $x_{\max}$ rather than towards $x_{\min}$.

A.16.2 Second Nonlinear Transformation

$$x = f(c, x_{\min}, x_{\max}) = \frac{x_{\max} \exp(c) + x_{\min} \exp(-c)}{\exp(c) + \exp(-c)}, \quad -\infty < c < +\infty. \tag{A.157}$$

It is clear that

$$x \to x_{\min},\ \text{as}\ c \to -\infty, \tag{A.158}$$

$$x \to x_{\max}, \text{ as } c \to +\infty. \tag{A.159}$$

It is straightforward to show that

$$\frac{\partial S_j}{\partial c} = \frac{dx}{dc}\frac{\partial S_j}{\partial x} = 2\frac{(x_{\max} - x)(x - x_{\min})}{x_{\max} - x_{\min}}\frac{\partial S_j}{\partial x}. \tag{A.160}$$

The two successive iterates x_{k+1} and x_k of x are related by

$$x_{k+1} = \frac{x_{\max}\exp(c_{k+1}) + x_{\min}\exp(-c_{k+1})}{\exp(c_{k+1}) + \exp(-c_{k+1})} = \frac{x_{\max}\exp(c_k)\exp(q_k) + x_{\min}\exp(-c_k)\exp(-q_k)}{\exp(c_k)\exp(q_k) + \exp(-c_k)\exp(-q_k)}, \tag{A.161}$$

where

$$c_k = \frac{1}{2}\ln\left(\frac{x_k - x_{\min}}{x_{\max} - x_k}\right). \tag{A.162}$$

Defining

$$p = 2\frac{(x_{\max} - x)(x - x_{\min})}{x_{\max} - x_{\min}}\, q = \frac{dx}{dc}q, \tag{A.163}$$

we obtain the following relationship between the two successive iterates x_{k+1} and x_k of x assuming an adjustable step-length υ_k along the search direction

$$x_{k+1} = \frac{x_{\max}(x_k - x_{\min})\exp(\alpha_k\ \upsilon_k\ p_k) + x_{\min}(x_{\max} - x_k)}{(x_k - x_{\min})\exp(\alpha_k\ \upsilon_k\ p_k) + (x_{\max} - x_k)},\ \text{for}\ \ p_k < 0, \tag{A.164}$$

and

$$x_{k+1} = \frac{x_{\max}(x_k - x_{\min}) + x_{\min}(x_{\max} - x_k)\exp(-\alpha_k\ \upsilon_k\ p_k)}{(x_k - x_{\min}) + (x_{\max} - x_k)\exp(-\alpha_k\ \upsilon_k\ p_k)},\ \text{for}\ \ p_k > 0, \tag{A.165}$$

where

$$\alpha_k = \frac{x_{\max} - x_{\min}}{(x_{\max} - x_k)(x_k - x_{\min})} \tag{A.166}$$

Note that

$$x_{k+1} \to x_{\min},\ \text{if}\ x_k \to x_{\min,} \tag{A.167}$$

$$x_{k+1} \to x_{\max},\ \text{if}\ x_k \to x_{\max}. \tag{A.168}$$

Hence, this transformation of equation (A.157) introduces false minima at $x = x_{\min}$ and $x = x_{\max}$ since $\partial S_j / \partial c$ vanishes at both $x = x_{\min}$ and $x = x_{\max}$. Notice that this transformation symmetrizes the emphasis on both $x_{\min}$ and $x_{\max}$.

A.16.3 Third Nonlinear Transformation

$$x = f(c, x_{\min}, x_{\max}) = \frac{x_{\max} + x_{\min}}{2} + \frac{x_{\max} - x_{\min}}{2}\sin(c), \quad -\infty < c < +\infty. \tag{A.169}$$

It is clear that

$$x \to x_{\min}, \text{ as } \sin(c) \to -1, \tag{A.170}$$

$$x \to x_{\max}, \text{ as } \sin(c) \to +1. \tag{A.171}$$

It is straightforward to show that

$$\frac{\partial S_j}{\partial c} = \frac{dx}{dc}\frac{\partial S_j}{\partial x} = \sqrt{(x_{\max} - x)(x - x_{\min})}\,\frac{\partial S_j}{\partial x}, \tag{A.172}$$

The two successive iterates x_{k+1} and x_k of x are related by

$$x_{k+1} = \frac{x_{\max} + x_{\min}}{2} + \frac{x_{\max} - x_{\min}}{2}\sin(c_{k+1}) = \frac{x_{\max} + x_{\min}}{2} + \frac{x_{\max} - x_{\min}}{2}\sin(c_k + q_k), \tag{A.173}$$

where

$$c_k = \arcsin\left(\frac{2x_k - x_{\max} - x_{\min}}{x_{\max} - x_{\min}}\right). \tag{A.174}$$

Defining

$$p = \sqrt{(x_{\max} - x)(x - x_{\min})}\;\; q = \frac{dx}{dc}q, \tag{A.175}$$

we obtain the following relationship between the two successive iterates x_{k+1} and x_k of x assuming an adjustable step-length υ_k along the search direction

$$x_{k+1} = \frac{x_{\max} + x_{\min}}{2} + \left(x_k - \frac{x_{\max} + x_{\min}}{2} \right) \cos\left(\frac{\upsilon_k \, p_k}{\alpha_k} \right) + \alpha_k \sin\left(\frac{\upsilon_k \, p_k}{\alpha_k} \right), \tag{A.176}$$

where

$$\alpha_k = \sqrt{(x_{\max} - x_k)(x_k - x_{\min})}. \tag{A.177}$$

A.17 CASCADE NONLINEAR INVERSION TECHNIQUE

The inversion algorithm employed in this work also takes advantage of a novel cascade optimization technique that incorporates a dual finite-difference gridding approach to accelerate the inversion associated with a large number of unknown model parameters. This highly efficient least-squares minimization technique is adapted from the work of Torres-Verdín et al. (2000).

A.17.1 Cascade Nonlinear Inversion Algorithm

Using shorthand notation, let us identify the inverse operator with the formula

$$\mathbf{x} = S^{-1}(\mathbf{m}), \tag{A.178}$$

where $S^{-1}(\mathbf{m})$ is in general nonlinear. In analogy with the forward and inverse operators defined above, we introduce auxiliary forward and inverse operators denoted as follows:

$$\hat{\mathbf{m}} = H(\hat{\mathbf{x}}) \tag{A.179}$$

and

$$\hat{\mathbf{x}} = H^{-1}(\hat{\mathbf{m}}), \tag{A.180}$$

respectively, where $\hat{\mathbf{m}}$ is a modified measurement vector yet to be defined. The symbol $\hat{\mathbf{x}}$ is used here only for labeling purposes to identify when a model vector has been derived from the operation $H^{-1}(\hat{\mathbf{m}})$. Heuristically, there are two important conditions we would like to impose on the construction of the above auxiliary forward and inverse operators:

(1) $H(\mathbf{x})$ should be much faster to compute than $S(\mathbf{x})$, and

(2) $H^{-1}(\hat{\mathbf{m}})$ should be bounded in a special way (to be defined later in this appendix).

Condition (1) is highly desirable from a practical point of view, because if a relationship exists between H^{-1} and S^{-1}, then solving for the former via repeated calls to $H(\mathbf{x})$ could potentially save, in principle, significant computational time. Condition (2), on the other hand, not only secures the possibility of inverting $H(\mathbf{x})$ in a stable manner, but if the bound is designed properly, it also could enforce a stable contractive mapping of the differences between $H(\mathbf{x})$ and $S(\mathbf{x})$, as is shown next.

The objective pursued here is to construct a series of approximations $\hat{\mathbf{x}}$ to $\mathbf{x}$ by performing inversions with the operator $H^{-1}(\hat{\mathbf{m}})$. On convergence, such series of approximations should yield $\hat{\mathbf{x}}$ equal to $\mathbf{x}$, but the computational efficiency still should be in favor of performing the repeated inversions of $\hat{\mathbf{x}}$. We construct this series of approximations through a fixed-point iteration recurrence given by

$$\hat{\mathbf{x}}_{k+1} = H^{-1}\left[H(\hat{\mathbf{x}}_k) - S(\hat{\mathbf{x}}_k) + \mathbf{m}\right] \tag{A.181}$$

where, the subscript k is used to denote iteration count. We first remark that if the above fixed-point iteration is to converge, then, on convergence,

$$\hat{\mathbf{x}}_{k+1} = \hat{\mathbf{x}}_k. \tag{A.182}$$

Recall also that by definition

$$\hat{\mathbf{x}}_k = H^{-1}\left[H(\hat{\mathbf{x}}_k)\right], \tag{A.183}$$

whereupon it follows that

$$\mathbf{m} - S(\hat{\mathbf{x}}_k) = \mathbf{0}. \tag{A.184}$$

If $S^{-1}(\mathbf{m})$ has a solution equal to $\mathbf{x}$, then it is obvious that

$$\hat{\mathbf{x}}_k = \mathbf{x}. \tag{A.185}$$

We therefore conclude that if the fixed-point iteration given by equation (A.181) is a contractive mapping it converges to the solution of the original inverse problem $S^{-1}(\mathbf{m})$. By direct inspection of equation (A.181), it also follows that

$$\hat{\mathbf{x}}_{k+1} = H^{-1}\left[H(\hat{\mathbf{x}}_k) - S(\hat{\mathbf{x}}_k) + \mathbf{m}\right] \tag{A.186}$$

The remaining important issue to deal with here concerns the operating conditions that will guarantee the fixed-point iteration given by equation (A.181) to converge. Evidently, the smaller the Euclidean norm of the difference $\left[H(\mathbf{x})-S(\mathbf{x})\right]$, the closer to global convergence the fixed-point iteration will be, but this is hardly a quantitative statement. In the following section, we prove that convergence is guaranteed when the following bounding condition is satisfied:

$$\left\|\partial H^{-1}(\hat{\mathbf{m}})\cdot\left[\partial H(\mathbf{x})-\partial S(\mathbf{x})\right]\right\| \leq 1, \tag{A.187}$$

where the operator ∂ designates the Jacobian matrix (Fréchet derivative) of the corresponding vector function; accordingly, using the notation introduced earlier, $\partial S(\mathbf{x})=\mathbf{J}(\mathbf{x})$. Apart from being a rigorous design restriction, the above bounding condition is not necessarily a practical recipe to construct the auxiliary forward modeling operator, $H(\mathbf{x})$. The message is simply that the closer the Jacobian matrix of $H(\mathbf{x})$ is to the Jacobian matrix of $S(\mathbf{x})$, the closer to global convergence the recurrence (A.181) will be, provided that $H^{-1}(\hat{\mathbf{m}})$ is bounded appropriately as well.

We summarize the proposed nonlinear inversion procedure with the following sequence of steps:

(1) Construct the auxiliary forward-modeling operator $H(\mathbf{x})$ to yield to a faster method of solution than the one used to compute $S(\mathbf{x})$, but subject to the condition $\left\|\partial H^{-1}(\hat{\mathbf{m}})\cdot\left[\partial H(\mathbf{x})-\partial S(\mathbf{x})\right]\right\| \leq 1$. This construction customarily would be achieved by trial and error, but would be done only once (and even perhaps only once for a large variety of data sets).

(2) Provide an initial guess $\mathbf{x}$.

(3) Compute $S(\mathbf{x})$; if the Euclidean norm of $[S(\mathbf{x})-\mathbf{m}]$ is below the specified threshold, then the inversion stops and the current value of $\mathbf{x}$ is accepted as the extremum of the least-squares cost function. Otherwise compute $\hat{\mathbf{m}} = H(\mathbf{x}) - S(\mathbf{x}) + \mathbf{m}$.

(4) Find the extremum of the auxiliary cost function in equation (A.3).

(5) Return to step (3).

Since the modified data vector $\hat{\mathbf{m}}$ is reset every time the above process reaches step (3) before convergence, each of the auxiliary cost functions of step (4) is defined in a cascade fashion whereby a given cost function depends on the results obtained from minimizing the previous cost function in the cascade. This is why we have adopted the term cascade minimization to refer to the new inversion procedure developed in this work.

The critical step in the cascade minimization is the construction of the auxiliary operator $H(\mathbf{x})$, which remains unchanged throughout this process. Without the loss of generality, in this work, we have chosen to define the auxiliary (approximate) forward operator by using a subset of the finite-difference grid used to simulate $S(\mathbf{x})$. The specific subset of the original finite-difference grid should be chosen to expedite significantly the computation of $H(\mathbf{x})$. Additionally, the choice of the subset grid should abide by condition (A.187). For the problems of interest of this dissertation, in order to determine the subset grid that provides the best balance between accuracy and efficiency, we performed extensive experimentations by trial and error with numerical simulations and checks to bounding condition (A.187).

A.17.2 Convergence of the Cascade Nonlinear Inversion Algorithm

In this section, we establish the necessary condition for the recurrence equation (A.181) to be convergent. In the Cauchy sense, local convergence is assured whenever

$$\left\|\hat{\mathbf{x}}_{k+1}-\hat{\mathbf{x}}_k\right\|=\left\|\hat{\mathbf{x}}_k-\hat{\mathbf{x}}_{k-1}\right\|. \tag{A.188}$$

From equation (A.181), we obtain

$$\hat{\mathbf{x}}_{k+1}-\hat{\mathbf{x}}_k=H^{-1}\left[H(\hat{\mathbf{x}}_k)-S(\hat{\mathbf{x}}_k)+\mathbf{m}\right]-H^{-1}\left[H(\hat{\mathbf{x}}_{k-1})-S(\hat{\mathbf{x}}_{k-1})+\mathbf{m}\right]. \tag{A.189}$$

When $\hat{\mathbf{x}}_{k+1}$ is close to convergence, we can approximate this equality as

$$\hat{\mathbf{x}}_{k+1}-\hat{\mathbf{x}}_k\approx\partial H^{-1}(\hat{\mathbf{m}}_k)\cdot\left\{\left[H(\hat{\mathbf{x}}_k)-H(\hat{\mathbf{x}}_{k-1})\right]-\left[S(\hat{\mathbf{x}}_k)-S(\hat{\mathbf{x}}_{k-1})\right]\right\}. \tag{A.190}$$

where

$$\hat{\mathbf{m}}_k=H(\hat{\mathbf{x}}_k)-S(\hat{\mathbf{x}}_k)+\mathbf{m} \tag{A.191}$$

and the operator ∂ denotes the Jacobian matrix (Fréchet derivative) of the corresponding vector function. Further substitution of

$$H(\hat{\mathbf{x}}_k)-H(\hat{\mathbf{x}}_{k-1})\approx\partial H(\hat{\mathbf{x}}_k)\cdot\left[\hat{\mathbf{x}}_k-\hat{\mathbf{x}}_{k-1}\right] \tag{A.192}$$

and

$$S(\hat{\mathbf{x}}_k)-S(\hat{\mathbf{x}}_{k-1})\approx\partial S(\hat{\mathbf{x}}_k)\cdot\left[\hat{\mathbf{x}}_k-\hat{\mathbf{x}}_{k-1}\right] \tag{A.193}$$

yields

$$\hat{\mathbf{x}}_{k+1} - \hat{\mathbf{x}}_k \approx \partial H^{-1}(\hat{\mathbf{m}}_k) \cdot \left[\partial H(\hat{\mathbf{x}}_k) - \partial S(\hat{\mathbf{x}}_k)\right] \cdot \left[\hat{\mathbf{x}}_k - \hat{\mathbf{x}}_{k-1}\right]. \tag{A.194}$$

Comparison of equations (A.188) and (A.194) then shows that for the recurrence of equation (A.181) to converge, the condition

$$\left\| \partial H^{-1}(\hat{\mathbf{m}}_k) \cdot \left[\partial H(\mathbf{x}_k) - \partial S(\mathbf{x}_k)\right] \right\| \leq 1 \tag{A.195}$$

is a necessary requirement.

A.18 A HYBRID GLOBAL OPTIMIZATION ALGORITHM FOR INVERSION

The optimization technique implemented for the solution of the inverse problems considered in this dissertation is based on the weighted least-squares method described in the previous sections of this appendix. In our implementation, the weighted least-squares algorithm makes use of a regularized Gauss-Newton search direction, hence, we coined the term, Weighted and Regularized Gauss-Newton method, (WRGN). In addition, two helper methods based on the Simultaneous Perturbation Stochastic Approximation (SPSA) technique are introduced to overcome the common WRGN pitfall of entrapment around a local minimum (Spall, 1992; Chin, 1994; Spall, 1998; Spall, 2003). When the helper method is active, the inversion algorithm marches toward the minimum with the steps of a global optimizer (SPSA). Once the model is deemed sufficiently close to the minimum, WRGN steps take over SPSA steps for ensuring rapid convergence. If local minimum entrapment is sensed (based on invariance of the model or insufficient reduction of the objective function), the hybrid algorithm automatically switches back to SPSA steps. Convergence of the algorithm is accepted only if (approximately) the same model minimum is achieved after a prescribed number of global-local (WRGN-SPSA)

interactions over the course of optimization. Figure A.1 is a graphical description of the hybrid inversion algorithm with automatically interchangeable global-local coupling. Following sections provide additional technical details of this highly efficient hybrid inversion algorithm.

A.18.1 Hybridization of WRGN with Helper Methods

The quadratic approximation of the cost functional, $C(\mathbf{x})$, shown in equation (A.3), lives in the space of model parameters sufficiently close to the minimum. As such, the WRGN direction is rendered a descent direction. When applied properly, regularization certainly helps to further increase the spectral radius of this model space by sharpening the objective function in the vicinity of minimum. However, for cases where a-priori information is significantly deficient, initial-guess locations may be located far away from the space described by the spectral radius of a WRGN step. Hence, an algorithm that relies solely on the WRGN approach may be trapped in a local minimum. A helper routine that implements a global optimization approach can be used to perform the minimization in the region of the model space where the quadratic approximation (with regularization) can locate the minimum accurately.

A great majority of global optimization techniques are plagued by the requirement of intensive forward modeling. Therefore, our inversion algorithm may be rendered prohibitively slow since we make use of robust and accurate forward solvers instead of proxy methods (i.e., artificial neural networks, etc.). The accuracy of such proxy techniques depend principally on the extent of initial simulation investment. For the purpose of maintaining the generality of the inverse solver, we avoid the use of proxy modeling approach. To mitigate a potential initial-guess related local-trapping problem, among the investigated global optimization techniques, Simultaneous Perturbation Stochastic Approximation (SPSA) technique, introduced by Spall (1992) and extended to

global optimization by Chin (1994), provided an optimal balance between accuracy and computational efficiency for our inversion algorithm. In our implementation, the user can activate an option such that the optimization will start with a global approach. Upon satisfaction of global convergence criteria, the inversion algorithm may switch to a WRGN technique until the WRGN convergence criteria are satisfied. If the WRGN technique fails to satisfy the convergence criteria, a global helper routine is automatically reactivated. If convergence is still not achieved after a given number of global-local interactions, inversion will restart itself by drawing a new initial-guess location using a random number generator. The selection of the new initial-guess location is constrained by the physical constraints already imposed on the SPSA and WRGN methods. The above-described two-way coupling between SPSA and WRGN techniques is graphically demonstrated in Figure A.1. This figure is generated for the hybridization of WRGN with ASPSA that will be described in a further section of Appendix A. Alternatively, depending upon the choice made by the user, SPSA or WRGN methods can also be run independently. Our hybrid optimizer developed in FORTRAN90 drives multi-physics simulation algorithms, which, in turn, together act as a cost functional evaluator. A UNIX interface establishes communication between the optimization routines and the multi-physics simulation.

Two variants of SPSA are implemented. The first helper algorithm is a standard implementation of SPSA with simple enhancements for imposing bounds and search direction efficiency, referred to as SSPA. A second helper routine implementation makes use of a stochastic gradient averaging approach within SPSA for determining smooth search directions to mitigate possible large jumps in model space. This helper approach is here referred to as ASPSA. Our implementations of SPSA follow detailed guidelines provided by Spall (1998) and Chin (1994).

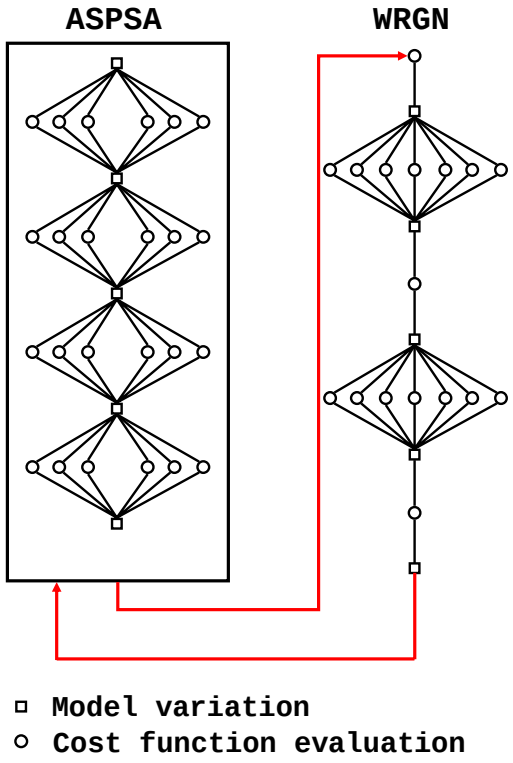

Figure A.1: Graphical description of the hybrid inversion technique with two-way coupling.

A.18.2 SSPSA Technique

Let us minimize a differentiable, modified cost functional

$$F(\mathbf{x}) = \left\{ \left\| \mathbf{W}_d \cdot \mathbf{e}(\mathbf{x}) \right\|^2 - \chi^2 \right\}, \tag{A.195}$$

where $F : R^N \rightarrow R^1$. At the minimum, the modified objective function satisfies

$$\nabla F(\mathbf{x}_k) = \mathbf{g}(\mathbf{x}_k) = 0. \tag{A.196}$$

A great majority of SA algorithms based on finite-difference methods require $2N$ evaluations of F at each iteration. However, the SPSA technique only requires $2Q$ $(Q \geq 1)$ evaluations of F at each iteration, where for large N one typically has $Q \ll N$. Therefore, SPSA may provide significant algorithmic efficiency as long as the number of iterations does not increase to counterbalance the reduced amount of modified cost functional evaluations per iteration (Spall, 1994).

Let $\mathbf{x}_k$ denote the estimate for $\mathbf{x}$ at the k^{th} iteration, the stochastic approximation algorithm has the following standard form

$$\mathbf{x}_{k+1} = \mathbf{x}_k - a_k \mathbf{g}_k(\mathbf{x}_k), \tag{A.197}$$

where a_k is the so-called "gain sequence" that satisfies the conditions listed by Spall (1992). The simultaneous perturbation estimate for $\mathbf{g}_k(\mathbf{x}_k)$ is determined as follows:

Let $\boldsymbol{\delta}_k \in R^N$ be a vector of N mutually independent zero-mean random variables, $\boldsymbol{\delta}_k = [\delta_{k1}, \ldots, \delta_{kN}]^T$, satisfying the conditions given by Spall (1992). The principal condition for the convergence of SPSA is that $E\{\| \boldsymbol{\delta}_k^{-1} \|\}$, or some higher inverse moment of $\boldsymbol{\delta}_k$ be bounded. This condition distinctly precludes $\boldsymbol{\delta}_k$ from being uniformly or normally distributed. Let $\{\boldsymbol{\delta}_k\}$ be a mutually independent sequence with $\boldsymbol{\delta}_k$ independent of $\mathbf{x}_o, \mathbf{x}_1, \ldots, \mathbf{x}_k$. Theoretically, no additional assumption is necessary for the specific distribution for $\boldsymbol{\delta}_k$. For the numerical implementation, as suggested by Spall (1998), we assume that $\boldsymbol{\delta}_k$ is symmetrically Bernoulli distributed. Also, let c_k be a positive scalar, and

$$Y^{(+)} = F(\mathbf{x}_k + c_k \boldsymbol{\delta}_k) \tag{A.198}$$

and

$$Y^{(-)} = F(\mathbf{x}_k - c_k \boldsymbol{\delta}_k). \tag{A.199}$$

Then, the estimate of $\mathbf{g}_k(\mathbf{x}_k)$ is given by

$$\mathbf{g}_k(\mathbf{x}_k) = \left[\frac{Y^{(+)} - Y^{(-)}}{2c_k\delta_{k1}} \quad \cdots \quad \frac{Y^{(+)} - Y^{(-)}}{2c_k\delta_{kN}} \right]^T \tag{A.200}$$

This estimate differs from the usual stochastic finite-difference approximation in that only two evaluations (instead of $2N$) are used. The name "simultaneous perturbation" as applied to equation (A.200) arises from the fact that all elements of the $\mathbf{x}_k$ vector are being varied simultaneously.

A.18.3 ASPSA Technique

Aside from evaluating equation (A.197) with $\mathbf{g}_k(\mathbf{x}_k)$ as in equation (A.200), in ASPSA we consider using equation (A.197) with several independent simultaneous perturbation approximations averaged at each iteration. Thus $\mathbf{g}_k(\mathbf{x}_k)$ in equation (A.200) is replaced by

$$\mathbf{g}_k(\mathbf{x}_k) = Q^{-1} \sum_{j=1}^{Q} \mathbf{g}_k^{(j)}(\mathbf{x}_k), \tag{A.201}$$

where each $\mathbf{g}_k^{(j)}(\mathbf{x}_k)$ is generated as in equation (A.200) based on a new pair of evaluations that are conditionally independent of the other measurement pairs. Spall (1992) demonstrates that averaging can enhance the performance of the SA algorithm.

A.19 SUMMARY

We reviewed a number of variants of Newton-type inversion techniques. Newton-type methods work efficiently for inversion applications where the number of inverted model parameters is limited which makes Newton-type techniques very desirable for parametric inversion algorithms. We formulate enhancements on the Newton-type inversion techniques using a family of nonlinear parameter transformations to impose physical bounds on the inverted model parameters and an efficient line search procedure to accelerate the convergence. In turn, a robust and efficient algorithm based on the Weighted and Regularized Gauss-Newton technique is implemented using an innovative multiplicative regularization approach. The formulation of the multiplicative regularization technique, originally developed for the gradient-based imaging algorithms, is extended and successfully applied to Newton-type parametric inversion algorithms.

We also describe an algorithm for nonlinear inversion that casts standard minimization procedures in the form of a cascade sequence of simpler, and hence, computationally more efficient, nonlinear inversions. In this work, we have chosen to construct these simple nonlinear inversions by using an approximate solution to the original forward problem. In this dissertation, we propose the possibility of constructing an approximate forward problem by taking a subset of the finite-difference grid that is used to simulate the measurements numerically. Other approximate forward problems could be used for the same purpose as long as they abide by the necessary requirements of convergence. On the other hand, the dual-grid approach proposed in this work is attractive because it allows great flexibility to adjust the degree of accuracy required to achieve a given rate of convergence.

In the final section of this appendix, we formulate and implement a robust and accurate hybrid optimization algorithm for inverse problems with potential multiple local

minima. The hybrid inversion algorithm allows a two-way coupling between the (global) Simultaneous Perturbation Stochastic Approximation (SPSA) technique, and the (local) Weighted and Regularized Gauss-Newton (WRGN) technique.

Appendix B: A Quantitative Study to Assess the Value of Pressure Data Acquired with In-Situ Permanent Sensors in Three-Dimensional Heterogeneous Reservoir Models Subject to Two-Phase Fluid Flow

B.1 INTRODUCTION

Recent advances in smart well completion technologies have enabled the dynamic acquisition of in-situ pressure measurements with sensors in direct hydraulic contact with rock formations. In addition to the immediate impact of in-situ sensors as tools for real-time, reactive reservoir management and control, usage of in-situ pressure sensors has long-term benefits. Devising an optimal macro-management strategy for hydrocarbon reservoirs requires more than a tool for instantaneous monitoring and control. Precise knowledge of the spatial distribution of petrophysical properties is essential for accurate reservoir delineation, management, and production forecasting. From the formation evaluation viewpoint, large volumes of flow-related data constitute an attractive prospect for robust and accurate characterization of reservoirs. In addition to static information in the form of geostatistical, seismic, and geologic data, usage of dynamic measurements remains imperative to construct accurate reservoir models amenable to production forecast.

In this chapter, we address the quantitative estimation of three-dimensional (3D) spatial distributions of permeability and porosity from pressure measurements acquired with in-situ permanent sensors. A pilot waterflood operation conducted with a conventional five-spot pattern is chosen as example for our numerical experiments. We assume in-situ permanent pressure sensors to be an integral part of the production-well completion and to remain completely isolated from the hydraulics of the wellbore. Therefore, these sensors perform uncorrupted measurements of in-situ formation fluid pressures. Quantitative estimation of spatial distributions of permeability and porosity is

approached with a novel subspace approach and a modified Gauss-Newton inversion algorithm. This inversion strategy incorporates an adjoint formulation for the efficient computation of model sensitivities. In our inversions, the physics of two-phase fluid-flow in the 3D spatial domain is rigorously incorporated into the assessment of distributions of petrophysical properties from in-situ permanent-sensor pressure data. Comparisons are shown of the enhancement in spatial resolution and reduction of uncertainty when using in-situ permanent sensors with respect to estimations performed via standard history matching techniques.

B.2 MOTIVATION

Traditional production sampling strategies consist of time records of bottom-hole pressure (BHP) and surface flow rates expressed in terms of water-oil ratio (WOR) for two-phase flow behavior. Albeit intrinsically useful, these measurements at best can provide large-scale average properties of flow units commingled through a well rather than the response of individual flow units. This work quantifies the use of in-situ pressure sensors to sample time records of individual layer pressures during the hydrocarbon production. As shown in Figure B.1, pressure sensors considered in this study are deployed in-situ behind casing, are hydraulically isolated from the wellbore, and remain in hydraulic communication with the formation during hydrocarbon production. It is shown that pressure data measured with an array of in-situ pressure sensors installed across multi-layer formations provide enhanced vertical resolution in reconstructing depth dependent petrophysical properties. Additionally, injection/production responses sampled with in-situ pressure arrays can provide enhanced inter-well spatial sensitivity to resolve main features of the lateral distribution of petrophysical properties.

The majority of the interpretation work for permanent sensor measurements reported in the literature have been based on the limiting assumption of single-phase fluid

flow regime throughout the production/injection history of the reservoir. On the contrary, numerical examples described in this study are intended to assess the spatial resolution properties of in-situ permanent sensors in the presence of two-phase flow within the context of a waterflood secondary recovery scheme.

Estimation of petrophysical properties is approached with a novel inversion algorithm that efficiently combines multidirectional-resolution properties and an adjoint formulation for sensitivity computations (Wu et al., 1999). This inversion algorithm also incorporates the use of water-cut data to further reduce uncertainty in the estimation of a 3D petrophysical model. Inversions of measurement data are performed to quantify the lateral and vertical resolution of in-situ permanent pressure sensor measurements. Reconstructions of the permeability and porosity model using pressure data acquired with in-situ permanent pressure sensors are compared to the inversion results of BHP data acquired with conventional wellbore sensors. We also consider the integration of in-situ permanent sensor data with water-cut measurements acquired in the late-time history of the waterflood. Comparisons of inversion results indicate substantial vertical resolution enhancement in the reconstruction of depth dependent petrophysical properties when in-situ permanent pressure data are included as input to the inversion. In comparison to the inversions of conventional wellbore data, relatively more accurate reconstructions of inter-well permeability and porosity are achieved with the use of in-situ permanent pressure data. Although to a less degree when compared to the vertical resolution enhancement, in-situ permanent-sensor data clearly extend the lateral resolution of inversions. Inversion results for the numerical test examples considered in this chapter constitute a practical proof of the reduction of uncertainty when using in-situ permanent sensors with respect to estimations performed with history matching techniques through sole use of conventional production data.

B.3 SIMULATION OF FLUID-FLOW MEASUREMENTS

Quantitative estimation of the spatial distribution of permeability and porosity is posed as an optimization problem. Accordingly, reservoir parameters such as permeability and porosity are adjusted to minimize the misfit between the observed and predicted time records of an arbitrary combination of in-situ permanent-sensor pressure, BHP, and water-cut measurements. The predicted measurements are generated from the numerical solution of coupled partial differential equations (PDE) that describe two-phase flow phenomena in porous media. In our formulation, we disregard the presence of chemical reactions, rock/fluid mass transfer, and diffusive/dispersive transport. The mass balance equation for the i^{th} fluid phase in a 3D spatial domain can be stated as follows (Aziz and Settari, 1979)

$$\frac{\partial}{\partial t}\left(\frac{\phi S_i}{B_i}\right)+\nabla\cdot\left(\frac{\mathbf{u}_i}{B_i}\right)=R_i^{sc}, \tag{B.1}$$

where B, $\mathbf{u}$, ϕ, R^{sc}, and S denote formation volume factor, fluid velocity vector, porosity, source/sink term for each phase at standard conditions, and phase saturation, respectively. No-flow boundary conditions are assumed at the external boundaries of the porous medium subject to simulation. For the modeled fluid-flow phenomenon, we assume mutual immiscibility between both fluid components (water and oil) meaning that the phases and components are the same. Darcy's law is the governing transport equation, i.e.,

$$\mathbf{u}_i=-\overline{\overline{\mathbf{k}}}\cdot\frac{k_{ri}}{\mu_i}\left(\nabla p_i-\gamma_i\nabla D_z\right), \tag{B.2}$$

where $\overline{\overline{\mathbf{k}}}$ is the single-phase permeability tensor of the porous medium and k_r denotes relative permeability. In addition, $\mu, p, \gamma,$ and D_z denote the phase viscosity, pressure, specific gravity, and the vertical location below some reference level, respectively. Finally, the constituent equation follows from the equation of state. The assumption is made that both fluid and rock compressibilities are functions of the pressure range of interest for the simulations and are given by

$$c_i = -\frac{1}{V_i}\frac{\partial V_i}{\partial p}\bigg|_T = \frac{1}{\rho_i}\frac{\partial \rho_i}{\partial p}\bigg|_T, \tag{B.3}$$

and

$$c_r = \frac{1}{\phi}\frac{\partial \phi}{\partial p}\bigg|_T, \tag{B.4}$$

respectively. Equations (B.3) and (B.4) are incorporated into equation (B.1) via constitutive relationships given by

$$B_i = B_i^o[1 - c_i(p - p^o)], \tag{B.5}$$

and

$$\phi(p) = \phi^o[1 + c_f(p - p^o)], \tag{B.6}$$

where B_i^o, p^o, and ϕ^o denote formation volume factor, pressure, and rock porosity at reference conditions. In our simulator, standard conditions are used as reference. On the other hand, capillary pressures and fluid saturations are governed by

$$P_c(S_w) = p_o - p_w, \tag{B.7}$$

and

$$S_o + S_w = 1.0, \tag{B.8}$$

respectively. The coupled set of PDEs described by equation (B.1) is solved numerically using a finite-difference stencil and an IMPES approach (Aziz and Settari, 1979).

B.4 A SUBSPACE INVERSION ALGORITHM

By making use of a Bayesian statistical rule, inversion can be stated as the minimization of the quadratic cost function (Wu et al., 1999) given by

$$J(\mathbf{x}) = (\mathbf{x} - \mathbf{x}_p)^T \mathbf{C}_x^{-1} (\mathbf{x} - \mathbf{x}_p) + (S(\mathbf{x}) - \mathbf{m})^T \mathbf{C}_d^{-1} (S(\mathbf{x}) - \mathbf{m}), \tag{B.9}$$

where $\mathbf{x} = [\log(k), \phi]^T$ is the size-N vector of reservoir parameters, $S(\mathbf{x})$ is the vector of simulated measurements, $\mathbf{m}$ is the vector of measurement data, $\mathbf{C}_d$ and $\mathbf{C}_x$ denote the covariance matrices of measured data and the model matrix, respectively. Given that, in general, physical values of absolute permeability encompass a large range, a convenient logarithmic transform for permeability remains suitable. This transformation is also useful in enforcing positivity constraints.

When the number of unknown reservoir parameters is large, numerous combinations of model domain parameters can equally satisfy the time record of fluid-flow measurements. Therefore, the inclusion of the first term in equation (B.9) aims at reducing the non-uniqueness of the solution as well as to stabilizing the estimation in the presence of noisy data. Precisely speaking, the first term biases the inversion toward a specific set of solutions in parameter space when the degree of non-uniqueness in the inversion remains high. The covariance matrix of the model may not be available due to the lack of a-priori knowledge about the model. In general, the Laplacian or an equivalent isotropic operator can be applied for the regularization of model parameters. In particular, Tarantola (1987) showed that the first-order difference approximation is analogous to the model covariance matrix. In the inversions performed in this chapter, we adopt an exponential covariance function introduced by Oliver (1994) to compute the covariance matrix.

A modified Gauss-Newton technique is employed for the minimization of equation (B.9). The iterative form of the modified Gauss-Newton method is given by

$$\mathbf{x}_{k+1} = \mathbf{x}_p - \mathbf{C}_x \mathbf{G}_k^T [\mathbf{C}_d + \mathbf{G}_k \mathbf{C}_x \mathbf{G}_k^T]^{-1} [S(\mathbf{x}) - \mathbf{m} + \mathbf{G}_k (\mathbf{x}_k - \mathbf{x}_p)]. \tag{B.10}$$

In equation (B.10), $\mathbf{G}_k$ is the matrix of sensitivity coefficients calculated at the k^{th} iteration. At each iteration, we solve the linear equation given by

$$[\mathbf{C}_d + \mathbf{G}_k \mathbf{C}_x \mathbf{G}_k^T] \boldsymbol{\eta} = S(\mathbf{x}) - \mathbf{m} + \mathbf{G}_k (\mathbf{x}^k - \mathbf{x}_p) \tag{B.11}$$

for the model update vector, $\boldsymbol{\eta}$. In this formulation, the dimension of the equations is equal to the number of observed data. Such a modified Gauss-Newton method operates

efficiently for the cases where the size of **m** (or the number of fluid-flow measurements) is relatively small. We also employ an adjoint procedure for the computation of the sensitivity coefficients of fluid-flow measurements with respect to petrophysical model parameters. At each iteration, the sensitivity coefficients are computed at the cost of a single forward simulation run and the solution of an adjoint system with multiple right-hand-side (RHS) vectors. The number of RHS vectors equals the size of **m**.

For inversion cases involving a large number of observed data, such as in the case of time records of production data, the size of the sensitivity matrix is considerably large. The high computational cost and computer memory requirements for calculating the sensitivity matrix makes the inversion algorithm in its current form impractical. Kennett et al. (1988) and Abacioglu et al. (2001) proposed a subspace approach to invert seismic data and pressure data, respectively. Similarly, in this work, we propose a new subspace approach that makes large-scale inversion tractable. Details of this inversion approach are described below.

Suppose that the modeling errors can be neglected and that only measurement errors are of interest. The relationship between the modeled response and measurements is given by

$$S(x)_{i,j} = m_{i,j} + e_{i,j} \text{ for } i = 1,\cdots,N_W \text{ and } j = 1,\cdots,N_D, \tag{B.12}$$

where $S(x)$ is the modeled response. In the above equation, e denotes the observed error for each data point, N_W is the number of producing wells, N_D is the number of measured data, such as in-situ permanent-pressure sensor data, water-oil data at each producer, etc. It is now remarked that the second term in equation (B.9) can be modified to read as

$$(S(\mathbf{x})-\mathbf{m})^T \mathbf{C}_d^{-1}(S(\mathbf{x})-\mathbf{m}) = \sum_{i=1}^{N_W}\sum_{j=1}^{N_D} \frac{\left[S(x)_{i,j} - m_{i,j}\right]^2}{\sigma_{i,j}^2}. \tag{B.13}$$

A motivation for developing a new subspace approach is based on the central limit theorem. The latter theorem states that the distribution of the sum of a large number of identically distributed random variables will be approximately normal, regardless of the individual distributions. If the error between the observed data and the model predicted data fall within the range of the standard deviation, the following property of the subspace cost function will hold

$$g_i = \left\{ \frac{1}{N_{D,i}} \sum_{j=1}^{N_D} \frac{e_{i,j}^{\ 2}}{\sigma_{i,j}^2} \right\} = 1, \quad i = 1, \ldots, N_w, \tag{B.14}$$

where the operator $\{\bullet\}$ denotes expectation and $\mathbf{g} = \left[g_1, \ldots, g_{N_w} \right]^T$. Thus, the inversion can be restated as "adjusting the model parameters by making the limit defined in equation (B.14) approach to 1 as closely as possible". If the observed data are matched with the model predicted data, the functional g_i should tend to 1. By making use of the latter property, the cost function defined in equation (B.9) can be restated as follows:

$$J(\mathbf{x}) = (\mathbf{x}-\mathbf{x}_p)^T \mathbf{C}_x^{-1}(\mathbf{x}-\mathbf{x}_p) + (S(\mathbf{x})-\mathbf{e})^T \mathbf{C}_b^{-1}(\mathbf{g}-\mathbf{e}). \tag{B.15}$$

Here, the matrix $\mathbf{C}_b$ denotes a weighting term that assigns a relative importance to the observed data at different production wells, and $\mathbf{e}$ is the vector given by $\mathbf{e} = [1, \ldots, 1]^T$. Minimization of the above-described new cost function only requires the computation of sensitivity coefficients of the subspace cost function with respect to model parameters.

As pointed out earlier, the adjoint procedure used in the computation of sensitivity coefficients requires the solution of a linear system with multiple RHS vectors. The number of RHS vectors depends on the number of observed data. Therefore, a reduction in the number of observed data automatically translates into a reduction in the number of adjoint systems to be solved at each iteration. Moreover, the size of the sensitivity coefficient matrix associated with the minimization of the cost function in equation (B.15), $M \times N_W$, is much smaller than the size of the sensitivity coefficient matrix associated with the minimization of the original cost function given by equation (B.9), $M \times N_W \times N_D$. Because of this, large volumes of observed data can be efficiently inverted into large reservoir petrophysical models using the subspace adjoint inversion algorithm.

B.5 COMPUTATION OF THE SUBSPACE GRADIENT VIA AN ADJOINT OPERATOR

Wu et al. (1999) describe an efficient adjoint method for the computation of sensitivities of production data with respect to model parameters for two-phase flow. Here, we extend the adjoint method to calculate the gradient of the subspace cost function with respect to permeability and porosity. The discretized form of the two-phase flow equation can be stated as follows:

$$F_p(\Psi^{q+1}, \Psi^q, t) = 0, \tag{B.16}$$

where $\Psi = (\psi_1, \psi_2, \ldots, \psi_P)^T$ is the vector of pressure and saturation in all P gridblocks and the superscript n stands for the n^{th} time step.

For all $q+1$ time steps, the two $P-$dimensional vectors of adjoint variables are defined by $\lambda_p^q = (\lambda_{p,1}^q, \lambda_{p,2}^q, \cdots, \lambda_{p,P}^q)^T$, where p stands for either water or oil phase. The flow equation (B.16) can be written in terms of an adjoint operator, whereupon a new functional J can be constructed using the expression,

$$J = J_i + \sum_{p=o,w} \sum_{q=0}^{N-1} (\lambda_p^{q+1})^T F_p^{q+1}, \tag{B.17}$$

where the cost function J_i is used to quantify the data misfit function for a given production well, for instance, and the subscript i designates a given well. Taking the variation of the cost functional into account and using the necessary condition for a functional extremum, one can obtain the adjoint equations given by

$$\left[\frac{\partial F_p^q}{\partial \Psi^q}\right]^T \lambda_p^q = -\left[\frac{\partial F_p^{q+1}}{\partial \Psi^q}\right]^T \lambda_p^{q+1} - \frac{\partial J_i}{\partial \Psi^q} \text{ for } n = 1, 2, \ldots, N-1, \tag{B.18}$$

where $\lambda = (\lambda_1, \lambda_2 \cdots \lambda_P)^T$ denotes the vector of adjoint variables. Once the adjoint variable λ is computed, the gradients with respect to permeability and porosity can be computed with the expressions

$$\frac{\partial J_i}{\partial k} = \sum_{p=w,o} \sum_{q=0}^{N} \left[\frac{\partial F_p^q}{\partial k}\right]^T \lambda_p^q, \tag{B.19}$$

and

$$\frac{\partial J_i}{\partial \phi} = \sum_{p=w,o} \sum_{q=0}^{N} \left\{\left[\frac{\partial F_p^q}{\partial \phi}\right]^T - \left[\frac{\partial F_p^{q+1}}{\partial \phi}\right]^T\right\} \lambda_p^q, \tag{B.20}$$

respectively. For the cost function J_i, one needs to compute its derivatives with respect to both pressure and saturation. These derivatives can be calculated via the equation

$$\frac{\partial J_i}{\partial \Psi} = \frac{\partial}{\partial \Psi} \sum_{q=0}^{N_D} (WOR_q^i - WOR_{obs,q}^i)^2, \tag{B.21}$$

where N_D is the number of the observed data, and

$$WOR_q^i = \frac{\sum_{k=1}^{K} (q_{w,k}^i)}{\sum_{k=1}^{K} (q_{o,k}^i)}. \tag{B.22}$$

In equation (B.22), K denotes the number of the penetrated layers. If the total flow rate is specified, the total flow rate at the k^{th} layer can be written as

$$q_{t,k}^i = q_t^i \frac{WI_k^i (\lambda_{o,k}^i / B_{o,k}^i + \lambda_w^i / B_{w,k}^i)}{\sum_{k=1}^{K} WI_k^i (\lambda_{o,k}^i / B_{o,k}^i + \lambda_{w,k}^i / B_{w,k}^i)}, \tag{B.23}$$

where WI_k^i denotes the well index for the k^{th} layer at well i, given by

$$WI_k^i = \frac{2\pi 1.127 \times 10^{-3} h_k^i \sqrt{k_{x,k}^i k_{y,k}^i}}{\ln(r_{o,k}^i / r_w^i) + S_i}. \tag{B.24}$$

In equation (B.24) $r_{o,k}^i$ is computed from

$$r_{o,k}^i = \frac{0.2873 \Delta x^i \sqrt{1 + k_{x,k}^i (\Delta y_k^i)^2 / (k_{y,k}^i (\Delta x_k^i)^2)}}{1 + \sqrt{k_{x,k}^i / k_{y,k}^i}}, \tag{B.25}$$

where r_w^i is the radius of well i, S_i is the skin factor for well i, and Δx_k^i and Δy_k^i denote the lengths of the gridblock containing well i (at k^{th} layer) in the x and y directions, respectively. Phase flow rates at each layer are computed via

$$q_{w,k}^i = q_{t,k}^i \frac{\lambda_{w,k}^i / B_{w,k}^i}{\lambda_{o,k}^i / B_{o,k}^i + \lambda_{w,k}^i / B_{w,k}^i} \tag{B.26}$$

and

$$q_{o,k}^i = q_{t,k}^i \frac{\lambda_{o,k}^i / B_{o,k}^i}{\lambda_{o,k}^i / B_{o,k}^i + \lambda_{w,k}^i / B_{w,k}^i}. \tag{B.27}$$

Here, water and oil mobilities ($\lambda_{w,k}^i$ and $\lambda_{o,k}^i$) are given by

$$\lambda_{o,k}^i = \frac{k_{ro,k}^i}{\mu_o}, \tag{B.28}$$

and

$$\lambda_{w,k}^i = \frac{k_{rw,k}^i}{\mu_w}. \tag{B.29}$$

By substituting equations (B.23) through (B.29) into equation (B.22), one obtains derivatives of water-oil ratio (WOR) with respect to pressure and saturation in a straightforward manner.

B.6 NUMERICAL EXAMPLES

With the purpose of quantifying the resolution properties of in-situ permanent sensors in a two-phase fluid-flow environment, we designed a realistic set of numerical examples. The reservoir volume is saturated with oil. A waterflood operation to sweep the reservoir volume is assumed to be the physical background of the inversion problem. We consider the deployment of cemented in-situ permanent pressure sensors along the production wells. Pressure measurements acquired with these sensors are inverted to yield spatial distributions of permeability and porosity. In order to establish a rigorous basis of comparison for the information content of in-situ permanent pressure measurements, we additionally consider the acquisition of conventional BHP and WOR measurements and perform inversions of these data to estimate spatial distributions of permeability and porosity. Assessment of the value of cemented in-situ permanent pressure sensors is performed directly in model space.

B.6.1 Reservoir Model

The reservoir model consists of a spatially heterogeneous 3D porous medium and is displayed in Figure B.2. Spatial dimensions are 1680 ft × 1680 ft × 50 ft and the model is discretized with a 21×21×5 Cartesian grid in the x, y, and z directions, respectively. The gridsize is uniform in each direction. Reservoir thickness is assumed uniform and equal to 50 ft. Each gridblock exhibits specific values of permeability and porosity. The permeability field is homogeneous, yet vertically anisotropic, with the vertical permeability assumed to be one-tenth of the horizontal permeability. Oil production in the reservoir of interest is assumed to be driven by a waterflood operation. A conventional 5-spot well pattern is used to sweep the hydrocarbons saturating the reservoir volume. The central well is used for water injection while the remaining wells are dedicated to oil production. Well locations are shown in Figure B.2. The injector well

is located at the gridblock [x, y] = [11, 11] and four producers, numbered 1 through 4, are located in the gridblocks [5, 17], [17, 5], [5, 5], and [17, 17]. The total flow rate at each producer is fixed at 400 STB/D and the flow rate at the injector is fixed at 2100 STB/D. Two-phase relative permeability and capillary pressure curves employed in the forward modeling of fluid-flow measurements are shown in Figures B.3 and B.4, respectively.

Permeability and porosity distributions for the synthetic 3D reservoir are generated by means of geostatistical simulation. Here, the mean for log-permeability is assumed to be 4.5 with variance equal to 0.5. On the other hand, the mean for porosity is assumed to be 0.18 with variance equal to 0.0025. Variogram ranges for both permeability and porosity are 800 ft. Each layer is assumed to exhibit a spherical variogram model. No correlation is assumed between the porosity and log-permeability. Spatial distributions of the permeability and porosity are generated using unconditional simulation computed from Cholesky decomposition of the covariance matrix and are shown in Figures B.5 and B.6, respectively. Measurements used in the inversions are generated using the permeability and porosity distributions in a forward simulation. Measurement errors are assumed independent and uncorrelated among themselves. Details of the reservoir fluid and rock properties along with the characteristics of the model's spatial architecture are given in Table B.1.

B.6.2 Inversion of In-Situ Permanent Sensor Pressure Measurements

Three in-situ permanent pressure sensors are assumed cemented behind casing in each production well. Sensor locations correspond to the centers of the upper-most, mid, and bottom-most layers, respectively. In-situ permanent sensor pressure measurements are acquired in response to oil production in each of the production wells. A 10 hr-long time-record of pressure responses is input to the inversion algorithm. Synthetically generated pressure measurements are contaminated with additive random Gaussian noise.

The standard deviation of noise is assumed equal to 2 psi. Inversions are initialized with uniform spatial distributions of permeability and porosity.

Figures B.7 and B.8 display results of the simultaneous inversion of in-situ pressure data for spatial distributions of permeability and porosity, respectively. Estimation of the spatial distribution of permeability remains successful in capturing the main features of the original distribution in both lateral and vertical directions. The main characteristic of the inversion results is the blurring of permeabilities for model domain voxels located far away from measurement locations. The quality in the reconstruction of permeability increases in the vicinity of the sensors. Yet, the inversion tends to yield an effective medium response close to that of average permeability away from the sensors. In this work, we explore not only the information inherent to in-situ pressure measurements but also attempt to integrate dynamic information provided by fluid-flow measurements into geostatistical models. In the absence of any a-priori information about the spatial statistics of the permeability model, a very good reconstruction of the permeability model is attained with in-situ permanent sensor data. Similar conclusions concerning spatial resolution apply to the spatial distributions of porosity. Overall, inversion results characteristically yield relatively enhanced vertical resolution in the vicinity of the in-situ sensors. However, reconstructions undergo a significant blurring in both lateral and vertical directions away from the sensors. On the other hand, approximate locations and parameter values of large model features are reconstructed in a robust manner. Post-inversion data-domain matches of measurements remain very good for all sensor locations. Figures B.9 through B.12 show the agreement between observed data and the predicted pressure data for various sensor locations. In-situ pressure sensors 1, 2, 3, and 4 are located in the production wells 1, 2, 3, and 4 from the top layer of the

reservoir, respectively. For completeness, time records of pressure computed from spatial distributions of initial guess model parameters are also shown in each of these figures.

Quantitative assessment of the model domain reconstructions is carried out by computing the correlation coefficient of post-inversion and true model domain parameters. The correlation coefficient varies between -1 and 1. It is equal to 1 when there is a perfect match between two model sets. In other words, for the case when inverted and true model parameters, e.g. permeabilities, match identically then the correlation coefficients are equal to 1. As inverted and true permeability fields become increasingly different, the correlation coefficient decreases toward zero. Thus, correlation coefficients can be utilized to diagnose the closeness of two parameter fields. Figures B.13 and B.14 display maps of correlation coefficients for initial guess and inverted permeability fields, respectively. In both figures, correlation coefficients are computed with respect to the actual spatial distributions of permeability. Figure B.13 indicates that the majority of the correlation coefficients are below 0.5 at the level of the initial guess. Yet, as displayed in Figure B.14, most of the correlation coefficients increase to approximately 0.70 after matching the in-situ permanent sensor measurements. The enhancement in the correlation coefficients can be effectively interpreted as the reduction of non-uniqueness achieved with the integration of dynamic in-situ measurements with respect to that of an initial guess model lacking a-priori information. On the other hand, Figures B.15 and B.16 display maps of correlation coefficients for initial guess and inverted porosity fields, respectively. In both these figures, correlation coefficients are computed with respect to the actual spatial distributions of porosity. The comparison of Figures B.15 and B.16 also indicates a trend of the correlation coefficients to increase for the post-inversion spatial distributions of porosity. However, the magnitude of the enhancement is relatively less significant in comparison to the case of spatial

distributions of permeability. Consistent with the physics of pressure measurements, in-situ permanent sensor data appear to be more sensitive to the spatial distribution of permeabilities in comparison to the spatial distribution of porosities.

If the oil production rate is measured on a layer-by-layer basis along each of the production wells, this information can play a similar role as in-situ sensor pressure does to reconstruct spatial distributions of permeability and porosity. Of course, in-situ flow rate measurements require special completions and permanent downhole flowmeters. To demonstrate the information content of in-situ flow rate measurements, we plot post-inversion layer-by-layer oil production rates in Figure B.17 for the case of the inversion of in-situ pressure data. Although layer flow rates do not vary as a function of time until the time of water breakthrough (not shown), individual flow rate substantially differ from each other. However, at the initial guess level, when uniform permeability and porosity distributions were assigned to all gridblocks, in-situ flow rates remain approximately equal to each other. This information alone evidences the sensitivity of in-situ flow rates to near-wellbore distributions of petrophysical model parameters. A full inversion of in-situ flow rates is still necessary to further assess the spatial resolution properties of this type of measurements.

B.6.3 Comparison of the Inversion of In-Situ Permanent Sensor Pressure Measurements to the Inversion of BHP Measurements

In the following numerical example, attention is focused to the inversions of BHP data acquired at each production well with a conventional downhole pressure gauge. We compare the inversion results to those yielded by the measurements acquired with in-situ permanent sensors.

The main difference between in-situ permanent sensor pressure and BHP data lies in the measurement conditions. Cemented in-situ permanent sensors are designed to establish a direct hydraulic communication with the formation fluids and are isolated

from the wellbore. As such, in-situ pressure gauges measure the time record of fluid pressures at a particular location within the reservoir. Under this measurement condition, pressure responses are acquired before the produced fluids from various layers undergo mixing and pressure equilibration within the wellbore. Hence, in-situ permanent sensor measurements exhibit a significant amount of sensitivity to the local distributions of flow properties of the formation. Subsequent to the flow of fluids from reservoir layers to the wellbore, fluid pressures from these layers equilibrate at wellbore conditions. This equilibrium pressure is also referred to as BHP. As such, BHP measurements can only be available on a well-to-well basis rather than on a sensor-by-sensor basis. Moreover, a significant amount of spatial resolution inherent to the in-situ pressures is sacrificed to the pressure equilibration within the wellbore. In contrast to in-situ pressure measurements, BHP measurements incorporate limited sensitivity to the local distributions of flow properties. Hence, effective average medium properties in the vicinity of the wellbore characterize the level of spatial resolution that can be recovered from BHP measurements.

Confirmation of the physical insights discussed above is provided by the inversions of BHP data acquired within the production wells. Measurement data are corrupted with the same noise contamination mechanism described in the previous numerical example. Spatial distributions of permeability and porosity yielded by the inversion of BHP data are shown in Figures B.18 and B.19, respectively. Post-inversion BHP data matches are shown in Figures B.20 through B.21 along with BHP time records computed from spatial distributions of initial guess model parameters. As shown in Figures B.18 and B.19, the spatial resolution of BHP measurements suffices only to asymptotically approximate an average permeability and porosity for the entire reservoir. Variations in the inverted permeability occur only in the vicinity of wells, where one can

observe slightly improved spatial resolutions inherent to the BHP measurements. However, the above conclusion does not hold true for porosity distributions. Such an observation is consistent with the first-order sensitivity of pressure measurements to permeability. Information about the location and magnitude of the main reservoir features is nonexistent in the inversions of BHP measurements. Poor reconstructions of the spatial distributions of permeability and porosity coupled to good matches between BHP measurements and post-inversion BHP simulations (shown in Figures B.20 through B.23) clearly indicate the high level of non-uniqueness in the inversions of BHP data.

Comparisons of Figures B.7 and B.17 for permeability, and Figures B.8 and B.19 for porosity domains indicate major differences in the resolution properties of BHP and in-situ permanent sensor data. Spatial distributions of permeability and porosity yielded by the inversions of in-situ pressure measurements exhibit significantly enhanced lateral as well as vertical resolution in comparison to the reconstruction of distributions inverted from BHP measurements.

B.6.4 Comparison of the Inversion of In-Situ Permanent Sensor Pressure Measurements to the Inversion of WOR Measurements

We also investigate the use of WOR measurements for the quantitative estimation of spatial distributions of permeability and porosity. In general, WOR data constitute a relatively late-time measurement in the economic life of a reservoir. Until the water breakthrough occurs in one or more production wells, WOR information is literally nonexistent. After water breakthrough, the ratio of the volumetric production rates of water and hydrocarbon components is measured at surface conditions. Hence, in this work, similar to BHP measurements, we focus on conventional WOR measurements acquired on a well-by-well basis. WOR measurements are contaminated with additive random noise using a procedure similar to that explained for the case of in-situ permanent pressure measurements. Figures B.24 and B.25 show inversion results from WOR data in

the form of spatial distributions of permeability and porosity, respectively. Post-inversion data domain fits are displayed in Figures B.26 through B.29 for each production well along with the WOR data simulated using a homogeneous distribution of parameters as initial guess.

Model domain reconstructions indicate that, in comparison to the inversion of BHP data, a relatively better reconstruction is obtained for the main features of the reservoir. However, when we compare the inversions obtained from in-situ pressure measurements to the inversions from WOR measurements, in-situ pressure measurements clearly yield higher resolution reconstructions of the spatial distributions of both permeability and porosity.

Similar to the BHP, WOR measurements contain average vertical information of reservoir parameters. Therefore, the vertical resolution of in-situ pressure measurements is far superior to that of WOR data especially in the vicinity of production wells. Moreover, inverted distributions remain highly influenced by the actual values of porosity and permeability in the vicinity of wells since the fluid flow rates are extremely sensitive to these gridblock parameters near production wells. On the other hand, in contrast to BHP measurements, WOR measurements incorporate a relatively extended lateral length of penetration evidenced by the comparatively improved sensitivity to the general reservoir features. As far as the lateral resolution of BHP and WOR measurements is concerned, in this work, we refer to “improved lateral sensitivity” rather than “improved lateral reconstruction” when considering the use of WOR data. As shown in Figure B.24 for the permeability domain, and in Figure B.25 for the porosity domain, WOR measurements clearly lack the lateral resolution necessary to identify the location of the main reservoir features. Yet, the comparison of Figures B.18 and B.24 for permeability domain and Figures B.19 and B.25 for porosity domain indicate that, in the

lateral direction, WOR measurements encompass more information in comparison to BHP measurements. However, when we compare the inversion results of in-situ permanent sensor measurements to that of WOR and BHP measurements, the lateral resolution of in-situ permanent sensor measurements is significantly superior to that of both WOR and BHP data. From a formation evaluation viewpoint, acquisition of pressure data with arrays of in-situ permanent sensors deployed in various lateral locations in the reservoir replicate multiple local pressure interference tests that are sensitive to local formation properties. In a much coarser sense, these measurements can be regarded as sensitive to the inter-well reservoir volume.

Figures B.26 through B.29 show good post-inversion data domain fits yielded by the inversion of WOR data. Along with the comparison of inverted and true spatial distributions for model domain parameters, the above observation provides a proof of concept for the high-level of non-uniqueness when estimating permeabilities and porosities from WOR data.

Another disadvantage of WOR measurements lies in the fact that, in general, they are not available in the early stages of the life of the reservoir. Once water breakthrough occurs, a significant reduction in the production rate takes place very quickly unless a remediation measure is taken. Late arrival of the information is a significant factor to reduce the value of WOR measurements.

B.6.5 Regularization

It must be pointed out that, in order to robustly invert parameter fields, one can incorporate the prior information under the Bayesian framework to bias the inversion toward a specific region in model space. In the absence of a-priori information, regularization can be used to impose a desired degree of freedom of the parameter fields. Thus, regularization appears to improve the resolution of permeability and porosity

around producers and injector wells. In all cases, we make use of the regularization term discussed within of the specific formulation implemented to solve the inverse problem. In the absence of a regularization term, very rough parameter fields caused convergence problems. We also observed that the regularization did contribute to improve the vertical resolution of the spatial distribution of permeability and porosity.

Figure B.30 shows the convergence rates associated with the subspace algorithm for inversions that incorporate different types of measurements. Minimization of the subspace cost function is performed for the inversions of in-situ permanent sensor pressure, BHP, and WOR measurements. The convergence behavior for each of these cases is shown in Figure B.30 as a function of the required number of iterations. For the purpose of comparison, convergence histories for all of the cases are plotted on the same graph. The cost function is efficiently reduced for all of the cases. The final value of the cost function is the lowest for the case of the inversion of WOR data followed by BHP data. Comparisons of the inverted and true spatial distributions of permeability and porosity for the inversions of all types of measurements indicate a significantly lower degree of non-uniqueness for the inversion of in-situ permanent sensor data.

B.7 SUMMARY AND CONCLUDING REMARKS

A robust and efficient subspace inversion algorithm was developed for the inversion of fluid-flow measurements acquired in two-phase flow environments, i.e., waterflood operations. The subspace inversion algorithm was applied to the quantitative appraisal of in-situ permanent sensor pressure measurements in the estimation of spatial distributions of permeability and porosity. Reconstruction of model parameters yielded by permanent pressure sensor pressure data was rigorously compared to the spatial distributions of model parameters inverted from BHP and WOR data, respectively.

When compared to the true permeability and porosity fields, reconstructions of spatial distributions of model parameters yielded by noisy in-situ permanent pressure measurements are more accurate than reconstructions performed with noisy BHP and WOR data. In both lateral and vertical directions the relative spatial resolution of in-situ permanent sensor data is significantly higher than the resolution provided by BHP and WOR measurements. Our test cases also indicate that the degree of sensitivity of in-situ permanent sensor measurements is higher for the spatial distributions of permeability than for the spatial distributions of porosity.

Inversion results clearly show the added value of in-situ permanent sensor measurements in providing enhanced spatial resolution of permeability and to a relatively less degree for porosity. Having established a practical proof of concept for the value of dynamic in-situ pressure measurements in the absence of a-priori information, in-situ pressure measurements could be further integrated into the construction of static geostatistical reservoir models. Such a strategy could provide more accurate spatial descriptions of porosity and permeability and hence a significant reduction of uncertainty in the forecast of hydrocarbon production.

Table B.1: Summary of geometrical, fluid, and reservoir properties of the synthetic reservoir model considered in this chapter.

	Property	Values
Fluid	Water density	62.40 lb/ft^3
	Oil density	52.88 lb/ft^3
	Water viscosity	1.00 cp
	Oil viscosity	0.92 cp
	Water compressibility	3.20×10^{-6} psi^{-1}
	Oil compressibility	1.00×10^{-5} psi^{-1}
	Water formation volume factor	1.00 RB/STB
	Oil formation volume factor	1.16 RB/STB
Reservoir	Initial water saturation	0.19
	Residual oil saturation	0.23
	Average porosity	0.18
	Average permeability	90.10 mD
	k_{rw}^{o} endpoint of water relative permeability	0.20
	k_{ro}^{o} endpoint of oil relative permeability	0.90
	k_x / k_y ratio of the two principal permeability directions	1.00
	k_x / k_z ratio of horizontal permeability to vertical permeability	0.10
Simulation	Number of gridblocks	21×21×5
	Gridblock size	80×80×10 ft
	Injection rate	400 STB/D
	Production rate	2100 STB/D
	Perforation information	All layers
	Number of production wells	4
	Number of injection wells	1

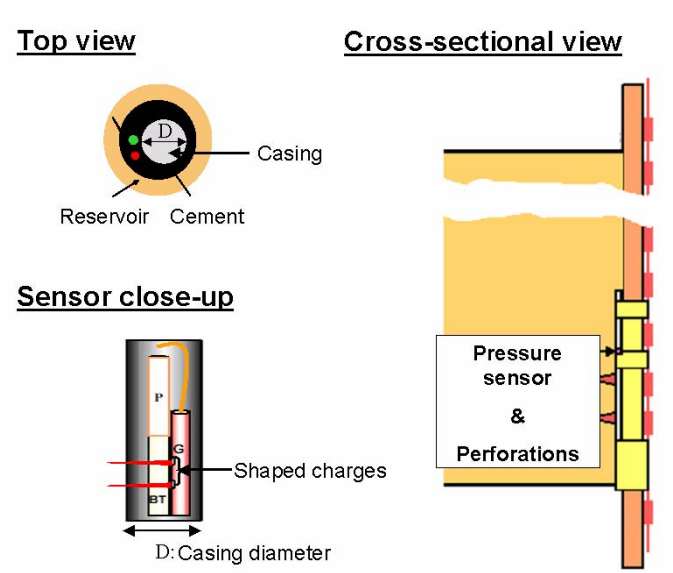

Figure B.1: Graphical description of the components of an in-situ pressure gauge. The gauge is cemented behind casing and operates in direct hydraulic contact with the formation.

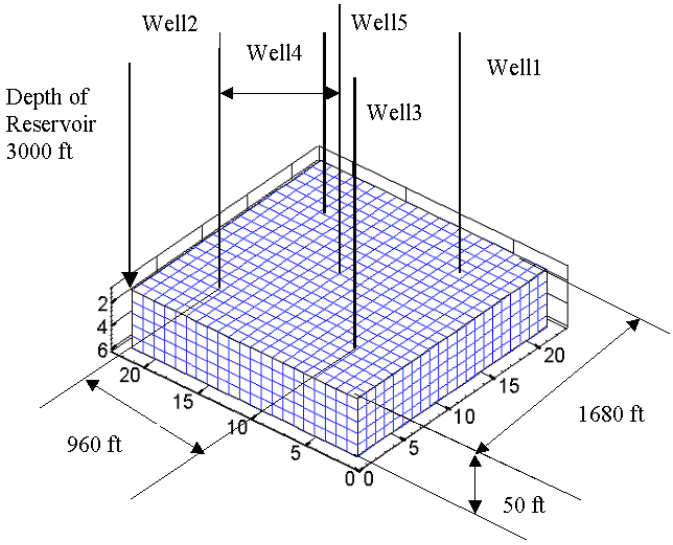

Figure B.2: Graphical description of the three-dimensional reservoir model. The diagram shows the 21x21 Cartesian finite-difference grid used to simulate fluid-flow measurements. Well locations for the conventional five-spot pattern are indicated with vertical lines penetrating through the reservoir. The injection well is located in the middle of the reservoir. Four production wells are distributed symmetrically, and remain closer to the edges of the reservoir.

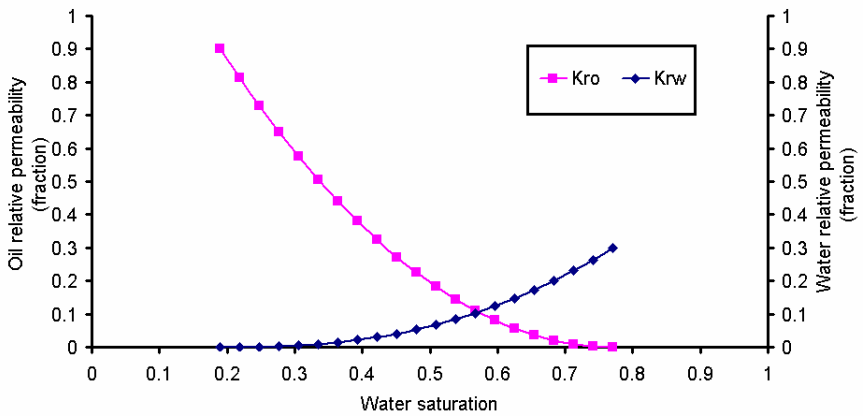

Figure B.3: Water-oil relative permeability curves used in the numerical simulation of water injection.

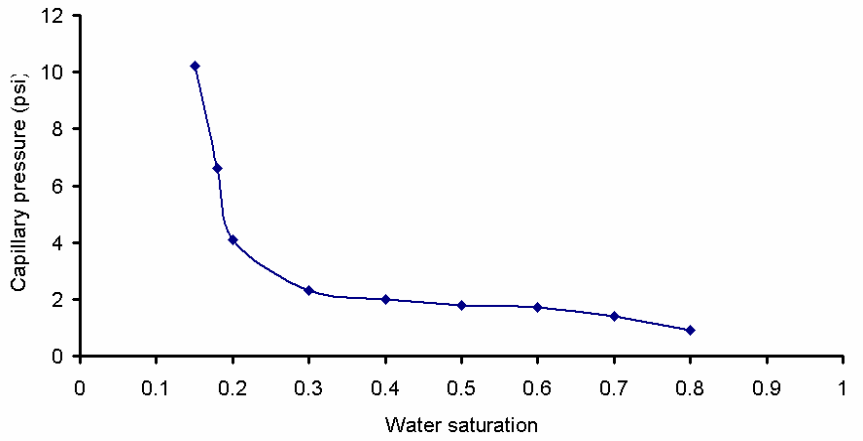

Figure B.4: Capillary pressure curve used in the numerical simulation of water injection.

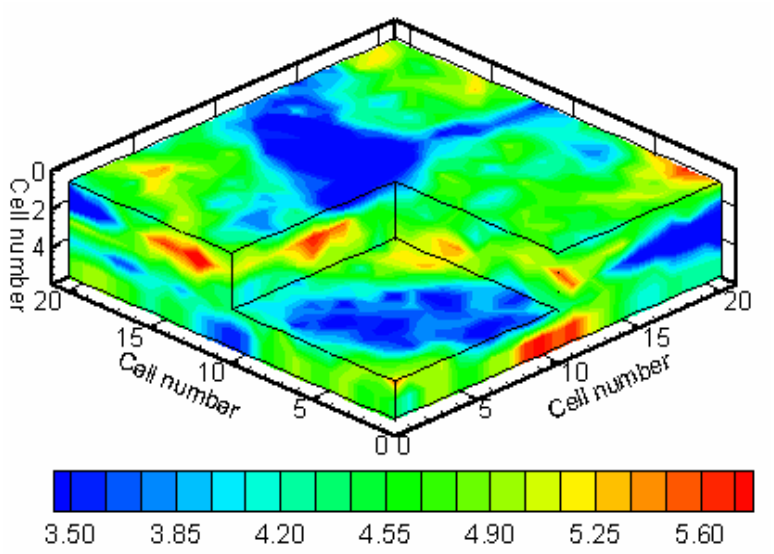

Figure B.5: Graphical description of the true spatial distribution of log-permeability [mD].

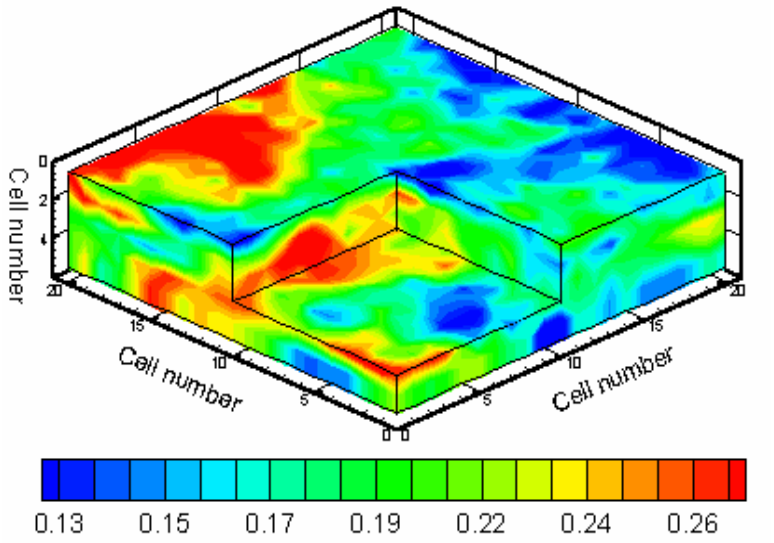

Figure B.6: Graphical description of the true spatial distribution of porosity [fraction].

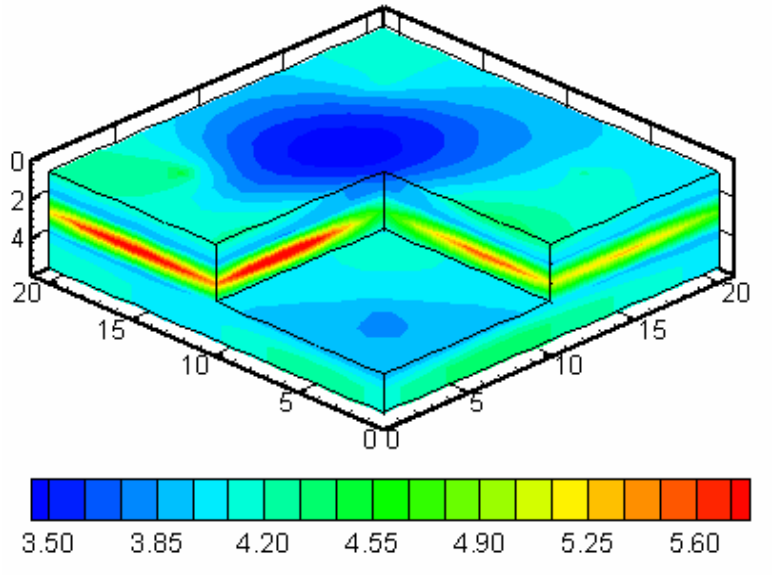

Figure B.7: Graphical description of the spatial distribution of log-permeability [mD] estimated from time-lapse in-situ permanent pressure measurements.

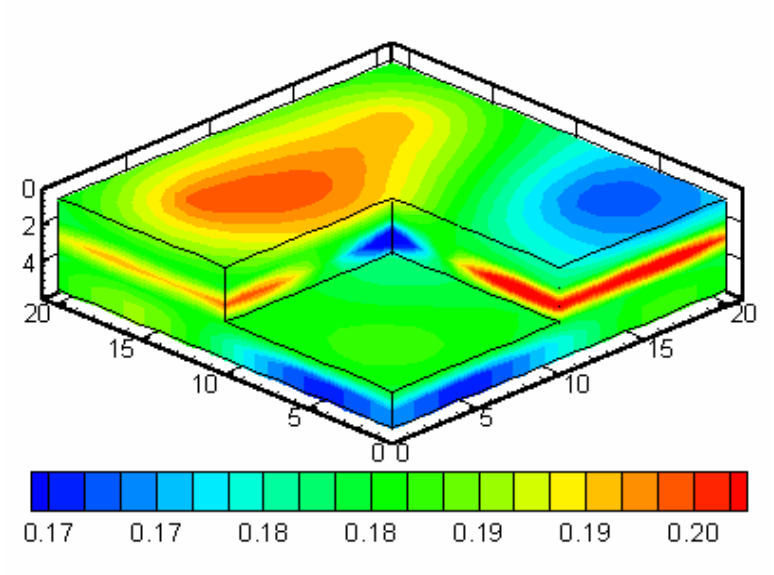

Figure B.8: Graphical description of the spatial distribution of porosity [fraction] estimated from time-lapse in-situ permanent pressure measurements.

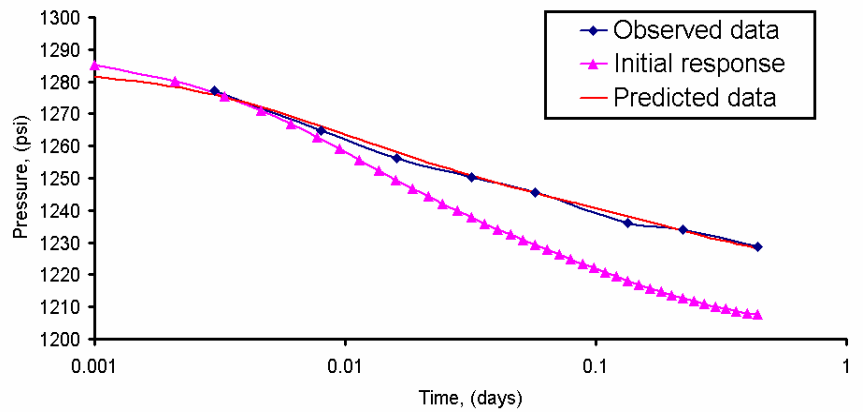

Figure B.9: Post-inversion match between simulated and measured in-situ permanent sensor pressure data for Sensor No. 1.

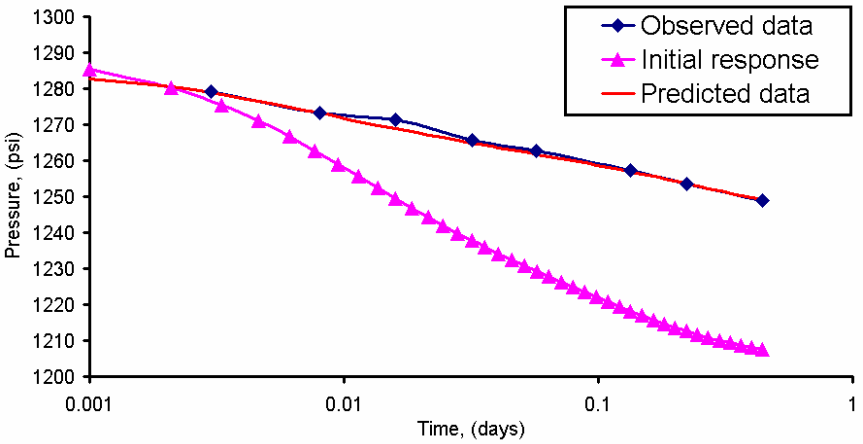

Figure B.10: Post-inversion match between simulated and measured in-situ permanent sensor pressure data for Sensor No. 2.

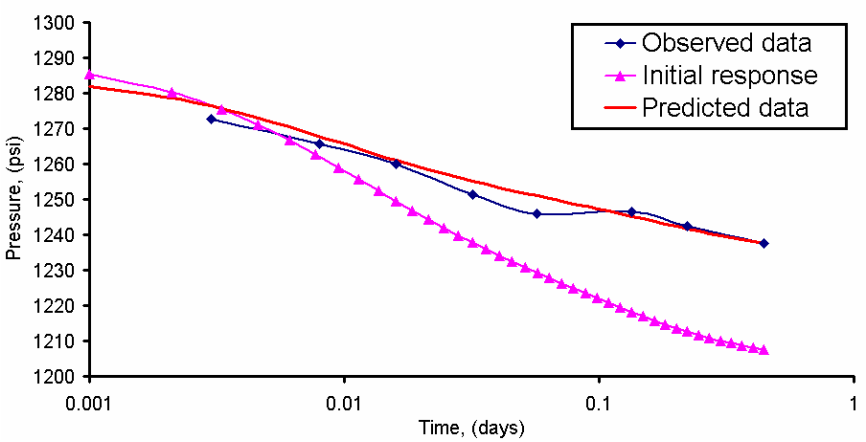

Figure B.11: Post-inversion match between simulated and measured in-situ permanent sensor pressure data for Sensor No. 3.

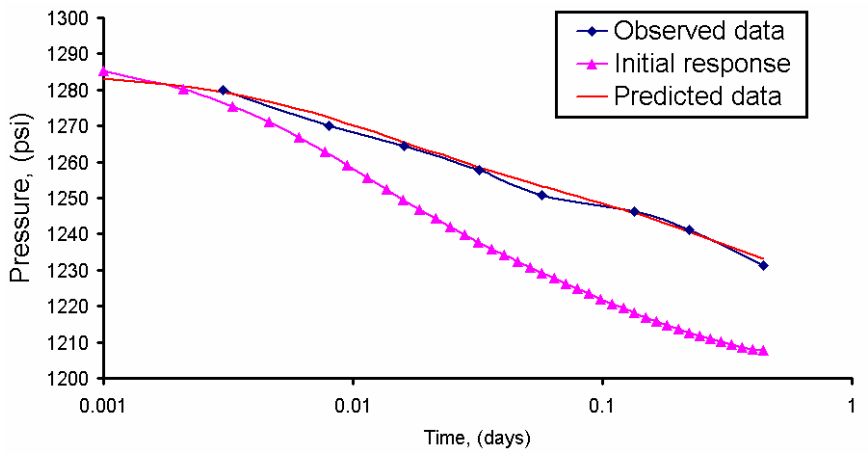

Figure B.12: Post-inversion match between simulated and measured in-situ permanent sensor pressure data for Sensor No. 4.

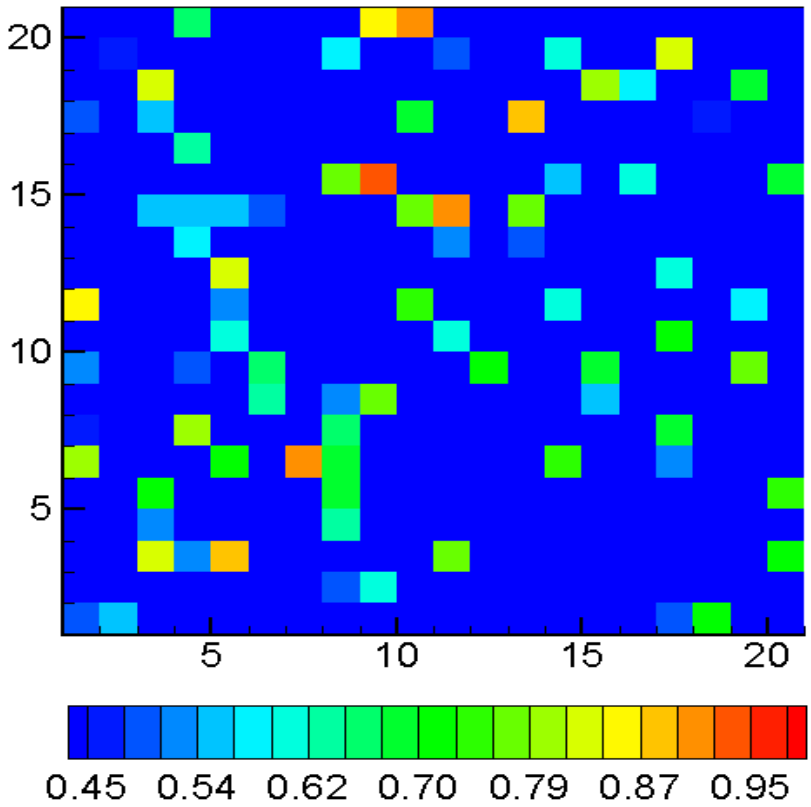

Figure B.13: A two-dimensional map of correlation coefficients for log-permeability computed to quantify the correlation between the initial guess and true distributions of log-permeability.

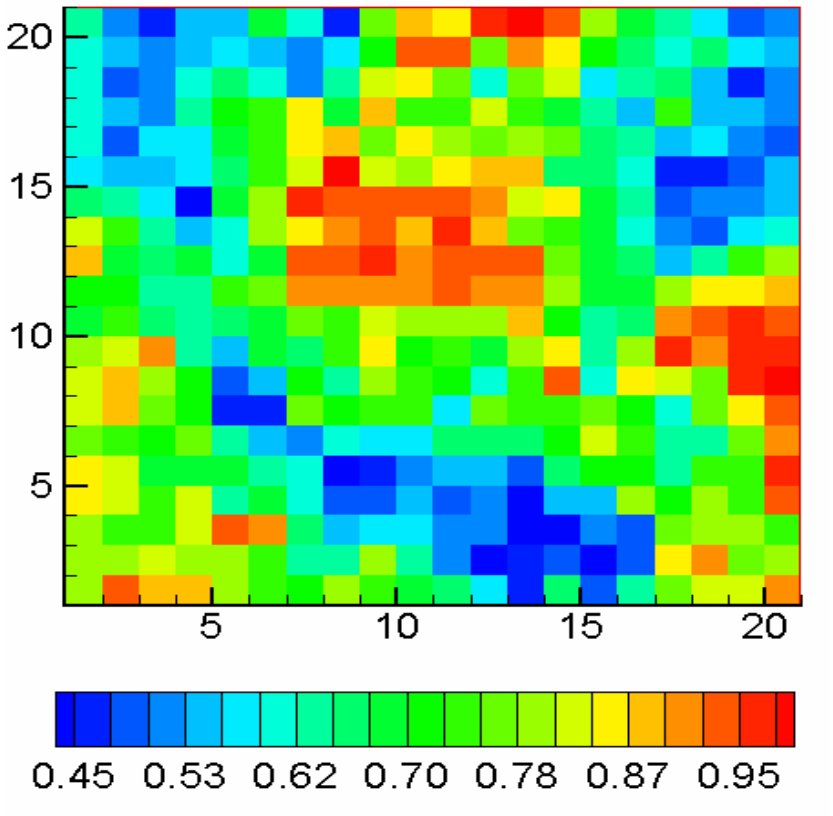

Figure B.14: A two-dimensional map of correlation coefficients for log-permeability computed to quantify the correlation between the inverted and true distributions of log-permeability.

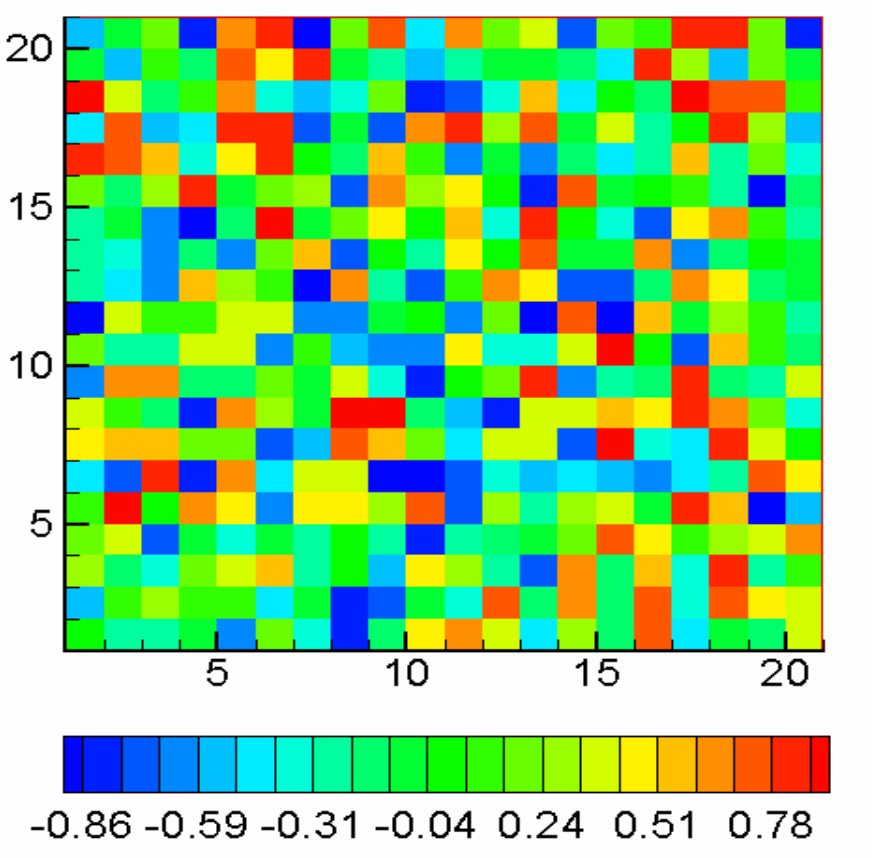

Figure B.15: A two-dimensional map of correlation coefficients for porosity computed to quantify the correlation between the initial guess and actual spatial distributions of porosity.

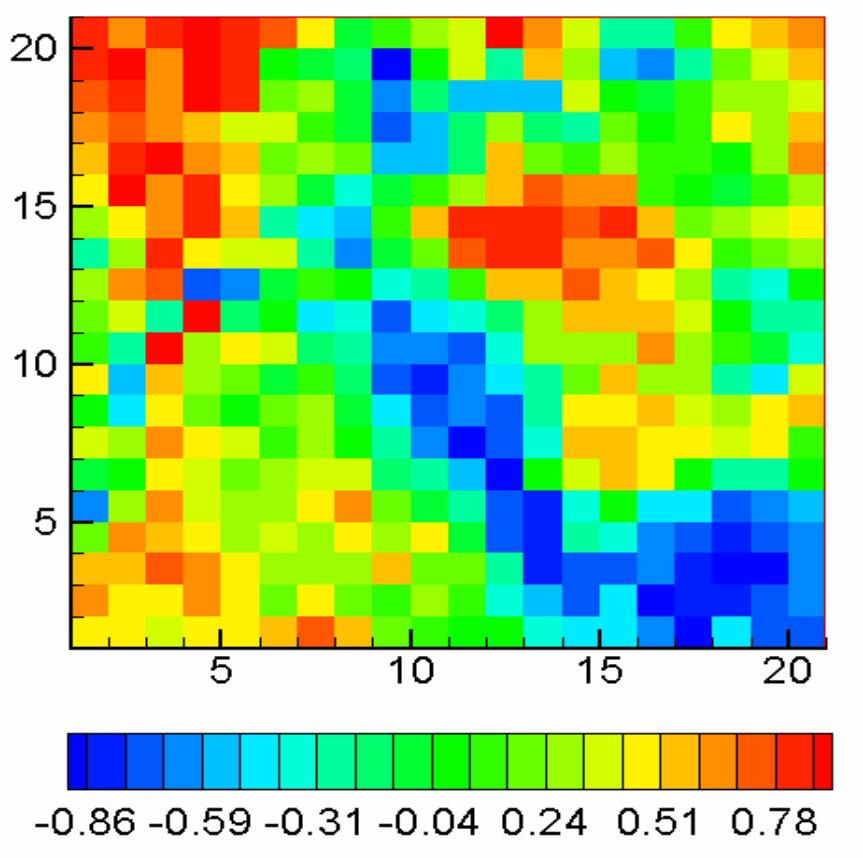

Figure B.16: A two-dimensional map of correlation coefficients for porosity computed to quantify the correlation between the inverted and actual spatial distributions of porosity.

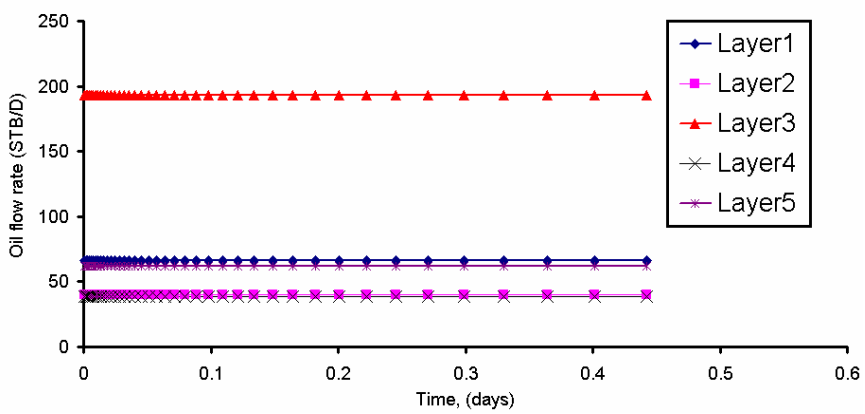

Figure B.17: Layer-by-layer oil production rates computed using post-inversion spatial distributions of permeability and porosity. Model parameters were estimated from time-lapse in-situ permanent sensor pressure data.

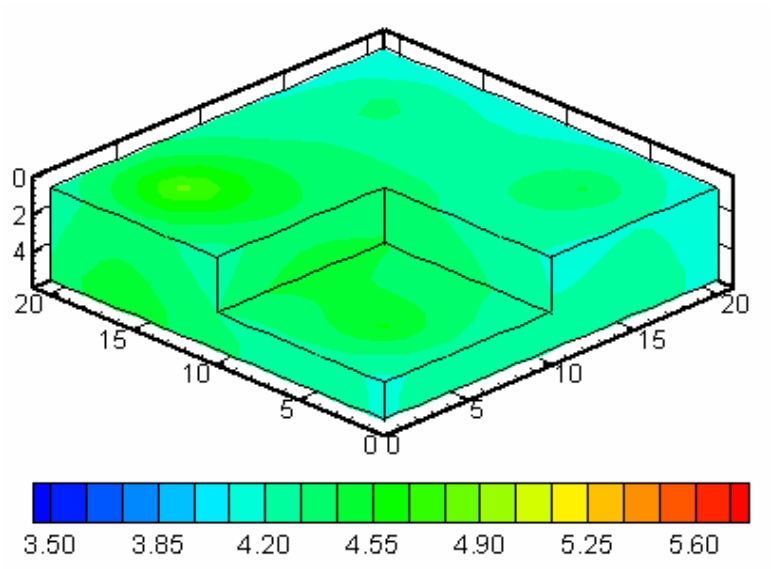

Figure B.18: Graphical description of the spatial distribution of log-permeability [mD] estimated from time-lapse bottom-hole pressure (BHP) measurements.

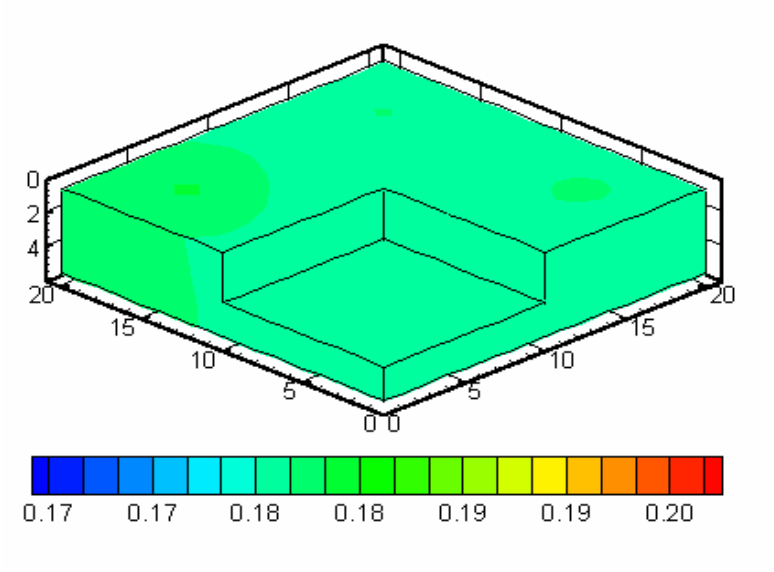

Figure B.19: Graphical description of the spatial distribution of porosity [fraction] estimated from time-lapse bottom-hole pressure (BHP) measurements.

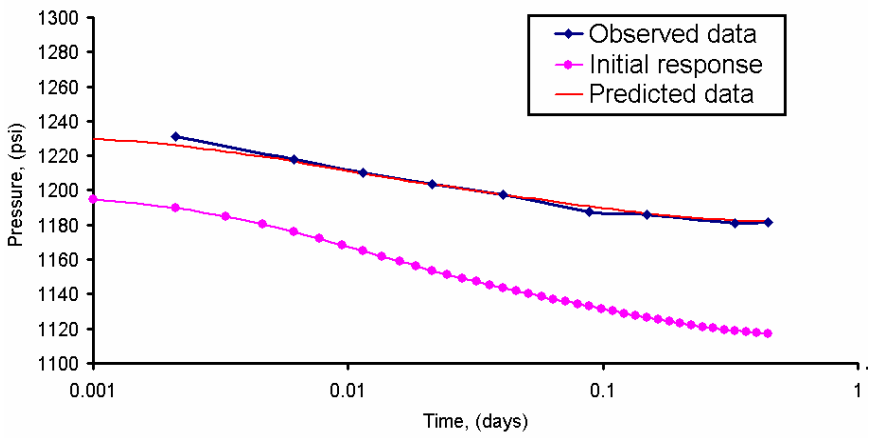

Figure B.20: Post-inversion match between simulated and measured bottom-hole pressure (BHP) data for the Production Well No. 1.

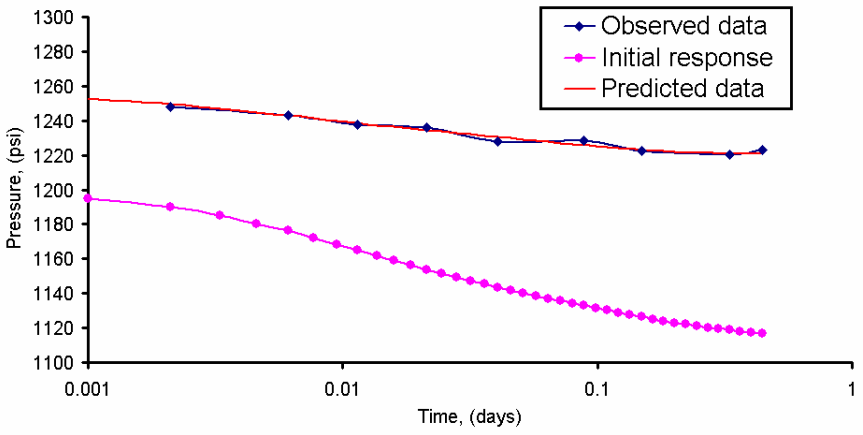

Figure B.21: Post-inversion match between simulated and measured bottom-hole pressure (BHP) data for the Production Well No. 2.

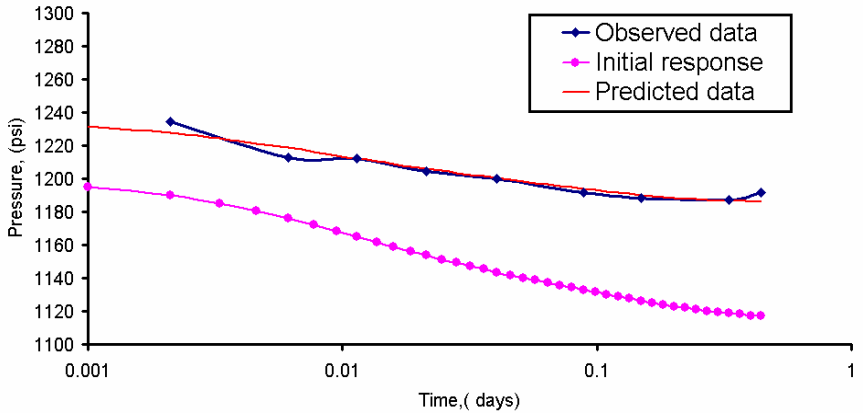

Figure B.22: Post-inversion match between simulated and measured bottom-hole pressure (BHP) data for the Production Well No. 3.

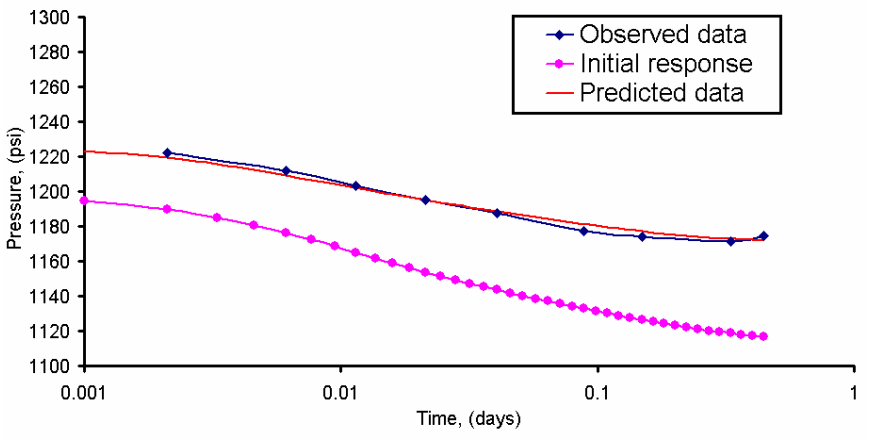

Figure B.23: Post-inversion match between simulated and measured bottom-hole pressure (BHP) data for the Production Well No. 4.

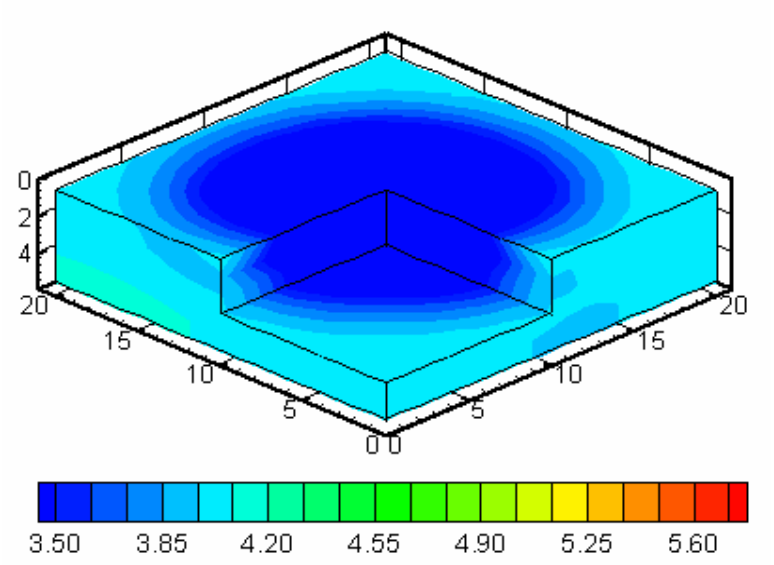

Figure B.24: Graphical description of the spatial distribution of log-permeability [mD] estimated from time-lapse water-oil ratio (WOR) measurements.

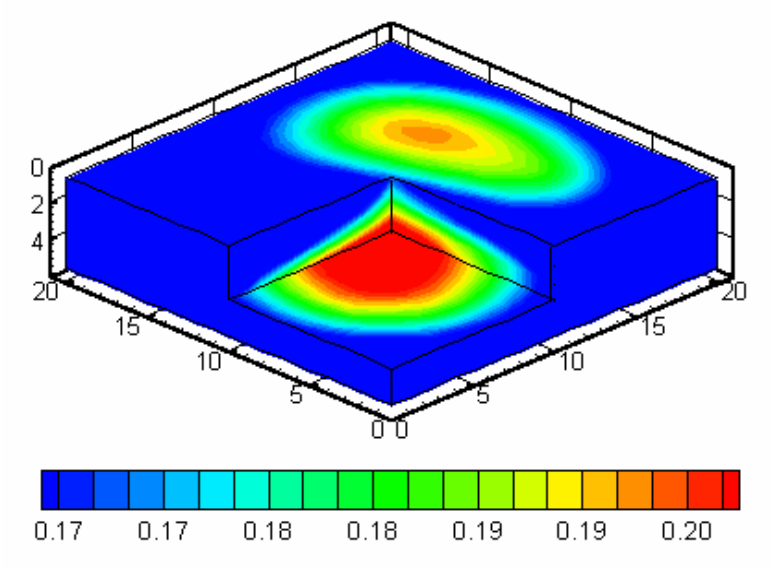

Figure B.25: Graphical description of the spatial distribution of porosity [fraction] estimated from time-lapse water-oil ratio (WOR) measurements.

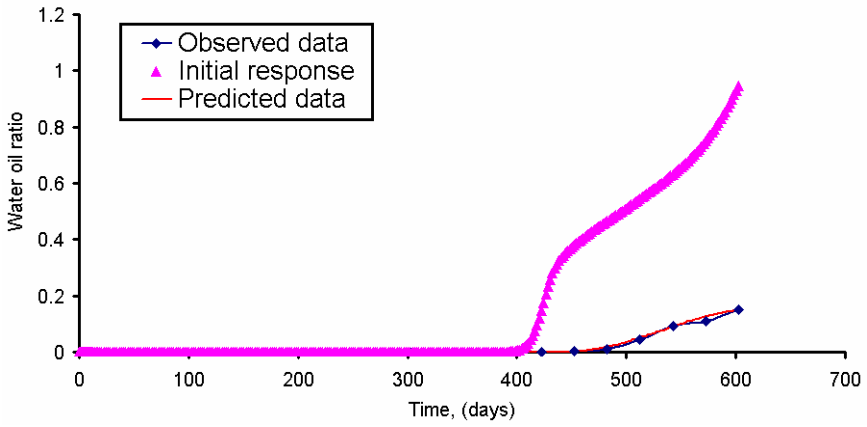

Figure B.26: Post-inversion match between simulated and measured water-oil ratio (WOR) data for the Production Well No. 1.

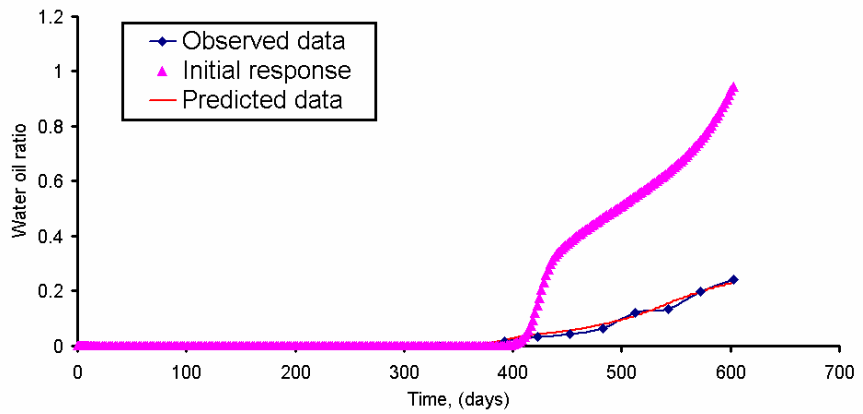

Figure B.27: Post-inversion match between simulated and measured water-oil ratio (WOR) data for the Production Well No. 2.

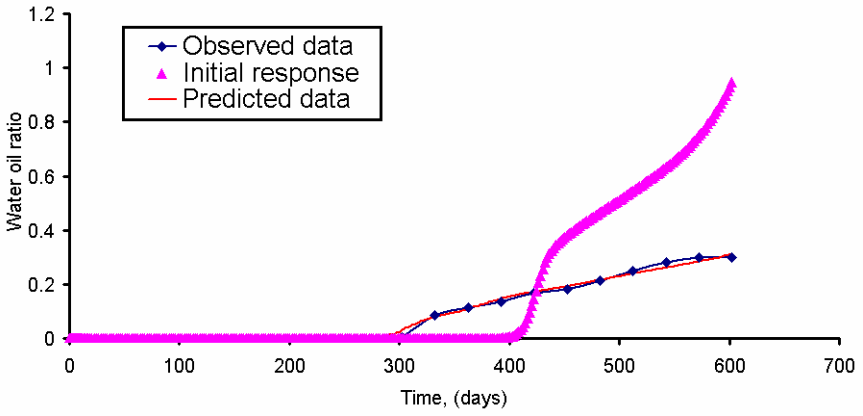

Figure B.28: Post-inversion match between simulated and measured water-oil ratio (WOR) data for the Production Well No. 3.

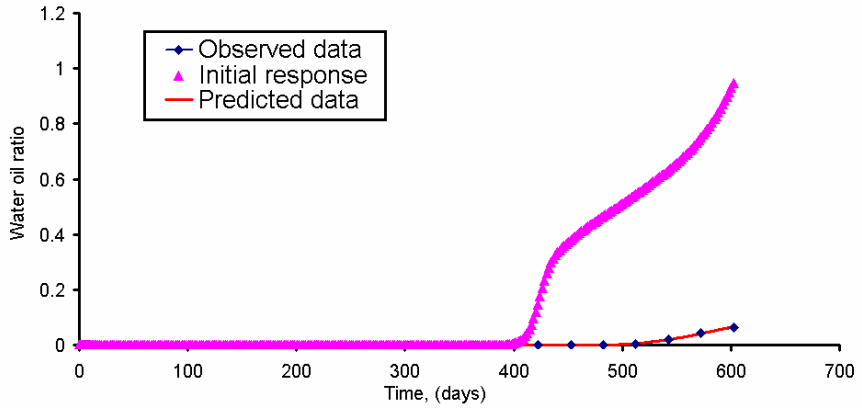

Figure B.29: Post-inversion match between simulated and measured water-oil ratio (WOR) data for the Production Well No. 4.

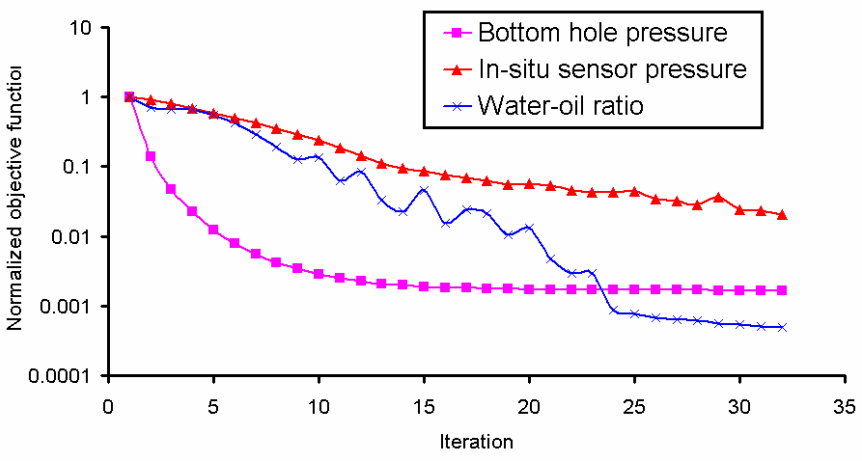

Figure B.30: Plot of the normalized cost (objective) function as a function of iteration number observed with the use of the subspace inversion algorithm. Curves are shown for inversions performed with three different types of time-lapse input data, namely, in-situ permanent sensor pressure, bottom-hole pressure (BHP), and water-oil ratio (WOR) measurements.

Bibliography

Abacioglu, Y., Oliver, D. S. and Reynolds, A.C. [2001]. Efficient history-matching using subspace vectors. *Computational Geoscience* **5**, 151-172.

Abubakar, A. and van den Berg, P. M. [2003]. Two- and three dimensional algorithms for microwave imaging and inverse scattering. *Journal of Electromagnetic Waves and Applications* **17**(2): 209-231.

Allers, A., Sezginer A. and Druskin V. [1994]. Solution of 2.5-dimensional problems using the Lanczos decomposition. *Radio Science* **29**(4): 955-963.

Alpak, F. O., Dussan V., E. B., Habashy, T. M. and Torres-Verdín, C. [2003a]. Numerical simulation of mud-filtrate invasion and sensitivity analysis of array induction tools. *Petrophysics* **44**(6): 396-411.

Alpak, F. O., Habashy, T. M., Torres-Verdín, C. and Dussan V., E. B. [2003b]. Joint inversion of pressure and time-lapse electromagnetic logging measurements. Paper SS, *Transactions of the 44th Annual Logging Symposium: Society of Well Log Analysts*, Galveston, Texas, June 22–25.

Alpak, F. O., Habashy, T. M., Torres-Verdín, C. and Dussan V., E. B. [2004a]. Joint inversion of transient-pressure and time-lapse electromagnetic logging measurements. *Petrophysics* **45**(3): 251-267.

Alpak, F. O., Torres-Verdín, C. and Habashy, T. M. [2004b]. Joint inversion of transient-pressure and dc resistivity measurements acquired with in-situ permanent sensors: a numerical study. *Geophysics* **69**(5): 1173-1191.

Alpak, F. O., Torres-Verdín, C. and Habashy, T. M. [2005b]. Petrophysical inversion of borehole electromagnetic-induction logging measurements. *Geophysics* (submitted for review).

Alpak, F. O., Torres-Verdín, C., Habashy, T. M. and Sepehrnoori, K. [2004c]. Simultaneous estimation of in-situ multi-phase petrophysical properties of rock formations from wireline formation tester and induction logging measurements. Paper SPE 90960, *Proceedings of the Annual Technical Conference and Exhibition: Society of Petroleum Engineers*, Houston, Texas, 26–29 September.

Alpak, F. O., Torres-Verdín, C. and Sepehrnoori, K. [2001]. Numerical simulation and inversion of pressure data acquired with permanent sensors. Paper SPE 71612,

Proceedings of the Annual Technical Conference and Exhibition: Society of Petroleum Engineers, New Orleans, Lousiana, 30 September–3 October.

Alpak, F. O., Torres-Verdín, C. and Sepehrnoori, K. [2004d]. Estimation of axisymmetric spatial distributions of permeability from pressure-transient data acquired with in-situ permanent sensors: a numerical study. *Journal of Petroleum Science and Engineering* **44**: 231-267.

Alpak, F. O., Torres-Verdín, C., Sepehrnoori, K. and Fang, S. [2002]. Numerical sensitivity studies for the joint inversion of pressure and dc resistivity measurements acquired with in-situ permanent sensors. Paper SPE 77621, *Proceedings of the Annual Technical Conference and Exhibition: Society of Petroleum Engineers*, San Antonio, Texas, 29 September–2 October.

Alpak, F. O., Torres-Verdín, C., Sepehrnoori, K., Fang, S. and Knizhnerman, L. [2003c]. An extended Krylov subspace method to simulate single-phase fluid flow phenomena in axisymmetric and anisotropic porous media. *Journal of Petroleum Science and Engineering* **40**: 121-144.

Alpak, F. O., Wu Z. and Torres-Verdín, C. [2005b]. A quantitative study to assess the value of pressure data acquired with in-situ permanent sensors in complex 3D reservoir models subject to two-phase fluid flow. *SPE Journal* (submitted for review).

Altunbay, M., Georgi, D. and Zhang, G. Q. [1998]. Pseudo capillary pressure from NMR data. *Proceedings of the International Petroleum Congress of Turkey*, October 12-14.

Altunbay, M., Martain, R. and Robinson, M. [2001]. Capillary pressure data from NMR logs and its implications on field economics. Paper SPE 71703, *Proceedings of the Annual Technical Conference and Exhibition: Society of Petroleum Engineers*, New Orleans, Lousiana, 30 September–3 October.

Anterion, F., Karcher, B. and Eymard, R. [1989]. Use of parameter gradients for reservoir history matching. Paper SPE 18433, *Proceedings of the Symposium on Reservoir Simulation: Society of Petroleum Engineers*, Houston, Texas, 6–8 February.

Archie, G. E. [1942]. The electrical resistivity log as an aid in determining some reservoir characteristics. *Petroleum Transactions of AIME* **146**: 54-62.

Athichanagorn, S., Horne, R.N. and Kikani, J. [1999]. Processing and interpretation of long term data from permanent downhole pressure gauges. Paper SPE 56419, *Proceedings of the Annual Technical Conference and Exhibition: Society of Petroleum Engineers*, Houston, Texas, 3–6 October.

Ayan, C., Hafez, H., Hurst, H., Kuchuk, F. J., O'Callaghan, A., Peffer, J., Pop, J. and Zeybek, M. [2001]. Characterizing permeability with formation testers. *Oilfield Review* Autumn issue: 1-23.

Aziz, K. and Settari, A. [1979]. *Petroleum Reservoir Simulation*. Applied Science Publishers, London.

Babour, K., Belani, A.K. and Pilla, J. [1995]. *Method and apparatus for long term monitoring of reservoirs*. United States Patent 5,467,823.

Babour, K., Belani, A.K. and Seeman, B. [1997]. *Method and apparatus for surveying and monitoring a reservoir penetrated by a well including fixing electrodes hydraulically isolated with a well*. United States Patent 5,462,051.

Baker, A., Gaskell, J., Jeffery, J., Thomas, A., Veneruso, T. and Unneland, T. [1995]. Permanent monitoring-looking at lifetime reservoir dynamics. *Oilfield Review* **7**(4): 32–46.

Barber, T., Anderson, B., Abubakar, A., Broussard, T., Chen, K-C., Davydycheva, S. Druskin, V., Habashy, T., Homan, D., Minerbo, G., Rosthal, R., Schlein, R. and Wang, H. [2004]. Determining formation anisotropy in the presence of invasion. Paper SPE 90526, *Proceedings of the Annual Technical Conference and Exhibition: Society of Petroleum Engineers*, Houston, Texas, 26–29 September.

Belani, A., Ramakrishnan, T. S., Habashy, T., Kuchuk, F. and Ayesteran, L. [2000]. *Method and apparatus for characterizing earth formation properties through joint pressure-resistivity inversion*. United States Patent 6,061,634.

Bissel, R. [1994]. Calculating optimal parameters for history matching. *Proceedings of the 4th European Conference on the Mathematics of Oil Recovery*, Topic E: History Match and Recovery Optimization, Roros, Norway, June 7–10.

Bissel, R., Sharma, Y. and Killough, J. E. [1994]. History matching using the method of gradients: two case studies. Paper SPE 28590, *Proceedings of the Annual Technical Conference and Exhibition: Society of Petroleum Engineers*, New Orleans, Lousiana, 25–28 September.

Bryant, I. D., Chen, M.-Y., Raghuraman, B., Raw, I., Delhomme, J.-P., Chouzenoux, C., Pohl, D., Manin, Y., Rioufol, E., Oddie, G., Swager, D. and Smith, J. [2002a]. An application of cemented resistivity arrays to monitor waterflooding of the Mansfield sandstone, Indiana, USA (paper SPE 81752). *SPE Reservoir Evaluation and Engineering* December issue: 447–454.

Bryant, I. D., Chen, M.-Y., Raghuraman, B., Schroeder, R., Supp, M., Navarro, J., Raw, I., Smith, J. and Scaggs, M. [2002b]. Real-time monitoring and control of water influx to a horizontal well using advanced completion equipped with permanent sensors. Paper SPE 77522, *Proceedings of the Annual Technical Conference and*

Exhibition: Society of Petroleum Engineers, San Antonio, Texas, 29 September–2 October.

Buckley, S. E. and Leverett, M. C. [1941]. Mechanism of fluid displacement in sands. *Journal of Petroleum Technology* May issue: 107-116.

Carter, R. D., Kemp, Jr., L. F., Pierce, A. C. and Williams, D. L. [1974]. Performance matching with constraints. *SPE Journal* **14**(2): 187-196.

Carter, R. D., Kemp, Jr., L. F., Pierce, A. C. and Williams, D. L. [1982]. Discussion of comparison of sensitivity coefficient calculation methods in automatic history matching. *SPE Journal* **22**: 205-208.

Chan, T. F. and Wong, C. K. [1998]. Total variation blind deconvolution. *IEEE Transactions on Image Processing* **7**: 370-375.

Charara, M., Manin, Y., Bacquet, C. and Delhomme, J.-P. [2002]. Use of permanent resistivity and transient-pressure measurement for time-lapse saturation mapping (paper SPE 80433). *SPE Reservoir Evaluation and Engineering* December issue: 472-479.

Chavent, G. M., Dupuy, M. and Lemonnier, P. [1975]. History matching by use of optimal control theory. *SPE Journal* **15**(1): 74-86.

Chen, W. H., Gavalas, G. R., Seinfeld, J. H. and Wasserman, M. L. [1974]. A new algorithm for automatic history matching. *SPE Journal* **14**(6): 593-608.

Chin, D. C. [1994]. A more efficient global optimization algorithm based on Styblinski and Tang. *Neural Networks* **7**(3): 573-574.

Chu, L., Reynolds, A. C. and Oliver, D. S. [1995]. Computation of sensitivity coefficients for conditioning the permeability field to well-test pressure data. *In Situ* **19**(2): 179-223.

Chu, L., Reynolds, A. C. and Oliver, D. S. [1995]. Reservoir description from static and well-test data using efficient gradient methods. Paper SPE 29999, *Proceedings of the Society of Petroleum Engineers International Meeting on Petroleum Engineering*, Beijing, People's Republic of China, 14–17 November.

Černy, V. [1985]. Thermodynamical approach to the traveling salesman problem: an efficient simulation algorithm. *Journal of Optimization and Applications* **45**: 41-51.

Delhomme, J.-P., Manin, Y., Charara, M. and Souhaite, P. [1998]. Potential applications of downhole electrical sensors for permanent reservoir monitoring. Extended abstract, *Proceedings of the EAGE Workshop on "Reservoir Monitoring: The Road to Greater Value"*.

Delshad, M., Pope, G. A. and Sepehrnoori, K. [1996]. A compositional simulator for modeling surfactant enhanced aquifer remediation. *Journal of Contaminant Hydrology* **23**: 303-327.

Dennis Jr., J. E. and Schnabel, R. B. [1983]. *Numerical Methods for Unconstrained Optimization and Nonlinear Equations*. Prentice Hall Inc., New Jersey.

Dey, A. and Morrison, H.F. [1979]. Resistivity modeling for arbitrarily shaped three dimensional structures. *Geophysics* **44**(4): 753-780.

Druskin, V. and Knizhnerman, L. A. [1987]. A method of solution of forward problems of electric well logging and electric exploration with direct current. *Izvestiya, Earth Physics* **23**: 317-323, (Russian; translated into English).

Druskin, V. and Knizhnerman, L. [1988]. Spectral differential-difference method for numeric solution of three-dimensional nonstationary problems in electric prospecting. *Izvestiya, Earth Physics* **24**: 63-74, (Russian; translated into English).

Druskin, V. and Knizhnerman, L. [1989]. Two polynomial methods to compute functions of symmetric matrices. *Journal of Computational Mathematics and Mathematical Physics* **29**: 112-121.

Druskin, V. and Knizhnerman, L. [1991]. Error bounds in the simple Lanczos procedure when computing functions of symmetric matrices and eigenvalues. *Journal of Computational Mathematics and Mathematical Physics* **31**: 20-30.

Druskin, V. and Knizhnerman, L. [1994a]. On application of the Lanczos method to solution of some partial differential equations. *Journal of Computational and Applied Mathematics* **50**: 255-262.

Druskin, V. and Knizhnerman, L. [1994b]. Spectral approach to solving three-dimensional Maxwell's diffusion equations in the time and frequency domains. *Radio Science* **29**(4): 937-953.

Druskin, V. and Knizhnerman, L. [1995]. Krylov subspace approximation of eigenpairs and matrix functions in exact and computer arithmetic. *Numerical Linear Algebra and Applications* **2**: 205-217.

Druskin, V. and Knizhnerman, L. [1998]. Extended Krylov subspaces: approximation of the matrix square root and related functions. *SIAM Journal on Matrix Analysis Applications* **19**: 755-771.

Druskin, V., Knizhnerman, L. and Lee, P. [1999]. New spectral Lanczos decomposition method for induction modeling in arbitrary 3D geometry. *Geophysics* **64**: 701-706.

Druskin, V. L. and Tamarchenko, T. V. [1988]. Fast variant of partial domain method for solution of the problem of induction logging. *Geologiya i Geofizika* **29**(3): 129-135, (in Russian; translated to English).

Dunbar, W. S. and Woodbury, A. D. [1989]. Application of the Lanczos algorithm to the solution of the groundwater flow equation. *Water Resources Research* **25**: 551-558.

Dumanoir, J. L., Tixier, M. P. and Martin, M. [1957]. Interpretation of the induction-electrical log in fresh mud. *Petroleum Transactions of the AIME* **210**: 202-217.

Dussan V., E. B., Anderson, B. I. and Auzerais, F. [1994]. Estimating vertical permeability from resistivity logs. Paper UU, *Transactions of the 35th Annual Logging Symposium: Society of Well Log Analysts*, Tulsa, Oklahoma, 19–22 June.

Ellis, R. G., Farquharson, C. G. and Oldenburg, D. W. [1993]. Approximate inverse mapping inversion of the COPROD2 data. *Journal of Geomagnetics and Geoelectrics* **45**: 1001-1012.

Epov, M., Yeltsov, I., Kashevarov, A., Sobolev, A. and Ulyanov, V. [2002]. Time evolution of the near borehole zone in sandstone reservoir through the time-lapse data of high-frequency electromagnetic logging. Paper ZZ, *Transactions of the 43rd Annual Logging Symposium: Society of Well Log Analysts*, Oiso, Japan, 2–5 June.

Fletcher, R. [1987]. *Practical Methods of Optimization*. John Wiley & Sons, New York City.

Freedman, R. and Minerbo, G. N. [1991]. Maximum entropy inversion of induction log data. *SPE Formation Evaluation* June issue: 259-268.

Gao, L. [2002]. Fast induction log inversion using quasi-Newton updates. Paper SPE 77716, *Proceedings of the Annual Technical Conference and Exhibition: Society of Petroleum Engineers*, San Antonio, Texas, 29 September–2 October.

Gavalas, G. R., Shah, P. C. and Seinfeld, J. H. [1976]. Reservoir history matching by Bayesian estimation. *SPE Journal* **16**(6): 337-350.

Geman, S. and Geman, D. [1984]. Stochastic relaxation, Gibbs distributions, and the Bayesian restoration of images. *IEEE Transactions on Pattern Analysis and Machine Intelligence* **6**(6): 721-741.

George, B. K., Torres-Verdín, C., Delshad, M., Sigal, R., Zouioueche, F. and Anderson, B. [2003]. A case study integrating the physics of mud-filtrate invasion with the physics of induction logging: assessment of in-situ hydrocarbon saturation in the presence of deep invasion and highly saline connate water. Paper K, *Transactions*

of the 44th Annual Logging Symposium: Society of Well Log Analysts, Galveston, Texas, June 22–25.

GeoQuest, Schlumberger [2000]. *ECLIPSE Reference Manual 2000A*.

Gill, P. E., Murray, W. and Wright, M. H. [1981]. *Practical Optimization*. Academic Press, London.

Goldberg, D. E. [1980]. *Genetic Algorithms in Search, Optimization and Machine Learning*. Addison-Wesley, Reading, Massachusetts.

Golub, G. H. and van Loan, C. F. [1993]. *Matrix Computations*. The Johns Hopkins University Press, Baltimore, Maryland.

Habashy, T. M. and Abubakar, A. [2004]. A general framework for constraint minimization for the inversion of electromagnetic measurements. *Progress in Electromagnetic Research (PIER)* **46**: 265-312.

Habashy, T. M., Chew, W. C. and Chow, E. Y. [1986]. Simultaneous reconstruction of permittivity and conductivity profiles in a radially inhomogeneous slab. *Radio Science* **21**: 635-645.

He, N., Reynolds, A. C. and Oliver, D. S. [1997]. Three-dimensional reservoir description from multiwell pressure data and prior information. *SPE Journal* **2**(3): 312-327.

He, N., Oliver, D. S. and Reynolds, A. C. [2000]. Conditioning stochastic reservoir models to well-test data. *SPE Reservoir Evaluation and Engineering* **3**(1): 74-79.

Honarpour M., Koederitz, L. F. and Harvey, A. H. [1986]. *Relative Permeability of Petroleum Reservoirs*. CRC Press Inc., Boca Raton.

Hunka, J. F., Barber, T. D., Rosthal, R. A., Minerbo, G. N., Head, E. A., Howard, A. Q., Hazen, G. A. and Chandler, R. N. [1990]. A new resistivity measurement system for deep formation imaging and high-resolution formation evaluation. Paper SPE 20559, *Proceedings of the Annual Technical Conference and Exhibition: Society of Petroleum Engineers*, New Orleans, Lousiana, 23–26 September, 295-307.

Jackson, R. R., Banerjee, R. and Thambynayagam, R. K. M. [2003]. An integrated approach to interval pressure transient test analysis using analytical and numerical methods. Paper SPE 81515, *Proceedings of the 13th Middle East Oil Show & Conference: Society of Petroleum Engineers*, Bahrain, 5–8 April.

Jacquard, P. and Jain, C. [1965]. Permeability distribution from field pressure data. *SPE Journal* **5**(4): 281-294.

Kennett, P. R., Sambridge, M. S. and Williamson, P. R. [1988]. Subspace Methods for Large Inverse Problems with Multiple Parameter Classes. *Geophysical Journal International* **94**: 237-247.

Killough, J. E., Sharma, Y., Dupuy, A., Bissel, R. and Wallis, J. [1995]. A multiple right hand side iterative solver for history matching. Paper SPE 29119, *Proceedings of the Symposium on Reservoir Simulation: Society of Petroleum Engineers*, San Antonio, Texas, 12–15 February.

Kirkpatrick, S., Gelatt Jr., C. and Vecchi, M. [1983]. Optimization by simulated annealing. *Science* **220**(4598): 671-680.

Knizhnerman, L., Druskin, V., Liu Q.-H. and Kuchuk, F. J. [1994]. Spectral Lanczos decomposition method for solving single-phase fluid flow in porous media. *Numerical Methods for Partial Differential Equations* **10**: 569-580.

Kuchuk, F. J., Ramakrishnan, T. S. and Dave, Y. [1994]. Interpretation of wireline formation tester packer and probe pressures. Paper SPE 28404, *Proceedings of the Annual Technical Conference and Exhibition: Society of Petroleum Engineers*, New Orleans, Lousiana, 25–28 September, 431-441.

Kuchuk, F. J. and Wilkinson, D. J. [1991]. Transient pressure behavior of commingled reservoirs. *SPE Formation Evaluation* March issue: 111-120.

Lake, L. W. [1989]. *Enhanced Oil Recovery*. Prentice Hall, Englewood Cliffs.

Lanczos, C. [1950]. An iteration method for the solution of the eigenvalue problem of linear differential and integral operators. *Journal of Research of the National Bureau of Standards* **45**: 255-282.

Landa, J. L. and Horne, R. N. [1997]. A procedure to integrate well-test data, reservoir performance history, and 4D seismic information into a reservoir description. Paper SPE 38653, *Proceedings of the Annual Technical Conference and Exhibition: Society of Petroleum Engineers*, San Antonio, Texas, 5–8 October.

Landa, J. L., Horne, R. N., Kamal, M. M. and Jenkins, C. D. [2000]. Reservoir characterization constrained to well-test data: a field example. *SPE Reservoir Evaluation and Engineering* **3**(4): 325-334.

Lee, T. Y. and Seinfeld, J. H. [1987]. Estimation of two-phase petroleum reservoir properties by regularization. *Journal of Computational Physics* **69**: 397-419.

Lee, T. Y. and Seinfeld, J. H. [1987]. Estimation of absolute and relative permeabilities in petroleum reservoirs. *Inverse Problems* **3**: 711-728.

Li, R., Reynolds, A. C. and Oliver, D. S. [2001]. History matching of three-phase flow production data. Paper SPE 66351, *Proceedings of the Symposium on Reservoir Simulation: Society of Petroleum Engineers*, Houston, Texas, 11–14 February.

Li, S. and Shen, L. C. [2003]. Dynamic Invasion Profiles and Time-Lapse Electrical Logs. Paper E, *Transactions of the 44th Annual Logging Symposium: Society of Well Log Analysts*, Galveston, Texas, June 22–25.

Lowry, T., Allen, M. B. and Shive P. N. [1989]. Singularity removal: a refinement of resistivity modeling techniques. *Geophysics* **54**(6): 766-774.

Luenberger, D. G. [1984]. *Linear and Nonlinear Programming*. Addison-Wesley, Reading, Massachusetts.

Makhlouf, E. M., Chen, W. H., Wasserman, M. L. and Seinfeld, J. H. [1993]. A general history matching algorithm for three-phase, three-dimensional petroleum reservoirs. *SPE Advanced Technology Series* **1**(2): 83-91.

Malinverno, A. and Torres-Verdín, C. [2000]. Bayesian inversion of dc electrical measurements with uncertainties for reservoir monitoring. *Inverse Problems* **16**: 1343-1356.

Metropolis, N., Rosenbluth, A., Rosenbluth, M., Teller, A. and Teller, E. [1953]. Equation of state calculations by fast computing machines. *Journal of Chemical Physics* **21**(6): 1087-1092.

Moskow, S., Druskin, V., Habashy, T., Lee, P. and Davydycheva, S. [1999]. A finite difference scheme for elliptic equations with rough coefficients using a Cartesian grid nonconforming to interfaces. *SIAM Journal on Numerical Analysis* **36**(2): 442-464.

Muskat, M. [1937]. *The Flow of Homogeneous Fluids Through Porous Media*. McGraw-Hill, New York.

Nocedal, J. and Wright, S. J. [1999]. *Numerical Optimization*. Springer-Verlag, New York.

Nour-Omid, B. [1987]. Lanczos method for heat conduction analysis. *International Journal for Numerical Methods in Engineering* **24**: 251-262.

Nour-Omid, B. and Clough, R. W. [1984]. Dynamic analysis of structure using Lanczos co-ordinates. *Earthquake Engineering and Structural Dynamics* **12**: 565-577.

Oldenburg, D. W. [1990]. Inversion of electromagnetic data: an overview of new techniques. *Surveys in Geophysics* **11**: 231-270.

Oliver, D. S. [1994]. Incorporation of transient pressure data into reservoir characterization. *In Situ* **18**(3): 243-275.

Oliver, D. S., He, N. and Reynolds, A. C. [1996]. Conditioning permeability fields to pressure data. *Proceedings of the 5th European Conference on the Mathematics of Oil Recovery*, 1-11, Leoben, Austria, 3–6 September.

Onur, M. and Kuchuk, F. J. [1999]. Integrated nonlinear regression analysis of multiprobe wireline formation tester packer and probe pressures and flow rate measurements. Paper SPE 56616, *Proceedings of the Annual Technical Conference and Exhibition: Society of Petroleum Engineers*, Houston, Texas, 3–6 October.

Onur, M. and Reynolds, A. C. [2002]. Nonlinear regression: the information content of pressure and pressure-derivative data. *SPE Journal* September issue: 243-249.

Oristaglio, M. and Blok, H. [1995]. *Wavefield imaging and inversion in electromagnetics and acoustics*. Report number: Et/EM 1995-21, Laboratory of Electromagnetic Research, Department of Electrical Engineering Centre for Technical Geoscience, Delft University of Technology, Delft, The Netherlands.

Paige, C. C. and Sounders, M. A. [1975]. Solution of sparse indefinite systems of linear equations. *SIAM Journal on Numerical Analysis* **12**: 617-629.

Parlett, B. N. [1980]. *The Symmetric Eigenvalue Problem*. Prentice-Hall, Englewood Cliffs, New Jersey.

Parlett, B. N. [1980]. A new look at the Lanczos algorithm for solving symmetric systems of linear equations. *Linear Algebra Applications* **29**: 323-346.

Peaceman, D. W. [1977]. *Fundamentals of Numerical Reservoir Simulation*. Elsevier, New York.

Pop, J., Badry, R., Morris, C., Wilkinson, D., Tottrup, P. and Jonas, J. [1993]. Vertical interference testing with a wireline-conveyed straddle-packer tool. Paper SPE 26481, *Proceedings of the Annual Technical Conference and Exhibition: Society of Petroleum Engineers*, Houston, Texas, 3–6 October, 665-680.

Press, W. H., Teukolsky, S. A., Vetterling, W. T. and Flannery, B. P. [1992]. *Numerical Recipes in FORTRAN 77*. Cambridge University Press, Cambridge, Massachusetts.

Raghavan, R. [1993]. *Well Test Analysis*. Prentice-Hall, Englewood Cliffs, New Jersey.

Raghuraman, B. and Ramakrishnan, T. S. [2001]. Interference analysis of cemented-permanent-sensor data from a field experiment. Expanded abstract M019,

Proceedings of the European Association of Geoscientists and Engineers Conference, Amsterdam, The Netherlands, 11–15 June.

Ramakrishnan, T. S., Al-Khalifa, J., Al-Waheed, H. H. and Cao-Minh, C. [1997]. Producibility estimation from array-Induction logs and comparison with measurements: a case study. Paper X, *Transactions of the 38th Annual Logging Symposium: Society of Well Log Analysts*, Houston, Texas, June 15-18.

Ramakrishnan, T. S. and Kuchuk, F. J. [1993]. Pressure transients during injection: constant rate and convolution solutions. *Transport in Porous Media* **10**: 103-136.

Ramakrishnan, T. S. and Wilkinson, D. J. [1997]. Formation producibility and fractional flow curves from radial resistivity variation caused by drilling fluid invasion. *Physics of Fluids* **9**(4): 833-844.

Ramakrishnan, T. S. and Wilkinson, D. J. [1999]. Water-cut and fractional flow logs from array-induction measurements. *SPE Reservoir Evaluation and Engineering* **2**(1): 85-94.

Reynolds, A. C., He, N., Chu, L. and Oliver, D. S. [1996]. Reparameterization techniques for generating reservoir descriptions conditioned to variograms and well-test pressure data. *SPE Journal* **1**(4): 413-426.

Reynolds, A. C., He, N. and Oliver, D. S. [1999]. Reducing uncertainty in geostatistical description with well testing pressure data. *Reservoir Characterization-Recent Advances*. R. A. Schatzinger and J. F. Jordan, eds., AAPG, 149-162.

Rudin, L., Osher, S. and Fatemi, C. [1992]. Nonlinear total variation based on noise removal algorithm. *Physica* **30D**: 259-268.

Scharf, L. L. [1991]. *Statistical Signal Processing, Detection, Estimation, and Time Series Analysis*. Addison-Wesley, Massachusetts.

Semmelbeck, M. E., Dewan, J. T. and Holditch, S. A. [1995]. Invasion-based method for estimating permeability from logs. Paper SPE 30581, *Proceedings of the Annual Technical Conference and Exhibition: Society of Petroleum Engineers*, Dallas, Texas, 22–25 October, 517-531.

Spall, J. C. [1992]. Multivariate stochastic approximation using a simultaneous perturbation gradient approximation. *IEEE Transactions on Automatic Control* **37**(3): 332-341.

Spall, J. C. [1998]. Implementation of the simultaneous perturbation algorithm for stochastic optimization. *IEEE Transactions on Aerospace and Electronic Systems* **34**(3): 817-823.

Spall, J. C. [2003]. *Introduction to Stochastic Search and Optimization: Estimation, Simulation, and Control*. Wiley and Sons Inc., Hoboken.

Tarantola, A. [1987]. *Inverse Problem Theory*. Elsevier, Amsterdam.

Tan, T. B. and Kalogerakis, N. [1991]. A fully implicit, three-dimensional, three-phase simulator with automatic history matching capability. Paper SPE 21205, *Proceedings of the Symposium on Reservoir Simulation: Society of Petroleum Engineers*, Anaheim, California, 17–20 February.

Tang, Y. N., Chen, Y. M. and Wasserman, M. L. [1989]. Generalized pulse-spectrum technique for 2-D and 2-phase history matching. *Applied Numerical Mathematics* **5**(6): 529-539.

Tobola, D. P. and Holditch, S. A. [1991]. Determination of reservoir permeability from repeated induction logging. *SPE Formation Evaluation* March issue: 20-26.

Torres-Verdín, C., Druskin, V. L., Fang, S., Knizhnerman, L. A. and Malinverno, A. [2000]. A dual-grid nonlinear inversion technique with applications to the interpretation of dc resistivity data. *Geophysics* **65**(6): 1733-1745.

Torres-Verdín, C., George, B. K., Delshad, M., Sigal, R., Zouioueche, F. and Anderson, B. [2003]. Assessment of in-situ hydrocarbon saturation in the presence of deep invasion and highly saline connate water. *Petrophysics* **45**: 141-156.

Torres-Verdín, C. and Habashy, T. M. [1994]. Rapid 2.5-D forward modeling and inversion via new nonlinear scattering approximation. *Radio Science* **29**: 1051-1079.

Treitel, S. and Lines, L. R. [1982]. Linear inverse theory and deconvolution. *Geophysics* **47**: 1153-1159.

van den Berg, P. M. and Abubakar, A. [2001]. Contrast source inversion method: state of art. *Progress in Electromagnetics Research (PIER)* **34**: 189-218.

van den Berg, P. M., Abubakar, A. and Fokkema, J. T. [2003]. Multiplicative regularization for contrast profile inversion. *Radio Science* **38**(2): 23.1-23.10.

van Kleef, R., Hakvoort, R., Bushan, V., Al-Khodhori, S., Boom, W., de Bruin, C., Babour, K., Chouzenoux, C., Delhomme, J.-P., Manin, Y., Pohl, D., Rioufol, E., Charara, M. and Harb, R. [2001]. Water flood monitoring in an Oman carbonate reservoir using a downhole permanent electrode array. Paper SPE 68078, *Proceedings of the Middle East Oil Show: Society of Petroleum Engineers*, Bahrain, 17-20 March.

van der Vorst, H. A. [1987]. An iterative solution method for solving $f(\mathbf{A})x = b,$ using Krylov subspace information obtained for the symmetric positive definite matrix $\mathbf{A}$. *Journal of Computational and Applied Mathematics* **18**: 249-263.

Volokitin, Y., Looyestijn, W. J., Slijkerman, W. F. J. and Hofman, J. P. [1999]. A practical approach to obtain 1st drainage capillary pressure curves from NMR core and log data. Paper SCA-9924, *Proceedings of the International Symposium: Society of Core Analysts*, Golden, Colorado, August 1-4.

Wang, H., Barber, T., Rosthal, R., Tabanou, J., Anderson, B. and Habashy, T. [2003]. Fast and rigorous inversion of triaxial induction logging data to determine formation resistivity anisotropy, bed boundary position, relative dip and azimuth angles. *Proceedings of the Annual Meeting: Society of Exploration Geophysicists*, Dallas, Texas, 24–31 October.

Wang, P. and Horne, R. N. [2000]. Integrating resistivity data with production data for improved reservoir modeling. Paper SPE 59425, *Proceedings of the 2000 SPE Asia Pacific Conference on Integrated Modelling for Asset Management*, 25–26 April, Yokohama, Japan.

Wen, X.-H., Deutsch, C. V. and Cullick, A. S. [1998]. High-resolution reservoir models integrating multiple-well production data. *SPE Journal* December issue: 344-355.

Wu, J. [2004]. *Numerical Simulation of Multi-Phase Mud-Filtrate Invasion and Inversion of Formation Tester Data*. Ph.D. dissertation, The University of Texas at Austin, Austin, Texas.

Wu, J., Torres-Verdín, C., Proett, M. A., Sepehrnoori, K. and Belanger, D. [2002]. Inversion of multi-phase petrophysical properties using pumpout sampling data acquired with a wireline formation tester. Paper SPE 77345, *Proceedings of the Annual Technical Conference and Exhibition: Society of Petroleum Engineers*, San Antonio, Texas, 29 September–2 October.

Wu, J., Torres- Verdín, C., Sepehrnoori, K. and Delshad, M. [2001]. Numerical simulation of mud filtrate invasion in deviated wells. Paper SPE 71739, *Proceedings of the Annual Technical Conference and Exhibition: Society of Petroleum Engineers*, New Orleans, Louisiana, September 30–October 3.

Wu, J., Torres-Verdín, C., Sepehrnoori, K., Proett, M. A. and van Dalen, S. C. [2003]. A new inversion technique determines in-situ relative permeabilities and capillary pressure parameters from pumpout wireline formation tester data. Paper GG, *Transactions of the 44th Annual Logging Symposium: Society of Well Log Analysts*, Galveston, Texas, June 22–25.

Wu, Z. and Datta-Gupta, A. [2002]. Rapid history matching using a generalized travel-time inversion method. *SPE Journal* June issue: 113-122.

Wu, Z., Reynolds, A. C. and Oliver, D. S. [1999]. Conditioning geostatistical models to two-phase production data. *SPE Journal* **3**(2): 142-155.

Yang, P., Watson, A. T. and Armasu, R. V. [1988]. Automatic history matching with variable-metric methods. *SPE Reservoir Engineering* **3**(3): 995-1001.

Yao, C. Y. and Holditch, S. A. [1996]. Reservoir permeability estimation from time-lapse log data. *SPE Formation Evaluation* June issue: 69-74.

Zeybek, M., Ramakrishnan, T. S., Al-Otaibi, S. S., Salamy, S. P. and Kuchuk, F. J. [2001]. Estimating multiphase flow properties using pressure and flowline water-cut data from dual-packer formation tester interval tests and openhole array resistivity measurements. Paper SPE 71568, *Proceedings of the Annual Technical Conference and Exhibition: Society of Petroleum Engineers*, New Orleans, Lousiana, 30 September–3 October.

Zeybek, M., Ramakrishnan, T. S., Al-Otaibi, S. S., Salamy, S. P. and Kuchuk, F. J. [2004]. Estimating multiphase-flow properties from dual-packer formation tester interval tests and openhole array resistivity measurements. *SPE Reservoir Evaluation and Engineering* February issue: 40-46.

Zhang, J-H., Hu, Q. and Liu, Z-H. [1999]. Estimation of true formation resistivity and water saturation with a time-lapse induction logging method. *The Log Analyst* **40**(2): 138-148.

Zhang, Y-C., Shen, L. C. and Liu, C. [1994]. Inversion of induction logs based on maximum flatness, maximum oil, and minimum oil algorithms. *Geophysics* **59**(9): 1320-1326.

Zhang, F. and Reynolds, A. C. [2002]. Optimization algorithms for automatic history matching of production data. Expanded abstract E48, *Proceedings of the 8th European Conference on the Mathematics of Oil Recovery*, Freiberg, Germany, 3–6 September.

Zhang, F., Reynolds, A. C. and Oliver, D. S. [2003]. Automatic history matching in a Bayesian framework, example applications. Paper SPE 84461, *Proceedings of the Annual Technical Conference and Exhibition: Society of Petroleum Engineers*, Denver, Colorado, 5–8 October.

Vita

Faruk Omer Alpak was born in Ankara, Turkey, on May 31, 1974, and he is the son of Osman Alpak and Mine Emine Alpak. After completing his high school education at Ankara Anadolu Gymnasium, Turkey, he entered the Middle East Technical University (METU), in Ankara, Turkey in the year 1992. He received his degree of Bachelor of Science in Petroleum and Natural Gas Engineering (with honors) in June, 1997. In December 1999, he received the degree of Master of Science in Petroleum Engineering from The University of Texas at Austin. Faruk Omer Alpak has one and one half years of industry experience through science/engineering internships and visiting scientist positions with Pipeline Transportation Company (BOTAS, Ankara, Turkey), Schlumberger Logelco Inc. (Cairo, Egypt), Schlumberger-Doll Research (Ridgefield, CT), and Shell International Exploration and Production (Houston, TX).

Permanent address: I. Konutkent, E6 Blok No. 21,
Ankara, Çayyolu, Turkey 06530

This dissertation was typed by the author.